

# PRINCIPLES OF COMPOSITE MATERIAL MECHANICS

THIRD EDITION

Ronald F. Gibson



CRC Press  
Taylor & Francis Group

# **PRINCIPLES OF COMPOSITE MATERIAL MECHANICS**

**THIRD EDITION**

**MECHANICAL ENGINEERING**  
A Series of Textbooks and Reference Books

*Founding Editor*

**L. L. Faulkner**

*Columbus Division, Battelle Memorial Institute  
and Department of Mechanical Engineering  
The Ohio State University  
Columbus, Ohio*

1. *Spring Designer's Handbook*, Harold Carlson
2. *Computer-Aided Graphics and Design*, Daniel L. Ryan
3. *Lubrication Fundamentals*, J. George Wills
4. *Solar Engineering for Domestic Buildings*, William A. Himmelman
5. *Applied Engineering Mechanics: Statics and Dynamics*, G. Boothroyd and C. Poli
6. *Centrifugal Pump Clinic*, Igor J. Karassik
7. *Computer-Aided Kinetics for Machine Design*, Daniel L. Ryan
8. *Plastics Products Design Handbook, Part A: Materials and Components; Part B: Processes and Design for Processes*, edited by Edward Miller
9. *Turbomachinery: Basic Theory and Applications*, Earl Logan, Jr.
10. *Vibrations of Shells and Plates*, Werner Soedel
11. *Flat and Corrugated Diaphragm Design Handbook*, Mario Di Giovanni
12. *Practical Stress Analysis in Engineering Design*, Alexander Blake
13. *An Introduction to the Design and Behavior of Bolted Joints*, John H. Bickford
14. *Optimal Engineering Design: Principles and Applications*, James N. Siddall
15. *Spring Manufacturing Handbook*, Harold Carlson
16. *Industrial Noise Control: Fundamentals and Applications*, edited by Lewis H. Bell
17. *Gears and Their Vibration: A Basic Approach to Understanding Gear Noise*, J. Derek Smith
18. *Chains for Power Transmission and Material Handling: Design and Applications Handbook*, American Chain Association
19. *Corrosion and Corrosion Protection Handbook*, edited by Philip A. Schweitzer
20. *Gear Drive Systems: Design and Application*, Peter Lynwander
21. *Controlling In-Plant Airborne Contaminants: Systems Design and Calculations*, John D. Constance
22. *CAD/CAM Systems Planning and Implementation*, Charles S. Knox
23. *Probabilistic Engineering Design: Principles and Applications*, James N. Siddall

24. *Traction Drives: Selection and Application*, Frederick W. Heilich III and Eugene E. Shube
25. *Finite Element Methods: An Introduction*, Ronald L. Huston and Chris E. Passerello
26. *Mechanical Fastening of Plastics: An Engineering Handbook*, Brayton Lincoln, Kenneth J. Gomes, and James F. Braden
27. *Lubrication in Practice: Second Edition*, edited by W. S. Robertson
28. *Principles of Automated Drafting*, Daniel L. Ryan
29. *Practical Seal Design*, edited by Leonard J. Martini
30. *Engineering Documentation for CAD/CAM Applications*, Charles S. Knox
31. *Design Dimensioning with Computer Graphics Applications*, Jerome C. Lange
32. *Mechanism Analysis: Simplified Graphical and Analytical Techniques*, Lyndon O. Barton
33. *CAD/CAM Systems: Justification, Implementation, Productivity Measurement*, Edward J. Preston, George W. Crawford, and Mark E. Coticchia
34. *Steam Plant Calculations Manual*, V. Ganapathy
35. *Design Assurance for Engineers and Managers*, John A. Burgess
36. *Heat Transfer Fluids and Systems for Process and Energy Applications*, Jasbir Singh
37. *Potential Flows: Computer Graphic Solutions*, Robert H. Kirchhoff
38. *Computer-Aided Graphics and Design: Second Edition*, Daniel L. Ryan
39. *Electronically Controlled Proportional Valves: Selection and Application*, Michael J. Tonyan, edited by Tobi Goldoftas
40. *Pressure Gauge Handbook*, AMETEK, U.S. Gauge Division, edited by Philip W. Harland
41. *Fabric Filtration for Combustion Sources: Fundamentals and Basic Technology*, R. P. Donovan
42. *Design of Mechanical Joints*, Alexander Blake
43. *CAD/CAM Dictionary*, Edward J. Preston, George W. Crawford, and Mark E. Coticchia
44. *Machinery Adhesives for Locking, Retaining, and Sealing*, Girard S. Haviland
45. *Couplings and Joints: Design, Selection, and Application*, Jon R. Mancuso
46. *Shaft Alignment Handbook*, John Piotrowski
47. *BASIC Programs for Steam Plant Engineers: Boilers, Combustion, Fluid Flow, and Heat Transfer*, V. Ganapathy
48. *Solving Mechanical Design Problems with Computer Graphics*, Jerome C. Lange
49. *Plastics Gearing: Selection and Application*, Clifford E. Adams
50. *Clutches and Brakes: Design and Selection*, William C. Orthwein
51. *Transducers in Mechanical and Electronic Design*, Harry L. Trietley
52. *Metallurgical Applications of Shock-Wave and High-Strain-Rate Phenomena*, edited by Lawrence E. Murr, Karl P. Staudhammer, and Marc A. Meyers
53. *Magnesium Products Design*, Robert S. Busk

54. *How to Integrate CAD/CAM Systems: Management and Technology*, William D. Engelke
55. *Cam Design and Manufacture: Second Edition; with cam design software for the IBM PC and compatibles, disk included*, Preben W. Jensen
56. *Solid-State AC Motor Controls: Selection and Application*, Sylvester Campbell
57. *Fundamentals of Robotics*, David D. Ardayfio
58. *Belt Selection and Application for Engineers*, edited by Wallace D. Erickson
59. *Developing Three-Dimensional CAD Software with the IBM PC*, C. Stan Wei
60. *Organizing Data for CIM Applications*, Charles S. Knox, with contributions by Thomas C. Boos, Ross S. Culverhouse, and Paul F. Muchnicki
61. *Computer-Aided Simulation in Railway Dynamics*, by Rao V. Dukkipati and Joseph R. Amyot
62. *Fiber-Reinforced Composites: Materials, Manufacturing, and Design*, P. K. Mallick
63. *Photoelectric Sensors and Controls: Selection and Application*, Scott M. Juds
64. *Finite Element Analysis with Personal Computers*, Edward R. Champion, Jr. and J. Michael Ensminger
65. *Ultrasonics: Fundamentals, Technology, Applications: Second Edition, Revised and Expanded*, Dale Ensminger
66. *Applied Finite Element Modeling: Practical Problem Solving for Engineers*, Jeffrey M. Steele
67. *Measurement and Instrumentation in Engineering: Principles and Basic Laboratory Experiments*, Francis S. Tse and Ivan E. Morse
68. *Centrifugal Pump Clinic: Second Edition, Revised and Expanded*, Igor J. Karassik
69. *Practical Stress Analysis in Engineering Design: Second Edition, Revised and Expanded*, Alexander Blake
70. *An Introduction to the Design and Behavior of Bolted Joints: Second Edition, Revised and Expanded*, John H. Bickford
71. *High Vacuum Technology: A Practical Guide*, Marsbed H. Hablanian
72. *Pressure Sensors: Selection and Application*, Duane Tandeske
73. *Zinc Handbook: Properties, Processing, and Use in Design*, Frank Porter
74. *Thermal Fatigue of Metals*, Andrzej Weronski and Tadeusz Hejwowski
75. *Classical and Modern Mechanisms for Engineers and Inventors*, Preben W. Jensen
76. *Handbook of Electronic Package Design*, edited by Michael Pecht
77. *Shock-Wave and High-Strain-Rate Phenomena in Materials*, edited by Marc A. Meyers, Lawrence E. Murr, and Karl P. Staudhammer
78. *Industrial Refrigeration: Principles, Design and Applications*, P. C. Koelet
79. *Applied Combustion*, Eugene L. Keating
80. *Engine Oils and Automotive Lubrication*, edited by Wilfried J. Bartz

81. *Mechanism Analysis: Simplified and Graphical Techniques, Second Edition, Revised and Expanded*, Lyndon O. Barton
82. *Fundamental Fluid Mechanics for the Practicing Engineer*, James W. Murdock
83. *Fiber-Reinforced Composites: Materials, Manufacturing, and Design, Second Edition, Revised and Expanded*, P. K. Mallick
84. *Numerical Methods for Engineering Applications*, Edward R. Champion, Jr.
85. *Turbomachinery: Basic Theory and Applications, Second Edition, Revised and Expanded*, Earl Logan, Jr.
86. *Vibrations of Shells and Plates: Second Edition, Revised and Expanded*, Werner Soedel
87. *Steam Plant Calculations Manual: Second Edition, Revised and Expanded*, V. Ganapathy
88. *Industrial Noise Control: Fundamentals and Applications, Second Edition, Revised and Expanded*, Lewis H. Bell and Douglas H. Bell
89. *Finite Elements: Their Design and Performance*, Richard H. MacNeal
90. *Mechanical Properties of Polymers and Composites: Second Edition, Revised and Expanded*, Lawrence E. Nielsen and Robert F. Landel
91. *Mechanical Wear Prediction and Prevention*, Raymond G. Bayer
92. *Mechanical Power Transmission Components*, edited by David W. South and Jon R. Mancuso
93. *Handbook of Turbomachinery*, edited by Earl Logan, Jr.
94. *Engineering Documentation Control Practices and Procedures*, Ray E. Monahan
95. *Refractory Linings Thermomechanical Design and Applications*, Charles A. Schacht
96. *Geometric Dimensioning and Tolerancing: Applications and Techniques for Use in Design, Manufacturing, and Inspection*, James D. Meadows
97. *An Introduction to the Design and Behavior of Bolted Joints: Third Edition, Revised and Expanded*, John H. Bickford
98. *Shaft Alignment Handbook: Second Edition, Revised and Expanded*, John Piotrowski
99. *Computer-Aided Design of Polymer-Matrix Composite Structures*, edited by Suong Van Hoa
100. *Friction Science and Technology*, Peter J. Blau
101. *Introduction to Plastics and Composites: Mechanical Properties and Engineering Applications*, Edward Miller
102. *Practical Fracture Mechanics in Design*, Alexander Blake
103. *Pump Characteristics and Applications*, Michael W. Volk
104. *Optical Principles and Technology for Engineers*, James E. Stewart
105. *Optimizing the Shape of Mechanical Elements and Structures*, A. A. Seireg and Jorge Rodriguez
106. *Kinematics and Dynamics of Machinery*, Vladimír Stejskal and Michael Valásek
107. *Shaft Seals for Dynamic Applications*, Les Horve
108. *Reliability-Based Mechanical Design*, edited by Thomas A. Cruse
109. *Mechanical Fastening, Joining, and Assembly*, James A. Speck

110. *Turbomachinery Fluid Dynamics and Heat Transfer*, edited by Chunill Hah
111. *High-Vacuum Technology: A Practical Guide, Second Edition, Revised and Expanded*, Marsbed H. Hablanian
112. *Geometric Dimensioning and Tolerancing: Workbook and Answerbook*, James D. Meadows
113. *Handbook of Materials Selection for Engineering Applications*, edited by G. T. Murray
114. *Handbook of Thermoplastic Piping System Design*, Thomas Sixsmith and Reinhard Hanselka
115. *Practical Guide to Finite Elements: A Solid Mechanics Approach*, Steven M. Lepi
116. *Applied Computational Fluid Dynamics*, edited by Vijay K. Garg
117. *Fluid Sealing Technology*, Heinz K. Muller and Bernard S. Nau
118. *Friction and Lubrication in Mechanical Design*, A. A. Seireg
119. *Influence Functions and Matrices*, Yuri A. Melnikov
120. *Mechanical Analysis of Electronic Packaging Systems*, Stephen A. McKeown
121. *Couplings and Joints: Design, Selection, and Application, Second Edition, Revised and Expanded*, Jon R. Mancuso
122. *Thermodynamics: Processes and Applications*, Earl Logan, Jr.
123. *Gear Noise and Vibration*, J. Derek Smith
124. *Practical Fluid Mechanics for Engineering Applications*, John J. Bloomer
125. *Handbook of Hydraulic Fluid Technology*, edited by George E. Totten
126. *Heat Exchanger Design Handbook*, T. Kuppan
127. *Designing for Product Sound Quality*, Richard H. Lyon
128. *Probability Applications in Mechanical Design*, Franklin E. Fisher and Joy R. Fisher
129. *Nickel Alloys*, edited by Ulrich Heubner
130. *Rotating Machinery Vibration: Problem Analysis and Troubleshooting*, Maurice L. Adams, Jr.
131. *Formulas for Dynamic Analysis*, Ronald L. Huston and C. Q. Liu
132. *Handbook of Machinery Dynamics*, Lynn L. Faulkner and Earl Logan, Jr.
133. *Rapid Prototyping Technology: Selection and Application*, Kenneth G. Cooper
134. *Reciprocating Machinery Dynamics: Design and Analysis*, Abdulla S. Rangwala
135. *Maintenance Excellence: Optimizing Equipment Life-Cycle Decisions*, edited by John D. Campbell and Andrew K. S. Jardine
136. *Practical Guide to Industrial Boiler Systems*, Ralph L. Vandagriff
137. *Lubrication Fundamentals: Second Edition, Revised and Expanded*, D. M. Pirro and A. A. Wessol
138. *Mechanical Life Cycle Handbook: Good Environmental Design and Manufacturing*, edited by Mahendra S. Hundal
139. *Micromachining of Engineering Materials*, edited by Joseph McGeough
140. *Control Strategies for Dynamic Systems: Design and Implementation*, John H. Lumkes, Jr.
141. *Practical Guide to Pressure Vessel Manufacturing*, Sunil Pullarcot

142. *Nondestructive Evaluation: Theory, Techniques, and Applications*, edited by Peter J. Shull
143. *Diesel Engine Engineering: Thermodynamics, Dynamics, Design, and Control*, Andrei Makartchouk
144. *Handbook of Machine Tool Analysis*, Ioan D. Marinescu, Constantin Ispas, and Dan Boboc
145. *Implementing Concurrent Engineering in Small Companies*, Susan Carlson Skalak
146. *Practical Guide to the Packaging of Electronics: Thermal and Mechanical Design and Analysis*, Ali Jamnia
147. *Bearing Design in Machinery: Engineering Tribology and Lubrication*, Avraham Harnoy
148. *Mechanical Reliability Improvement: Probability and Statistics for Experimental Testing*, R. E. Little
149. *Industrial Boilers and Heat Recovery Steam Generators: Design, Applications, and Calculations*, V. Ganapathy
150. *The CAD Guidebook: A Basic Manual for Understanding and Improving Computer-Aided Design*, Stephen J. Schoonmaker
151. *Industrial Noise Control and Acoustics*, Randall F. Barron
152. *Mechanical Properties of Engineered Materials*, Wolé Soboyejo
153. *Reliability Verification, Testing, and Analysis in Engineering Design*, Gary S. Wasserman
154. *Fundamental Mechanics of Fluids: Third Edition*, I. G. Currie
155. *Intermediate Heat Transfer*, Kau-Fui Vincent Wong
156. *HVAC Water Chillers and Cooling Towers: Fundamentals, Application, and Operation*, Herbert W. Stanford III
157. *Gear Noise and Vibration: Second Edition, Revised and Expanded*, J. Derek Smith
158. *Handbook of Turbomachinery: Second Edition, Revised and Expanded*, edited by Earl Logan, Jr. and Ramendra Roy
159. *Piping and Pipeline Engineering: Design, Construction, Maintenance, Integrity, and Repair*, George A. Antaki
160. *Turbomachinery: Design and Theory*, Rama S. R. Gorla and Ajaz Ahmed Khan
161. *Target Costing: Market-Driven Product Design*, M. Bradford Clifton, Henry M. B. Bird, Robert E. Albano, and Wesley P. Townsend
162. *Fluidized Bed Combustion*, Simeon N. Oka
163. *Theory of Dimensioning: An Introduction to Parameterizing Geometric Models*, Vijay Srinivasan
164. *Handbook of Mechanical Alloy Design*, edited by George E. Totten, Lin Xie, and Kiyoshi Funatani
165. *Structural Analysis of Polymeric Composite Materials*, Mark E. Tuttle
166. *Modeling and Simulation for Material Selection and Mechanical Design*, edited by George E. Totten, Lin Xie, and Kiyoshi Funatani
167. *Handbook of Pneumatic Conveying Engineering*, David Mills, Mark G. Jones, and Vijay K. Agarwal
168. *Clutches and Brakes: Design and Selection, Second Edition*, William C. Orthwein
169. *Fundamentals of Fluid Film Lubrication: Second Edition*, Bernard J. Hamrock, Steven R. Schmid, and Bo O. Jacobson

170. *Handbook of Lead-Free Solder Technology for Microelectronic Assemblies*, edited by Karl J. Puttlitz and Kathleen A. Stalter
171. *Vehicle Stability*, Dean Karnopp
172. *Mechanical Wear Fundamentals and Testing: Second Edition, Revised and Expanded*, Raymond G. Bayer
173. *Liquid Pipeline Hydraulics*, E. Shashi Menon
174. *Solid Fuels Combustion and Gasification*, Marcio L. de Souza-Santos
175. *Mechanical Tolerance Stackup and Analysis*, Bryan R. Fischer
176. *Engineering Design for Wear*, Raymond G. Bayer
177. *Vibrations of Shells and Plates: Third Edition, Revised and Expanded*, Werner Soedel
178. *Refractories Handbook*, edited by Charles A. Schacht
179. *Practical Engineering Failure Analysis*, Hani M. Tawancy, Anwar Ul-Hamid, and Nureddin M. Abbas
180. *Mechanical Alloying and Milling*, C. Suryanarayana
181. *Mechanical Vibration: Analysis, Uncertainties, and Control, Second Edition, Revised and Expanded*, Haym Benaroya
182. *Design of Automatic Machinery*, Stephen J. Derby
183. *Practical Fracture Mechanics in Design: Second Edition, Revised and Expanded*, Arun Shukla
184. *Practical Guide to Designed Experiments*, Paul D. Funkenbusch
185. *Gigacycle Fatigue in Mechanical Practice*, Claude Bathias and Paul C. Paris
186. *Selection of Engineering Materials and Adhesives*, Lawrence W. Fisher
187. *Boundary Methods: Elements, Contours, and Nodes*, Subrata Mukherjee and Yu Xie Mukherjee
188. *Rotordynamics*, Agnieszka (Agnes) Muszýska
189. *Pump Characteristics and Applications: Second Edition*, Michael W. Volk
190. *Reliability Engineering: Probability Models and Maintenance Methods*, Joel A. Nachlas
191. *Industrial Heating: Principles, Techniques, Materials, Applications, and Design*, Yeshvant V. Deshmukh
192. *Micro Electro Mechanical System Design*, James J. Allen
193. *Probability Models in Engineering and Science*, Haym Benaroya and Seon Han
194. *Damage Mechanics*, George Z. Voyatzis and Peter I. Kattan
195. *Standard Handbook of Chains: Chains for Power Transmission and Material Handling, Second Edition*, American Chain Association and John L. Wright, Technical Consultant
196. *Standards for Engineering Design and Manufacturing*, Wasim Ahmed Khan and Abdul Raouf S.I.
197. *Maintenance, Replacement, and Reliability: Theory and Applications*, Andrew K. S. Jardine and Albert H. C. Tsang
198. *Finite Element Method: Applications in Solids, Structures, and Heat Transfer*, Michael R. Gosz
199. *Microengineering, MEMS, and Interfacing: A Practical Guide*, Danny Banks

- 200. *Fundamentals of Natural Gas Processing*, Arthur J. Kidnay and William Parrish
- 201. *Optimal Control of Induction Heating Processes*, Edgar Rapoport and Yulia Pleshivtseva
- 202. *Practical Plant Failure Analysis: A Guide to Understanding Machinery Deterioration and Improving Equipment Reliability*, Neville W. Sachs, P.E.
- 203. *Shaft Alignment Handbook, Third Edition*, John Piotrowski
- 204. *Advanced Vibration Analysis*, S. Graham Kelly
- 205. *Principles of Composite Materials Mechanics, Second Edition*, Ronald F. Gibson
- 206. *Applied Combustion, Second Edition*, Eugene L. Keating
- 207. *Introduction to the Design and Behavior of Bolted Joints, Fourth Edition: Non-Gasketed Joints*, John H. Bickford
- 208. *Analytical and Approximate Methods in Transport Phenomena*, Marcio L. de Souza-Santos
- 209. *Design and Optimization of Thermal Systems, Second Edition*, Yogesh Jaluria
- 210. *Friction Science and Technology: From Concepts to Applications, Second Edition*, Peter J. Blau
- 211. *Practical Guide to the Packaging of Electronics, Second Edition: Thermal and Mechanical Design and Analysis*, Ali Jamnia
- 212. *Practical Stress Analysis in Engineering Design, Third Edition*, Ronald L. Huston and Harold Josephs
- 213. *Principles of Biomechanics*, Ronald L. Huston
- 214. *Mechanical Vibration Analysis, Uncertainties, and Control, Third Edition*, Haym Benaroya and Mark L. Nagurka
- 215. *Solid Fuels Combustion and Gasification: Modeling, Simulation, and Equipment Operations, Second Edition, Third Edition*, Marcio L. de Souza-Santos
- 216. *Asset Management Excellence*, edited by John D. Campbell, Andrew K. S. Jardine, Joel McGlynn
- 217. *Mechanical Tolerance Stackup and Analysis, Second Edition*, Bryan R. Fischer
- 218. *Principles of Composite Materials Mechanics, Third Edition*, Ronald F. Gibson

This page intentionally left blank

# PRINCIPLES OF COMPOSITE MATERIAL MECHANICS

THIRD EDITION

Ronald F. Gibson



CRC Press  
Taylor & Francis Group  
Boca Raton London New York

---

CRC Press is an imprint of the  
Taylor & Francis Group, an **informa** business

CRC Press  
Taylor & Francis Group  
6000 Broken Sound Parkway NW, Suite 300  
Boca Raton, FL 33487-2742

© 2012 by Taylor & Francis Group, LLC  
CRC Press is an imprint of Taylor & Francis Group, an Informa business

No claim to original U.S. Government works  
Version Date: 20110810

International Standard Book Number-13: 978-1-4398-5006-0 (eBook - PDF)

This book contains information obtained from authentic and highly regarded sources. Reasonable efforts have been made to publish reliable data and information, but the author and publisher cannot assume responsibility for the validity of all materials or the consequences of their use. The authors and publishers have attempted to trace the copyright holders of all material reproduced in this publication and apologize to copyright holders if permission to publish in this form has not been obtained. If any copyright material has not been acknowledged please write and let us know so we may rectify in any future reprint.

Except as permitted under U.S. Copyright Law, no part of this book may be reprinted, reproduced, transmitted, or utilized in any form by any electronic, mechanical, or other means, now known or hereafter invented, including photocopying, microfilming, and recording, or in any information storage or retrieval system, without written permission from the publishers.

For permission to photocopy or use material electronically from this work, please access [www.copyright.com](http://www.copyright.com) (<http://www.copyright.com/>) or contact the Copyright Clearance Center, Inc. (CCC), 222 Rosewood Drive, Danvers, MA 01923, 978-750-8400. CCC is a not-for-profit organization that provides licenses and registration for a variety of users. For organizations that have been granted a photocopy license by the CCC, a separate system of payment has been arranged.

**Trademark Notice:** Product or corporate names may be trademarks or registered trademarks, and are used only for identification and explanation without intent to infringe.

Visit the Taylor & Francis Web site at  
<http://www.taylorandfrancis.com>

and the CRC Press Web site at  
<http://www.crcpress.com>

*To my wonderful family, Maryanne, Tracy, Tola, Sophie, and  
Aidan, and the memory of my parents,*

*Jim and Lora Gibson*

This page intentionally left blank

---

# *Contents*

---

Preface.....	xxi
Preface to the Second Edition.....	xxiii
Preface to the First Edition.....	xxv
Author.....	xxix
<b>1 Introduction .....</b>	<b>1</b>
1.1 Basic Concepts .....	1
1.2 Constituent Materials for Composites .....	6
1.2.1 Reinforcement Materials, Including Nanoreinforcements.....	10
1.2.2 Matrix and Filler Materials.....	14
1.3 Structural Applications of Composites .....	15
1.4 Multifunctional Applications of Composites.....	25
1.5 Fabrication Processes.....	28
1.6 Elements of Mechanical Behavior of Composites .....	38
1.7 Review of Basic Mechanics of Materials Equations .....	40
Problems.....	47
References .....	51
<b>2 Lamina Stress–Strain Relationships .....</b>	<b>53</b>
2.1 Introduction .....	53
2.2 Effective Moduli in Stress–Strain Relationships.....	54
2.3 Symmetry in Stress–Strain Relationships .....	59
2.4 Orthotropic and Isotropic Engineering Constants .....	64
2.5 Specially Orthotropic Lamina.....	67
2.6 Generally Orthotropic Lamina .....	71
Problems.....	84
References .....	87
<b>3 Effective Moduli of a Continuous Fiber-Reinforced Lamina .....</b>	<b>89</b>
3.1 Introduction .....	89
3.2 Elementary Mechanics of Materials Models.....	97
3.2.1 Longitudinal Modulus .....	99
3.2.2 Transverse Modulus .....	103
3.2.3 Shear Modulus and Poisson’s Ratio .....	105
3.3 Improved Mechanics of Materials Models.....	108
3.4 Elasticity Models .....	113
3.4.1 Finite Difference Models.....	114
3.4.2 Finite Element Models.....	116
3.4.3 Closed-Form and Variational Models.....	121

3.5	Semiempirical Models.....	123
Problems.....		126
References .....		131
<b>4</b>	<b>Strength of a Continuous Fiber-Reinforced Lamina .....</b>	<b>135</b>
4.1	Introduction .....	135
4.2	Multiaxial Strength Criteria .....	138
4.2.1	Maximum Stress Criterion .....	140
4.2.2	Maximum Strain Criterion.....	145
4.2.3	Quadratic Interaction Criteria.....	147
4.3	Micromechanics Models for Lamina Strength .....	155
4.3.1	Longitudinal Strength.....	156
4.3.2	Transverse Strength.....	164
4.3.3	In-Plane Shear Strength .....	169
4.3.4	Multiaxial Strength.....	169
Problems.....		173
References .....		175
<b>5</b>	<b>Analysis of Lamina Hygrothermal Behavior .....</b>	<b>181</b>
5.1	Introduction .....	181
5.2	Hygrothermal Degradation of Properties .....	183
5.3	Lamina Stress–Strain Relationships Including Hygrothermal Effects .....	195
5.4	Micromechanics Models for Hygrothermal Properties .....	202
Problems.....		211
References .....		215
<b>6</b>	<b>Analysis of a Discontinuously Reinforced Lamina .....</b>	<b>219</b>
6.1	Introduction .....	219
6.2	Aligned Discontinuous Fibers .....	220
6.2.1	Stress and Strength Analysis .....	221
6.2.2	Modulus Analysis.....	229
6.3	Off Axis–Aligned Discontinuous Fibers .....	239
6.3.1	Stress and Strength Analysis .....	239
6.3.2	Modulus Analysis.....	242
6.4	Randomly Oriented Discontinuous Fibers .....	245
6.4.1	Stress and Strength Analysis .....	245
6.4.2	Modulus Analysis.....	247
6.5	Nanofibers and Nanotubes.....	258
6.5.1	Stress and Strength Analysis .....	259
6.5.2	Modulus Analysis.....	260
6.6	Particulates.....	265
6.6.1	Stress and Strength Analysis .....	266
6.6.2	Modulus Analysis.....	267
6.7	Hybrid Multiscale Reinforcements.....	271

Problems.....	275
References .....	278
<b>7 Analysis of Laminates.....</b>	<b>283</b>
7.1 Introduction .....	283
7.2 Theory of Laminated Beams .....	284
7.2.1 Flexural Stresses and Deflections.....	284
7.2.2 Shear Stresses and Deflections .....	290
7.3 Theory of Laminated Plates with Coupling.....	296
7.4 Stiffness Characteristics of Selected Laminate Configurations.....	304
7.4.1 Specially Orthotropic Laminates.....	305
7.4.2 Generally Orthotropic Laminates .....	305
7.4.3 Symmetric Laminates .....	306
7.4.4 Antisymmetric Laminates.....	308
7.4.5 Quasi-Isotropic Laminates .....	310
7.5 Derivation and Use of Laminate Compliances.....	314
7.5.1 Inversion of Laminate Force–Deformation Equations.....	315
7.5.2 Determination of Lamina Stresses and Strains.....	316
7.5.3 Determination of Laminate Engineering Constants .....	320
7.5.4 Comparison of Measured and Predicted Compliances .....	324
7.6 Hygrothermal Effects in Laminates.....	327
7.6.1 Hygrothermal Degradation of Laminates.....	327
7.6.2 Hygrothermal Stresses in Laminates.....	328
7.6.3 Laminate Hygrothermal Expansion Coefficients .....	332
7.7 Interlaminar Stresses.....	333
7.8 Laminate Strength Analysis.....	339
7.8.1 First Ply Failure and Subsequent Ply Failures Due to In-Plane Stresses .....	340
7.8.2 Delamination Due to Interlaminar Stresses .....	352
7.9 Deflection and Buckling of Laminates .....	357
7.9.1 Analysis of Small Transverse Deflections .....	358
7.9.2 Buckling Analysis.....	364
7.10 Selection of Laminate Designs.....	367
7.11 Application of Laminate Analysis to Composite Structures .....	375
7.11.1 Composite Sandwich Structures .....	376
7.11.2 Composite Grid Structures.....	382
Problems.....	387
References .....	395
<b>8 Analysis of Viscoelastic and Dynamic Behavior.....</b>	<b>399</b>
8.1 Introduction .....	399

8.2	Linear Viscoelastic Behavior of Composites .....	402
8.2.1	Boltzmann Superposition Integrals for Creep and Relaxation.....	405
8.2.2	Differential Equations and Spring–Dashpot Models .....	411
8.2.3	Quasielastic Analysis .....	421
8.2.4	Sinusoidal Oscillations and Complex Modulus Notation.....	424
8.2.5	Elastic–Viscoelastic Correspondence Principle .....	430
8.2.6	Temperature and Aging Effects.....	436
8.3	Dynamic Behavior of Composites .....	443
8.3.1	Longitudinal Wave Propagation and Vibrations in Specially Orthotropic Composite Bars .....	444
8.3.2	Flexural Vibration of Composite Beams.....	450
8.3.3	Transverse Vibration of Laminated Plates .....	454
8.3.4	Analysis of Damping in Composites .....	464
8.4	Nanoenhancement of Viscoelastic and Dynamic Properties .....	476
	Problems.....	479
	References .....	487
<b>9</b>	<b>Analysis of Fracture .....</b>	<b>493</b>
9.1	Introduction .....	493
9.2	Fracture Mechanics Analyses of Through-Thickness Cracks .....	493
9.2.1	Stress Intensity Factor Approach.....	496
9.2.2	Strain Energy Release Rate Approach .....	502
9.2.3	Virtual Crack Closure Technique .....	506
9.3	Stress Fracture Criteria for Through-Thickness Notches.....	508
9.4	Interlaminar Fracture .....	515
9.5	Nanoenhancement of Fracture Toughness .....	527
	Problems.....	530
	References .....	534
<b>10</b>	<b>Mechanical Testing of Composites and Their Constituents .....</b>	<b>541</b>
10.1	Introduction.....	541
10.2	Measurement of Constituent Material Properties.....	542
10.2.1	Fiber Tests .....	542
10.2.2	Neat Resin Matrix Tests .....	545
10.2.3	Constituent Volume Fraction Measurement .....	549
10.3	Measurement of Basic Composite Properties .....	549
10.3.1	Tensile Tests .....	550
10.3.2	Compressive Tests.....	555
10.3.3	Shear Tests.....	561
10.3.4	Flexure Tests .....	570

10.3.5	Interlaminar Fracture Tests .....	571
10.3.6	Fiber/Matrix Interface Tests .....	574
10.3.7	Open Hole and Filled Hole Tests .....	576
10.3.8	Bearing Tests .....	577
10.3.9	Pull-Through Tests .....	579
10.4	Measurement of Viscoelastic and Dynamic Properties .....	581
10.4.1	Creep Tests .....	581
10.4.2	Vibration Tests .....	585
10.5	Measurement of Hygrothermal Properties .....	593
10.5.1	Glass Transition Temperature Tests .....	593
10.5.2	Thermal Expansion Tests .....	594
10.5.3	Moisture Absorption Tests .....	595
Problems .....	596	
References .....	600	
<b>Appendix A: Matrix Concepts and Operations .....</b>	<b>609</b>	
<b>Appendix B: Stress Equilibrium Equations .....</b>	<b>619</b>	
<b>Appendix C: Strain–Displacement Equations .....</b>	<b>623</b>	
<b>Index .....</b>	<b>627</b>	

This page intentionally left blank

---

## *Preface*

---

The goals for the third edition are to continue to present a unique blended coverage of classical and state-of-the-art mechanics of composites technologies, while striving to incorporate the most worked-out example problems and homework problems of any available textbook on mechanics of composite materials. A high priority has been placed on writing a textbook that is easily understood by students. Pedagogical improvements include a total of 81 worked-out example problems (25 of which are new for the third edition); 177 homework problems (25 of which are new); 388 figures (46 of which are new); a new appendix on matrix concepts and operations; new coverage of particle composites, nanocomposites, nanoenhancement of conventional fiber composites, hybrid multiscale composites; and additional coverage of finite element modeling and test methods. Although the book is written first as a textbook covering classical methods, frequent references to current state-of-the-art composites technology and research findings are included. Extensive references are provided, including many current journal articles along with classic and historical publications.

I continue to be indebted to my colleagues, graduate students, and sponsors for their encouragement and support over the years. Most recently, my professional affiliations with Wayne State University (WSU) and the University of Nevada, Reno (UNR) have provided the necessary positive environments for teaching and research that made the development of this new edition possible. I have been particularly motivated by the interactions with students in my composites classes at WSU and UNR. As with the earlier editions of this book, my wife and best friend, Maryanne, continues to be my most enthusiastic supporter, and there is no way that I could have completed this project without her.

**Ronald F. Gibson**

This page intentionally left blank

---

## *Preface to the Second Edition*

---

There have been many developments in mechanics of composite materials since the first edition of this book was published. Accordingly, the second edition has new sections on recent applications of composite mechanics to nanocomposites, composite grid structures, and composite sandwich structures. In order to strengthen the emphasis on the basic principles of mechanics, I have added a review of the basic mechanics of materials equations in the Introduction, and appendices covering the derivations of stress equilibrium equations and strain–displacement relations from elasticity theory. Coverage of micromechanics in Chapter 3 has been revised to include more detailed discussions of elasticity and finite element models. Chapter 4 on strength analysis has been updated to include results from the World Wide Failure Exercise. Chapter 8 has been improved by adding a phenomenological approach to understanding linear viscoelastic behavior of composites. Chapter 9 on fracture has been updated to include coverage of the finite element implementation of the virtual crack closure technique. Chapter 10 on testing of composites and their constituents has been extensively updated to include coverage of both new and revised ASTM standard test methods. Finally, more example problems and homework problems have been added to most chapters, and new references have been cited throughout.

As with the first edition, I am indebted to many colleagues, graduate students, and sponsors. I am grateful to Wayne State University for providing a nurturing environment for my teaching and research, and for granting me sabbatical leave, which were essential to the completion of this project. My graduate students have been particularly helpful in identifying the inevitable errors in the first edition, and their thesis research findings have enabled me to add important new dimensions in the second edition. And as with the first edition, my wife and best friend, Maryanne, has continued to be my strongest supporter, and I will be forever grateful for her love, encouragement, patience, and understanding.

**Ronald F. Gibson**

This page intentionally left blank

---

## Preface to the First Edition

---

Composite materials is truly an interdisciplinary subject, and the number of students taking courses in this area is steadily increasing. Books on the subject tend to emphasize either the mechanics or the materials science aspects of composites. *Principles of Composite Material Mechanics* is mechanics oriented. Composite materials technology is new enough for many working engineers who have had no training in this area, and so a textbook in composite material mechanics should be useful not only for the education of new engineers, but also for the continuing education of practicing engineers and for reference. The high level of interest in composite materials, the interdisciplinary nature of the subject, the need to reeducate practicing engineers, and the need for a new composite mechanics textbook at the introductory level all led to my decision to write this book.

Chapters 1 through 7 form the basis of a one-semester senior/graduate-level course in mechanical engineering, which I have taught for the last 15 years. Chapters 8 through 10, along with selected papers from technical journals and student research projects/presentations, form the basis of a second one-semester course, which is taken only by graduate students, and which I have taught for the last 4 years. The book could also be the basis for a two-quarter sequence by omitting some topics. Prerequisites for the course are knowledge of mechanics of materials, introduction to materials engineering, and ordinary differential equations, and previous exposure to linear algebra is highly desirable. For some of the graduate-level material, earlier courses in advanced mechanics of materials, elasticity, and partial differential equations are recommended, but not required.

Some of the basic elements of composite mechanics covered in this book have not changed since the first books on the subject were published in the 1960s and 1970s, and, where possible, I have tried to use the accepted terminology and nomenclature. For example, the coverage of stress-strain relationships and transformation of properties for anisotropic materials in Chapter 2 and the classical lamination theory in Chapter 7 is consistent with that of previous textbooks such as the *Primer on Composite Materials* by Ashton, Halpin, and Petit, and *Mechanics of Composite Materials* by Jones. However, rather than beginning the study of laminates by jumping directly into classical lamination theory, I have concluded that a better pedagogical approach is to introduce first basic laminate concepts by using the simpler theory of laminated beams in pure flexure. Also, I believe that the concept of an effective modulus of an equivalent homogeneous material, which had previously been covered only in advanced books such as *Mechanics of Composite Materials* by Christensen, is essential for the proper development of heterogeneous composite micromechanics. Thus, effective modulus

concepts are emphasized from their introduction in Chapter 2 to their use in the analysis of viscoelastic and dynamic behavior in Chapter 8.

Although many basic concepts have been presented in earlier textbooks, numerous new developments in composite mechanics over the last two decades have made it increasingly necessary to supplement these books with my own notes. Thus, I have added coverage of such important topics as hygrothermal effects in Chapter 5, discontinuous fiber composites in Chapter 6, viscoelastic behavior and dynamic behavior in Chapter 8, fracture in Chapter 9, and mechanical testing in Chapter 10. The coverage of experimental mechanics of composites has been expanded to include summaries of the most important ASTM standard test methods, many of which did not exist when the early mechanics of composites books were published. A variety of example problems and homework problems, a number of them related to practical composite structures, are also included.

The contents of this book represent the cumulative effects of more than 25 years of interactions with colleagues and students, and I would be remiss if I did not mention at least some of them. My fascination with composites began in 1965 with my first engineering position in what is now part of Oak Ridge National Laboratory in Tennessee, where I was involved in the design and development of high-speed rotating equipment. At that time I realized that the advantages of using composites in rotating equipment are numerous, as is the case in many other applications. My experiences working with Dean Waters and other colleagues in the mechanical development group in Oak Ridge have had a strong influence on my later career decision to emphasize composites research and education. My doctoral research on vibration damping characteristics of composites with Robert Plunkett at the University of Minnesota further cemented my desire to continue working in the composites area and ultimately led to my career in university teaching and research.

After beginning my academic career at Iowa State University in 1975, I began a long and productive association with C.T. Sun, and later had the pleasure of spending a one-year leave working with C.T. and his colleagues Robert Sierakowski and Shive Chaturvedi at the University of Florida. I owe much of my understanding of composite mechanics to interactions with them. The notes leading to this book were developed by teaching composite mechanics courses at Iowa State University, the University of Idaho, the University of Florida, Michigan State University, and Wayne State University, and I am indebted to the students who took my classes and helped me to "debug" these notes over the years. Most recently, my students at Wayne State University have been particularly effective at finding the inevitable errors in my notes. Interaction with my graduate students over the years has contributed immeasurably to my understanding of composite mechanics, and the work of several of those students has been referred to in this book. I am particularly indebted to Stalin Suarez, Lyle Deobald, Raju Mantena, and Jimmy Hwang, all former graduate students at the University of Idaho.

Serious work on this book actually began during a sabbatical leave at Michigan State University in 1987, and I am indebted to Larry Drzal and his colleagues for our many stimulating discussions during that year. Particularly important was the interaction with Cornelius Horgan, with whom I team-taught a course on advanced mechanics of composites. Most recently, my collaboration with John Sullivan and his colleagues of the Ford Scientific Research Laboratory has proved to be very rewarding, and I am indebted to John for his careful review of the manuscript and helpful comments. I am grateful to Carl Johnson, also of the Ford Scientific Research Laboratory, for his encouragement and support and for providing several of the figures in Chapter 1. The strong support of Wayne State University, which made it possible to establish the Advanced Composites Research Laboratory there in 1989, is gratefully acknowledged. The support and encouragement of my department chairman, Ken Kline, has been particularly important. Generous support for my composites research from numerous funding agencies over the years has also helped to make this book possible. Grants from the Air Force Office of Scientific Research, the National Science Foundation, the Army Research Office, the Boeing Company, and the Ford Motor Company have been particularly important.

McGraw-Hill and I would like to thank the following reviewers for their many helpful comments and suggestions: Charles W. Bert, University of Oklahoma; Olivier A. Bauchau, Rensselaer Polytechnic Institute; Shive Chaturvedi, Ohio State University; Vincent Choo, New Mexico State University; John M. Kennedy, Clemson University; Vikram K. Kinra, Texas A & M University; C.T. Sun, University of Florida; and Steven W. Yurgartis, Clarkson University.

Finally, my wife and best friend, Maryanne, has been my strongest supporter as I labored on this project, and there is no way that I could have done it without her love, encouragement, patience, and understanding.

**Ronald F. Gibson**

This page intentionally left blank

---

## **Author**

---

**Dr. Ronald F. Gibson** is currently a distinguished research professor of mechanical engineering at the University of Nevada, Reno. He has a PhD in mechanics from the University of Minnesota, an MS in mechanical engineering from the University of Tennessee, and a BS in mechanical engineering from the University of Florida. His industrial/government experience includes a position as development engineer for Union Carbide Corporation, Nuclear Division and a summer faculty fellowship at the NASA Langley Research Center. He has held full-time faculty positions at Iowa State University, The University of Idaho, and Wayne State University, as well as visiting faculty positions at Stanford University, the University of Florida, and Michigan State University. He is an elected Fellow of the American Society of Mechanical Engineers and the American Society for Composites, and a member of the American Society for Engineering Education, the American Institute for Aeronautics and Astronautics, the Society for Experimental Mechanics, and the Society for Advancement of Material and Process Engineering. He served as the president of the American Society for Composites in 2004–2005, and as vice president during 2002–2003. Dr. Gibson's awards include the Hetenyi Award for Best Research Paper of the Year from the Society for Experimental Mechanics, the College of Engineering Outstanding Faculty Award from the University of Idaho, the Distinguished Faculty Fellowship Award, the DeVlieg Professorship, and the Outstanding Graduate Faculty Mentor Award from Wayne State University. The results of his research have been published in numerous scholarly journal articles and presented at a variety of national and international meetings. His current research interests include mechanical characterization of composite materials and structures, noise and vibration control with composites, design and manufacturing of composite structures, characterization of energy-absorbing materials, multifunctional composites, and nanocomposites.

This page intentionally left blank

# 1

---

## *Introduction*

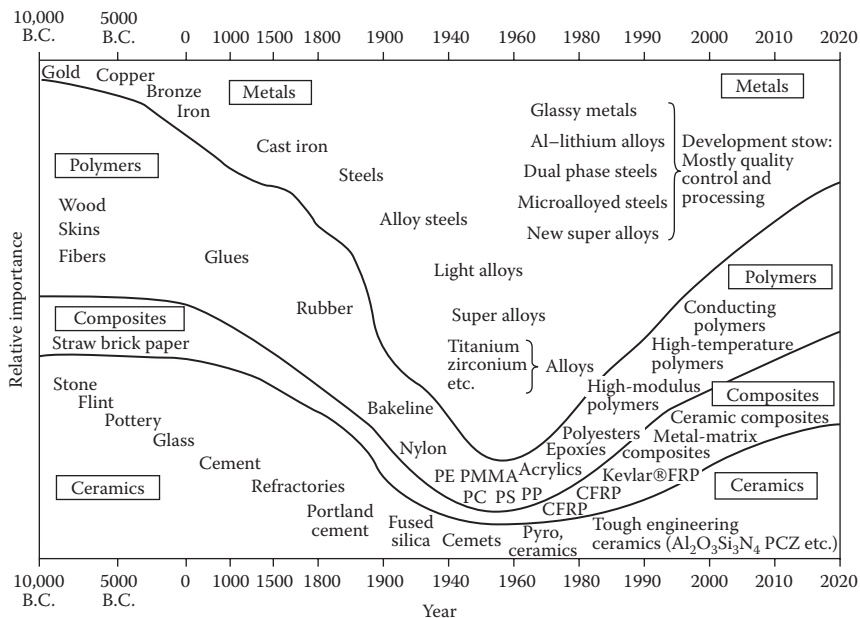
---

### **1.1 Basic Concepts**

Structural materials can be divided into four basic categories as metals, polymers, ceramics, and composites. Composites, which consist of two or more separate materials combined in a structural unit, are typically made from various combinations of the other three materials. In the early days of modern man-made composite materials, the constituents were typically macroscopic. As composites technology advanced over the last few decades, the constituent materials, particularly the reinforcement materials, steadily decreased in size. Most recently, there has been considerable interest in “nanocomposites” having nanometer-sized reinforcements such as carbon nanoparticles, nanofibers, and nanotubes, because of the extraordinary properties of these materials.

The relative importance of the four basic materials in a historical context has been presented by Ashby [1], as shown schematically in Figure 1.1 that clearly shows the steadily increasing importance of polymers, composites, and ceramics and the decreasing role of metals. Composites are generally used because they have desirable properties that cannot be achieved by any of the constituent materials acting alone. The most common example is the fibrous composite consisting of reinforcing fibers embedded in a binder or matrix material. Particle or flake reinforcements are also used, but they are generally not as effective as fibers.

Although it is difficult to say with certainty when or where humans first learned about fibrous composites, nature provides us with numerous examples. Wood consists mainly of fibrous cellulose in a matrix of lignin, whereas most mammalian bone is made up of layered and oriented collagen fibrils in a protein–calcium phosphate matrix [2]. The book of Exodus in the Old Testament recorded what surely must be one of the first examples of man-made fibrous composites, the straw-reinforced clay bricks used by the Israelites. The early natives of South America and Central America apparently used plant fibers in their pottery. These early uses of fibrous reinforcement, however, were probably based on the desire to keep the clay from cracking during drying rather than on structural reinforcement. Much later, humans

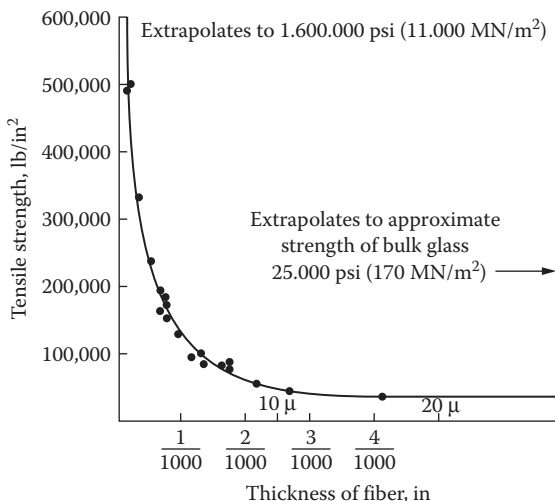
**FIGURE 1.1**

The relative importance of metals, polymers, composites, and ceramics as a function of time. The diagram is schematic and describes neither tonnage nor value. The timescale is nonlinear. (Ashby, M. F. 1987. Technology of the 1990s: Advanced materials and predictive design. *Philosophical Transactions of the Royal Society of London*, A322, 393–407. Reproduced by permission of The Royal Society.)

developed structural composites such as steel-reinforced concrete, polymers reinforced with fibers such as glass and carbon, and many other materials.

Fibrous reinforcement is very effective because many materials are much stronger and stiffer in fiber form than they are in bulk form. It is believed that this phenomenon was first demonstrated scientifically in 1920 by Griffith [3], who measured the tensile strengths of glass rods and glass fibers of different diameters. Griffith found that as the rods and fibers got thinner, they got stronger (see Figure 1.2 from Ref. [3], as shown in Ref. [4]), apparently because the smaller the diameter, the smaller the likelihood that failure-inducing surface cracks would be generated during fabrication and handling. By extrapolating these results, Griffith found that for very small diameters, the fiber strength approached the theoretical cohesive strength between adjacent layers of atoms, whereas for large diameters, the fiber strength dropped to nearly the strength of bulk glass.

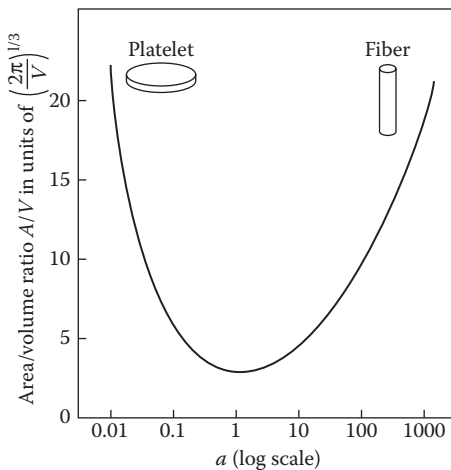
Results similar to those published by Griffith have been reported for a wide variety of other materials. The reasons for the differences between fiber and bulk behavior, however, are not necessarily the same for the other materials. For example, polymeric fibers are stronger and stiffer than bulk polymers

**FIGURE 1.2**

Griffith's measurements of tensile strength as a function of fiber thickness for glass fibers. (Griffith, A. A. 1920. The phenomena of rupture and flow in solids. *Philosophical Transactions of the Royal Society*, 221A, 163–198. Reproduced by permission of The Royal Society; Gordon, J. E. 1976. *The New Science of Strong Materials*, 2nd ed. Princeton University Press, Princeton, NJ. With permission.)

because of the highly aligned and extended polymer chains in the fibers and the randomly oriented polymer chains in the bulk polymer. A similar effect occurs in crystalline materials such as graphite. In addition, a single crystal tends to have a lower dislocation density than a polycrystalline solid; so single-crystal "whisker" materials are much stronger than the same material in polycrystalline bulk form. Whiskers typically have dimensions in the micrometer range, and for many years, it was thought that whiskers were the strongest and stiffest reinforcement materials available. However, it is now believed that carbon nanotubes, which have dimensions in the nanometer range, are the strongest and stiffest reinforcement materials in existence [5,6].

There can be no doubt that fibers allow us to obtain the maximum tensile strength and stiffness of a material, but there are obvious disadvantages of using a material in fiber form. Fibers alone cannot support longitudinal compressive loads and their transverse mechanical properties are often not as good as the corresponding longitudinal properties. Thus, fibers are generally useless as structural materials unless they are held together in a structural unit with a binder or matrix material and unless some transverse reinforcement is provided. Fortunately, the geometrical configuration of fibers also turns out to be very efficient from the point of view of interaction with the binder or matrix. As shown in Figure 1.3 from Ref. [7], the ratio of surface area to volume for a cylindrical particle is greatest when the particle is in either platelet or fiber form. For a platelet, the particle aspect ratio, that

**FIGURE 1.3**

Surface area-to-volume ratio  $A/V$  of a cylindrical particle of given volume plotted vs. particle aspect ratio  $a = l/d$ . (McCrum, N. G., Buckley, C. P., and Bucknall, C. B. *Principles of Polymer Engineering*, 1988, by permission of Oxford University Press, New York.)

is,  $a = l/d$  (i.e., the length-to-diameter ratio) is very small, whereas for a fiber, the aspect ratio is very large. Thus, the fiber/matrix interfacial area available for stress transfer per unit volume of fiber increases with increasing fiber length-to-diameter ratio. It is also important to note that, for a fiber-reinforced composite, the total fiber/matrix interfacial area will be increased if the fiber diameter is decreased while maintaining constant fiber volume and fiber length.

### Example 1.1

Compare the total fiber surface area of a group of  $N$  small-diameter fibers with that of a single large-diameter fiber having the same length and volume.

### SOLUTION

Assuming that the fibers are perfectly round, for a single large-diameter fiber of diameter  $d_L$ , the circumferential fiber surface area per unit length is

$$A_L = \pi d_L$$

while the fiber volume per unit length is

$$V_L = \frac{\pi d_L^2}{4}$$

For a single small-diameter fiber of diameter  $d_s$ , the corresponding circumferential surface area and volume per unit length are, respectively,

$$A_s = \pi d_s$$

and

$$V_s = \frac{\pi d_s^2}{4}$$

For  $N$  small-diameter fibers having the same volume and length as a single large-diameter fiber,

$$NV_s = V_L$$

so that

$$N = \frac{V_L}{V_s} = \left( \frac{d_L}{d_s} \right)^2$$

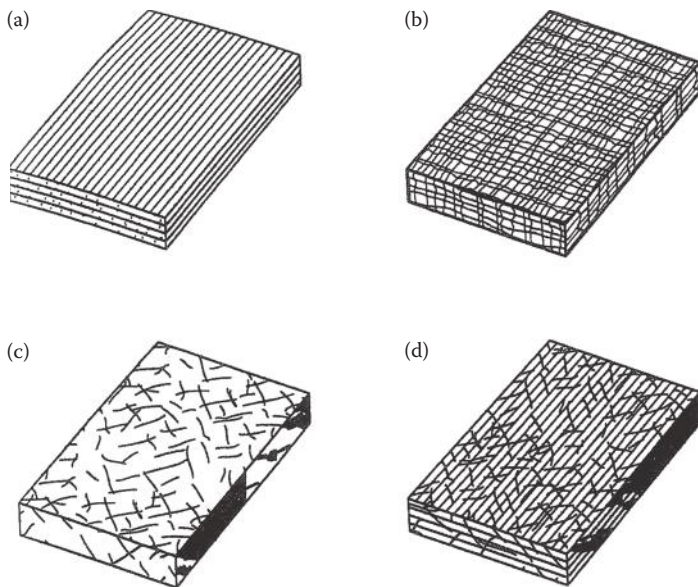
The ratio of the total surface area of  $N$  small-diameter fibers to the surface area of a single large-diameter fiber having the same volume and length is then

$$R = \frac{NA_s}{A_L} = \frac{Nd_s}{d_L} = \left( \frac{d_L}{d_s} \right)^2 \frac{d_s}{d_L} = \frac{d_L}{d_s}$$

For example, if a large fiber is replaced by a group of fibers having diameters 1000 times smaller,  $d_L = 1000 d_s$ , and the total fiber surface area for a constant fiber length and volume will increase by a factor of 1000. It can be easily shown that the same result holds for spherical particles. So in addition to their superior strength and stiffness, small-diameter fibers such as nanofibers have the additional advantage of significantly larger fiber/matrix interfacial surface area per unit volume than larger-diameter fibers.

The matrix also serves to protect the fibers from external damage and environmental attack. Transverse reinforcement is generally provided by orienting fibers at various angles according to the stress field in the component of interest. Filler particles are also commonly used in composites for a variety of reasons such as weight reduction, cost reduction, flame and smoke suppression, and prevention of ultraviolet degradation due to exposure to sunlight.

The need for fiber placement in different directions according to the particular application has led to various types of composites, as shown in Figure 1.4. In the continuous fiber composite laminate (Figure 1.4a), individual continuous fiber/matrix laminae are oriented in the required directions and bonded together to form a laminate. Although the continuous fiber laminate is used extensively, the potential for delamination, or separation of the laminae, is still a major problem because the interlaminar strength is matrix dominated. Woven fiber composites (Figure 1.4b) do not have distinct laminae and are not susceptible to delamination, but strength and stiffness are sacrificed

**FIGURE 1.4**

Types of fiber-reinforced composites. (a) Continuous fiber composite, (b) woven composite, (c) chopped fiber composite, and (d) hybrid composite.

because the fibers are not as straight as in the continuous fiber laminate. Chopped fiber composites may have short fibers randomly dispersed in the matrix, as shown in Figure 1.4c. Chopped fiber composites are used extensively in high-volume applications due to their low manufacturing cost, but their mechanical properties are considerably poorer than those of continuous fiber composites. Finally, hybrid composites may consist of mixed chopped and continuous fibers, as shown in Figure 1.4d, or mixed fiber types such as glass and carbon. Another common composite configuration, the sandwich structure (Figure 1.5), consists of high-strength composite facing sheets (which could be any of the composites shown in Figure 1.4) bonded to a lightweight foam or honeycomb core. Sandwich structures have extremely high flexural stiffness-to-weight ratios and are widely used in aerospace structures. The design flexibility offered by these and other composite configurations is obviously quite attractive to designers, and the potential exists to design not only the structure but also the structural material itself.

---

## 1.2 Constituent Materials for Composites

Fiberglass-reinforced plastics were one of the first structural composites. Composites incorporating glass or other relatively low-modulus fibers (less

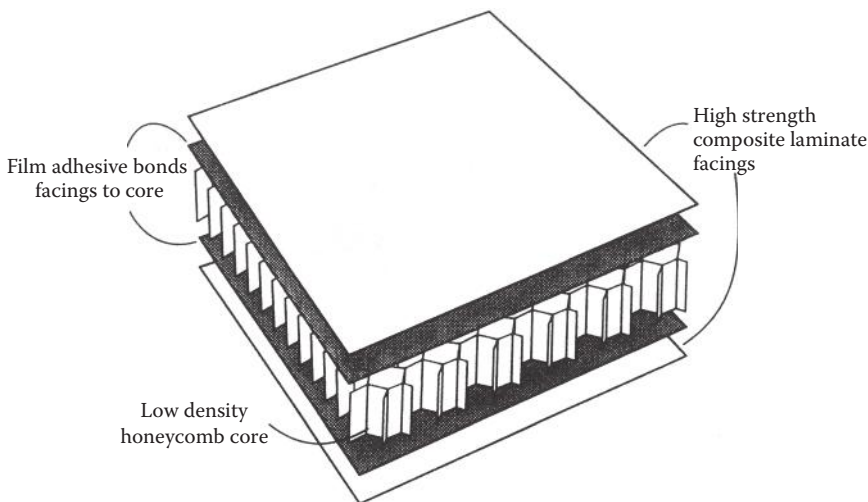


**FIGURE 1.5**  
Composite sandwich structure.

than about 83 GPa [ $12 \times 10^6$  psi] are used in many high-volume applications such as automotive vehicles because of their low cost, and are sometimes referred to as “basic” composites. The so-called “advanced” composites made from carbon, silicon carbide, aramid polymer, boron, or other higher-modulus fibers are used mainly in more demanding applications such as aerospace structures where their higher cost can be justified by improved performance.

The tremendous advantages of advanced fibers over glass fibers and conventional bulk materials are shown in Table 1.1, by comparing selected properties. The main advantages are higher modulus, higher strength, and lower density. In many applications, such as aerospace and automotive structures, structural weight is very important. Depending on whether the structural design is strength-critical or stiffness-critical, the material used should have a high strength-to-weight ratio (or specific strength) or a high stiffness-to-weight ratio (or specific stiffness). As shown in Figure 1.6, advanced fibers also have significant advantages over conventional materials in both these attributes, and this is the principal reason that composites will be used with increasing frequency in aerospace structures, fiber-reinforced automotive structures, and other structures where these properties are important. When the reinforcing fibers are combined with a matrix or binder material to form a composite, there is obviously some reduction in the tremendously high specific strengths and specific moduli shown for the reinforcing fibers in Figure 1.6, but the composites still have an overwhelming advantage with respect to these properties. Table 1.1 also shows that the ultimate strain, or strain to failure (a measure of ductility), is one attribute where reinforcing fibers are typically not as good as conventional bulk

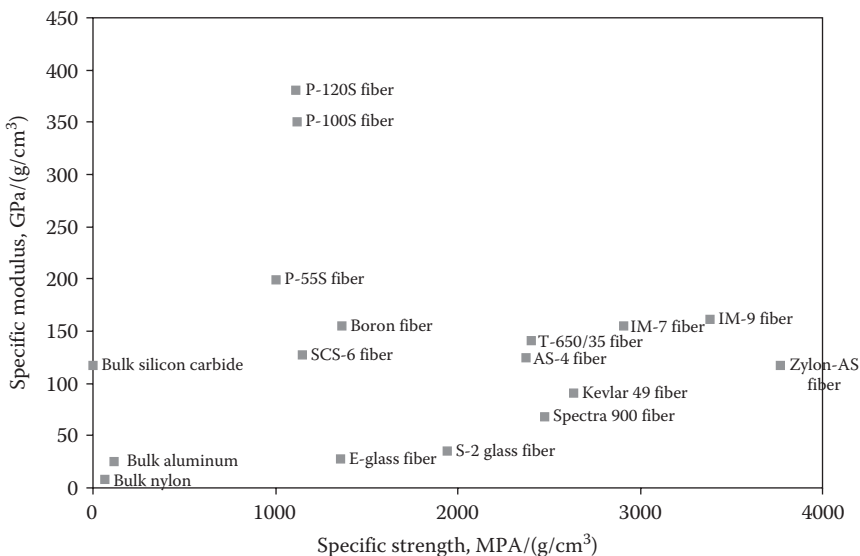
**TABLE 1.1**

Selected Properties of Bulk and Fibrous Materials

Material	Tensile Strength (MPa)	Tensile Modulus (GPa)	Density (g/cm <sup>3</sup> )	Specific Strength (MPa/[g/cm <sup>3</sup> ])	Specific Modulus (GPa/[g/cm <sup>3</sup> ])	Ultimate Strain	Manufacturer
<i>Bulk Metals</i>							
6061T6 Aluminum	310	69	2.71	114.4	25.5	0.17	
4340 Steel	1030	200	7.83	131.5	25.5	0.19	
AZ80 Magnesium	345	45	1.8	191.7	25	0.06	
6AL4V Titanium	880	114	4.43	198.6	25.7	0.14	
<i>Bulk Polymers</i>							
Nylon 6/6	75	2.8	1.14	65.8	2.5	0.5	
Polycarbonate	65	2.4	1.2	54.2	2	1.1	
Polyvinylchloride	40	3.1	1.44	27.8	2.2	0.4	
<i>Bulk Polymer Matrix Materials</i>							
Hexply 8551-7 epoxy	99	4.1	1.27	78	3.2	0.044	Hexcel
Hexply 8552 epoxy	121	4.7	1.3	93.1	3.6	0.017	Hexcel
CYCOM 934 epoxy	83	4.1	1.3	63.8	3.1	0.007	Cytec
Hexply 954-3A cyanate	56	3.3	1.19	47	2.8	0.019	Hexcel
Derakane 411-350 vinylester	86	3.2	1.14	75.4	2.8	0.05	Ashland
Ultem 2300 polyetherimide	158	9.3	1.51	104.6	6.2	0.03	Sabic
Victrex 150G polyetherether-ketone	97	3.5	1.3	74.6	2.7	0.6	Victrex
Fortron 0214B1 polyphenylene sulfide	86	4.1	1.4	61.4	2.9	0.03	Ticona
<i>Bulk Ceramics</i>							
Alumina (Al <sub>2</sub> O <sub>3</sub> )	2600 <sup>a</sup>	375 <sup>a</sup>	3.89	668.3	96.4		Accuratus
Silicon carbide (SiC)	3900 <sup>a</sup>	410 <sup>a</sup>	3.1	1258	132.2		Accuratus
Silica (SiO <sub>2</sub> )	1100 <sup>a</sup>	73 <sup>a</sup>	2.2	500	33.2		Accuratus
Aluminum nitride (AlN)	2100 <sup>a</sup>	330 <sup>a</sup>	3.26	644.2	101.2		Accuratus
<i>Glass Fibers</i>							
E-glass	3448	72	2.54	1357.5	28.3	0.048	Owens-Corning
S-2 glass	4890	87	2.46	1987.8	35.8	0.057	Owens-Corning

<i>PAN-Based Carbon Fibers</i>							
AS4, 12K filaments	4475	231	1.79	2500	129	0.018	Hexcel
IM7, 12K	5670	276	1.78	3185.4	155	0.0178	Hexcel
IM9, 12K	6140	304	1.8	3411.1	168.9	0.019	Hexcel
IM10, 12K	6964	303	1.79	3890.5	169.3	0.021	Hexcel
T-300, 12K	3650	231	1.76	2073.9	131.3	0.014	Cytec
T-650/35, 12K	4550	248	1.7	2676.4	145.9	0.0175	Cytec
T-400H, 6K	4410	250	1.8	2450.0	138.9	0.018	Toray
M-40, 12K	2740	392	1.81	1513.8	216.6	0.007	Toray
T700S, 12K	4900	230	1.8	2722.2	127.8	0.021	Toray
T-800S, 24K	5880	294	1.8	3266.7	163.3	0.02	Toray
T-1000G, 12K	6370	294	1.8	3538.9	163.3	0.022	Toray
<i>Pitch-Based Carbon Fibers</i>							
P-55S, 2K	1900	380	2.0	950	190	0.005	Cytec
P-100S, 2K	2100	760	2.13	985.9	356.8	0.002	Cytec
P-120S, 2K	2240	830	2.13	1051.6	389.7	0.0042	Cytec
<i>Polymeric Fibers</i>							
Kevlar 29 aramid	3620	70	1.44	2514	48.6	0.036	DuPont
Kevlar 49 aramid	3620	112	1.44	2514	77.8	0.024	DuPont
Spectra 900/650 polyethylene	2600	79	0.97	2680	81.4	0.036	Honeywell
Spectra 2000/100 polyethylene	3340	124	0.97	3443.3	127.8	0.03	Honeywell
Technora aramid	3430	73	1.39	2467.6	52.5	0.046	Teijin
Zylon-AS PBO	5800	180	1.54	3766.2	116.9	0.035	Toyobo
Dyneema SK60 polyethylene	3500	110	0.97	3608.2	113.4		Toyobo
<i>Other Fibers</i>							
Boron 4.0 mil dia	3600	400	2.54	1417.3	157.5	0.008	Specialty Materials
SCS-6 silicon carbide	3900	380	3	1300	126.7	0.0013	Specialty Materials
Carbon nanotubes	13,000–52,000	320–1470	1.3–1.4				
Carbon nanofibers	2700–7000	400–600	1.8–2.1				Applied Sciences

<sup>a</sup> Denotes compressive property.

**FIGURE 1.6**

Specific modulus versus specific strength for a variety of fibers and conventional bulk materials. The specific value is the value of the property divided by the density.

metals and polymers, but are still better than bulk ceramics. Many advanced fibers exhibit nearly linear stress-strain curves to failure, and such behavior is generally considered to be characteristic of brittle materials. It is important to remember, however, that the fiber strength, fiber modulus, and fiber ultimate strain values in Table 1.1 are based on tensile tests with the load acting along the fiber axis. As shown later, these properties all change substantially for off-axis loading, and applied loads are rarely aligned perfectly with the fiber axis. It will be shown later, for example, that a composite laminate can be constructed in such a way that its overall behavior is similar to that of ductile metals, even though the reinforcing fibers may exhibit brittle behavior.

### 1.2.1 Reinforcement Materials, Including Nanoreinforcements

Glass fibers consist primarily of silica (silicon dioxide) and metallic oxide modifying elements and are generally produced by mechanical drawing of molten glass through a small orifice. E-glass (named for its electrical properties) accounts for most of the glass fiber production and is the most widely used reinforcement for composites. The second most popular glass fiber, S-glass, has roughly 40% greater tensile strength and 20% greater modulus of elasticity than E-glass (Table 1.1), but it is not as widely used, because of its higher cost. S-glass actually has greater strength and elongation than many advanced fibers, but its relatively low modulus limits its application.

Glass/epoxy and glass/polyester composites are used extensively in applications ranging from fishing rods to storage tanks and aircraft parts.

Graphite or carbon fibers are the most widely used advanced fibers, and graphite/epoxy or carbon/epoxy composites are now used routinely in aerospace structures. Unfortunately, the names "carbon" and "graphite" are often used interchangeably to describe fibers based on the element carbon. These fibers are usually produced by subjecting organic precursor fibers such as polyacrylonitrile (PAN) or rayon to a sequence of heat treatments, so that the precursor is converted to carbon by pyrolysis. The major difference is that graphite fibers are subjected to higher-temperature pyrolysis than carbon fibers. The result is that carbon fibers typically are less than 95% carbon, whereas graphite fibers are at least 99% carbon [8]. Although carbon fibers were once prohibitively expensive, the cost has dropped significantly as production capacity and demand has increased. Development of new carbon and graphite fibers continues at a rapid pace. For example, fibers based on a pitch precursor (P-120S) with a modulus more than four times that of steel are now available (Table 1.1). High-strength carbon fibers such as IM10 and T-1000G, which are based on a PAN precursor, have a tensile strength more than six times that of steel. Either high strength or high modulus is obtained by using the appropriate heat treatment.

Advanced polymeric fibers such as Kevlar® aramid fibers by DuPont, Spectra® polyethylene fibers by Honeywell, Technora® aramid fibers by Teijin, and Zylon® *para*-phenylene benzobisoxazole (PBO) fibers by Toyobo have extremely high specific strengths because of their combinations of high strength and low density. The polymeric fibers also have higher failure strains (i.e., better ductility) than the glass or carbon fibers. The main disadvantages of the polymeric fibers are that they are generally not suitable for use at extremely high temperatures, and some of them are also susceptible to moisture-induced degradation. The effects of temperature and moisture on polymers and polymer composites will be discussed in more detail in Chapter 5.

Boron fibers are actually composites consisting of a boron coating on a substrate of tungsten or carbon, and the diameter of boron fibers is among the largest of all the advanced fibers, typically 0.002–0.008 in. (0.05–0.2 mm). Boron fibers not only have much higher moduli than most carbon fibers (Table 1.1), but they also have higher density. Boron/epoxy and boron/aluminum composites are widely used in aerospace structures where high stiffness is needed, but high cost still prevents more widespread use.

Silicon carbide (SiC) fibers are used primarily in high-temperature metal and ceramic matrix composites because of their excellent oxidation resistance and high-temperature strength retention. At room temperature, the strength and stiffness of SiC fibers are about the same as those of boron. SiC whisker-reinforced metals are also receiving considerable attention as alternatives to unreinforced metals and continuous fiber-reinforced metals. SiC whiskers are very small, typically 8–20  $\mu\text{m}$  (20–51 nm) in diameter and about

0.0012 in (0.03 mm) long, so that standard metal-forming processes such as extrusion, rolling, and forging can be easily used [7].

The ultimate reinforcement material to date is the carbon nanotube (CNT). Carbon nanotubes, which were first observed in 1991, are two-dimensional hexagonal networks of carbon atoms (graphene sheets) that have been rolled up to form a cage-like hollow tube having a diameter of several nanometers [5,6]. The properties for nanotubes presented in Table 1.1 are only approximate, as nanotubes have so many different possible configurations. For example, they can be single walled or multiwalled, and they may occur in the form of bundles or ropes. Carbon nanofibers have greater diameters and lengths, but lower mechanical properties than carbon nanotubes. Nanofibers are typically less expensive than nanotubes. Both carbon nanotubes and nanofibers are discontinuous, having rather low aspect ratios compared to conventional fibers such as glass and carbon. Discontinuous reinforcement is discussed in Chapter 6.

Particulate reinforcements, especially nanoparticles, are increasingly used to improve the mechanical and/or thermal properties of polymer matrix materials in fiber-reinforced composites. The longitudinal compressive strength, transverse tensile strength, and shear strength of fiber composites can be significantly enhanced by reinforcing the matrix with particles. Ceramic particles and nanoparticles such as silicon dioxide ( $\text{SiO}_2$ ) have much lower thermal expansion coefficients than polymer matrix materials, and can be used to reduce undesirable thermal expansion mismatches between fiber and matrix materials in fiber composites.

Hybrids consisting of mixed fiber materials can be used when a single fiber material does not have all the desired properties. More complete descriptions of fiber materials and their properties can be found in several composites handbooks [8–13]. Chapter 3 deals with further discussion on fiber properties, including anisotropic behavior.

### **Example 1.2**

A thin-walled pressure vessel of mean radius  $r$  and wall thickness  $t$  is to contain gas at an internal pressure  $p$ . Compare the maximum internal pressures that can be withstood by an IM 10 carbon fiber composite vessel and a 6061T6 aluminum vessel. Assume that both vessels have the same radius and wall thickness, that the carbon fibers are all oriented in the circumferential direction, and neglect the contribution of the matrix in the composite.

#### **SOLUTION**

From the mechanics of materials thin-walled pressure vessel theory, the circumferential hoop stress in the vessel is given by

$$\sigma = \frac{pr}{t}$$

so the pressure is given by

$$p = \frac{\sigma t}{r}$$

Therefore, for the same radius and thickness, the ratio of the pressures that can be withstood by the two vessels is given by the ratio of the tensile strengths for the two materials, as given in Table 1.1.

$$\frac{P_{IM10}}{P_{6061T6}} = \frac{\sigma_{IM10}}{\sigma_{6061T6}} = \frac{6964}{310} = 22.46$$

So the IM10 carbon fiber vessel can withstand 22.46 times the pressure that the 6061T6 vessel can withstand.

### Example 1.3

A cantilever beam of rectangular cross-section and made of 6061T6 aluminum is to be replaced by an IM10 carbon fiber composite beam having the same length  $L$  and width  $b$ , and it must have the same tip deflection  $w$  under the same tip load  $P$ . Compare the thicknesses and weights of the two beams, neglecting the contribution of the matrix material in the composite.

#### SOLUTION

From the mechanics of materials beam theory, the tip deflection of the cantilever beam is given by

$$w = \frac{Pl^3}{3EI}$$

where  $I = bh^3/12$  is the area moment of inertia of the cross-section about the neutral axis, or centroidal axis,  $b$  is the width,  $h$  is the thickness, and  $E$  is the modulus of elasticity from Table 1.1. The ratio of the tip deflections for the two beams having the same length, width, and load is

$$\left( \frac{h_{IM10}}{h_{6061T6}} \right)^3 \frac{E_{IM10}}{E_{6061T6}} = 1$$

So the corresponding ratio of thicknesses is

$$\frac{h_{IM10}}{h_{6061T6}} = \left( \frac{E_{6061T6}}{E_{IM10}} \right)^{1/3} = \left( \frac{69}{303} \right)^{1/3} = 0.61$$

and the carbon fiber beam only needs to be 61% as thick as the aluminum beam. The ratio of the weights of the two beams is given by

$$\frac{W_{IM10}}{W_{6061T6}} = \frac{bh_{IM10}L\rho_{IM10}}{bh_{6061T6}L\rho_{6061T6}} = \frac{h_{IM10}\rho_{IM10}}{h_{6061T6}\rho_{6061T6}} = 0.61 \frac{1.79}{2.71} = 0.403$$

where  $W$  is the beam weight and  $\rho$  is the beam material density from Table 1.1. So the carbon fiber composite beam only weighs 40% as much as the aluminum beam, but it satisfies the same design criteria. These examples demonstrate some of the advantages of composites over conventional materials without considering the matrix material. The contributions of the matrix material will be discussed in later chapters, especially Chapters 3 and 4.

### **1.2.2 Matrix and Filler Materials**

Polymers, metals, and ceramics are all used as matrix materials in composites, depending on the particular requirements. The matrix holds the fibers together in a structural unit and protects them from external damage, transfers and distributes the applied loads to the fibers, and, in many cases, contributes some needed property such as ductility, toughness, or electrical insulation. A strong interface bond between the fiber and matrix is obviously desirable, and so the matrix must be capable of developing a mechanical or chemical bond with the fiber. The fiber and matrix materials should also be chemically compatible, so that undesirable reactions do not take place at the interface. Such reactions tend to be more of a problem in high-temperature composites. Service temperature is often the main consideration in the selection of a matrix material. Thus, the materials will be discussed below in order of increasing temperature capability.

Polymers are unquestionably the most widely used matrix materials in modern composites (Table 1.1). Polymers are described as being either thermosets (e.g., epoxy, polyester, phenolic) or thermoplastics (e.g., polyimide (PI), polysulfone (PSU), polyetheretherketone (PEEK), polyphenylene sulfide (PPS)). On curing, thermosets form a highly cross-linked, three-dimensional molecular network that does not melt at high temperatures. Thermoplastics, however, are based on polymer chains that do not cross-link. As a result, thermoplastics will soften and melt at high temperatures, then harden again on cooling.

Epoxies and polyesters have been the principal polymer matrix materials for several decades, but advanced thermoplastics such as PEEK and PPS are now receiving considerable attention for their excellent toughness and low moisture absorption properties, their simple processing cycles, and their higher-temperature capabilities. Aerospace grade epoxies are typically cured at about 177°C (350°F) and are generally not used at temperatures above 150°C (300°F), whereas advanced thermoplastics such as PPS, PI, and PEEK have melting temperatures in the range 315–370°C (600–700°F). At this time, it appears that polymer matrix materials for use up to 425°C (800°F) are

feasible. For higher temperatures, metal, ceramic, or carbon matrix materials are required.

By using lightweight metals such as aluminum, titanium, and magnesium and their alloys and intermetallics such as titanium aluminide and nickel aluminide, operating temperatures can be extended to about 1250°C (2280°F). Other advantages of metal matrices are higher strength, stiffness, and ductility than polymers but at the expense of higher density. Ceramic matrix materials such as silicon carbide and silicon nitride can be used at temperatures up to 1650°C (3000°F). Ceramics have poor tensile strength and are notoriously brittle, however, and there is a need for much research before these materials can be routinely used. Finally, carbon fiber/carbon matrix composites can be used at temperatures approaching 2760°C (5000°F), but the cost of these materials is such that they are used only in a few critical aerospace applications. For further details on matrix materials and their properties, the reader is referred to any of several handbooks [8–13].

The third constituent material of a composite, the filler material, is mixed in with the matrix material during fabrication. Fillers are not generally used to improve mechanical properties but, rather, are used to enhance some other aspect of composite behavior. For example, hollow glass microspheres are used to reduce weight, clay or mica particles are used to reduce cost, carbon black particles are used for protection against ultraviolet radiation, and alumina trihydrate is used for flame and smoke suppression [11]. Fillers truly add another dimension to the design flexibility we have in composites.

---

### 1.3 Structural Applications of Composites

Composite structural elements are now used in a variety of components for automotive, aerospace, marine, and architectural structures in addition to consumer products such as skis, golf clubs, and tennis rackets. Since much of the current composites technology evolved from aerospace applications, it is appropriate to begin this brief overview from there.

Military aircraft designers were among the first to realize the tremendous potential of composites with high specific strength and high specific stiffness, since performance and maneuverability of those vehicles depend so heavily on weight. Composite construction also leads to smooth surfaces (no rivets or sharp transitions as in metallic construction), which reduce drag. Since boron and graphite fibers were first developed in the early 1960s, applications of advanced composites in military aircraft have accelerated quickly. Carbon fiber composite structural elements such as horizontal and vertical stabilizers, flaps, wing skins, and various control surfaces have been used in fighter aircraft for many years. More recently, carbon fiber composite fuselage and wing structures have been incorporated in fighter aircraft such as

**FIGURE 1.7**

Lockheed Martin F-35 Lightning II Joint Strike Fighter with composite fuselage and wing structures. (Courtesy of Lockheed Martin Corporation.)

the F-35 Lightning II Joint Strike Fighter (Figure 1.7) and in the entire structure of the B2 stealth bomber (Figure 1.8). The steady growth in the use of composite structures in military fighter aircraft over the years has been documented in Ref. [14].

Composites applications in commercial aircraft have been steadily increasing as material costs come down, as design and manufacturing technology evolves, and as the experience with composites in aircraft continues to build. A 1994 NASA report [15] indicated excellent in-service performance of composite components in commercial aircraft over a 15-year evaluation period, and such results have encouraged increased usage of composites in aircraft structures, including small business-type aircraft and large, commercial-transport aircraft. Initial use in these aircraft was restricted to smaller, lightly loaded secondary structures, but recently, composites are being used increasingly in large, heavily loaded primary structures such as the wings and the fuselage. For example, the Cirrus SR-22 single-engine, a four-passenger aircraft shown in Figure 1.9, has a composite fuselage and wings. As an excellent example of innovative design made possible by composites, the use of composites in this airplane resulted in enough weight savings to accommodate the extra weight of an airframe parachute system for safe descent of the entire aircraft in the event of a loss of engine power. The application of composites in commercial airliners has shown steady, conservative growth, but based on the increased prices of fuels, demands by airlines for more efficient aircraft, and other recent trends, this growth promises to be rapid in the future. For example, the Boeing 787 (Figure 1.10) is the first commercial



**FIGURE 1.8**

Northrup Grumman B2 Spirit stealth bomber with composite structure. (Courtesy of Northrup Grumman Corporation.)



**FIGURE 1.9**

Cirrus SR-22 single-engine, four-passenger composite aircraft. (Courtesy of Cirrus Design Corporation.)

**FIGURE 1.10**

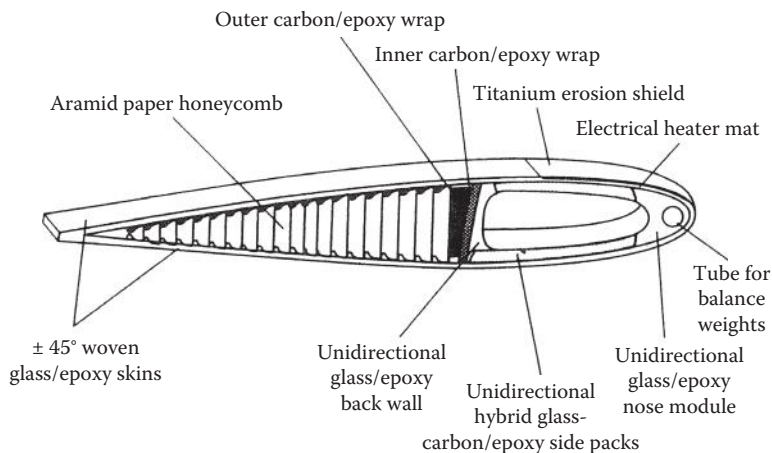
Boeing 787—first commercial airliner with composite fuselage and wings. (Courtesy of Boeing Company.)

airliner with a composite fuselage and wings. As much as 50% of the primary structure—including the fuselage and wings—on the 787 consists of carbon fiber/epoxy composite materials, or carbon fiber-reinforced plastics (CFRP). A similar new composite airliner, the Airbus A350 XWB, is currently under development.

The level of sophistication attained in aircraft composite construction is strikingly illustrated by the composite helicopter rotor blade in Figure 1.11. The construction of such a component obviously requires a multistep fabrication procedure involving many materials, and some of these fabrication processes will be discussed in the next section.

Due to the tremendous cost per unit weight to place an object in space, the value of weight saved is even greater for spacecraft. Thus, composites are extremely attractive for spacecraft applications. The NASA Space Shuttle has a number of composite parts, including graphite/epoxy cargo bay doors and experimental graphite/epoxy solid rocket-booster motor cases. For large space structures such as the proposed space station, the key properties of the structural materials are high stiffness-to-weight ratio, low thermal expansion coefficient, and good vibration-damping characteristics. In all three of these areas, composites offer significant advantages over conventional metallic materials.

Scaled Composite's SpaceShipOne (Figure 1.12), the first private manned spacecraft to achieve suborbital flight, is constructed primarily from composite materials, and promises to lead the way to commercial manned space travel. In other spacecraft components such as precision reflectors

**FIGURE 1.11**

Composite construction of a helicopter rotor blade. (McCrum, N. G., Buckley, C. P., and Bucknall, C. B. *Principles of Polymer Engineering*, 1988, by permission of Oxford University Press, New York.)

(Figure 1.13), special composite structures such as carbon fiber-reinforced isogrids are used for their superior dimensional stability characteristics. As shown later, some advanced fibers such as carbon have extremely low (and in some cases, negative) thermal expansion coefficients, which makes it possible to design composite structures having excellent dimensional stability.

**FIGURE 1.12**

SpaceShipOne and its mother ship White Knight. (Copyright 2004, Mojave Aerospace Ventures LLC, photograph by Scaled Composites. SpaceShipOne is a Paul G. Allen project.)

**FIGURE 1.13**

Composite isogrid spacecraft reflector. (Courtesy of Composite Optics, Inc.)

Structural weight is also very important in automotive vehicles, and the use of composite automotive components continues to grow. Glass fiber-reinforced polymers continue to dominate the automotive composites market, but advanced composites with carbon fiber reinforcement are getting increased attention as the cost of carbon fibers continues to drop. In cargo trucks, the reduced weight of composite components translates into increased payloads, which can have a significant economic impact. For example, the composite concrete mixer drum shown in Figure 1.14 weighs 2000 lb less than the conventional steel mixer drum that it replaced. According to the manufacturer, this means that an additional one-half cubic yard of concrete per load can be transported, which translates into an estimated productivity gain of \$7500 per year.

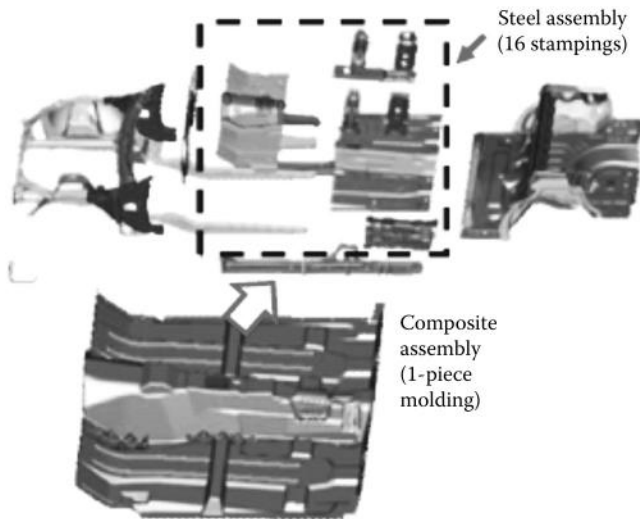
Weight savings on specific components such as composite leaf springs can exceed 70% compared with steel springs (composite leaf springs have also proved to be more fatigue resistant). Experimental composite engine blocks

**FIGURE 1.14**

Composite mixer drum on concrete transporter truck weighs 2000 lb less than conventional steel mixer drum. (Courtesy of Oshkosh Truck Corporation.)

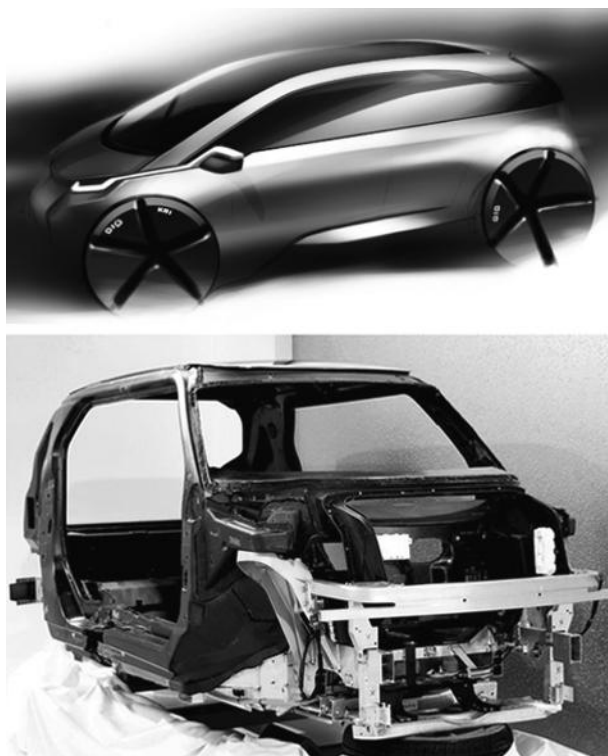
have been fabricated from graphite-reinforced thermoplastics, but the ultimate goal is a ceramic composite engine that would not require water cooling. Chopped glass fiber-reinforced polymers have been used extensively in body panels where stiffness and appearance are the principal design criteria. Composite structures such as Automotive Composites Consortium's composite underbody (Figure 1.15) are only experimental at this point, but they offer weight reduction, fewer parts, and smaller assembly and manufacturing costs. So far, the applications of composites in automotive vehicles have been mainly in secondary structural elements and appearance parts, and the full potential of composite primary structures remains to be explored. With the increased interest in electric vehicles comes a need for composite structures to reduce vehicle structural weight to compensate for the heavy batteries that are required. For example, the proposed BMW Megacity electric vehicle in Figure 1.16 would have a carbon fiber composite passenger compartment integrated with an aluminum spaceframe.

Other applications of structural composites are numerous, and so only a few examples will be given here. I-beams, channel sections, and other structural elements (Figure 1.17) used in civil infrastructure may be made of fiber-reinforced plastic using the pultrusion process, which will be discussed in the next section. Corrosion resistance and electrical and thermal insulation are added advantages of composites over steel in such applications. Wind turbines (Figure 1.18) are getting increased attention as environmentally

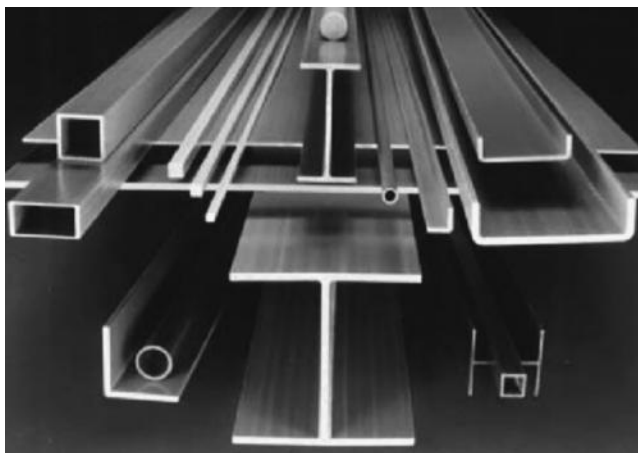
**FIGURE 1.15**

Automotive Composite Consortium's preliminary composite underbody design, replacing 16 steel stampings with one molded component. This work was sponsored by an agency of the United States Government. Neither the United States Government nor any agency thereof, nor any of their employees makes any warranty, express or implied, or assumes any legal liability or responsibility for the accuracy completeness, or usefulness of any information, apparatus, product or process disclosed, or represents that its use would not infringe privately owned rights. Reference herein to any specific commercial product, process or service by trade name, trademark, manufacturer, or otherwise does not necessarily constitute or imply its endorsement, recommendation, or favoring by the United States Government or any agency thereof. The views and opinions of authors expressed herein do not necessarily state or reflect those of the United States Government or any agency thereof. (This material is based on work supported by the Department of Energy National Energy Technology Laboratory under Award Number DE-FC26-02OR22910. With permission.)

attractive, alternative energy sources, and their blades are typically made from composites due to their high strength-to-weight ratio, high stiffness-to-weight ratio, excellent vibration damping, and fatigue resistance. The bodies of large mass-transportation vehicles such as airport people movers (Figure 1.19) are often fabricated from composites for the same reasons that they are used in many other transportation vehicles, and because, as shown in the next section, high-volume, low-cost processes for fabricating such large structures are now believed to be relatively mature technologies. One of the fastest-growing applications of composites in civil infrastructure is in pre-fabricated bridge decks for either new bridges or rehabilitation of older bridges. Fiber-reinforced polymer (FRP) composite bridge decks (Figure 1.20) have many advantages over conventional concrete and steel decks: FRP decks weigh much less, are more resistant to corrosion and freeze-thaw cycles, and are more easily and quickly installed. A major related application is the now common practice of seismic retrofitting of conventional

**FIGURE 1.16**

Concept sketch, carbon fiber composite cockpit and aluminum spaceframe for BMW Megacity electric vehicle. (Courtesy of BMW.)

**FIGURE 1.17**

Pultruded fiberglass composite structural elements. (Courtesy of Strongwell Corporation.)

**FIGURE 1.18**

Composite wind turbine blades. (Courtesy of GE Energy.)

concrete–steel bridge columns by wrapping them with composite tapes in earthquake-prone areas. In these examples, as well as in many of the previous examples, cost is a major consideration limiting the more widespread use of composites. The fabrication process is the key to cost control, and the next section will describe the fabrication processes used to make the components described here.

**FIGURE 1.19**

Airport people mover with composite body. (Courtesy of TPI Composites.)

**FIGURE 1.20**

Installation of FRP composite deck for bridge rehabilitation. (Courtesy of Strongwell Corporation.)

---

## 1.4 Multifunctional Applications of Composites

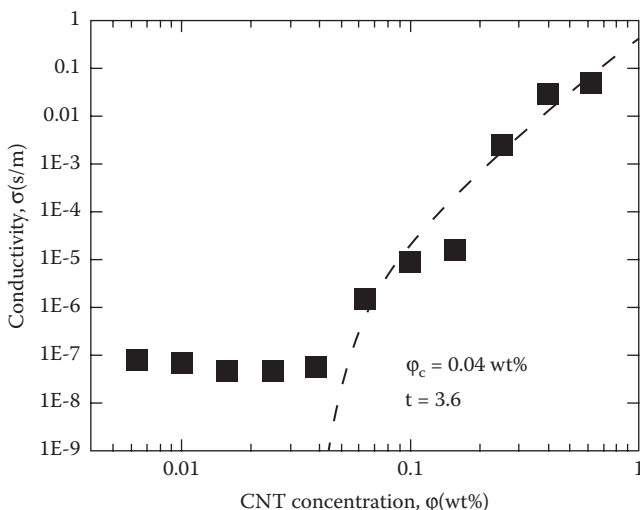
Interest in the mechanics of multifunctional materials and structures has increased markedly in recent years [16]. The increased interest in multifunctional materials and structures is driven by the need for the development of new materials and structures that simultaneously perform (a) multiple structural functions, (b) combined nonstructural and structural functions, or (c) both. One example of a multifunctional structure of type (a) would be a composite structure that has high strength, high stiffness, low thermal expansion, and high damping. An example of type (b) would be a load-bearing structure that has the capability of providing its own noise and vibration control, self-repair, thermal insulation, and energy harvesting/storage, whereas an example of type (c) would be a structure combining the functions of both type (a) and type (b). Most of the recent developments in multifunctional materials and structures tend to be of type (b).

Multifunctional materials are necessarily composite materials, and the strong growth in the use of composites has been greatly influenced by multifunctional design requirements. The traditional approach to the development of structures is to address the load-carrying function and other functional requirements separately, resulting in a suboptimal load-bearing structure with add-on attachments that perform the nonstructural functions with the penalty of added weight. Recently, however, there has been increased interest in the development of load-bearing materials and structures that

have integral nonload-bearing functions, guided by recent discoveries about how multifunctional biological systems work.

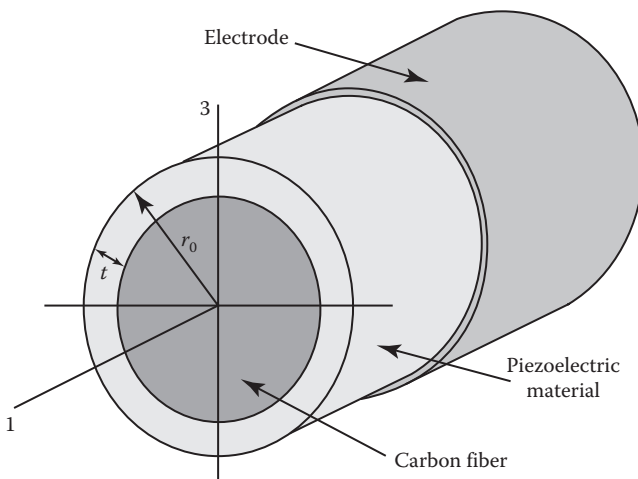
Among the most important nonstructural functions that a structure may need are electrical and thermal conductivity, but the most widely used composites have polymer matrix materials, which are typically poor conductors. So, conductive polymer nanocomposites are being investigated as possible replacements for nonconducting polymer matrix materials. Very small concentrations of CNTs or other conducting nanoreinforcements in polymers lead to disproportionately large improvements in the electrical conductivity of the nanocomposite. Figure 1.21 shows that the electrical conductivity of CNT/epoxy nanocomposites increases by nearly six decades when the CNT concentration is increased by only two decades [17]. The “percolation threshold,”  $\varphi_c$ , which is the CNT concentration in the polymer that characterizes the insulator-conductor transition, is only 0.04 wt% in this case.

Sensing and actuation are two closely related nonstructural functions, and in many cases, the same material or device can be used for both functions, as well as for other functions like energy harvesting/storage and structural health monitoring. Piezoelectric materials such as lead zirconate titanate (PZT), can be embedded in structures for sensing and actuation, as they naturally possess the required electromechanical coupling. As shown in Figure 1.22, piezoelectric structural fibers for sensing and actuation consist of conductive structural fibers such as carbon coated with a piezoelectric



**FIGURE 1.21**

Electrical conductivity of CNT/epoxy nanocomposites at various CNT concentrations. Percolation threshold is 0.04 wt%. (Reprinted from *Composites Science and Technology*, 69(10), Bauhofer, W. and Kovacs, J. Z., A review and analysis of electrical percolation in carbon nanotube polymer composites, 1486–1498, Copyright (2009), with permission from Elsevier.)

**FIGURE 1.22**

Multifunctional piezoelectric structural fiber. (Reprinted from *Composites Science and Technology*, 68(7-8), Lin, Y. and Sodano, H.A., Concept and model of a piezoelectric structural fiber for multifunctional composites, 1911–1918, Copyright (2008), with permission from Elsevier.)

interphase layer and an outer electrode layer [18]. Piezoelectric structural fiber composites are suitable for vibration control, damping, energy harvesting, or structural health monitoring.

A truly autonomous multifunctional structure will be capable of healing itself when damaged, as a biological system would, and recent research has demonstrated the feasibility of self-healing polymers and polymer composites based on the use of a microencapsulated healing agent and a catalyst for polymerizing the healing agent [19]. As shown in Figure 1.23, when damage causes cracks in the polymer, the cracks break open the microcapsules, causing the healing agent to leak into the crack by capillary action. The healing agent then reacts with the catalyst, causing polymerization that bonds the crack faces together.

Structurally integrated electronics such as batteries for energy storage are another recent application of multifunctional structure design. The effectiveness of a multifunctional system is best defined by using a metric that characterizes the particular system, such as flight endurance time for an aircraft vehicle. For example, by integrating a polymer lithium-ion battery in the carbon/epoxy composite wing skin structure of the DARPA Wasp micro air vehicle (MAV), a record-setting flight endurance time for the vehicle was achieved [20]. A photo of this vehicle is shown in Figure 1.24.

Other important nonstructural functions that are being integrated into multifunctional composite structures include thermal stability, thermal conductivity, electromagnetic interference (EMI) shielding, recyclability and biodegradability, optical transparency, and morphing capability. A more

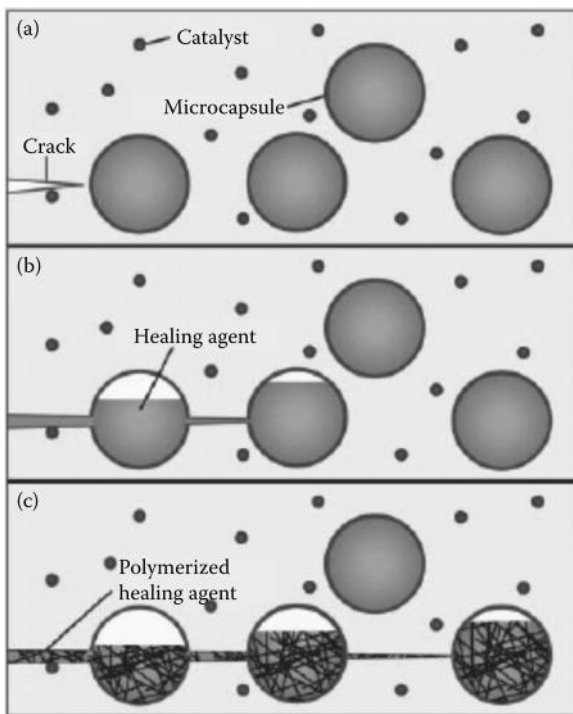
**FIGURE 1.23**

Illustration of self-healing of cracks in polymers by the use of a microencapsulated healing agent and a catalyst for polymerizing the healing agent. (a) Cracks form in the matrix; (b) the crack ruptures the microcapsules, releasing the healing agent into the crack through capillary action; and (c) the healing agent contacts the catalyst, triggering polymerization that bonds the crack faces closed. (With kind permission from Springer Science + Business Media: *Experimental Mechanics*, Fracture testing of a selfhealing polymer composite, 42(4), 2002, 372–379, Brown, E. N., Sottos, N. R., and White, S. R.)

detailed review of research on mechanics of multifunctional composite materials and structures can be found in Ref. [16].

## 1.5 Fabrication Processes

Although this book is concerned primarily with the mechanics of composite materials, it is essential for the reader to know how these materials are made. This is because, with composites, we design and build not only the structure, but also the structural material itself. The selection of a fabrication process obviously depends on the constituent materials in the composite, with the matrix material being the key (i.e., the processes for polymer matrix, metal

**FIGURE 1.24**

First generation DARPA Wasp microair vehicle (MAV) with polymer lithium-ion battery (silver quadrilaterals) integrated in composite wing skin structure. (With kind permission from Springer Science + Business Media: *JOM*, The design and application of multifunctional structure-battery material systems, 57(3), 2005, 18–24. Thomas, J. P. and Qidwai, M. A.)

matrix, and ceramic matrix composites are generally quite different). In this summary of fabrication processes, only those used for polymer matrix composite fabrication will be discussed, and the reader is referred to other books for details on metal matrix and ceramic matrix composite fabrication [8–13]. More details on composites manufacturing processes and analytical modeling of the processes can be found in Ref. [21].

A summary of fabrication processes used for polymer composites with various types of fiber reinforcement is given in Table 1.2. The open-mold process with hand lay-up of woven fiber mat or chopped strand mat (Figure 1.25) or spray-up of chopped fibers (Figure 1.26) is used for development work, prototype fabrication, and production of large components in relatively small quantities. A mold having the desired shape is first coated with a mold release, which prevents bonding of the resin matrix material to the mold. If a smooth surface on the part is desired (i.e., boat hulls or aircraft exterior parts), a gel coat is then applied to the mold, followed by a thermosetting polymer resin and the fibers. A roller may then be used for consolidation, followed by curing the polymer resin at the required temperature.

A major breakthrough in composite manufacturing technology was the development of “prepreg tape,” which is a tape consisting of fibers precoated with the polymer resin. This innovation means that the fabricator no longer has to worry about consistently mixing the resin components in the right proportions and combining the resin with the fibers in the correct fashion. Most prepreg tapes are made by the hot-melt process (Figure 1.27). If a thermosetting resin is used, the resin coating is partially cured, and the tape

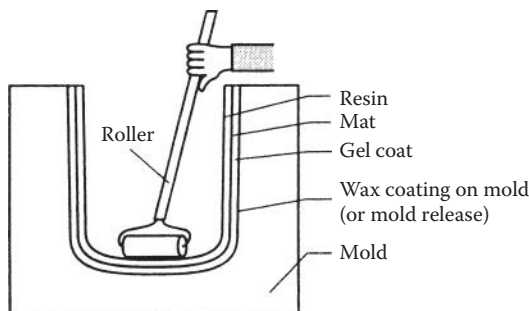
**TABLE 1.2**

Fabrication Processes for Polymer Matrix Composites

Process	Type of Reinforcement			
	Continuous	Chopped	Woven	Hybrid
Open mold				
Hand lay-up		X	X	
Spray-up		X		
Autoclave	X		X	
Compression molding	X	X	X	X
Filament winding	X			
Roll-wrapping	X		X	
Pultrusion	X		X	
Liquid composite molding	X	X	X	X
Reinforced reaction injection molding		X		
Resin infusion	X	X	X	X
Automated fiber placement	X		X	
Thermoplastic molding	X	X	X	X
Programmable powdered preform process		X		

must be kept refrigerated to prevent full curing until final use. If a thermoplastic resin is used, the tape can be stored at room temperature until it is melted during final use. The fabrication of a laminated structure with prepreg tape involves simply “laying-up” the tapes at the required orientations on a mold, stacking layers of tape in the required stacking sequence, and then curing the assembly under elevated temperature and pressure.

Autoclave molding (Figure 1.28) is the standard aerospace industry process for fabrication with prepreg tapes. The autoclave is simply a heated pressure vessel into which the mold (with lay-up) is placed and subjected to the required temperature and pressure for curing. The mold and lay-up are often covered with a release fabric, a bleeder cloth, and a vacuum bag. A vacuum line is then

**FIGURE 1.25**

Open-mold, hand lay-up composite fabrication.

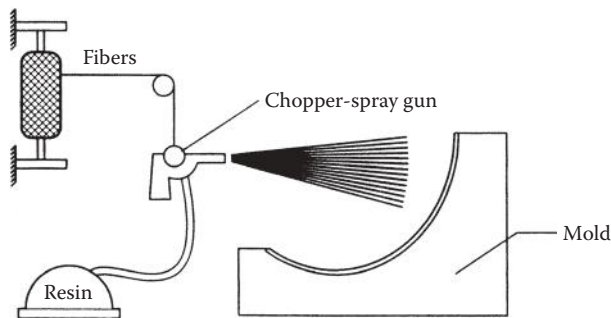


**FIGURE 1.26**  
Open-mold, spray-up composite fabrication.

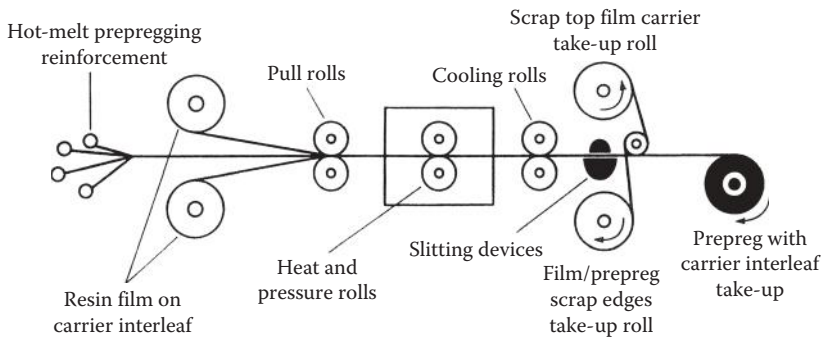


**FIGURE 1.27**  
Hot-melt prepregging process. (Courtesy of Suppliers of Advanced Composite Materials Association [SACMA].)

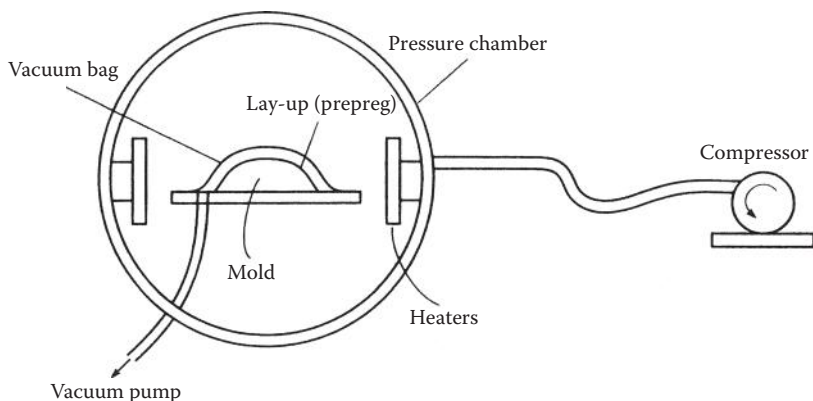


**FIGURE 1.28**  
Autoclave molding.

attached to the mold for evacuation of volatile gases during the cure process. Without the vacuum bagging, these gases would be trapped and could cause void contents of greater than 5% in the cured laminate. With the vacuum bag, void contents of the order of 0.1% are attainable. Autoclaves come in a wide range of sizes, from bench-top laboratory versions to the room-sized units used to cure large aircraft structures. Due to the expense and physical size of autoclaves for large structures, there is considerable interest in the development of “out-of-autoclave” processes and prepreg materials. One such process, Quickstep™, involves the use of a fluid-filled, balanced pressure, heated floating mold technology, and works by rapid heating of the laminate that is positioned between a mold that floats in a special heat transfer fluid. The mold and laminate are separated from the circulating heat transfer fluid by a flexible bladder. The autoclave-style press cure [22] is often used to cure small samples for research. In this case, a vacuum-bagged mold assembly (Figure 1.29) is inserted between the heated platens of a hydraulic press, and the press then generates the temperature and pressure required for curing. A vacuum press is a variation on this concept involving the use of a vacuum chamber surrounding the platen-mold assembly, and a sealed door on this chamber eliminates the need for a vacuum bag.

Owing to the cost and energy consumption of autoclaves (especially the large room-sized autoclaves in use by the aerospace industry), increased research activity has been directed toward the development of out-of-autoclave (OOA) processing of prepreg composite lay-ups using specially formulated prepreg resins with different cure cycles that enable the lay-up to be cured using vacuum pressure alone. One version of the OOA, vacuum bag only (VBO) processing, involves the use of an oven and a vacuum bag instead of an autoclave. Another version involves direct heating of the lay-up from the mold itself instead of an external oven. Due to the reduced pressure on the mold in OOA processing, the required tooling can be made of lightweight composites instead of heavy metallic materials such as Invar.

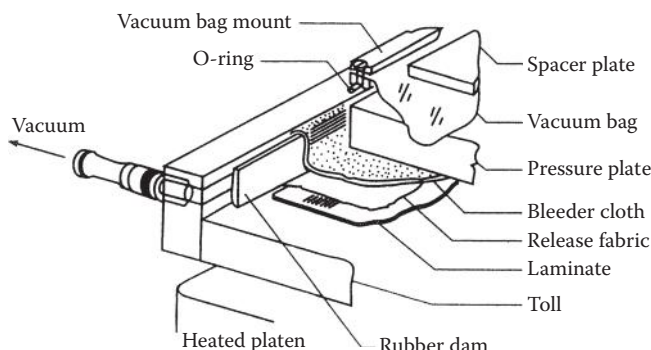
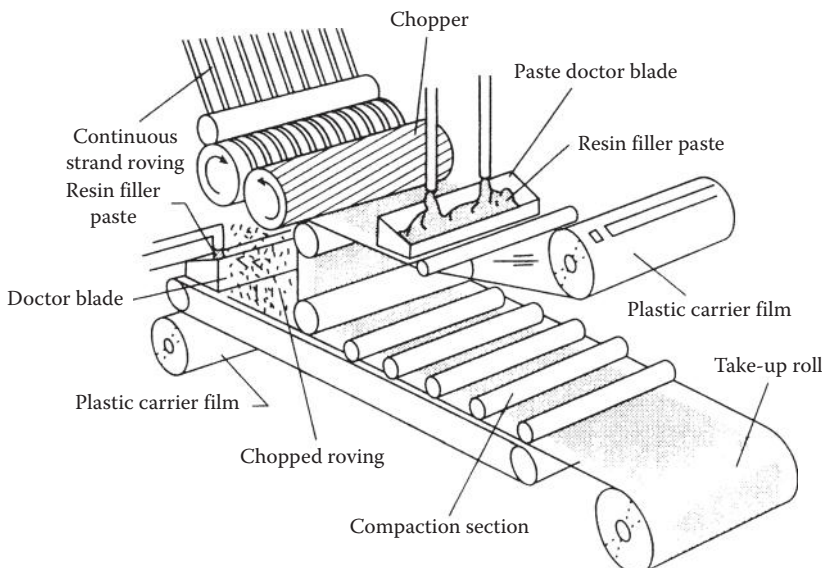


**FIGURE 1.29**  
Lay-up sequence for autoclave-style press molding.

Significant advances in OOA have been made in recent years, and it has been demonstrated that OOA-cured prepgres have properties essentially equivalent to those of autoclave-cured prepgres that have been previously qualified for aerospace primary structure use.

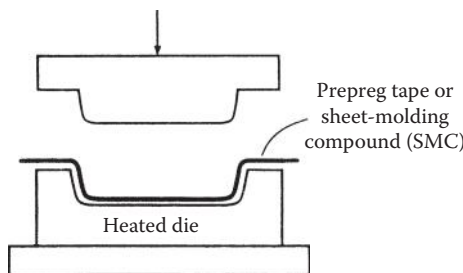
Sheet-molding compounds (SMCs) are an important innovation in composite manufacturing that are used extensively in the automobile industry. SMCs are similar to prepreg tape in that the fibers and the resin are "prepackaged" in a form that is more easily utilized by fabricators. SMCs consist of a relatively thick, chopped fiber-reinforced resin sheet, whereas a prepreg usually has continuous fibers in a thin tape. A machine for producing SMCs is shown schematically in Figure 1.30. An alternative to SMCs are bulk-molding compounds (BMCs), which consist of the chopped fiber/resin mixture in bulk form. SMCs or BMCs may be molded by using the matched metal die process (Figure 1.31).

Filament winding (Figure 1.32), which involves winding resin-coated fibers onto a rotating mandrel, may be used to produce any composite structure having the form of a body of revolution. Fiber orientation is controlled by the traverse speed of the fiber winding head and the rotational speed of the mandrel. Another advantage of this process is that by controlling the winding tension on the fibers, they can be packed together very tightly to produce high-fiber-volume fractions. On completion of the winding process, the composite structure may be cured by placing the mandrel in an oven or by passing hot fluid through the mandrel itself.



**FIGURE 1.30**

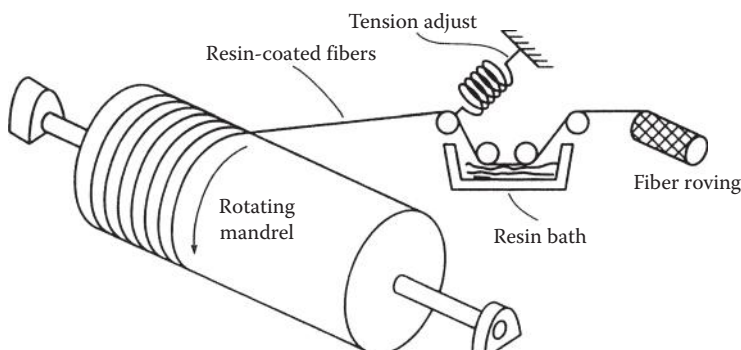
Machine for producing SMCs. (From Reinhart, T.J. et al. eds. 1987. *Engineered Materials Handbook*, Vol. 1, *Composites*. ASM International, Materials Park, OH. Reprinted by permission of ASM International.)



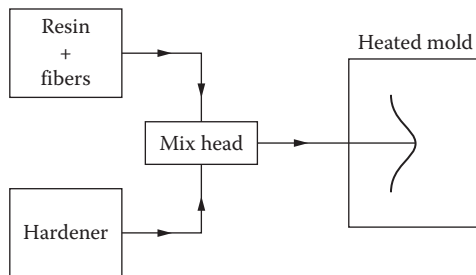
**FIGURE 1.31**  
Compression molding with matched metal dies.

Filament winding is widely used to produce such structures as rocket motor cases, pressure vessels, power transmission shafts, piping, and tubing. Prepreg tape is often produced by filament winding and removing the tape from the mandrel before curing. Imaginative variations on the filament-winding process have produced a variety of structures such as leaf springs for automotive vehicles. A composite leaf spring may be fabricated by winding on an ellipsoidal mandrel, then cutting the cured shell into the required pieces. Experimental programs are underway to produce large, complex structures such as aircraft fuselages and automobile body structures by filament winding. Filament-winding machines for such structures will require the liberal use of computer control and robotics.

The roll wrapping (or tube rolling) process also involves the placement of resin-impregnated fibers on a cylindrical mandrel to produce a composite tube or other body of revolution. However, in the case of roll wrapping, sheets of composite prepreg tape are wrapped around the mandrel by rolling the mandrel over the prepreg, which lies flat on a table. In this manner, prepreg tape is wrapped around the mandrel at a rate of one layer per revolution, and the mandrel is indexed after each revolution so that the abutting



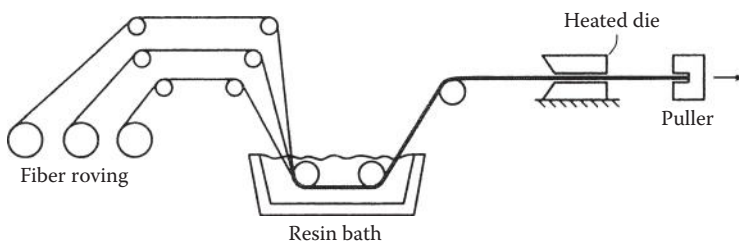
**FIGURE 1.32**  
Filament winding process.



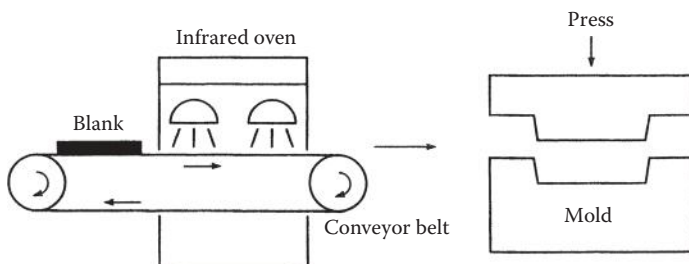
**FIGURE 1.33**  
RRIM process.

joints of prepreg tape are offset by some amount, thus avoiding an undesirable region of weakness that would be generated if all the abutting joints line up along a radial line. Once the wrapping process is completed, the mandrel is externally pressurized and heated at the required cure pressure and temperature. One advantage of roll wrapping over filament winding is that the fibers can be oriented in the true circumferential direction for maximum hoop strength, whereas in filament winding, some amount of deviation from circumferential fiber orientation will be introduced as the winding head traverses along the rotating mandrel. Either unidirectional fiber or woven fabric-reinforced prepreg can be used in roll wrapping, whereas filament winding is typically restricted to unidirectional fiber tows. Roll wrapping is often used to produce fishing rods, golf club shafts, hockey sticks, and tubing for bicycle frames.

Many of the processes described above are fairly time consuming. Processes with faster production cycles are needed for high-volume applications such as automotive parts. For example, reinforced reaction injection molding (RRIM) is a very fast process that is widely used to produce such components as automobile body panels. The RRIM process (Figure 1.33) involves the injection of a chopped fiber/resin mixture into a mold under high pressure and then curing it at the required temperature. Pultrusion (Figure 1.34) is the process of pulling a continuous fiber/resin mixture through a heated

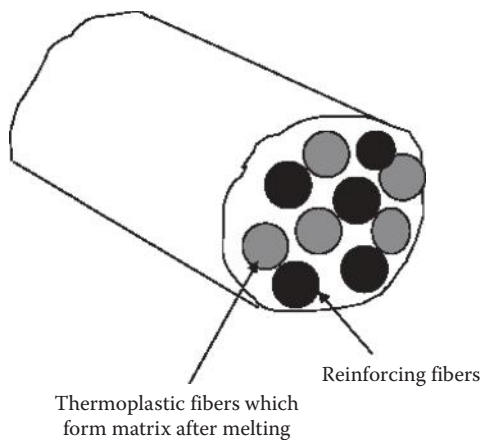


**FIGURE 1.34**  
Pultrusion process.

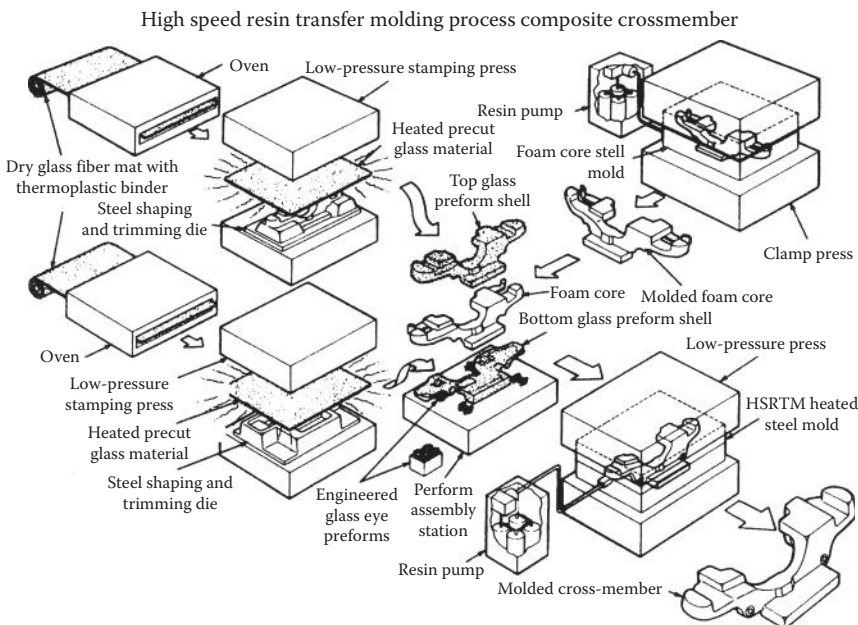


**FIGURE 1.35**  
Thermoplastic molding process.

die to form structural elements such as I-beams and channel sections (Figure 1.17). This process is relatively fast but is restricted to structures whose shapes do not change along the length. In the thermoplastic molding process (Figure 1.35), a blank (an uncured laminate consisting of thermoplastic prepreg tape layers) is passed through an infrared oven where it is heated to near the melting point of the thermoplastic resin. Thermoplastic yarn or woven textiles consisting of commingled reinforcing fibers and thermoplastic matrix fibers (Figure 1.36) are also used. The heated blank is then quickly placed in a matched metal die mold for final forming. In another form of thermoplastic molding, solid cylindrical pellets containing either long or short chopped fibers in a thermoplastic resin are melted and molded by using a screw injection machine, or by compression molding. Resin transfer molding (RTM) and structural reaction injection molding (SRIM) are attracting considerable attention because of their relatively fast production cycles and the near-net-shape of resulting parts. In both the RTM process



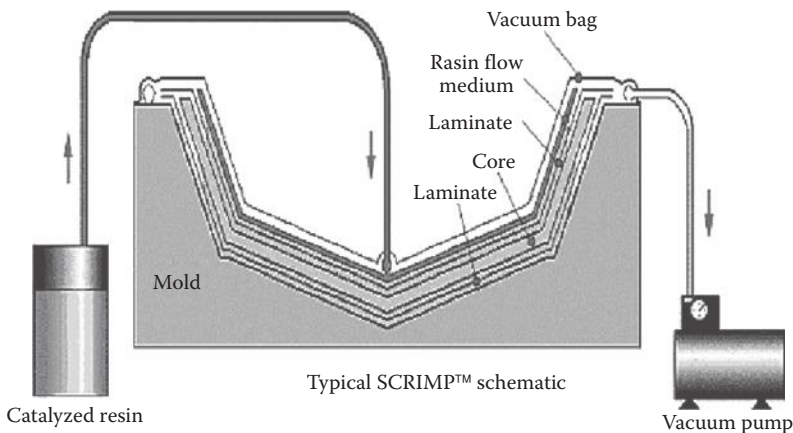
**FIGURE 1.36**  
Commingled reinforcing fibers and thermoplastic matrix fibers in a thermoplastic yarn.



**FIGURE 1.37**  
RTM process. (Courtesy of Ford Motor Company, Research Staff.)

(Figure 1.37) and the SRIM process, a “preform” consisting of fibers and possibly a foam core is first produced in the general shape of the finished part. The preform is then placed in a closed metal mold and the liquid resin is injected under pressure. The major difference between the two processes is that with RTM, the resin and hardener are premixed before injection into the mold, whereas with SRIM, the resin and hardener are mixed by impingement as they are injected into the mold. Three-dimensionally shaped parts with foam cores can be produced with both RTM and SRIM, but SRIM tends to be faster than RTM.

In the vacuum-assisted RTM (VARTM) process, a vacuum pump is connected to the closed mold to pull the resin through the fiber preform. The SCRIMP™ (Seeman composites resin infusion molding process), shown in Figure 1.38, is an open-mold/vacuum bag version of the VARTM process; it is effective for fabricating very large composite structures. The resin film infusion (RFI) process is similar to the SCRIMP™ process except that a solid resin film is used instead of a liquid resin. In RFI, the lay-up consists of the fiber preform and a solid resin film covered with a vacuum bag in an open mold, followed by heating and melting of the resin film, which infuses the fiber preform. Finally, the composite part is cured and released from the mold. The automated fiber placement process involves robotic placement of thermoset or thermoplastic prepreg tapes on a mold and is widely used in the aerospace industry. In processing methods that involve fiber preforms,

**FIGURE 1.38**

Schematic of SCRIMP™ (Seeman composites resin infusion molding process). (Courtesy of TPI Composites.)

one of the costliest and most time-consuming steps is the fabrication of the fiber preform itself. An innovative breakthrough in preform fabrication involves the use of robotic fiber placement in the so-called P4 (programmable powder preform process). In the P4 process, continuous fibers are chopped and sprayed onto a mold screen by a programmable robot, along with a small amount of resin binder to hold the fibers in place. A vacuum also helps to hold the fibers in place on the screen. The completed fiber preform is removed from the screen and placed in a mold where it is infiltrated with resin that is cured to form the composite part.

In conclusion, many innovative processes exist for manufacturing polymer composites. Much of the success that composite materials have had in the past several decades is due to innovative fabrication technology, and the future success of composites will surely depend on further advances in this area. Computer-aided-manufacturing technology and robotics are expected to play important roles in the continuing drive to reduce cost and to improve the quality of composite structures.

## 1.6 Elements of Mechanical Behavior of Composites

This book is concerned with the analysis of both the micromechanical and the macromechanical behavior of fiber-reinforced composite materials. As shown schematically in Figure 1.39, micromechanics is concerned with the mechanical behavior of constituent materials (in this case, fiber and matrix materials), the interaction of these constituents, and the resulting behavior of

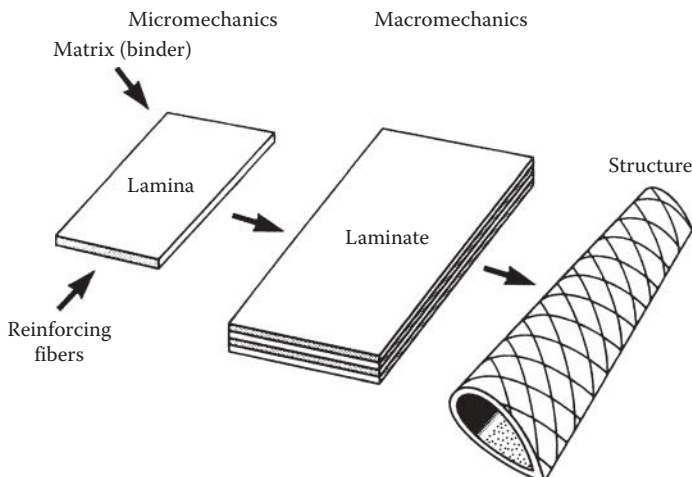


**FIGURE 1.39**  
Micromechanics and macromechanics of composites.

the basic composite (in this case, a single lamina in a laminate). Macromechanics is concerned with the gross mechanical behavior of composite materials and structures (in this case, lamina, laminate, and structure), without regard for the constituent materials or their interactions. As we will see in Chapter 2, this macromechanical behavior may be characterized by averaged stresses and strains and averaged, or “effective,” mechanical properties in an equivalent homogeneous material. As shown in Chapters 3 through 6, the focus in micromechanics is on the relationships between the effective composite properties and the effective constituent properties. Subsequent chapters deal with macromechanical behavior of laminates and structures.

When dealing with composite materials, we find very quickly that we can no longer draw upon the “intuition” about material behavior that we developed from years of experience with conventional metallic structural materials, and that we must learn to “think composites.” Most metallic structural materials are homogeneous (properties do not vary from point to point in the material) and isotropic (properties do not depend on orientation), whereas most composites are heterogeneous and anisotropic. That is, the properties in a composite change as we move from matrix to fiber and as we change the direction along which they are measured. For example, in a “unidirectional” composite, that is, having reinforcement in only one direction, the strength and stiffness are much greater along the reinforcement direction than in the transverse direction.

The relationships between forces and deformations (or between stresses and strains) are much more complicated in anisotropic composites than in conventional isotropic materials, and this can lead to unexpected behavior. For example, in an isotropic material, a normal stress induces only normal

strains (extensions and/or contractions), and a shear stress induces only shear strains (distortions). In an anisotropic composite, however, a normal stress may induce both normal strains and shear strains, and a shear stress may induce both shear strains and normal strains. A temperature change in an isotropic material causes expansion or contraction that is uniform in all directions, whereas a temperature change in an anisotropic material may cause nonuniform expansion or contraction plus distortion. These so-called “coupling” effects have important implications not only for the analytical mechanics of composites, but for the experimental characterization of composite behavior as well.

It is hoped that these general observations regarding composite materials will provide motivation for further study in subsequent chapters, where the analytical and experimental characterization of mechanical behavior of composites is discussed in more detail.

---

## **1.7 Review of Basic Mechanics of Materials Equations**

The basic equations of the mechanics of materials are used throughout this book, and this section briefly reviews and reinforces those equations, with examples of application to composite systems. As shown in many textbooks on mechanics of solids [23,24], when the loading is static or quasistatic in nature, three basic categories of equations are typically used, separately or in combination, to solve problems in elementary mechanics of materials. They are:

- Equations of static equilibrium based on Newton’s Second Law
- Force–deformation or stress–strain relationships for the materials
- Geometric compatibility equations or assumed relationships regarding the geometry of deformation

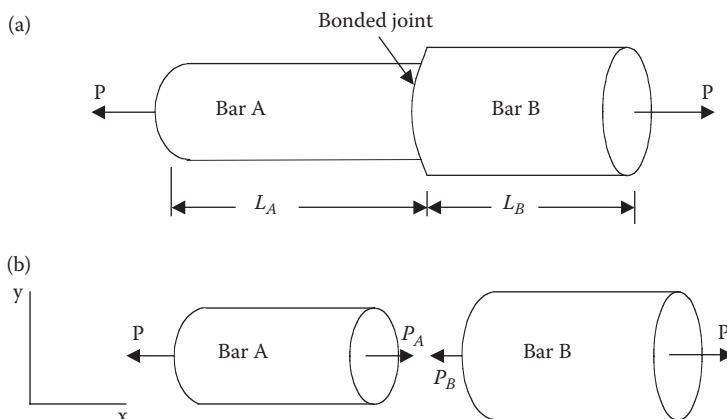
In addition, using accurate free-body diagrams is essential to set up the correct equations of static equilibrium. The equations of mechanics of materials are often algebraic, but in some cases involving differential equations, a fourth category of equations, usually referred to as boundary conditions, is also needed. For example, the well-known beam-deflection equations are second-order ordinary linear differential equations whose solution requires two boundary conditions. In problems involving dynamic loading, equations of motion are used instead of static equilibrium equations, and the equations of motion may be either ordinary or partial differential equations, depending on whether the mass is assumed to be discretely or continuously distributed, respectively. Most of the cases considered in this book will

involve static or quasistatic loading, and dynamic loading is discussed mainly in Chapter 8. Finally, it is important to recognize that, for statically determinant systems, the three categories of equations described above can be solved independently, but for statically indeterminate systems, they must be solved simultaneously.

The remainder of this section consists of examples demonstrating the application of the basic equations of mechanics of materials to the analysis of composite systems. These preliminary examples involve only simple composite systems having isotropic constituents, and the force-deformation and stress-strain relationships of isotropic materials should be familiar from previous studies of elementary mechanics of materials. However, it is important to realize that many composites and their constituents are anisotropic, and the corresponding force-deformation and stress-strain relationships of anisotropic materials are complex compared with those of isotropic materials. The study of anisotropic materials will begin in Chapter 2.

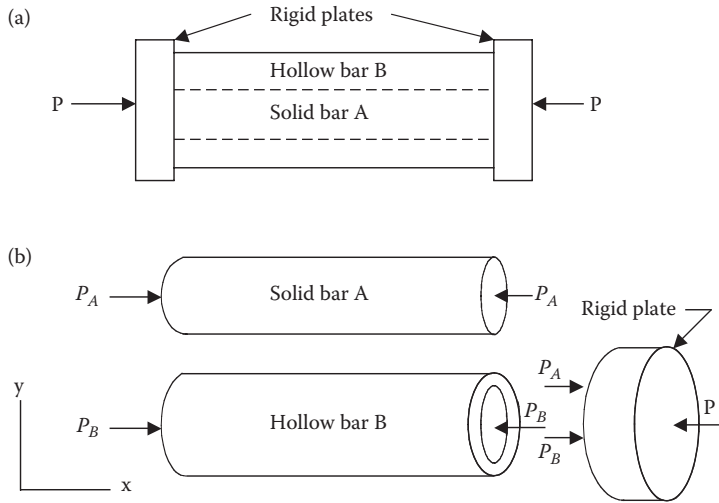
### Example 1.4

We wish to find the stresses and deformations in the axially loaded composite bar system in Figure 1.40a. The composite bar consists of two bars made of different isotropic materials A and B having different diameters and which are securely bonded together in a series arrangement and loaded by an axial load  $P$ . The bar of material A has length  $L_A$ , cross-sectional area  $A_A$ , and modulus of elasticity  $E_A$ , while the bar of material B has length  $L_B$ , cross-sectional area  $A_B$ , and modulus of elasticity  $E_B$ . Free-body diagrams of the two bars are shown in Figure 1.40b.



**FIGURE 1.40**

Composite bar system for Example 1.4. (a) Series arrangement of axially loaded bars and (b) free-body diagrams for bars A and B.

**FIGURE 1.41**

Composite bar system for Example 1.5. (a) Parallel arrangement of axially loaded bars and (b) free-body diagrams of members.

### SOLUTION

For static equilibrium of bar  $A$ , which has internal force  $P_A$ ,

$$\sum F_x = P_A - P = 0$$

Similarly, for bar  $B$ , which has internal force  $P_B$ ,

$$\sum F_x = P - P_B = 0$$

so that  $P = P_A = P_B$  and the load is the same for each bar in the series arrangement.

The axial stresses in the two bars are therefore

$$\sigma_A = \frac{P_A}{A_A} \quad \text{and} \quad \sigma_B = \frac{P_B}{A_B}$$

The axial elongations of the bars are given by the familiar force-deformation equations

$$\delta_A = \frac{P_A L_A}{A_A E_A} \quad \text{and} \quad \delta_B = \frac{P_B L_B}{A_B E_B}$$

Since the bars are assumed to be securely joined together in a series arrangement, the total axial elongation is given by the geometric compatibility equation,

$$\delta_{\text{total}} = \delta_A + \delta_B$$

So, for the series arrangement, the forces are the same in each member, and the total deformation is the sum of the deformations in the members. This is also an example of a statically determinate system, since the forces in the members can be determined from the static equilibrium equations alone. For such a system, the force-deformation equations and the geometric compatibility equation are not needed to find the forces in the members. The next example will be a statically indeterminate composite system, where the three basic types of equations must be solved simultaneously to find the forces in the members.

### Example 1.5

Now we wish to find the stresses and deformations in the composite system of Figure 1.41a, where a solid isotropic bar A is securely bonded inside a hollow isotropic bar B of the same length and both bars are axially loaded by a load P that is transmitted through rigid plates. The free-body diagrams for the bars and one of the rigid plates are shown in Figure 1.41b.

#### SOLUTION

Static equilibrium of the rigid plate requires that the applied force  $P$  must be related to the internal forces in the members,  $P_A$  and  $P_B$ , by the equation

$$\sum F_x = P_A + P_B - P = 0 \quad \text{or} \quad P = P_A + P_B$$

This is the only nontrivial static equilibrium equation for this system, but the equation contains two unknown forces,  $P_A$  and  $P_B$ . Thus, unlike Example 1.4, the forces in the members cannot be determined from the static equilibrium equations alone, and the system is said to be statically indeterminate. A second equation is needed to solve for the two unknown forces, and that equation may be generated by combining the force-deformation relationships and the geometric compatibility condition. As with Example 1.4, the force-deformation relationships for the bars are

$$\delta_A = \frac{P_A L_A}{A_A E_A} \quad \text{and} \quad \delta_B = \frac{P_B L_B}{A_B E_B}$$

Since the bars are assumed to be securely bonded together, the geometric compatibility condition for the parallel arrangement is

$$\delta_A = \delta_B$$

So for the parallel arrangement, the deformations in the members are equal and the total applied force is equal to the sum of the member forces. By combining the

force-deformation and geometric compatibility equations, we obtain a second equation in the two unknown forces  $P_A$  and  $P_B$  that can be solved simultaneously with the static equilibrium equation. Once the forces  $P_A$  and  $P_B$  are found, the stresses and deformations in the members can be found.

### Example 1.6

In the composite system shown in Figure 1.42a, a rigid L-shaped bar is hinged at point O and is also supported by a wood post and a steel cable. Before the load P is applied, the system is unstressed, and we wish to find the stresses and deformations in the steel cable and the wood post after the load P is applied.

#### SOLUTION

For a two-dimensional problem such as this, three static equilibrium equations are available, but from the free-body diagram of the L-shaped bar in Figure 1.42b, it is seen that there are four unknown reaction forces: the force in the steel cable,  $F_s$ , the hinge forces  $O_x$  and  $O_y$ , and the force in the wood post,  $F_w$ . The hinge forces are not of interest here, and can be eliminated from the problem by writing the equation for static equilibrium of moments about an axis through the hinge point O, as

$$\sum M_O = Pc - F_w b - F_s a = 0$$

We now have one equation in two unknowns,  $F_w$  and  $F_s$ , and although there are two remaining available static equations, those equations would involve the hinge forces  $O_x$  and  $O_y$ , and so nothing can be gained by considering them. Thus, the problem is statically indeterminate, and we must develop the geometric compatibility and force-deformation equations and solve all the equations simultaneously. The geometry of deformation of the rigid L-shaped bar that rotates about the hinge point O is shown in Figure 1.42c. From this drawing, it is clear that the geometric compatibility equation is

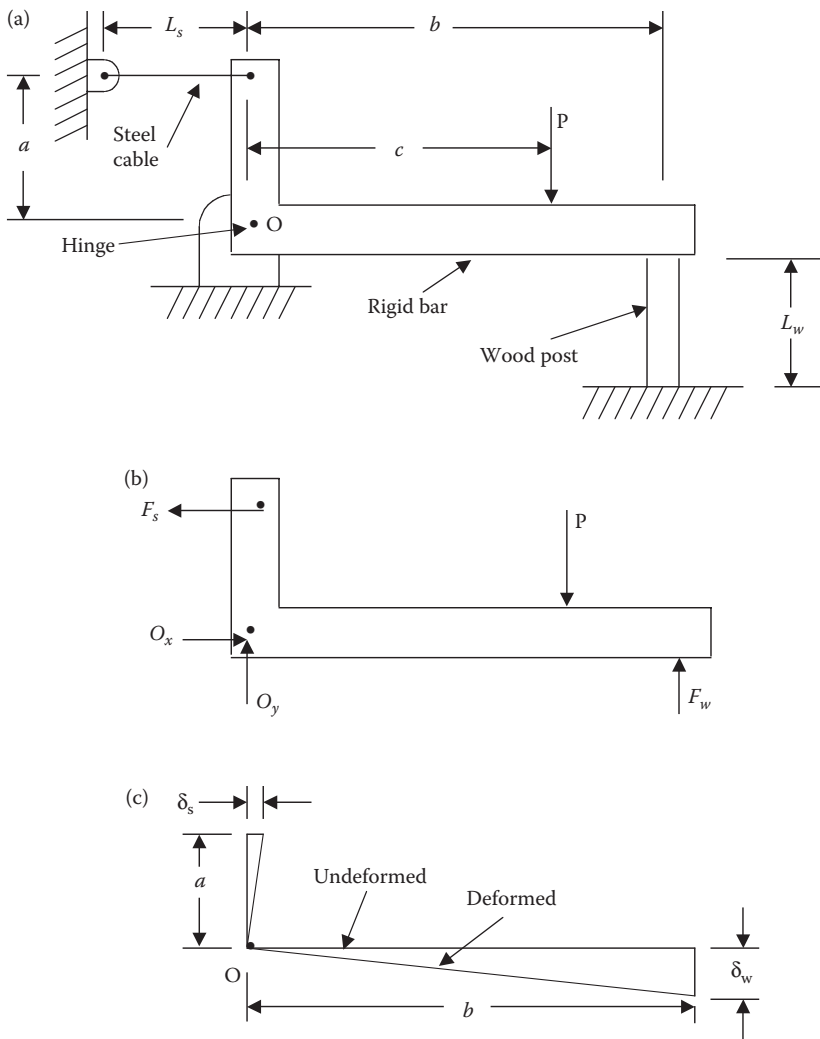
$$\frac{\delta_w}{b} = \frac{\delta_s}{a}$$

where  $\delta_w$  and  $\delta_s$  are the deformations in the wood post and the steel cable, respectively. The corresponding force-deformation equations are

$$\delta_w = \frac{F_w L_w}{A_w E_w} \quad \text{and} \quad \delta_s = \frac{F_s L_s}{A_s E_s}$$

where  $A_w$  and  $A_s$  are the cross-sectional areas and  $E_w$  and  $E_s$ , the elastic moduli of the wood post and the steel cable, respectively. Now the equilibrium, compatibility, and force-deformation equations can be solved simultaneously for the forces  $F_w$  and  $F_s$ ; the forces and areas can then be used to determine the stresses.

Thus, the general procedure for analyzing statically indeterminate structures is to solve the static equilibrium equations, the force-deformation equations, and

**FIGURE 1.42**

Composite system for Example 1.6. (a) Arrangement of composite system, (b) free-body diagram of rigid L-shaped bar, and (c) geometry of deformation for rigid L-shaped bar.

the geometric compatibility equations simultaneously for the forces in the members, then use the member forces to find the corresponding stresses and deformations. Although these same basic principles are used throughout this book, we find that it is often more convenient and practical to work with the stresses rather than the forces, the strains rather than the deformations, and the stress-strain relationships rather than the force-deformation relationships. Example 1.7 illustrates these concepts.

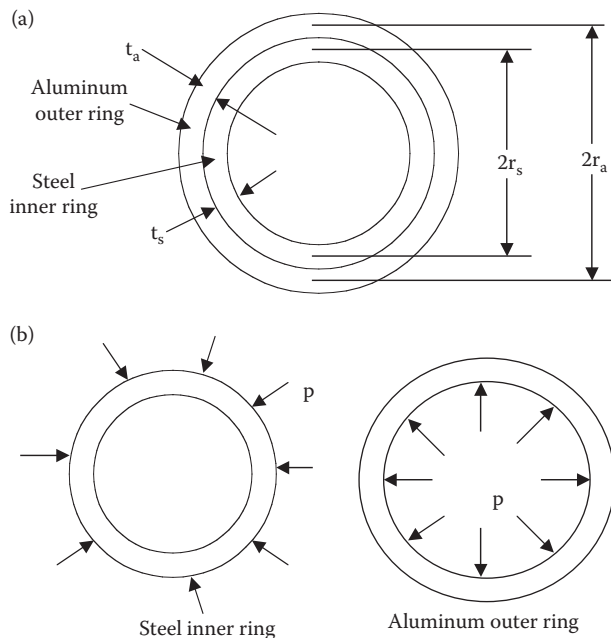


**FIGURE 1.43**  
Composite ring system for Example 1.7. (a) Assembled rings and (b) free body diagrams of rings after cooling.

### Example 1.7

The composite ring assembly in Figure 1.43a consists of a thin steel inner ring of mean radius  $r_s$ , wall thickness  $t_s$ , modulus of elasticity  $E_s$ , and coefficient of thermal expansion  $\alpha_s$ , which just fits inside an aluminum outer ring of mean radius  $r_a$ , wall thickness  $t_a$ , modulus of elasticity  $E_a$ , and coefficient of thermal expansion  $\alpha_a$ , so that both rings are initially unstressed at room temperature. We wish to determine the stresses in each ring after the assembly has been cooled by an amount  $\Delta T < 0$ , where  $\Delta T$  is the temperature drop.

### SOLUTION

From material property tables, we find that  $\alpha_a \gg \alpha_s$ , so that when the assembly is cooled, the aluminum ring tries to contract more than the steel ring. As a result of this differential contraction, a radial pressure,  $p$ , develops at the aluminum–steel interface, as shown in the free-body diagrams in Figure 1.43b. The effect of the interface pressure  $p$  is to put the inner steel ring in compression and the outer aluminum ring in tension. From the static equilibrium analysis of thin-walled cylinders or rings, which is found in any mechanics of materials book, the tangential (hoop) stresses in the two rings are

$$\sigma_a = \frac{pr_a}{t_a} \quad \text{and} \quad \sigma_s = -\frac{pr_s}{t_s}$$

However, it is clear from the free-body diagrams in Figure 1.43b that the pressure  $p$  and the corresponding stresses above cannot be found from the static equilibrium equations alone. Thus, the system must be statically indeterminate, and we must develop additional equations based on geometric compatibility and stress-strain relationships.

From mechanics of materials, the tangential (hoop) strains in the rings must be

$$\varepsilon_a = \frac{\Delta r_a}{r_a} \quad \text{and} \quad \varepsilon_s = \frac{\Delta r_s}{r_s}$$

where  $\Delta r_a$  and  $\Delta r_s$  are the radial displacements in the aluminum and steel rings, respectively. Since the two rings are securely bonded together, geometric compatibility requires that  $\Delta r_a = \Delta r_s$ , so that

$$\varepsilon_a = \frac{r_s}{r_a} \varepsilon_s$$

The tangential stress-strain relationships for the two materials including thermal effects are

$$\varepsilon_a = \frac{\sigma_a}{E_a} + \alpha_a \Delta T \quad \text{and} \quad \varepsilon_s = \frac{\sigma_s}{E_s} + \alpha_s \Delta T$$

By combining the above equations, we can reduce the problem to one equation in one unknown, the interfacial pressure  $p$ , as shown below.

$$\frac{pr_a}{t_a E_a} + \alpha_a \Delta T = \frac{r_s}{r_a} \left( -\frac{pr_s}{t_s E_s} + \alpha_s \Delta T \right)$$

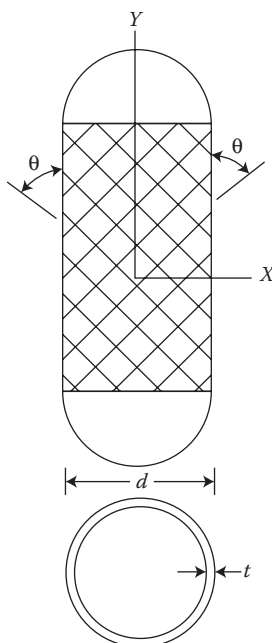
By substituting the known geometrical and material properties along with the temperature change, we can solve this equation for  $p$ . Once  $p$  is determined, the corresponding stresses in the rings can be easily calculated.

## PROBLEMS

- For a cylindrical particle, derive the relationship between the ratio of surface area to volume,  $A/V$ , and the particle aspect ratio,  $l/d$ , and verify the shape of the curve shown in Figure 1.3.
- Explain qualitatively why sandwich structures (Figure 1.5) have such high flexural stiffness-to-weight ratios. Describe the key parameters affecting the flexural stiffness-to-weight ratio of a sandwich panel.
- Describe a possible sequence of fabrication processes that might be used to manufacture the helicopter rotor blade in Figure 1.11. Note that several different materials and fiber lay-ups are used.
- Which of the reinforcing fibers listed in Table 1.1 would be best for use in an orbiting space satellite antenna structure that is subjected

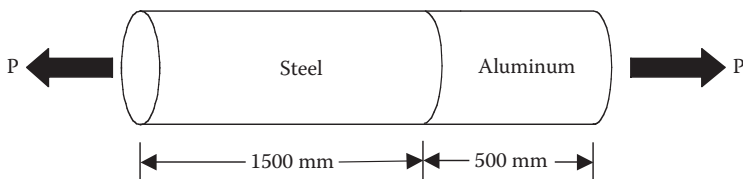
to relatively low stresses but has very precise dimensional stability requirements? The answer should be based only on the properties given in Table 1.1.

5. A thin-walled filament-wound composite pressure vessel has fibers wound at a helical angle  $\theta$ , as shown in Figure 1.44. Ignore the resin matrix material and assume that the fibers carry the entire load. Also assume that all fibers are uniformly stressed in tension. This gross oversimplification is the basis of the so-called "netting analysis," which is actually more appropriate for stress analysis of all-fiber textile fabrics. Using this simplified analysis, show that the angle  $\theta$  must be  $54.74^\circ$  in order to support both the hoop (tangential) and axial stresses that are generated in a thin-walled pressure vessel. (See any mechanics of materials book for the stress analysis of a thin-walled pressure vessel.)
6. A filament-wound E-glass/epoxy pressure vessel has a diameter of 50 in (127 cm), a wall thickness of 0.25 in (6.35 mm), and a helical wrap angle  $\theta = 54.74^\circ$ . Using a netting analysis and a safety factor of 2, estimate the allowable internal pressure in the vessel. Compare with the allowable internal pressure in a 6061-T6 aluminum alloy pressure vessel having the same dimensions. For the aluminum vessel, assume that the tensile yield stress is 40,000 psi (276 MPa) and use the Maximum Shear Stress yield criterion. Although the netting analysis is greatly oversimplified, these approximate



**FIGURE 1.44**

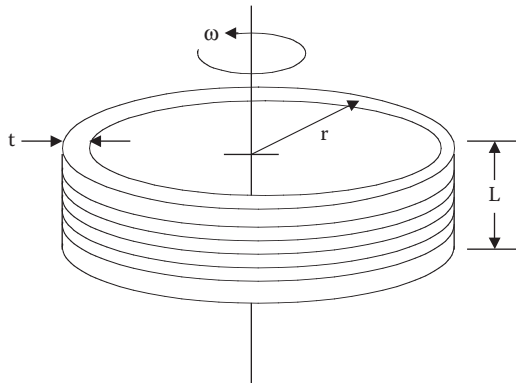
Filament-wound composite pressure vessel for Problem 5.

**FIGURE 1.45**

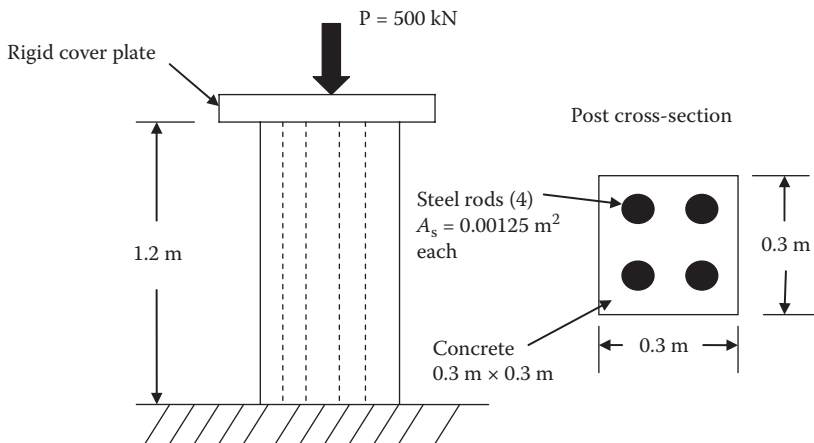
Composite bar system for Problem 7.

results should demonstrate the significant advantages of fiber composite construction over conventional metallic construction.

7. The 2000 mm long composite bar shown in Figure 1.45 consists of an aluminum bar having a modulus of elasticity  $E_{Al} = 70 \text{ GPa}$  and length  $L_{Al} = 500 \text{ mm}$ , which is securely fastened to a steel bar having modulus of elasticity  $E_{St} = 210 \text{ GPa}$  and length  $L_{St} = 1500 \text{ mm}$ . After the force  $P$  is applied, a tensile normal strain of  $\epsilon_{AL} = 1000 \times 10^{-6}$  is measured in the aluminum bar. Find the tensile normal stress in each bar and the total elongation of the composite bar.
8. A support cable in a structure must be 5 m long and must withstand a tensile load of 5 kN with a safety factor of 2.0 against tensile failure. Assuming a solid cylindrical cross-section for the cable as an approximation, (a) determine and compare the weights of cables made of 4340 steel and AS-4 carbon fibers that meet the above requirements and (b) for an AS-4 carbon fiber cable having the same weight, length, and safety factor as the 4340 steel cable from part (a). How much tensile load will the carbon fiber cable be able to withstand?
9. A flywheel for energy storage is modeled as a rotating thin-walled cylindrical ring ( $t \ll r$ ) as shown in Figure 1.46. Find the equation for the tensile stress in the ring as a function of the mean radius,  $r$ , the rotational speed,  $\omega$ , and the mass density,  $\rho$ , of the ring, then compare the maximum peripheral speed (tangential velocity) and

**FIGURE 1.46**

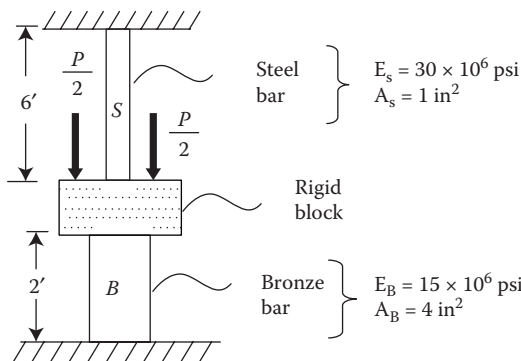
Simplified model of flywheel for Problem 9.

**FIGURE 1.47**

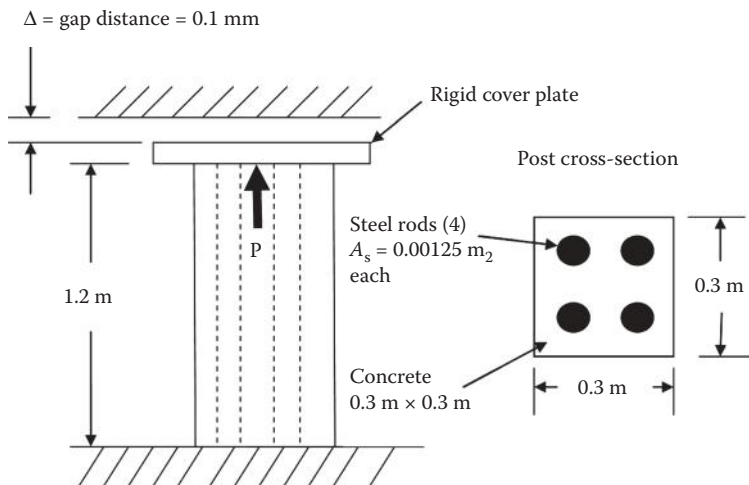
Concrete composite post for Problem 11.

the kinetic energy stored per unit mass of a ring made from 4340 steel with that of a ring made from IM-7 carbon fibers. For the carbon fiber ring, assume that the fibers are oriented in the circumferential direction, and that the entire tensile load is supported by the fibers.

10. Compare the total surface area of a group of  $N$  small-diameter spherical particles with that of a single large-diameter spherical particle having the same volume.
11. The concrete composite post in Figure 1.47 is 1.2 m long with a  $0.3 \text{ m} \times 0.3 \text{ m}$  square cross-section. The post is reinforced by four vertical steel rods of the same length having a cross-sectional area of  $A_s = 0.00125 \text{ m}^2$  each, and is loaded by a single vertical load  $P = 500 \text{ kN}$  applied on the rigid cover plate as shown below. The modulus of elasticity for concrete is  $E_c = 17 \text{ GPa}$ , while the modulus

**FIGURE 1.48**

Composite bar system for Problem 12.

**FIGURE 1.49**

Composite post for Problem 13. See Problem 11 for material properties.

of elasticity of steel is  $E_s = 200 \text{ GPa}$ . Determine the stresses in the steel rods and the concrete.

12. The composite bar system in Figure 1.48 consists of a steel bar and a bronze bar that are both securely attached to a rigid block and rigid supports. The system is loaded with a total load  $P$  at the rigid block. If the total applied load is  $P = 42,000 \text{ lb}$ , determine the stresses in the two bars.
13. The composite post in Figure 1.49 has the same properties and dimensions as in Problem 11, except that there is a gap  $\Delta = 0.1 \text{ mm}$  between the top of the cover plate on the post and the upper support. An upward load  $P$  is applied to the rigid cover plate, which is securely attached to the concrete and the steel reinforcing rods. If the deformation due to the load  $P$  is just enough to close the gap  $\Delta$ , determine the resulting stresses in the concrete and the steel rods, and the magnitude of the load  $P$ . Note that Figure 1.49 shows the position of the cover plate before the gap  $\Delta$  has been closed.

## References

1. Ashby, M. F. 1987. Technology of the 1990s: Advanced materials and predictive design. *Philosophical Transactions of the Royal Society of London*, A322, 393–407.
2. Wainwright, S. A., Biggs, W. D., Currey, J. D., and Gosline, J. M. 1976. *Mechanical Design in Organisms*. Princeton University Press, Princeton, NJ.
3. Griffith, A. A. 1920. The phenomena of rupture and flow in solids. *Philosophical Transactions of the Royal Society*, 221A, 163–198.

4. Gordon, J. E. 1976. *The New Science of Strong Materials*, 2nd ed. Princeton University Press, Princeton, NJ.
5. Thostenson, E. R., Ren, Z., and Chou, T.-W. 2001. Advances in the science and technology of carbon nanotubes and their composites: A review. *Composites Science and Technology*, 61, 1899–1912.
6. Qian, D., Wagner, J. G., Liu, W. K., Yu, M. F., and Ruoff, R. S. 2002. Mechanics of carbon nanotubes. *Applied Mechanics Reviews*, 55(6), 495–533.
7. McCrum, N. G., Buckley, C. P., and Bucknall, C. B. 1988. *Principles of Polymer Engineering*. Oxford University Press, New York.
8. Schwartz, M. M. 1984. *Composite Materials Handbook*. McGraw-Hill, Inc., New York.
9. Weeton, J. W., Peters, D. M., and Thomas, K. L. eds. 1987. *Engineer's Guide to Composite Materials*, ASM International, Materials Park, OH.
10. Lubin, G. ed. 1982. *Handbook of Composites*. Van Nostrand Reinhold Co., New York, NY.
11. Katz, H. S. and Milewski, J. V. eds. 1978. *Handbook of Fillers and Reinforcements for Plastics*. Van Nostrand Reinhold Co. New York, NY.
12. Reinhart, T. J. et al. eds. 1987. *Engineered Materials Handbook*, vol. 1, *Composites*. ASM International, Materials Park, OH.
13. Mallick, P. K. ed. 1997. *Composites Engineering Handbook*. Marcel Dekker, Inc., New York, NY.
14. Harris, C. E., Starnes, J. H., Jr., and Shuart, M. J. 2001. *An Assessment of the State-of-the-Art in the Design and Manufacturing of Large Composite Structures for Aerospace Vehicles*. NASA TM-2001-210844.
15. Dexter, H. B. and Baker, D. J. 1994. Flight service environmental effects on composite materials and structures. *Advanced Performance Materials*, 1, 51–85.
16. Gibson, R. F. 2010. A review of recent research on mechanics of multifunctional composite materials and structures. *Composite Structures*, 92(12), 2793–2810.
17. Bauhofer W. and Kovacs, J. Z. 2009. A review and analysis of electrical percolation in carbon nanotube polymer composites. *Composites Science and Technology*, 69(10), 1486–1498.
18. Lin, Y. and Sodano, H.A. 2008. Concept and model of a piezoelectric structural fiber for multifunctional composites. *Composites Science and Technology*, 68(7-8), 1911–1918.
19. Brown, E. N., Sottos, N. R., and White, S. R. 2002. Fracture testing of a self-healing polymer composite. *Experimental Mechanics*, 42(4), 372–379.
20. Thomas, J. P. and Qidwai, M. A. 2005. The design and application of multifunctional structure-battery material systems. *JOM* 57(3), 18–24.
21. Gutowski, T. G. ed. 1997. *Advanced Composites Manufacturing*. John Wiley & Sons, Inc., New York, NY.
22. Gibson, R. F., Suarez, S. A., and Deobald, L. R. 1985. Laboratory production of discontinuous-aligned fiber composite plates using an autoclave-style press cure. *Journal of Composites Technology and Research*, 7(2), 391–400.
23. Crandall, S. H., Dahl, N. C., and Lardner, T. J. 1978. *An Introduction to the Mechanics of Solids* (2nd ed. with SI units). McGraw Hill, New York, NY.
24. Riley, W. F., Sturges, L. D., and Morris, D. H. 2002. *Statics and Mechanics of Materials—An Integrated Approach*, 2nd ed. John Wiley & Sons, Inc., New York, NY.

# 2

---

## *Lamina Stress–Strain Relationships*

---

### 2.1 Introduction

The basic building block of a composite structure is the lamina, which usually consists of one of the fiber/matrix configurations shown in Figure 1.4. For the purposes of mechanics analysis, however, the “unidirectionally reinforced” or “unidirectional” lamina with an arrangement of parallel, continuous fibers is the most convenient starting point. As shown in subsequent chapters, the stress–strain relationships for the unidirectional lamina form the basis for the analysis of not only the continuous fiber composite laminate (Figure 1.4a), but also of woven fiber (Figure 1.4b) and chopped fiber composites (Figure 1.4c) and (Figure 1.4d).

A composite material is obviously heterogeneous at the constituent material level, with properties possibly changing from point to point. For example, the stress–strain relationships at a point are different for a point in the fiber material from how they are for a point in the matrix material. If we take the composite lamina as the basic building block, however, the “macromechanical” stress–strain relationships of the lamina can be expressed in terms of average stresses and strains and effective properties of an equivalent homogeneous material [1]. This chapter is concerned with the development and manipulation of these macromechanical stress–strain relationships. The “micromechanical” relationships between the constituent material properties and the effective lamina properties will be discussed in more detail in Chapter 3, but the basic concept of an effective modulus will be discussed here.

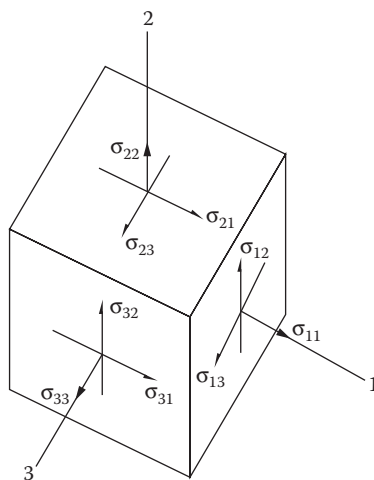
To complicate matters further, the properties of a composite are usually anisotropic. That is, the properties associated with an axis passing through a point in the material generally depend on the orientation of the axis. By comparison, conventional metallic materials are nearly isotropic since their properties are essentially independent of orientation. Fortunately, each type of composite has characteristic material property symmetries that make it possible to simplify the general anisotropic stress–strain relationships. In particular, the symmetry possessed by the unidirectional lamina makes it a so-called orthotropic material. The symmetries associated with various types of composite laminae and the resulting lamina stress–strain relationships are discussed in this chapter, along with certain mathematical

manipulations that make it easier to deal with the directional nature of composite properties.

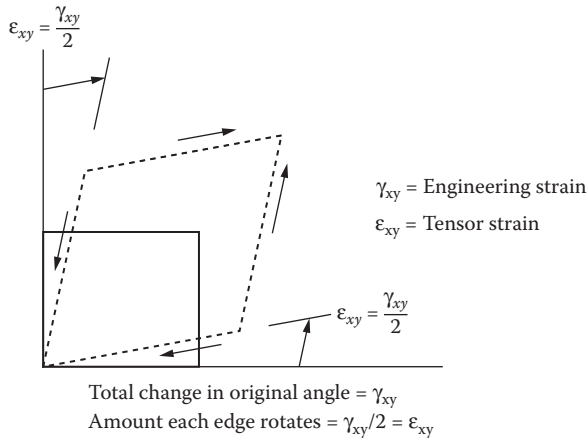
## 2.2 Effective Moduli in Stress–Strain Relationships

A general 3-D state of stress at a point in a material can be described by nine stress components  $\sigma_{ij}$  (where  $i, j = 1, 2, 3$ ), as shown in Figure 2.1. According to the conventional subscript notation, when  $i = j$ , the stress component  $\sigma_{ii}$  is a normal stress; and when  $i \neq j$ , the stress component is a shear stress. The first subscript refers to the *direction of the outward normal* to the face on which the stress component acts, and the second subscript refers to the direction in which the stress component itself acts.

Corresponding to each of the stress components, there is a strain component  $\epsilon_{ij}$  describing the deformation at the point. Normal strains ( $i = j$ ) describe the extension or contraction per unit length along the  $x_i$  direction, and shear strains ( $i \neq j$ ) describe the distortional deformations associated with lines that were originally parallel to the  $x_i$  and  $x_j$  axes. It is very important to distinguish between the “tensor” strain  $\epsilon_{ij}$  and the “engineering” strain  $\gamma_{ij}$ . In the case of normal strain, the engineering strain is the same as the tensor strain, but for shear strain,  $\epsilon_{ij} = \gamma_{ij}/2$ . Thus, the engineering shear strain  $\gamma_{ij}$  describes the total distortional change in the angle between lines that were originally parallel to the  $x_i$  and  $x_j$  axes, but the tensor shear strain  $\epsilon_{ij}$  describes the amount of rotation of either of the lines (Figure 2.2).



**FIGURE 2.1**  
3-D state of stress.

**FIGURE 2.2**

Geometric interpretation of engineering shear strain and tensor shear strain.

In the most general stress–strain relationship *at a point* in an elastic material, each stress component is related to each of the nine strain components by an equation of the form

$$\sigma_{ij} = f_{ij}(\varepsilon_{11}, \varepsilon_{12}, \varepsilon_{13}, \varepsilon_{21}, \varepsilon_{22}, \varepsilon_{23}, \varepsilon_{31}, \varepsilon_{32}, \varepsilon_{33}) \quad (2.1)$$

where the functions  $f_{ij}$  may be nonlinear. For the linear elastic material, which is of primary concern in this book, the most general linear stress–strain relationships *at a point* in the material (excluding effects of environmental conditions) are given by equations of the form

$$\left\{ \begin{matrix} \sigma_{11} \\ \sigma_{22} \\ \sigma_{33} \\ \sigma_{23} \\ \sigma_{31} \\ \sigma_{12} \\ \sigma_{32} \\ \sigma_{13} \\ \sigma_{21} \end{matrix} \right\} = \left[ \begin{matrix} C_{1111} & C_{1122} & C_{1133} & C_{1123} & C_{1131} & C_{1112} & C_{1132} & C_{1113} & C_{1121} \\ C_{2211} & C_{2222} & C_{2233} & C_{2223} & C_{2231} & C_{2212} & C_{2232} & C_{2213} & C_{2221} \\ C_{3311} & C_{3322} & C_{3333} & C_{3323} & C_{3331} & C_{3312} & C_{3332} & C_{3313} & C_{3321} \\ \dots & \dots \\ \dots & \dots \\ \dots & \dots \\ \dots & \dots \\ \dots & \dots \\ C_{2111} & C_{2122} & C_{2133} & C_{2123} & C_{2131} & C_{2112} & C_{2132} & C_{2113} & C_{2121} \end{matrix} \right] \left\{ \begin{matrix} \varepsilon_{11} \\ \varepsilon_{22} \\ \varepsilon_{33} \\ \varepsilon_{23} \\ \varepsilon_{31} \\ \varepsilon_{12} \\ \varepsilon_{32} \\ \varepsilon_{13} \\ \varepsilon_{21} \end{matrix} \right\} \quad (2.2)$$

where  $[C]$  is a fully populated  $9 \times 9$  matrix of stiffnesses or elastic constants (or moduli) having 81 components. Note that the first two subscripts on the elastic constants correspond to those of the stress, whereas the last two

subscripts correspond to those of the strain. If no further restrictions are placed on the elastic constants, the material is called anisotropic and Equation 2.2 is referred to as the generalized Hooke's law for anisotropic materials. In practice, there is no need to deal with this equation and its 81 elastic constants because various symmetry conditions simplify the equations considerably.

As shown in any mechanics of materials book [2], both stresses and strains are symmetric (i.e.,  $\sigma_{ij} = \sigma_{ji}$  and  $\epsilon_{ij} = \epsilon_{ji}$ ), so that there are only six independent stress components and six independent strain components. This means that the elastic constants must be symmetric with respect to the first two subscripts and with respect to the last two subscripts (i.e.,  $C_{ijkl} = C_{jikl}$  and  $C_{ijkl} = C_{ijlk}$  where  $i, j, k$ , and  $l$  each take on the values 1, 2, and 3) and that the number of nonzero elastic constants is now reduced to 36. These simplifications lead to a contracted notation that reduces the number of subscripts based on the following changes in notation [3–6]:

$$\begin{array}{ll}
 \sigma_{11} = \sigma_1 & \epsilon_{11} = \epsilon_1 \\
 \sigma_{22} = \sigma_2 & \epsilon_{22} = \epsilon_2 \\
 \sigma_{33} = \sigma_3 & \epsilon_{33} = \epsilon_3 \\
 \sigma_{23} = \sigma_{32} = \sigma_4 & 2\epsilon_{23} = 2\epsilon_{32} = \gamma_{23} = \gamma_{32} = \epsilon_4 \\
 \sigma_{13} = \sigma_{31} = \sigma_5 & 2\epsilon_{13} = 2\epsilon_{31} = \gamma_{13} = \gamma_{31} = \epsilon_5 \\
 \sigma_{12} = \sigma_{21} = \sigma_6 & 2\epsilon_{12} = 2\epsilon_{21} = \gamma_{12} = \gamma_{21} = \epsilon_6
 \end{array}$$

With this contracted notation, the generalized Hooke's law can now be written as

$$\sigma_i = C_{ij}\epsilon_j, \quad i, j = 1, 2, \dots, 6 \quad (2.3)$$

and the repeated subscript  $j$  implies summation on that subscript. Alternatively, in matrix form,

$$\{\sigma\} = [C]\{\epsilon\} \quad (2.4)$$

where the elastic constant matrix or stiffness matrix  $[C]$  is now  $6 \times 6$  with 36 components and the stresses  $\{\sigma\}$  and strains  $\{\epsilon\}$  are column vectors, each having six elements. Alternatively, the generalized Hooke's law relating strains to stresses can be written as

$$\epsilon_i = S_{ij}\sigma_j, \quad i, j = 1, 2, \dots, 6 \quad (2.5)$$

or in matrix form as

$$\{\epsilon\} = [S]\{\sigma\} \quad (2.6)$$

where  $[S]$  is the compliance matrix, which is the inverse of the stiffness matrix ( $[S] = [C]^{-1}$ ). For a brief review of matrix operations, please refer to Appendix A. As shown later, due to the existence of the strain energy density, the stiffness and compliance matrices are symmetric. Note that nothing has been said thus far about any symmetry that the material itself may have. All real materials have some form of symmetry, however, and no known material is completely anisotropic.

Before discussing the various simplifications of the stress–strain relationships, it is appropriate to deal with the problem of heterogeneity in the composite material. Recall that the stress–strain relationships presented up to now are only valid *at a point* in the material, and that the stresses, strains, and elastic moduli will change as we move from point to point in a composite (i.e., the elastic moduli for the matrix material are different from those of the fiber). In order to analyze the macromechanical behavior of the composite, it is more convenient to deal with *averaged* stresses and strains that are related by “effective moduli” of an equivalent homogeneous material. Figure 2.3 shows schematically how the stresses in a heterogeneous composite may be nonuniform even though the imposed strain is uniform.

As shown in Figure 2.3, if the scale of the inhomogeneity in a material can be characterized by some length dimension,  $d$ , then the length dimension,  $L$ , over which the macromechanical averaging is to take place, must be much larger than  $d$  if the average stresses and strains are to be related by effective moduli of an equivalent homogeneous material. We now define the average

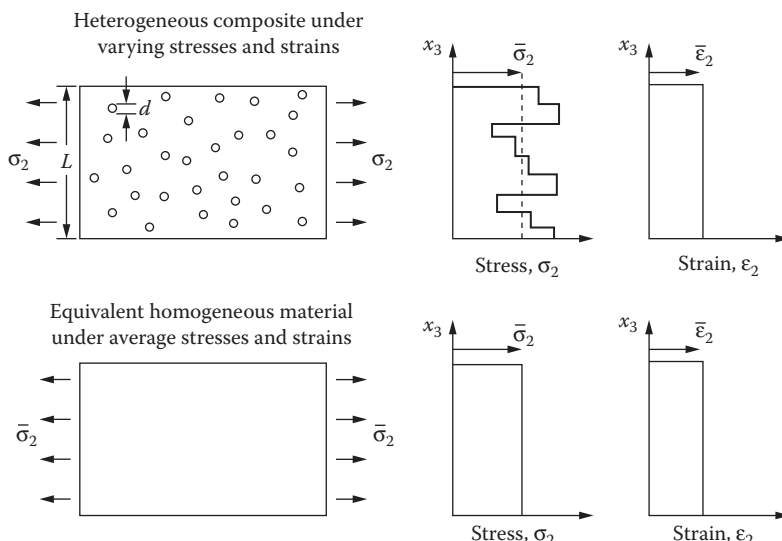


**FIGURE 2.3**  
Concept of an equivalent homogeneous material.

stresses,  $\bar{\sigma}_i$ , and the average strains,  $\bar{\varepsilon}_i$ , ( $i = 1, 2, \dots, 6$ ) to be averaged over a volume  $V$ , which is characterized by the dimension  $L$ , so that [1]

$$\bar{\sigma}_i = \frac{\int_V \sigma_i dV}{\int_V dV} = \frac{\int_V \sigma_i dV}{V} \quad (2.7)$$

$$\bar{\varepsilon}_i = \frac{\int_V \varepsilon_i dV}{\int_V dV} = \frac{\int_V \varepsilon_i dV}{V} \quad (2.8)$$

where  $i = 1, 2, \dots, 6$  and  $\sigma_i$  and  $\varepsilon_i$  are the position-dependent stresses and strains at a point, respectively. If these averaged stresses and strains are used in place of the stresses and strains at a point, the generalized Hooke's law (i.e., Equation 2.3) becomes

$$\bar{\sigma}_i = C_{ij} \bar{\varepsilon}_j \quad (2.9)$$

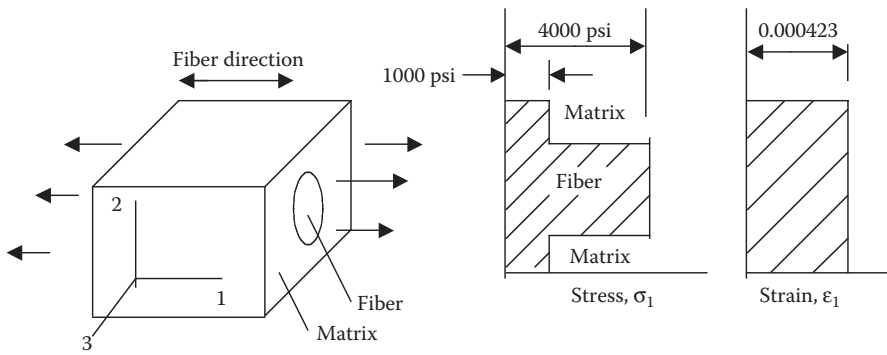
and the elastic moduli  $C_{ij}$  then become the "effective moduli" of the equivalent homogeneous material in volume  $V$ . Similarly, the "effective compliances"  $S_{ij}$  may be defined by

$$\bar{\varepsilon}_i = S_{ij} \bar{\sigma}_j \quad (2.10)$$

For example, in Figure 2.3, the scale of the inhomogeneity is assumed to be the diameter of the fiber,  $d$ , and the averaging dimension,  $L$ , is assumed to be a characteristic lamina dimension such that  $L \gg d$ . The effective modulus  $C_{22}$  of the lamina is thus defined as  $C_{22} = \bar{\sigma}_2 / \bar{\varepsilon}_2$ . In the remainder of this book, lamina properties are assumed to be effective properties as described above.

### Example 2.1

A representative volume element (RVE) from a fiber-reinforced composite lamina is shown in Figure 2.4, along with the longitudinal stress and strain distributions across the fiber and matrix materials in the section. The fiber has a uniform longitudinal stress of 4000 psi (along the 1 direction) and a diameter of 0.0003 in., while the matrix has a uniform longitudinal stress of 1000 psi. A uniform longitudinal strain of 0.000423 in./in. acts over the entire section. The RVE has edge dimensions 0.0004 in.  $\times$  0.0004 in. in the 23 plane. Assume that the cross-sectional dimensions of the section do not change along the longitudinal direction, and use the concept of the effective modulus of an equivalent homogeneous material to find the numerical value of the effective longitudinal modulus,  $E_1$  (or  $E_{11}$ ) of the composite.

**FIGURE 2.4**

Stress and strain distributions for calculation of effective modulus in Example 2.1.

### SOLUTION

The effective longitudinal modulus is given by

$$E_1 = \frac{\bar{\sigma}_1}{\bar{\epsilon}_1}$$

where the average stress is

$$\begin{aligned} \bar{\sigma}_1 &= \frac{\int \sigma_1 dV}{\int dV} = \frac{\int \sigma_1 dA}{\int dA} = \frac{\sigma_f A_f + \sigma_m A_m}{A_f + A_m} \\ &= \frac{(4000) \frac{\pi}{4} (0.0003)^2 + (1000) \left[ (0.0004)^2 - \frac{\pi}{4} (0.0003)^2 \right]}{(0.0004)^2} = 2325 \text{ psi} \end{aligned}$$

and the stresses and cross-sectional areas of the fiber and matrix are denoted by the subscripts f and m, respectively. The average strain is  $\bar{\epsilon}_1 = 0.000423$ , so the effective modulus is

$$E_1 = \frac{\bar{\sigma}_1}{\bar{\epsilon}_1} = \frac{2325}{0.000423} = 5.496(10^6) \text{ psi}$$

## 2.3 Symmetry in Stress–Strain Relationships

In this section, the generalized anisotropic Hooke's law will be simplified and specialized using various symmetry conditions. The first symmetry

condition, which has nothing to do with material symmetry, is strictly a result of the existence of a strain energy density function [3,6]. The strain energy density function,  $W$ , is such that the stresses can be derived according to the equation

$$\sigma_i = \frac{\partial W}{\partial \epsilon_i} = C_{ij}\epsilon_j \quad (2.11)$$

where

$$W = \frac{1}{2}C_{ij}\epsilon_i\epsilon_j \quad (2.12)$$

By taking a second derivative of  $W$ , we find that

$$\frac{\partial^2 W}{\partial \epsilon_i \partial \epsilon_j} = C_{ij} \quad (2.13)$$

and by reversing the order of differentiation, we find that

$$\frac{\partial^2 W}{\partial \epsilon_j \partial \epsilon_i} = C_{ji} \quad (2.14)$$

Since the result must be the same regardless of the order of the differentiation,  $C_{ij} = C_{ji}$ , the stiffness matrix is symmetric. Similarly,  $W$  can be expressed in terms of compliances and stresses, and by taking two derivatives with respect to stresses, it can be shown that  $S_{ij} = S_{ji}$ . Thus, the compliance matrix is also symmetric. Due to these mathematical manipulations, only 21 of the 36 anisotropic elastic moduli or compliances are independent, and we still have not said anything about any inherent symmetry of the material itself.

According to the above developments, the stiffness matrix for the linear elastic anisotropic material without any material property symmetry is of the form

$$C_{ij} = \begin{bmatrix} C_{11} & C_{12} & C_{13} & C_{14} & C_{15} & C_{16} \\ & C_{22} & C_{23} & C_{24} & C_{25} & C_{26} \\ & & C_{33} & C_{34} & C_{35} & C_{36} \\ & & & C_{44} & C_{45} & C_{46} \\ & & & & C_{55} & C_{56} \\ & & & & & C_{66} \end{bmatrix} \quad (2.15)$$

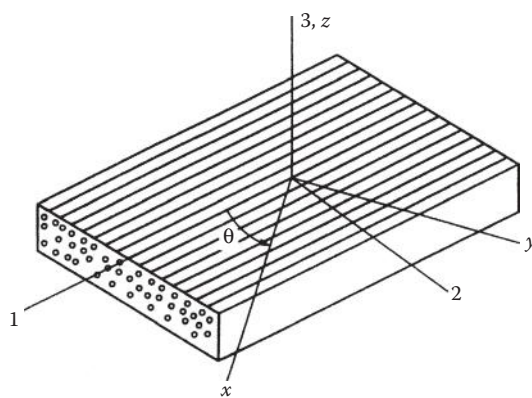
SYM

Further simplifications of the stiffness matrix are possible only if the material properties have some form of symmetry. For example, a *monoclinic* material

has one plane of material property symmetry. It can be shown [3,7] that since the  $C_{ij}$  for such a material must be invariant under a transformation of coordinates corresponding to reflection in the plane of symmetry, the number of independent elastic constants for the monoclinic material is reduced to 13. Such a symmetry condition is generally not of practical interest in composite material analysis, however.

As shown in Figure 2.5, a unidirectional composite lamina has three mutually orthogonal planes of material property symmetry (i.e., the 12, 23, and 13 planes) and is called an *orthotropic* material. The term “orthotropic” alone is not sufficient to describe the form of the stiffness matrix, however. Unlike the anisotropic stiffness matrix (Equation 2.15), which has the same form (but different terms) for different coordinate systems, the form of the stiffness matrix for the orthotropic material depends on the coordinate system used. The 123 coordinate axes in Figure 2.5 are referred to as the *principal material coordinates* since they are associated with the reinforcement directions. Invariance of the  $C_{ij}$  under transformations of coordinates corresponding to reflections in two orthogonal planes [3,7] may be used to show that the stiffness matrix for a so-called *specially orthotropic* material associated with the principal material coordinates is of the form

$$C_{ij} = \begin{bmatrix} C_{11} & C_{12} & C_{13} & 0 & 0 & 0 \\ C_{21} & C_{22} & C_{23} & 0 & 0 & 0 \\ C_{31} & C_{32} & C_{33} & 0 & 0 & 0 \\ \text{SYM} & & & C_{44} & 0 & 0 \\ & & & & C_{55} & 0 \\ & & & & & C_{66} \end{bmatrix} \quad (2.16)$$

**FIGURE 2.5**

Orthotropic lamina with principal (123) and nonprincipal (xyz) coordinate systems.

A stiffness matrix of this form in terms of engineering constants will be obtained in the next section using observations from simple experiments. Note that there are only 12 nonzero elastic constants and 9 independent elastic constants for the specially orthotropic material.

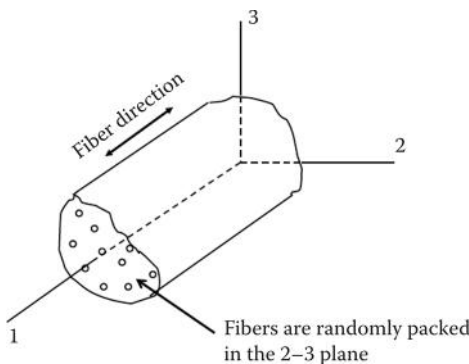
Table 2.1 summarizes similar results for the different combinations of materials and coordinate systems used in this book. It will also be shown later that if the stress-strain relationships for the same orthotropic material are developed for a nonprincipal coordinate system  $xyz$  as shown in Figure 2.5, the stiffness matrix is of the same form as that of the anisotropic material in Equation 2.15. In such a nonprincipal or off-axis coordinate system, the material is called *generally orthotropic* (Table 2.1). There are two other types of material symmetry that are important in the study of composites. The details will be developed in the next section, but the general forms of the stiffness matrices are given here for completeness. In most composites, the fiber-packing arrangement is statistically random in nature (Figure 2.6), so that the properties are nearly the same in any direction perpendicular to the fibers (i.e., properties along the 2 direction are the same as those along the 3 direction, and properties are invariant to rotations about the 1 axis), and the material is *transversely isotropic*. If the fibers were packed in a regular array, such as a square array or a triangular array, the material would not be transversely isotropic. As shown later in Chapter 3, real composites typically have random fiber packing, and can be considered transversely isotropic.

For such a material, we would expect that  $C_{22} = C_{33}$ ,  $C_{12} = C_{13}$ ,  $C_{55} = C_{66}$ , and that  $C_{44}$  would not be independent from the other stiffnesses. It can be

**TABLE 2.1**

Elastic Coefficients in the Stress–Strain Relationships for Different Materials and Coordinate Systems

Material and Coordinate System	Number of Nonzero Coefficients	Number of Independent Coefficients
<i>3-D Case</i>		
Anisotropic	36	21
Generally orthotropic (nonprincipal coordinates)	36	9
Specially orthotropic (principal coordinates)	12	9
Specially orthotropic, transversely isotropic	12	5
Isotropic	12	2
<i>2-D Case (Lamina)</i>		
Anisotropic	9	6
Generally orthotropic (nonprincipal coordinates)	9	4
Specially orthotropic (principal coordinates)	5	4
Balanced orthotropic, or square symmetric (principal coordinates)	5	3
Isotropic	5	2

**FIGURE 2.6**

Specially orthotropic, transversely isotropic material.

shown [1] that the complete stiffness matrix for a specially orthotropic, transversely isotropic material is of the form

$$C_{ij} = \begin{bmatrix} C_{11} & C_{12} & C_{12} & 0 & 0 & 0 \\ & C_{22} & C_{23} & 0 & 0 & 0 \\ & & C_{22} & 0 & 0 & 0 \\ \text{SYM} & & & (C_{22} - C_{23}) / 2 & 0 & 0 \\ & & & & C_{66} & 0 \\ & & & & & C_{66} \end{bmatrix} \quad (2.17)$$

where the 23 plane and all parallel planes are assumed to be planes of isotropy. In the next section, a stiffness matrix of the same form will be derived, except that the so-called *engineering constants* will be used instead of the  $C_{ij}$ . Note that now there are still 12 nonzero elastic moduli but that only 5 are independent (Table 2.1).

The simplest form of the stress–strain relationship occurs when the material is *isotropic* and every coordinate axis is an axis of symmetry. Now we would expect that  $C_{11} = C_{22} = C_{33}$ ,  $C_{12} = C_{13} = C_{23}$ , that  $C_{44} = C_{55} = C_{66}$ , and that  $C_{44}$  again would not be independent from the other  $C_{ij}$ . The isotropic stiffness matrix is of the form [1]

$$C_{ij} = \begin{bmatrix} C_{11} & C_{12} & C_{12} & 0 & 0 & 0 \\ & C_{11} & C_{12} & 0 & 0 & 0 \\ & & C_{11} & 0 & 0 & 0 \\ \text{SYM} & & & (C_{11} - C_{12}) / 2 & 0 & 0 \\ & & & & (C_{11} - C_{12}) / 2 & 0 \\ & & & & & (C_{11} - C_{12}) / 2 \end{bmatrix} \quad (2.18)$$

Now there are still 12 nonzero elastic constants, but only 2 are independent (Table 2.1). Similar equations based on the engineering constants will be derived in the next section. Equations of this form can be found in any mechanics of materials book, and the design of metallic components is usually based on such formulations.

---

## 2.4 Orthotropic and Isotropic Engineering Constants

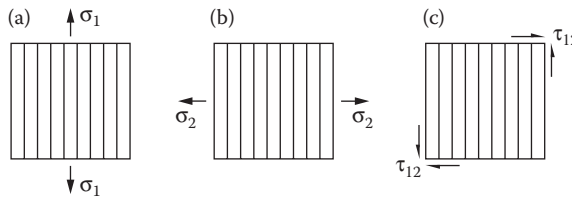
In the previous section, symmetry conditions were shown to reduce the number of elastic constants (the  $C_{ij}$  or  $S_{ij}$ ) in the stress-strain relationships for several important classes of materials and the general forms of the relationships were presented. When a material is characterized experimentally, however, the so-called “engineering constants” such as Young’s modulus (or modulus of elasticity), shear modulus, and Poisson’s ratio are usually measured instead of the  $C_{ij}$  or the  $S_{ij}$ . The engineering constants are also widely used in analysis and design because they are easily defined and interpreted in terms of simple states of stress and strain. In this section, several simple tests and their resulting states of stress and strain will be used to develop the 3-D and 2-D stress-strain relationships for orthotropic and isotropic materials.

Consider a simple uniaxial tensile test consisting of an applied longitudinal normal stress,  $\sigma_1$ , along the reinforcement direction (i.e., the 1 direction) of a specimen from an orthotropic material, as shown in Figure 2.7a. It is assumed that all other stresses are equal to zero. Typical experimental stress-strain data from such a test on a carbon/epoxy composite are shown in Figure 2.8a from Ref. [8], where both longitudinal strains  $\varepsilon_1$  and transverse Poisson strains  $\varepsilon_2$  are shown. More details on testing of composites will be provided in Chapter 10.

Within the linear range the experimental observation is that the resulting strains associated with the 123 axes can be expressed empirically in terms of “engineering constants” as

$$\begin{aligned}\varepsilon_1 &= \frac{\sigma_1}{E_1} \\ \varepsilon_2 &= -v_{12}\varepsilon_1 = -\frac{v_{12}\sigma_1}{E_1} \\ \varepsilon_3 &= -v_{13}\varepsilon_1 = -\frac{v_{13}\sigma_1}{E_1} \\ \gamma_{12} &= \gamma_{23} = \gamma_{13} = 0\end{aligned}\tag{2.19}$$

where  $E_1$  = longitudinal modulus of elasticity associated with the 1 direction, and  $v_{ij} = -\varepsilon_j/\varepsilon_i$  is the Poisson’s ratio, the ratio of the strain in the  $j$  direction to

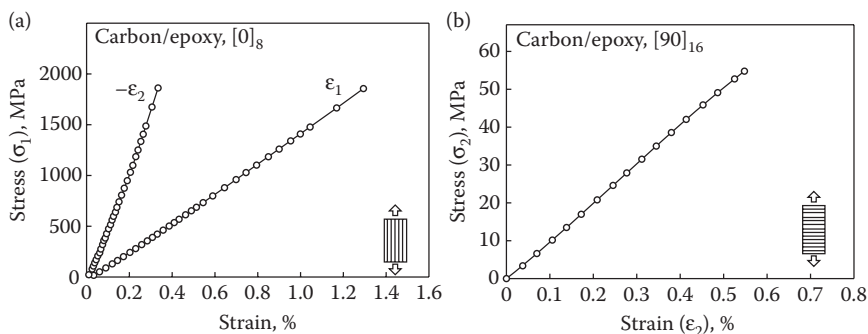
**FIGURE 2.7**

Simple states of stress used to define lamina engineering constants. (a) Applied longitudinal normal stress, (b) applied transverse normal stress, and (c) applied in-plane shear stress.

the strain in the perpendicular  $i$  direction when the applied stress is in the  $i$  direction.

Recall from mechanics of materials [2] that for isotropic materials, no subscripts are needed on properties such as the modulus of elasticity and Poisson's ratio because the properties are the same in all directions. This is not the case with orthotropic materials, however, and subscripts are needed on these properties because of their directional nature. For example,  $E_1 \neq E_2$  and  $v_{12} \neq v_{21}$ . Note that, as with isotropic materials, a negative sign must be used in the definition of Poisson's ratio. A property like  $v_{12}$  is usually called a *major Poisson's ratio*, whereas a property like  $v_{21}$  is called a *minor Poisson's ratio*. As with isotropic materials, a normal stress induces only normal strains, and all shear strains are equal to zero. This lack of shear/normal interaction is observed only for the principal material coordinate system, however. For any other set of coordinates, the so-called "shear-coupling" effect is present. This effect will be discussed in more detail later.

Now consider a similar experiment where a transverse normal stress,  $\sigma_2$ , is applied to the same material as shown in Figure 2.7b, with all other stresses

**FIGURE 2.8**

Typical stress–strain data from (a) longitudinal tensile test and (b) transverse tensile test of carbon/epoxy composite. (Reprinted from Adams, D. F., Carlsson, L. A., and Pipes, R. B. 2003. *Experimental Characterization of Advanced Composite Materials*, Third Edition, CRC Press, Boca Raton, FL. With permission.)

being equal to zero. Typical stress-strain data from such a test on a carbon/epoxy composite are shown in Figure 2.8b from Ref. [8]. Now the experimental observation is that the resulting strains can be expressed as

$$\begin{aligned}\varepsilon_2 &= \frac{\sigma_2}{E_2} \\ \varepsilon_1 &= -v_{21}\varepsilon_2 = -\frac{v_{21}\sigma_2}{E_2} \\ \varepsilon_3 &= -v_{23}\varepsilon_2 = -\frac{v_{23}\sigma_2}{E_2} \\ \gamma_{12} &= \gamma_{23} = \gamma_{13} = 0\end{aligned}\tag{2.20}$$

where  $E_2$  is the transverse modulus of elasticity associated with the 2 direction. A similar result for an applied transverse normal stress,  $\sigma_3$ , can be obtained by changing the appropriate subscripts in Equation 2.20.

Next, consider a shear test where a pure shear stress,  $\sigma_{12} = \tau_{12}$ , is applied to the material in the 12 plane, as shown in Figure 2.7c. Now the experimental observation is that the resulting strains can be written as

$$\begin{aligned}\gamma_{12} &= \frac{\tau_{12}}{G_{12}} \\ \varepsilon_1 &= \varepsilon_2 = \varepsilon_3 = \gamma_{13} = \gamma_{23} = 0\end{aligned}\tag{2.21}$$

where  $G_{12}$  is the shear modulus associated with the 12 plane. Similar results can be obtained for pure shear in the 13 and 23 planes by changing the appropriate subscripts in Equation 2.21. Again, notice that there is no shear/normal interaction (or shear coupling). As before, however, this is only true for the principal material axes.

Finally, consider a general 3-D state of stress consisting of all possible normal and shear stresses associated with the 123 axes as shown in Figures 2.1 and 2.6. Since we are dealing with linear behavior, it is appropriate to use superposition and add all the resulting strains due to the simple uniaxial and shear tests, as given in Equations 2.19 through 2.21, and similar equations as described above. The resulting set of equations is given below:

$$\left\{ \begin{array}{l} \varepsilon_1 \\ \varepsilon_2 \\ \varepsilon_3 \\ \gamma_{23} \\ \gamma_{31} \\ \gamma_{12} \end{array} \right\} = \left[ \begin{array}{cccccc} 1/E_1 & -v_{21}/E_2 & -v_{31}/E_3 & 0 & 0 & 0 \\ -v_{12}/E_1 & 1/E_2 & -v_{32}/E_3 & 0 & 0 & 0 \\ -v_{13}/E_1 & -v_{23}/E_2 & 1/E_3 & 0 & 0 & 0 \\ 0 & 0 & 0 & 1/G_{23} & 0 & 0 \\ 0 & 0 & 0 & 0 & 1/G_{31} & 0 \\ 0 & 0 & 0 & 0 & 0 & 1/G_{12} \end{array} \right] \left\{ \begin{array}{l} \sigma_1 \\ \sigma_2 \\ \sigma_3 \\ \tau_{23} \\ \tau_{31} \\ \tau_{12} \end{array} \right\} \tag{2.22}$$

Note that the compliance matrix is of the same form as the stiffness matrix for a specially orthotropic material (Equation 2.16) as it should be because  $[S] = [C]^{-1}$ . Note also that due to symmetry of the compliance matrix,  $v_{ij}/E_i = v_{ji}/E_j$  and only nine of the engineering constants are independent.

If we now consider a simple uniaxial tensile test consisting of an applied normal stress,  $\sigma_x$ , along some arbitrary  $x$  axis as shown in Figure 2.5 we find that the full complement of normal strains and shear strains are developed. The generation of shear strains due to normal stresses and normal strains due to shear stresses is often referred to as the “shear-coupling effect.” As a result of shear coupling, all the zeros disappear in the compliance matrix and it becomes fully populated for the general 3-D state of stress associated with the arbitrary  $xyz$  axes; this is the *generally orthotropic* material. The stiffness or compliance matrices for the generally orthotropic material are of the same form as those for the general anisotropic material (Equation 2.15), although the material still has its orthotropic symmetries with respect to the principal material axes. Obviously then, the experimental characterization of such a material is greatly simplified by testing it as a specially orthotropic material along the principal material directions. As shown later, once we have the stiffnesses or compliances associated with the 123 axes, we can obtain those for an arbitrary off-axis coordinate system such as  $xyz$  by transformation equations involving the angles between the axes.

If the material being tested is specially orthotropic and transversely isotropic as shown in Figure 2.6, the subscripts 2 and 3 in Equation 2.22 are interchangeable, and we have  $G_{13} = G_{12}$ ,  $E_2 = E_3$ ,  $v_{21} = v_{31}$ , and  $v_{23} = v_{32}$ . In addition, the familiar relationship among the isotropic engineering constants [2] is now valid for the engineering constants associated with the 23 plane, so that

$$G_{23} = \frac{E_2}{2(1 + v_{32})} \quad (2.23)$$

Now the compliance matrix is of the same form as Equation 2.17 and only five of the engineering constants are independent.

Finally, for the isotropic material, there is no need for subscripts and  $G_{13} = G_{23} = G_{12} = G$ ,  $E_1 = E_2 = E_3 = E$ ,  $v_{12} = v_{23} = v_{13} = v$ , and  $G = E/2(1 + v)$ . Now the compliance matrix is of the same form as Equation 2.18 and only two of the engineering constants are independent.

## 2.5 Specially Orthotropic Lamina

As shown later in the analysis of laminates, the lamina is often assumed to be in a simple 2-D state of stress (or plane stress). In this case the specially

orthotropic stress-strain relationships in Equation 2.22 can be simplified by letting  $\sigma_3 = \tau_{23} = \tau_{31} = 0$ , so that

$$\begin{Bmatrix} \varepsilon_1 \\ \varepsilon_2 \\ \gamma_{12} \end{Bmatrix} = \begin{bmatrix} S_{11} & S_{12} & 0 \\ S_{21} & S_{22} & 0 \\ 0 & 0 & S_{66} \end{bmatrix} \begin{Bmatrix} \sigma_1 \\ \sigma_2 \\ \tau_{12} \end{Bmatrix} \quad (2.24)$$

where the compliances  $S_{ij}$  and the engineering constants are related by the equations

$$\begin{aligned} S_{11} &= \frac{1}{E_1}, & S_{22} &= \frac{1}{E_2}, \\ S_{12} = S_{21} &= -\frac{v_{21}}{E_2} = -\frac{v_{12}}{E_1}, & S_{66} &= \frac{1}{G_{12}} \end{aligned} \quad (2.25)$$

Thus, there are five nonzero compliances and only four independent compliances for the specially orthotropic lamina (Table 2.1). The lamina stresses in terms of *tensor* strains are given by

$$\begin{Bmatrix} \sigma_1 \\ \sigma_2 \\ \tau_{12} \end{Bmatrix} = \begin{bmatrix} Q_{11} & Q_{12} & 0 \\ Q_{21} & Q_{22} & 0 \\ 0 & 0 & 2Q_{66} \end{bmatrix} \begin{Bmatrix} \varepsilon_1 \\ \varepsilon_2 \\ \frac{\gamma_{12}}{2} \end{Bmatrix} \quad (2.26)$$

where the  $Q_{ij}$  are the components of the lamina stiffness matrix, which are related to the compliances and the engineering constants by (see the discussion of matrix inversion in Appendix A)

$$\begin{aligned} Q_{11} &= \frac{S_{22}}{S_{11}S_{22} - S_{12}^2} = \frac{E_1}{1 - v_{12}v_{21}} \\ Q_{12} &= -\frac{S_{12}}{S_{11}S_{22} - S_{12}^2} = \frac{v_{12}E_2}{1 - v_{12}v_{21}} = Q_{21} \\ Q_{22} &= \frac{S_{11}}{S_{11}S_{22} - S_{12}^2} = \frac{E_2}{1 - v_{12}v_{21}} \\ Q_{66} &= \frac{1}{S_{66}} = G_{12} \end{aligned} \quad (2.27)$$

Note that the factor of 2 has been introduced in the  $Q_{66}$  term of Equation 2.26 to compensate for the use of tensor shear strain  $\varepsilon_{12} = \gamma_{12}/2$ . The reason for

this will become apparent in the next section. As shown later, the experimental characterization of the orthotropic lamina involves the measurement of four independent engineering constants such as  $E_1$ ,  $E_2$ ,  $G_{12}$ , and  $v_{12}$ . Typical values of these properties for several composites are shown in Table 2.2.

The balanced orthotropic lamina shown schematically in Figure 2.9 often occurs in practice when the fiber reinforcement is woven or cross-plyed at  $0^\circ$  and  $90^\circ$ . In this case, the number of independent elastic constants in Equations 2.24 through 2.27 is reduced to 3 because of the double symmetry of properties with respect to the 1 and 2 axes (Table 2.1).

Thus, for the balanced orthotropic lamina, we have  $E_1 = E_2$ ,  $Q_{11} = Q_{22}$ , and  $S_{11} = S_{22}$ .

### Example 2.2

An orthotropic, transversely isotropic material is subjected to a two-dimensional stress condition along the principal material axes 1,2,3 as shown in Figure 2.10 and the engineering constants for the material are as follows:

$$E_1 = 20 \times 10^6 \text{ psi}, G_{12} = 1 \times 10^6 \text{ psi}, E_2 = 1.5 \times 10^6 \text{ psi}, v_{12} = 0.3, v_{23} = 0.2$$

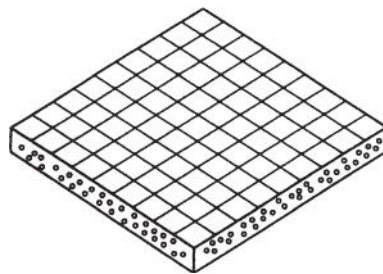
Determine all strains associated with the 1,2,3 axes.

**TABLE 2.2**

Typical Values of Lamina Engineering Constants for Several Composites Having Fiber Volume Fraction  $v_f$

Material	$E_1$ (Msi [GPa])	$E_2$ (Msi [GPa])	$G_{12}$ (Msi [GPa])	$v_{12}$	$v_f$
T300/934 carbon/epoxy	19.0 (131)	1.5 (10.3)	1.0 (6.9)	0.22	0.65
AS/3501 carbon/epoxy	20.0 (138)	1.3 (9.0)	1.0 (6.9)	0.3	0.65
P-100/ERL 1962 pitch/carbon/epoxy	68.0 (468.9)	0.9 (6.2)	0.81 (5.58)	0.31	0.62
IM7/8551-7 carbon/toughened epoxy	23.5(162)	1.21(8.34)	0.3(2.07)	0.34	0.6
AS4/APC2 carbon/PEEK	19.1(131)	1.26(8.7)	0.73(5.0)	0.28	0.58
Boron/6061 boron/aluminum	34.1(235)	19.9(137)	6.8(47.0)	0.3	0.5
Kevlar™ 49/934 aramid/epoxy	11.0 (75.8)	0.8 (5.5)	0.33 (2.3)	0.34	0.65
Scotchply™ 1002 E-glass/epoxy	5.6 (38.6)	1.2 (8.27)	0.6 (4.14)	0.26	0.45
Boron/5505 boron/epoxy	29.6 (204.0)	2.68 (18.5)	0.81 (5.59)	0.23	0.5
Spectra™ 900/826 polyethylene/epoxy	4.45 (30.7)	0.51 (3.52)	0.21 (1.45)	0.32	0.65
E-glass/470-36 E-glass/vinylester	3.54 (24.4)	1.0 (6.87)	0.42 (2.89)	0.32	0.30

*Note:* Kevlar™ is a registered trademark of DuPont Company, Wilmington, Delaware; Scotchply™ is a registered trademark of 3M Company, St. Paul, Minnesota; and Spectra™ is a registered trademark of Honeywell International, Inc.

**FIGURE 2.9**

Balanced orthotropic lamina consisting of fibers oriented at 0° and 90°.

### SOLUTION

Due to Symmetry of the Compliance Matrix in Equation 2.22

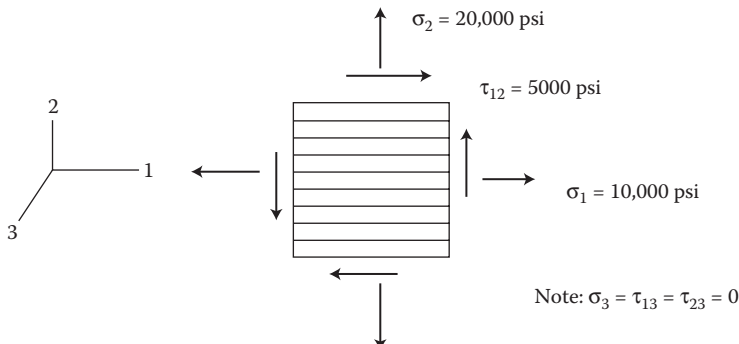
$$\frac{v_{21}}{E_2} = \frac{v_{12}}{E_1}$$

and due to transverse isotropy,  $v_{13} = v_{12}$ . Therefore, from Equation 2.22, the strains are

$$\epsilon_1 = \frac{\sigma_1}{E_1} - \frac{v_{12}}{E_1} \sigma_2 = \frac{10 \times 10^3}{20 \times 10^6} - \frac{0.3(20 \times 10^3)}{20 \times 10^6} = 0.002$$

$$\epsilon_2 = -\frac{v_{12}}{E_1} \sigma_1 + \frac{\sigma_2}{E_2} = -\frac{0.3(10 \times 10^3)}{20 \times 10^6} + \frac{20 \times 10^3}{1.5 \times 10^6} = 0.01318$$

$$\epsilon_3 = -\frac{v_{12}}{E_1} \sigma_1 - \frac{v_{23}}{E_2} \sigma_2 = -\frac{0.3(10 \times 10^3)}{20 \times 10^6} - \frac{0.2(20 \times 10^3)}{1.5 \times 10^6} = -0.002816$$

**FIGURE 2.10**

Stress condition for Example 2.2.

$$\gamma_{12} = \frac{\tau_{12}}{G_{12}} = \frac{5 \times 10^3}{1 \times 10^6} = 0.005$$

$$\gamma_{31} = \frac{\tau_{31}}{G_{31}} = 0$$

$$\gamma_{23} = \frac{\tau_{23}}{G_{23}} = 0$$

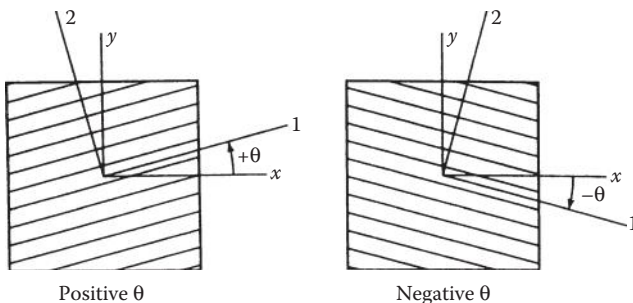
So even though the stress condition is two-dimensional, the resulting strains are three-dimensional due to the Poisson strain  $\varepsilon_3$ .

## 2.6 Generally Orthotropic Lamina

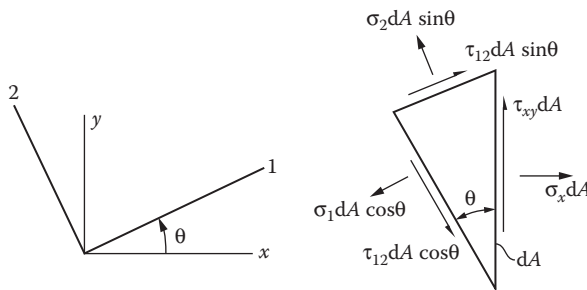
In the analysis of laminates having multiple laminae, it is often necessary to know the stress–strain relationships for the *generally orthotropic lamina* in nonprincipal coordinates (or “off-axis” coordinates) such as  $x$  and  $y$  in Figure 2.5. Fortunately, the elastic constants in these so-called “off-axis” stress–strain relationships are related to the four independent elastic constants in the principal material coordinates and the lamina orientation angle. The sign convention for the lamina orientation angle,  $\theta$ , is given in Figure 2.11. The relationships are found by combining the equations for transformation of stress and strain components from the 12 axes to the  $xy$  axes.

Relationships for transformation of stress components between coordinate axes may be obtained by writing the equations of static equilibrium for the wedge-shaped differential element in Figure 2.12. For example, the force equilibrium along the  $x$  direction is given by

$$\sum F_x = \sigma_x dA - \sigma_1 dA \cos^2 \theta - \sigma_2 dA \sin^2 \theta + 2\tau_{12} dA \sin \theta \cos \theta = 0 \quad (2.28)$$



**FIGURE 2.11**  
Sign convention for lamina orientation.

**FIGURE 2.12**

Differential element under static equilibrium with forces in two coordinate systems.

which, after dividing through by  $dA$ , gives an equation relating  $\sigma_x$  to the stresses in the 12 system:

$$\sigma_x = \sigma_1 \cos^2 \theta + \sigma_2 \sin^2 \theta - 2\tau_{12} \sin \theta \cos \theta \quad (2.29)$$

Using a similar approach, the complete set of transformation equations for the stresses in the  $xy$ -coordinate system can be developed and written in matrix form as

$$\begin{Bmatrix} \sigma_x \\ \sigma_y \\ \tau_{xy} \end{Bmatrix} = \begin{bmatrix} c^2 & s^2 & -2cs \\ s^2 & c^2 & 2cs \\ cs & -cs & c^2 - s^2 \end{bmatrix} \begin{Bmatrix} \sigma_1 \\ \sigma_2 \\ \tau_{12} \end{Bmatrix} = [T]^{-1} \begin{Bmatrix} \sigma_1 \\ \sigma_2 \\ \tau_{12} \end{Bmatrix} \quad (2.30)$$

and the stresses in the 12 system can be written as

$$\begin{Bmatrix} \sigma_1 \\ \sigma_2 \\ \tau_{12} \end{Bmatrix} = [T] \begin{Bmatrix} \sigma_x \\ \sigma_y \\ \tau_{xy} \end{Bmatrix} \quad (2.31)$$

where  $c = \cos \theta$ ,  $s = \sin \theta$ , and the transformation matrix,  $[T]$ , is defined as

$$[T] = \begin{bmatrix} c^2 & s^2 & 2cs \\ s^2 & c^2 & -2cs \\ -cs & cs & c^2 - s^2 \end{bmatrix} \quad (2.32)$$

A procedure for determining the matrix inverse  $[T]^{-1}$  is described in Appendix A. It can also be shown [2,3] that the *tensor strains* transform the same way as the stresses, and that

$$\begin{Bmatrix} \varepsilon_1 \\ \varepsilon_2 \\ \gamma_{12}/2 \end{Bmatrix} = [T] \begin{Bmatrix} \varepsilon_x \\ \varepsilon_y \\ \gamma_{xy}/2 \end{Bmatrix} \quad (2.33)$$

Substituting Equation 2.33 into Equation 2.26, and then substituting the resulting equations into Equation 2.30, we find that

$$\begin{Bmatrix} \sigma_x \\ \sigma_y \\ \tau_{xy} \end{Bmatrix} = [T]^{-1}[Q^*][T] \begin{Bmatrix} \varepsilon_x \\ \varepsilon_y \\ \gamma_{xy}/2 \end{Bmatrix} \quad (2.34)$$

where the components of the stiffness matrix  $[Q^*]$  in Equations 2.34 are defined as  $Q_{ij}^* = Q_{ij}$  for all  $ij$  except  $Q_{66}^* = 2Q_{66}$  as shown in Equations 2.26.

Carrying out the indicated matrix multiplications and converting back to engineering strains, we find that

$$\begin{Bmatrix} \sigma_x \\ \sigma_y \\ \tau_{xy} \end{Bmatrix} = \begin{bmatrix} \bar{Q}_{11} & \bar{Q}_{12} & \bar{Q}_{16} \\ \bar{Q}_{12} & \bar{Q}_{22} & \bar{Q}_{26} \\ \bar{Q}_{16} & \bar{Q}_{26} & \bar{Q}_{66} \end{bmatrix} \begin{Bmatrix} \varepsilon_x \\ \varepsilon_y \\ \gamma_{xy} \end{Bmatrix} \quad (2.35)$$

where the  $\bar{Q}_{ij}$  are the components of the transformed lamina stiffness matrix which are defined as follows:

$$\begin{aligned} \bar{Q}_{11} &= Q_{11}c^4 + Q_{22}s^4 + 2(Q_{12} + 2Q_{66})s^2c^2 \\ \bar{Q}_{12} &= (Q_{11} + Q_{22} - 4Q_{66})s^2c^2 + Q_{12}(c^4 + s^4) \\ \bar{Q}_{22} &= Q_{11}s^4 + Q_{22}c^4 + 2(Q_{12} + 2Q_{66})s^2c^2 \\ \bar{Q}_{16} &= (Q_{11} - Q_{12} - 2Q_{66})c^3s - (Q_{22} - Q_{12} - 2Q_{66})cs^3 \\ \bar{Q}_{26} &= (Q_{11} - Q_{12} - 2Q_{66})cs^3 - (Q_{22} - Q_{12} - 2Q_{66})c^3s \\ \bar{Q}_{66} &= (Q_{11} + Q_{22} - 2Q_{12} - 2Q_{66})s^2c^2 + Q_{66}(s^4 + c^4) \end{aligned} \quad (2.36)$$

Although the transformed lamina stiffness matrix now has the same form as that of an anisotropic material with nine nonzero coefficients, only four of the coefficients are independent because they can all be expressed in terms of the four independent lamina stiffnesses of the specially orthotropic material. That is, the material is still orthotropic, but it is not recognizable as such in the off-axis coordinates. As in the 3-D case, it is obviously much easier to characterize the lamina experimentally in the principal material coordinates than in the off-axis coordinates. Recall that the engineering constants, the properties that are normally measured, are related to the lamina stiffnesses by Equation 2.27.

Alternatively, the strains can be expressed in terms of the stresses as

$$\begin{Bmatrix} \boldsymbol{\varepsilon}_x \\ \boldsymbol{\varepsilon}_y \\ \gamma_{xy} \end{Bmatrix} = \begin{bmatrix} \bar{S}_{11} & \bar{S}_{12} & \bar{S}_{16} \\ \bar{S}_{12} & \bar{S}_{22} & \bar{S}_{26} \\ \bar{S}_{16} & \bar{S}_{26} & \bar{S}_{66} \end{bmatrix} \begin{Bmatrix} \sigma_x \\ \sigma_y \\ \tau_{xy} \end{Bmatrix} \quad (2.37)$$

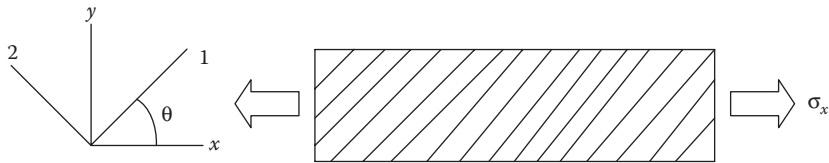
where the  $\bar{S}_{ij}$  are the components of the transformed lamina compliance matrix that are defined by  $[\bar{S}] = [\bar{Q}]^{-1}$ , or in expanded form

$$\begin{aligned} \bar{S}_{11} &= S_{11}c^4 + (2S_{12} + S_{66})s^2c^2 + S_{22}s^4 \\ \bar{S}_{12} &= S_{12}(s^4 + c^4) + (S_{11} + S_{22} - S_{66})s^2c^2 \\ \bar{S}_{22} &= S_{11}s^4 + (2S_{12} + S_{66})s^2c^2 + S_{22}c^4 \\ \bar{S}_{16} &= (2S_{11} - 2S_{12} - S_{66})sc^3 - (2S_{22} - 2S_{12} - S_{66})s^3c \\ \bar{S}_{26} &= (2S_{11} - 2S_{12} - S_{66})s^3c - (2S_{22} - 2S_{12} - S_{66})sc^3 \\ \bar{S}_{66} &= 2(2S_{11} + 2S_{22} - 4S_{12} - S_{66})s^2c^2 + S_{66}(s^4 + c^4) \end{aligned} \quad (2.38)$$

The lamina engineering constants can also be transformed from the principal material axes to the off-axis coordinates. For example, the off-axis longitudinal modulus of elasticity associated with uniaxial loading along the  $x$  direction as shown in Figure 2.13 is defined as

$$E_x = \frac{\sigma_x}{\varepsilon_x} = \frac{\sigma_x}{\bar{S}_{11}\sigma_x} = \frac{1}{\bar{S}_{11}} \quad (2.39)$$

where the strain  $\varepsilon_x$  in the denominator has been found by substituting the stress conditions  $\sigma_x \neq 0$ ,  $\sigma_y = \tau_{xy} = 0$  in Equations 2.37.

**FIGURE 2.13**

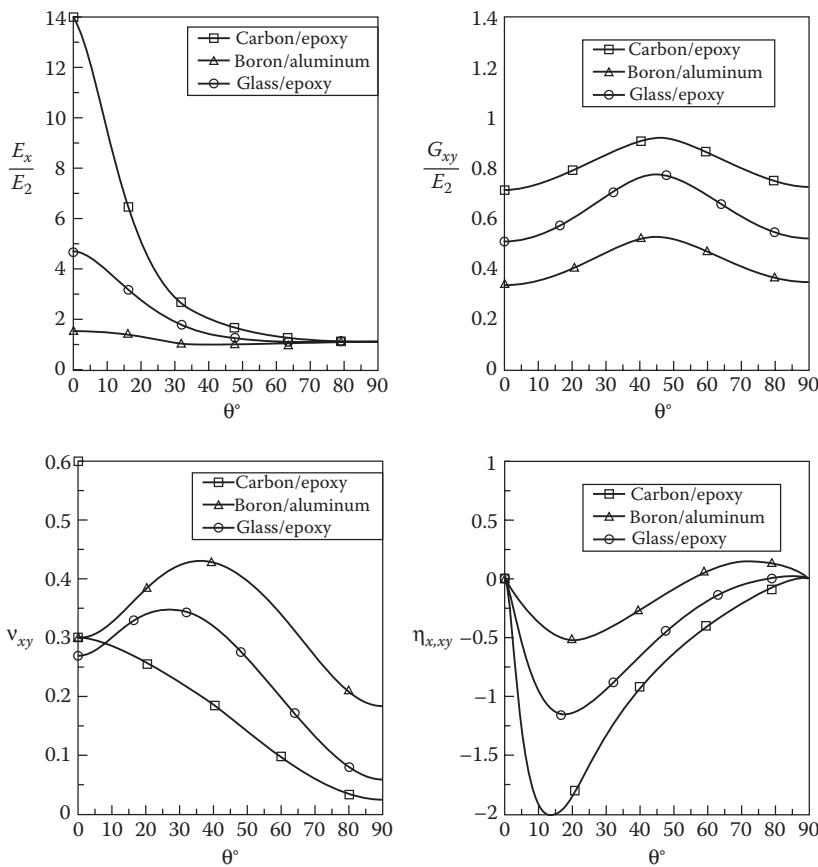
Off-axis loading for determination of off-axis longitudinal modulus of elasticity  $E_x$ .

By substituting  $\bar{S}_{11}$  from the first of Equation 2.38 into Equation 2.39 and then using Equations 2.25, we get the first of Equation 2.40:

$$\begin{aligned} E_x &= \left[ \frac{1}{E_1} c^4 + \left( \frac{1}{G_{12}} - \frac{2v_{12}}{E_1} \right) s^2 c^2 + \frac{1}{E_2} s^4 \right]^{-1} \\ E_y &= \left[ \frac{1}{E_1} s^4 + \left( \frac{1}{G_{12}} - \frac{2v_{12}}{E_1} \right) s^2 c^2 + \frac{1}{E_2} c^4 \right]^{-1} \\ G_{xy} &= \left[ \frac{1}{G_{12}} (s^4 + c^4) + 4 \left( \frac{1}{E_1} + \frac{1}{E_2} + \frac{2v_{12}}{E_1} - \frac{1}{2G_{12}} \right) s^2 c^2 \right]^{-1} \\ v_{xy} &= E_x \left[ \frac{v_{12}}{E_1} (s^4 + c^4) - \left( \frac{1}{E_1} + \frac{1}{E_2} - \frac{1}{G_{12}} \right) s^2 c^2 \right] \end{aligned} \quad (2.40)$$

where  $c = \cos \theta$  and  $s = \sin \theta$  as before. The rest of Equation 2.40 for the off-axis transverse modulus  $E_y$ , the off-axis shear modulus  $G_{xy}$ , and the off-axis major Poisson's ratio  $v_{xy}$  can be obtained from similar derivations.

The variation of these properties with lamina orientation for several composites is shown graphically in Figure 2.14 from Ref. [9]. As intuitively expected,  $E_x$  varies from a maximum at  $\theta = 0^\circ$  to a minimum at  $\theta = 90^\circ$  for this particular material. It is not necessarily true that the extreme values of such material properties occur along the principal material directions, however [6]. What may not be intuitively expected is the sharp drop in the off-axis modulus  $E_x$  as the angle changes slightly from  $0^\circ$  and the fact that over much of the range of lamina orientations the modulus  $E_x$  is very low. This is why transverse reinforcement is needed in unidirectional fiber composites which are subjected to multiaxial loading. The maximum value of the off-axis shear modulus  $G_{xy}$  at  $\theta = 45^\circ$  and minimum values of  $G_{xy}$  at  $\theta = 0^\circ$  and  $\theta = 90^\circ$  indicate that off-axis reinforcement is also essential for good shear stiffness in unidirectional composites. A good analogy here is the effect of diagonal bracing in a truss structure—without such bracing, the structure would be much more susceptible to collapse under shear loading. For filament-wound composite power transmission shafts under torsional loading,

**FIGURE 2.14**

Variations of off-axis engineering constants with lamina orientation for unidirectional carbon/epoxy, boron/aluminum and glass/epoxy composites. (Sun, C.T. *Mechanics of Aircraft Structures*, 1998, John Wiley & Sons, New York. Reproduced with permission.)

off-axis reinforcement is required for acceptable shear stiffness. Later in Chapter 7, it will become clear that off-axis laminae are essential in the design of laminates which are subjected to shear loading.

The shear-coupling effect has been described previously as the generation of shear strains by off-axis normal stresses and the generation of normal strains by off-axis shear stresses. One way to quantify the degree of shear coupling is by defining dimensionless shear-coupling ratios [4,5] or mutual influence coefficients [10] or shear-coupling coefficients [11]. For example, when the state of stress is defined as  $\sigma_x \neq 0$ ,  $\sigma_y = \tau_{xy} = 0$ , the ratio

$$\eta_{x,xy} = \frac{\gamma_{xy}}{\varepsilon_x} = \frac{\bar{S}_{16}}{\bar{S}_{11}} = E_x \left[ \left( \frac{2}{E_1} + \frac{2v_{12}}{E_1} - \frac{1}{G_{12}} \right) sc^3 - \left( \frac{2}{E_2} + \frac{2v_{12}}{E_1} - \frac{1}{G_{12}} \right) s^3 c \right] \quad (2.41)$$

is a measure of the amount of shear strain generated in the  $xy$  plane per unit normal strain along the direction of the applied normal stress,  $\sigma_x$ . Thus, the shear-coupling ratio is analogous to the Poisson's ratio, which is a measure of the coupling between normal strains. As shown in Figure 2.14,  $\eta_{x,xy}$  strongly depends on orientation and has its maximum value at some intermediate angle which depends on the material. Since there is no coupling along principal material directions,  $\eta_{x,xy} = 0$  for  $\theta = 0^\circ$  and  $\theta = 90^\circ$ . As the shear-coupling ratio increases, the amount of shear coupling increases. Other shear-coupling ratios can be defined for different states of stress. For example, when the stresses are  $\tau_{xy} \neq 0$ ,  $\sigma_x = \sigma_y = 0$ , the ratio

$$\eta_{xy,y} = \frac{\varepsilon_y}{\gamma_{xy}} = \frac{\bar{S}_{26}}{\bar{S}_{66}} = G_{xy} \left[ \left( \frac{2}{E_1} + \frac{2\nu_{12}}{E_1} - \frac{1}{G_{12}} \right) s^3 c - \left( \frac{2}{E_2} + \frac{2\nu_{12}}{E_1} - \frac{1}{G_{12}} \right) sc^3 \right] \quad (2.42)$$

characterizes the normal strain response along the  $y$  direction due to a shear stress in the  $xy$  plane.

Finally, for a generally orthotropic lamina under plane stress, the stress–strain relationship for the normal strain  $\varepsilon_x$  in terms of off-axis engineering constants can be expressed as:

$$\varepsilon_x = \frac{1}{E_x} \sigma_x - \frac{\nu_{yx}}{E_y} \sigma_y + \frac{\eta_{xy,x}}{G_{xy}} \tau_{xy} \quad (2.43)$$

with similar relationships for  $\varepsilon_y$  and  $\gamma_{xy}$ . As with the specially orthotropic case and the general anisotropic case, the stiffness and compliance matrices are still symmetric. So, for example, the off-axis compliances  $\bar{S}_{12} = \bar{S}_{21}$ , or in terms of off-axis engineering constants,  $(\nu_{yx}/E_y) = (\nu_{xy}/E_x)$ .

### Example 2.3

A  $45^\circ$  off-axis tensile test is conducted on a generally orthotropic test specimen by applying a normal stress  $\sigma_x$  as shown in Figure 2.15. The specimen has strain gages attached so as to measure the normal strains  $\varepsilon_x$  and  $\varepsilon_y$  along the  $x$  and  $y$  directions, respectively. How many engineering constants for this material can be determined from the measured parameters  $\sigma_x$ ,  $\varepsilon_x$ , and  $\varepsilon_y$ ?

### SOLUTION

The off-axis modulus of elasticity along the  $x$  direction is determined from

$$E_x = \frac{\sigma_x}{\varepsilon_x}$$

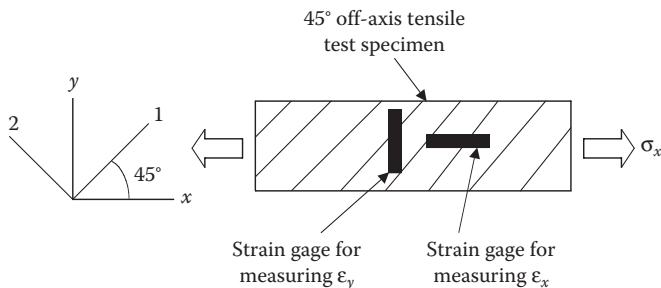


**FIGURE 2.15**  
Strain-gaged specimen for a  $45^\circ$  off-axis tensile test.

The off-axis major Poisson's ratio is given by

$$\nu_{xy} = -\frac{\epsilon_y}{\epsilon_x}$$

Although it may not seem obvious, the in-plane shear modulus  $G_{12}$  may also be found from these measurements by using the appropriate transformations of stress and strain. Using  $\theta = 45^\circ$  in Equation 2.33, the shear strain  $\gamma_{12}$  is found from

$$\frac{\gamma_{12}}{2} = -\cos 45^\circ \sin 45^\circ \epsilon_x + \cos 45^\circ \sin 45^\circ \epsilon_y + (\cos^2 45^\circ - \sin^2 45^\circ) \frac{\gamma_{xy}}{2}$$

or

$$\gamma_{12} = -\epsilon_x + \epsilon_y$$

Note that the  $\gamma_{xy}$  term drops out of the above equation only when  $\theta = 45^\circ$ . For any other value of  $\theta$ , we would need to know  $\gamma_{xy}$  as well as  $\epsilon_x$  and  $\epsilon_y$  in order to find  $\gamma_{12}$  from this transformation equation. Likewise, the shear stress  $\tau_{12}$  is found by substituting the tensile test conditions  $\sigma_x \neq 0$ ,  $\sigma_y = \tau_{xy} = 0$  in Equation 2.31:

$$\tau_{12} = -\cos 45^\circ \sin 45^\circ \sigma_x = -\frac{\sigma_x}{2}$$

Finally, the shear modulus  $G_{12}$  may now be calculated from the third line of Equation 2.24 as

$$G_{12} = \frac{1}{S_{66}} = \frac{\tau_{12}}{\gamma_{12}}$$

Note that this equation holds even though the stresses  $\sigma_1 \neq 0$  and  $\sigma_2 \neq 0$  in the first two lines of Equation 2.24.

The effects of lamina orientation on stiffness are difficult to assess from a quick inspection of stiffness transformation equations such as Equations 2.36 and 2.40. In addition, the eventual incorporation of lamina stiffnesses into laminate analysis requires integration of lamina stiffnesses over the laminate thickness, and integration of such complicated equations is also difficult. In view of these difficulties, a more convenient “invariant” form of the lamina stiffness transformation equations has been proposed by Tsai and Pagano [12]. By using trigonometric identities to convert from power functions to multiple angle functions and then using additional mathematical manipulations, Tsai and Pagano showed that Equations 2.36 could also be written as

$$\begin{aligned}\bar{Q}_{11} &= U_1 + U_2 \cos 2\theta + U_3 \cos 4\theta \\ \bar{Q}_{12} &= U_4 - U_3 \cos 4\theta \\ \bar{Q}_{22} &= U_1 - U_2 \cos 2\theta + U_3 \cos 4\theta \\ \bar{Q}_{16} &= \frac{U_2}{2} \sin 2\theta + U_3 \sin 4\theta \\ \bar{Q}_{26} &= \frac{U_2}{2} \sin 2\theta - U_3 \sin 4\theta \\ \bar{Q}_{66} &= \frac{1}{2}(U_1 - U_4) - U_3 \cos 4\theta\end{aligned}\quad (2.44)$$

where the set of “invariants” is defined as

$$\begin{aligned}U_1 &= \frac{1}{8}(3Q_{11} + 3Q_{22} + 2Q_{12} + 4Q_{66}) \\ U_2 &= \frac{1}{2}(Q_{11} - Q_{22}) \\ U_3 &= \frac{1}{8}(Q_{11} + Q_{22} - 2Q_{12} - 4Q_{66}) \\ U_4 &= \frac{1}{8}(Q_{11} + Q_{22} + 6Q_{12} - 4Q_{66})\end{aligned}\quad (2.45)$$

As the name implies, the invariants, which are simply linear combinations of the  $Q_{ij}$ , are invariant to rotations in the plane of the lamina. Note that there are four independent invariants, just as there are four independent elastic constants. Equation 2.44 is obviously easier to manipulate and interpret than Equations 2.36. For example, all the stiffness expressions except those for the coupling stiffnesses consist of one constant term and terms that vary with lamina orientation. Thus, the effects of lamina orientation on stiffness are easier to interpret.

Invariant formulations of lamina compliance transformations are also useful. It can be shown [5,11] that the off-axis compliance components in Equation 2.37 can be written as

$$\begin{aligned}\bar{S}_{11} &= V_1 + V_2 \cos 2\theta + V_3 \cos 4\theta \\ \bar{S}_{12} &= V_4 - V_3 \cos 4\theta \\ \bar{S}_{22} &= V_1 - V_2 \cos 2\theta + V_3 \cos 4\theta \\ \bar{S}_{16} &= V_2 \sin 2\theta + 2V_3 \sin 4\theta \\ \bar{S}_{26} &= V_2 \sin 2\theta - 2V_3 \sin 4\theta \\ \bar{S}_{66} &= 2(V_1 - V_4) - 4V_3 \cos 4\theta\end{aligned}\tag{2.46}$$

where the invariants are

$$\begin{aligned}V_1 &= \frac{1}{8}(3S_{11} + 3S_{22} + 2S_{12} + S_{66}) \\ V_2 &= \frac{1}{2}(S_{11} - S_{22}) \\ V_3 &= \frac{1}{8}(S_{11} + S_{22} - 2S_{12} - S_{66}) \\ V_4 &= \frac{1}{8}(S_{11} + S_{22} + 6S_{12} - S_{66})\end{aligned}\tag{2.47}$$

Invariant formulations also lend themselves well to graphical interpretation. As shown in any mechanics of materials book [2], stress transformation equations such as Equation 2.30 can be combined and manipulated so as to generate the equation of Mohr's circle. As shown in Figure 2.16, the transformation of a normal stress component  $\sigma_x$  can be described by the invariant formulation

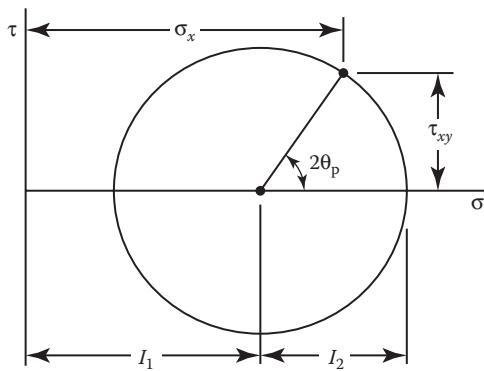
$$\sigma_x = I_1 + I_2 \cos 2\theta_p\tag{2.48}$$

where

$$\begin{aligned}I_1 &= \frac{\sigma_x + \sigma_y}{2} = \text{invariant} \\ I_2 &= \sqrt{\left[\frac{\sigma_x - \sigma_y}{2}\right]^2 + \tau_{xy}^2} = \text{invariant}\end{aligned}$$

$\theta_p$  = angle between the  $x$  axis and the principal stress axis

In this case the invariants are  $I_1$ , which defines the position of the center of the circle, and  $I_2$ , which is the radius of the circle. Note the similarity between

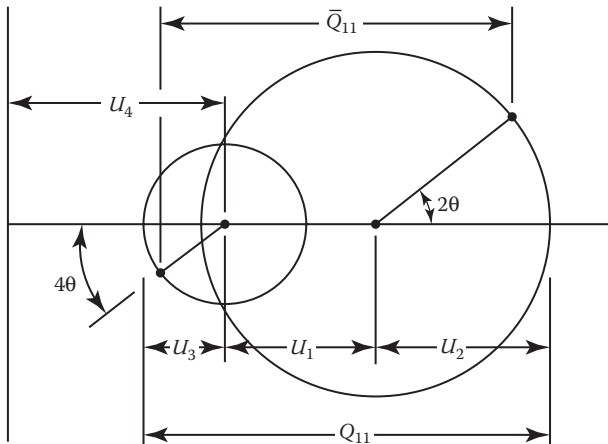
**FIGURE 2.16**

Mohr's circle for stress transformation.

Equation 2.48 and the first of Equation 2.44 in that the invariant formulation typically consists of a constant term and a term or terms that vary with orientation. Similarly, the invariant forms of the stiffness transformations can also be interpreted graphically using Mohr's circles. For example, Tsai and Hahn [11] have shown that the stiffness transformation equation

$$\bar{Q}_{11} = U_1 + U_2 \cos 2\theta + U_3 \cos 4\theta \quad (2.49)$$

can be represented graphically by using two Mohr's circles, as shown in Figure 2.17. The distance between points on each of the two circles represents

**FIGURE 2.17**

Mohr's circles for stiffness transformation. (From Tsai, S.W. and Hahn, H.T. 1980. *Introduction to Composite Materials*. Technomic Publishing Co., Lancaster, PA. Reprinted by permission of Technomic Publishing Co.)

the total stiffness  $\bar{Q}_{11}$ , whereas the distance between the centers of the two circles is given by  $U_1$ . The radius and angle associated with one circle are  $U_2$  and  $2\theta$ , respectively, and the radius and angle associated with the other circle are  $U_3$  and  $4\theta$ , respectively. Thus, the distance between the centers of the circles is a measure of the isotropic component of stiffness, whereas the radii of the circles indicate the strength of the orthotropic component. If  $U_2 = U_3 = 0$ , the circles collapse to points and the material is isotropic.

Invariants will prove to be very useful later in the analysis of randomly oriented short fiber composites and laminated plates. For additional applications of invariants in composite analysis, the reader is referred to books by Halpin [5] and Tsai and Hahn [11].

### Example 2.4

A filament-wound cylindrical pressure vessel (Figure 2.18) of mean diameter  $d = 1$  m and wall thickness  $t = 20$  mm is subjected to an internal pressure,  $p$ . The filament-winding angle  $\theta = 53.1^\circ$  from the longitudinal axis of the pressure vessel, and the glass/epoxy material has the following properties:  $E_1 = 40$  GPa =  $40(10^3)$  MPa,  $E_2 = 10$  GPa,  $G_{12} = 3.5$  GPa, and  $v_{12} = 0.25$ . By the use of a strain gage, the normal strain along the fiber direction is determined to be  $\epsilon_1 = 0.001$ . Determine the internal pressure in the vessel.

### SOLUTION

From mechanics of materials, the stresses in a thin-walled cylindrical pressure vessel are given by

$$\sigma_x = \frac{pr}{2t} = \frac{0.5p}{2(0.02)} = 12.5p, \quad \tau_{xy} = 0$$

$$\sigma_y = \frac{pr}{t} = \frac{0.5p}{0.02} = 25p$$

(Note that  $r = d/2 = 0.5$  m.)

These equations are based on static equilibrium and geometry only. Thus, they apply to a vessel made of any material. Since the given strain is along the fiber

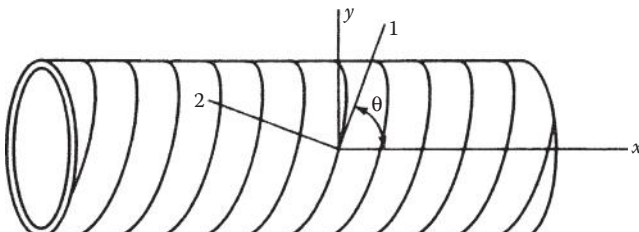


**FIGURE 2.18**  
Filament-wound vessel.

direction, we must transform the above stresses to the 12 axes. Recall that in the “netting analysis” in Problems 5 and 6 of Chapter 1, only the fiber longitudinal normal stress was considered. This was because the matrix was ignored, and the fibers alone cannot support transverse or shear stresses. In the current problem, however, the transverse normal stress,  $\sigma_2$ , and the shear stress,  $\tau_{12}$ , are also considered because the fiber and matrix are now assumed to act as a composite. From Equations 2.31, the stresses along the 12 axes are

$$\begin{aligned}\sigma_1 &= \sigma_x \cos^2 \theta + \sigma_y \sin^2 \theta + 2\tau_{xy} \sin \theta \cos \theta \\&= (12.5p)(0.6)^2 + (25p)(0.8)^2 + 0 = 20.5p(\text{MPa}) \\ \sigma_2 &= \sigma_x \sin^2 \theta + \sigma_y \cos^2 \theta - 2\tau_{xy} \sin \theta \cos \theta \\&= (12.5p)(0.8)^2 + (25p)(0.6)^2 - 0 = 17.0p(\text{MPa}) \\ \tau_{12} &= -\sigma_x \sin \theta \cos \theta + \sigma_y \sin \theta \cos \theta + \tau_{xy} (\cos^2 \theta - \sin^2 \theta) \\&\quad - (12.5p)(0.8)(0.6) + (25p)(0.6)(0.8) + 0 = 6.0p(\text{MPa})\end{aligned}$$

where the pressure  $p$  is in MPa. From the first of Equation 2.24, the normal strain  $\epsilon_1$  is

$$\epsilon_1 = \frac{\sigma_1}{E_1} - \frac{v_{12}\sigma_2}{E_1} = \frac{20.5p}{40(10^3)} - \frac{0.25(17.0p)}{40(10^3)} = 0.001$$

and the resulting pressure is  $p = 2.46$  MPa.

### Example 2.5

A tensile test specimen is cut out along the  $x$  direction of the pressure vessel described in Example 2.4. What effective modulus of elasticity would you expect to get during a test of this specimen?

#### SOLUTION

The off-axis modulus of elasticity,  $E_x$ , associated with the  $x$  direction is given by the first of equations (2.40) with  $\theta = 53.1^\circ$ .

$$\begin{aligned}E_x &= \frac{1}{(1/E_1)c^4 + [-(2v_{12}/E_1) + 1/G_{12}]c^2s^2 + (1/E_2)s^4} \\ E_x &= \frac{1}{(1/40)(0.6)^4 + [-(2(0.25)/40) + (1/3.5)](0.6)^2(0.8)^2 + (1/10)(0.8)^4} \\ &= 9.33 \text{ GPa}\end{aligned}$$

### Example 2.6

A lamina consisting of continuous fibers randomly oriented in the plane of the lamina is said to be “planar isotropic,” and the elastic properties in the plane are

isotropic in nature. Find expressions for the lamina stiffnesses for a planar isotropic lamina.

### SOLUTION

Since the fibers are assumed to be randomly oriented in the plane, the “planar isotropic stiffnesses” can be found by averaging the transformed lamina stiffnesses as follows:

$$\tilde{Q}_{ij} = \frac{\int_0^\pi \bar{Q}_{ij} d\theta}{\int_0^\pi d\theta}$$

where the superscript ( $\sim$ ) denotes an averaged property.

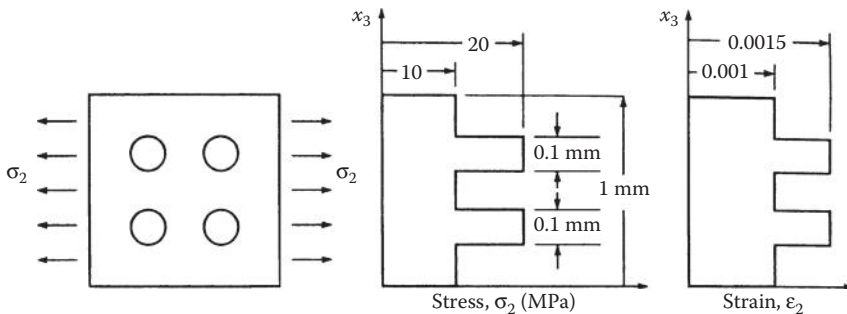
It is convenient to use the invariant forms of the transformed lamina stiffnesses because they are easily integrated. For example, if we substitute the first of Equation 2.44 in the above equation, we get

$$\tilde{Q}_{11} = \frac{\int_0^\pi \bar{Q}_{11} d\theta}{\int_0^\pi d\theta} = \frac{\int_0^\pi [U_1 + U_2 \cos 2\theta + U_3 \cos 4\theta] d\theta}{\pi} = U_1$$

Note that the averaged stiffness equals the isotropic part of the transformed lamina stiffness, and that the orthotropic parts drop out in the averaging process. Similarly, the other averaged stiffnesses can be found in terms of the invariants. The derivations of the remaining expressions are left as an exercise.

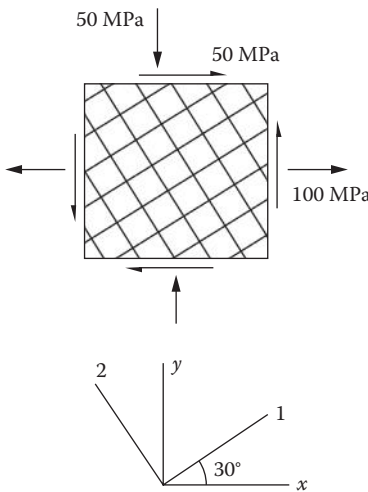
### PROBLEMS

1. A representative section from a composite lamina is shown in Figure 2.19 along with the transverse stress and strain distributions across the fiber and matrix materials in the section. The composite section is  $1 \text{ mm} \times 1 \text{ mm}$  square, and the diameter of each of the four fibers is  $0.1 \text{ mm}$ . Assuming that the dimensions of the section do not change along the longitudinal direction (perpendicular to the page), find the numerical value of the effective transverse modulus for the section.
2. Derive the first of Equation 2.40 for the off-axis modulus,  $E_x$ .
3. Derive the third of Equation 2.40 for the off-axis shear modulus,  $G_{xy}$ .
4. Using the result from Problem 3:
  - a. Find the value of the angle  $\theta$  (other than  $0^\circ$  or  $90^\circ$ ) where the curve of  $G_{xy}$  vs.  $\theta$  has a possible maximum, minimum, or inflection point.
  - b. For the value of  $\theta$  found in part (a), find the bounds on  $G_{12}$  which must be satisfied if  $G_{xy}$  is to have a maximum or minimum.

**FIGURE 2.19**

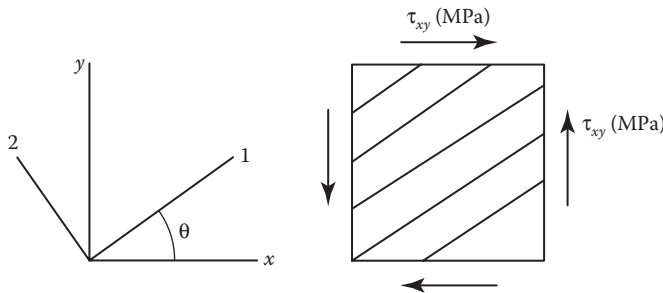
Transverse stress and strain distribution over a section of lamina.

- c. Qualitatively sketch the variation of  $G_{xy}$  vs.  $\theta$  for the different cases and identify each curve by the corresponding bounds on  $G_{12}$ , which give that curve.
- d. Using the bounds on  $G_{12}$  from part (b), find which conditions apply for E-glass/epoxy composites. The bounds on  $G_{12}$  in part (b) should be expressed in terms of  $E_1$ ,  $E_2$ , and  $v_{12}$ .
5. Describe a series of tensile tests that could be used to measure the four independent engineering constants for an orthotropic lamina without using a pure shear test. Give the necessary equations for the data reduction.
6. A balanced orthotropic, or square symmetric lamina, is made up of  $0^\circ$  and  $90^\circ$  fibers woven into a fabric and bonded together, as shown in Figure 2.9.
  - a. Describe the stress–strain relationships for such a lamina in terms of the appropriate engineering constants.
  - b. For a typical glass/epoxy composite lamina of this type, sketch the expected variations of all the engineering constants for the lamina from  $0^\circ$  to  $90^\circ$ . Numerical values are not required.
7. An element of a balanced orthotropic carbon/epoxy lamina is under the state of stress shown in Figure 2.20. If the properties of the woven carbon fabric/epoxy material are  $E_1 = 70$  GPa,  $v_{12} = 0.25$ ,  $G_{12} = 5$  GPa, determine all the strains along the fiber directions.
8. Derive Equation 2.27.
9. Express the stress–strain relationships in Equation 2.37 in terms of off-axis engineering constants such as the moduli of elasticity, shear modulus, Poisson’s ratios, and shear-coupling ratios.
10. Derive the first two equations of Equations 2.44.
11. Find all components of the stiffness and compliance matrices for a specially orthotropic lamina made of AS/3501 carbon/epoxy.
12. Using the results of Problem 11, determine the invariants  $U_i$  and  $V_i$  for the AS/3501 lamina, where  $i = 1, 2, 3, 4$ .
13. Using the results of Problem 11 or Problem 12, compare the transformed lamina stiffnesses for AS/3501 carbon/epoxy plies oriented at  $+45^\circ$  and  $45^\circ$ .

**FIGURE 2.20**

Stresses acting on an element of balanced orthotropic lamina.

14. Show how the Mohr's circles in Figure 2.17 can be used to interpret the transformed lamina stiffness  $\bar{Q}_{12}$ .
15. Using the approach described in Example 2.5, derive the expressions for all the averaged stiffnesses for the planar isotropic lamina in terms of invariants. Use these results to find the corresponding averaged engineering constants (modulus of elasticity, shear modulus, and Poisson's ratio) in terms of invariants.
16. For a specially orthotropic, transversely isotropic material the "plane strain bulk modulus,"  $K_{23}$ , is an engineering constant that is defined by the stress conditions  $\sigma_2 = \sigma_3 = \sigma$  and the strain conditions  $\epsilon_1 = 0, \epsilon_2 = \epsilon_3 = \epsilon$ . Show that these conditions lead to the stress-strain relationship  $\sigma = 2K_{23}\epsilon$ , and find the relationship among  $K_{23}, E_1, E_2, G_{23}$ , and  $v_{12}$ .
17. Describe the measurements that would have to be taken and the equations that would have to be used to determine  $G_{23}, v_{32}$ , and  $E_2$  for a specially orthotropic, transversely isotropic material from a single tensile test.
18. A 45° off-axis tensile test specimen has three strain gages attached. Two of the gages are mounted as shown in Figure 2.15 so as to measure the normal strains  $\epsilon_x$  and  $\epsilon_y$ , and a third gage is mounted at  $\theta = 45^\circ$  so as to measure the normal strain  $\epsilon_1$ . If the applied stress  $\sigma_x = 100$  MPa and the measured strains are  $\epsilon_x = 0.00647, \epsilon_y = -0.00324$  and  $\epsilon_1 = 0.00809$ , determine the off-axis modulus of elasticity  $E_x$ , the off-axis major Poisson's ratio  $v_{xy}$  and the shear coupling ratio  $\eta_{x,xy}$ .
19. A off-axis tensile test (Figure 2.13) of a unidirectional AS/3501 carbon/epoxy specimen is conducted with  $\theta = 45^\circ$  and the applied stress is found to be  $\sigma_x = 15.44$  MPa. Determine the resulting strain  $\epsilon_x$ .

**FIGURE 2.21**

Description of off-axis lamina and stresses for Problem 20.

20. An element of an orthotropic lamina is subjected to an off-axis shear stress  $\tau_{xy}$  at an angle  $\theta$  as shown in Figure 2.21. (a) for an angle  $\theta = 45^\circ$ , determine the value of the applied shear stress  $\tau_{xy}$  that would generate the following stresses along the 1,2 axes:  $\sigma_1 = 1000 \text{ MPa}$ ,  $\sigma_2 = -1000 \text{ MPa}$ ,  $\tau_{12} = 0$ . (b) Assuming that the lamina described in part (a) is made from T300/934 carbon/epoxy and that the stresses are also given in part (a), determine the strains along the 1,2 axes.
21. Use invariants to find the optimum lamina orientation for maximizing the shear stiffness  $\bar{Q}_{66}$ , then find the corresponding maximum shear stiffness in terms of invariants.

## References

1. Christensen, R. M. 1979. *Mechanics of Composite Materials*. John Wiley & Sons, New York, NY.
2. Crandall, S. H., Dahl, N. C., and Lardner, T. J. 1978. *An Introduction to the Mechanics of Solids*, 2nd ed. with SI units. McGraw-Hill, Inc., New York, NY.
3. Sokolnikoff, I. S. 1956. *Mathematical Theory of Elasticity*. McGraw-Hill, Inc., New York, NY.
4. Ashton, J. E., Halpin, J. C., and Petit, P. H. 1969. *Primer on Composite Materials: Analysis*. Technomic Publishing Co., Lancaster, PA.
5. Halpin, J. C. 1984. *Primer on Composite Materials: Analysis*, rev. ed. Technomic Publishing Co., Lancaster, PA.
6. Jones, R. M. 1999. *Mechanics of Composite Materials*, 2nd ed. Taylor and Francis, Inc., Philadelphia, PA.
7. Vinson, J. R. and Sierakowski, R. L. 1986. *The Behavior of Structures Composed of Composite Materials*. Martinus Nijhoff Publishers, Dordrecht, The Netherlands.
8. Adams, D. F., Carlsson, L. A., and Pipes, R. B. 2003. *Experimental Characterization of Advanced Composite Materials*, 3rd ed., CRC Press, Boca Raton, FL.
9. Sun, C. T. 1998. *Mechanics of Aircraft Structures*. John Wiley & Sons, New York, NY.

10. Lekhnitski, S. G. 1981. *Theory of Elasticity of an Anisotropic Body*. Mir Publishing Co., Moscow, USSR.
11. Tsai, S. W. and Hahn, H. T. 1980. *Introduction to Composite Materials*. Technomic Publishing Co., Lancaster, PA.
12. Tsai, S. W. and Pagano, N. J. 1968. Invariant properties of composite materials, in Tsai, S. W., Halpin, J. C., and Pagano N. J. eds., *Composite Materials Workshop*, pp. 233–253. Technomic Publishing Co., Lancaster, PA.

# 3

---

## *Effective Moduli of a Continuous Fiber-Reinforced Lamina*

---

### 3.1 Introduction

In the previous chapter, the concept of an effective modulus was found to be essential to the development of practical engineering stress-strain relationships for composite materials. Recall that for some representative volume element (RVE) in a heterogeneous composite, the volume-averaged stresses can be related to the volume-averaged strains by the effective moduli of an equivalent homogeneous material. Chapter 2 was primarily concerned with the development and manipulation of macromechanical stress-strain relationships involving the lamina effective moduli, however, and the roles of lamina constituent materials were not examined in detail. In this chapter, we will discuss various micromechanical models for predicting the effective moduli of continuous fiber-reinforced laminae in terms of the corresponding material properties, relative volume contents, and geometric arrangements of the fiber and matrix materials. Corresponding models for predicting strength and hygrothermal properties will be presented in Chapters 4 and 5, respectively. Micromechanics of discontinuously reinforced composites, including nanocomposites, is covered in Chapter 6.

Before proceeding further, it is appropriate to briefly discuss the term “micromechanics.” To a materials scientist, the term may imply the study of mechanical behavior at the level of molecular or crystal structures. Since the behavior of composite material structures such as laminates is referred to as “macromechanics,” it has been suggested that, perhaps, mechanics of composites at the constituent material level should be referred to as “minimechanics” [1]. In the present context, and in much of the composites literature, however, the analysis of effective composite properties in terms of constituent material properties is called “micromechanics.” The terms “structure-property relationships” and “effective modulus theories” are also used in the literature. Many analytical approaches have been developed over the years, and comprehensive literature surveys have been published by Chamis and Sendeckyj [2], Christensen [3], Hashin [1], and Halpin [4].

Micromechanical analyses are based on either the mechanics of materials or the elasticity theory. In the mechanics of materials approach, simplifying

assumptions make it unnecessary to specify the details of the stress and strain distributions at the micromechanical level, and fiber-packing geometry is generally arbitrary. The theory of elasticity models involves the solution for actual stresses and strains at the micromechanical level, and fiber-packing geometry is taken into account. The elasticity approach often involves numerical solutions of the governing equations because of the complex geometries and boundary conditions. Although the simplifying assumptions used in the mechanics of materials approach violate some of the laws of elasticity theory, some of the results are sufficiently accurate that they are often used in design. A third category involves empirical solutions that are based on curve-fitting to elasticity solutions or experimental data, and some of these equations are often used along with the mechanics of materials equations to formulate a complete set of simple lamina design equations.

Ideally, micromechanical models should enable us to answer quickly "What if?" questions regarding the effects of various fiber/matrix combinations without actually fabricating and testing the composites in question. On the other hand, experience has shown that there are pitfalls in such an approach and that there is no substitute for experimental characterization. Experimental data on the constituent material properties are required as input to the models, and similar data on the corresponding composite properties are required to assess the validity of the models. Indeed, as we will see later, some properties such as fiber transverse moduli are usually inferred from the micromechanical model and other measured properties because of the difficulty of direct measurement. Once a micromechanical model has been shown to be sufficiently accurate by comparison with experiment, however, it can become part of a powerful design methodology that enables us to design the material as well as the structure. Aside from design implications, micromechanical analysis and experimental characterization are both essential if we are to understand better "how composites work."

One of the key elements in micromechanical analysis is the characterization of the relative volume or weight contents of the various constituent materials. We will find that the micromechanics equations involve constituent volume fractions, but actual measurements are often based on weight fractions. Measurements are discussed later, but the relationships between volume fractions and weight fractions will be presented here.

For any number of constituent materials,  $n$ , the sum of the constituent volume fractions must be unity:

$$\sum_{i=1}^n v_i = 1 \quad (3.1)$$

where  $v_i = V_i/V_c$  = volume fraction of the  $i$ th constituent,  $V_i$  = volume of the  $i$ th constituent, and  $V_c$  = total volume of the composite.

In many cases, this equation reduces to

$$v_f + v_m + v_v = 1 \quad (3.2)$$

where  $v_f$ ,  $v_m$ , and  $v_v$  are the volume fractions of the fiber, matrix, and voids, respectively. The corresponding equations for weight fractions are

$$\sum_{i=1}^n w_i = 1 \quad (3.3)$$

and

$$w_f + w_m = 1 \quad (3.4)$$

where  $w_i = W_i/W_c$ ,  $w_f = W_f/W_c$ ,  $w_m = W_m/W_c$ , and  $W_i$ ,  $W_f$ ,  $W_m$ , and  $W_c$  are the weights of the  $i$ th constituent, fiber, matrix, and composite, respectively. Note that the weight of the voids has been neglected here. Substituting the product of density and volume for weight in each term of Equations 3.3 and 3.4 and solving for the composite density, we get the “rule of mixtures”:

$$\rho_c = \sum_{i=1}^n \rho_i v_i \quad (3.5)$$

or

$$\rho_c = \rho_f v_f + \rho_m v_m \quad (3.6)$$

where  $\rho_i$ ,  $\rho_f$ ,  $\rho_m$ , and  $\rho_c$  are the densities of the  $i$ th constituent, fiber, matrix, and composite, respectively. Similarly, Equations 3.1 and 3.2 can be rearranged as

$$\rho_c = \frac{1}{\sum_{i=1}^n (w_i / \rho_i)} \quad (3.7)$$

and

$$\rho_c = \frac{1}{(w_f / \rho_f) + (w_m / \rho_m)} \quad (3.8)$$

Equation 3.2 can also be rearranged so that the void fraction can be calculated from measured weights and densities:

$$v_v = 1 - \frac{(W_f/\rho_f) + (W_c - W_f)/\rho_m}{W_c/\rho_c} \quad (3.9)$$

Typical autoclave-cured composites may have void fractions in the range 0.1–1%. Without vacuum bagging, however, volatiles trapped in the composite during the cure cycle can cause void contents of the order of 5%.

Since micromechanics equations are typically expressed in terms of volume fractions, but measurements are usually based on weight fractions, it is useful to know the relationships between these two parameters. For example, the fiber weight fraction is related to the fiber volume fraction by

$$w_f = \frac{W_f}{W_c} = \frac{\rho_f V_f}{\rho_c V_c} = \frac{\rho_f}{\rho_c} v_f \quad (3.10)$$

So that

$$v_f = \frac{\rho_c}{\rho_f} w_f \quad (3.11)$$

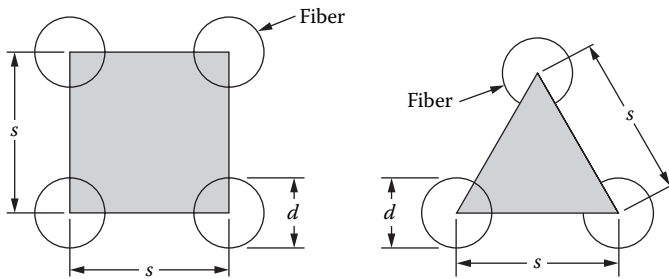
Similarly, the matrix weight fractions and volume fractions are related by

$$w_m = \frac{W_m}{W_c} = \frac{\rho_m V_m}{\rho_c V_c} = \frac{\rho_m}{\rho_c} v_m \quad (3.12)$$

and

$$v_m = \frac{\rho_c}{\rho_m} w_m \quad (3.13)$$

In order to get some idea as to the range of constituent volume fractions that may be expected in fiber composites, it is useful to consider representative area elements for idealized fiber-packing geometries such as the square and triangular arrays shown in Figure 3.1. It is assumed that fibers are oriented perpendicular to the page, that the fiber center-to-center spacing,  $s$ , and the fiber diameter,  $d$ , do not change along the fiber length, and that the area fractions are equal to the volume fractions. Indeed, measurement of such area fractions is possible from photomicrographs and image analysis software. The fiber volume fraction for the square array is found by dividing

**FIGURE 3.1**

Representative area elements for idealized square and triangular fiber-packing geometries.

the area of fiber enclosed in the shaded square by the total area of the shaded square [5]:

$$v_f = \frac{\pi}{4} \left( \frac{d}{s} \right)^2 \quad (3.14)$$

Clearly, the maximum theoretical fiber volume fraction occurs when  $s = d$ . In this case,

$$v_{f \max} = \frac{\pi}{4} = 0.785 \quad (3.15)$$

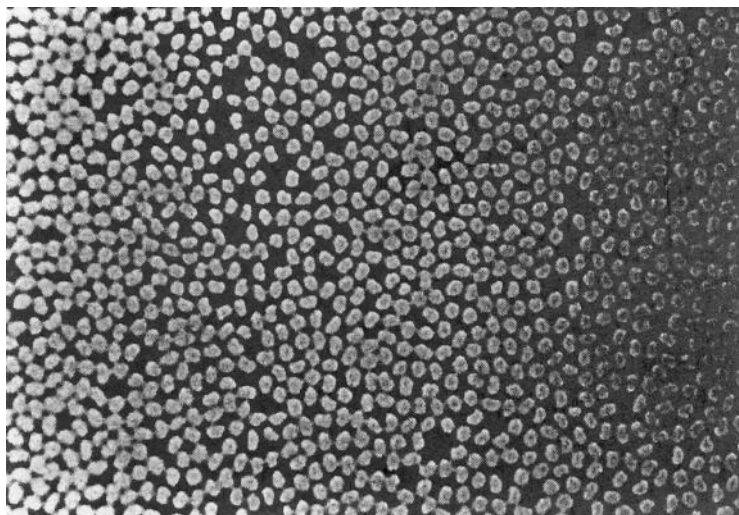
A similar calculation for the triangular array shows that

$$v_f = \frac{\pi}{2\sqrt{3}} \left( \frac{d}{s} \right)^2 \quad (3.16)$$

and when  $s = d$ , the maximum fiber volume fraction is

$$v_{f \max} = \frac{\pi}{2\sqrt{3}} = 0.907 \quad (3.17)$$

The close packing of fibers required to produce these theoretical limits is generally not achievable in practice, however. In most continuous fiber composites, the fibers are not perfectly round and are packed in a random fashion as shown in Figure 3.2, so that the fiber volume fractions typically range from 0.5 to 0.8. In short fiber composites, fiber volume fractions are usually much lower due to processing limitations (e.g., the viscosity of the fiber/resin mixture must be controlled for proper flow during molding) and the random orientation of fibers. Since fiber-packing geometry is never entirely

**FIGURE 3.2**

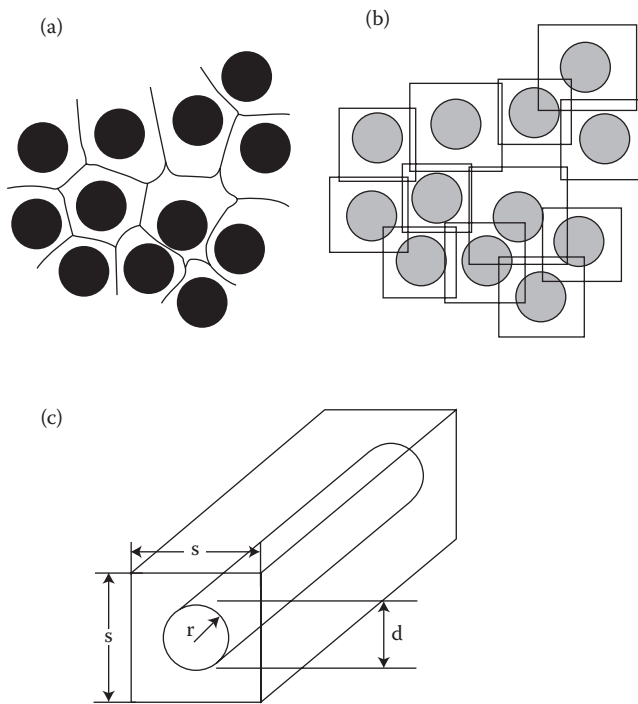
Photomicrograph of carbon/epoxy composite showing actual fiber-packing geometry at  $400 \times$  magnification.

reproducible from one piece of material to another, we should not expect our micromechanics predictions to be exact.

The random nature of the fiber-packing geometry in real composites such as the one shown in Figure 3.2 can be quantified by the use of the Voronoi cell (Figure 3.3) and a statistical distribution describing the Voronoi cell size [6]. Each point within the space of a Voronoi cell for a particular fiber is closer to the center of that fiber than it is to the center of any other fiber. If we can approximate the Voronoi cell in Figure 3.3a as an equivalent square area as shown in Figure 3.3b and Figure 3.3c, then Equation 3.14 can be used to describe the relationship between the fiber diameter  $d$ , the fiber volume fraction  $v_f$ , and the Voronoi cell size  $s$  (which is assumed to be the same as the center-to-center spacing). Yang and Colton [6] have used digital image processing to show that the Weibull distribution

$$f(s) = \frac{\beta}{\delta} \left( \frac{s - \gamma}{\delta} \right)^{\beta-1} \exp \left[ - \left( \frac{s - \gamma}{\delta} \right)^\beta \right] \quad \text{when } s \geq \gamma \\ f(s) = 0 \quad \text{otherwise} \quad (3.18)$$

adequately characterizes the probability density function for the Voronoi cell size for several composites, where  $\beta$ ,  $\delta$ , and  $\gamma$  are the Weibull parameters associated with the shape, scale, and location of the distribution, respectively. A typical histogram of measured Voronoi distances for a thermoplastic matrix

**FIGURE 3.3**

Voronoi cell and its approximation. (Yang, H. and Colton, J. S.: Microstructure-based processing parameters of thermoplastic composite materials. Part I: Theoretical models. *Polymer Composites*. 1994. 51(1). 34–41. Copyright Wiley-VCH Verlag GmbH & Co. KGaA. Reproduced with permission.)

composite and the corresponding Weibull distribution from regression analysis are shown in Figure 3.4.

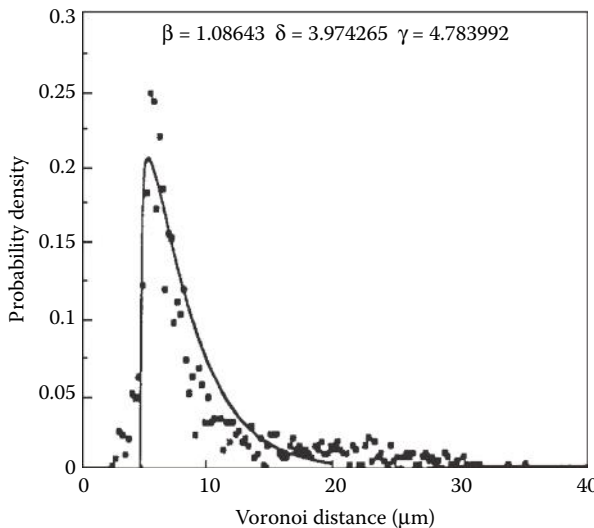
### Example 3.1

A carbon/epoxy composite specimen has dimensions of  $2.54 \text{ cm} \times 2.54 \text{ cm} \times 0.3 \text{ cm}$  and a weight of 2.98 g. After “resin digestion” in an acid solution, the remaining carbon fibers weigh 1.863 g. From independent tests, the densities of the carbon fibers and epoxy matrix materials are found to be 1.9 and  $1.2 \text{ g/cm}^3$ , respectively. Determine the volume fractions of fibers, epoxy matrix, and voids in the specimen.

### SOLUTION

The composite density is

$$\rho_c = \frac{2.98 \text{ g}}{(2.54)(2.54)(0.3) \text{ cm}^3} = 1.54 \text{ g/cm}^3$$

**FIGURE 3.4**

Typical histogram of Voronoi distances and corresponding Weibull distribution for a thermoplastic matrix composite. (Yang, H. and Colton, J. S.: Microstructure-based processing parameters of thermoplastic composite materials. Part I: Theoretical models. *Polymer Composites*. 1994. 51(1). 34–41. Copyright Wiley-VCH Verlag GmbH & Co. KGaA. Reproduced with permission.)

From Equation 3.9, the void fraction is

$$v_v = 1 - \frac{(1.863/1.9) + (2.98 - 1.863)/1.2}{2.98/1.54} = 0.0122 \text{ or } 1.22\%$$

From Equation 3.2,

$$v_f + v_m = 1 - v_v = 1.0 - 0.0122 = 0.988$$

Then, from Equation 3.6,

$$1.54 = 1.9v_f + 1.2(0.988 - v_f)$$

Therefore, the fiber volume fraction is

$$v_f = 0.506 \text{ or } 50.6\%$$

and the matrix volume fraction is

$$v_m = 0.988 - 0.506 = 0.482 \text{ or } 48.2\%$$

### Example 3.2

Assume that the carbon fibers in the specimen from Example 3.1 have been uniformly coated with an epoxy “sizing” of thickness  $t$  before bonding of the fibers

and matrix together to form a unidirectional composite. If the bare fibers have a diameter  $d = 0.0005$  in. (0.0127 mm) and the coated fibers are assumed to be packed together in the tightest possible square array, what is the thickness of the sizing?

### SOLUTION

The fiber spacing,  $s$ , which in this case must be equal to the coated fiber diameter,  $d_c$ , can be found from Equation 3.14:

$$s = d_c = \sqrt{\frac{\pi d^2}{4v_f}} = \sqrt{\frac{\pi(0.0005)^2}{4(0.506)}} = 0.000623 \text{ in. (0.0158 mm)}$$

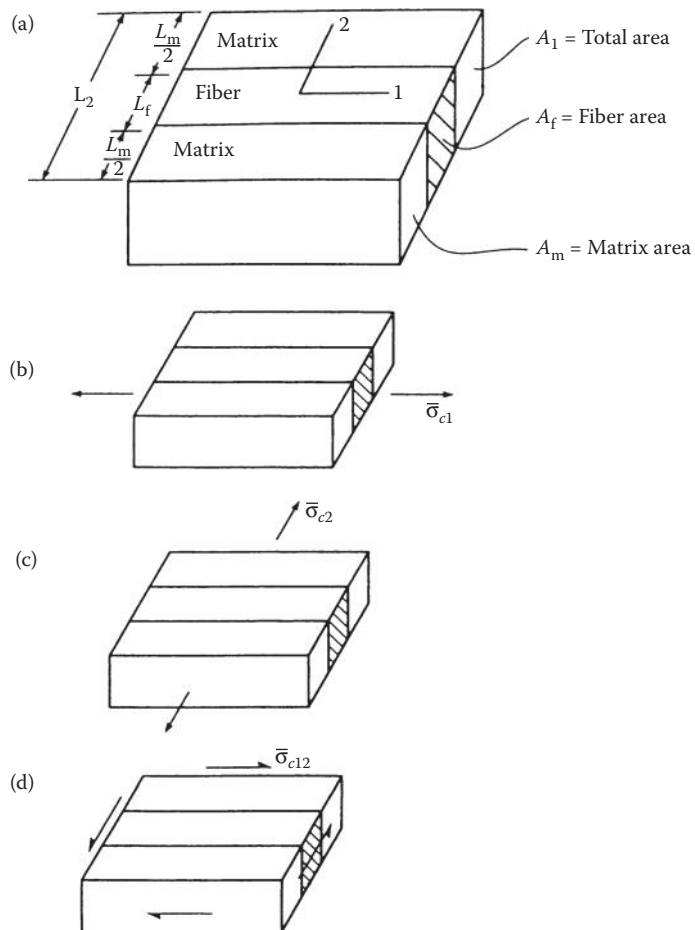
The thickness is then  $t = (d_c - d)/2 = 0.0000615$  in. (0.00156 mm).

## 3.2 Elementary Mechanics of Materials Models

The objective of this section is to present elementary mechanics of materials models for predicting four independent effective moduli of an orthotropic continuous fiber-reinforced lamina. In the elementary mechanics of materials approach to micromechanical modeling, fiber-packing geometry is not specified, so that the RVE may be a generic composite block consisting of fiber material bonded to matrix material, as shown in Figure 3.5. More sophisticated mechanics of materials models, which do consider fiber-packing geometry, will be discussed later.

The constituent volume fractions in the RVE are assumed to be the same as those in the actual composite. Since it is assumed that the fibers remain parallel and that the dimensions do not change along the length of the element, the area fractions must equal the volume fractions. Perfect bonding at the interface is assumed, so that no slip occurs between fiber and matrix materials. The fiber and matrix materials are assumed to be linearly elastic and homogeneous. The matrix is assumed to be isotropic, but the fiber can be either isotropic or orthotropic. Following the concept of the RVE, the lamina is assumed to be macroscopically homogeneous, linearly elastic, and orthotropic.

Micromechanics equations will be developed from either equilibrium or compatibility relationships, and assumptions about either stresses or strains in the RVE that has been subjected to a simple state of stress. Since the mechanics of materials approach does not require the specification of the stresses, strains, and displacements at each point, we only deal with the corresponding volume-averaged quantities. Finally, since it is assumed that the stresses,

**FIGURE 3.5**

RVE and simple stress states used in elementary mechanics of materials models. (a) Representative volume element, (b) longitudinal normal stress, (c) transverse normal stress, and (d) in-plane shear stress.

strains, displacements, and RVE dimensions do not change along the length, we can just use area averages:

$$\bar{\sigma} = \frac{1}{V} \int \sigma dV = \frac{1}{A} \int \sigma dA \quad (3.19)$$

$$\bar{\varepsilon} = \frac{1}{V} \int \varepsilon dV = \frac{1}{A} \int \varepsilon dA \quad (3.20)$$

$$\bar{\delta} = \frac{1}{V} \int \delta dV = \frac{1}{A} \int \delta dA \quad (3.21)$$

where the overbar denotes an averaged quantity, and  $\sigma$  = stress,  $\epsilon$  = strain,  $\delta$  = displacement,  $V$  = volume, and  $A$  = area associated with the face on which loading is applied.

The volume averaging (or area averaging) may occur over the composite lamina, the fiber, or the matrix, and the corresponding parameters will be identified by using subscripts as defined in the following derivations.

### 3.2.1 Longitudinal Modulus

If the RVE in Figure 3.5a is subjected to a longitudinal normal stress,  $\bar{\sigma}_{c1}$ , as shown in Figure 3.5b, the response is governed by the effective longitudinal modulus,  $E_1$ . Static equilibrium requires that the total resultant force on the element must equal the sum of the forces acting on the fiber and matrix. Combining the static equilibrium condition with Equation 3.19, we get

$$\bar{\sigma}_{c1}A_1 = \bar{\sigma}_{f1}A_f + \bar{\sigma}_{m1}A_m \quad (3.22)$$

where subscripts c, f, and m refer to composite, fiber, and matrix, respectively, and the second subscript refers to the direction. Since area fractions are equal to the corresponding volume fractions, Equation 3.22 can be rearranged to give a “rule of mixtures” for longitudinal stress:

$$\bar{\sigma}_{c1} = \bar{\sigma}_{f1}v_f + \bar{\sigma}_{m1}v_m \quad (3.23)$$

Under the assumptions that the matrix is isotropic, that the fiber is orthotropic, and that all materials follow a 1-D Hooke's law (i.e., Poisson strains are neglected),

$$\bar{\sigma}_{c1} = E_1\bar{\epsilon}_{c1}; \quad \bar{\sigma}_{f1} = E_{f1}\bar{\epsilon}_{f1}; \quad \bar{\sigma}_{m1} = E_m\bar{\epsilon}_{m1} \quad (3.24)$$

and Equation 3.23 becomes

$$E_1\bar{\epsilon}_{c1} = E_{f1}\bar{\epsilon}_{f1}v_f + E_m\bar{\epsilon}_{m1}v_m \quad (3.25)$$

Double subscripts are used for the fiber modulus since the fiber is assumed to be orthotropic. That is, the longitudinal fiber modulus,  $E_{f1}$ , is not necessarily equal to the transverse fiber modulus,  $E_{f2}$ . For example, carbon and aramid fibers exhibit orthotropic behavior, whereas glass and boron are practically isotropic. For the isotropic case, it is a simple matter to let  $E_{f1} = E_{f2}$ . Since the matrix is assumed to be isotropic, the matrix modulus,  $E_m$ , does not need a second subscript.

Finally, the key assumption is that, due to perfect bonding the average displacements and strains in the composite, fiber, and matrix along the 1 direction are all equal:

$$\bar{\epsilon}_{c1} = \bar{\epsilon}_{f1} = \bar{\epsilon}_{m1} \quad (3.26)$$

Substitution of Equation 3.26 in Equation 3.25 then yields the rule of mixtures for the longitudinal modulus:

$$E_1 = E_f v_f + E_m v_m \quad (3.27)$$

This equation predicts a linear variation of the longitudinal modulus with fiber volume fraction, as shown in Figure 3.6. Although simple in form, Equation 3.27 agrees well with experimental data from Ref. [7] (Figure 3.6b) and is a useful design equation. The validity of the key assumptions leading to this equation will now be examined by using a strain energy approach.

Further insight into the micromechanics of the longitudinal loading case is possible by using a strain energy approach. Under the given state of stress, the total strain energy stored in the composite,  $U_c$ , can be represented as the sum of the strain energy in the fibers,  $U_f$ , and the strain energy in the matrix,  $U_m$ :

$$U_c = U_f + U_m \quad (3.28)$$

Again making the mechanics of materials assumption that the stresses and strains are uniform over the RVE and using Equation 3.24, the strain energy terms can be simplified as

$$U_c = \frac{1}{2} \int_{V_e} \sigma_{c1} \epsilon_{c1} dV = \frac{1}{2} E_1 \bar{\epsilon}_{c1}^2 V_c \quad (3.29a)$$

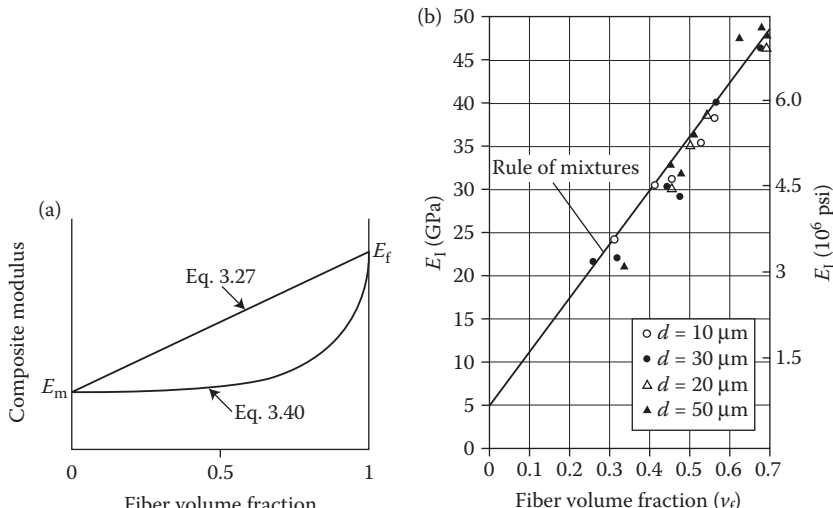


**FIGURE 3.6**

Variation of composite moduli with fiber volume fraction (a) predicted  $E_1$  and  $E_2$  from elementary mechanics of materials models and (b) comparison of predicted and measured  $E_1$  for E-glass/polyester. (From Adams, R. D. 1987. *Engineered Materials Handbook*, Vol. 1, Composites, pp. 206–217. With permission.)

$$U_f = \frac{1}{2} \int_{V_f} \sigma_{f1} \epsilon_{f1} dV = \frac{1}{2} E_{f1} \bar{\epsilon}_{f1}^2 V_f \quad (3.29b)$$

$$U_m = \frac{1}{2} \int_{V_m} \sigma_{m1} \epsilon_{m1} dV = \frac{1}{2} E_{m1} \bar{\epsilon}_{m1}^2 V_m \quad (3.29c)$$

In this approximation, the strain energy due to the mismatch in Poisson strains at the fiber/matrix interface has been neglected (recall the assumptions leading to Equation 3.24). This neglected term has been shown to be of the order of the square of the difference between the Poisson's ratios of the fiber and the matrix, so the approximation is justified [8]. It is easily shown that substitution of Equation 3.29 into Equation 3.28, along with the assumption of equal strains from Equation 3.26, again leads to the rule of mixtures given by Equation 3.27. But the strain energy approach also allows us to ask, "What happens if the assumption of equal strains is not made?" In order to proceed, let the stresses in the fibers and the matrix be defined in terms of the composite stress as follows:

$$\bar{\sigma}_{f1} = a_1 \bar{\sigma}_{c1}; \quad \bar{\sigma}_{m1} = b_1 \bar{\sigma}_{c1} \quad (3.30)$$

where  $a_1$  and  $b_1$  are constants. Substitution of Equation 3.30 in the rule of mixtures for stress, Equation 3.23, leads to

$$a_1 v_f + b_1 v_m = 1 \quad (3.31)$$

Substitution of Equation 3.30, Equation 3.24, and Equation 3.29 in Equation 3.28 leads to

$$\frac{1}{E_1} = a_1^2 \frac{v_f}{E_{f1}} + b_1^2 \frac{v_m}{E_m} \quad (3.32)$$

Note that we did not assume equal strains in fibers and matrix to derive these equations. In order to check the strain distribution, however, Equations 3.31 and 3.32 can be solved simultaneously for  $a_1$  and  $b_1$  when composite, fiber, and matrix properties are known. The ratio of the fiber strain to the matrix strain can then be found. For example, using the measured properties of an E-glass/epoxy composite [9],

$$\begin{aligned} E_1 &= 5.05 \times 10^6 \text{ psi} \quad (34.82 \text{ GPa}); \quad v_m = 0.55 \\ E_2 &= 1.53 \times 10^6 \text{ psi} \quad (10.55 \text{ GPa}); \quad v_f = 0.45 \\ E_{f1} &= E_{f2} = 10.5 \times 10^6 \text{ psi} \quad (72.4 \text{ GPa}) \\ E_m &= 0.55 \times 10^6 \text{ psi} \quad (3.79 \text{ GPa}) \end{aligned} \quad (3.33)$$

we find that  $a_1 = 2.0884$ ,  $b_1 = 0.1093$ ,  $a_1/b_1 = \bar{\sigma}_{f1}/\bar{\sigma}_{m1} = 19.1$ , and  $\bar{\epsilon}_{f1}/\bar{\epsilon}_{m1} = 1.00$ . Thus, the assumption of equal strains, which led to Equation 3.27, is valid for this material, as it apparently is for other composites. The strain energy approach will be used again in the next section to check the validity of an assumption leading to the equation for the transverse modulus.

### Example 3.3

Determine the longitudinal modulus  $E_1$  of the reinforced concrete post described in Problem 11 of Chapter 1. Assume that the steel rods and the concrete are linear elastic and isotropic, and that they are perfectly bonded together.

#### SOLUTION

In this case, the steel rods act as the fibers and the concrete acts as the matrix. The fiber volume fraction (same as the area fraction, if the rod and post cross-sections do not change along the length) is

$$v_f = \frac{4(0.00125)}{(0.3)^2} = 0.055$$

Therefore, the matrix volume fraction is

$$v_m = 1 - 0.055 = 0.945$$

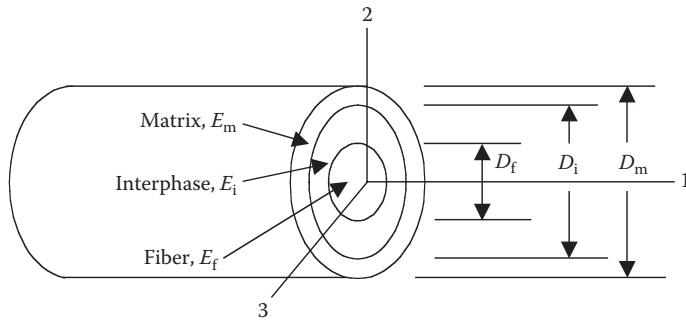
From Equation 3.27, the longitudinal modulus is

$$E_1 = E_{f1} v_f + E_m v_m = 200(0.055) + 17(0.945) = 27.065 \text{ GPa}$$

Note that, even though the volume fraction of the steel rods is only 5.5%, the steel contributes about 40% of the longitudinal composite modulus because of the high modulus of steel (200 GPa) relative to that of concrete (17 GPa).

### Example 3.4

As shown in Figure 3.7, an RVE for a three-phase unidirectional composite is approximated by three concentric cylinders representing the fiber, the matrix, and the fiber/matrix interphase. The fiber/matrix interphase is a region surrounding the fiber, which has different properties from either the fiber or the matrix. Interphase regions may be created during processing as a result of interactions between the matrix materials and either the fiber material or a fiber-sizing material. Since the geometrical features of this model are not associated with any specific fiber-packing array geometry, it has been referred to as a “self-consistent model” [8]. Assuming that the three materials are linear elastic, isotropic, and securely bonded together, derive the micromechanics equation for the longitudinal modulus,  $E_1$ , of the composite.

**FIGURE 3.7**

Self-consistent RVE for three-phase composite, including fiber, matrix, and fiber/matrix interphase.

### SOLUTION

The three constituent materials are arranged in parallel; so static equilibrium requires that the total resultant force on the composite must equal the sum of the forces acting on the three materials. Accordingly, the rule of mixtures for longitudinal composite stress in Equation 3.23 applies here, with the addition of a third term representing the interphase, as denoted by the subscript  $i$

$$\bar{\sigma}_{c1} = \bar{\sigma}_f v_f + \bar{\sigma}_m v_m + \bar{\sigma}_i v_i$$

Now supplementing Equation 3.24 with a similar stress-strain relationship for the interphase material and extending the assumption of equal strains in the constituents (Equation 3.26) to the interphase material as well, we get another rule of mixtures:

$$E_1 = E_f v_f + E_m v_m + E_i v_i = E_f \left( \frac{D_f^2}{D_m^2} \right) + E_m \left( \frac{D_m^2 - D_i^2}{D_m^2} \right) + E_i \left( \frac{D_i^2 - D_f^2}{D_m^2} \right)$$

where the diameters  $D_f$ ,  $D_m$ , and  $D_i$  are defined in Figure 3.7. Indeed, for a composite having any number of constituents,  $n$ , that are securely bonded together and arranged in parallel as in Figure 3.7, the generalized rule of mixtures for the longitudinal composite modulus is

$$E_1 = \sum_{j=1}^n E_j v_j$$

where  $E_j$  and  $v_j$  are the modulus and volume fraction of the  $j$ th constituent, respectively, and  $j = 1, 2, \dots, n$ .

#### 3.2.2 Transverse Modulus

If the RVE in Figure 3.5a is subjected to a transverse normal stress,  $\bar{\sigma}_{c2}$ , as shown in Figure 3.5c, the response is governed by the effective transverse

modulus,  $E_2$ . Geometric compatibility requires that the total transverse composite displacement,  $\bar{\delta}_{c2}$ , must equal the sum of the corresponding transverse displacements in the fiber,  $\bar{\delta}_{f2}$ , and the matrix,  $\bar{\delta}_{m2}$ :

$$\bar{\delta}_{c2} = \bar{\delta}_{f2} + \bar{\delta}_{m2} \quad (3.34)$$

It follows from the definition of normal strain that

$$\bar{\epsilon}_{c2} = \bar{\epsilon}_{c2}L_2, \quad \bar{\epsilon}_{f2} = \bar{\epsilon}_{f2}L_f, \quad \bar{\epsilon}_{m2} = \bar{\epsilon}_{m2}L_m \quad (3.35)$$

and Equation 3.34 now becomes

$$\bar{\epsilon}_{c2}L_2 = \bar{\epsilon}_{f2}L_f + \bar{\epsilon}_{m2}L_m \quad (3.36)$$

Since the dimensions of the RVE do not change along the 1 direction, the length fractions must be equal to the volume fractions, and Equation 3.36 can be rearranged to get the rule of mixtures for transverse strains:

$$\bar{\epsilon}_{c2} = \bar{\epsilon}_{f2}v_f + \bar{\epsilon}_{m2}v_m \quad (3.37)$$

The 1-D Hooke's laws for this case are

$$\bar{\sigma}_{c2} = E_2\bar{\epsilon}_{c2}, \quad \bar{\sigma}_{f2} = E_{f2}\bar{\epsilon}_{f2}, \quad \bar{\sigma}_{m2} = E_m\bar{\epsilon}_{m2} \quad (3.38)$$

where the Poisson strains have again been neglected. As with the longitudinal case, the inclusion of such strains would lead to a much more complex state of stress due to the mismatch in Poisson strains at the interface [10,11]. This is another example of the difference between a mechanics of materials solution and a more rigorous theory of elasticity solution. Combining Equations 3.38 and 3.37, we get

$$\frac{\bar{\sigma}_{c2}}{E_2} = \frac{\bar{\sigma}_{f2}}{E_{f2}}v_f + \frac{\bar{\sigma}_{m2}}{E_m}v_m \quad (3.39)$$

If we assume that the stresses in the composite, matrix, and fiber are all equal, Equation 3.39 reduces to the "inverse rule of mixtures" for the transverse modulus:

$$\frac{1}{E_2} = \frac{v_f}{E_{f2}} + \frac{v_m}{E_m} \quad (3.40)$$

From the RVE in Figure 3.5, it would seem that the assumption of equal stresses is valid because equilibrium requires that the forces must be equal for the series arrangement, and both fiber and matrix blocks have equal areas normal to the 2 direction. In the actual composite, however, the fiber-packing arrangement is such that the forces and areas for the fiber and matrix are not

necessarily equal, and we will use a strain energy approach to show that the resulting stresses are not equal. *Thus, Equation 3.40 is generally not acceptable for design use.* As shown in Figure 3.5a, Equation 3.40 gives the same result as Equation 3.27 at the extreme values of fiber volume fraction (i.e.,  $v_f = 0$  and  $v_f = 1.0$ ), but it predicts significant improvement in the transverse modulus  $E_2$  only at high fiber volume fractions. This turns out to be the correct trend, but, as shown in Section 3.5, the experimental data fall well above the predicted curve based on Equation 3.40.

As with the longitudinal case, the strain energy approach provides additional insight into the micromechanics of the transverse loading case. We now express the fiber and matrix strains in terms of the composite strain:

$$\bar{\varepsilon}_{f2} = a_2 \bar{\varepsilon}_{c2}, \quad \bar{\varepsilon}_{m2} = b_2 \bar{\varepsilon}_{c2} \quad (3.41)$$

where  $a_2$  and  $b_2$  are constants. Substitution of Equation 3.41 in the compatibility expression, Equation 3.37 yields

$$a_2 v_f + b_2 v_m = 1 \quad (3.42)$$

By substituting Equations 3.41 and 3.38 in equations analogous to Equation 3.29 for the transverse loading case and the strain energy expression, Equation 3.28, we find that

$$E_2 = a_2^2 E_{f2} v_f + b_2^2 E_m v_m \quad (3.43)$$

where the strain energy due to the Poisson strain mismatch at the interface has again been neglected. It is important to note that we did not assume equal stresses in the fibers and the matrix to obtain Equation 3.43. Using the properties for the E-glass/epoxy given in Equation 3.33 and solving Equations 3.42 and 3.43 simultaneously, we find that  $a_2 = 0.432$ ,  $b_2 = 1.465$ , the strain ratio  $a_2/b_2 = \bar{\varepsilon}_{f2}/\bar{\varepsilon}_{m2} = 0.295$ , and the corresponding stress ratio is  $\bar{\sigma}_{f2}/\bar{\sigma}_{m2} = 5.63$ . Thus, the assumption of equal stresses in fibers and matrix, which led to Equation 3.40, is not justified for this material and is apparently not valid for most other composites as well. More accurate alternative design equations for the transverse modulus will be discussed later.

### 3.2.3 Shear Modulus and Poisson's Ratio

The major Poisson's ratio,  $v_{12}$ , and the in-plane shear modulus,  $G_{12}$ , are most often used as the two remaining independent elastic constants for the orthotropic lamina. The major Poisson's ratio, which is defined as

$$v_{12} = -\frac{\bar{\varepsilon}_{c2}}{\bar{\varepsilon}_{c1}} \quad (3.44)$$

when the only nonzero stress is a normal stress along the 1 direction (Figure 3.5b), can be found by solving the geometric compatibility relationships associated with both the 1 and the 2 directions. The result is another rule of mixtures formulation:

$$v_{12} = v_{f12}v_f + v_m v_m \quad (3.45)$$

where  $v_{f12}$  is the major Poisson's ratio of the fiber and  $v_m$  is the Poisson's ratio of the matrix.

*Equation 3.45 is generally accepted as being sufficiently accurate for design purposes.* As in the case for the longitudinal modulus, the geometric compatibility relationships leading to the solution are valid.

The effective in-plane shear modulus is defined as (Figure 3.5d)

$$G_{12} = \frac{\bar{\sigma}_{c12}}{\bar{\gamma}_{c12}} \quad (3.46)$$

where  $\bar{\sigma}_{c12}$  is the average composite shear stress in the 12 plane and  $\bar{\gamma}_{c12} = 2\bar{\epsilon}_{c12}$ , the average engineering shear strain in the 12 plane.

An equation for the in-plane shear modulus can be derived using an approach similar to that which was used for the transverse modulus. That is, geometric compatibility of the shear deformations, along with the assumption of equal shear stresses in fibers and matrix, leads to another inverse rule of mixtures:

$$\frac{1}{G_{12}} = \frac{v_f}{G_{f12}} + \frac{v_m}{G_m} \quad (3.47)$$

where  $G_{f12}$  is the shear modulus of the fiber in the 12 plane and  $G_m$  is the shear modulus of the matrix.

*As we might expect, this equation is not very accurate because the shear stresses are not equal as assumed.* A strain energy approach similar to that used in Section 3.2.2 can be used here to show that the shear stresses are in fact not equal. *As with the transverse modulus, we need to find better equations for estimating the in-plane shear modulus. Such equations will be discussed in the following sections.*

### Example 3.5

The constituent materials in the composite described in Examples 3.1 and 3.2 have the properties  $E_f = 32.0 \times 10^6$  psi (220 GPa),  $E_{f2} = 2.0 \times 10^6$  psi (13.79 GPa), and  $E_m = 0.5 \times 10^6$  psi (3.45 GPa). Estimate the longitudinal and transverse moduli of the composite. Given these fiber and matrix materials, what are the maximum possible values of  $E_1$  and  $E_2$ ?

### SOLUTION

The longitudinal modulus is given by the rule of mixtures in Equation 3.27

$$E_1 = (32 \times 10^6)0.506 + (0.5 \times 10^6)0.482 = 16.43 \times 10^6 \text{ psi (113 GPa)}$$

The transverse modulus is roughly estimated by the inverse rule of mixtures in Equation 3.40:

$$E_2 = \frac{1}{\frac{0.506}{2 \times 10^6} + \frac{0.482}{0.5 \times 10^6}} = 0.82 \times 10^6 \text{ psi (5.65 GPa)}$$

However, as shown later, the inverse rule of mixtures prediction is typically well below the actual values of  $E_2$ , and is not recommended for design use. As expected, the composite is highly anisotropic with  $E_1 \gg E_2$ . If the composite has the theoretical maximum fiber volume fraction of 0.907 for a close-packed triangular array (Equation 3.17), the corresponding composite properties are still highly anisotropic, with  $E_1 = 29 \times 10^6$  psi (200 GPa) and  $E_2 = 1.56 \times 10^6$  psi (10.75 GPa). Note that even with this maximum fiber content, the transverse modulus is still very low. Thus, some transverse reinforcement is usually necessary in practical applications. Note also that the longitudinal modulus of the carbon/epoxy composite is now about the same as the modulus of steel, but the density of the composite is only about 20% of the density of steel. Composites typically have much greater stiffness-to-weight ratios than conventional metallic structural materials.

### **Example 3.6**

For longitudinal loading of the composites in Example 3.5, compare the stresses in the fiber and matrix materials. Compare the strain energy stored in the fibers with that stored in the matrix.

### SOLUTION

From Equations 3.24 and 3.26, the ratio of fiber stress to matrix stress is

$$\frac{\bar{\sigma}_{f1}}{\bar{\sigma}_{m1}} = \frac{E_{f1}\bar{\epsilon}_{f1}}{E_m\bar{\epsilon}_{m1}} = \frac{E_{f1}}{E_m} = \frac{32.0}{0.5} = 64.0$$

Thus, the fiber carries most of the stress since the fiber modulus is always higher than the matrix modulus. From Equations 3.29b, c and 3.26, the ratio of fiber strain energy to matrix strain energy is

$$\frac{U_f}{U_m} = \frac{E_{f1}V_f}{E_mV_m} = \frac{32.0(0.506)}{0.5(0.482)} = 67.0$$

that is almost the same as the stress ratio. If the composite had the maximum possible fiber volume fraction of 0.907, the stress ratio would remain the same since it is independent of the fiber volume fraction. However, the strain energy ratio would increase dramatically to 624, since it is proportional to the ratio of fiber volume fraction to the matrix volume fraction.

### 3.3 Improved Mechanics of Materials Models

As shown in the previous section, the elementary mechanics of materials models for  $E_1$  and  $v_{12}$  are good enough for design use. However, the corresponding models for  $E_2$  and  $G_{12}$  are of questionable value, because they are based on invalid assumptions, and agreement with experimental results is generally poor. We will now discuss several refinements of the elementary mechanics of materials models.

Due to the simplified RVE that was used for the elementary mechanics of materials approach (Figure 3.5), the resulting equations were not tied to any particular fiber-packing geometry. Since the results for  $E_1$  and  $v_{12}$  were so favorable, we can conclude that those properties must be essentially independent of fiber-packing geometry. By the same reasoning, it appears that  $E_2$  and  $G_{12}$  may be more sensitive to fiber-packing geometry. Thus, the assumption of a specific fiber-packing array is one possible refinement of the models. Although real composites have random-packing arrays, the assumption of a regular array is a logical simplification if we are to have any hope of developing simple design equations. Such an assumption allows us to use simple relations among fiber size, spacing, and volume fraction. Hopkins and Chamis [12] have developed a refined model for transverse and shear properties based on a square fiber-packing array and a method of dividing the RVE into subregions. The following derivation is adapted from Ref. [12].

A square array of fibers is shown in Figure 3.1, and the RVE for such an array is shown in Figure 3.8. The RVE is easily divided into subregions for more detailed analysis if we convert to a square fiber having the same area as the round fiber. The equivalent square fiber shown in Figure 3.8 must then have the dimension

$$s_f = \sqrt{\frac{\pi}{4}}d \quad (3.48)$$

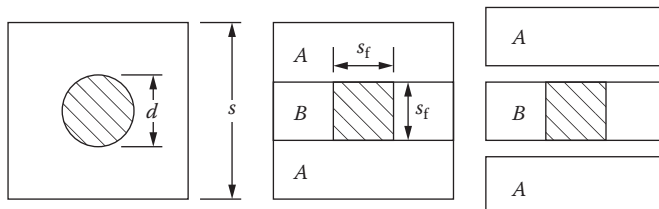


**FIGURE 3.8**

Division of RVE into subregions based on square fiber having equivalent fiber volume fraction.

and from Equation 3.14, the size of the RVE is

$$s = \sqrt{\frac{\pi}{4v_f}} d \quad (3.49)$$

The RVE is divided into subregions *A* and *B*, as shown in Figure 3.8. In order to find the effective transverse modulus for the RVE, we first subject the series arrangement of fiber and matrix in subregion *B* to a transverse normal stress. Following the procedure of Section 3.2.2, the effective transverse modulus for this subregion,  $E_{B2}$ , is found to be

$$\frac{1}{E_{B2}} = \frac{1}{E_{f2}} \frac{s_f}{s} + \frac{1}{E_m} \frac{s_m}{s} \quad (3.50)$$

where the matrix dimension is  $s_m = s - s_f$ . From Equations 3.48 and 3.49, it is seen that

$$\frac{s_f}{s} = \sqrt{v_f} \quad \text{and} \quad \frac{s_m}{s} = 1 - \sqrt{v_f} \quad (3.51)$$

so that Equation 3.50 now becomes

$$E_{B2} = \frac{E_m}{1 - \sqrt{v_f}(1 - E_m/E_{f2})} \quad (3.52)$$

The parallel combination of subregions *A* and *B* is now loaded by a transverse normal stress and the procedure of Section 3.2.1 is followed to find the effective transverse modulus of the RVE. The result, of course, is the rule of mixtures analogous to Equation 3.27

$$E_2 = E_{B2} \frac{s_f}{s} + E_m \frac{s_m}{s} \quad (3.53)$$

Substitution of Equations 3.51 and 3.52 in Equation 3.53 then gives the final result,

$$E_2 = E_m \left[ \left( 1 - \sqrt{v_f} \right) + \frac{\sqrt{v_f}}{1 - \sqrt{v_f}(1 - E_m/E_{f2})} \right] \quad (3.54)$$

A similar result may be found for  $G_{12}$ . The detailed derivation in Ref. [12] also includes the effect of a third phase, a fiber/matrix interphase material, which is assumed to be an annular volume surrounding the fiber. Such

interphase regions exist in many metal matrix [12] and polymer matrix [13] composites. When the fiber diameter is equal to the interphase diameter, the equation for  $E_2$  in [12] reduces to Equation 3.54. The complete set of equations for effective moduli of the three-phase model is given in [12].

In separate publications, Chamis [14,15] presented the so-called simplified micromechanics equations (SMEs), which are based on this same method of subregions, except that only the terms for subregion  $B$  (Figure 3.8) are retained. Thus, the SME for  $E_2$  would be the same as that for  $E_{B2}$  in Equation 3.52, and similar equations for the other effective moduli are given in Refs. [14,15]. Also included in these references are tables of fiber and matrix properties to be used as input to the SME, and these tables are reproduced here in Tables 3.1 and 3.2. It is important to note that in such tables, the transverse fiber modulus,  $E_{f2}$ , and the longitudinal fiber shear modulus,  $G_{f12}$ , are not actually measured but are inferred by substitution of measured composite properties and matrix properties in the SME. The inferred properties show that fibers such as carbon and aramid are highly anisotropic, whereas glass and boron are essentially isotropic. Similar back-calculations of anisotropic fiber properties using other analytical models have been reported by Kriz and Stinchcomb [16] and by Kowalski [17]. More recently, direct measurement of fiber transverse moduli has been reported by Kawabata [18]. Kawabata's measurements, based on transverse diametral compression of single carbon and aramid fibers, show even greater anisotropy than the inferred properties in Tables 3.1 and 3.2. However, Caruso and Chamis [19] have shown that the SME and the corresponding tables of properties give results that agree well with 3-D finite element models, as shown in Figure 3.9. Finite element models will be discussed in more detail in the next section. Since the SME for  $E_1$  and  $v_{12}$  are the same as Equations 3.27 and 3.45, respectively, this comparison provides further evidence of the validity of those equations.

Another set of equations for  $E_2$  and  $G_{12}$  has been derived by Spencer [20] who used a square array model that included the effects of the strain concentration at points of minimum clearance between fibers in the RVE. Spencer's equation is

$$\frac{M_c}{M_m} = \frac{\Gamma - 1}{\Gamma} + \frac{1}{k} \left[ -\frac{\pi}{2} + \frac{2\Gamma}{\sqrt{\Gamma^2 - k^2}} \tan^{-1} \sqrt{\frac{\Gamma + k}{\Gamma - k}} \right] \quad (3.55)$$

where  $M_c = E_2$ ,  $M_m = E_m$ , and  $k = 1 - E_m/E_{f2}$  for the transverse modulus equation and  $M_c = G_{12}$ ,  $M_m = G_m$ , and  $k = 1 - G_m/G_{f12}$  for the longitudinal shear modulus equation. The parameter  $\Gamma = s/d$  in both the equations. Spencer also suggests that  $\Gamma$  can be accurately approximated for a variety of packing geometries over the full range of fiber volume fractions,  $v_f$ , by the equation

$$\Gamma = \frac{1}{\sqrt{(1.1v_f^2 - 2.1v_f + 2.2)v_f}} \quad (3.56)$$

**TABLE 3.1**

Fiber Properties for Use in Chamis Simplified Micromechanics Equations (SME)

Properties	Units	Boron	HMS	AS	T300	KEV	S-G	E-G
Number of fibers per end	—	1	<b>10,000</b>	10,000	3000	580	204	204
Fiber diameter	in.	0.0056	<b>0.0003</b>	0.0003	0.0003	0.00046	0.00036	0.00036
Density	lb/in. <sup>3</sup>	0.095	<b>0.070</b>	0.063	0.064	0.053	0.090	0.090
Longitudinal modulus	10 <sup>6</sup> psi	58	<b>55.0</b>	31.0	32.0	22	12.4	10.6
Transverse modulus	10 <sup>6</sup> psi	58	<b>0.90</b>	2.0	2.0	0.6	12.4	10.6
Longitudinal shear modulus	10 <sup>6</sup> psi	24.2	<b>1.1</b>	2.0	1.3	0.42	5.17	4.37
Transverse shear modulus	10 <sup>6</sup> psi	24.2	<b>0.7</b>	1.0	0.7	0.22	5.17	4.37
Longitudinal Poisson's ratio	—	0.20	<b>0.20</b>	0.20	0.20	0.35	0.20	0.22
Transverse Poisson's ratio <sup>a</sup>	—	0.20	<b>0.00327</b>	0.0129	0.0125	0.00954	0.20	0.22
Heat capacity	btu/1b/°F	0.31	<b>0.20</b>	0.20	0.22	0.25	0.17	0.17
Longitudinal heat conductivity	btu/h/ft <sup>2</sup> /°F/in	22	<b>580</b>	580	580	1.7	21	7.5
Transverse heat conductivity	btu/h/ft <sup>2</sup> /°F/in	22	<b>58</b>	58	58	1.7	21	7.5
Longitudinal thermal expansion coefficient	10 <sup>-6</sup> in./in./°F	2.8	<b>- 0.55</b>	- 0.55	- 0.55	- 2.2	2.8	2.8
Transverse thermal expansion coefficient	10 <sup>-6</sup> in./in./°F	2.8	<b>5.6</b>	5.6	5.6	30	2.8	2.8
Longitudinal tensile strength	ksi	600	<b>250</b>	350	350	400	600	400
Longitudinal compression strength	ksi	700	<b>200</b>	260	300	75	—	—
Shear strength	ksi	100	—	—	—	—	—	—

<sup>a</sup> Estimates of Transverse Poisson's ratio based on assumed symmetry of fiber compliance matrix.

Note: Transverse, shear, and compression properties are estimates inferred from corresponding composite properties. HMS, AS, and T300 are carbon fibers, KEV is Kevlar, S-G is S-glass, and E-G is E-glass.

Source: From Chamis, C.C. 1987. In Weeton, J.W., Peters, D.M., Thomas, K.L. eds. *Engineers' Guide to Composite Materials*. ASM International, Materials Park, OH. With permission.

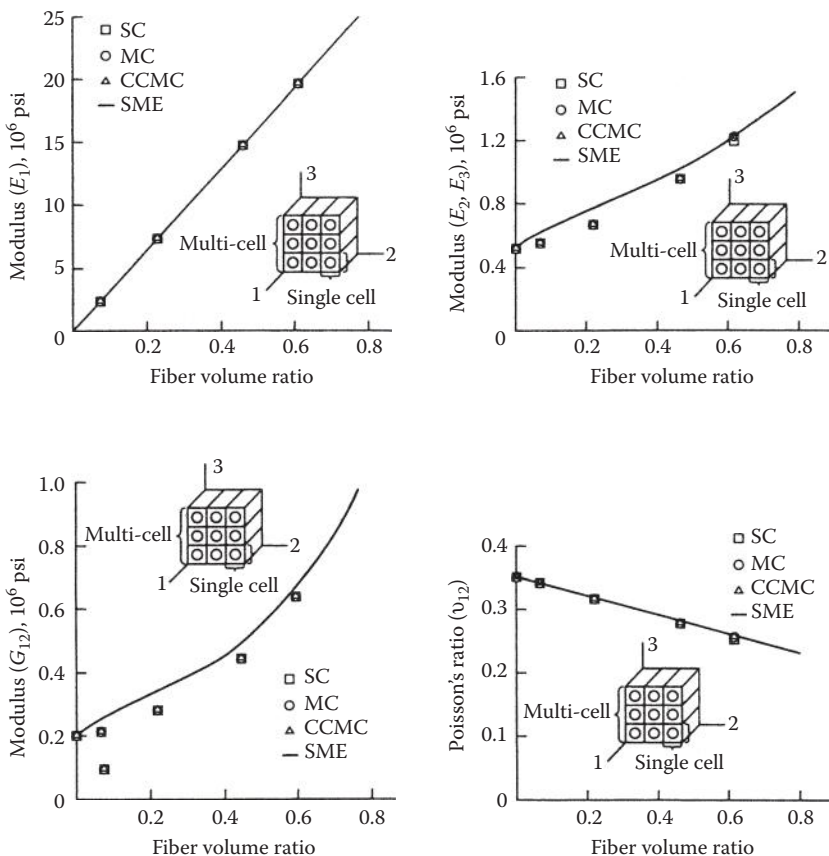
**TABLE 3.2**

Matrix Properties for Use in Chamis Simplified Micromechanics Equations

Parameters	Units	LM	IMLS	IMHS	HM	Polyimide	PMR
Density	1b/in. <sup>3</sup>	0.042	0.046	0.044	0.045	0.044	0.044
Modulus	10 <sup>6</sup> psi	0.32	0.50	0.50	0.75	0.50	0.47
Shear modulus	10 <sup>6</sup> psi	—	—	—	—	—	—
Poisson's ratio	—	0.43	0.41	0.35	0.35	0.35	0.36
Heat capacity	btu/1b/°F	0.25	0.25	0.25	0.25	0.25	0.25
Heat conductivity	btu/h/ft <sup>2</sup> /°F/in.	1.25	1.25	1.25	1.25	1.25	1.25
Thermal expansion coefficient	10 <sup>-6</sup> in./in./°F	57	57	36	40	20	28
Diffusivity	10 <sup>-10</sup> in. <sup>2</sup> /s	0.6	0.6	0.6	0.6	0.6	0.6
Moisture expansion coefficient	in./in./M	0.33	0.33	0.33	0.33	0.33	0.33
Tensile strength	ksi	8	7	15	20	15	8
Compression strength	ksi	15	21	35	50	30	16
Shear strength	ksi	8	7	13	15	13	8
Tensile fracture strain	in./in. (%)	8.1	1.4	2.0	2.0	2.0	2.0
Compressive fracture strain	in./in. (%)	15	4.2	5.0	5.0	4.0	3.5
Shear fracture strain	in./in. (%)	10	3.2	3.5	4.0	3.5	5.0
Air heat conductivity	btu/h/ft <sup>2</sup> /°F/in.	0.225	0.225	0.225	0.225	0.225	0.225
Glass transition temperature (dry)	°F	350	420	420	420	700	700

Note: LM, low modulus; IMLS, intermediate modulus low strength; IMHS, intermediate modulus high strength; HM, high modulus. Thermal, hygral, compression, and shear properties are estimates only;  $G_m = E_m / 2(1 + \nu_m)$ . LM, IMLS, IMHS, and HM refer to typical epoxy matrix resins.

Source: From Chamis, C. C., 1987. In Weeton, J. W., Peters, D. M., and Thomas, K. L. eds. *Engineers' Guide to Composite Materials*. ASM International, Materials Park, OH. With permission.

**FIGURE 3.9**

Comparison of 3-D finite element results for lamina elastic constants with predictions from SMEs for carbon/epoxy. (From Caruso, J. J. and Chamis, C. C. 1986. *Journal of Composites Technology and Research*, 8(3), 77–83. With permission.)

Spencer does not include a table of suggested properties for use with these equations.

### 3.4 Elasticity Models

The theory of elasticity approach to micromechanical modeling begins in the same way as the mechanics of materials approach, by selecting the RVE and then subjecting it to uniform stress or displacement at the boundary. The two approaches differ substantially in the solution of the resulting boundary value problem, however. The equations of elasticity must be satisfied at every

point in the model, and no simplifying assumptions are made regarding the stress or strain distributions as in the mechanics of materials approach. Fiber-packing geometry is generally specified in the elasticity approach. A variety of closed-form and numerical solutions of the governing equations of elasticity have been reported in the literature [1–4], and a complete review of the work in this area is beyond the scope of this book. However, the stress equilibrium equations and the strain–displacement relations from elasticity theory are derived in Appendices B and C, respectively. The objective here is to discuss several representative numerical and closed-form solutions in order to show what additional knowledge of micromechanical behavior can be obtained from the more rigorous elasticity approach. Particular emphasis is placed on finite element numerical solutions.

### 3.4.1 Finite Difference Models

Numerical solutions of the governing elasticity equations are often necessary for complex structural geometries such as those found in the RVEs used in micromechanics models. For example, Adams and Doner [21] used a finite difference solution to determine the shear modulus  $G_{12}$  for a rectangular array of fibers. A displacement boundary value problem was solved for one quadrant of the RVE, as shown in Figure 3.10. Note that Adams and Doner use the  $z$  axis to define the fiber direction, whereas the  $x$  and  $y$  axes correspond to the transverse directions. The displacement components  $u$ ,  $v$ , and  $w$  correspond to the displacements along the  $x$ ,  $y$ , and  $z$  axes, respectively. The

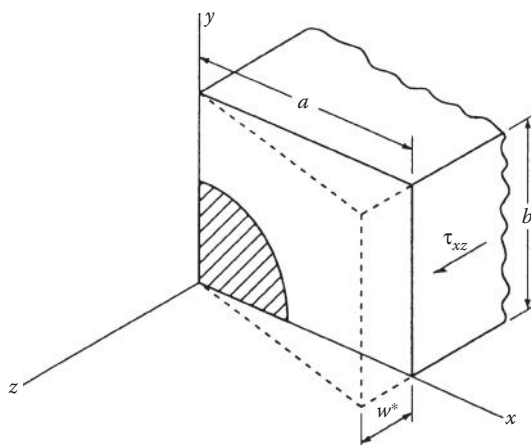


**FIGURE 3.10**

One quadrant of an RVE from Adams and Doner elasticity solution for shear modulus  $G_{12}$ . (From Adams, D. F. and Doner, D. R. 1967. *Journal of Composite Materials*, 1, 4–17. With permission.)

imposed displacement  $w^*$  along  $x = a$  causes a displacement field of the form

$$u = v = 0, \quad w = w(x, y) \quad (3.57)$$

From the strain-displacement equations (Appendix C) and Hooke's law, the only nonvanishing stress components are

$$\tau_{xz} = G \frac{\partial w}{\partial x} \quad \text{and} \quad \tau_{zy} = G \frac{\partial w}{\partial y} \quad (3.58)$$

where the shear modulus,  $G$ , may be either the fiber shear modulus,  $G_f$ , or the matrix shear modulus,  $G_m$ , depending on whether the coordinates  $x$  and  $y$  locate a point in the fiber or in the matrix. Isotropic behavior was assumed for both fiber and matrix materials. Substitution of Equations 3.58 in the only nontrivial stress equilibrium equation (Appendix B) yielded the governing partial differential equation

$$G \left[ \frac{\partial^2 w}{\partial x^2} + \frac{\partial^2 w}{\partial y^2} \right] = 0 \quad (3.59)$$

which was solved subject to the displacement boundary conditions

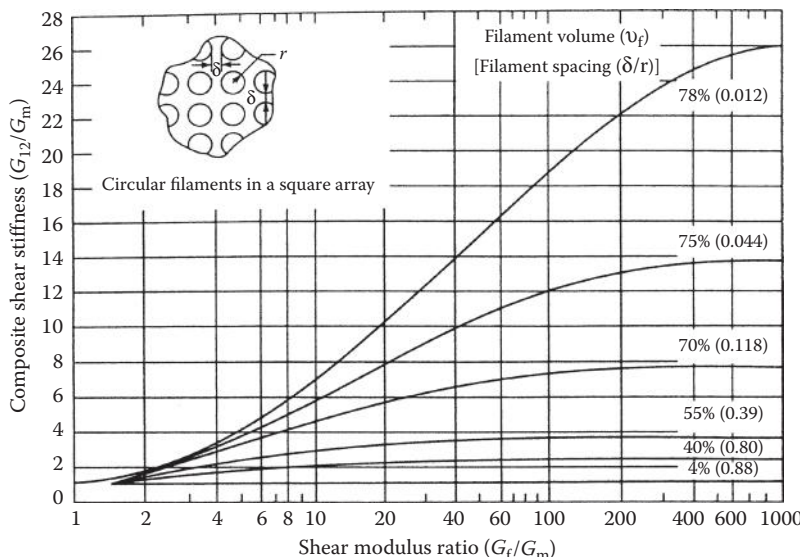
$$\begin{aligned} w(0, y) &= 0, \quad w(a, y) = w^* \\ G \frac{\partial w}{\partial y} &= 0 \quad \text{along} \quad y = 0 \quad \text{and} \quad y = b \end{aligned} \quad (3.60)$$

and continuity conditions at the fiber/matrix interface by using a finite difference scheme. The solution yielded the values of the displacements  $w(x, y)$  at each node of the finite difference grid. Stresses were found by substituting these displacements in the finite difference forms of Equation 3.58, and the effective shear modulus was then determined from

$$G_{xz} = \frac{\bar{\tau}_{xz}}{w^*/a} \quad (3.61)$$

where  $\bar{\tau}_{xz}$  is the average shear stress along  $x = a$ . A similar boundary value problem for shear along  $y = b$  yields the associated shear modulus  $G_{yz}$ . Typical results are shown in Figure 3.11, where the ratio of the composite shear modulus to the matrix shear modulus,  $G_{12}/G_m$ , is plotted versus the shear modulus ratio  $G_f/G_m$  for various fiber volume fractions.

In a separate paper, Adams and Doner [22] used a similar approach to determine the transverse modulus  $E_2$  and typical results are shown in Figure 3.12. It is seen in Figures 3.11 and 3.12 that the reinforcement effect for

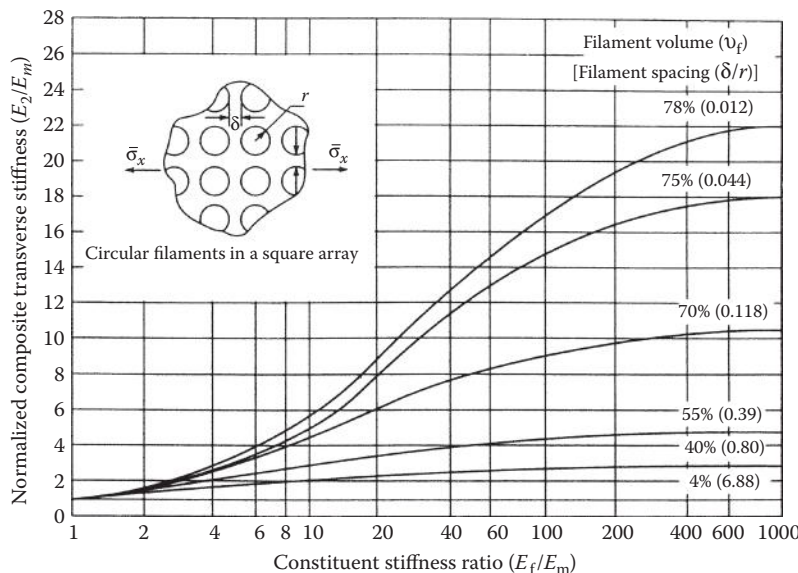
**FIGURE 3.11**

Normalized composite shear stiffness,  $G_{12}/G_m$ , vs. shear modulus ratio,  $G_f/G_m$ , for circular fibers in a square array. (From Adams, D. F. and Doner, D. R. 1967. *Journal of Composite Materials*, 1, 4-17. With permission.)

both  $G_{12}$  and  $E_2$  only becomes significant for fiber volume fractions above about 50%, but that combinations of high fiber stiffness and high fiber volume fractions can significantly increase  $G_{12}$  and  $E_2$ . Unfortunately, these same combinations also generate very high stress concentration factors at the fiber/matrix interfaces, as shown in the same papers [21,22]. One of the advantages of the elasticity approach is that the complete stress and strain distributions in the RVE are generated, and the calculation of stress concentration factors is possible. One advantage of numerical solutions such as finite differences is the capability for analysis of complex geometries. For example, stiffness and stress concentration factors were also obtained for a variety of fiber cross-sectional shapes such as squares and ellipses in a rectangular array [21,22].

### 3.4.2 Finite Element Models

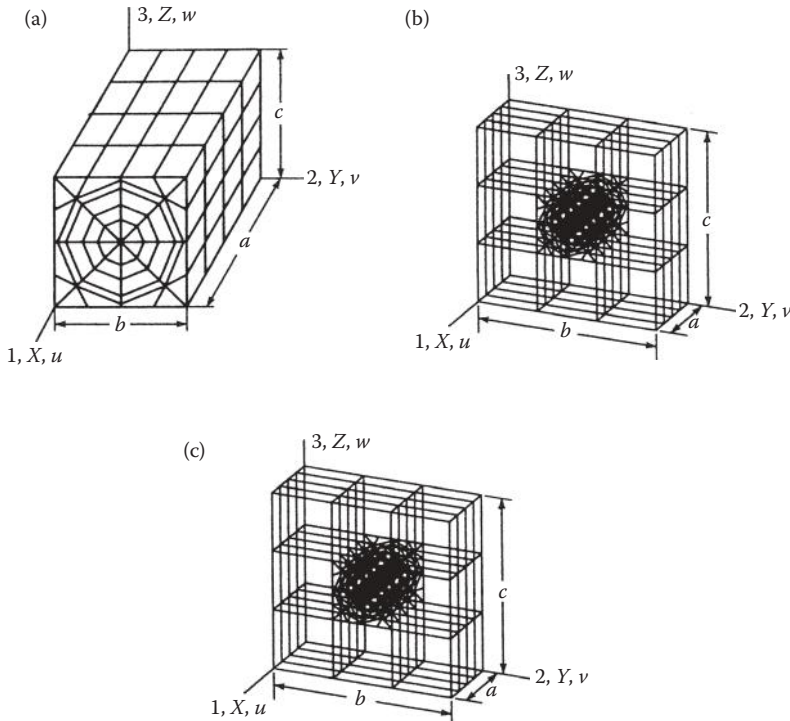
The most widely used numerical approach to micromechanics modeling is finite element analysis (FEA). The previously mentioned FEA of Caruso and Chamis [19] and Caruso [23] is one example of such an approach. In this case, a single-cell (SC) finite element model was developed from 192 3-D isoparametric brick elements (Figure 3.13). This SC model was then used as a building block for a multicell (MC) model consisting of nine SC models in a  $3 \times 3$  array (Figure 3.9). A third model (CCMC) used only the center cell in the

**FIGURE 3.12**

Normalized composite transverse stiffness,  $E_2/E_m$ , versus modulus ratio,  $E_f/E_m$ , for circular fibers in a square array. (From Adams, D. F. and Doner, D. R. 1967. *Journal of Composite Materials*, 1, 152–164. With permission.)

nine-cell MC model for the calculations. Boundary and load conditions were consistent with those used for the previously discussed SME mechanics of materials solutions, so that the finite element results could be compared with the SME results. For example, Equation 3.61 and similar equations were used to determine stiffnesses from finite element results. Material properties for AS graphite fibers in an intermediate-modulus-high-strength (IMHS) epoxy matrix were used (Tables 3.1 and 3.2). Fibers were assumed to be orthotropic, whereas the matrix was assumed to be isotropic. As shown in Figure 3.9, the finite element results show good agreement with SME results.

As with the previously discussed finite difference approach used in Refs. [21,22], the quarter domain model of a representative volume can also be analyzed by using finite elements. Typical 2-D and 3-D quarter domain finite element models are shown in Figure 3.14 from [24]. For example, in one study, 3-D finite element quarter domain models similar to the one in Figure 3.14 were subjected to transverse normal loading as in Figure 3.15 [24,25], and the effect of model aspect ratio  $L/(D/2)$  on the transverse modulus was determined, as shown in Figure 3.16. In this model, the fiber axis is assumed to lie along the  $z$  direction, while  $x$  and  $y$  are transverse to the fiber axis. This particular model included a fiber coating or interphase region between the fiber and the matrix (see Example 3.4 for further discussion of the interphase). For the quarter domain model, boundary conditions are that along the plane  $x = 0$ , displacements perpendicular to the plane are prevented, while along

**FIGURE 3.13**

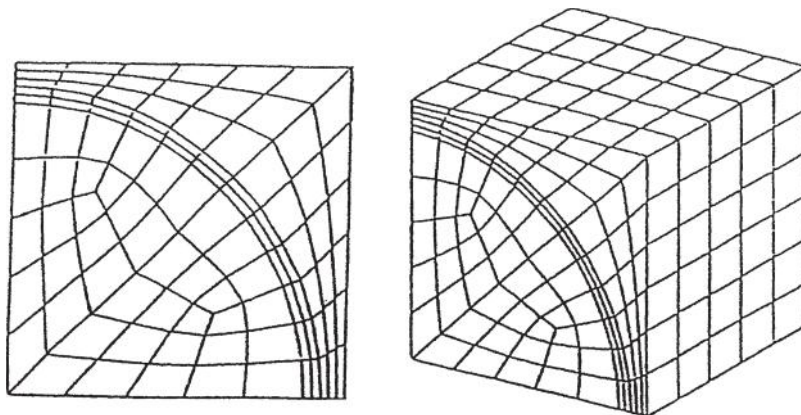
3-D finite element models of RVEs. (a) The single-cell model used for the SC calculation, (b) the multicell model which is used for the MC calculation, and (c) the multicell model which only the center cell is used for the CCMC calculation. (From Caruso, J. J. and Chamis, C. C. 1986. *Journal of Composites Technology and Research*, 8(3), 77–83. Copyright ASTM. With permission.)

the plane  $y = 0$ , displacements perpendicular to that plane are also prevented. The transverse modulus was calculated by imposing a uniform displacement  $U_x$  along the plane  $x = D/2$  and then using the calculated stresses from the finite element model to evaluate Equation 3.62:

$$E_x = \frac{\bar{\sigma}_x}{\bar{\epsilon}_x} = \frac{\int_V \sigma_x dV}{\frac{\int_V \epsilon_x dV}{V}} \quad (3.62)$$

where  $\bar{\sigma}_x$  = average stress acting along plane  $x = D/2$  in Figure 3.15,

$$\bar{\epsilon}_x = \frac{U_x}{(D/2)} = \text{average strain along plane } x = D/2$$

**FIGURE 3.14**

Examples of 2-D and 3-D finite element quarter domain micromechanics models. (From Finegan, I. C. and Gibson, R. F. 1997. In Farabee, T. M. ed. *Proceedings of ASME Noise Control and Acoustics Division*. NCA-Vol. 24, pp. 127–138. With permission.)

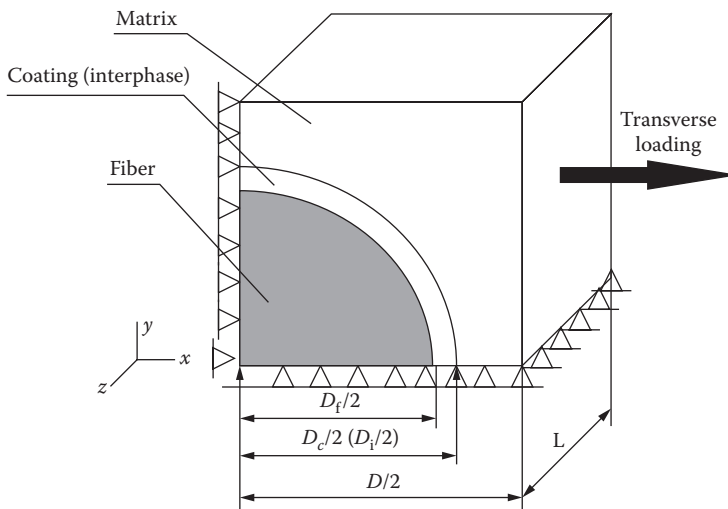
where

$D/2$  = dimension defined in Figure 3.15

$U_x$  = imposed displacement along  $x = D/2$

$L$  = length of model along  $z$ , the fiber direction

$V$  = volume

**FIGURE 3.15**

Quarter domain of RVE under transverse normal loading. (From Finegan, I. C. and Gibson, R. F. 1998. *Journal of Vibration and Acoustics*, 120(2), 623–627. With permission.)

It is seen from Figure 3.16 that the transverse modulus varies from a minimum value for low-model aspect ratios to a maximum for high-model aspect ratios [24,25]. It was also shown that the low-model aspect ratio results from 3-D models coincided with the results obtained by using 2-D plane stress elements (i.e., with longitudinal stress  $\sigma_z = 0$ ), while the high-model aspect ratio results from 3-D models coincided with the results obtained by using 2-D plane strain elements (i.e., with longitudinal strain  $\epsilon_z = 0$ ). For a unidirectional composite having continuous fibers oriented along the  $z$  direction, the plane strain condition is more realistic than the plane stress condition. The importance of this observation is that 2-D plane strain elements can be used for these types of models instead of 3-D elements, and this leads to significant reductions in the number of elements and the corresponding computation time.

Proper treatment of boundary conditions on the RVEs of micromechanical FEA models is particularly important [26]. Since the composite is assumed to consist of large numbers of identical and adjacent RVEs as repeating elements, the deformations on the boundaries of a given RVE must be geometrically compatible with those of the adjacent RVEs. Figure 3.17a shows an example of a boundary deformation pattern that is not geometrically compatible with that of the adjacent identical RVEs (i.e.,

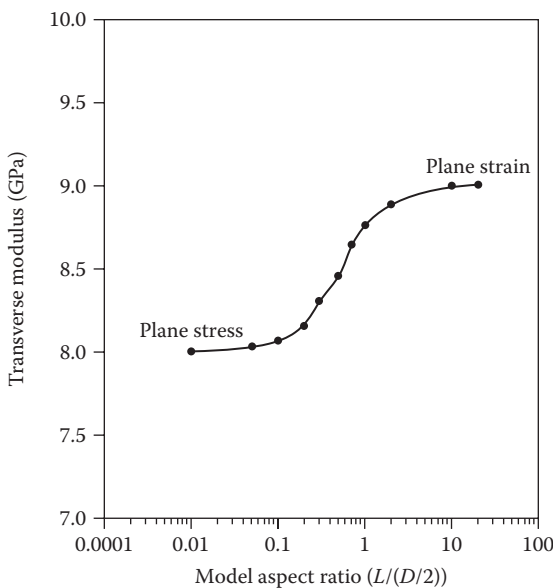


**FIGURE 3.16**

Variation of transverse modulus with model aspect ratio for graphite/epoxy composite from 3-D finite element models. (From Finegan, I. C. and Gibson, R. F. 1998. *Journal of Vibration and Acoustics*, 120(2), 623–627. With permission.)

symmetry arguments tell us that the deformed RVEs will not “fit together” to form a continuous composite without gaps). By contrast, Figure 3.17b shows a boundary deformation pattern that is geometrically compatible with that of its neighboring RVEs (i.e., the deformed RVEs will all “fit together” to form a continuous composite without gaps). These are often referred to as “periodic boundary conditions,” since they are repeated over and over again from one RVE to another as we move through the composite. For normal loading as in Figure 3.15, geometric compatibility is assured if each boundary surface is constrained to deform parallel to itself as in Figure 3.17b. Such constraints on displacements of a plane can be accomplished in FEA by using the so-called multipoint constraint (MPC) elements which are available in many FEA codes. MPC elements allow the user to specify a “master node” in a plane such that all nodes in that plane will have the same displacement under load. For shear loading as in Figure 3.10, geometric compatibility is assured if the deformed shape is a parallelogram, although, as pointed out by Sun and Vaidya [26], it is not necessary for the edges of the parallelogram to remain straight as they rotate in shear distortion. Note that, when the displacement is imposed, as in the example described above and in [25], geometric compatibility is assured by the imposed planar displacement. When the applied stress is imposed, however, displacement constraints must be specified to assure geometric compatibility.

### 3.4.3 Closed-Form and Variational Models

As an example of a closed-form elasticity solution, Whitney and Riley [8] used axisymmetric Airy stress functions to solve for the stresses and strains in a so-called “self-consistent” model having a single isotropic fiber embedded in a concentric cylinder of isotropic matrix material. The cylindrical

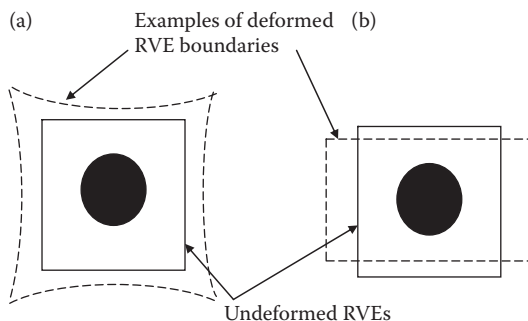


**FIGURE 3.17**

Boundary deformations for RVEs of micromechanical models: (a) boundary deformations are geometrically incompatible with those of identical adjacent RVEs and (b) boundary deformations are geometrically compatible with those of identical adjacent RVEs.

geometry of the self-consistent model is such that the model is not associated with any specific fiber-packing geometry. The resulting micromechanical stresses and strains were then used in energy balance equations similar to Equations 3.28 and 3.29 to solve for  $E_1$  and  $E_2$ . The equation for  $E_1$  reduces to the rule of mixtures when the Poisson's ratio of the fiber is equal to that of the matrix. The additional term is due to the mismatch in Poisson strains at the fiber/matrix interface (recall that this term was neglected in Equations 3.28 and 3.29). Predictions showed good agreement with experimental data for boron/epoxy. In a later paper, Whitney extended the analysis to include anisotropic, transversely isotropic fibers [27].

Another closed-form micromechanical elasticity approach, the method of cells was developed by Aboudi [28]. A representative cell consisting of a square fiber embedded in a square of matrix material was divided into four subcells. Equilibrium equations were then solved subject to continuity of displacements and tractions at the interfaces between the subcells and between neighboring cells on an average basis, along with the assumption of linear variations of displacements in each subcell. The equations are too lengthy to present here, but excellent agreement was observed with the experimental data on graphite/epoxy from Ref. [16]. One advantage of this approach is that it yields not only the in-plane lamina properties, but also the through-the-thickness properties such as  $G_{23}$  and  $v_{23}$ .

Paul [29] obtained closed-form solutions for the bounds on the transverse modulus of a fiber composite (or Young's modulus of an isotropic-particle-reinforced composite) by using a variational approach. By applying the theorem of minimum complementary energy to the situation where the composite is subjected to a uniaxial normal stress, Paul found the lower bound on  $E_2$  to be the inverse rule of mixtures (3.40). The application of the theorem of minimum potential energy to the situation where the composite is subjected to a simple extensional strain gave the upper bound on  $E_2$ , which reduces to the rule of mixtures (3.27) when the Poisson's ratios of fiber and matrix materials are taken to be the same.

The bounds derived by Paul [29] are independent of packing geometry and are referred to as the elementary bounds. Thus, it should be no surprise that the bounds are very far apart, as shown in Figure 3.6. Tighter bounds require the specification of packing geometry. For example, Hashin and Rosen [30] applied the principles of minimum potential and complementary energy to fiber composites with hexagonal and random arrays. Detailed summaries of these and other related results have been reported by Hashin [1] and Christensen [3]. More recently, Torquato [31] has reviewed advances in the calculation of improved bounds on the effective properties of random heterogeneous media. Such improved bounds are determined by using statistical correlation functions to model the random variations in the microstructure. Since the fiber-packing geometry in composites is of a random nature, such bounds should be more realistic than the bounds that are based on some idealized fiber-packing array.

---

### 3.5 Semiempirical Models

In Section 3.3, improved mechanics of materials models for the prediction of  $E_2$  and  $G_{12}$  were discussed. Another general approach to estimating these properties involves the use of semiempirical equations that are adjusted to match experimental results or elasticity results by the use of curve-fitting parameters. The equations are referred to as being “semiempirical” because, although they have terms containing curve-fitting parameters, they also have some basis in mechanics. The most widely used semiempirical equations were developed by Halpin and Tsai [32]. The Halpin–Tsai equation for the transverse modulus is

$$\frac{E_2}{E_m} = \frac{1 + \xi\eta v_f}{1 - \eta v_f} \quad (3.63)$$

where

$$\eta = \frac{(E_f/E_m) - 1}{(E_f/E_m) + \xi} \quad (3.64)$$

and  $\xi$  is the curve-fitting parameter, which is also a measure of the degree of reinforcement of the matrix by the fibers. The corresponding equation for  $G_{12}$  is obtained by replacing Young's moduli  $E_2$ ,  $E_f$ , and  $E_m$  in the above equations by the shear moduli  $G_{12}$ ,  $G_f$ , and  $G_m$ , respectively. Note that the values for the curve-fitting parameter may be different for  $E_2$  and  $G_{12}$ . Halpin and Tsai found that the value  $\xi = 2$  gave an excellent fit to the finite difference elasticity solution of Adams and Doner [22] for the transverse modulus of a square array of circular fibers having a fiber volume fraction of 0.55. For the same material and fiber volume fraction, a value of  $\xi = 1$  gave excellent agreement with the Adams and Doner solution for  $G_{12}$  [21].

Jones [11] shows that when  $\xi = 0$ , the Halpin–Tsai equation reduces to the inverse rule of mixtures (3.40), whereas a value of  $\xi = \infty$  yields the rule of mixtures (3.27). Recall that Paul [29] proved that these equations also represent the bounds on  $E_2$ . Thus, the interpretation of the curve-fitting parameter,  $\xi$ , as a measure of the degree of fiber reinforcement has a theoretical basis. The use of the Halpin–Tsai equations in a variety of other applications and related empirical equations for estimating the curve-fitting parameter are discussed in more detail by Jones [11] and Halpin [4]. Zhu et al. [33] have shown that the predicted elastic constants for Kevlar/epoxy from the Halpin–Tsai equations agree closely with predictions from finite element micro-mechanics models similar to those discussed in Section 3.4.2.

Tsai and Hahn [10] have proposed another semiempirical approach to calculating  $E_2$  and  $G_{12}$ , that is based on the fact that the stresses in the fibers and

the matrix are not equal under the corresponding loading conditions. Recall that the proof of such differences was demonstrated using a strain energy approach in Section 3.2.2. The method involves the use of empirical “stress-partitioning parameters” in derivations paralleling those used for the elementary mechanics of materials models. For example, the Tsai–Hahn equation for  $E_2$  is found by introducing a stress-partitioning parameter,  $\eta_2$ , and using the relationship

$$\bar{\sigma}_{m2} = \eta_2 \bar{\sigma}_{f2} \quad (3.65)$$

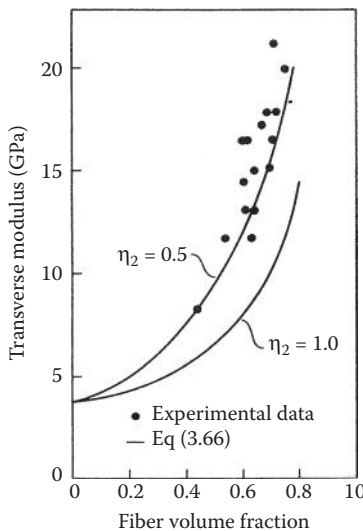
in a derivation similar to that used for the elementary mechanics of materials model for  $E_2$  in Section 3.2.2. The derivation was also based on the assumption that a rule of mixtures for stress similar to Equation 3.23 also held for the transverse direction (2 direction). Although such an assumption is obviously not consistent with the RVE configuration and the loading condition shown in Figure 3.5c, it would be valid for a real composite with fiber packing such as that shown in Figure 3.2. The result of this derivation is

$$\frac{1}{E_2} = \frac{1}{v_f + \eta_2 v_m} \left[ \frac{v_f}{E_f} + \frac{\eta_2 v_m}{E_m} \right] \quad (3.66)$$

Note that Equation 3.66 reduces to the inverse rule of mixtures (Equation 3.40) when the stress-partitioning parameter  $\eta_2 = 1.0$ . This is to be expected since Equation 3.40 was based on the assumption that the stresses in the fiber and the matrix are the same. A similar equation can be derived for the shear modulus,  $G_{12}$ , as shown in Ref. [10]. Figure 3.18 from Ref. [10] shows experimental data for the transverse modulus of a glass/epoxy composite compared with the predicted values from Equation 3.66 for two different assumed values of the stress-partitioning parameter. Clearly, the experimental data fall well above the prediction for  $\eta_2 = 1.0$ , which corresponds to the inverse rule of mixtures (Equation 3.40). This further validates the statement following Equation 3.40 that the inverse rule of mixtures is not acceptable for design use. A much better agreement is seen for  $\eta_2 = 0.5$ , which means that the stress in the matrix is only one-half of the stress in the fiber. The stress-partitioning parameter  $\eta_2 = 0.5$  was also found to yield accurate predictions of  $G_{12}$  based on comparisons with experimental data for the same glass/epoxy [10]. Formulas for estimating the stress-partitioning parameters from constituent material properties are also given in [10].

### Example 3.7

For the composite in Example 3.5, compare the transverse modulus values calculated by the inverse rule of mixtures (3.40), the method of subregions (3.54),

**FIGURE 3.18**

Transverse modulus for glass/epoxy according to Tsai–Hahn equation (3.66). (From Tsai, S. W. and Hahn, H. T. 1980. *Introduction to Composite Materials*. Technomic Publishing Co., Lancaster, PA. With permission.)

Spencer's equation (3.55), the Halpin–Tsai equation (3.63), and the Tsai–Hahn equation (3.66).

### SOLUTION

The result from the inverse rule of mixtures (3.40), as previously calculated in Example 3.5, is

$$E_2 = 0.82 \times 10^6 \text{ psi} (5.65 \text{ GPa})$$

For the method of subregions (3.54):

$$\begin{aligned} E_2 &= E_m \left[ \left( 1 - \sqrt{v_f} \right) + \frac{\sqrt{v_f}}{1 - \sqrt{v_f} \left( 1 - (E_m/E_{i2}) \right)} \right] \\ &= 0.5 \times 10^6 \left[ \left( 1 - \sqrt{0.506} \right) + \frac{\sqrt{0.506}}{1 - \sqrt{0.506} \left( 1 - (0.5/2) \right)} \right] \\ &= 0.9 \times 10^6 \text{ psi} (6.2 \text{ GPa}) \end{aligned}$$

For Spencer's equation (3.55):

First estimate  $\Gamma = 1.18$  from Equation 3.56. Note that the actual value of  $\Gamma$  from example 3.2 is  $\Gamma = s/d = 0.000623/0.0005 = 1.25$ . Using  $\Gamma = 1.18$  in Equation 3.55, we have  $E_2 = 0.98 \times 10^6 \text{ psi} (6.76 \text{ GPa})$ .

For the Halpin–Tsai equation (3.63):

$$\eta = \frac{(E_f/E_m) - 1}{(E_f/E_m) + \xi} = \frac{(2/0.5) - 1}{(2/0.5) + 2} = 0.5$$

$$E_2 = E_m \left( \frac{1 + \xi \eta v_f}{1 - \eta v_f} \right) = 0.5 \times 10^6 \left( \frac{1 + 2(0.5)(0.506)}{1 - 0.5(0.506)} \right)$$

$$= 1.00 \times 10^6 \text{ psi (6.89 GPa)}$$

For the Tsai–Hahn equation (3.66):

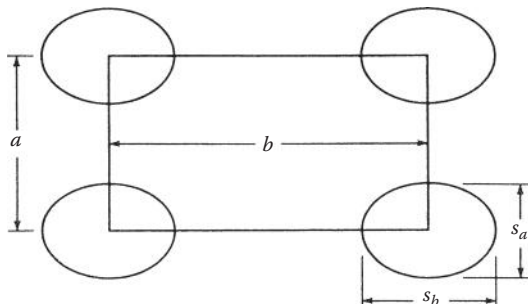
$$\frac{1}{E_2} = \frac{1}{v_f + \eta_2 v_m} \left[ \frac{v_f}{E_f} + \frac{\eta_2 v_m}{E_m} \right] = \frac{1}{0.506 + 0.5(0.482)} \left[ \frac{0.506}{2 \times 10^6} + \frac{0.5(0.482)}{0.5 \times 10^6} \right]$$

so that  $E_2 = 1.016 \times 10^6 \text{ psi (7 GPa)}$ .

As previously mentioned, the inverse rule of mixtures prediction for the transverse modulus is considerably lower than experimentally determined values. However, the higher values given by the method of subregions, Spencer's equation, the Halpin–Tsai equation, and the Tsai–Hahn equation are in good agreement with each other and with experimental values, and so these equations are recommended for design use.

### PROBLEMS

1. A rectangular array of elliptical fibers is shown in Figure 3.19. Derive the relationship between the fiber volume fraction and the given geometrical parameters. What is the maximum possible fiber volume fraction for this packing geometry?
2. The fibers in a E-glass/epoxy composite are 0.0005 in. (0.0127 mm) in diameter before coating with an epoxy sizing 0.0001 in. (0.00254 mm) thick. After the sizing has been applied, the fibers

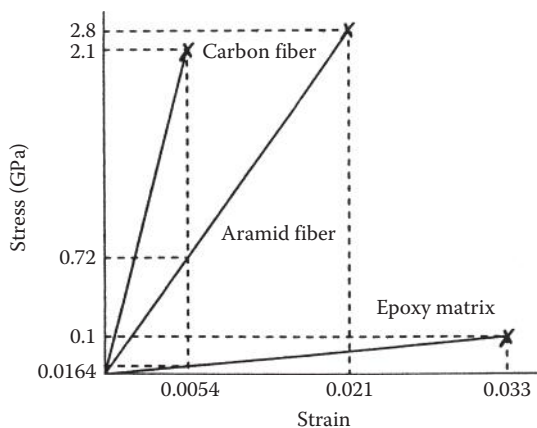


**FIGURE 3.19**

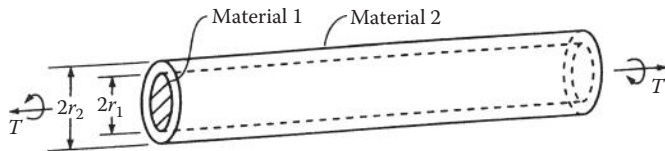
Rectangular array of elliptical fibers.

are bonded together with more epoxy of the same type. What is the maximum fiber volume fraction that can be achieved? Using the fiber and matrix moduli given in Equation 3.33, determine the composite longitudinal modulus  $E_1$  and the composite transverse modulus  $E_2$  corresponding to the maximum fiber volume fraction.

3. A hybrid carbon–aramid/epoxy composite is made by randomly mixing continuous aligned fibers of the same diameter, so that there are two carbon fibers for each aramid fiber. The fibers are assumed to be arranged in a square array with the closest possible packing. The stress–strain curves for longitudinal tensile loading of fiber and matrix materials are shown in Figure 3.20. Determine the composite longitudinal modulus  $E_1$ .
4. Derive Equation 3.45.
5. Derive Equation 3.47.
6. Using an elementary mechanics of materials approach, find the micromechanics equation for predicting the minor Poisson's ratio,  $\nu_{21}$ , for a unidirectional fiber composite in terms of the corresponding fiber and matrix properties and volume fractions. Assume that the fibers are orthotropic, the matrix is isotropic, and all materials are linear elastic. This derivation should be independent of the one in Problem 4.
7. A composite shaft is fabricated by bonding an isotropic solid shaft having shear modulus  $G_1$ , and outside radius  $r_1$ , inside a hollow isotropic shaft having shear modulus  $G_2$  and outside radius  $r_2$ . The composite shaft is to be loaded by a twisting moment,  $T$ , that is distributed over the end of the shaft, as shown in Figure 3.21. Using an elementary mechanics of materials approach, derive the equations for the stresses and deformations at any radius and the equation for the effective torsional shear modulus of the composite

**FIGURE 3.20**

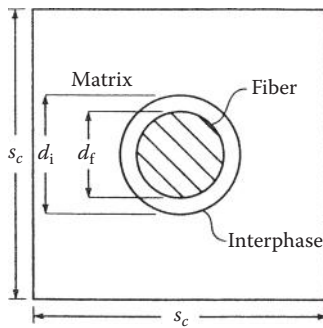
Stress–strain curves for fiber and matrix materials in a hybrid composite.

**FIGURE 3.21**

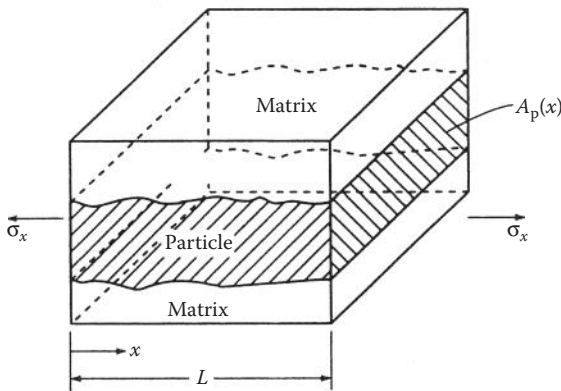
Composite shaft under torsional load.

shaft in terms of the material and geometrical properties of shafts 1 and 2.

8. Using the method of subregions, derive an equation for the transverse modulus,  $E_2$ , for the RVE, which includes a fiber/matrix interphase region, as shown in Figure 3.22. Hint: The equation should reduce to Equation 3.54 when the fiber diameter is the same as the interphase diameter.
9. Derive Equation 3.59.
10. For a unidirectional composite with a rectangular fiber array (Figure 3.10), use the equations of elasticity to set up the displacement boundary value problem for the determination of the transverse modulus,  $E_2$ . That is, find the governing partial differential equations for displacements  $u$  and  $v$  in the RVE, and specify the boundary and continuity conditions. Assume plane strain ( $\varepsilon_z = 0$ ). Do not attempt to solve the equations, but explain briefly how  $E_2$  would be found. Assume that both fiber and matrix are isotropic.
11. Derive Equation 3.66.
12. Show that a value of  $\xi = 0$  reduces the Halpin–Tsai equation (Equation 3.63) to the inverse rule of mixtures Equation 3.40, whereas a value  $\xi = \infty$  reduces it to the rule of mixtures Equation 3.27.
13. An RVE from a particle-reinforced composite is shown in Figure 3.23. The particle has a cross-sectional area  $A_p(x)$  that varies with the distance  $x$ , and the stresses and strains in particle and matrix materials also vary with  $x$ . Find the expression for the effective

**FIGURE 3.22**

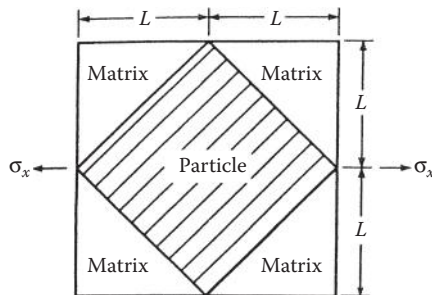
RVE with fiber/matrix interphase region.

**FIGURE 3.23**

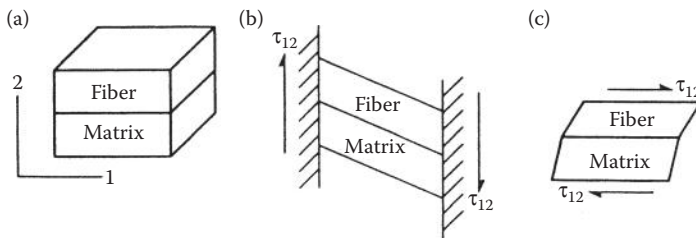
RVE for a particle-reinforced composite with a particle that has a varying cross-sectional area  $A_p(x)$ .

Young's modulus of the composite,  $E_x$ , along the  $x$  direction. The answer should be left in terms of an integral involving the length,  $L$ ; the particle modulus,  $E_p$ ; the matrix modulus,  $E_m$ ; and the particle area fraction  $a_p(x) = A_p(x)/A_c$ , where  $A_c$  is the total composite cross-sectional area. Assume that both the particle and the matrix are isotropic.

14. Using the result from Problem 13, determine the effective Young's modulus,  $E_x$ , for the RVE shown in Figure 3.24. In Figure 3.24 the reinforcing particle has a square cross-section and is oriented as shown. For a particle having a Young's modulus  $E_p = 10 \times 10^6$  psi (68.95 GPa) and a matrix having a Young's modulus  $E_m = 0.5 \times 10^6$  psi (3.45 GPa), determine the value of  $E_x$  and compare with the values from the rule of mixtures Equation 3.27 and the inverse rule of mixtures Equation 3.40. Discuss your results in the context of the comments on theoretical bounds on the transverse modulus in Section 3.4.3.

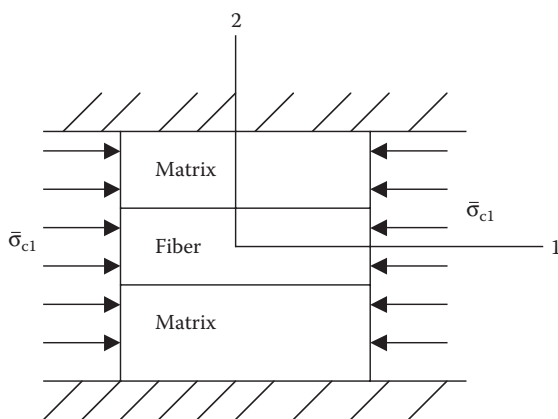
**FIGURE 3.24**

RVE for a composite reinforced with a square particle and loaded along the diagonal of the particle.

**FIGURE 3.25**

RVE with two different loading and boundary conditions for problem 15. (a) Representative volume element, (b) ends of RVE fixed against rotation, and (c) ends of RVE free to rotate.

15. A unidirectional composite is to be modeled by the RVE shown in Figure 3.25a, where the fiber and matrix materials are assumed to be isotropic and perfectly bonded together. Using a mechanics of materials approach, derive the micromechanics equations for the effective in-plane shear modulus,  $G_{12}$ , for the following cases:
- The ends of the RVE are perfectly bonded to supports that are rigid against rotation, then subjected to the uniform in-plane shear stress,  $\tau_{12}$ , by the nonrotating supports, as shown in Figure 3.25b.
  - The top and bottom surfaces of the RVE are subjected to the uniform in-plane shear stress,  $\tau_{12}$ , and the ends of the RVE are free to rotate, as shown in Figure 3.25c.
16. Figure 3.26 shows an RVE for an elementary mechanics of materials model of the same type as shown in Figure 3.5, but with transverse deformation along the 2 direction prevented by rigid supports along the top and bottom edges. For an applied longitudinal normal

**FIGURE 3.26**

RVE for elementary mechanics of materials model with rigid supports that prevent transverse deformation.

stress as shown in Figure 3.26, find a micromechanics equation for the longitudinal modulus  $E_1$ . Do not neglect the Poisson strains in the general derivation, and show what happens to the general equation for  $E_1$  when the Poisson's ratios for composite, fiber, and matrix are all equal.

17. A unidirectional IM-9 carbon fiber/Hexply 8551-7 epoxy composite is to be designed to replace a 6061-T6 aluminum alloy rod which is to be loaded in longitudinal tension. (a) What fiber volume fraction of the carbon fibers would be required if the composite longitudinal modulus is to be equal to that of the 6061-T6 aluminum? (b) For the composite rod of part (a), what would be the percentage reduction in density compared with that of aluminum rod? Use the properties in Table 1.1, and neglect voids in the composite.
18. For the quarter domain of an RVE in Figure 3.15, a uniform transverse normal stress  $\bar{\sigma}_x$  is applied on the plane  $x = D/2$ . Set up the equations describing the boundary conditions and the constraints on geometrically compatible displacements for a finite element micromechanics analysis of this model.

---

## References

1. Hashin, Z. 1983. Analysis of composite materials—A survey. *Journal of Applied Mechanics*, 50, 481–505.
2. Chamis, C. C. and Sendeckyj, G. P. 1968. Critique on theories predicting thermoelastic properties of fibrous composites. *Journal of Composite Materials*, 2(3), 332–358.
3. Christensen, R. M. 1979. *Mechanics of Composite Materials*. John Wiley & Sons, New York, NY.
4. Halpin, J. C. 1984. *Primer on Composite Materials: Analysis* (rev.). Technomic Publishing Co., Lancaster, PA.
5. Gibson, R. F. 1975. Elastic and dissipative properties of fiber reinforced composite materials in flexural vibration. Ph.D. Dissertation, University of Minnesota.
6. Yang, H. and Colton, J. S. 1994. Microstructure-based processing parameters of thermoplastic composite materials. Part I: Theoretical models. *Polymer Composites*, 15(1), 34–41.
7. Adams, R. D. 1987. Damping properties analysis of composites, in Reinhart, T. J., Dostal, C. A., Woods, M. S., Frissell, H. J., and Ronke, A. W., eds., *Engineered Materials Handbook*, vol. 1, *Composites*, pp. 206–217. ASM International, Materials Park, OH.
8. Whitney, J. M. and Riley, M. B. 1966. Elastic properties of fiber reinforced composite materials. *AIAA Journal*, 4(9), 1537–1542.
9. Gibson, R. F. and Plunkett, R. 1976. Dynamic mechanical behavior of fiber-reinforced composites: Measurement and analysis. *Journal of Composite Materials*, 10, 325–341.
10. Tsai, S. W. and Hahn, H. T. 1980. *Introduction to Composite Materials*. Technomic Publishing Co., Lancaster, PA.

11. Jones, R. M. 1999. *Mechanics of Composite Materials*, 2nd ed. Taylor & Francis, Philadelphia, PA.
12. Hopkins, D. A. and Chamis, C. C. 1988. A unique set of micromechanics equations for high temperature metal matrix composites, in DiGiovanni, P. R. and Adsit, N. R. eds., *Testing Technology of Metal Matrix Composites*, ASTM STP 964, pp. 159–176. American Society for Testing and Materials, Philadelphia, PA.
13. Drzal, L. T., Rich, M. J., Koenig, M. F., and Lloyd, P. F. 1983. Adhesion of graphite fibers to epoxy matrices. II. The effect of fiber finish. *Journal of Adhesion*, 16, 133–152.
14. Chamis, C. C. 1984. Simplified composite micromechanics equations for hygral, thermal and mechanical properties. *SAMPE Quarterly*, 15(3), 14–23.
15. Chamis, C. C. 1987. Simplified composite micromechanics equations for mechanical, thermal and moisture-related properties, in Weeton, J. W., Peters, D. M., and Thomas, K. L., eds., *Engineers' Guide to Composite Materials*. ASM International, Materials Park, OH.
16. Kriz, R. D. and Stinchcomb, W. W. 1979. Elastic moduli of transversely isotropic graphite fibers and their composites. *Experimental Mechanics*, 19, 41–49.
17. Kowalski, I. M. 1986. Determining the transverse modulus of carbon fibers. *SAMPE Journal*, 22(4), 38–42.
18. Kawabata, S. 1988. Measurements of anisotropic mechanical property and thermal conductivity of single fiber for several high performance fibers. *Proceedings of 4th Japan–U.S. Conference on Composite Materials*, pp. 253–262, Washington, D.C.
19. Caruso, J. J. and Chamis, C. C. 1986. Assessment of simplified composite micromechanics using three-dimensional finite element analysis. *Journal of Composites Technology and Research*, 8(3), 77–83.
20. Spencer, A. 1986. The transverse moduli of fibre composite material. *Composites Science and Technology*, 27, 93–109.
21. Adams, D. F. and Doner, D. R. 1967. Longitudinal shear loading of a unidirectional composite. *Journal of Composite Materials*, 1, 4–17.
22. Adams, D. F. and Doner, D. R. 1967. Transverse normal loading of a unidirectional composite. *Journal of Composite Materials*, 1, 152–164.
23. Caruso, J. J. 1984. Application of finite element substructuring to composite micromechanics. NASA TM 83729.
24. Finegan, I. C. and Gibson, R. F. 1997. Analytical and experimental characterization of damping and stiffness in polymer composites having coated fibers as reinforcement, in Farabee, T. M., ed., *Proceedings of ASME Noise Control and Acoustics Division*, NCA-Vol. 24, American Society of Mechanical Engineers, New York, NY, pp. 127–138.
25. Finegan, I. C. and Gibson, R. F. 1998. Improvement of damping at the micromechanical level in polymer composite materials under transverse normal loading by the use of special fiber coatings. *Journal of Vibration and Acoustics*, 120(2), 623–627.
26. Sun, C. T. and Vaidya R. S. 1996. Prediction of composite properties from a representative volume element. *Composites Science and Technology*, 56, 171–179.
27. Whitney, J. M. 1967. Elastic moduli of unidirectional composites with anisotropic fibers. *Journal of Composite Materials*, 1, 188–193.
28. Aboudi, J. 1989. Micromechanical analysis of composites by the method of cells. *Applied Mechanics Reviews*, 42(7), 193–221.

29. Paul, B. 1960. Prediction of elastic constants of multi-phase materials. *Transactions of AIME*, 218, 36–41.
30. Hashin, Z. and Rosen, B. W. 1964. The elastic moduli of fiber reinforced materials. *Journal of Applied Mechanics*, 31, 223–232. Errata, p. 219 (March 1965).
31. Torquato, S. 1991. Random heterogeneous media: microstructure and improved bounds on effective properties. *Applied Mechanics Reviews*, 44(2), 37–76.
32. Halpin, J. C. and Tsai, S. W. 1969. Effects of environmental factors on composite materials. AFML-TR-67-423.
33. Zhu, H., Sankar, B. V., and Marrey, R. V., 1998. Evaluation of failure criteria for fiber composites using finite element micromechanics. *Journal of Composite Materials*, 32, 766–782.

This page intentionally left blank

# 4

---

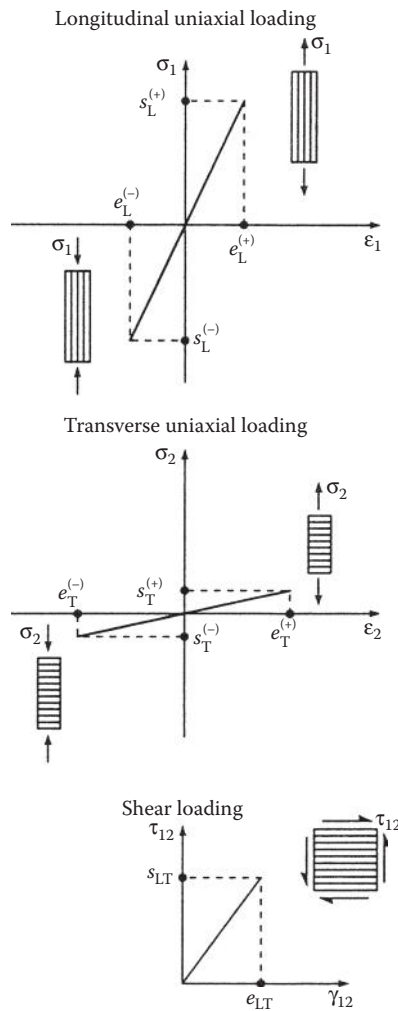
## *Strength of a Continuous Fiber-Reinforced Lamina*

---

### 4.1 Introduction

Because of the variety of failure modes that can occur in composites, the analysis of composite strength is more difficult than the analysis of elastic behavior, which was discussed in Chapters 2 and 3. As shown in Chapter 1, the strength of a composite is derived from the strength of the fibers, but this strength is highly directional in nature. For example, the longitudinal strength of the continuous fiber-reinforced lamina,  $s_L$ , is much greater than the transverse strength,  $s_T$ . In addition, the compressive strengths  $s_L^{(-)}$  and  $s_T^{(-)}$  associated with these directions may be different from the corresponding tensile strengths  $s_L^{(+)}$  and  $s_T^{(+)}$ , and the transverse tensile strength  $s_T^{(+)}$  is typically the smallest of all the lamina strengths for reasons that will be explained later. The in-plane shear strength  $s_{LT}$  associated with the principal material axes is still another independent property. These five lamina strengths form the basis of a simplified lamina strength analysis, which, in turn, will be used later in a simplified laminate strength analysis. The relationships among these five lamina strengths and the allowable lamina strengths under off-axis or multiaxial loading are discussed in this chapter, as are several micromechanical models for predicting the lamina strengths. Interlaminar strengths will be discussed in Chapters 7 and 9.

As shown in Chapters 2 and 3, the linear elastic stress-strain relationships for the orthotropic lamina are simplified by the use of “effective moduli.” The effective moduli, which relate the volume-averaged lamina stresses to the volume-averaged lamina strains (recall Equations 2.7 through 2.9), are defined by simple uniaxial or shear stress conditions associated with the lamina principal material axes. Using a similar approach, the “effective strengths” of the lamina may be defined as ultimate values of the volume-averaged stresses that cause failure of the lamina under these same simple states of stress. The stress-strain curves in Figure 4.1 show the graphical interpretation of these simple states of stress, the effective strengths  $s_L^{(+)}, s_L^{(-)}, s_T^{(+)}, s_T^{(-)}$ , and  $s_{LT}$ , and the corresponding ultimate strains  $e_L^{(+)}, e_L^{(-)}, e_T^{(+)}, e_T^{(-)}$ , and  $e_{LT}$ . If we assume

**FIGURE 4.1**

Stress-strain curves for uniaxial and shear loading showing lamina in-plane strengths and ultimate strains.

linear elastic behavior up to failure, the ultimate stresses are related to the ultimate strains by

$$\begin{aligned} s_L^{(+)} &= E_1 e_L^{(+)}; \quad s_T^{(+)} = E_2 e_T^{(+)}; \quad s_{LT} = G_{12} e_{LT} \\ s_L^{(-)} &= E_1 e_L^{(-)}; \quad s_T^{(-)} = E_2 e_T^{(-)} \end{aligned} \quad (4.1)$$

Typical experimental values of the effective lamina strengths for selected composites are given in Table 4.1 [1,2]. Note that the transverse tensile

**TABLE 4.1**

Typical Values of Lamina Strengths for Several Composites at Room Temperature

Material	$s_L^{(+)}$ ksi (MPa)	$s_L^{(-)}$ ksi (MPa)	$s_T^{(+)}$ ksi (MPa)	$s_T^{(-)}$ ksi (MPa)	$s_{LT}$ ksi (MPa)
Boron/5505 boron/epoxy $v_f = 0.5^a$	230(1586)	360(2482)	9.1(62.7)	35.0(241)	12.0(82.7)
AS/3501 carbon/epoxy $v_f = 0.6^a$	210(1448)	170(1172)	7.0(48.3)	36.0(248)	9.0(62.1)
T300/5208 carbon/epoxy $v_f = 0.6^a$	210(1448)	210(1448)	6.5(44.8)	36.0(248)	9.0(62.1)
IM7/8551-7 carbon/epoxy $v_f = 0.6^b$	400(2578)	235(1620)	11.0(75.8)		
AS4/APC2 carbon/PEEK $v_f = 0.58^c$	298.6(2060)	156.6(1080)	11.3(78)	28.4(196)	22.8(157)
B4/6061 Boron/ aluminum $v_f = 0.50^c$	199(1373)	228(1573)	17.1(118)	22.8(157)	18.5(128)
Kevlar® 49/ epoxy aramid/epoxy $v_f = 0.6^a$	200(1379)	40(276)	4.0(27.6)	9.4(64.8)	8.7(60.0)
Scotchply® 1002 E-glass/epoxy $v_f = 0.45^a$	160(1103)	90(621)	4.0(27.6)	20.0(138)	12.0(82.7)
E-glass/470-36 E-glass/vinyl ester $v_f = 0.30^d$	85(584)	116(803)	6.2(43)	27.1(187)	9.3(64.0)

<sup>a</sup> From Chamis, C.C. 1987. *Engineers' Guide to Composite Materials*, 3-8-3-24, ASM International, Materials Park, OH. With permission.

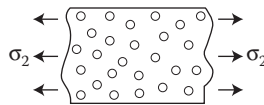
<sup>b</sup> From Hexcel Website, <http://www.hexcel.com>.

<sup>c</sup> From Daniel, I.M. and Ishai, O. 1994, *Engineering Mechanics of Composite Materials*, Oxford University Press, New York. With permission.

<sup>d</sup> Courtesy of Ford Motor Company, Research Staff.

Note: Kevlar® is a registered trademark of DuPont Company, and Scotchply® is a registered trademark of 3M Company.

strength,  $s_T^{(+)}$ , is the lowest of all the strengths. This is because, when the loading is perpendicular to the fibers as shown in Figure 4.2, stress and strain concentrations occur in the matrix around the fibers (i.e., the fibers create discontinuities in the matrix) and this reduces the tensile strength of the matrix material.

**FIGURE 4.2**

For composites under transverse loading, the fibers create discontinuities in the matrix that lead to stress and strain concentrations.

As shown later, this condition is often responsible for the so-called “first ply failure” in a laminate. It is also interesting to note in Table 4.1 that the compressive strengths are not necessarily equal to the corresponding tensile strengths; the transverse compressive strengths are generally greater than the transverse tensile strengths, and the longitudinal compressive strengths are usually less than or equal to the longitudinal tensile strengths. The intrinsic compressive strength of composites has always been difficult to determine experimentally, however, and the validity of such compression test results is a subject of continuing debate. Recent test results indicate that if the proper technique is used, the compression strength may be about the same as the tensile strength. Measurement of composite properties will be discussed in more detail later in Chapter 10.

In this section, the lamina effective strengths under simple states of stress have been defined. In the next section, we will discuss the use of these properties in several theories for predicting lamina strength under off-axis or multiaxial loading conditions. Elementary mechanics of materials models for micromechanical prediction of several of the lamina strengths will also be described in this chapter for illustrative purposes.

## 4.2 Multiaxial Strength Criteria

In the cases of off-axis or multiaxial loading, we assume that lamina failure can be characterized by using a multiaxial strength criterion (or failure criterion) that incorporates the gross mechanical strengths described in the previous section. The objective of such a theory is to provide the designer with the capability to estimate quickly when lamina failure will occur under complex loading conditions other than simple uniaxial or shear stresses. In this semiempirical “mechanics of materials” approach, we do not concern ourselves with the details of specific micromechanical failure modes such as fiber pullout, fiber breakage, fiber microbuckling, matrix cracking, and delamination. The actual failure process is complicated by the fact that these microfailure modes may occur in various combinations and sequences. Indeed, as pointed out by Hashin [3], our knowledge of the details of failure at the micromechanical level is so incomplete that “the failure process cannot be followed analytically.” The existence and growth of cracks and other

defects in the composite are also ignored with this approach. Studies of micromechanical failure modes generally require the use of more advanced approaches such as fracture mechanics and are the subjects of numerous journal publications. Additional discussion of such topics will be made in Section 4.3 and in Chapter 9.

Available multiaxial composite failure criteria have been reviewed and discussed by Hashin [4], Wu [5], Sendeckyj [6], Chamis [7], Kaminski and Lantz [8], Franklin [9], Tsai [10], Christensen [11], and Zhu et al. [12]. During the period from 1998 to 2004, Soden, Hinton, and Kaddour reported on the various aspects of the so-called World Wide Failure Exercise (WWFE) in a series of journal articles [13–22] and a book [23]. The WWFE was an international exercise in which the developers of 19 leading composite material failure theories were asked to apply their theories to predict failure in unidirectional laminae and in multiply laminates under 14 different test cases involving complex states of stress. The results from the different theories were compared with each other and with experimental data. Since this chapter only covers prediction of failure in unidirectional laminae, only the key results of the WWFE that are relevant to lamina failure prediction will be discussed here, and the results that are relevant to laminate failure prediction will be deferred until later in Chapter 7. Complete coverage of the WWFE is beyond the scope of this book, and the reader is referred to the previously mentioned journal articles [13–22] and the book [23] for details. All the criteria are phenomenological, having evolved from attempts to develop analytical models to describe experimental observations of failure under combined stresses. As pointed out by Wu [5], a large experimental database alone could form the basis for an empirical failure criterion, but the semiempirical mathematical model is preferable because it can reduce the number of required experiments and provide a more systematic approach to design. None of the available theories has been shown to accurately predict failure for all materials and loading conditions, however, and there is no universal agreement as to which theory is best.

Many of the failure criteria for anisotropic composites are based on generalizations of previously developed criteria for predicting the transition from elastic to plastic behavior in isotropic metallic materials. As such, they make use of the concept of a “failure surface” or “failure envelope” generated by plotting stress components in stress space. The coordinate axes for the stress space generally correspond to the stresses along the principal material axes. The theory predicts that those combinations of stresses whose loci fall inside the failure surface will not cause failure, whereas those combinations of stresses whose loci fall on or outside the surface will cause failure. *Thus, in the application of all the failure criteria, the first step is the transformation of calculated stresses to the principal material axes using transformation equations like Equation 2.31.* Since we are only dealing with two-dimensional stress states in a lamina at this point, the failure surface would be 2-D. Failure surfaces for each of the criteria will be presented as they are discussed here.

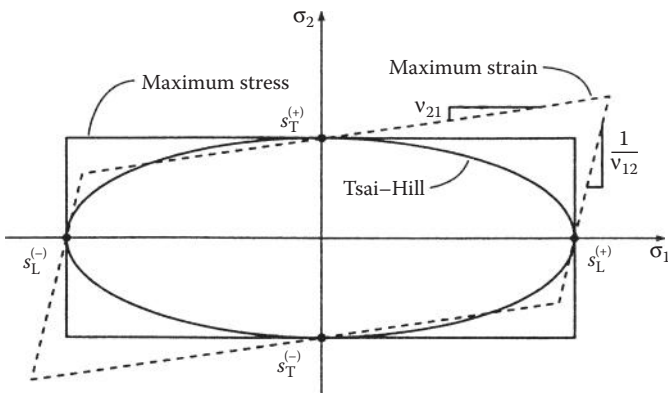
### 4.2.1 Maximum Stress Criterion

The Maximum Stress Criterion for orthotropic laminae was apparently first suggested in 1920 by Jenkins [24] as an extension of the Maximum Normal Stress Theory (or Rankine's Theory) for isotropic materials, which is covered in elementary mechanics of materials courses [25]. This criterion predicts failure when any principal material axis stress component exceeds the corresponding strength. Thus, to avoid failure according to this criterion, the following set of inequalities must be satisfied:

$$\begin{aligned} -s_L^{(-)} &< \sigma_1 < s_L^{(+)} \\ -s_T^{(-)} &< \sigma_2 < s_T^{(+)} \\ |\tau_{12}| &< s_{LT} \end{aligned} \quad (4.2)$$

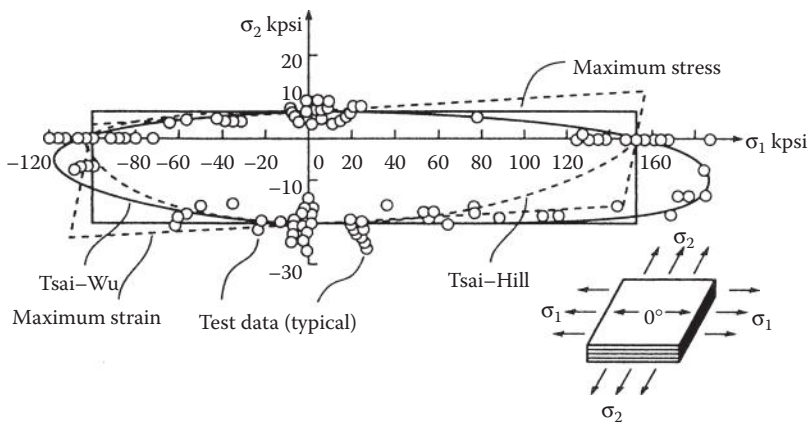
where the numerical values of  $s_L^{(-)}$  and  $s_T^{(-)}$  are assumed to be positive. It is assumed that shear failure along the principal material axes is independent of the sign of the shear stress  $\tau_{12}$ . Thus, only the magnitude of  $\tau_{12}$  is important, as shown in the last of Equations 4.2. As shown later, however, the shear strength for off-axis loading may depend on the sign of the shear stress.

The failure surface for the Maximum Stress Criterion in  $\sigma_1$ ,  $\sigma_2$  space is a rectangle, as shown in Figure 4.3. Note that this failure surface is independent of the shear stress  $\tau_{12}$ , and that the criterion does not account for possible interaction between the stress components. That is, the predicted limiting value of a particular stress component is the same whether or not other stress components are present. Figure 4.4 shows a comparison of theoretical failure surfaces with experimental biaxial failure data for a unidirectional graphite/epoxy composite [26]. Since the strengths along the principal material directions provide the input to the criterion, we would expect the agreement to be



**FIGURE 4.3**

Maximum stress, maximum strain, and Tsai–Hill failure surfaces in  $\sigma_1$ ,  $\sigma_2$  space.

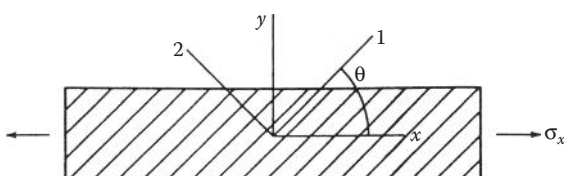
**FIGURE 4.4**

Comparison of predicted failure surfaces with experimental failure data for graphite/epoxy. (From Burk, R. C. 1983. *Astronautics and Aeronautics*, 21(6), 58–62. Copyright AIAA. Reprinted with permission.)

good when the applied stress is uniaxial along those directions. Due to lack of stress interaction in the Maximum Stress Criterion, however, the agreement is not so good in biaxial stress situations. The scatter in the experimental data is unfortunately typical for composite strength tests.

Experimental biaxial failure data for comparison with predicted failure surfaces can be obtained by applying biaxial loading directly to the test specimens. Biaxial stress fields can also be generated indirectly by using off-axis uniaxial loading tests [27] or off-axis shear-loading tests. According to Equation 2.31, the applied normal stress,  $\sigma_x$ , in the off-axis uniaxial loading test shown in Figure 4.5 produces the following biaxial stress state along the principal material axes

$$\begin{aligned}\sigma_1 &= \sigma_x \cos^2 \theta \\ \sigma_2 &= \sigma_x \sin^2 \theta \\ \tau_{12} &= -\sigma_x \sin \theta \cos \theta\end{aligned}\tag{4.3}$$

**FIGURE 4.5**

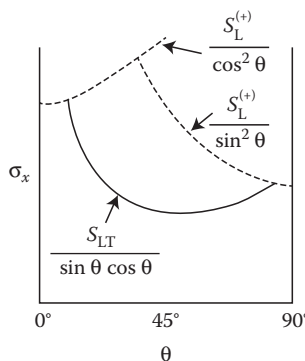
Off-axis uniaxial test of a unidirectional lamina specimen.

where the applied normal stress,  $\sigma_x$ , may be positive or negative. The importance of the sign of the applied stress in the interpretation of the test results here is obvious. These stress components may then be substituted into equations similar to Equation 4.2 to generate failure surfaces. By plotting the predicted and measured values of  $\sigma_x$  at failure versus lamina orientation,  $\theta$ , the various failure criteria can be evaluated [28].

For example, for the off-axis tensile test in Figure 4.5, the predicted values of the failure stress  $\sigma_x$  as functions of  $\theta$  according to this theory are shown as three curves in Figure 4.6. For a given angle  $\theta$ , the corresponding predicted failure stress  $\sigma_x$  would be found by drawing a vertical line at that angle  $\theta$  and finding where it intersects the three curves—predicted failure would correspond to the smallest of the three resulting values of  $\sigma_x$ . It is seen that, for small  $\theta$  near  $\theta = 0^\circ$ , predicted failure is governed by the longitudinal tensile strength,  $s_L^{(+)}$ , for intermediate values of  $\theta$ , failure is dominated by the shear strength,  $s_{LT}$ , and for large  $\theta$  near  $\theta = 90^\circ$ , failure is dominated by the transverse tensile strength,  $s_T^{(+)}$ . The predictions of the Maximum Stress Criterion agree reasonably well with experimental off-axis tensile test data when  $\theta$  is near  $0^\circ$  or  $90^\circ$ , but not so well for intermediate angles. In addition, the cusps and discontinuities in the predicted curves are not reflected in experimental data, which tend to be smoother and more continuous.

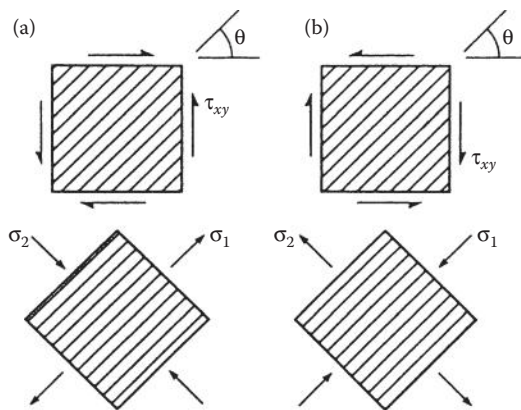
For the off-axis shear test described in Figure 4.7, the applied shear stress,  $\tau_{xy}$ , generates the following biaxial stress state along the principal material axes according to Equation 2.31:

$$\begin{aligned}\sigma_1 &= 2\tau_{xy} \cos \theta \sin \theta \\ \sigma_2 &= -2\tau_{xy} \cos \theta \sin \theta \\ \tau_{12} &= \tau_{xy} (\cos^2 \theta - \sin^2 \theta)\end{aligned}\quad (4.4)$$



**FIGURE 4.6**

Predicted values of off-axis uniaxial tensile strength for various off-axis fiber orientations according to the Maximum Stress Criterion.

**FIGURE 4.7**

Off-axis shear test of a unidirectional lamina specimen. (a) Positive  $\tau_{xy}$  at  $\theta = 45^\circ$  and resulting stresses along 1,2 axes; (b) negative  $\tau_{xy}$  at  $\theta = 45^\circ$  and resulting stresses along 1,2 axes.

The importance of the sign of the applied shear stress in the interpretation of test results may not be so obvious here, and further discussion is warranted. For example, if the angle  $\theta = 45^\circ$ , Equation 4.4 reduces to  $\sigma_1 = \tau_{xy}$ ,  $\sigma_2 = -\tau_{xy}$ , and  $\tau_{12} = 0$ . Thus, a positive applied shear stress,  $\tau_{xy}$ , would produce longitudinal tension and transverse compression along the principal material axes, as shown in the lower part of Figure 4.7a. On the other hand, a negative applied shear stress would produce longitudinal compression and transverse tension, as shown in the lower part of Figure 4.7b. Given the fact that the transverse tensile strength is so much lower than the other strengths (Table 4.1), the importance of the sign of the applied off-axis shear stress should now be obvious. It is easy to visualize a situation where a negative shear stress of a certain magnitude could cause a transverse tensile failure, whereas a positive shear stress of the same magnitude would not cause failure. A similar development for pure shear along the principal material axes shows that the sign of the shear stress makes no difference in that case. Similarly, recall from elementary mechanics of materials that the sign of the shear stress also has no effect on failure of isotropic materials. The importance of the sign of the shear stress for orthotropic materials extends beyond the interpretation of tests results as described here; it has implications for all phases of stress analysis in composite materials.

### Example 4.1

An element of an orthotropic lamina made of T300/5208 carbon/epoxy material is subjected to a positive off-axis shear stress,  $\tau_{xy}$ , at an angle  $\theta = 45^\circ$  as shown in Figure 4.7a. Determine the value of the off-axis shear stress  $\tau_{xy}$  that would cause failure according to the Maximum Stress Criterion.

### SOLUTION

From Figure 4.7a, it is seen that a positive off-axis shear stress produces longitudinal tension and transverse compression along the principal material axes. Employing Equation 2.31 and the Maximum Stress Criterion, along with the strength data for T300/5208 from Table 4.1, the calculations are as follows:

For failure by the longitudinal tensile stress,

$$\sigma_1 = 2\tau_{xy} \cos \theta \sin \theta = 2\tau_{xy} \cos 45^\circ \sin 45^\circ = \tau_{xy} = s_L^{(+)} = 1448 \text{ MPa}$$

So the corresponding off-axis shear stress required to produce this mode of failure is

$$\tau_{xy} = 1448 \text{ MPa}$$

For failure by the transverse compressive stress:

$$\sigma_2 = -2\tau_{xy} \cos \theta \sin \theta = -2\tau_{xy} \cos 45^\circ \sin 45^\circ = -\tau_{xy} = -s_T^{(-)} = -248 \text{ MPa}$$

So the corresponding off-axis shear stress required to produce this mode of failure is

$$\tau_{xy} = 248 \text{ MPa}$$

There is no shear stress along the principal material axes, since

$$\tau_{12} = \tau_{xy}(\cos^2 \theta - \sin^2 \theta) = \tau_{xy}(\cos^2 45^\circ - \sin^2 45^\circ) = 0$$

So transverse compression is the governing mode of failure, and the value of the off-axis shear stress required to produce failure is

$$\tau_{xy} = 248 \text{ MPa}$$

### Example 4.2

Repeat example 4.1 if the off-axis shear stress in Example 4.1 is negative, as shown in Figure 4.7b.

### SOLUTION

From Figure 4.7b, it is seen that a negative off-axis shear stress produces longitudinal compression and transverse tension along the principal material axes. Employing Equation 2.31 and the Maximum Stress Criterion, along with the strength data for T300/5208 from Table 4.1, the calculations are now as follows:

For failure by the longitudinal compressive stress,

$$\sigma_1 = -2\tau_{xy} \cos \theta \sin \theta = -2\tau_{xy} \cos 45^\circ \sin 45^\circ = -\tau_{xy} = -s_L^{(-)} = -1448 \text{ MPa}$$

So the corresponding off-axis shear stress required to produce this mode of failure is

$$\tau_{xy} = 1448 \text{ MPa}$$

For failure by the transverse tensile stress,

$$\sigma_2 = 2\tau_{xy} \cos \theta \sin \theta = 2\tau_{xy} \cos 45^\circ \sin 45^\circ = \tau_{xy} = S_T^{(+)} = 44.8 \text{ MPa}$$

So the corresponding off-axis shear stress required to produce this mode of failure is

$$\tau_{xy} = 44.8 \text{ MPa}$$

Again there is no shear stress along the principal material axes, since

$$\tau_{12} = \tau_{xy}(\cos^2 \theta - \sin^2 \theta) = \tau_{xy}(\cos^2 45^\circ - \sin^2 45^\circ) = 0$$

So transverse tension is now the governing mode of failure, and the corresponding value of the off-axis shear stress required to produce failure is now only

$$\tau_{xy} = 44.8 \text{ MPa}$$

So, simply changing the sign of the off-axis shear stress from positive to negative produces a completely different mode of failure and a much lower failure stress.

#### 4.2.2 Maximum Strain Criterion

In 1967, Waddoups [29] proposed the Maximum Strain Criterion for orthotropic laminae as an extension of the Maximum Normal Strain Theory (or Saint Venant's Theory) for isotropic materials, which is also discussed in elementary mechanics of materials courses [25]. This criterion predicts failure when any principal material axis strain component exceeds the corresponding ultimate strain. In order to avoid failure according to this criterion, the following set of inequalities must be satisfied:

$$\begin{aligned} -e_L^{(-)} &< \varepsilon_1 < e_L^{(+)} \\ -e_T^{(-)} &< \varepsilon_2 < e_T^{(+)} \\ |\gamma_{12}| &< e_{LT} \end{aligned} \tag{4.5}$$

where the numerical values of  $e_L^{(-)}$  and  $e_T^{(-)}$  are assumed to be positive and the ultimate strains are all *engineering strains* as defined by Equation 4.1. As with the Maximum Stress Criterion, it is assumed that shear failure along the principal material axes is independent of the sign of the shear strain  $\gamma_{12}$ .

Due to the similarity of Equations 4.5 and 4.2, the failure surface for the Maximum Strain Criterion in  $\varepsilon_1, \varepsilon_2$  space is a rectangle similar to that of the Maximum Stress Criterion in  $\sigma_1, \sigma_2$  space. In  $\sigma_1, \sigma_2$  space, however, the Maximum Strain Criterion failure surface is a skewed parallelogram, as shown in Figures 4.3 and 4.4. The shape of the parallelogram can be deduced by combining the lamina stress-strain relationships in Equation 2.24, with the relationships given in Equation 4.1. For example, the limiting strain associated with the positive 1 direction is

$$\varepsilon_1 = \frac{s_L^{(+)}}{E_1} = \frac{\sigma_1}{E_1} - \frac{v_{12}\sigma_2}{E_1} \quad (4.6)$$

Therefore

$$\sigma_2 = \frac{\sigma_1 - s_L^{(+)}}{v_{12}} \quad (4.7)$$

which is the equation of a straight line having intercept  $(s_L^{(+)}, 0)$  and slope  $1/v_{12}$  (Figure 4.3). A similar development using the limiting strain along the positive 2 direction yields the equation

$$\sigma_2 = v_{21}\sigma_1 + s_T^{(+)} \quad (4.8)$$

which is the equation for a straight line having intercept  $(0, s_T^{(+)})$  and slope  $v_{21}$ . These lines form the right and top sides, respectively, of the parallelogram shown in Figure 4.3, and similar consideration of the limiting strains in the negative 1 and 2 directions yields equations for the remaining two sides. It should be noted, however, that depending on the magnitudes of the lamina strengths and stiffnesses, the intercepts of the Maximum Strain Criterion parallelogram may not be the same as those of the Maximum Stress Criterion rectangle in stress space. For some materials, the lines defining the top and bottom of the Maximum Strain Criterion parallelogram intercept the horizontal axis at stresses less than the measured tensile and compressive longitudinal strengths, which contradicts experimental evidence [5,8]. According to Wu [5], such contradictions develop as a result of an ambiguous conversion from strain space to stress space unless certain mathematical constraints on the properties are satisfied. Only for isotropic materials are the intercepts always the same for the Maximum Stress and Maximum Strain Criteria. As with the Maximum Stress Criterion, the Maximum Strain Criterion does not account for possible interaction between stress components, and the predicted failure surface does not show good agreement with experimental biaxial failure data for graphite/epoxy in Figure 4.4. Off-axis uniaxial test data have led to similar conclusions [28], but both criteria are still used for orthotropic materials because the resulting equations are relatively simple.

### 4.2.3 Quadratic Interaction Criteria

The so-called quadratic interaction criteria also evolved from early failure theories for isotropic materials, but they differ from the Maximum Stress and Maximum Strain Criteria in that they include terms to account for interaction between the stress components, and the quadratic forms of the equations for plane stress lead to elliptical failure surfaces. As shown in any mechanics of materials book, the maximum distortional energy criterion or von Mises Criterion (circa early 1900s) is the most widely used quadratic interaction criteria for predicting the onset of yielding in isotropic metals [25]. In 1948, Hill [30] suggested that the von Mises Criterion could be modified to include the effects of induced anisotropic behavior in initially isotropic metals during large plastic deformations. For a general three-dimensional state of stress along the principal axes of anisotropy (the 123 axes) in such a material, the failure surface (or yield surface) for the Hill Criterion in  $\sigma_1$ ,  $\sigma_2$ ,  $\sigma_3$  space is described by the equation

$$A(\sigma_2 - \sigma_3)^2 + B(\sigma_3 - \sigma_1)^2 + C(\sigma_1 - \sigma_2)^2 + 2D\tau_{23}^2 + 2E\tau_{31}^2 + 2F\tau_{12}^2 = 1 \quad (4.9)$$

where  $A$ ,  $B$ ,  $C$ ,  $D$ ,  $E$ , and  $F$  are determined from yield strengths in uniaxial or shear loading. In order to avoid failure, the left-hand side of Equation 4.9 must be  $<1$ , and failure is predicted if the left-hand side is  $\geq 1$ . For a uniaxial test along the 1 direction with  $\sigma_1 = Y_1$  and all other stresses equal to zero Equation 4.9 reduces to

$$B + C = \frac{1}{Y_1^2} \quad (4.10)$$

where  $Y_1$  is the yield strength along 1 direction. Similarly, uniaxial tests along the 2 and 3 directions give the equations

$$A + C = \frac{1}{Y_2^2}; \quad A + B = \frac{1}{Y_3^2} \quad (4.11)$$

where  $Y_2$  and  $Y_3$  are the uniaxial yield strengths along the 2 and 3 directions, respectively. The yield strengths in tension and compression are assumed to be the same. Solving Equations 4.10 and 4.11 simultaneously for  $A$ ,  $B$ , and  $C$ , we find that

$$\begin{aligned} 2A &= \frac{1}{Y_2^2} + \frac{1}{Y_3^2} - \frac{1}{Y_1^2} \\ 2B &= \frac{1}{Y_3^2} + \frac{1}{Y_1^2} - \frac{1}{Y_2^2} \\ 2C &= \frac{1}{Y_1^2} + \frac{1}{Y_2^2} - \frac{1}{Y_3^2} \end{aligned} \quad (4.12)$$

Similarly, for pure shear tests along the 23, 31, and 12 planes, Equation 4.9 gives

$$2D = \frac{1}{Y_{23}^2}; \quad 2E = \frac{1}{Y_{31}^2}; \quad 2F = \frac{1}{Y_{12}^2} \quad (4.13)$$

where  $Y_{12}$ ,  $Y_{23}$ , and  $Y_{31}$  are the yield strengths in shear associated with the 12, 23, and 31 planes, respectively.

The extension of the Hill Criterion to prediction of failure in an orthotropic, transversely isotropic lamina was suggested by Azzi and Tsai [31] and Tsai [32]; the resulting equation is often referred to as the Tsai–Hill Criterion. If the 123 directions are assumed to be the principal material axes of the orthotropic transversely isotropic lamina, with the 1 direction being along the reinforcement direction, if plane stress is assumed ( $\sigma_3 = \tau_{31} = \tau_{23} = 0$ ), and if Hill's anisotropic yield strengths are replaced by the corresponding effective lamina strengths, then  $Y_1 = s_L$ ,  $Y_2 = Y_3 = s_T$ , and  $Y_{12} = s_{LT}$ , and Equations 4.9, 4.12, and 4.13 reduce to the equation for the Tsai–Hill failure surface:

$$\frac{\sigma_1^2}{s_L^2} - \frac{\sigma_1\sigma_2}{s_L^2} + \frac{\sigma_2^2}{s_T^2} + \frac{\tau_{12}^2}{s_{LT}^2} = 1 \quad (4.14)$$

As with the Hill equation, failure is avoided if the left-hand side of Equation 4.14 is  $< 1$ , and failure is predicted if the left-hand side is  $\geq 1$ . The failure surface generated by this equation is an ellipse, as shown in Figure 4.3. The ellipse shown in Figure 4.3 is symmetric about the origin because of the assumption of equal strengths in tension and compression. The Tsai–Hill equation can be used when tensile and compressive strengths are different by simply using the appropriate value of  $s_L$  and  $s_T$  for each quadrant of stress space. For example, if  $\sigma_1$  is positive and  $\sigma_2$  is negative, the values of  $s_L^{(+)}$  and  $s_L^{(-)}$  would be used in Equation 4.14. The resulting failure surface is no longer symmetric about the origin, as shown for the case of graphite/epoxy in Figure 4.4. Although such a procedure is inconsistent with the assumptions used in formulating the original von Mises and Hill Criteria, it has been successfully used for some composites [25,32]. As shown in Figure 4.4, the procedure seems to work reasonably well for the graphite/epoxy material except for the fourth quadrant of stress space. One way to account for different strengths in tension and compression is to include terms that are linear in the normal stresses  $\sigma_1$ ,  $\sigma_2$ , and  $\sigma_3$ , as suggested by Hoffman [33].

The off-axis tensile test can also be used to evaluate the Tsai–Hill Criterion. When the off-axis stress transformation Equation 4.3 is substituted into Equation 4.14, the resulting off-axis failure stress is

$$\sigma_x = \left[ \frac{1}{\frac{\cos^4 \theta}{s_L^2} + \left( \frac{1}{s_{LT}^2} - \frac{1}{s_L^2} \right) \sin^2 \theta \cos^2 \theta + \frac{\sin^4 \theta}{s_T^2}} \right]^{1/2} \quad (4.15)$$

and the corresponding curve of  $\sigma_x$  versus  $\theta$  is shown in Figure 4.8. Note that Equation 4.15 yields a single continuous curve in Figure 4.8 which varies from  $\sigma_x = s_L$  when  $\theta = 0^\circ$  to  $\sigma_x = s_T$  when  $\theta = 90^\circ$ , as opposed to the three separate curves produced by the Maximum Stress Criterion in Figure 4.6. Experimental data tend to follow continuous curves such as the one in Figure 4.8 more closely than the discontinuous curves of Figure 4.6.

In addition to the previously mentioned limitations of the quadratic interaction criteria based on the von Mises model, there is another problem. Since the von Mises and Hill Criteria are phenomenological theories for the prediction of yielding in ductile metals, the equations are based on principal stress differences and the corresponding shear stresses and strains that drive slip and dislocation movement in metallic crystals. Experimental evidence suggests that a hydrostatic state of stress does not cause the slip and dislocation movements that are associated with yielding, and the Hill Criterion predicts that failure will never occur under a hydrostatic state of stress  $\sigma_1 = \sigma_2 = \sigma_3$ , and  $\tau_{12} = \tau_{23} = \tau_{31} = 0$ . Due to shear coupling, however, a hydrostatic state of stress in an anisotropic material can produce shear strains and failure. Hoffman's equation [33], by virtue of its linear terms, could predict

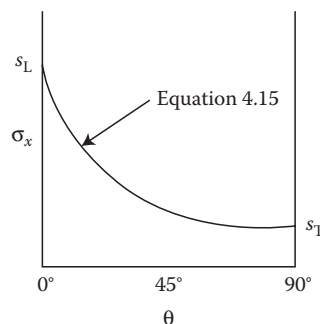


**FIGURE 4.8**

Predicted values of off-axis uniaxial tensile strength for various off-axis fiber orientations according to the Tsai–Hill Criterion.

failure for the hydrostatic state of stress. However, all these theories turn out to be special cases of a more general quadratic interaction criterion, which will be discussed next.

In 1971, Tsai and Wu [34] proposed an improved and simplified version of a tensor polynomial failure theory for anisotropic materials that had been suggested earlier by Gol'denblat and Kopnov [35]. In the Tsai–Wu general quadratic interaction criteria, the failure surface in stress space is described by the tensor polynomial:

$$F_i\sigma_i + F_{ij}\sigma_i\sigma_j = 1 \quad (4.16)$$

where the contracted notation  $i, j = 1, 2, \dots, 6$  is used, and  $F_i$  and  $F_{ij}$  are experimentally determined strength tensors of the second and fourth rank, respectively. In order to avoid failure, the left-hand side of Equation 4.16 must be <1, and failure is predicted when the left-hand side is ≥1. For the case of plane stress with  $\sigma_3 = \sigma_{33} = 0$ ,  $\sigma_4 = \tau_{23} = 0$ , and  $\sigma_5 = \tau_{31} = 0$ , Equation 4.16 becomes

$$F_{11}\sigma_1^2 + F_{22}\sigma_2^2 + F_{66}\sigma_6^2 + F_1\sigma_1 + F_2\sigma_2 + 2F_{12}\sigma_1\sigma_2 = 1 \quad (4.17)$$

where the linear terms in the shear stress  $\sigma_6 = \tau_{12}$  have been dropped because the shear strength along the principal material axes is not affected by the sign of the shear stress. Thus, only a quadratic term in the shear stress  $\sigma_6$  remains. However, the linear terms in the normal stresses  $\sigma_1 = \sigma_{11}$  and  $\sigma_2 = \sigma_{22}$  are retained because they take into account the different strengths in tension and compression. In addition, the term  $2F_{12}\sigma_1\sigma_2$  takes into account interaction between the normal stresses. With the exception of  $F_{12}$ , all the strength tensors in Equation 4.17 can be expressed in terms of the uniaxial and shear strengths using the same approach that was used with the Hill Criterion. For example, for the tension and compression tests with uniaxial stresses  $\sigma_1 = s_L^{(+)}$  and  $\sigma_1 = s_L^{(-)}$ , respectively, simultaneous solution of the two equations resulting from Equation 4.17 yields

$$F_{11} = \frac{1}{s_L^{(+)}s_L^{(-)}} \quad \text{and} \quad F_1 = \frac{1}{s_L^{(+)}} - \frac{1}{s_L^{(-)}} \quad (4.18)$$

where the numerical value of  $s_L^{(-)}$  is assumed to be positive as in Table 4.1. From similar uniaxial and shear tests, it can be shown that

$$F_{22} = \frac{1}{s_T^{(+)}s_T^{(-)}}; \quad F_2 = \frac{1}{s_T^{(+)}} - \frac{1}{s_T^{(-)}}; \quad F_{66} = \frac{1}{s_{LT}^2} \quad (4.19)$$

where the numerical value of  $s_T^{(-)}$  is assumed to be positive.

In order to find the interaction parameter,  $F_{12}$ , it is necessary to use a biaxial test involving both  $\sigma_1$  and  $\sigma_2$ . For example, an expression for  $F_{12}$  can be obtained by substituting the biaxial stress conditions  $\sigma_1 = \sigma_2 = P$  and  $\sigma_6 = 0$

into Equation 4.17, where  $P$  is the biaxial failure stress [34]. Thus, to find  $F_{12}$  for this condition, we need to know  $P$  in addition to the previously defined uniaxial and shear failure stresses. There is no a priori reason that  $\sigma_1$  must equal  $\sigma_2$ , however. Indeed, as pointed out by Hashin [3],  $F_{12}$  can have four different values, because there are four different failure pairs  $\sigma_1, \sigma_2$ . Wu [5,36] has suggested that in order to determine  $F_{12}$  accurately, the biaxial ratio  $B = \sigma_1/\sigma_2$  must be optimized to account for the sensitivity of  $F_{12}$  to experimental scatter in the applied stresses. The optimization procedure is complicated, however, and the reader is referred to the articles by Wu [5,36] for details. The Tsai-Wu failure surface for graphite/epoxy shown in Figure 4.4 was based on such an optimization procedure for  $F_{12}$ . In Figure 4.4 the agreement with experimental data seems to be much better for the Tsai-Wu failure surface than for the others, particularly in the fourth quadrant.

More recently, Tsai and Hahn [37] have proposed the equation

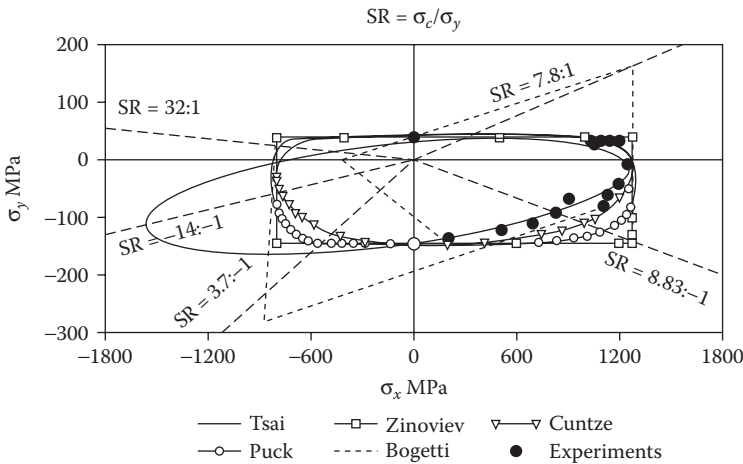
$$F_{12} = -\frac{(F_{11}F_{22})^{1/2}}{2} \quad (4.20)$$

which causes Equation 4.17 to take on the form of a generalized von Mises Criterion for the yielding of isotropic materials. It is also interesting to note that Equation 4.17 reduces to Equation 4.14, the Tsai-Hill Criterion, when the tensile and compressive strengths are assumed to be equal and

$$F_{12} = -\frac{1}{2s_L^2} \quad (4.21)$$

On the basis of the quantitative evaluation procedure used in the previously mentioned WWFE [13–23], the organizers of the exercise selected what they considered to be the best five of the original 19 failure theories with regard to recommended use by designers. The predicted failure surfaces for the five selected criteria are compared with experimental test results for unidirectional E-glass/epoxy materials under the biaxial normal stresses  $\sigma_x$  and  $\sigma_y$  in Figure 4.9 and under combined transverse normal stresses  $\sigma_y$  and in-plane shear stresses  $\tau_{xy}$  in Figure 4.10. In Figures 4.9 and 4.10, the notations Zinoviev, Bogetti, Tsai, Puck, and Cuntze refer to the following five failure criteria:

- Zinoviev et al. [38,39] used the Maximum Stress Criterion (i.e., Equation [4.2]) to predict failure of a single lamina. Linear elastic behavior was assumed up to initial failure. For laminate failure prediction, additional features were included after first ply failure.
- Bogetti et al. [40,41] employed a three-dimensional version of the Maximum Strain Criterion (i.e., Equations 4.5 are for the two-dimensional version only). Linear elastic behavior was assumed up

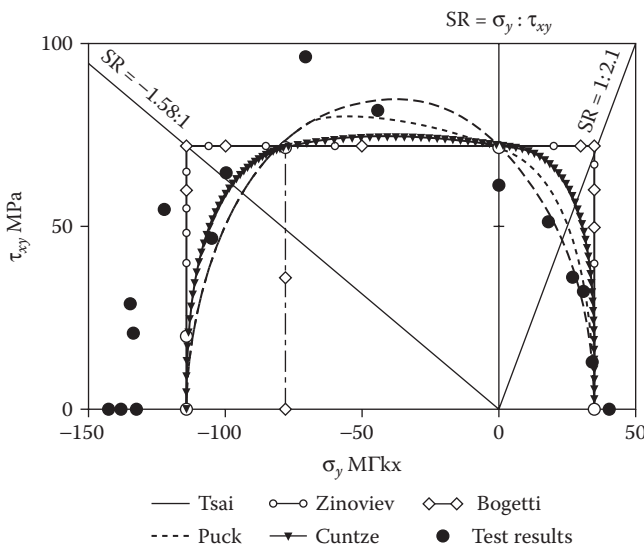
**FIGURE 4.9**

Comparison of predicted and measured biaxial failure surface for unidirectional E-glass/epoxy laminae under combined normal stresses in directions parallel ( $\sigma_x$ ) and perpendicular ( $\sigma_y$ ) to the fibers. (Reprinted from *Composites Science and Technology*, 64(3–4), Soden, P. D., Kaddour, A. S., and Hinton, M. J., Recommendations for designers and researchers resulting from the world-wide failure exercise, 589–604, Copyright (2004), with permission from Elsevier.)

to initial failure in the normal stress–normal strain relationships, but nonlinear shear stress–shear strain behavior was assumed. Additional features including progressive lamina failure were included for laminate analysis.

- Tsai et al. [42,43] used the Tsai–Wu Criterion (i.e., Equation 4.17) and assumed linear elastic behavior up to initial ply failure. For laminate failure prediction, a progressive failure analysis feature was added.
- Puck and Schurmann [44,45] and Cuntze et al. [46,47] employed similar three-dimensional progressive failure theories, which are beyond the scope of this book.

From Figures 4.9 and 4.10, the organizers of the WWFE observed that the predictions of Tsai, Puck, and Cuntze gave the best overall agreement with available experimental data [19]. However, the Tsai predictions were believed to be potentially unconservative in the compression–compression quadrant of Figure 4.9 where there is a lack of experimental data. The Puck predictions appeared to be unconservative in the tension–compression of Figure 4.9, but fared better overall in Figure 4.10. The predictions of Zinoviev and Bogetti were observed to be unconservative in several regions of both Figures 4.9 and 4.10. Finally, it was recommended that the combined theories of Tsai, Puck, and Cuntze be used in such a way that, for a given quadrant of the failure surface, the theory that produces the innermost portion of the failure surface in that quadrant should be selected for the purpose of lamina design.

**FIGURE 4.10**

Comparison of predicted and measured failure surfaces for unidirectional E-glass/epoxy laminae under combined in-plane shear stress ( $\tau_{xy}$ ) and normal stress perpendicular to the fibers ( $\sigma_y$ ). (Reprinted from *Composites Science and Technology*, 64(3–4), Soden, P. D., Kaddour, A. S., and Hinton, M. J., Recommendations for designers and researchers resulting from the world-wide failure exercise, 589–604, Copyright (2004), with permission from Elsevier.)

The development of improved multiaxial strength criteria for composites continues to be the subject of numerous publications. For example, Hashin [3,4] has suggested that for a given composite, each failure mode and its contributing stresses should be identified, and that each of these failure modes should be modeled separately by a quadratic criterion. Tennyson et al. [48] have extended the tensor polynomial criterion to include cubic terms. Obviously, the evaluation of the strength parameters in such an equation is a formidable task. It was shown, however, that in the particular case of failure in laminated tubes under internal pressure loading, the cubic criterion is more accurate than the quadratic criterion. Although considerable progress has been made, there is still a need for systematic experimental verification of the various theories for a variety of stress conditions. Finally, the theories discussed in this section are based on the macromechanical behavior of the composite without regard for the micromechanical behavior of fiber and matrix materials. In the next section, several micromechanical models for predicting composite strength will be presented.

### Example 4.3

The filament-wound pressure vessel described in Example 2.4 is fabricated from E-glass/epoxy having the lamina strengths listed in Table 4.1. Determine the internal

pressure  $p$ , which would cause failure of the vessel according to (a) the Maximum Stress Criterion and (b) the Tsai–Hill Criterion.

### SOLUTION

The first step in the application of both theories is to determine the stresses along the principal material axes. From the results of Example 2.4,  $\sigma_1 = 20.5 p$ ,  $\sigma_2 = 17.0 p$ , and  $\tau_{12} = 6.0 p$  (all in MPa). Note that both normal stresses are positive, so that the tensile strengths should be used in the failure theories.

- For the Maximum Stress Criterion, the three possible values of  $p$  at failure are found as follows:

$$\sigma_1 = 20.5 p = s_L^{(+)} = 1103 \text{ MPa}; \quad \text{therefore, } p = 53.8 \text{ MPa}$$

$$\sigma_2 = 17.0 p = s_T^{(+)} = 27.6 \text{ MPa}; \quad \text{therefore, } p = 1.62 \text{ MPa}$$

$$\tau_{12} = 6.0 p = s_{LT} = 82.7 \text{ MPa}; \quad \text{therefore, } p = 13.78 \text{ MPa}$$

Thus, the transverse tensile failure governs, and failure occurs first at  $p = 1.62 \text{ MPa}$ .

- For the Tsai–Hill Criterion, Equation 4.14 yields

$$\left(\frac{20.5 p}{1103}\right)^2 - \left(\frac{(20.5 p)(17.0 p)}{(1103)^2}\right) + \left(\frac{17.0 p}{27.6}\right)^2 + \left(\frac{6.0 p}{82.7}\right)^2 = 1$$

Solving for  $p$ , we find that  $p = 1.61 \text{ MPa}$ . Thus, for this case, the two criteria yield approximately the same result. This is not always true, however.

### Example 4.4

Using the Maximum Strain Criterion, determine the uniaxial failure stress,  $\sigma_x$ , for off-axis loading of the unidirectional lamina in Figure 4.5 if the material is AS/3501 carbon/epoxy and the angle  $\theta = 30^\circ$ .

### SOLUTION

First, the strains along the principal material axes must be found in terms of the applied stress,  $\sigma_x$ . On substituting the stress transformation (Equation 4.3) in the lamina stress–strain Equations 2.24 and 2.25, we find that

$$\varepsilon_1 = \frac{1}{E_1} (\cos^2 \theta - v_{12} \sin^2 \theta) \sigma_x$$

$$\varepsilon_2 = \frac{1}{E_2} (\sin^2 \theta - v_{21} \cos^2 \theta) \sigma_x$$

and

$$\gamma_{12} = -\frac{1}{G_{12}}(\sin \theta \cos \theta) \sigma_x$$

Assuming linear elastic behavior up to failure and using the stress-strain relations in Equation 4.1, the Maximum Strain Criterion (Equation 4.5) becomes

$$\sigma_x < \frac{s_L^{(+)}}{\cos^2 \theta - v_{12} \sin^2 \theta}$$

$$\sigma_x < \frac{s_T^{(+)}}{\sin^2 \theta - v_{21} \cos^2 \theta}$$

$$\sigma_x < \frac{s_{LT}}{\sin \theta \cos \theta}$$

where only the tensile strengths have been used because  $\sigma_x$  is positive. Using the AS/3501 data in Table 2.2 and Table 4.1, we find that to avoid longitudinal tensile failure

$$\sigma_x < \frac{1448}{(0.886)^2 - 0.3(0.5)^2} \text{ MPa} \quad \text{or} \quad \sigma_x < 2145 \text{ MPa}$$

In order to avoid transverse tensile failure,

$$\sigma_x < \frac{48.3}{(0.5)^2 - 0.0195(0.866)^2} \text{ MPa} \quad \text{or} \quad \sigma_x < 205 \text{ MPa}$$

and to avoid shear failure,

$$\sigma_x < \frac{62.1}{0.886(0.5)} \text{ MPa} \quad \text{or} \quad \sigma_x < 143 \text{ MPa}$$

Thus, according to the Maximum Strain Criterion, the mode of failure is shear, and the applied stress at failure is  $\sigma_x = 143$  MPa. The reader is encouraged to check that for compressive loading or other loading angles both the mode of failure and the failure stress may be different. The off-axis tensile test has been used to check the validity of the various failure criteria [27,28].

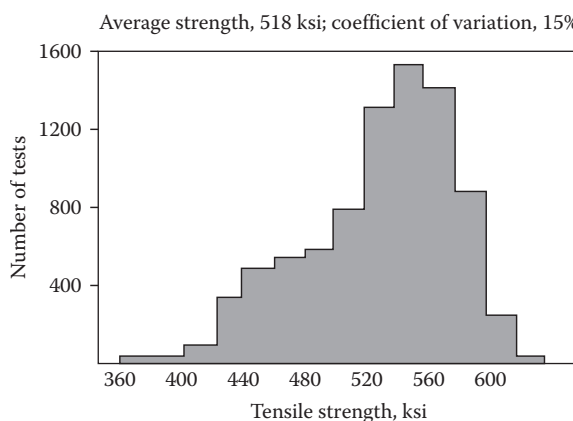
### 4.3 Micromechanics Models for Lamina Strength

In this section, the use of elementary mechanics of materials approaches to micromechanical modeling of lamina strength will be described. We

should not expect such simple models for strength to be as accurate as those for stiffness, because the strength is affected more than the stiffness by material and geometric nonhomogeneity and the resulting local perturbations in the stress and strain distributions. As shown in Chapter 3, the effects of such local stress and strain perturbations on stiffness are reduced due to the smoothing effect of integration in the effective modulus theories. On the other hand, material failure is often initiated at the sites of such stress and strain concentrations, so the effect on strength is much greater. For example, as shown in Figure 4.11 from Reference [49], the variability of strength in reinforcing fibers alone may be quite significant and statistical methods must be used for accurate analysis. In addition, differences between tensile and compressive modes of failure make it necessary to develop different micromechanics models for tensile strengths and compressive strengths.

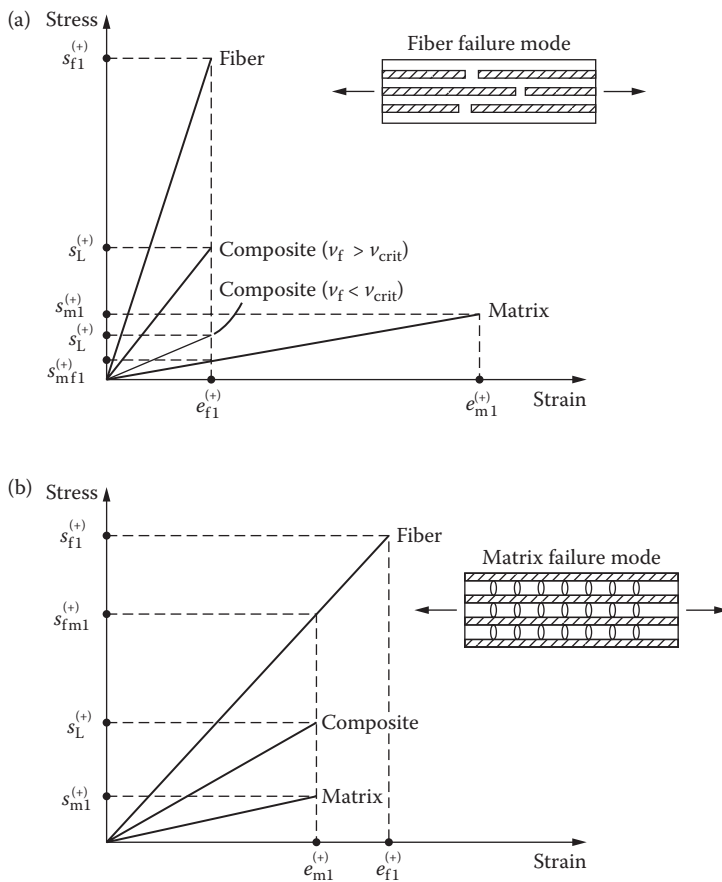
#### 4.3.1 Longitudinal Strength

Simple micromechanics models for composite longitudinal tensile strength can be developed from the rule of mixtures for longitudinal stress (Equation 3.23), and the representative stress-strain curves for fiber, matrix, and composite materials are shown in Figure 4.12a,b. In Figure 4.12a, the matrix failure strain,  $e_{m1}^{(+)}$ , is assumed to be greater than the fiber failure strain,  $e_{f1}^{(+)}$ , which is typical for many polymer matrix composites. A model for this case by Kelly and Davies [50] will be summarized here. Figure 4.12b shows the case where the fiber failure strain is greater than the matrix-failure strain, which is typical for ceramic matrix composites. A model based on the one



**FIGURE 4.11**

Statistical distribution of tensile strength for boron filaments. (From Weeton, J. W., Peters, D. M., and Thomas, K. L., eds. 1987. *Engineers' Guide to Composite Materials*. ASM International, Materials Park, OH. Reprinted by permission of ASM International.)

**FIGURE 4.12**

Representative stress-strain curves for typical fiber, matrix, and composite materials. (a) Matrix failure strain greater than fiber failure strain; (b) fiber failure strain greater than matrix failure strain.

proposed by Hull [51] will be described for this case. For both cases shown in Figure 4.12, the analyses will be developed on the assumptions of (1) equal strengths in all fibers, (2) linear elastic behavior up to failure, and (3) equal longitudinal strains in composite, fiber, and matrix (recall Equation 3.26).

For the case described in Figure 4.12a, the composite must fail at a strain level corresponding to the fiber tensile failure strain,  $e_{f1}^{(+)}$  =  $s_{f1}^{(+)}/E_{f1}$ . Theoretically, if the matrix could support the full applied load after fiber failure, the strain could be increased to the matrix failure strain. For all practical purposes, however, fiber failure means composite failure. Thus, when the fiber longitudinal stress reaches the fiber tensile strength,  $s_{f1}^{(+)}$ , the matrix longitudinal

stress reaches a value  $s_{\text{mf1}}^{(+)} = E_{\text{m}}e_{\text{f1}}^{(+)}$ , the composite longitudinal stress reaches the composite tensile strength,  $s_L^{(+)}$ , and Equation 3.23 becomes

$$s_L^{(+)} = s_{\text{f1}}^{(+)}v_f + s_{\text{mf1}}^{(+)}v_m = s_{\text{f1}}^{(+)}v_f + s_{\text{mf1}}^{(+)}(1 - v_f) \quad (4.22)$$

However, Equation 4.22 only has a meaning if the fiber volume fraction is sufficiently large. As shown in Figures 4.12a and 4.13a, if the fiber volume fraction  $v_f < v_{\text{fcrit}}$ , the composite strength from Equation 4.22 is less than the matrix strength, where

$$v_{\text{fcrit}} = \frac{s_{\text{m1}}^{(+)} - s_{\text{mf1}}^{(+)}}{s_{\text{f1}}^{(+)} - s_{\text{mf1}}^{(+)}} \quad (4.23)$$

Once the fibers fail in composites having  $v_f < v_{\text{fcrit}}$ , however, the remaining cross-sectional area of matrix that can support the load is such that

$$s_L^{(+)} = s_{\text{m1}}^{(+)}v_m = s_{\text{m1}}^{(+)}(1 - v_f) \quad (4.24)$$

As shown in Figure 4.13a, Equations 4.22 and 4.24 intersect at

$$v_{\text{fmin}} = \frac{s_{\text{m1}}^{(+)} - s_{\text{mf1}}^{(+)}}{s_{\text{f1}}^{(+)} - s_{\text{mf1}}^{(+)} + s_{\text{m1}}^{(+)}} \quad (4.25)$$

For practical composites, however,  $v_{\text{fcrit}}$  is generally less than 5%. Since  $v_{\text{fmin}} < v_{\text{fcrit}}$ , both of these values must be much smaller than the actual volume fraction of the composite, and the composite longitudinal strength for the case of Figure 4.12(a) would therefore be given by Equation 4.22.

For the case described in Figure 4.12b, composite failure may be defined in two ways, depending on whether we choose to use fiber failure or matrix failure as the criterion. If matrix failure is the criterion, composite failure will occur at the strain level corresponding to the matrix tensile failure strain,  $e_{\text{m1}}^{(+)}$ . Thus, when the matrix stress reaches the matrix tensile strength,  $s_{\text{m1}}^{(+)}$ , the fiber stress reaches the value  $s_{\text{fm1}}^{(+)} = E_{\text{f1}}e_{\text{f1}}^{(+)}$ , the composite stress reaches the composite strength,  $s_L^{(+)}$ , and Equation 3.23 becomes

$$s_L^{(+)} = s_{\text{fm1}}^{(+)}v_f + s_{\text{m1}}^{(+)}(1 - v_f) \quad (4.26)$$

As with Equation 4.22, this equation only has a physical meaning for a certain range of fiber volume fractions. As shown in Figure 4.12b, if the fibers could still withstand additional loading after matrix failure, the fiber strain may reach the fiber failure strain,  $e_{\text{f1}}^{(+)}$ . Due to the matrix failure, however, the

remaining load-bearing area of fibers is such that the composite strength is now given by

$$s_L^{(+)} = s_{f1}^{(+)} v_f \quad (4.27)$$

As shown in Figure 4.13b, and Equations 4.26 and 4.27 intersect at

$$v_{f\min} = \frac{s_{m1}^{(+)}}{s_{f1}^{(+)} - s_{fm1}^{(+)} + s_{m1}^{(+)}} \quad (4.28)$$

Thus, for  $v_f < v_{f\min}$ , the composite strength would be given by Equation 4.26, and for  $v_f > v_{f\min}$  the composite strength would be given by Equation 4.27. For practical composites, however,  $v_{f\min}$  is much smaller than the actual

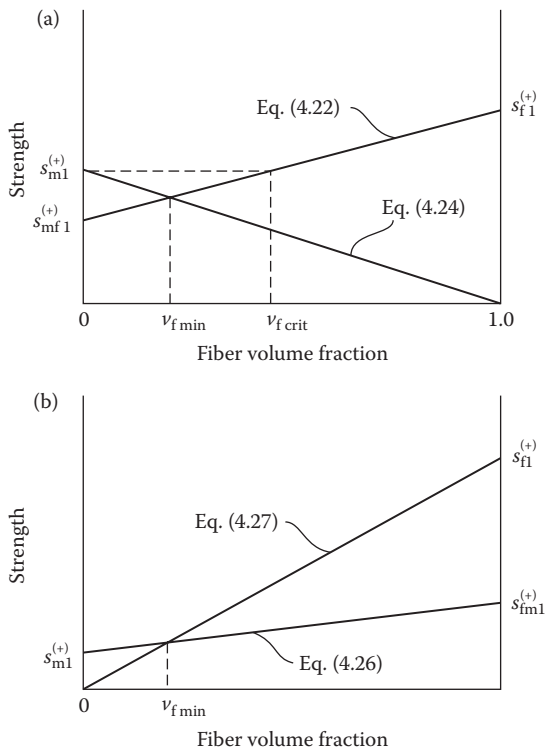


**FIGURE 4.13**

Variation of composite longitudinal tensile strength with fiber volume fraction for composite having (a) matrix failure strain greater than fiber failure strain; (b) fiber failure strain greater than matrix failure strain.

fiber volume fraction, so the composite longitudinal strength for the case of Figure 4.12b would be given by Equation 4.27.

Of the three assumptions made at the beginning of this section, the weakest one is that all fibers in the composite have the same strength,  $s_{fl}^{(+)}$ . As shown in Figure 4.11, fiber strength is not uniform, and some fibers fail at stresses well below the ultimate composite strength. In addition, fiber strength decreases with increasing fiber length due to the increased probability of imperfections in the fiber. Various statistical models have been proposed for the sequence of events beginning with the first fiber failure and culminating with overall composite failure [52,53]. Such analyses are beyond the scope of this book, however, and the reader is referred to the article by Rosen [54] for a review of the various models.

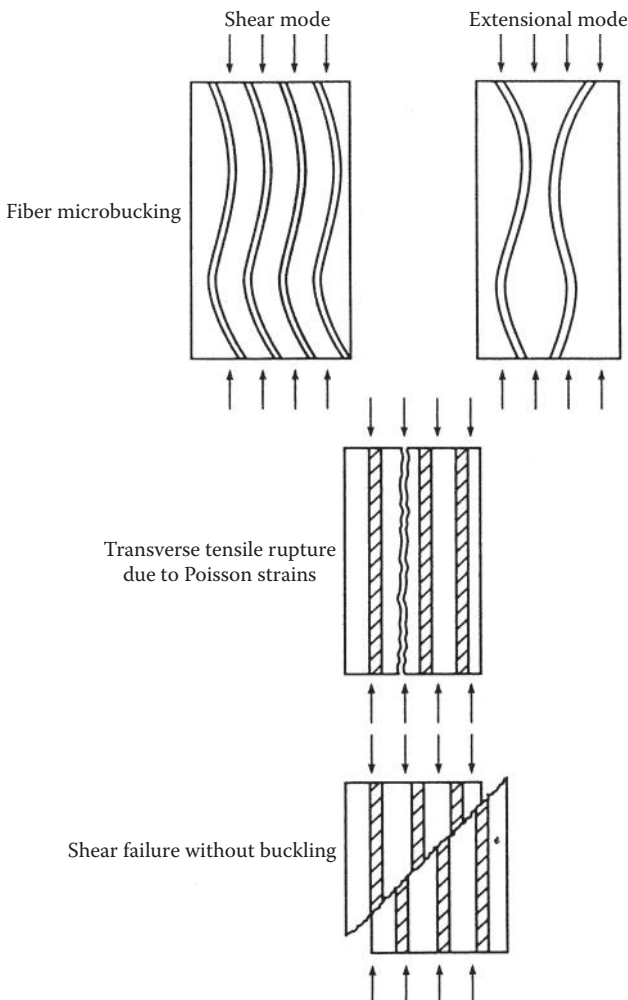
While the assumption regarding linear elastic behavior up to failure is not valid for many ductile matrix materials, the errors generated by this assumption are believed to be small. For example, the contribution of the matrix strength to the composite strength in Equation 4.22 is small, and the matrix strength does not appear at all in Equation 4.27. If the matrix has yielded before or during fiber failure, the term  $s_{mfi}$  in Equations 4.22, 4.23, and 4.25 can be replaced by the matrix yield strength,  $s_y$ . Excellent agreement has been reported between Equation 4.22 modified in this way, and experimental results for a tungsten fiber/copper matrix system over a wide range of fiber volume fractions [55].

It has long been assumed that the models for longitudinal tensile strength cannot be used for longitudinal compressive strength, because the modes of failure are different. This assumption has been supported by observed differences in measured tensile and compressive strengths, as shown in Table 4.1. Accurate measurement of the intrinsic compressive strength has proved to be very difficult, however, and test results to date typically depend on specimen geometry and/or test method. Whitney [56] has pointed out that the failure mode is the key issue because different compression test methods may produce different failure modes. Whether the failure mode in the test is the same as the failure mode in the composite structure being designed is another question. There appears to be three basic longitudinal compression failure modes, which are shown schematically in Figure 4.14:

1. Microbuckling of fibers in either shear or extensional mode
2. Transverse tensile rupture due to Poisson strains
3. Shear failure of fibers without buckling

Variations on these basic mechanisms have also been observed. For example, the shear mode of fiber microbuckling (Figure 4.14) often leads to "shear crippling" due to kink band formation [51,57]. Although these problems make it difficult to assess the accuracy of various micromechanics models for compressive strength, several representative models will be summarized.

Mechanics of materials models for local buckling or microbuckling of fibers in the matrix have been developed by Rosen [58] and Schuerch [59]. It is assumed that fiber buckling occurs in either the extensional mode, where fibers buckle in an out-of-phase pattern and the matrix is extended or compressed, or the shear mode, where fibers buckle in an in-phase pattern and the matrix is sheared (Figure 4.14). Two-dimensional models were used, with the fibers represented as plates separated by matrix blocks. By the energy method, the work done by external forces during deformation,  $W$ , is equal to

**FIGURE 4.14**

Three possible failure modes for longitudinal compressive loading of a unidirectional composite.

the corresponding change in the strain energy of the fibers,  $\Delta U_f$ , plus the change in the strain energy of the matrix,  $\Delta U_m$ :

$$\Delta U_f + \Delta U_m = W \quad (4.29)$$

Assuming a sinusoidally buckled shape, the buckling stress (or compressive strength) for the extensional, or out-of-phase mode, was found to be

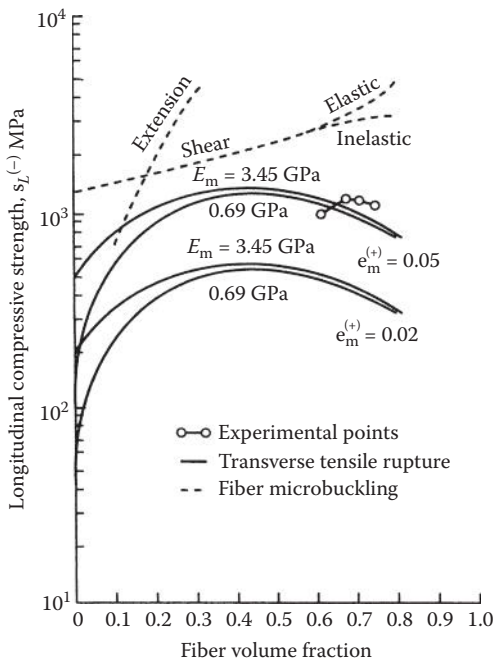
$$s_L^{(-)} = 2v_f \left[ \frac{v_f E_m E_{f1}}{3(1 - v_f)} \right]^{1/2} \quad (4.30)$$

whereas the buckling stress for the shear, or in-phase mode, was found to be

$$s_L^{(+)} = \frac{G_m}{(1 - v_f)} \quad (4.31)$$

The extensional mode turns out to be important only for very low fiber volume fractions, where it predicts the lowest buckling stress and is not important for practical composites (Figure 4.15). While the shear mode gives the lowest buckling stress over the range of practical fiber volume fractions, it overpredicts considerably by comparing with test results. One way to reduce the buckling stress predicted by Equation 4.31 is to take into account the possible inelastic deformation of the matrix material by using a reduced value of the matrix shear modulus,  $G_m$ , but predictions still tend to be too high. The nonlinear model of Hahn and Williams [57] includes the effects of initial fiber curvature and material nonlinearity, and reasonable predictions of compressive strength for graphite/epoxy were reported. Greszczuk [60] has shown that if the matrix shear modulus is high enough, the mode of failure shifts from microbuckling to compressive failure of the reinforcement. Since advanced composites tend to have high-modulus matrix materials, this may explain why attempts to apply microbuckling failure theories to these materials have not succeeded. For such cases, Greszczuk recommended that Equation 4.22 be used with  $s_{f1}^{(-)}$  in place of  $s_{f1}^{(+)}$ . It should be added, however, that this conclusion was based on tests of laminates consisting of aluminum strips bonded together with urethane or epoxy resins. The difficulty in measurement of fiber compressive strength,  $s_{ff}^{(-)}$ , may preclude the use of this model for fiber composites.

A model for transverse tensile rupture due to Poisson strains (Figure 4.14) has been presented by Agarwal and Broutman [61]. The model is based on the application of the Maximum Strain Criterion to the tensile transverse

**FIGURE 4.15**

Variation of predicted compressive strength of glass/epoxy with fiber volume fraction for fiber microbuckling and transverse tensile rupture modes of failure. (Agarwal, B. D. and Broutman, L. J., *Analysis and Performance of Fiber Composites*, 2nd ed., 1990. Copyright John Wiley & Sons, Inc., New York, NY. Reproduced with permission.)

Poisson strain under longitudinal compressive loading. Under the applied longitudinal stress,  $\sigma_1$ , the resulting transverse Poisson strain is

$$\varepsilon_2 = -v_{12}\varepsilon_1 = -v_{12} \frac{\sigma_1}{E_1} \quad (4.32)$$

Thus, when the Poisson strain  $\varepsilon_2 = e_T^{(+)}$ , the corresponding longitudinal stress is  $\sigma_1 = s_L^{(-)}$ , and the compressive strength is

$$s_L^{(-)} = \frac{E_1 e_T^{(+)}}{v_{12}} \quad (4.33)$$

As shown in Figure 4.15, Equation 4.33 shows better agreement with measured compressive strengths of glass/epoxy than the microbuckling theories do [61].

Failure of the fibers in direct shear due to the maximum shear stress  $\tau_{\max} = s_L^{(-)} / 2$  at an angle of  $45^\circ$  to the loading axis is a third possible failure mode under longitudinal compression (Figure 4.14). Hull [51] reports good agreement with experimental data for graphite/epoxy when the maximum shear stress is given by a rule of mixtures, so that the compressive strength is

$$s_L^{(-)} = 2(s_{f12}v_f + s_{m12}v_m) \quad (4.34)$$

where  $s_{f12}$  and  $s_{m12}$  are the shear strengths of fiber and matrix, respectively. The direct shear mode of failure for graphite/epoxy has been reported in several other publications as well [62,63]. For example, Crasto and Kim [63] have used a novel minisandwich beam to attain shear failure of the fibers in the composite facing without buckling—the resulting compressive strengths are much higher than those obtained with conventional compression testing.

A number of other factors have been shown to affect longitudinal compressive strength, and this continues to be a very active research area. For example, although the fiber/matrix interfacial strength does not appear in any of the equations presented here, it would appear to be very important in the case of transverse tensile rupture due to Poisson strains. The experiments of Madhukar and Drzal [64] have shown that the compressive strength of graphite/epoxy is strongly related to the interfacial shear strength, and that fiber surface treatments that improve the interfacial shear strength also improve the compressive strength.

#### 4.3.2 Transverse Strength

Since failure of the lamina under transverse tension occurs at such low stresses (Table 4.1), this mode of failure is often the first to occur. In laminates, the so-called “first ply failure” is generally due to transverse tension. The low value of the transverse tensile strength,  $s_T^{(+)}$ , and the corresponding transverse failure strain,  $e_T^{(+)}$ , are due to strain concentration in the matrix around the fibers, as shown in Equation 4.35:

$$e_T^{(+)} = \frac{e_{m2}^{(+)}}{F} = \frac{e_m^{(+)}}{F} \quad (4.35)$$

where  $e_{m2}^{(+)} = e_m^{(+)}$ , the matrix tensile failure strain (matrix is assumed to be isotropic) and  $F$  is the strain concentration factor ( $F > 1$ ).

Thus, the strain concentration causes the composite transverse tensile failure strain to be less than the matrix failure strain. The strain concentration factor is more appropriate than the stress concentration factor here because the stress-strain relationships for transverse loading are often nonlinear, reflecting the nonlinear behavior of many matrix materials. However, if

linear behavior to failure can be assumed, the corresponding transverse strength is

$$s_T^{(+)} = \frac{E_2 s_m^{(+)}}{E_m F} \quad (4.36)$$

It is assumed here that the fiber is perfectly bonded to the matrix, and so in composites having poor interfacial strength, the composite transverse strength would be less than that predicted by Equation 4.36. For example, de Kok and Peijs [65] conducted experiments and incorporated an interfacial model in a finite element micromechanics model to show that, although the fiber/matrix interface does not affect the transverse modulus, it has a significant effect on the transverse strength. More specifically, it was found that the transverse strength increases in proportion to the interfacial bond strength when the interfacial bond failure is the dominant mode of failure, but this proportionality does not hold when matrix failure dominates.

A mechanics of materials approximation for the strain concentration factor has been developed by Kies [66], who considered an element in a transversely loaded lamina, as shown in Figure 4.16a. For the shaded strip shown in Figure 4.16a, the total elongation is found by summing the deformations in the fiber and matrix

$$\bar{\delta}_{c2} = \bar{\delta}_{f2} + \bar{\delta}_{m2} = s \bar{\epsilon}_{c2} = d \bar{\epsilon}_{f2} + (s - d) \bar{\epsilon}_{m2} \quad (4.37)$$

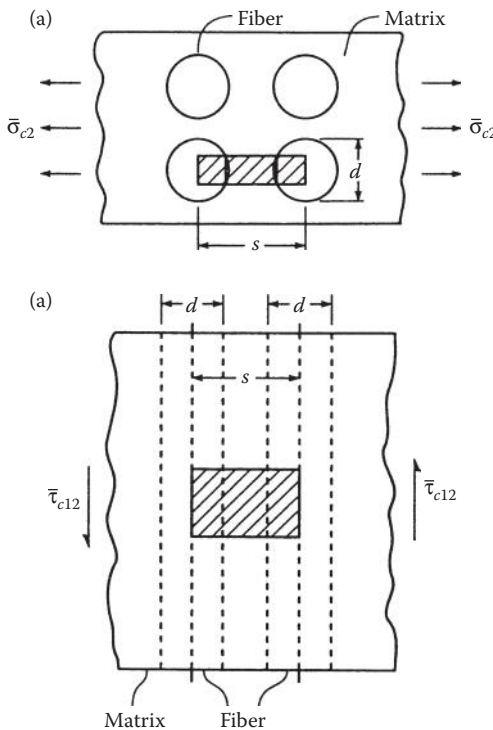
where the symbols are defined in Section 3.2.2 and Figure 4.16a. For the series arrangement of fiber and matrix materials in the shaded strip, it is assumed that the stresses in composite, matrix, and fiber are equal and that each material satisfies Hooke's law (Equation 3.38), as in Section 3.2.2. Equation 4.37 can then be written as

$$s \bar{\epsilon}_{c2} = \left( d \frac{E_{m2}}{E_{f2}} + s - d \right) \bar{\epsilon}_{m2} \quad (4.38)$$

which can be rearranged to give the expression for the strain concentration factor

$$F = \frac{\bar{\epsilon}_m}{\bar{\epsilon}_{c2}} = \frac{1}{d \left[ \frac{E_m}{E_{f2}} - 1 \right] + 1} \quad (4.39)$$

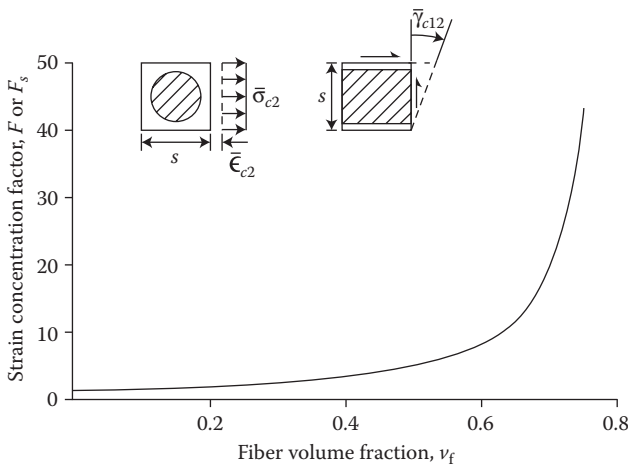
where the subscript "2" for matrix properties has been dropped due to the assumption of isotropy. Recall from Equations 3.14 and 3.16 that the ratio of

**FIGURE 4.16**

(a) Mechanics of materials model for strain concentration under transverse loading. (b) Mechanics of materials model for strain concentration under in-plane shear loading.

fiber diameter to fiber spacing,  $d/s$ , is related to the fiber volume fraction,  $v_f$ . For example, from substitution of the properties listed in Equation 3.33 in Equations 3.16 and 4.39, the strain concentration factor for a triangular array of E-glass fibers in an epoxy matrix ( $v_f = 0.45$ ) is  $F = 3.00$ . This value is in good agreement with experimentally determined values based on the ratio of matrix failure strain to transverse composite failure strain or the ratio of matrix yield strain to transverse composite yield strain [67]. A slightly higher value is predicted by a finite difference solution of the theory of elasticity model [68].

It is important to note that according to Equation 4.39, the strain concentration factor increases with increasing  $v_f$  and increasing  $E_{f2}$ . For example, the variation of  $F$  with fiber volume fraction is shown in Figure 4.17 for  $E_m/E_{f2} \ll 1$  [69]. The sharp rise in  $F$  for  $v_f > 0.6$  is particularly noteworthy. Thus, as we strive to improve the composite longitudinal properties by using higher fiber volume fractions and higher modulus fibers, we pay the penalty of lower composite transverse strength!

**FIGURE 4.17**

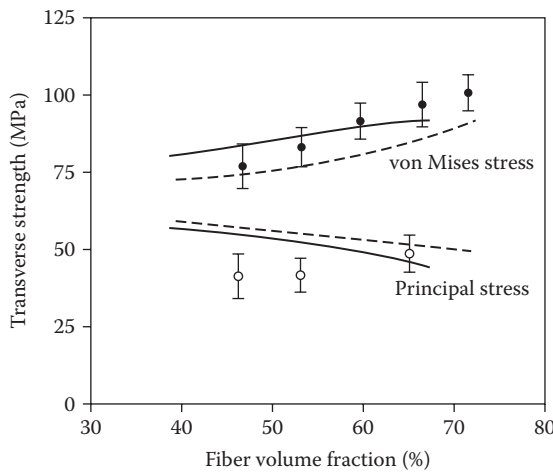
Variation of strain concentration factor  $F$  or  $F_s$  with fiber volume fraction. Valid for  $F$  when  $E_m/E_{f2} \ll 1$  and for  $F_s$  when  $G_m/G_{f12} \ll 1$ . (From Chamis, C. C. 1974. In Broutman, L.J. ed., *Composite Materials*, Vol. 5, Fracture and Fatigue, Chapter 3. Academic Press, New York. With permission.)

The same method outlined above can be used to estimate the transverse compressive strength,  $s_T^{(-)}$ , by replacing the tensile strains or strengths with the corresponding compressive strains or strengths. Alternatively, the corresponding matrix strength can be used as an upper bound on the composite strength, but the actual composite strength would be lower because of fiber/matrix interfacial bond failure, strain concentrations around fibers and/or voids, or longitudinal fiber splitting [70].

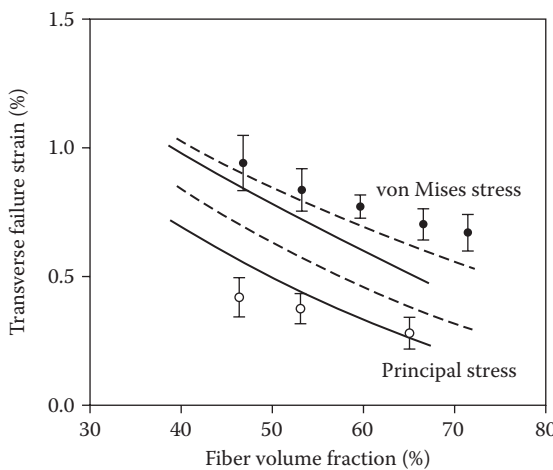
While substitution of Equation 4.39 in Equation 4.36 shows that  $s_T^{(+)}$  decreases with increasing  $v_f$ , there is some evidence in the literature that  $s_T^{(+)}$  increases slightly with increasing  $v_f$ . For example, de Kok and Meijer [71] studied the effect of fiber volume fraction on the transverse strength of glass/epoxy using experiments and finite element micromechanical models. Experiments and a finite element micromechanical model based on the von Mises failure criterion for the epoxy matrix showed that the transverse strength of the composite increased slightly with increasing fiber volume fraction (Figure 4.18), but since the transverse modulus,  $E_2$ , also increases with increasing  $v_f$ , the transverse failure strain decreased with increasing  $v_f$  (Figure 4.19). According to the von Mises yield criterion, yielding occurs in the matrix when the equivalent axial stress or von Mises stress

$$\sigma_{eq} = \frac{1}{\sqrt{2}} \sqrt{(\sigma_a - \sigma_b)^2 + (\sigma_b - \sigma_c)^2 + (\sigma_c - \sigma_a)^2} \quad (4.40)$$

reaches the uniaxial yield strength of the matrix material, where  $\sigma_a$ ,  $\sigma_b$ , and  $\sigma_c$  are the three principal stresses in the matrix. The corresponding predicted

**FIGURE 4.18**

Transverse strength of E-glass/epoxy composite as a function of fiber volume fraction, as measured in tension (○) and three-point bending (●), and predicted with the square (solid lines) and hexagonal (dotted lines) fiber packing models, using a von Mises criterion and an ultimate stress criterion. (Reprinted from *Composites Part A: Applied Science and Manufacturing*, 30(7), de Kok, J. M. M. and Peijs, T., Deformation, yield and fracture of unidirectional composites in transverse loading: 2. Influence of fibre-matrix adhesion, 905–916. Copyright (1999), with permission from Elsevier.)

**FIGURE 4.19**

Transverse failure strain of E-glass/epoxy composite as a function of fiber volume fraction, as measured in tension (○) and three-point bending (●), and predicted with the square (solid lines) and hexagonal (dotted lines) fiber packing models, using a von Mises criterion and an ultimate stress criterion. (Reprinted from *Composites Part A: Applied Science and Manufacturing*, 30(7), de Kok, J. M. M. and Peijs, T., Deformation, yield and fracture of unidirectional composites in transverse loading: 2. Influence of fibre-matrix adhesion, 905–916. Copyright (1999), with permission from Elsevier.)

transverse strength decreased with increasing  $v_f$  when only the ultimate principal stress in the matrix was considered in the micromechanics model. In addition, the predicted transverse strength based on the von Mises criterion was significantly higher than that predicted by the ultimate principal stress model (Figure 4.18). So it appears that the predicted transverse strength based on the 1-D stress model described in Equations 4.35 through 4.39 is conservative by comparison with the corresponding prediction based on the actual triaxial state of stress and the von Mises failure criterion.

### 4.3.3 In-Plane Shear Strength

The in-plane shear strength,  $s_{LT}$ , can also be estimated using the procedure outlined in the previous section. For the shaded element shown in Figure 4.16b, the expression analogous to Equation 4.37 for the in-plane shear strain is

$$s\bar{\gamma}_{c12} = d\bar{\gamma}_{f12} + (s - d)\bar{\gamma}_{m12} \quad (4.41)$$

and the in-plane shear strain concentration factor is

$$F_s = \frac{\bar{\gamma}_{m12}}{\bar{\gamma}_{c12}} = \frac{1}{d \left[ \frac{G_{m12}}{G_{f12}} - 1 \right] + 1} \quad (4.42)$$

where

$\bar{\gamma}_{m12}$  = average matrix in-plane shear strain

$\bar{\gamma}_{c12}$  = average composite in-plane shear strain

$\bar{\gamma}_{f12}$  = average fiber in-plane shear strain

$G_{f12}$  = fiber in-plane shear modulus

Note that this equation has the same form as Equation 4.39. Thus, Figure 4.17 also gives the variation of  $F_s$  with  $v_f$  when  $G_m/G_{f12} \ll 1$ , and the previous comments regarding the effect of  $v_f$  on  $F$  are also valid for  $F_s$ . The other necessary equations are obtained by replacing the tensile strains or strengths in Equations 4.35 and 4.36 with the corresponding in-plane shear strains or strengths. Again, the matrix shear strength can be used as an upper bound on the composite shear strength, as the actual composite strength would be lower for the same reasons mentioned in the previous section.

### 4.3.4 Multiaxial Strength

Sections 4.3.1 through 4.3.3 have summarized micromechanical models for prediction of the five basic unidirectional lamina strengths, and most of the micromechanical strength modeling efforts have been focused in these areas. However, micromechanical models have also been used to evaluate

multiaxial strength criteria such as those described in Section 4.2. For example, Zhu, Sankar, and Marrey [72] developed finite element unit cell micromechanics models and used them to evaluate the Maximum Stress, Maximum Strain and Tsai-Wu criteria as well as the combination of Tsai-Wu and Maximum Stress criteria for several biaxial loading conditions on a unidirectional composite. The approach was referred to as a direct micromechanics method (DMM). As shown in Figure 4.20, two types of failure criteria for the fiber and matrix materials were employed in the finite element DMM for predicting failure in each element of the model: (a) maximum principal stress criterion and (b) von Mises criterion, while fiber/matrix interfacial failure at the element level was modeled using the maximum tensile interfacial stress and the maximum interfacial shear stress. Failure envelopes were generated using the DMM and compared with the corresponding failure envelopes that were generated using the applied macromechanical stresses in the Tsai-Wu criterion, the Maximum Stress Criterion, the Maximum Strain Criterion, and the combined Tsai-Wu and Maximum Stress Criteria. From all the different cases examined, it was found that the combination of the Tsai-Wu and Maximum Stress Criteria led to the most conservative failure envelope in the biaxial stress space, and that the failure criteria for the matrix and the fiber/matrix interface played dominant roles in the failure criteria for the composite. For off-axis tensile test models, the Tsai-Wu criterion showed the best agreement with the DMM approach for fiber orientations in the range  $0 < \theta < 30^\circ$ , the Maximum Stress Criterion gave the best agreement in the range  $60^\circ < \theta < 90^\circ$ , and the criterion that gave the lowest strength prediction of the two criteria worked best in the range  $30^\circ < \theta < 60^\circ$ .

In conclusion, only the basics of micromechanical strength prediction have been discussed here. More detailed micromechanics analyses of strength under other types of loading such as interlaminar shear and flexure as well as micromechanical effects of voids and residual stresses on strength have been summarized by Chamis [69]. More recently, a critical review of the state

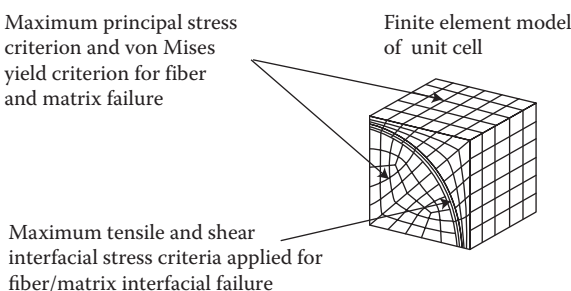


**FIGURE 4.20**

Failure criteria employed in the finite element unit cells using the Direct Micromechanics Method (DMM), (Adapted from Zhu, H., Sankar, B. V., and Marrey, R. V. 1998. *Journal of Composite Materials*, 32, 766–782.)

of the art in methodologies for material constitutive modeling and composite failure theories has been published by Orifici et al. [73].

### Example 4.5

Determine the longitudinal and transverse tensile strengths of the carbon/epoxy material described in Examples 3.1, 3.2, and 3.5 if the tensile strengths of fiber and matrix materials are 2413 and 103 MPa, respectively.

#### SOLUTION

The fiber tensile failure strain is

$$e_{f1}^{(+)} = \frac{s_{f1}^{(+)}}{E_{f1}} = \frac{2.413}{220} = 0.011$$

The matrix tensile failure strain is

$$e_m^{(+)} = \frac{s_m^{(+)}}{E_m} = \frac{0.103}{3.45} = 0.03$$

Thus, the material fails as described in Figure 4.12a at a strain level of  $e_{f1}^{(+)} = 0.011$ . Since  $v_f = 0.506$  and  $v_m = 0.482$ , from Example 3.1, the composite longitudinal tensile strength is given by Equation 4.22:

$$\begin{aligned} s_L^{(+)} &= s_{f1}^{(+)}v_f + s_{mf1}v_m \\ &= s_{f1}^{(+)}v_f + E_m e_{f1}^{(+)} v_m \\ &= 2413(0.506) + 3450(0.011)(0.482) \\ &= 1239 \text{ MPa (180,000 psi)} \end{aligned}$$

Note that the matrix contribution here is only 18.3 MPa out of 1239 MPa or about 1.5%.

The strain concentration factor for the calculation of the transverse tensile strength is given by Equation 4.39:

$$F = \frac{1}{\frac{d}{s} \left[ \frac{E_m}{E_{f2}} - 1 \right] + 1} = \frac{1}{\frac{0.0127}{0.0158} \left[ \frac{3.45}{13.79} - 1 \right] + 1} = 2.52$$

If linear elastic behavior to failure can be assumed, the transverse tensile strength is given by Equation 4.36.

$$s_T^{(+)} = \frac{E_2 S_m^{(+)}}{E_m F} = \frac{5.65(103)}{3.45(2.52)} = 66.9 \text{ MPa (9703 psi)}$$

### Example 4.6

Determine the longitudinal tensile strength of the hybrid carbon/aramid/epoxy composite described in Problem 3 and Figure 3.20 of Chapter 3 if the fiber packing array is triangular with the closest possible packing.

#### SOLUTION

For the triangular array of fibers of the same diameter with the closest possible packing, the maximum fiber volume fraction is given by Equation 3.17:

$$v_{f\max} = \frac{\pi}{2\sqrt{3}} = 0.907$$

Therefore, the sum of the fiber volume fractions of carbon and aramid fibers must be

$$v_c + v_a = v_{f\max} = 0.907$$

Since there are two carbon fibers for each aramid fiber

$$v_c = 2v_a$$

Neglecting voids, the sum of the volume fractions for the carbon, aramid, and epoxy must be

$$v_c + v_a + v_e = 1$$

Solving the above equations simultaneously, it is found that the volume fractions for the carbon, aramid, and epoxy, respectively, are

$$v_c = 0.604, \quad v_a = 0.302, \quad v_e = 0.094$$

From Figure 3.20, it is seen that the carbon fibers fail first at a strain level of 0.0054. At this strain level, the corresponding stresses in the carbon, aramid, and epoxy, respectively, are

$$s_{c1}^{(+)} = 2.1 \text{ GPa}, \quad s_{ac1}^{(+)} = 0.72 \text{ GPa}, \quad s_{ec1}^{(+)} = 0.0164 \text{ GPa}$$

Finally, generalizing Equation 4.22 for the case of the hybrid composite with three constituents, we find that the composite longitudinal tensile strength is

$$\begin{aligned} s_L^{(+)} &= s_{c1}^{(+)}v_c + s_{ac1}^{(+)}v_a + s_{ec1}^{(+)}v_e = 2.1(0.604) + 0.72(0.302) \\ &\quad + 0.0164(0.094) = 1.487 \text{ GPa} \end{aligned}$$

## PROBLEMS

1. An orthotropic lamina has the following properties:

$$\begin{array}{ll} E_1 = 160 \text{ GPa} & s_L^{(+)} = 1800 \text{ MPa} \\ E_2 = 10 \text{ GPa} & s_L^{(-)} = 1400 \text{ MPa} \\ v_{12} = 0.3 & s_T^{(+)} = 40 \text{ MPa} \\ G_{12} = 7 \text{ GPa} & s_T^{(-)} = 230 \text{ MPa} \\ s_{LT} = 100 \text{ MPa} & \end{array}$$

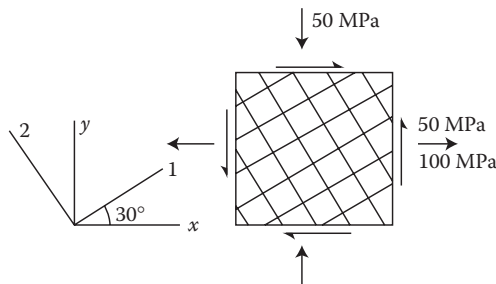
Construct the failure surfaces in the  $\sigma_1 - \sigma_2$  stress space for this material according to: (a) the Maximum Stress Criterion, (b) the Maximum Strain Criterion, and (c) the Tsai-Hill Criterion.

2. Using the material properties from Problem 1 and assuming that the stiffnesses are the same in tension and compression, determine the allowable off-axis shear stress,  $\tau_{xy}$ , at  $\theta = 45^\circ$  (refer to Figure 4.7) according to: (a) the Maximum Stress Criterion, (b) the Maximum Strain Criterion, and (c) the Tsai-Hill Criterion. Compare and discuss the results and check both positive and negative values of  $\tau_{xy}$ .
3. An element of a balanced orthotropic lamina is under the state of stress shown in Figure 4.21. The properties of the lamina are:

$$\begin{array}{ll} E_1 = E_2 = 70 \text{ GPa} & s_L^{(+)} = s_L^{(-)} = s_T^{(+)} = s_T^{(-)} = 560 \text{ MPa} \\ v_{12} = v_{21} = 0.25 & s_{LT} = 25 \text{ MPa} \\ G_{12} = 5 \text{ GPa} & \end{array}$$

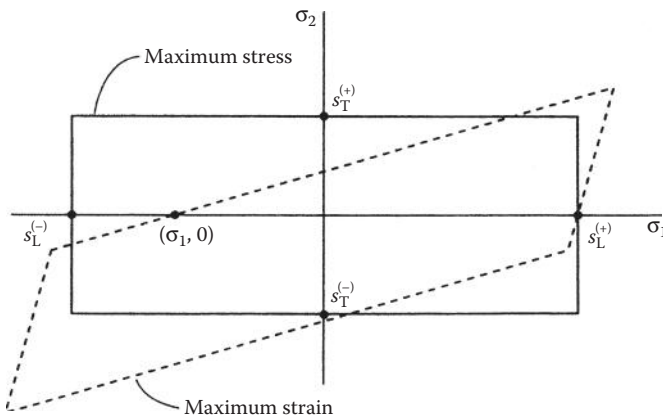
Using the Maximum Strain Criterion, determine whether or not failure will occur.

4. If some of the compliances and strengths of an orthotropic lamina satisfy certain conditions, the Maximum Strain Criterion failure surface will intercept the horizontal axis at a point like  $(\sigma_1, 0)$  instead of at  $(s_L^{(-)}, 0)$  as shown in Figure 4.22. Express these conditions in terms of an inequality.
5. An element of an orthotropic lamina having the properties given in Problem 1 is subjected to an off-axis tensile test, as shown in



**FIGURE 4.21**

Stresses acting on element of balanced orthotropic lamina.

**FIGURE 4.22**

Example showing that intercepts for Maximum Strain Criterion failure surface are not always the same as those for Maximum Stress Criterion.

Figure 4.5. Using the Maximum Strain Criterion, determine the values of  $\sigma_x$  at failure and the mode of failure for each of the following values of the angle  $\theta$ : (a)  $2^\circ$ , (b)  $30^\circ$ , and (c)  $75^\circ$ .

6. Repeat Problem 5 for an off-axis compression test.
7. A material having the properties given in Problem 1 is subjected to a biaxial tension test, and the biaxial failure stress is found to be  $\sigma_1 = \sigma_2 = 35$  MPa. Determine the Tsai-Wu interaction parameter  $F_{12}$  and then use the Tsai-Wu Criterion to determine whether or not failure will occur for the stress condition  $\sigma_1 = 100$  MPa,  $\sigma_2 = -50$  MPa,  $\sigma_1 = 90$  MPa.
8. The Tsai-Wu interaction parameter  $F_{12}$  is determined from biaxial failure stress data. One way to generate a biaxial state of stress is by using a uniaxial  $45^\circ$  off-axis tension test. Derive the expression for  $F_{12}$  based on such a test, assuming that all the uniaxial and shear strengths are known.
9. Determine the longitudinal tensile strength of the hybrid carbon/aramid/epoxy composite described in Problem 3 of Chapter 3 and Figure 3.20.
10. Compare and discuss the estimated longitudinal compressive strengths of Scotchply 1002 E-glass/epoxy based on (a) fiber microbuckling and (b) transverse tensile rupture. Assume linear elastic behavior to failure. For the epoxy matrix, assume that the modulus of elasticity is  $E_m = 3.79$  GPa, the Poisson's ratio is  $v_m = 0.35$ , and the fiber volume fraction is  $v_f = 0.45$ .
11. An element of an orthotropic lamina is subjected to an off-axis shear stress,  $\tau_{xy}$ , as shown in Figure 4.7a. Using the Tsai-Hill Criterion and assuming that the lamina strengths are the same in tension and compression, develop an equation relating the allowable value of  $\tau_{xy}$  to the lamina strengths,  $s_L$ ,  $s_T$ , and  $s_{LT}$ , and the fiber orientation  $\theta$ .

12. A uniaxial off-axis tensile test is conducted as shown in Figure 4.5a. Using the Tsai–Hill Criterion and assuming that the lamina strengths are the same in tension and compression, develop an equation relating the applied stress,  $\sigma_x$ , to the lamina strengths  $s_L$ ,  $s_T$ , and  $s_{LT}$ , and the lamina orientation,  $\theta$ , and (b) using the result from part (a), for a unidirectional composite having strengths  $s_L = 1500 \text{ MPa}$ ,  $s_T = 100 \text{ MPa}$ ,  $s_{LT} = 70 \text{ MPa}$ , and fiber orientation  $\theta = 60^\circ$ , determine whether or not an applied stress  $\sigma_x = 200 \text{ MPa}$  would cause failure according to the Tsai–Hill Criterion.
13. Using the Maximum Strain Criterion and micromechanics, set up the equations for predicting the averaged isotropic strength of a randomly oriented continuous fiber composite. Your answer should be expressed in terms of the appropriate fiber and matrix properties and volume fractions, the variable fiber orientation angle  $\theta$ , and the appropriate strengths of the corresponding unidirectional lamina that consists of the same fiber and matrix materials and volume fractions. In the micromechanics analysis, assume that the matrix failure strain is greater than the fiber failure strain (i.e., that the materials behave as shown in Figure 4.12a). Define all parameters used, but do not try to solve the equation.
14. Assuming that the failure mode for longitudinal compression of unidirectional E-glass/epoxy with fiber volume fraction  $v_f = 0.6$  is transverse tensile rupture due to Poisson strains, (a) estimate the longitudinal compressive strength of this material and (b) if the volume fraction of the material in part (a) is varied, what effect would this have on the longitudinal compressive strength?
15. An orthotropic AS/3501 carbon/epoxy lamina (see Tables 2.2 and 4.1) is subjected to the plane stress condition  $\sigma_x = 1000 \text{ MPa}$ ,  $\sigma_y = 50 \text{ MPa}$ ,  $\tau_{xy} = 50 \text{ MPa}$ . If the lamina orientation is  $\theta = 0^\circ$ , will the lamina fail according to (a) the Maximum Stress Criterion or (b) the Maximum Strain Criterion?
16. For the IM-9/8551-7 carbon/epoxy composite rod design of Problem 17 in Chapter 3, what would be the increase in the longitudinal tensile strength compared with that of the original 6061-T6 aluminum alloy design?
17. How would the answer to Problem 9 in Chapter 1 change if the flywheel ring is made of IM-7/8552 carbon/epoxy composite with fibers oriented in the circumferential direction? Assume a fiber volume fraction  $v_f = 0.6$ .

---

## References

1. Chamis, C. C. 1987. Simplified composite micromechanics thermal and moisture-related properties, in Weeton, J.W., Peters, D. M., and Thomas, K. L. eds. *Engineers' Guide to Composite Materials*, pp. 3-8-3-24. ASM International, Materials Park, OH.

2. Daniel, I. M. and Ishai, O. 1994. *Engineering Mechanics of Composite Materials*. Oxford University Press, New York, NY.
3. Hashin, Z. 1983. Analysis of composite materials—A survey. *Journal of Applied Mechanics*, 50, 481–505.
4. Hashin, Z. 1980. Failure criteria for unidirectional fiber composites. *Journal of Applied Mechanics*, 47, 329–334.
5. Wu, E. M. 1974. Phenomenological anisotropic failure criterion, in Sendeckyj, G. P. ed., *Composite Materials*, Vol. 2, *Mechanics of Composite Materials*, pp. 353–431. Academic Press, New York, NY.
6. Sendeckyj, G. P. 1972. A brief survey of empirical multiaxial strength criteria for composites. *Composite Materials: Testing and Design (Second Conference)*, ASTM STP 497, pp. 41–51. American Society for Testing and Materials, Philadelphia, PA.
7. Chamis, C. C. 1969. Failure criteria for filamentary composites. *Composite Materials: Testing and Design*, ASTM STP 460, pp. 336–351. American Society for Testing and Materials, Philadelphia, PA.
8. Kaminski, B. E. and Lantz, R. B. 1969. Strength theories of failure for anisotropic materials. *Composite Materials: Testing and Design*, ASTM STP 460, pp. 160–169. American Society for Testing and Materials, Philadelphia, PA.
9. Franklin, H. G. 1968. Classical theories of failure of anisotropic materials. *Fiber Science and Technology*, 1(2), 137–150.
10. Tsai, S. W. 1984. A survey of macroscopic failure criteria for composite materials. *Journal of Reinforced Plastics and Composites*, 3, 40–62.
11. Christensen, R. M. 1997. Stress based yield/failure criteria for fiber composites. *International Journal of Solids and Structures*, 34(5), 529–543.
12. Zhu, H., Sankar, B. V., and Marrey, R. V. 1998. Evaluation of failure criteria for fiber composites using finite element micromechanics. *Journal of Composite Materials*, 32(8), 766–782.
13. Soden, P. D., Hinton, M. J., and Kaddour, A.S. 1998. A comparison of the predictive capabilities of current failure theories for composite laminates. *Composites Science and Technology*, 58(7), 1125–1254.
14. Soden, P. D., Hinton, M. J., and Kaddour, A.S. 1998. Lamina properties, lay-up configurations and loading conditions for a range of fibre-reinforced composite laminates. *Composites Science and Technology*, 58(7), 1011–1022.
15. Hinton, M. J. and Soden, P. D. 1998. Predicting failure in composite laminates: the background to the exercise. *Composites Science and Technology*, 58(7), 1001–1010.
16. Hinton, M. J., Kaddour, A. S., and Soden, P. D. 2002. A comparison of the predictive capabilities of current failure theories for composite laminates, judged against experimental evidence. *Composites Science and Technology*, 62(12–13), 1725–1797.
17. Soden, P. D., Hinton, M. J., and Kaddour, A. S. 2002. Biaxial test results for strength and deformation of a range of E-glass and carbon fibre reinforced composite laminates: Failure exercise benchmark data. *Composites Science and Technology*, 62(12–13), 1489–1514.
18. Hinton, M. J., Kaddour, A. S., and Soden, P. D. 2002. Evaluation of failure prediction in composite laminates: Background to “Part B” of the exercise. *Composites Science and Technology*, 62(12–13), 1481–1488.
19. Soden, P. D., Kaddour, A. S., and Hinton, M. J. 2004. Recommendations for designers and researchers resulting from the world-wide failure exercise. *Composites Science and Technology*, 64(3–4), 589–604.

20. Hinton, M. J., Kaddour, A. S., and Soden, P. D. 2004. A further assessment of the predictive capabilities of current failure theories for composite laminates: Comparison with experimental evidence. *Composites Science and Technology*, 64(3–4), 549–588.
21. Kaddour, A. S., Hinton, M. J., and Soden, P. D. 2004. A comparison of the predictive capabilities of current failure theories for composite laminates: Additional contributions. *Composites Science and Technology*, 64(3–4), 449–476.
22. Hinton, M. J., Kaddour, A. S., and Soden, P. D. 2004. Evaluation of failure prediction in composite laminates: Background to 'part C' of the exercise. *Composites Science and Technology*, 64(3–4), 321–327.
23. Hinton, M. J., Soden, P. D., and Kaddour, A. S. 2004. *Failure Criteria in Fibre-Reinforced Polymer Composites*. Elsevier, London.
24. Jenkins, C. F. 1920. Report on materials of construction used in aircraft and aircraft engines. Great Britain Aeronautical Research Council, London, UK.
25. Higdon, A., Ohlsen, E. H., Stiles, W. B., Weese, J. A., and Riley, W. F. 1976. *Mechanics of Materials*, 3rd ed. John Wiley & Sons, New York, NY.
26. Burk, R. C. 1983. Standard failure criteria needed for advanced composites. *Astronautics and Aeronautics*, 21(6), 58–62.
27. Pipes, R. B. and Cole, B. W. 1973. On the off-axis strength test for anisotropic materials. *Journal of Composite Materials*, 7, 246–256.
28. Jones, R. M. 1999. *Mechanics of Composite Materials*, 2nd ed. Taylor & Francis, Philadelphia, PA.
29. Waddoups, M. E. 1967. Advanced composite material mechanics for the design and stress analyst. General Dynamics. Fort Worth Division Report FZM-4763, Fort Worth, TX.
30. Hill, R. 1948. A theory of the yielding and plastic flow of anisotropic metals, in *Proceedings of the Royal Society of London, Series A*, 193, 281–297.
31. Azzi, V. D. and Tsai, S. W. 1965. Anisotropic strength of composites, in *Proceedings of the Society for Experimental Stress Analysis*, XXII(2), 283–288.
32. Tsai, S. W. 1968. Strength theories of filamentary structures, in Schwartz, R. T. and Schwartz, H. S. eds., *Fundamental Aspects of Fiber Reinforced Plastic Composites*, Chapter 1, pp. 3–11. Wiley Interscience, New York, NY.
33. Hoffman, O. 1967. The brittle strength of orthotropic materials. *Journal of Composite Materials*, 1, 200–206.
34. Tsai, S.W. and Wu, E.M. 1971. A general theory of strength for anisotropic materials. *Journal of Composite Materials*, 5, 58–80.
35. Goldenblat, I. and Kopnov, V. A. 1965. Strength of glass reinforced plastics in the complex stress state. *Mekhanika Polimerov*, 1, 70–78 (English translation: *Polymer Mechanics*, 1, 54–60, 1966).
36. Wu, E.M. 1972. Optimal experimental measurements of anisotropic failure tensors. *Journal of Composite Materials*, 6, 472–489.
37. Tsai, S. W. and Hahn, H. T. 1980. *Introduction to Composite Materials*. Technomic Publishing Co., Lancaster, PA.
38. Zinoviev, P., Grigoriev, S. V., Lebedeva, O. V., and Tairova, L. R. 1998. Strength of multilayered composites under plane stress state. *Composites Science and Technology*, 58(7), 1209–1224.
39. Zinoviev, P. A., Lebedeva, O. V., and Tairova, L. R. 2002. Coupled analysis of experimental and theoretical results of the deformation and failure of laminated

- composites under a plane state of stress. *Composites Science and Technology*, 62(12–13), 1711–1723.
- 40. Bogetti, T. A., Hoppel, C. P. R., Harik, V. M., Newill, J. F., and Burns, B. P. 2004. Predicting the nonlinear response and progressive failure of composite laminates. *Composites Science and Technology*, 64(3–4), 329–342.
  - 41. Bogetti, T. A., Hoppel, C. P. R., Harik, V. M., Newill, J. F., and Burns, B. P. 2004. Predicting the nonlinear response and progressive failure of composite laminates: Correlation with experimental results. *Composites Science and Technology*, 64(3–4), 477–485.
  - 42. Liu, K. S. and Tsai, S. W. 1998. A progressive quadratic failure criterion for a laminate. *Composites Science and Technology*, 58(7), 1023–1032.
  - 43. Kuraishi, A., Tsai, S. W., and Liu, K. S. 2002. A progressive quadratic failure criterion. Part B. *Composites Science and Technology*, 62(12–13), 1683–1695.
  - 44. Puck, A. and Schurmann, H. 1998. Failure analysis of FRP laminates by means of physically based phenomenological models. *Composites Science and Technology*, 58(7), 1045–1067.
  - 45. Puck, A. and Schurmann, H. 2002. Failure analysis of FRP laminates by means of physically based phenomenological models. *Composites Science and Technology*, 62(12–13), 1633–1662.
  - 46. Cuntze, R. G. and Freund, A. 2004. The predictive capability of failure mode concept-based strength criteria for multidirectional laminates. *Composites Science and Technology*, 64(3–4), 343–377.
  - 47. Cuntze, R. G. 2004. The predictive capability of failure mode concept-based strength criteria for multidirectional laminates—part B. *Composites Science and Technology*, 64(3–4), 487–516.
  - 48. Tennyson, R. C., MacDonald, D., and Nanyaro, A. P. 1978. Evaluation of the tensor polynomial failure criterion for composite materials. *Journal of Composite Materials*, 12, 63–75.
  - 49. Weeton, J. W., Peters, D. M., and Thomas, K. L. eds. 1987. *Engineers' Guide to Composite Materials*. ASM International, Materials Park, OH.
  - 50. Kelly, A. and Davies, G. J. 1965. The principles of the fibre reinforcement of metals. *Metallurgical Review*, 10, 1–77.
  - 51. Hull, D. 1981. *An Introduction to Composite Materials*. Cambridge University Press, Cambridge, MA.
  - 52. Rosen, B. W. 1964. Tensile failure of fibrous composites. *AIAA Journal*, 2, 1985–1991.
  - 53. Zweben, C. and Rosen, B. W. 1970. A statistical theory of material strength with applications to composite materials. *Journal of Mechanics and Physics of Solids*, 18, 180–206.
  - 54. Rosen, B. W. 1987. Composite materials analysis and design, in Reinhart, T. J. ed., *Engineered Materials Handbook*, vol. 1, Composites, Section 4. ASM International, Materials Park, OH.
  - 55. Holister, G. S. and Thomas, C. 1966. *Fibre Reinforced Materials*. Elsevier Publishing Co., Ltd., New York, NY.
  - 56. Whitney, J. M. 1991. Failure modes in compression testing of composite materials, *How Concept Becomes Reality, Proceedings of 36th International SAMPE Symposium*, 36, pp. 1069–1078. Society for Advancement of Material and Process Engineering, Covina, CA.

57. Hahn, H. T. and Williams, J. G. 1986. Compression failure mechanisms in unidirectional composites, in Whitney, J. M. ed., *Composite Materials: Testing and Design (Seventh Conference)*, ASTM STP 893, pp. 115–139. American Society for Testing and Materials, Philadelphia, PA.
58. Rosen, B. W. 1965. Mechanics of composite strengthening. *Fiber Composite Materials*. American Society for Metals, Metals Park, OH.
59. Schuerch, H. 1966. Prediction of compressive strength in uniaxial boron fiber metal matrix composites. *AIAA Journal*, 4, 102–106.
60. Greszczuk, L. B. 1974. Microbuckling of lamina-reinforced composites, in Berg, C. A., McGarry, F. J., and Elliott, S. Y. eds., *Composite Materials: Testing and Design (Third Conference)*, ASTM STP 546, pp. 5–29. American Society for Testing and Materials, Philadelphia, PA.
61. Agarwal, B. D. and Broutman, L. J. 1990. *Analysis and Performance of Fiber Composites*, 2nd ed. John Wiley & Sons, Inc., New York, NY.
62. Hancox, N. L. 1975. The compression strength of unidirectional carbon fibre reinforced plastics. *Journal of Materials Science*, 10(2), 234–242.
63. Crasto, A. S. and Kim, R. Y. 1991. Compression strengths of advanced composites from a novel mini-sandwich beam. *SAMPE Quarterly*, 22(3), 29–39.
64. Madhukar, M. S. and Drzal, L. T. 1990. Effect of fiber-matrix adhesion on longitudinal compressive properties of graphite/epoxy composites, in *Proceedings of the American Society for Composites Fifth Technical Conference*, pp. 849–858. Technomic Publishing Co., Lancaster, PA.
65. de Kok, J. M. M. and Peijs, T. 1999. Deformation, yield and fracture of unidirectional composites in transverse loading: 2. Influence of fibre-matrix adhesion. *Composites Part A: Applied Science and Manufacturing*, 30(7), 917–932.
66. Kies, J. A. 1962. Maximum strains in the resin of fiber glass composites. U.S. Naval Research Laboratory Report No. 5752.
67. Gibson, R. F. 1975. Elastic and dissipative properties of fiber reinforced composite materials in flexural vibration. Ph.D. Dissertation, University of Minnesota, Minneapolis, MN.
68. Adams, D. F. and Doner, D. R. 1967. Transverse normal loading of a unidirectional composite. *Journal of Composite Materials*, 1, 152–164.
69. Chamis, C. C. 1974. Micromechanics strength theories, in Broutman, L. J. ed., *Composite Materials*, Vol. 5, *Fracture and Fatigue*, Chapter 3. Academic Press, New York, NY.
70. Piggott, M. R. 1980. *Load Bearing Fibre Composites*. Pergamon Press Ltd., Oxford, England.
71. de Kok, J. M. M. and Meijer, H. E. H. 1999. Deformation, yield and fracture of unidirectional composites in transverse loading: 1. Influence of fibre volume fraction and test temperature. *Composites Part A: Applied Science and Manufacturing*, 30(7), 905–916.
72. Zhu, H., Sankar, B. V., and Marrey, R. V. 1998. Evaluation of failure criteria for fiber composites using finite element micromechanics. *Journal of Composite Materials*, 32, 766–782.
73. Orifici, A. C., Herszberg, I., and Thomson, R. S. 2008, Review of methodologies for composite material modeling incorporating failure. *Composite Structures*, 86, 194–210.

This page intentionally left blank

# 5

---

## *Analysis of Lamina Hygrothermal Behavior*

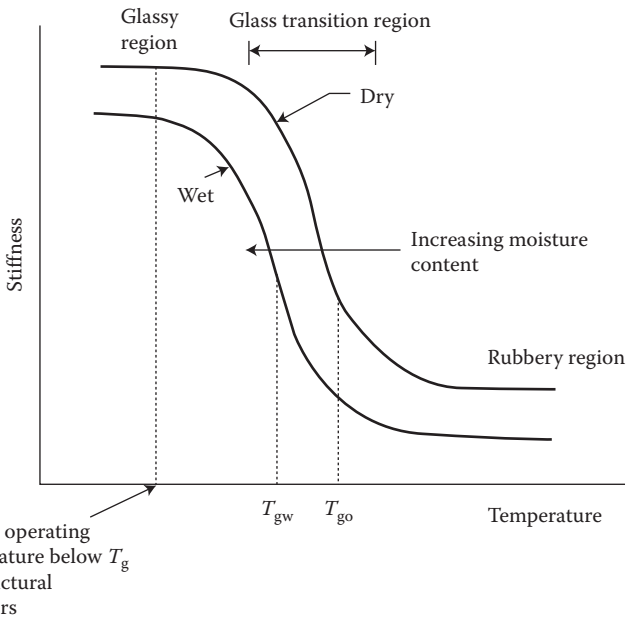
---

### 5.1 Introduction

The analytical models for composite mechanical behavior presented up to now have been based on the assumption of constant environmental conditions. Composites are usually subjected to changing environmental conditions during both initial fabrication and final use, however, and it is important to be able to include the effects of such changes in the analysis. Among the many environmental conditions that may influence composite mechanical behavior, changes in temperature and moisture content are singled out for discussion here because of the particularly important effects they have on polymer matrix materials and those properties of polymer composites that are matrix dominated. Effects of temperature are usually referred to as "thermal" effects, whereas those of moisture are often referred to as "hygroscopic" effects. The word "hygrothermal" has evolved as a way of describing the combined effects of temperature and moisture.

There are two principal effects of changes in the hygrothermal environment on mechanical behavior of polymer composites:

1. Matrix-dominated properties such as stiffness and strength under transverse, off-axis, or shear loading are altered. Increased temperature causes a gradual softening of the polymer matrix material up to a point. If the temperature is increased beyond the so-called "glass transition" region (indicating a transition from glassy behavior to rubbery behavior), however, the polymer becomes too soft for use as a structural material (Figure 5.1). Plasticization of the polymer by absorbed moisture causes a reduction in the glass transition temperature,  $T_g$ , and a corresponding degradation of composite properties. As shown in Figure 5.1, the glass transition temperature of the dry material is characterized by  $T_{go}$  (i.e., the "dry"  $T_g$ ), and when the material is fully saturated with moisture content  $M_m$ , it is characterized by  $T_{gw}$  (the "wet"  $T_g$ ). Saturation moisture contents of 3–4% by weight, and moisture-induced reductions in  $T_g$  on the order of 20% are typical for polymer matrix materials, as shown by the numerical data in Table 5.1. Figure 5.1 also shows that, at a typical operating

**FIGURE 5.1**

Variation of stiffness with temperature for a typical polymer showing the glass transition temperature,  $T_g$ , and the effect of absorbed moisture on  $T_g$ . Note:  $T_{g0}$  = dry  $T_g$  and  $T_{gw}$  = wet  $T_g$ .

temperature below  $T_g$ , the stiffness is significantly reduced as the material picks up moisture. Table 5.1 shows that the maximum service temperature is typically well below the  $T_g$ , as properties such as stiffness become undesirably sensitive to temperature if the service temperature gets too close to the glass transition region.

2. Hygrothermal expansions or contractions change the stress and strain distributions in the composite. Increased temperature and/or moisture content causes swelling of the polymer matrix, whereas reduced temperature and/or moisture content causes contraction. Since the fibers are typically not affected as much by hygrothermal conditions, the swelling or contraction of the matrix is resisted by the fibers and residual stresses develop in the composite. A similar effect at the laminate level is due to differential expansions or contractions of constituent laminae.

This chapter is therefore concerned with analytical modeling of hygrothermal degradation of matrix-dominated properties and modification of the lamina stress-strain relationships to include hygrothermal effects. Micro-mechanical prediction of mechanical and thermophysical properties will also be discussed because of its importance in the analytical modeling of both the effects.

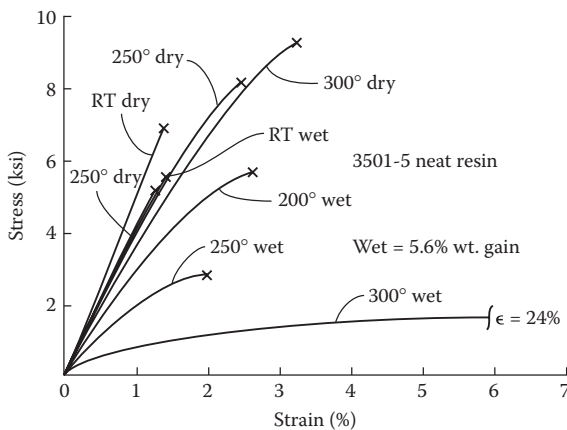
**TABLE 5.1**

Hygrothermal Properties for Various Polymer Matrix Materials

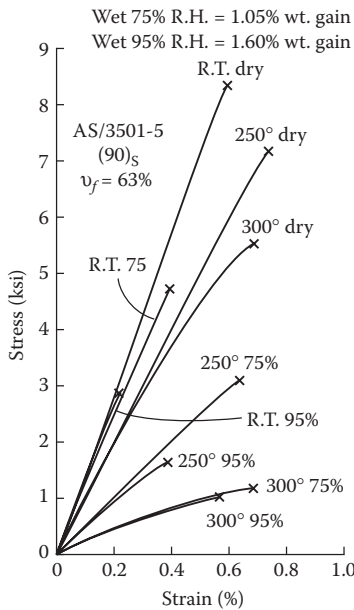
Material	Supplier	Saturation Moisture Content, $M_m$ (Weight %)	$T_{go}$ (Dry) [°F (°C)]	$T_{gw}$ (Wet) [°F (°C)]	Maximum Service Temperature (Dry) [°F (°C)]
Hexply® F655 bismaleimide	Hexcel	4.1	550(288)	400(204)	400(204)
Hexply® 8551-7 epoxy	Hexcel	3.1	315(157)	240(116)	200(93)
Hexply® 8552 epoxy	Hexcel	—	392(200)	309(154)	250(121)
Hexply® 954-3A cyanate	Hexcel	—	400(204)	—	—
CyCom® 2237 polyimide	Cytec	4.4	640(338)	509(265)	550(208)
CyCom® 934 epoxy	Cytec	—	381(194)	320(160)	350(177)
Avimid® R polyimide	Cytec	2.8	581(305)	487(253)	550(288)
Derakane® 411-350 vinylester	Ashland	1.5	250(120)	—	220(105)
Ultem® 2300 polyetherimide	Sabic	0.9	419(215)	—	340(171)
Victrex® 150G polyetherether- ketone	Victrex plc	0.5	289(143)	—	356(180)
Cetex® polyphenylene sulfide	Tencate	0.02	194(90)	—	212(100)

## 5.2 Hygrothermal Degradation of Properties

As evidence of hygrothermal degradation of properties, consider the data of Browning et al. [1], who tested graphite/epoxy composites and their epoxy matrix materials under various hygrothermal conditions. Figure 5.2 shows the stress-strain curves for a typical epoxy matrix material under the various combinations of temperature and absorbed moisture. The corresponding stress-strain curves for the graphite/epoxy composite under transverse loading are shown in Figure 5.3. Note that the imposed hygrothermal conditions cause substantial reductions of both strength and stiffness in both cases, with the so-called “hot-wet” conditions (combined high temperature and high moisture content) generating the most severe degradation. Similar

**FIGURE 5.2**

Stress-strain curves for 3501-5 epoxy resin at different temperatures and moisture contents. (Reprinted from Browning, C. E., Husman, G. E., and Whitney, J. M. 1977. *Composite Materials: Testing and Design: Fourth Conference*, ASTM STP 617, pp. 481–496. American Society for Testing and Materials, Philadelphia, PA. Copyright ASTM. With permission.)

**FIGURE 5.3**

Stress-strain curves for AS/3501-5 graphite/epoxy composite under transverse loading at different temperatures and moisture contents. (Reprinted from Browning, C. E., Husman, G. E., and Whitney, J. M. 1977. *Composite Materials: Testing and Design: Fourth Conference*, ASTM STP 617, pp. 481–496. American Society for Testing and Materials, Philadelphia, PA. Copyright ASTM. With permission.)

degradation was observed in the case of in-plane shear loading of the composite since the behavior is matrix dominated in both the cases. On the other hand, the corresponding stress-strain curves for the composite under longitudinal loading showed little effect because longitudinal strength and stiffness are fiber dominated.

Another example of the hygrothermal sensitivity of matrix-dominated composite properties are the data of Gibson et al. [2], who used a vibrating beam method to measure the flexural moduli of several E-glass/polyester sheet-molding compounds after soaking at various times in a water bath. Table 5.2 gives a description of the materials, Figure 5.4 shows the percent weight gain due to moisture pickup, and Figure 5.5 shows the variation in modulus with soaking time. Composites having some continuous fibers and high fiber contents absorbed little moisture and showed negligible change in modulus with soaking time. On the other hand, composites having matrix-dominated behavior (those with chopped fibers only and low fiber contents) exhibited the most moisture pickup and the greatest reduction in modulus.

Considerable insight into the physics of temperature and moisture distribution in a material is gained from the analysis of Shen and Springer [3], who considered the 1-D distributions of temperature,  $T$ , and moisture concentration,  $c$ , in a plate of thickness,  $h$ , which is suddenly exposed on both sides to an environment of temperature,  $T_a$ , and moisture concentration,  $c_a$  (Figure 5.6). The temperature and moisture concentration are assumed to vary only through the thickness along the  $z$  direction and the initial temperature,  $T_i$ , and initial moisture concentration,  $c_i$ , are assumed to be uniform. The temperature distribution is governed by the Fourier heat conduction equation:

$$\rho C \frac{\partial T}{\partial t} = \frac{\partial}{\partial z} K_z \frac{\partial T}{\partial z} \quad (5.1)$$

**TABLE 5.2**

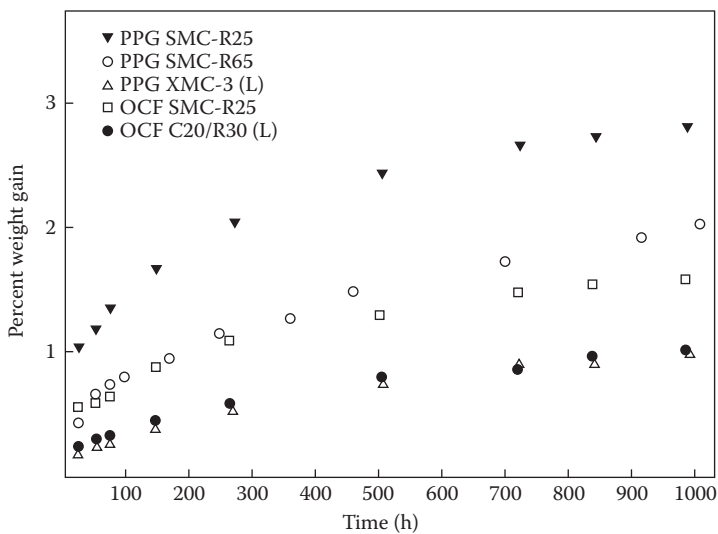
Description of Composite Materials for Figures 5.4 and 5.5

Material	Weight Percentages of Constituents		
	Chopped E-Glass Fibers	Continuous E-Glass Fibers	Polyester Resin, Fillers, etc.
PPG SMC-R25 <sup>a</sup>	25	0	75
PPG SMC-R65	65	0	35
PPG XMC-3	25	50 ( $\pm 7.5^\circ$ , X-pattern)	25
OCF SMC-R25 <sup>b</sup>	25	0	75
OCF C20/R30	30	20 (aligned)	50

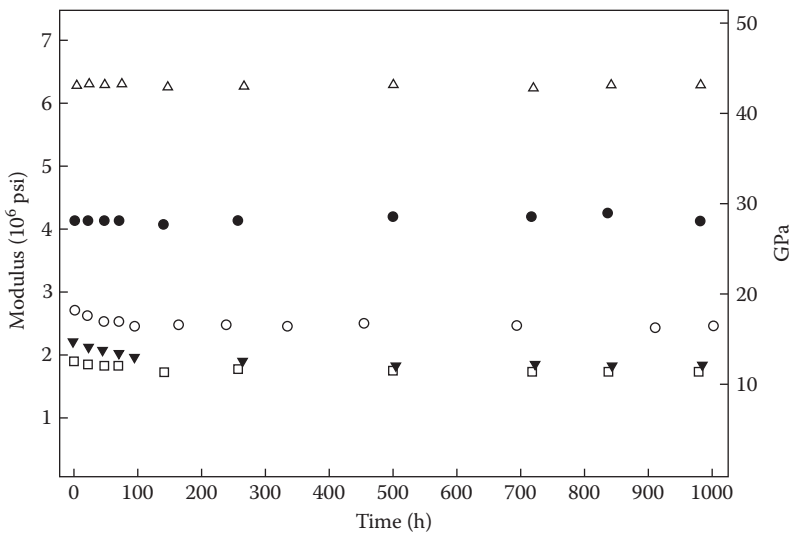
Source: Gibson, R. F. et al. 1982. *Journal of Reinforced Plastics and Composites*, 1(3), 225–241. With permission.

<sup>a</sup> Manufactured by PPG Industries, Fiber Glass Division, Pittsburgh, PA.

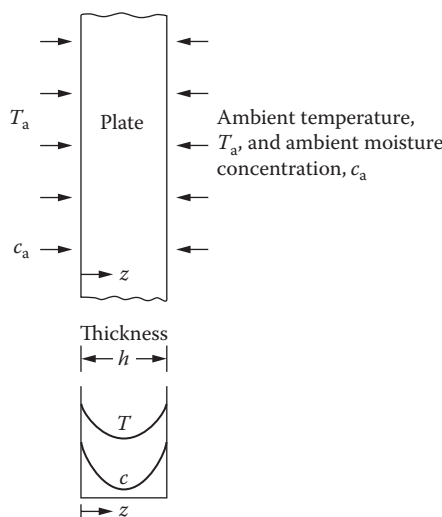
<sup>b</sup> Manufactured by Owens-Corning Fiberglas Corporation, Toledo, OH.

**FIGURE 5.4**

Percent weight gain due to moisture pickup vs. soaking time for several E-glass/polyester sheet-molding compounds. Materials described in Table 5.2. (From Gibson, R. F. et al. 1982. *Journal of Reinforced Plastics and Composites*, 1(3), 225–241. Reprinted by permission of Technomic Publishing Co.)

**FIGURE 5.5**

Variation of flexural modulus of several E-glass/polyester sheet-molding compounds with soaking time in distilled water at 21°C to 24°C. Materials described in Table 5.2 and in Figure 5.4. (From Gibson, R. F. et al. 1982. *Journal of Reinforced Plastics and Composites*, 1(3), 225–241. Reprinted by permission of Technomic Publishing Co.)

**FIGURE 5.6**

Schematic representation of temperature and moisture distributions through the thickness of a plate that is exposed to an environment of temperature,  $T_a$ , and moisture concentration,  $c_a$ , on both sides.

whereas the moisture distribution is governed by Fick's second law,

$$\frac{\partial c}{\partial t} = \frac{\partial}{\partial z} D_z \frac{\partial c}{\partial z} \quad (5.2)$$

where

$\rho$  = density of the material

$C$  = specific heat of the material

$K_z$  = thermal conductivity of the material along the  $z$  direction

$D_z$  = mass diffusivity along the  $z$  direction

$t$  = time

These equations are solved subject to the initial and boundary conditions,

$$\left. \begin{array}{l} T = T_i \\ c = c_i \end{array} \right\} 0 < z < h, \quad t \leq 0$$

$$\left. \begin{array}{l} T = T_a \\ c = c_a \end{array} \right\} z = 0; \quad z = h; \quad t > 0$$

Shen and Springer [3] point out that, due to the numerical values of the thermophysical properties  $C$ ,  $K_z$ ,  $D_z$ , and  $\rho$  for typical polymer composites,

the temperature approaches equilibrium about 1 million times faster than the moisture concentration. Thus, the material temperature can usually be assumed to be the same as the ambient temperature, but the moisture distribution requires further analysis. If the diffusivity is assumed to be constant, Fick's second law becomes

$$\frac{\partial c}{\partial t} = D_z \frac{\partial^2 c}{\partial z^2} \quad (5.3)$$

The solution to this equation subject to the previously stated initial and boundary conditions is [3,4]

$$\frac{c - c_i}{c_m - c_i} = 1 - \frac{4}{\pi} \sum_{j=0}^{\infty} \frac{1}{(2j+1)} \sin \frac{(2j+1)\pi z}{h} \times \exp \left[ -\frac{(2j+1)^2 \pi^2 D_z t}{h^2} \right] \quad (5.4)$$

where the moisture concentration at the surface of the material,  $c_m$ , is related to the moisture content of the environment,  $c_a$ . Browning et al. [1] used Equation 5.4 to predict moisture profiles for a graphite/epoxy plate after drying out for various periods of time, as shown in Figure 5.7. While Equation 5.4 gives the *local* moisture concentration,  $c(z,t)$ , we normally measure the

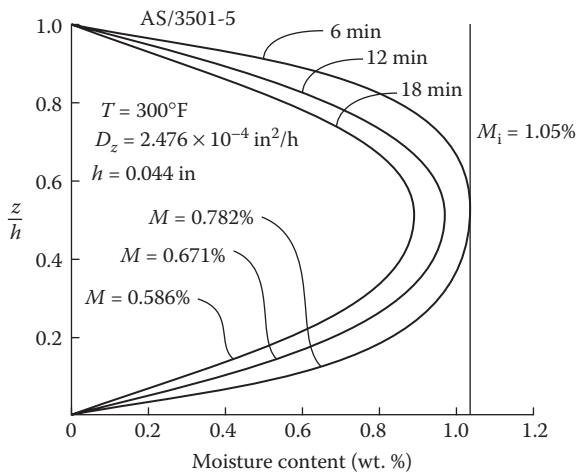


**FIGURE 5.7**

Predicted moisture profiles through the thickness of a graphite/epoxy plate after drying out for various periods of time. (From Browning, C. E., Husman, G. E., and Whitney, J. M. 1977. *Composite Materials: Testing and Design: Fourth Conference*, ASTM STP 617, pp. 481–496. American Society for Testing and Materials, Philadelphia, PA. Copyright ASTM. Reprinted with permission.)

total amount of moisture averaged over the sample. The average concentration is given by [4]

$$\bar{c} = \frac{1}{h} \int_0^h c(z, t) dz = (c_m - c_i) \times \left[ 1 - \frac{8}{\pi^2} \sum_{j=0}^{\infty} \frac{\exp[-(2j+1)^2 \pi^2 (D_z t / h^2)]}{(2j+1)^2} \right] + c_i \quad (5.5)$$

The weight percent moisture,  $M$ , is the quantity that is normally measured, and since  $\bar{c}$  is linearly related to  $M$ , we can write [3]

$$G = \frac{M - M_i}{M_m - M_i} = 1 - \frac{8}{\pi^2} \sum_{j=0}^{\infty} \frac{\exp[-(2j+1)^2 \pi^2 (D_z t / h^2)]}{(2j+1)^2} \quad (5.6)$$

where  $M_i$  is the initial weight percent of moisture in the material and  $M_m$  is the weight percent of moisture in the material when the material reaches fully saturated equilibrium with the ambient conditions. Thus, the parameter  $G$  describes the moisture weight gain as a function of time. Such data can be obtained experimentally by weighing the specimen at various times during exposure to a moist environment. Figure 5.8 from Ref. [3] shows a

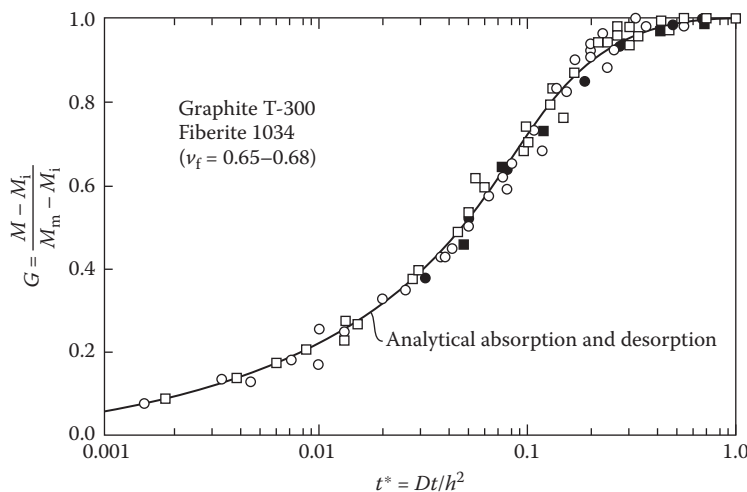


**FIGURE 5.8**

Comparison of predicted (Equation 5.6) and measured moisture absorption and desorption of T300/1034 graphite/epoxy composites. Open symbols represent measured absorption and dark symbols represent measured desorption. (From Shen, C. H. and Springer, G. S. 1976. *Journal of Composite Materials*, 10, 2–20. Reprinted by permission of Technomic Publishing Co.)

comparison of measured and predicted values of  $G$  as a function of the dimensionless ratio  $D_z t / h^2$  for graphite/epoxy. The agreement is seen to be excellent. Thus, the moisture diffusion process in these composites seems to follow Fick's law. In fact, the diffusivity is often determined indirectly by fitting the Fick's law prediction to such experimental moisture pickup data, using the diffusivity as a curve-fitting parameter. Non-Fickian diffusion has also been observed in some cases where microcracking is developed as a result of the hygrothermal degradation [5]. The time-dependent viscoelastic response of polymers has also been found to lead to non-Fickian moisture diffusion in polymer composites [6]. For more information on these and various other moisture effects in polymer composites, the reader is referred to several review articles by Weitsman [7] and Weitsman and Elahi [8].

The hygrothermal degradation of composite strength and/or stiffness can be estimated by using an empirical equation to degrade the corresponding matrix property, then by using the degraded matrix property in the appropriate micromechanics equation. Chamis and Sinclair [9] and Chamis [10] have demonstrated such a procedure based on the equation

$$F_m = \frac{P}{P_o} = \left[ \frac{T_{gw} - T}{T_{go} - T_o} \right]^{1/2} \quad (5.7)$$

where

$F_m$  = matrix mechanical property retention ratio

$P$  = matrix strength or stiffness after hygrothermal degradation

$P_o$  = reference matrix strength or stiffness before degradation

$T$  = temperature at which  $P$  is to be predicted ( $^{\circ}$ F)

$T_{go}$  = glass transition temperature for reference dry condition ( $^{\circ}$ F)

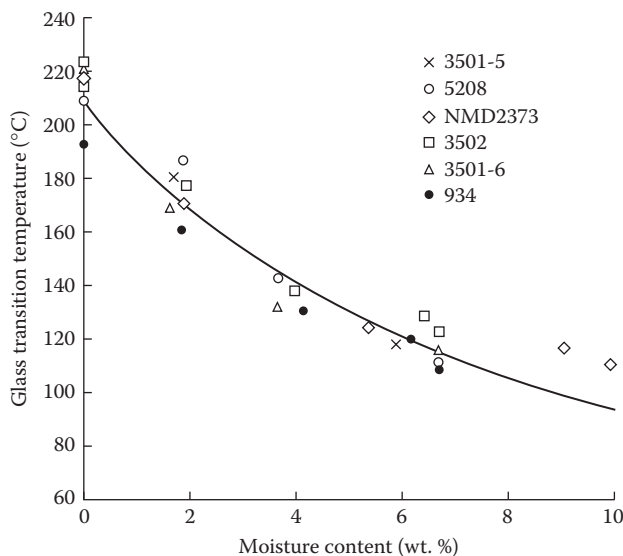
$T_{gw}$  = glass transition temperature for wet matrix material at moisture content corresponding to property  $P$  ( $^{\circ}$ F) (Figure 5.1)

$T_o$  = test temperature at which  $P_o$  was measured ( $^{\circ}$ F)

(All temperatures are in  $^{\circ}$ F.)

The form of Equation 5.7 is based on the experimental observation that degradation is gradual until the temperature  $T$  approaches  $T_{gw}$  whereupon the degradation accelerates. The value of  $T_{gw}$  can be obtained from experimental data on the glass transition temperature of the matrix resin as a function of absorbed moisture. For example, the data of DeIasi and Whiteside [11] show the reduction in  $T_{gw}$  with increasing moisture content for six epoxy resins (Figure 5.9). Chamis [10] suggests that  $T_{gw}$  can be estimated by using the following empirical equation:

$$T_{gw} = (0.005 M_r^2 - 0.10 M_r + 1.0) T_{go} \quad (5.8)$$

**FIGURE 5.9**

Variation of glass transition temperature with equilibrium moisture content for several epoxy resins. (Reprinted from DeIasi, R. and Whiteside, J. B. 1987. In Vinson, J. R. ed., *Advanced Composite Materials—Environmental Effects*, ASTM STP 658, pp. 2–20. American Society for Testing and Materials, Philadelphia, PA. Copyright ASTM. With permission.)

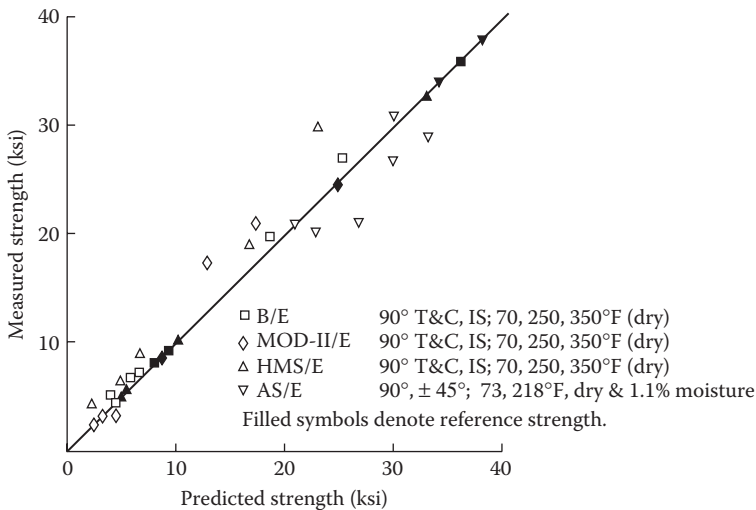
where  $M_r$  is the weight percent of moisture in the matrix resin and values of  $T_{go}$  for several matrix materials are found in Tables 3.2 and 5.1. DeIasi and Whiteside [11] and Browning et al. [1] also found that data such as that in Figure 5.9 are in good agreement with predictions from the theory of polymer plasticization by diluents.

Once the mechanical property retention ratio is found from Equation 5.7, it is used to degrade the matrix property in the appropriate micromechanics equation. For example, the rule of mixtures for the longitudinal modulus (Equation 3.27) now becomes

$$E_1 = E_{f1}v_f + F_m E_{mo}v_m \quad (5.9)$$

where  $E_{mo}$  is the reference value of the matrix modulus in the dry condition. It is assumed that Poisson's ratio is not hygrothermally degraded [10].

Reasonably accurate predictions are also obtained when Equation 5.7 is applied directly to matrix-dominated composite properties (i.e.,  $P$  and  $P_o$  are taken to be matrix-dominated composite properties instead of matrix properties). For example, Chamis and Sinclair [9] found good agreement between the predictions of Equation 5.7 and experimental data on hygrothermal degradation of transverse compression, transverse tension, and intralaminar shear strengths of boron/epoxy and graphite/epoxy composites (Figure 5.10).

**FIGURE 5.10**

Comparison of predicted (Equation 5.7) and measured strengths of several hygrothermally degraded composites. (Reprinted from Chamis, C. C. and Sinclair, J. H. 1982. In Daniel, I. M. ed., *Composite Materials: Testing and Design (Sixth Conference)*, ASTM STP 787, pp. 498–512. American Society for Testing and Materials, Philadelphia, PA. Copyright ASTM. With permission.)

Thus, the hygrothermally degraded composite property may be estimated by applying Equation 5.7 directly to the matrix-dominated composite property measured under reference conditions, or by applying Equation 5.7 to matrix data measured under reference conditions, then substituting the result into the appropriate micromechanics equation.

Empirical equations such as Equations 5.7 and 5.8 should always be used with caution. Curve-fitting parameters such as the exponent of 1/2 in Equation 5.7 and the coefficients of  $M_r$  in Equation 5.8 are based on experimental data for epoxy matrix materials. While the equations may be suitable for other composites as well, the user should check predictions against available experimental data where possible.

The procedure just outlined is based on the combined effects of temperature and moisture, and the two effects were seen to be coupled by the lowering of the glass transition temperature due to absorbed moisture. There is another important connection between the two effects. Moisture absorption occurs by diffusion, which is known to be a thermally activated process. The diffusivity  $D$  that appears in Fick's law is related to temperature by the Arrhenius relationship:

$$D = D_0 \exp\left(\frac{-E_a}{RT}\right) \quad (5.10)$$

where

$D_o$  = material constant

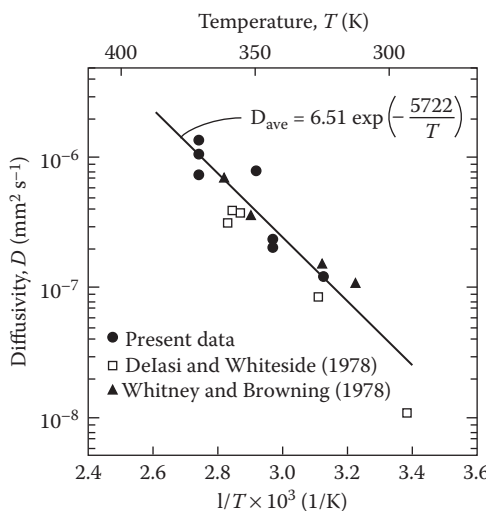
$E_a$  = activation energy for diffusion

$R$  = universal gas constant

$T$  = absolute temperature

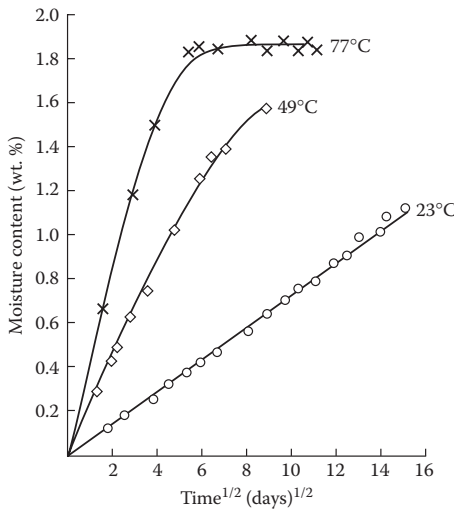
Proof that this relationship holds for composites is given by the fact that plots of experimentally determined values of  $\log D$  versus  $1/T$  fall on a straight line, as shown in Figure 5.11 from Loos and Springer [12]. The result of this relationship is that increased temperature causes an increase in the rate of moisture absorption, as shown in Figure 5.12.

The applied stress also has an effect on moisture absorption in polymers and polymer composites [13–15]. For example, Fahmy and Hurt [13] have shown that the diffusivity of a polymer is increased under tensile stress and decreased under compressive stress. Thus, in a composite, the residual stresses due to differential thermal expansion of fiber and matrix materials may cause increased moisture absorption along a path running through a tensile stress field. Starting from the basic principles of continuum mechanics and irreversible thermodynamics, Weitsman [15] showed that, for both elastic and viscoelastic materials, both the diffusion process and the saturation moisture levels are stress dependent, and that the diffusion process is nonlinear with respect to stress.



**FIGURE 5.11**

Variation of transverse diffusivity with temperature for AS/3501-5 graphite/epoxy composite. (From Loos, A. C. and Springer, G. S. 1981. In Springer, G. S. ed., *Environmental Effects on Composite Materials*, pp. 34–50. Technomic Publishing Co., Lancaster, PA. Reprinted by permission of Technomic Publishing Co.)

**FIGURE 5.12**

Effect of temperature on rate of moisture absorption in AS/3501-5 graphite/epoxy composite. (Reprinted from Delasi, R. and Whiteside, J. B. 1987. In Vinson, J. R. ed., *Advanced Composite Materials—Environmental Effects*, ASTM STP 658, pp. 2–20. American Society for Testing and Materials, Philadelphia, PA. Copyright ASTM. With permission.)

### Example 5.1

An epoxy resin sample has a thickness  $h = 5$  mm and a diffusivity  $D = 3 \times 10^{-8}$  mm<sup>2</sup>/s. Determine the moisture absorption of an initially dry sample after a time  $t = 100$  days.

### SOLUTION

The moisture absorption is predicted by Equation 5.6, which involves an infinite series. In order to examine the convergence characteristics of the series, we will look at the first four terms. Each term in the series contains the dimensionless ratio  $\pi^2 D t / h^2$ , which has the numerical value

$$\frac{\pi^2 D t}{h^2} = \frac{\pi^2 (3 \times 10^{-8}) (100)}{(5)^2} = 0.102$$

Since the sample was initially dry, the initial weight of moisture in the material is  $M_t = 0$ . Thus, Equation 5.6 reduces to the ratio  $M/M_m$ , which is the ratio of the weight percent of moisture at time  $t$  to the weight percent of moisture in the fully saturated equilibrium condition. The first four terms are

$$\begin{aligned} \frac{M}{M_m} &= 1 - \frac{8}{\pi^2} \left[ \exp(-0.102) + \frac{\exp(-9(0.102))}{9} \right. \\ &\quad \left. + \frac{\exp(-25(0.102))}{25} + \frac{\exp(-49(0.102))}{49} + \dots \right] \end{aligned}$$

The values of  $M/M_m$  corresponding to the different number of terms are: 0.267 (one term), 0.230 (two terms), 0.228 (three terms), and 0.228 (four terms). Thus, the series has converged after three terms. Rapid convergence is a characteristic of this solution, and in many cases, only one term is sufficient [4].

### Example 5.2

The composite described in Examples 3.1, 3.2, and 3.5 is to be used in a "hot-wet" environment with temperature  $T = 200^\circ\text{F}$  ( $93^\circ\text{C}$ ) and resin moisture content  $M_r = 3\%$ . If the glass transition temperature of the dry matrix resin is  $350^\circ\text{F}$  ( $177^\circ\text{C}$ ) and if the properties given in Examples 3.1, 3.2, and 3.5 are for a temperature of  $70^\circ\text{F}$  ( $21^\circ\text{C}$ ), determine the hygrothermally degraded values of the longitudinal and transverse moduli.

#### SOLUTION

From Equation 5.8, the glass transition temperature in the wet condition is

$$T_{gw} = [0.005(3)^2 - 0.1(3) + 1.0]350 = 261^\circ\text{F} (127^\circ\text{C})$$

From Equation 5.7, the hygrothermally degraded Young's modulus of the epoxy resin is

$$E_m = [(261 - 200)/(350 - 70)]^{1/2} (0.5)(10^6) = 0.233(10^6) \text{ psi (1.61 GPa)}$$

From Equation 5.9, the hygrothermally degraded longitudinal modulus is

$$E_1 = 32(10^6)(0.506) + 0.233(10^6)(0.482) = 16.3(10^6) \text{ psi (112 GPa)}$$

Thus, the hygrothermally degraded value of  $E_1$  is 99.2% of the reference value calculated in Example 3.5. As stated earlier, the fiber-dominated properties are not affected much by temperature and moisture.

Similarly, using the degraded value of  $E_m$  in Equation 3.40, we find that the hygrothermally degraded transverse modulus is estimated to be  $E_2 = 0.434(10^6)$  psi (3.0 GPa), which is only 53% of the reference value calculated in Example 3.5. Thus, the matrix-dominated properties such as the transverse modulus are strongly affected by hygrothermal conditions.

---

### 5.3 Lamina Stress–Strain Relationships Including Hygrothermal Effects

In Chapter 2, the lamina stress–strain relationships were developed for linear elastic behavior and constant environmental conditions. The thermal expansion or contraction of structural materials due to temperature change

is a well-known phenomenon, however, and the thermal strains for an *isotropic* material are usually described by an equation of the form

$$\varepsilon_i^T = \begin{cases} \alpha\Delta T, & \text{if } i = 1, 2, 3 \\ 0, & \text{if } i = 4, 5, 6 \end{cases} \quad (5.11)$$

where

$i = 1, 2, \dots, 6$  (recall contracted notation)

$\Delta T$  = temperature change ( $T - T_o$ )

$T$  = final temperature

$T_o$  = initial temperature where  $\varepsilon_i^T = 0$  for all  $i$

$\alpha$  = coefficient of thermal expansion (CTE)

This relationship is based on the experimental observation that a temperature change in an unrestrained isotropic material induces an equal expansion or contraction in all directions, with no distortion due to shear deformation. In this case  $\alpha > 0$ , because an increase in temperature causes an increase in thermal strain. As we will see later, however, some anisotropic fiber materials have *negative* CTEs along the fiber axis and positive CTEs along the transverse direction. In general, the strain–temperature relationship is nonlinear, but the assumption of linearity is valid over a sufficiently narrow temperature range. Typical thermal expansion data for an epoxy resin are shown in Figure 5.13. If operation over a wide temperature range is expected, the reader is referred to data such as that of Cairns and Adams [16], who have developed cubic polynomial expressions to fit experimental thermal expansion data for epoxy, glass/epoxy, and graphite/epoxy from  $-73^\circ\text{C}$  to  $175^\circ\text{C}$ . A procedure for estimating the hygrothermal degradation of matrix-dominated thermal properties will be discussed in Section 5.4.

In polymeric materials, moisture has been shown to cause hygroscopic expansions or contractions analogous to thermal strains. For example, the experimentally determined moisture-induced swelling of several epoxy resins is shown in Figure 5.14. The experimental observation is that the moisture-induced strains in *isotropic* materials can be expressed as

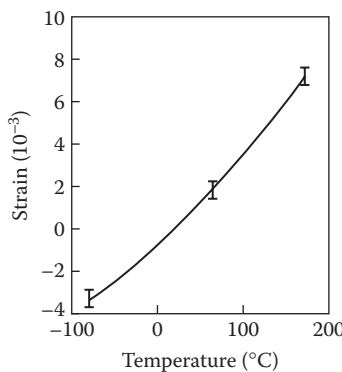
$$\varepsilon_i^M = \begin{cases} (\beta)c, & \text{if } i = 1, 2, 3 \\ 0, & \text{if } i = 4, 5, 6 \end{cases} \quad (5.12)$$

where

$c$  = moisture concentration = (mass of moisture in unit volume/mass of dry material in unit volume)

$\beta$  = coefficient of hygroscopic expansion (CHE).

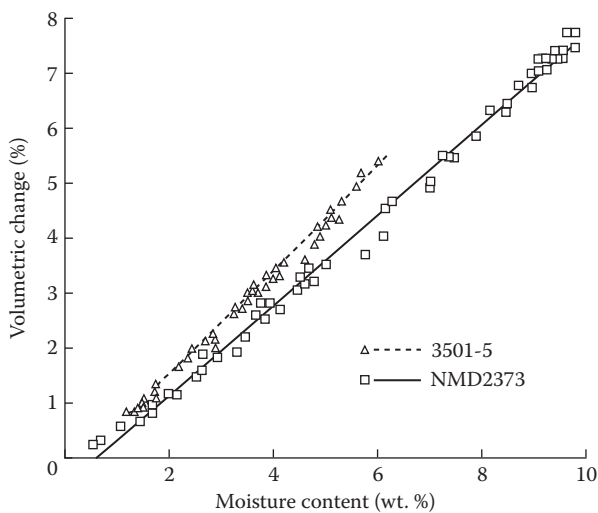
The reference condition is assumed to be the moisture-free state  $c = 0$ , where  $\varepsilon_i^M = 0$ . Hygroscopic strains are generally nonlinear functions of

**FIGURE 5.13**

Thermal expansion vs. temperature for 3501-6 epoxy resin. (From Cairns, D. S. and Adams, D. F. 1984. In Springer, G. S. ed., *Environmental Effects on Composite Materials*, Vol. 2, pp. 300–316. Technomic Publishing Co., Lancaster, PA. Reprinted by permission of Technomic Publishing Co.)

moisture content [16], but the linear relationship in Equation 5.12 is valid if the range of moisture contents is not too wide. Thus, in an *isotropic* material, the total hygrothermal strain can be written as

$$\varepsilon_i^H = \varepsilon_i^T + \varepsilon_i^M \quad (5.13)$$

**FIGURE 5.14**

Hygroscopic expansion vs. moisture content for two epoxy resins. (Reprinted from Delasi, R. and Whiteside, J. B. 1987. In Vinson, J. R. ed., *Advanced Composite Materials—Environmental Effects*, ASTM STP 658, pp. 2–20. American Society for Testing and Materials, Philadelphia, PA. Copyright ASTM. With permission.)

Because fibers usually have CTEs and CHEs that are quite different from those of matrix materials, the hygrothermal strains in a composite lamina are different in longitudinal and transverse directions. For example, the experimental thermal strain versus temperature data in Figure 5.15 (from Ref. [18]) shows the large differences between longitudinal ( $\epsilon_1$ ) and transverse ( $\epsilon_2$ ) thermal strains for unidirectional Kevlar 49/epoxy and S-glass/epoxy composites. Notice that the longitudinal thermal strains  $\epsilon_1$  for Kevlar 49/epoxy are negative, while the corresponding transverse thermal strains  $\epsilon_2$  are positive, which implies that the longitudinal CTE,  $\alpha_1$ , is negative and the transverse CTE,  $\alpha_2$ , is positive for this material. Carbon fiber-reinforced composites often have similar characteristics. Notice also in Table 3.1 that the longitudinal CTEs of some other fibers are negative, whereas the transverse CTEs are positive. As shown later, this leads to the interesting possibility of designing a composite with a CTE of near zero. Thus, subscripts are needed for  $\alpha$  and  $\beta$ , and the hygrothermal strains associated with the 1,2 principal material axes in the specially orthotropic lamina should be expressed as

$$\epsilon_i^H = \begin{cases} \alpha_i \Delta T + \beta_i c, & \text{if } i = 1, 2, 3 \\ 0, & \text{if } i = 4, 5, 6 \end{cases} \quad (5.14)$$

If the material is transversely isotropic,  $\alpha_2 = \alpha_3$  and  $\beta_2 = \beta_3$ . Typical values of  $\alpha_i$  and  $\beta_i$  for several composites are given in Table 5.3 from Ref. [17]. Representative CTEs for fiber and matrix materials and CHEs for polymer matrix materials are given in Tables 3.1 and 3.2. Notice that the negative

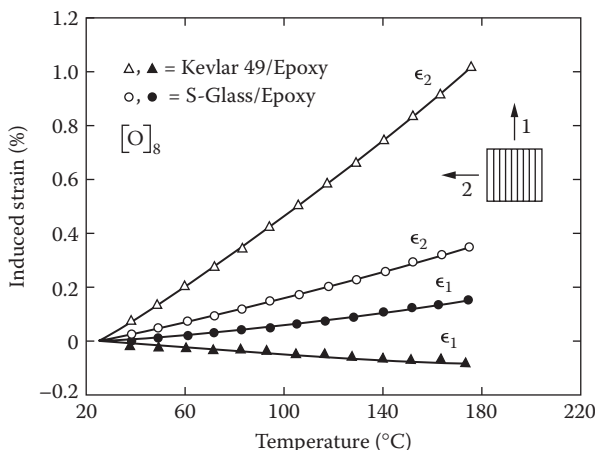


**FIGURE 5.15**

Variation of measured longitudinal and transverse thermal strains for unidirectional Kevlar 49/epoxy and S-glass/epoxy with temperature. (From Adams, D. F., Carlsson, L. A. and Pipes, R. B., 2003. *Experimental Characterization of Advanced Composite Materials*. CRC Press, Boca Raton, FL. With permission.)

**TABLE 5.3**

Typical Thermal and Hygroscopic Expansion Properties

Material	Thermal Expansion Coefficients ( $[10^{-6} \text{ m/m}]^{\circ}\text{C}$ )		Hygroscopic Expansion Coefficients (m/m)	
	$\alpha_1$	$\alpha_2$	$\beta_1$	$\beta_2$
AS carbon/epoxy	0.88	31.0	0.09	0.30
E-glass/epoxy	6.3	20.0	0.014	0.29
AF-126-2 adhesive	29.0	29.0	0.20	0.20
1020 steel	12.0	12.0	—	—

Source: From Graves, S. R. and Adams, D. F. 1981. *Journal of Composite Materials*, 15, 211–224. With permission.

longitudinal CTE of carbon fibers leads to a very small longitudinal CTE for the carbon/epoxy lamina. Notice also the large differences between longitudinal and transverse hygrothermal coefficients.

The total strains along the principal material axes in the specially orthotropic lamina are found by summing the mechanical strains due to applied stresses (Equation 2.24) and the hygrothermal strains (Equation 5.14):

$$\begin{Bmatrix} \varepsilon_1 \\ \varepsilon_2 \\ \gamma_{12} \end{Bmatrix} = \begin{bmatrix} S_{11} & S_{12} & 0 \\ S_{21} & S_{22} & 0 \\ 0 & 0 & S_{66} \end{bmatrix} \begin{Bmatrix} \sigma_1 \\ \sigma_2 \\ \tau_{12} \end{Bmatrix} + \begin{Bmatrix} \alpha_1 \\ \alpha_2 \\ 0 \end{Bmatrix} \Delta T + \begin{Bmatrix} \beta_1 \\ \beta_2 \\ 0 \end{Bmatrix} c \quad (5.15)$$

or, in more concise matrix notation,

$$\{\varepsilon\} = [S]\{\sigma\} + \{\alpha\}\Delta T + \{\beta\}c \quad (5.16)$$

whereupon the stresses are given by

$$\{\sigma\} = [S]^{-1}(\{\varepsilon\} - \{\alpha\}\Delta T - \{\beta\}c) \quad (5.17)$$

Note that if the material is unrestrained during the hygrothermal exposure, there are no stresses generated and the strains are given by

$$\{\varepsilon\} = \{\alpha\}\Delta T + \{\beta\}c \quad (5.18)$$

If the material is completely restrained during hygrothermal exposure, however, the total strain must be zero. Thus,

$$\{\varepsilon\} = 0 = [S]\{\sigma\} + \{\alpha\}\Delta T + \{\beta\}c \quad (5.19)$$

and the resulting hygrothermal stresses are given by

$$\{\sigma\} = [S]^{-1}(-\{\alpha\}\Delta T - \{\beta\}c) \quad (5.20)$$

Note that there are no hygrothermal shear strains or shear stresses along the principal material axes. This is not true for the generally orthotropic (off-axis) case, however. For an arbitrary set of axes  $xy$  oriented at an angle  $\theta$  to the 12 axes, the stress-strain relationships can be transformed as in Chapter 2. The complete stress-strain relations for the generally orthotropic lamina are

$$\begin{Bmatrix} \varepsilon_x \\ \varepsilon_y \\ \gamma_{xy} \end{Bmatrix} = \begin{bmatrix} \bar{S}_{11} & \bar{S}_{12} & \bar{S}_{16} \\ \bar{S}_{12} & \bar{S}_{22} & \bar{S}_{26} \\ \bar{S}_{16} & \bar{S}_{26} & \bar{S}_{66} \end{bmatrix} \begin{Bmatrix} \sigma_x \\ \sigma_y \\ \tau_{xy} \end{Bmatrix} + \begin{Bmatrix} \alpha_x \\ \alpha_y \\ \alpha_{xy} \end{Bmatrix} \Delta T + \begin{Bmatrix} \beta_x \\ \beta_y \\ \beta_{xy} \end{Bmatrix} c \quad (5.21)$$

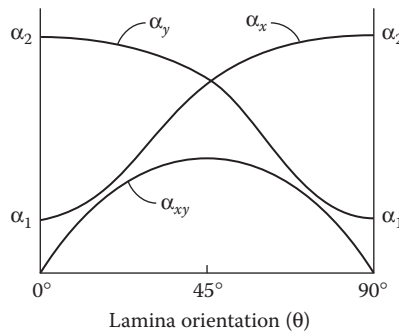
In the transformations, it must be remembered that the CTEs and the CHEs transform like *tensor strains* (recall Equation 2.33), so that

$$\begin{Bmatrix} \alpha_x \\ \alpha_y \\ \alpha_{xy}/2 \end{Bmatrix} = [T]^{-1} \begin{Bmatrix} \alpha_1 \\ \alpha_2 \\ 0 \end{Bmatrix} \quad (5.22)$$

and a similar equation is used for the CHEs. Notice that the hygrothermal effects *do* induce shear strains in the off-axis case due to  $\alpha_{xy}$  and  $\beta_{xy}$ , the shear coefficients of thermal and hygroscopic expansion, respectively. This is quite different from the case of isotropic materials, where hygrothermal effects do not cause shear strains along any axes. The variations of  $\alpha_x$ ,  $\alpha_y$ , and  $\alpha_{xy}$  with lamina orientation according to Equations 5.22 are shown in Figure 5.16. Similar curves could also be used for  $\beta_x$ ,  $\beta_y$ , and  $\beta_{xy}$ . The hygrothermal shear coefficients  $\alpha_{xy}$  and  $\beta_{xy}$  have their maximum values at  $\theta = 45^\circ$  and are proportional to the differences  $(\alpha_1 - \alpha_2)$  and  $(\beta_1 - \beta_2)$ , respectively. Thus, the greater the degree of anisotropy (i.e., the larger the ratio  $\alpha_1/\alpha_2$  or  $\beta_1/\beta_2$ ), the greater the hygrothermally induced shear strains. It is important to note that if  $\alpha_1 < 0$  and  $\alpha_2 > 0$ , it is possible to find an angle  $\theta$  where  $\alpha_x = 0$ . Thus, we can design a laminate consisting of plies of such a material, so that the CTE along a particular direction is zero.

### Example 5.3

An orthotropic lamina forms one layer of a laminate which is initially at temperature  $T_o$ . Assuming that the lamina is initially stress free, that adjacent laminae are rigid, that the properties do not change as a result of the temperature change, and

**FIGURE 5.16**

Variation of lamina thermal expansion coefficients with lamina orientation for a lamina having  $\alpha_2 > \alpha_1 > 0$ .

that the lamina picks up no moisture, determine the maximum temperature that the lamina can withstand according to the Maximum Stress Criterion.

### SOLUTION

Owing to the assumption that adjacent laminae are rigid, deformation is prevented and the total strains must all be zero. The resulting hygrothermal stresses are therefore given by Equation 5.20 with  $c = 0$ ,

$$\{\sigma\} = -[S]^{-1} \{\alpha\} (T - T_o) = -[Q]\{\alpha\} (T - T_o)$$

Thus, for the Maximum Stress Criterion, it is necessary to check each of the following conditions:

For tensile stresses

$$-(Q_{11}\alpha_1 + Q_{12}\alpha_2)(T - T_o) = s_L^{(+)}$$

$$-(Q_{12}\alpha_1 + Q_{22}\alpha_2)(T - T_o) = s_T^{(+)}$$

For compressive stresses

$$-(Q_{11}\alpha_1 + Q_{12}\alpha_2)(T - T_o) = s_L^{(-)}$$

$$-(Q_{12}\alpha_1 + Q_{22}\alpha_2)(T - T_o) = s_T^{(-)}$$

(Note: There are no hygrothermal shear stresses along the 12 axes.)

After substituting numerical values for the initial temperature,  $T_o$ , the lamina stiffness,  $Q_{ij}$ , the coefficients of thermal expansion,  $\alpha_i$ , the strengths  $s_L^{(+)}$ , and so on, in the above equations, the equation that yields the lowest temperature  $T$  would be the condition governing failure. It is worthwhile to note that adjacent laminae are not really rigid, but we will need to use laminate theory later to consider deformations of adjacent laminae. It is also worthwhile to note that if hygrothermal degradation of properties is to be taken into account, Equation 5.7 could be used to express the hygrothermally degraded lamina strengths and stiffnesses in terms

of the temperature  $T$ . In this case,  $T$  would appear on both sides of the above equations and the problem would be more difficult to solve.

### Example 5.4

A sample of a unidirectional E-glass/epoxy lamina is completely unrestrained as it is heated from 20°C to 70°C. Determine all components of stress and strain associated with the 1,2 axes and the  $x,y$  axes if the  $x,y$  axes are oriented at  $\theta = 45^\circ$ . See Table 5.3 for the required properties of E-glass/epoxy.

#### SOLUTION

Since the lamina is unrestrained during heating, there are no stresses along either the 1,2 or the  $x,y$  axes, but the thermal strains are found as follows:

From Equation 5.15 with no stresses or hygroscopic strains, the thermal strains along the 1,2 axes for  $\Delta T = 50^\circ\text{C}$  are

$$\begin{Bmatrix} \epsilon_1 \\ \epsilon_2 \\ \gamma_{12} \end{Bmatrix} = \begin{Bmatrix} \alpha_1 \\ \alpha_2 \\ 0 \end{Bmatrix} \Delta T = \begin{Bmatrix} 6.3(10^{-6}) \\ 20.0(10^{-6}) \\ 0 \end{Bmatrix} (50) = \begin{Bmatrix} 0.000315 \\ 0.001 \\ 0 \end{Bmatrix}$$

From the inverted form of Equation 2.33, with  $\theta = 45^\circ$ , the thermal strains along the  $x,y$  axes can be found directly as

$$\begin{Bmatrix} \epsilon_x \\ \epsilon_y \\ \frac{\gamma_{xy}}{2} \end{Bmatrix} = [T]^{-1} \begin{Bmatrix} \epsilon_1 \\ \epsilon_2 \\ \gamma_{12}/2 \end{Bmatrix} = \begin{bmatrix} 0.5 & 0.5 & -1.0 \\ 0.5 & 0.5 & 1.0 \\ 0.5 & -0.5 & 0 \end{bmatrix} \begin{Bmatrix} 0.000315 \\ 0.001 \\ 0 \end{Bmatrix} = \begin{Bmatrix} 0.00066 \\ 0.00066 \\ -0.00034 \end{Bmatrix}$$

Alternatively, the same result for the thermal strains along the  $x,y$  axes can be obtained by first transforming the CTE values from the 1,2 axes to the  $x,y$  axes using Equation 5.22, then substituting the transformed CTEs in Equation 5.21 to calculate the thermal strains along the  $x,y$  axes. Note that, although there was no thermal shear strain along the 1,2 axes, there is an off-axis thermal shear strain along the  $x,y$  axes. Thus, there will be thermal distortion associated with the off-axis directions, and this is another example of the shear coupling phenomenon.

## 5.4 Micromechanics Models for Hygrothermal Properties

We have seen in Chapters 3 and 4 that the mechanical properties of a composite lamina can be estimated from the corresponding properties of the constituent

materials using micromechanics models. Similarly, micromechanics equations for the thermophysical properties that appear in hygrothermal analysis can be developed. Various theoretical approaches ranging from elementary mechanics of materials to energy methods and finite element analysis have been used.

An equation for the longitudinal coefficient of thermal expansion,  $\alpha_1$ , can be developed using the elementary mechanics of materials approach from Chapter 3. Recall that in the derivation of the rule of mixtures for the longitudinal modulus (Equation 3.27), the 1-D forms of the stress-strain relationships along the 1 direction for the lamina, fiber, and matrix materials (Equation 3.24) were substituted in the rule of mixtures for longitudinal stress, Equation 3.23. The corresponding 1-D form of the lamina stress-strain relationship including the thermal effect is

$$\bar{\epsilon}_{c1} = \frac{\bar{\sigma}_{c1}}{E_1} + \alpha_1 \Delta T \quad (5.23)$$

or

$$\bar{\sigma}_{c1} = E_1(\bar{\epsilon}_{c1} - \alpha_1 \Delta T) \quad (5.24)$$

If we now substitute equations similar to Equation 5.24 for composite, fiber, and matrix, respectively, into Equation 3.23, the result is

$$E_1(\bar{\epsilon}_{c1} - \alpha_1 \Delta T) = E_{f1}(\bar{\epsilon}_{f1} - \alpha_{f1} \Delta T)v_f + E_{m1}(\bar{\epsilon}_{m1} - \alpha_{m1} \Delta T)v_m \quad (5.25)$$

where  $\alpha_{f1}$  and  $\alpha_{m1}$  are the longitudinal CTEs of fiber and matrix materials, respectively (see Tables 3.1 and 3.2), and the remaining terms are defined in Chapter 3. By combining Equations 5.25, 3.26, and 3.27, we get a modified rule of mixtures for the longitudinal CTE:

$$\alpha_1 = \frac{E_{f1}\alpha_{f1}v_f + E_{m1}\alpha_{m1}v_m}{E_1} = \frac{E_{f1}\alpha_{f1}v_f + E_{m1}\alpha_{m1}v_m}{E_{f1}v_f + E_{m1}v_m} \quad (5.26)$$

For the case of isotropic constituents, the above equation becomes

$$\alpha_1 = \frac{E_f\alpha_f v_f + E_m\alpha_m v_m}{E_f v_f + E_m v_m} \quad (5.27)$$

This equation, derived by a mechanics of materials approach, turns out to be the same as the result obtained by Schapery [19], who used a more rigorous energy method. This should not be surprising, given the proven validity of the assumptions that were used in the derivation of the rule of mixtures for

$E_1$  and the accuracy of Equation 3.27. Hashin [20] derived a more complicated expression for the case of orthotropic constituents.

Similarly, an elementary mechanics of materials approach can be used to find a micromechanics equation for  $\alpha_2$ , the transverse CTE of the lamina. In this case, the appropriate 1-D form of the lamina stress-strain relationship including the thermal effect is

$$\bar{\epsilon}_{c2} = \frac{\bar{\sigma}_{c2}}{E_2} + \alpha_2 \Delta T \quad (5.28)$$

Substituting equations similar to Equation 5.28 for composite, fiber and matrix, respectively, in the transverse geometric compatibility condition given by Equation 3.37, the result is

$$\frac{\bar{\sigma}_{c2}}{E_2} + \alpha_2 \Delta T = \left( \frac{\bar{\sigma}_{f2}}{E_{f2}} + \alpha_{f2} \Delta T \right) v_f + \left( \frac{\bar{\sigma}_{m2}}{E_{m2}} + \alpha_{m2} \Delta T \right) v_m \quad (5.29)$$

where  $\alpha_{f2}$  and  $\alpha_{m2}$  are the transverse CTEs of fiber and matrix materials, respectively (see Tables 3.1 and 3.2) and the remaining terms are defined in Chapter 3. By combining Equation 5.29 with Equation 3.39 and assuming that the stresses in the composite, fiber, and matrix are all equal (as in the development of Equation 3.40), we get another rule of mixtures type equation

$$\alpha_2 = \alpha_{f2} v_f + \alpha_{m2} v_m \quad (5.30)$$

In many cases, the matrix is isotropic, so  $E_{m1} = E_{m2} = E_m$  and  $\alpha_{m1} = \alpha_{m2} = \alpha_m$ . If both fiber and matrix materials are isotropic, Equation 5.30 becomes

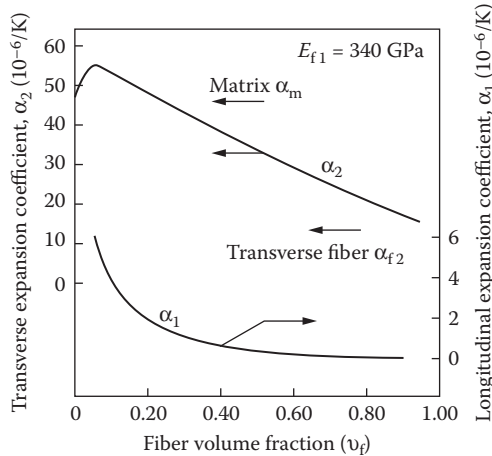
$$\alpha_2 = \alpha_f v_f + \alpha_m v_m \quad (5.31)$$

However, as indicated earlier, the assumption of equal stresses in composite, fiber, and matrix leading to the inverse rule of mixtures for  $E_2$  in Equation 3.40 is not very accurate, so Equations 5.30 and 5.31 should only be considered as rough estimates for  $\alpha_2$ .

Schapery [19] used a more rigorous energy method to derive the following expression for the transverse CTE of a composite with isotropic constituents:

$$\alpha_2 = (1 + v_m) \alpha_m v_m + (1 + v_f) \alpha_f v_f - \alpha_1 v_{12} \quad (5.32)$$

where  $\alpha_1$  is the longitudinal CTE given by Equation 5.27 and  $v_{12}$  is the major Poisson's ratio of the lamina given by Equation 3.45. The variations of  $\alpha_1$  and  $\alpha_2$  with fiber-volume fraction for a typical graphite/epoxy composite are shown in Figure 5.17. Rosen [21] has observed that for such composites

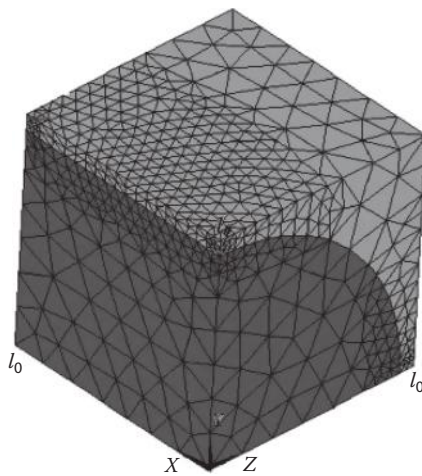
**FIGURE 5.17**

Variation of predicted longitudinal and transverse coefficients of thermal expansion with fiber-volume fraction for typical unidirectional graphite/epoxy composite. (From Rosen, B. W. 1987. In Reinhart, T. J. ed., *Engineered Materials Handbook*, Vol. 1, Composites, Sec. 4. ASM International, Materials Park, OH. Reprinted by permission of ASM International.)

having high fiber-volume fractions, the predicted  $\alpha_1$  is practically zero. Measurements of the CTEs for such materials by Ishikawa et al. [22] have confirmed that  $\alpha_1$  is so small as to fluctuate between positive and negative values due to small changes in temperature or fiber-volume fraction. Over the range of practical fiber-volume fractions,  $\alpha_2$  is much greater than  $\alpha_1$ . It is also interesting to note that at low fiber-volume fractions,  $\alpha_2$  can be greater than  $\alpha_m$ .

Finite element analysis (FEA) of unit cells is a versatile numerical approach to micromechanical modeling of composite CTEs. FEA unit cells similar to those described in Section 3.4.2 are subjected to a temperature change,  $\Delta T$ , and then the resulting FEA-calculated thermally induced displacements are used to determine the CTEs. Required input properties are the elastic constants and the CTEs of each finite element in the fiber and matrix materials, and either orthotropic or isotropic constituents are easily accommodated. Dimensions of the unit cell are selected so as to simulate the appropriate fiber volume fraction. In fact, the FEA approach is just a numerical simulation of the experiment that is done to measure the CTE, as discussed later in Chapter 10. For example, Karadeniz and Kumlutus [23] developed 3-D FEA unit cell models such as the one shown in Figure 5.18 to predict  $\alpha_1$  and  $\alpha_2$  for several types of composites.

In the model shown in Figure 5.18, the fiber lies along the X axis, while Y and Z are the transverse directions. Displacements of the model along the fixed reference planes  $X = 0$ ,  $Y = 0$ ,  $Z = 0$  in Figure 5.18 were restricted to be perpendicular to those planes. The free boundary planes  $X = l_0$ ,  $Y = l_0$ ,  $Z = l_0$  were restricted to move parallel to their original positions after the change in

**FIGURE 5.18**

Typical FEA unit cell for prediction of composite longitudinal and transverse CTEs. (Reprinted from *Composite Structures*, 78, Karadeniz, Z. and Kumlutas, D., A numerical study on the coefficients of thermal expansion of fiber reinforced composite materials, 1–10, Copyright (2007), with permission from Elsevier.)

temperature  $\Delta T$  in order to maintain geometric compatibility with neighboring unit cells (see Figure 3.17 and corresponding discussion of geometric compatibility and multipoint constraint in Section 3.4.2). The longitudinal CTE,  $\alpha_1$  (same as  $\alpha_X$  in Figure 5.18), was then calculated from

$$\alpha_1 = \alpha_X = \frac{\Delta l_X}{l_0} \frac{1}{\Delta T} \quad (5.33)$$

where  $\Delta l_X$  is the FEA-calculated thermal displacement of the plane  $X = l_0$  along the  $X$  direction. Similarly, the transverse CTE,  $\alpha_2$  (same as  $\alpha_Z$  or  $\alpha_Y$  in Figure 5.18, assuming transverse isotropy), was calculated from

$$\alpha_2 = \alpha_Z = \frac{\Delta l_Z}{l_0} \frac{1}{\Delta T} = \alpha_Y = \frac{\Delta l_Y}{l_0} \frac{1}{\Delta T} \quad (5.34)$$

where  $\Delta l_Z$  and  $\Delta l_Y$  are the FEA-calculated thermal displacements of the planes  $Z = l_0$  and  $Y = l_0$ , along the  $Z$  and  $Y$  directions, respectively. In [23], predictions from these FEA models were compared with experimental data for several composites from Sideris [24] and with results from other micro-mechanics models such as the rule of mixtures equations, the Schapery equations [19], and the Rosen–Hashin equations [25]. It was concluded that all of the models, including the FEA models, were in good agreement with experiments for the longitudinal CTE, but that the FEA models and the

Rosen–Hashin models agreed most closely with experiments for the transverse CTE. While the Rosen–Hashin models were found to be quite accurate, they are difficult to use, and are beyond the scope of this text. The accuracy of the FEA approach has been demonstrated for the transverse CTE calculation by Dong [26]. In Figure 5.19, Gibson and Muller [27] compared analytical solutions from Equation 5.27 (longitudinal CTE) and Equation 5.32 (transverse CTE) with FEA numerical predictions from Equations 5.33 and 5.34, respectively, for a SiO<sub>2</sub>/epoxy composite. The FEA micromechanics model was based on the simple block model shown in Figure 3.5a, and the agreement is seen to be excellent. Both materials were assumed to be isotropic with the following properties:

For the SiO<sub>2</sub> fibers;  $E_f = 70$  GPa,  $v_f = 0.17$ ,  $\alpha_f = 5 \times 10^{-6}/^\circ\text{C}$

For the epoxy matrix;  $E_m = 2.83$  GPa,  $v_m = 0.3$ ,  $\alpha_m = 57.85 \times 10^{-6}/^\circ\text{C}$

In summary, FEA has proven to be a very useful and accurate method for micromechanical prediction of composite CTEs.

By substituting the 1-D forms of the stress–strain relationships with hygroscopic effects into Equation 3.23 and following the procedure outlined in the derivation of Equation 5.26, a similar relationship is found for the longitudinal CHE:

$$\beta_1 = \frac{E_{f1}\beta_{f1}v_f + E_{m1}\beta_{m1}v_m}{E_{f1}v_f + E_{m1}v_m} \quad (5.35)$$

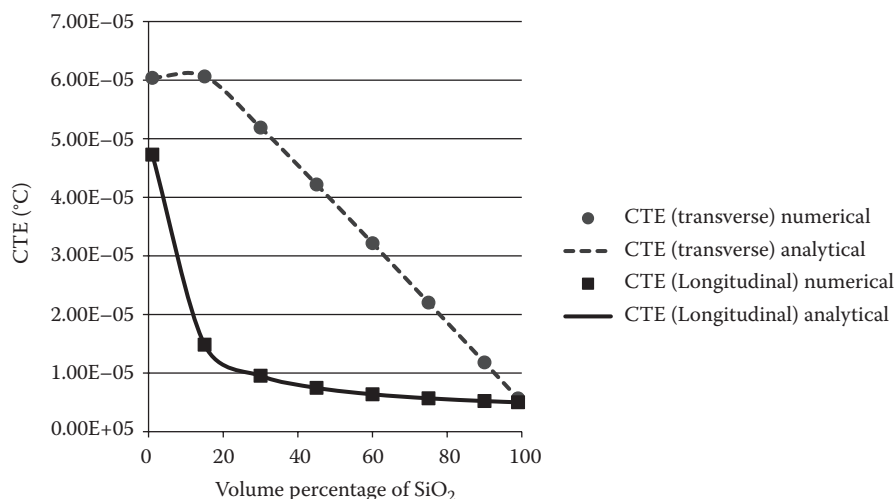


**FIGURE 5.19**

Comparison of analytical and FEA numerical predictions of longitudinal and transverse CTEs for SiO<sub>2</sub>/epoxy composites of various SiO<sub>2</sub> volume fractions. (Adapted from Gibson, R. F. and Muller, A. 2010. Unpublished research, University of Nevada, Reno.)

Similarly, the hygroscopic counterpart of Equation 5.30 is found to be

$$\beta_2 = \beta_{f2}v_f + \beta_{m2}v_m \quad (5.36)$$

In polymer matrix composites, the amount of moisture absorbed by the fibers is usually negligible in comparison with the moisture absorbed by the matrix, so that the terms involving  $\beta_{f1}$  and  $\beta_{f2}$  can often be ignored. For isotropic constituents, the equation for  $\beta_i$  would be analogous to Equation 5.31. According to Ashton et al. [28], the equations derived by Schapery (i.e., Equations 5.27 and 5.32) can be used for any expansional coefficients such as the CTE or the CHE. Thus, the transverse CHE for isotropic constituents would be given by

$$\beta_2 = (1 + v_m)\beta_m v_m + (1 + v_f)\beta_f v_f - \beta_1 v_{12} \quad (5.37)$$

where  $\beta_i$  is given by the isotropic form of Equation 5.35. FEA micromechanics models for composite CHEs may be developed using a procedure similar to that previously outlined for composite CTEs, assuming that the FEA code being used has the capability of calculating hygroscopic strains.

Recall that in the equations governing the temperature and moisture distributions (Equations 5.1 and 5.2), thermophysical properties such as specific heat, thermal conductivity, and diffusivity appeared. According to Chamis [10], the composite specific heat is given by

$$C_c = \frac{1}{\rho_c}(\rho_f C_f v_f + \rho_m C_m v_m) \quad (5.38)$$

where  $C_f$  and  $C_m$  are the specific heat of fiber and matrix, respectively; the composite density,  $\rho_c$ , is given by Equation 3.6, and the remaining terms are defined in Chapter 3. Ashton et al. [28] and Shen and Springer [3] have observed that the rule of mixtures formulations,

$$K_1 = K_f v_f + K_m v_m \quad (5.39)$$

and

$$D_1 = D_f v_f + D_m v_m \quad (5.40)$$

can be used to find the longitudinal thermal conductivity and mass diffusivity, respectively, as well as other transport properties. Equations for the transverse thermal conductivity and diffusivity based on the method of sub-regions (see Section 3.3) have been presented by Hopkins and Chamis [29] and Chamis [10]. These equations can be formed by substituting the appropriate properties (thermal conductivities or diffusivities instead of transverse moduli) in an equation of the form shown in Equation 3.54. Ashton et al. [27] have suggested that the Halpin–Tsai equations (see Section 3.5) can also be used for transverse transport properties such as thermal conductivity and

mass diffusivity. Off-axis properties can be found by recognizing that thermal conductivity and diffusivity are both second-order tensor quantities that transform according to the form shown in Equation 2.30.

Finally, a procedure for estimating hygrothermal degradation of matrix properties such as  $\alpha$ ,  $\beta$ ,  $K$ , and  $C$  has been proposed by Chamis [10]. Based on the observation that the effect of increased temperature on these properties is opposite to the corresponding effect on strength and stiffness, Chamis suggests that the matrix hygrothermal property retention ratio can be approximated by

$$F_h = \frac{R}{R_o} = \left[ \frac{T_{go} - T_o}{T_{gw} - T} \right]^{1/2} \quad (5.41)$$

where

$R$  = matrix hygrothermal property after hygrothermal degradation

$R_o$  = reference matrix hygrothermal property before degradation

Following a procedure similar to that outlined in Section 5.2, the matrix hygrothermal property is degraded according to Equation 5.34. Then the degraded matrix property is used in a micromechanics equation such as Equations 5.26 through 5.40 to estimate the hygrothermally degraded composite property.

### Example 5.5

A composite lamina is to be designed to have a specified coefficient of thermal expansion along a given direction. Outline a procedure to be used in the design.

#### SOLUTION

First, it is necessary to use micromechanics equations such as Equations 5.26 and 5.30 to find a combination of fiber and matrix materials having constituent CTEs and moduli and volume fractions, so that the specified CTE lies between the values of  $\alpha_1$  and  $\alpha_2$ . As shown by Equations 5.22 and Figure 5.16, the value of the specified  $\alpha_x$  along the direction defined by the angle must lie between the values of  $\alpha_1$  and  $\alpha_2$ . The required angle  $\theta$  is then found by setting  $\alpha_x$  equal to the specified value and solving the first of Equations 5.22. In a practical design problem, other requirements such as strength and stiffness may have to be considered as well.

### Example 5.6

Develop an analytical model for determination of the coefficient of hygroscopic expansion,  $\beta$ , for a randomly oriented continuous fiber composite in terms of fiber

and matrix properties and volume fractions. Assume that the composite is planar isotropic, and find the  $\beta$  for in-plane hygroscopic expansion.

### SOLUTION

For the planar isotropic case,  $\beta$  is independent of orientation in the plane, and it is appropriate to use an averaging approach similar to that used in Example 2.6. Thus, the isotropic  $\beta$  is found by first using a transformation equation similar to Equation 5.22 to find the  $\beta_x$  for the orthotropic lamina of the same material along the  $x$  direction as

$$\beta_x = \beta_1 \cos^2 \theta + \beta_2 \sin^2 \theta$$

This value is now averaged over all possible angles between  $\theta = 0$  to  $\theta = \pi$  to get the isotropic property as

$$\begin{aligned} \beta &= \frac{\int_0^\pi \beta_x d\theta}{\int_0^\pi d\theta} \\ &= \frac{\int_0^\pi (\beta_1 \cos^2 \theta + \beta_2 \sin^2 \theta) d\theta}{\pi} \\ &= \frac{\beta_1 \left[ \frac{\sin 2\theta}{4} + \frac{\theta}{2} \right]_0^\pi + \beta_2 \left[ \frac{-\sin 2\theta}{4} + \frac{\theta}{2} \right]_0^\pi}{\pi} \\ &= \frac{\beta_1 + \beta_2}{2} \end{aligned}$$

where the orthotropic properties  $\beta_1$  and  $\beta_2$  may be estimated from fiber and matrix properties and volume fractions by using micromechanics equations such as Equations 5.35 and 5.36.

### Example 5.7

A hybrid unidirectional S-glass/Kevlar/HM epoxy composite lamina has twice as many S-glass fibers as Kevlar fibers and the total fiber volume fraction is 0.6. Determine the longitudinal and transverse CTEs for the composite.

### SOLUTION

From Table 3.1 the properties for the S-glass fibers are

$$E_{S1} = 12.4 \times 10^6 \text{ psi}$$

$$\alpha_{S1} = 2.8 \times 10^{-6} \text{ in./in./}^\circ\text{F}$$

$$\alpha_{S2} = 2.8 \times 10^{-6} \text{ in./in./}^\circ\text{F}$$

The properties for the Kevlar fibers are

$$E_{K1} = 22 \times 10^6 \text{ psi}$$

$$\alpha_{K1} = -2.2 \times 10^{-6} \text{ in./in./}^\circ\text{F}$$

$$\alpha_{K2} = 30 \times 10^{-6} \text{ in./in./}^\circ\text{F}$$

From Table 3.2, the properties of the HM epoxy matrix are

$$E_m = 0.75 \times 10^6 \text{ psi}$$

$$\alpha_{m1} = \alpha_{m2} = \alpha_m = 40 \times 10^{-6} \text{ in./in./}^\circ\text{F}$$

The fiber volume fractions for S-glass and Kevlar are related by  $v_s = 2v_k$  and  $v_s + v_k = 0.6$  and all of the constituent volume fractions are related by

$$v_s + v_k + v_m = 1.0$$

so  $v_s = 0.4$ ,  $v_k = 0.2$ ,  $v_m = 0.4$ .

Generalizing Equation 5.26 for the hybrid composite with three constituents, the longitudinal CTE is

$$\alpha_1 = \frac{E_{S1}\alpha_{S1}v_s + E_{K1}\alpha_{K1}v_k + E_m\alpha_mv_m}{E_{S1}v_s + E_{K1}v_k + E_mv_m} = 1.68 \times 10^{-6} \text{ /in./in./}^\circ\text{F}$$

Similarly, generalizing Equation (5.30) for the hybrid composite, the transverse CTE is estimated to be

$$\alpha_2 = \alpha_{S2}v_s + \alpha_{K2}v_k + \alpha_mv_m = 23 \times 10^{-6} \text{ /in./in./}^\circ\text{F}$$

Note that  $\alpha_2 \gg \alpha_1$ . This is due to the negative longitudinal CTE of the Kevlar fibers, the large positive transverse CTE of the Kevlar fibers and the strong influence of the matrix CTE on  $\alpha_2$ .

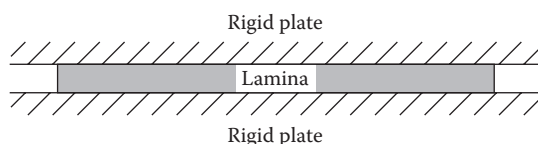
## PROBLEMS

1. Using Equation 5.6 for moisture diffusion, derive an equation for the time required for an initially dry material to reach 99.9% of its fully saturated equilibrium moisture content. The series in Equation 5.6 converges rapidly, so for the purposes of this problem, it is necessary only to consider the first term. The answer should be expressed in terms of the thickness,  $h$ , and the diffusivity,  $D_z$ .
2. The dependence of the transverse (through-the-thickness) diffusivity of unidirectional AS/3501-5 graphite/epoxy composite on temperature is given in Figure 5.11. For a temperature of 77°C and a thickness of 2.54 mm, use the results from Figure 5.11 and Problem 5.1 to estimate the time required for this material to reach 99.9% of its fully saturated equilibrium moisture content from an initially

dry condition. Compare your estimate with the experimental data in Figure 5.12. Does the estimate seem to be reasonable?

3. For the material described in Problems 1 and 2 above at a temperature of 77°C, determine the time required for drying the material from 99.9% to 50% of its fully saturated equilibrium moisture content.
4. Using only the linear part of the moisture absorption curve for a temperature of 77°C in Figure 5.12, and assuming a thickness of 2.54 mm, estimate the diffusivity  $D_z$ . Compare this value with the estimate from Figure 5.11.
5. For the composite properties and environmental conditions described in Examples 3.5, 4.5, and 5.2, determine the hygrothermally degraded values of the longitudinal and transverse tensile strengths. Compare with the reference values of these strengths from Example 4.5.
6. For the composite properties and environmental conditions described in Examples 3.5, 4.5, and 5.2, compare the reference and hygrothermally degraded values of the longitudinal compressive strength. Assume  $v_{12} = 0.3$ . Compare and discuss the different effects that hygrothermal conditions have on longitudinal tensile and compressive strengths.
7. The filament-wound E-glass/epoxy pressure vessel described in Example 4.3 is to be used in a hot-wet environment with temperature  $T = 100^\circ\text{F}$  ( $38^\circ\text{C}$ ) and moisture content  $M_r = 4\%$ . The glass transition temperature of the dry epoxy resin is  $250^\circ\text{F}$  ( $121^\circ\text{C}$ ), and the lamina strengths listed in Table 4.1 are for a temperature of  $70^\circ\text{F}$  ( $21^\circ\text{C}$ ) and a moisture content of zero. Determine the internal pressure  $p$  that would cause failure of the vessel according to the Maximum Stress Criterion. Compare with the result from Example 4.3.
8. A carbon/epoxy lamina is clamped between rigid plates in a mold (Figure 5.20) while curing at a temperature of  $125^\circ\text{C}$ . After curing, the lamina/mold assembly (still clamped together) is cooled from  $125^\circ\text{C}$  to  $25^\circ\text{C}$ . The cooling process occurs in moist air and the lamina absorbs 0.5% of its weight in moisture. The lamina has the following properties:

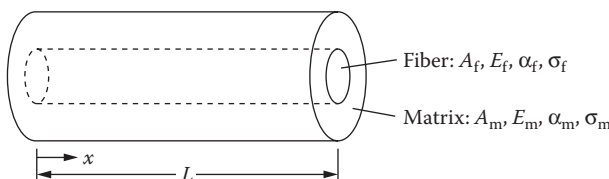
$$\begin{array}{ll} E_1 = 140 \text{ GPa} & \alpha_1 = -0.3 \times 10^{-6}/\text{K} \\ E_2 = 10 \text{ GPa} & \alpha_2 = 28 \times 10^{-6}/\text{K} \\ v_{12} = 0.3 & \beta_1 = 0 \\ G_{12} = 7 \text{ GPa} & \beta_2 = 0.44 \end{array}$$



**FIGURE 5.20**  
Lamina clamped between rigid plates in a mold.

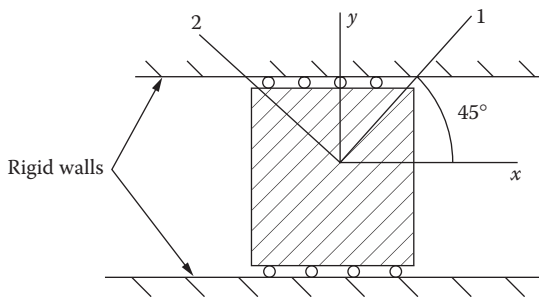
Assuming that the lamina properties do not change over this temperature range and that the lamina is initially dry and stress free, determine the residual hygrothermal stresses in the lamina at 25°C for angles  $\theta = 0^\circ$  and  $45^\circ$ .

9. A unidirectional continuous fiber composite is to be made from T300 graphite fibers in a high-modulus (HM) epoxy matrix, and the composite is to have a longitudinal coefficient of thermal expansion of zero. Using the fiber and matrix properties in Tables 3.1 and 3.2, determine the required fiber-volume fraction. Is this a practical composite? Sketch a graph showing the longitudinal CTE of the composite versus the fiber-volume fraction, and show the range of fiber-volume fractions over which the longitudinal CTE would be negative.
10. A unidirectional graphite/epoxy lamina having the properties described in Problem 8 is to be designed to have a coefficient of thermal expansion of zero along a particular axis. Determine the required lamina orientation for such a design.
11. A representative volume element (RVE) consisting of a cylindrical isotropic fiber embedded and perfectly bonded in a cylinder of isotropic matrix material is shown in Figure 5.21. If the ends of the RVE at  $x = 0$  and  $x = L$  and the outer surface of the RVE are stress free and the RVE is subjected to a uniform temperature change  $\Delta T$ , determine the fiber stress,  $\sigma_f$ , and the matrix stress,  $\sigma_m$ , along the fiber direction at the midpoint of the RVE (at  $x = L/2$ ). Use a mechanics of materials approach and express answers in terms of the coefficients of thermal expansion  $\alpha_f$  and  $\alpha_m$ , the cross-sectional areas  $A_f$  and  $A_m$ , the Young's moduli  $E_f$  and  $E_m$ , and the temperature change,  $\Delta T$ , where the subscripts f and m refer to fiber and matrix, respectively.
12. Samples of unidirectional Kevlar 49/epoxy and S-glass/epoxy composites are subjected to elevated temperatures in an oven and the resulting thermal strains are measured by using strain gages oriented along the 1 and 2 directions, as shown in Figure 5.15. From the data in Figure 5.15, estimate the longitudinal thermal expansion coefficient  $\alpha_1$  and the transverse thermal expansion coefficient  $\alpha_2$  for both materials.
13. A unidirectional 45° off-axis E-glass/epoxy composite lamina is supported on frictionless rollers between rigid walls as shown



**FIGURE 5.21**

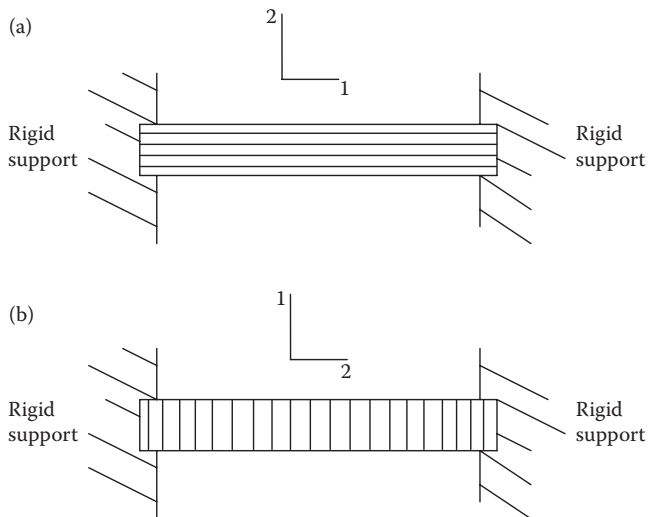
Representative volume element for Problem 11.

**FIGURE 5.22**

Off-axis composite lamina fixed between rigid walls for Problem 13.

in Figure 5.22. The lamina is fixed against displacements in the  $y$  direction, but is free to move in the  $x$  direction. Determine all of the lamina strains associated with the  $x,y$  axes if the lamina is heated from  $20^{\circ}\text{C}$  to  $120^{\circ}\text{C}$ . The required properties for E-glass/epoxy are given in Tables 2.2 and 5.3.

14. A hybrid unidirectional E-glass/T-300 carbon/IMHS epoxy composite is to be designed to have an overall longitudinal thermal expansion coefficient of zero in order to insure the best possible thermal stability under varying service temperatures. It is also required that in order to ensure that the material will be sufficiently stiff, the volume fraction of T-300 carbon fibers is to be twice the volume fraction of the E-glass fibers. (a) Using the properties in Tables 3.1 and 3.2 and neglecting voids in the material, determine the required volume fractions of T-300 carbon fibers and E-glass fibers. (b) Assuming that the T-300 carbon fibers and E-glass fibers have approximately the same diameters, and that the fibers are packed in a triangular array, is the composite design of part (a) feasible?
15. An orthotropic lamina has thermal expansion coefficients  $\alpha_1 = -4.0 \times 10^{-6} \text{ m/m/K}$  and  $\alpha_2 = 79 \times 10^{-6} \text{ m/m/K}$ . Determine (a) the angle  $\theta$  for which the thermal expansion coefficient  $\alpha_y = 0$ , and (b) the angle  $\theta$  for which the thermal expansion coefficient  $\alpha_{xy}$  has its maximum value.
16. A carbon/epoxy lamina having the properties listed in Problem 8 is clamped between two rigid plates as shown in Figure 5.20. If the lamina is heated from  $20^{\circ}\text{C}$  to  $120^{\circ}\text{C}$ , determine the thermal stresses associated with the principal material axes of the lamina.
17. A unidirectional E-glass/epoxy lamina is securely attached to rigid supports on both ends in two different ways as shown in Figure 5.23. In Figure 5.23a, the fiber direction is perpendicular to the rigid supports, and in Figure 5.23b the fibers are oriented parallel to the rigid supports. The lamina is to be heated by the amount  $\Delta T$  in both cases. Using the properties in Tables 2.2, 4.1, and 5.3, determine the maximum temperature increase  $\Delta T$  that the composites can withstand in both Figure 5.23a and b according

**FIGURE 5.23**

Rigidly supported E-glass epoxy lamina in two different orientations for Problem 17.

to the Maximum Stress Criterion. Based on the maximum service temperatures for typical epoxies in Table 5.1, what can you say about the practical limits on  $\Delta T$  in these cases?

18. Derive Equations 5.26 and 5.30.

## References

1. Browning, C. E., Husman, G. E., and Whitney, J. M. 1977. Moisture effects in epoxy matrix composites. *Composite Materials: Testing and Design: Fourth Conference*. ASTM STP 617, pp. 481–496, American Society for Testing and Materials, Philadelphia, PA.
2. Gibson, R. F., Yau, A., Mende, E. W., and Osborn, W. E. 1982. The influence of environmental conditions on the vibration characteristics of chopped fiber reinforced composite materials. *Journal of Reinforced Plastics and Composites*, 1(3), 225–241.
3. Shen, C. H. and Springer, G. S. 1976. Moisture absorption and desorption of composite materials. *Journal of Composite Materials*, 10, 2–20.
4. Jost, W. 1952. *Diffusion in Solids, Liquids, Gases*. Academic Press, Inc., New York.
5. Loos, A. C., Springer, G. S., Sanders, B. A., and Tung, R. W. 1981. Moisture absorption of polyester-E glass composites, in Springer, G. S., ed., *Environmental Effects on Composite Materials*, pp. 51–62. Technomic Publishing Co., Lancaster, PA.
6. Cai, L. W. and Weitsman, Y. 1994. Non-Fickian moisture diffusion in polymeric composites. *Journal of Composite Materials*, 28(2), 130–154.

7. Weitsman, Y. 2000. Effects of fluids on polymeric composites—A review, in Kelly, A. and Zweben, C., editors-in-chief, *Comprehensive Composite Materials*, Talreja, R. and Manson, J.-A. E., eds., *Polymeric Matrix Composites*, Vol. 2, pp. 369–401. Elsevier Science Publishers, Amsterdam.
8. Weitsman, Y. and Elahi, M. 2000. Effects of fluids on the deformation, strength and durability of polymeric composites—An overview. *Mechanics of Time-Dependent Materials*, 4, 107–126.
9. Chamis, C. C. and Sinclair, J. H. 1982. Durability/life of fiber composites in hygrothermomechanical environments, in Daniel, I. M. ed., *Composite Materials: Testing and Design (Sixth Conference)*, ASTM STP 787, pp. 498–512. American Society for Testing and Materials, Philadelphia, PA.
10. Chamis, C. C. 1987. Simplified composite micromechanics equations for mechanical, thermal, and moisture-related properties, in Wheeton, J. W. et al., eds., *Engineers' Guide to Composite Materials*, pp. 3-8-3-24. ASM International, Materials Park, OH.
11. Delasi, R. and Whiteside, J. B. 1987. Effect of moisture on epoxy resins and composites, in Vinson, J. R. ed., *Advanced Composite Materials—Environmental Effects*, ASTM STP 658, pp. 2–20. American Society for Testing and Materials, Philadelphia, PA.
12. Loos, A. C. and Springer, G. S. 1981. Moisture absorption of graphite/epoxy composites immersed in liquids and in humid air, in Springer, G. S. ed., *Environmental Effects on Composite Materials*, pp. 34–50. Technomic Publishing Co., Lancaster, PA.
13. Fahmy, A. A. and Hurt, J. C. 1980. Stress dependence of water diffusion in epoxy resins. *Polymer Composites*, 1(2), 77–80.
14. Marom, G. and Broutman, L. J. 1981. Moisture penetration into composites under external stress. *Polymer Composites*, 2(3), 132–136.
15. Weitsman, Y. 1987. Stress assisted diffusion in elastic and viscoelastic materials. *Journal of the Mechanics and Physics of Solids*, 35(1), 73–94.
16. Cairns, D. S. and Adams, D. F. 1984. Moisture and thermal expansion properties of unidirectional composite materials and the epoxy matrix, in Springer, G. S. ed., *Environmental Effects on Composite Materials*, Vol. 2, pp. 300–316. Technomic Publishing Co., Lancaster, PA.
17. Graves, S. R. and Adams, D. F. 1981. Analysis of a bonded joint in a composite tube subjected to torsion. *Journal of Composite Materials*, 15, 211–224.
18. Adams, D. F., Carlsson, L. A., and Pipes, R. B., 2003. *Experimental Characterization of Advanced Composite Materials*. CRC Press, Boca Raton, FL.
19. Schapery, R. A. 1968. Thermal expansion coefficients of composite materials based on energy principles. *Journal of Composite Materials*, 2(3), 380–404.
20. Hashin, Z. 1979. Analysis of properties of fiber composites with anisotropic constituents. *Journal of Applied Mechanics*, 46, 543–550.
21. Rosen, B. W. 1987. Composite materials analysis and design, in Reinhart, T. J. ed., *Engineered Materials Handbook*, Vol. 1, *Composites*, Sec. 4. ASM International, Materials Park, OH.
22. Ishikawa, T., Koyama, K., and Kobayashi, S. 1978. Thermal expansion coefficients of unidirectional composites. *Journal of Composite Materials*, 12, 153–168.
23. Karadeniz, Z. and Kumluatas, D. 2007. A numerical study on the coefficients of thermal expansion of fiber reinforced composite materials. *Composite Structures*, 78, 1–10.

24. Sideridis, E. 1994. Thermal expansion coefficient of fiber composites defined by the concept of an interphase. *Composites Science and Technology*, 51, 301–317.
25. Rosen, B. W. and Hashin, Z. 1970. Effective thermal expansion coefficients and specific heats of composite materials. *International Journal of Engineering Science*, 8, 157–173.
26. Dong, C. 2008. Development of a model for predicting the transverse coefficients of thermal expansion of unidirectional carbon fibre reinforced composite materials. *Applied Composite Materials*, 15, 171–182.
27. Gibson, R. F. and Muller, A. 2010. Unpublished research, University of Nevada, Reno.
28. Ashton, J. E., Halpin, J. C., and Petit, P. H. 1969. *Primer on Composite Materials: Analysis*. Technomic Publishing Co., Lancaster, PA.
29. Hopkins, D. A. and Chamis, C. C. 1988. A unique set of micromechanics equations for high temperature metal matrix composites, in DiGiovanni, P. R. and Adsit, N. R., eds., *Testing Technology of Metal Matrix Composites*, ASTM STP 964, pp. 159–176. American Society for Testing and Materials, Philadelphia, PA.

This page intentionally left blank

# 6

---

## *Analysis of a Discontinuously Reinforced Lamina*

---

### 6.1 Introduction

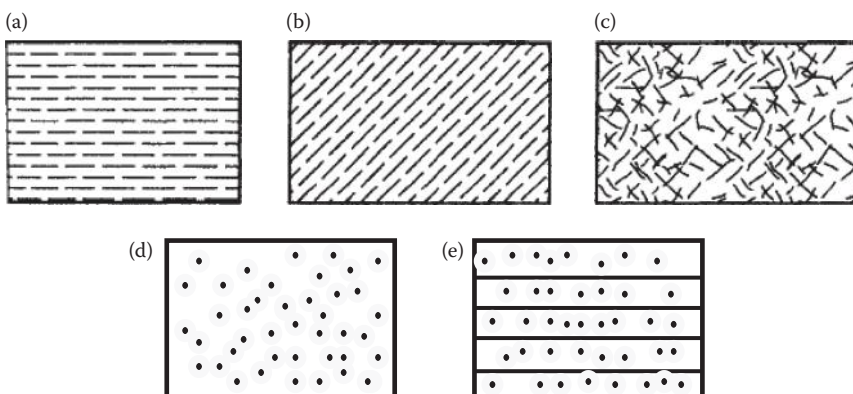
In Chapters 2 through 5, we have discussed the analysis of continuous fiber-reinforced composites. The effects of fiber discontinuity or fiber length on composite mechanical behavior were not taken into account in these analyses since it was assumed that the fibers extended from one end of the lamina to the other. This chapter is concerned with the mechanical behavior of laminae featured by discontinuous fiber or particulate reinforcement.

Short-fiber-reinforced or particulate-reinforced composites are typically not as strong or as stiff as continuous fiber-reinforced composites and are not likely to be used in critical structural applications such as aircraft primary structures (but this may change as the full potential of new discontinuous reinforcements such as carbon nanotubes (CNTs) or nanoparticles is realized). On the other hand, discontinuously reinforced composites do have several attractive characteristics that make them worthy of consideration for other applications. For example, in components characterized by complex geometrical contours, continuous fibers may not be practical because they may not conform to the desired shape without being damaged or distorted from the desired pattern. However, short fibers or particles can be easily mixed with the liquid matrix resin, and the resin/fiber or resin/particle mixture can be injection or compression molded to produce parts with complex shapes. Such processing methods are also fast and inexpensive, which makes them very attractive for high-volume applications. Composites having randomly oriented, short-fiber reinforcements or particulate reinforcements are nearly isotropic, whereas unidirectional continuous fiber composites are highly anisotropic. In many applications the advantages of low cost, the ease of fabricating complex parts, and isotropic behavior are enough to make short-fiber or particulate composites the material of choice. This has been especially true since the 1991 discovery of CNTs (the “ultimate short fibers,” which are currently believed to be the strongest materials that mankind is capable of producing), and much attention has been directed toward their use as reinforcement in composites.

Short-fiber composites with three types of fiber reinforcement will be considered here: aligned discontinuous fibers (Figure 6.1a), off-axis-aligned discontinuous fibers (Figure 6.1b), and randomly oriented discontinuous fibers (Figure 6.1c). Particulate-reinforced composites (Figure 6.1d) and hybrid multiscale composites having both fiber and particulate reinforcements of different size scales (Figure 6.1e) are also considered. Nanofibers, nanoparticles, or nanotubes can be used in any of these arrangements, but because of their extremely tiny dimensions, they are most often randomly oriented in all three dimensions. As indicated earlier in Section 1.4, nanoenhancement of the matrix materials (i.e., replacing the polymer matrix material with a nanocomposite) in conventional fiber-reinforced composites has made possible the development of a variety of new multifunctional composites. Although the randomly oriented, short-fiber composites (Figure 6.1c) are currently the most widely used, the development of the analytical models logically begins with the simplest case, that of aligned short fibers in Figure 6.1a.

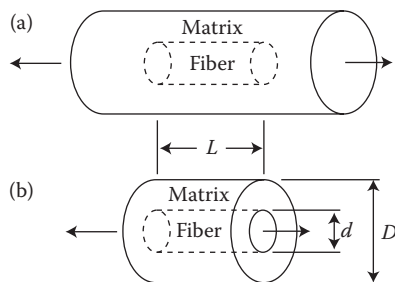
## 6.2 Aligned Discontinuous Fibers

The analysis of the specially orthotropic aligned discontinuous fiber composite in Figure 6.1a begins with the selection of an RVE consisting of a short fiber embedded in a cylinder of matrix material, as shown in Figure 6.2. Several models are based on the simplified RVE in Figure 6.2b, which does not include matrix material at the ends of the fiber as the model in Figure 6.2a does. Before beginning the analysis, however, it is instructive to consider the



**FIGURE 6.1**

Types of discontinuous reinforcement. (a) Aligned discontinuous fibers, (b) off-axis aligned discontinuous fibers, (c) randomly oriented discontinuous fibers, (d) particulate reinforcement, and (e) hybrid multiscale reinforcement.

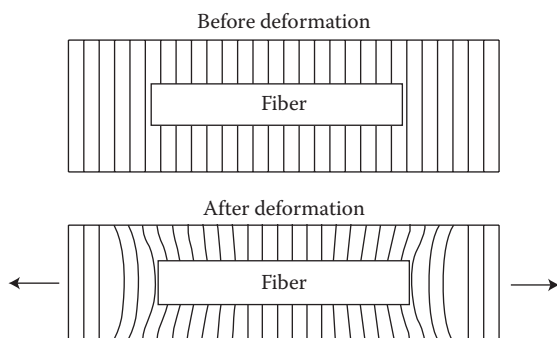
**FIGURE 6.2**

RVEs for aligned discontinuous fiber composite. (a) Matrix material included at ends of fiber and (b) matrix material not included at ends of fiber.

geometry of deformation in the RVE of Figure 6.2a. As shown by the grid lines before and after deformation in Figure 6.3, the stiffness mismatch between fiber and matrix ( $E_f \gg E_m$ ) leads to large shear deformations near the fiber ends but no shear deformation at the middle of the fiber. That is, if  $E_f = E_m$ , there is no mismatch in stiffness between fiber and matrix, and no fiber–matrix interfacial shear takes place. But as  $E_f$  increases relative to  $E_m$ , the interfacial shear stress and distortion increases. As we will see later, the stress transfer between matrix and fiber occurs primarily through interfacial shear, which is the greatest near the fiber ends. On the other hand, the normal stress in the fiber builds from a minimum at the fiber ends to a maximum in the middle of the fiber.

### 6.2.1 Stress and Strength Analysis

The above observations based on the geometry of deformation will now be confirmed by considering the free-body diagram of a differential element of

**FIGURE 6.3**

Schematic representation of matrix shear deformation in a short-fiber composite.

the fiber from the RVE, as shown in Figure 6.4. For static equilibrium of the forces along the  $x$ -direction,

$$\sum F_x = (\sigma_f + d\sigma_f) \frac{\pi d^2}{4} - \sigma_f \frac{\pi d^2}{4} - \tau(\pi d) dx = 0 \quad (6.1)$$

where

$\sigma_f$  = fiber normal stress along the  $x$ -direction at a distance  $x$  from the end of the fiber

$F_x$  = force along the  $x$ -direction

$\tau$  = interfacial shear stress at a distance  $x$  from the end of the fiber

$d$  = fiber diameter, a constant

$dx$  = length of the differential element

$d\sigma_f$  = differential change in stress  $\sigma_f$ .

Simplifying and rearranging the above equation, we obtain the differential equation relating the rate of change of the fiber normal stress along the  $x$ -direction to the interfacial shear stress:

$$\frac{d\sigma_f}{dx} = \frac{4\tau}{d} \quad (6.2)$$

Separating variables and integrating, we find that

$$\int_{\sigma_0}^{\sigma_f} d\sigma_f = \frac{4}{d} \int_0^x \tau dx \quad (6.3)$$

It is commonly assumed that essentially all of the stress transfer from matrix to fiber occurs by interfacial shear around the periphery of the

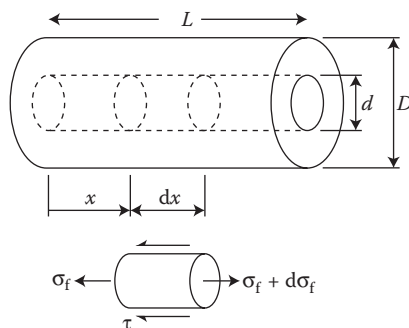


**FIGURE 6.4**  
Stresses acting on a differential element of fiber.

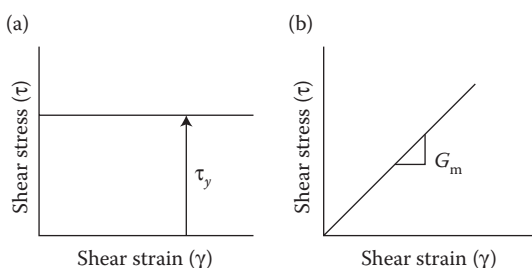
fiber, and that the fiber normal stress,  $\sigma_0$ , which is transferred across the ends of the fiber, is negligible. With this assumption, Equation 6.3 becomes

$$\sigma_f = \frac{4}{d} \int_0^x \tau \, dx \quad (6.4)$$

Thus, if we want to determine the fiber stress,  $\sigma_f$ , we must know the interfacial shear stress,  $\tau$ , as a function of the distance  $x$ . Two basic approaches have been proposed, both of which are based on assumptions regarding the behavior of the matrix material. Kelly and Tyson [1] assumed that the matrix is rigid plastic, as shown in the stress-strain curve in Figure 6.5a. Cox [2] assumed that the matrix is linear elastic, as shown in Figure 6.5b. Both models are based on the assumption of linear elastic fibers. We will consider both models, but it is convenient to use the Kelly-Tyson model for illustrative purposes at this point. The Kelly-Tyson model is much simpler than the Cox model because the interfacial shear stress,  $\tau$ , is everywhere equal to the matrix yield stress in shear,  $\tau_y$ . Thus, for the Kelly-Tyson model, the resulting fiber stress from Equation 6.4 is now

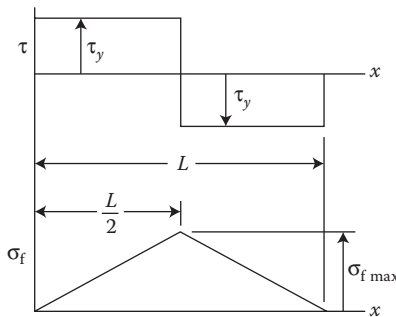
$$\sigma_f = \frac{4}{d} \tau_y x \quad (6.5)$$

This equation tells us that the fiber stress varies linearly with the distance from the fiber end, but we also know that the fiber stress distribution must be symmetric about  $x = L/2$ . Since it has been assumed that  $\sigma_f = \sigma_0 = 0$  at  $x = 0$  and, by symmetry, at  $x = L$ , the fiber stress distribution and the corresponding shear stress distribution must be as shown in Figure 6.6. The stress distributions in Figure 6.6 are actually valid only for fibers having lengths less than a certain value, as we will see later. The maximum fiber stress for such



**FIGURE 6.5**

Assumed stress-strain curves for matrix material in the (a) Kelly-Tyson and (b) Cox models.

**FIGURE 6.6**

Variation of interfacial shear stress,  $\tau$ , and fiber normal stress,  $\sigma_f$ , with distance along the fiber according to the Kelly-Tyson model.

a fiber occurs at  $x = L/2$  and is given by

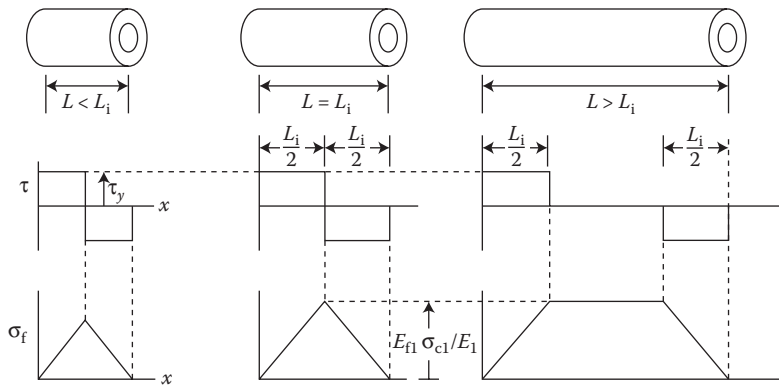
$$\sigma_{f \text{ max}} = \frac{4}{d} \tau_y \frac{L}{2} = \frac{2\tau_y L}{d} \quad (6.6)$$

The maximum fiber stress cannot keep increasing indefinitely as the fiber length  $L$  is increased, however. If the fiber is assumed to be elastic,  $\sigma_{f \text{ max}}$  cannot exceed the value  $E_{f1} \sigma_{cl}/E_1$ , which is the fiber stress in a continuous fiber composite under longitudinal composite stress,  $\sigma_{cl}$  (recall Section 3.2.1). Thus, as  $\sigma_{f \text{ max}}$  approaches the limiting value  $E_{f1} \sigma_{cl}/E_1$ , the fiber length,  $L$ , approaches a value  $L_i$ , which has been referred to as the “ineffective length” [3], or the “load transfer length” [4]. The equation for  $L_i$  is therefore

$$L_i = \frac{d E_{f1} \sigma_{cl}}{2 \tau_y E_1} \quad (6.7)$$

The effect of increasing fiber length on the fiber stress and shear stress distributions is shown graphically in Figure 6.7. Note that no matter how long the fiber is, the load transfer between fiber and matrix (by virtue of the interfacial shear stress,  $\tau$ ) only occurs over the length,  $L_i$ . The length  $L_i$  has been referred to as the “ineffective length” because the fiber stress is less than its maximum value for this portion of the fiber. The term “load transfer length” comes from the fact that the load transfer between fiber and matrix only occurs over this portion of the fiber. Although these results are for the Kelly-Tyson model, similar results are obtained from the Cox model.

Another limiting value of the fiber stress occurs when  $\sigma_{f \text{ max}}$  is equal to the fiber tensile strength,  $s_{f1}^{(+)}$ . In this case, the applied composite stress is such that

**FIGURE 6.7**

Effect of fiber length on stress distributions along the fiber according to the Kelly-Tyson model.

$$\frac{E_{f1}\sigma_{c1}}{E_1} = \sigma_{f \max} = s_{fi}^{(+)} \quad (6.8)$$

The corresponding fiber length now becomes \$L = L\_c\$, where \$L\_c\$ is referred to as the "critical length." For this condition, substitution of Equation 6.8 into Equation 6.6 yields the equation for the critical length as

$$L_c = \frac{ds_{fi}^{(+)}}{2\tau_y} \quad (6.9)$$

The critical length has important implications for the calculation of longitudinal composite strength. Recall from Equation 3.23 that the average longitudinal composite stress for loading along the fiber direction is given by

$$\bar{\sigma}_{c1} = \bar{\sigma}_{f1}v_f + \bar{\sigma}_{m1}v_m \quad (3.23)$$

Then Equation 4.22 for longitudinal composite strength of a continuous fiber-reinforced lamina was developed from Equation 3.23 by assuming that the continuous fibers were uniformly stressed along their entire lengths, and that the fibers failed before the matrix when the average fiber stress \$\bar{\sigma}\_{f1}\$ reached the fiber tensile strength \$s\_{fi}^{(+)}. However, in the case of discontinuous fibers, it should be clear from the previous developments in this section that the fibers are not uniformly stressed along their entire lengths, and that the fiber length must be taken into account. For the discontinuous fibers, the average longitudinal fiber stress in Equation 3.23 may be found from

$$\bar{\sigma}_{f1} = \frac{\int_0^{L/2} \sigma_{f1} dx}{L/2} \quad (6.10)$$

Evaluation of this integral depends on the fiber length. From Figure 6.7, it can be seen that for  $L \leq L_i$ , the fiber stress varies linearly with  $x$  as

$$\sigma_{fl} = \frac{\sigma_{f\ max}x}{L_i/2} \quad (6.11)$$

and Equation 6.10 becomes

$$\bar{\sigma}_{fl} = \frac{\int_0^{L/2} [\sigma_{f\ max}x/(L_i/2)]dx}{L/2} = \frac{\sigma_{f\ max}L}{2L_i} \quad (6.12)$$

whereas for the case  $L \geq L_i$ , the corresponding average stress is

$$\bar{\sigma}_{fl} = \frac{\int_0^{L_i/2} [\sigma_{f\ max}x/(L_i/2)]dx + \int_{L_i/2}^{L/2} \sigma_{f\ max} dx}{L/2} = \left(1 - \frac{L_i}{2L}\right) \sigma_{f\ max} \quad (6.13)$$

It should be kept in mind here that  $L$  is the variable fiber length and  $L_i$  is the specific value of fiber length over which load transfer takes place. Therefore, for the specific case of fiber failure and corresponding composite failure, substitution of the conditions  $\sigma_{f\ max} = s_{fl}^{(+)}$ ,  $\bar{\sigma}_{cl} = s_L^{(+)}$ ,  $\bar{\sigma}_m = s_{mf1}^{(+)}$ , and  $L_i = L_c$  along with Equation 6.12 into Equation 3.23 gives the longitudinal composite strength as

$$s_L^{(+)} = \frac{s_{fl}^{(+)}L}{2L_c} v_f + s_{mf1}^{(+)}(1 - v_f) \quad \text{for } L \leq L_c \quad (6.14)$$

while similar substitution of the conditions  $\sigma_{f\ max} = s_{fl}^{(+)}$ ,  $\bar{\sigma}_{cl} = s_L^{(+)}$ ,  $\bar{\sigma}_m = s_{mf1}^{(+)}$ , and  $L_i = L_c$  along with Equation 6.13 into Equation 3.23 gives the longitudinal composite strength as

$$s_L^{(+)} = \left(1 - \frac{L_c}{2L}\right) s_{fl}^{(+)} v_f + s_{mf1}^{(+)}(1 - v_f) \quad \text{for } L \geq L_c \quad (6.15)$$

It has been assumed in Equations 6.14 and 6.15 that the average stress in the matrix at fiber failure is  $\bar{\sigma}_m = s_{mf1}^{(+)}$  in accordance with Figure 4.12a and Equation 4.22. Note that, when  $L \gg L_c$ , Equation 6.15 approaches Equation 4.22 for continuous fibers.

Alternatively, Equation 6.9 can be rearranged to give the interfacial shear strength,  $\tau_y$ , corresponding to the critical length

$$\tau_y = \frac{ds_{fl}^{(+)}}{2L_c} \quad (6.16)$$

This equation has been used by Drzal et al. [5,6] and others to determine the interfacial shear strength from measurements of critical length. In such an experiment, a specimen consisting of a single fiber embedded in a strip of translucent matrix material is mounted under a microscope and then subjected to an increasing tensile load. Once the fiber stress reaches  $s_{fl}^{(+)}$ , the fiber breaks up into segments having a statistical distribution about the critical length,  $L_c$ , and the corresponding statistical parameters describing the interfacial shear strength are calculated using Equation 6.9.

### Example 6.1

If the distribution of the interfacial shear stress,  $\tau$ , along the discontinuous fiber in Figure 6.4 is described by the linear function shown in Figure 6.8a, find the corresponding expression for the fiber tensile normal stress,  $\sigma_f$ , and sketch its distribution.

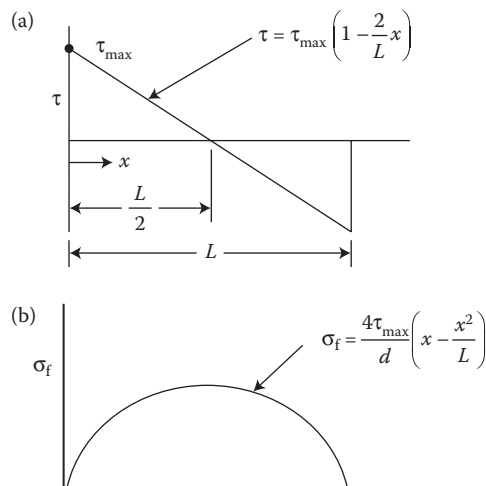


**FIGURE 6.8**

(a) Interfacial shear stress distribution along the short fiber in Example 6.1 and (b) corresponding fiber tensile normal stress distribution.

### SOLUTION

The equation for the linear variation of the interfacial shear stress in Figure 6.8a is

$$\tau = \tau_{\max} \left( 1 - \frac{2}{L} x \right)$$

Substituting this equation into Equation 6.4, the fiber tensile normal stress distribution is found to be

$$\sigma_f = \frac{4}{d} \int_0^x \tau dx = \frac{4}{d} \int_0^x \tau_{\max} \left( 1 - \frac{2}{L} x \right) dx = \frac{4\tau_{\max}}{d} \left( x - \frac{x^2}{L} \right)$$

This distribution is shown graphically in Figure 6.8b. The maximum value of this stress occurs at  $x = L/2$ .

### Example 6.2

An aligned short-fiber carbon–epoxy composite is to be fabricated so that it behaves as a continuous fiber composite with a composite modulus of  $E_1 = 80$  GPa. The 0.01-mm-diameter fibers have a modulus of elasticity  $E_{f1} = 240$  GPa and a tensile strength  $s_{f1}^{(+)} = 2.5$  GPa. The epoxy matrix can be assumed to be a rigid plastic material with a yield strength of 20 MPa in shear. Determine (a) the fiber length necessary to just reach the “continuous fiber stress” at the midpoint for a composite stress of 50 MPa and (b) the fiber length and the composite stress necessary to develop the ultimate tensile strength in the fiber.

### SOLUTION

a. The “continuous fiber stress” is

$$\sigma_{f\ max} = \frac{E_{f1}\sigma_{c1}}{E_1} = \frac{240(50)}{80} = 150 \text{ MPa}$$

and the corresponding fiber length from Equation 6.6 is

$$L = \frac{d\sigma_{f\ max}}{2\tau_y} = \frac{0.01(150)}{2(20)} = 0.0375 \text{ mm}$$

b. The fiber length corresponding to a fiber stress  $s_{f1}^{(+)}$  is found from Equation 6.9:

$$L_c = \frac{ds_{f1}^{(+)}}{2\tau_y} = \frac{0.01(2500)}{2(20)} = 0.625 \text{ mm}$$

and the corresponding composite stress is

$$\sigma_{cl} = \frac{E_l s_{fl}^{(+)}}{E_{fl}} = \frac{80(2.5)}{240} = 0.833 \text{ GPa} = 833 \text{ MPa}$$

### 6.2.2 Modulus Analysis

Expressions for the longitudinal modulus of the aligned discontinuous fiber composite can be found using either the Kelly-Tyson model or the Cox model, but only the derivation of the Cox model, extended further by Kelly [7], will be discussed here. A similar model, which is often referred to as a “shear lag” model, was developed by Rosen [8]. For the RVE of Figure 6.2b, recall from Equation 6.2 that the rate of change of the axial load in the fiber with respect to distance along the fiber is a linear function of the interfacial shear stress. Cox further assumed that the interfacial shear stress is proportional to the difference between  $u$  and  $v$ , where  $u$  is the axial displacement at a point in the fiber, and  $v$  is the axial displacement that the matrix would have at the same point in the RVE with no fiber present. Thus, the rate of change of the fiber axial load  $P$  is given by

$$\frac{dP}{dx} = H(u - v) \quad (6.17)$$

where  $H$  is a proportionality constant to be determined from geometrical and material property data. Differentiating Equation 6.17 once with respect to  $x$ , we find that

$$\frac{d^2P}{dx^2} = H\left(\frac{du}{dx} - \frac{dv}{dx}\right) = H\left(\frac{p}{A_f E_{fl}} - e\right) \quad (6.18)$$

where the expression

$$\frac{du}{dx} = \frac{P}{A_f E_{fl}}$$

is taken from elementary mechanics of materials and

$$\frac{dv}{dx} = e$$

is the matrix strain with no fiber present.

Equation 6.18 can be rearranged in the standard form of a second-order differential equation with constant coefficients as

$$\frac{d^2P}{dx^2} - \beta^2 P = -He \quad (6.19)$$

where

$$\beta^2 = \frac{H}{A_f E_{f1}}$$

The solution to Equation 6.19 is of the form

$$P = P_p + P_h \quad (6.20)$$

where

$$P_p = \text{particular solution} = A_f E_{f1} e$$

$$P_h = \text{homogeneous solution} = R \sinh \beta x + S \cosh \beta x$$

The coefficients  $R$  and  $S$  must be determined from the boundary conditions  $P = 0$  at  $x = 0$  and  $x = L$ . After using trigonometric identities and further manipulation, the resulting fiber stress is

$$\sigma_{f1} = \frac{P}{A_f} = E_{f1} e \left[ 1 - \frac{\cosh \beta(0.5L - x)}{\cosh(0.5\beta L)} \right] \quad (6.21)$$

The average fiber stress is then

$$\bar{\sigma}_{f1} = \frac{\int_0^{L/2} \sigma_{f1} dx}{L/2} = E_{f1} e \left[ 1 - \frac{\tanh(\beta L/2)}{\beta L/2} \right] \quad (6.22)$$

From the equilibrium of the composite for longitudinal loading, recall the rule of mixtures for stress (Equation 3.22), which is also valid for the RVE of Figure 6.2b:

$$\bar{\sigma}_{c1} = \bar{\sigma}_{f1} v_f + \bar{\sigma}_m v_m \quad (6.23)$$

Substituting Equation 6.22 into Equation 6.23, dividing Equation 6.23 by  $e$ , assuming that the applied composite stress produces a strain,  $e$ , in composite,

fiber, and matrix, and using Hooke's law for composite and matrix, we find the equation for the longitudinal modulus of the Cox model:

$$E_{cl} = E_{fl} \left[ 1 - \frac{\tanh(\beta L/2)}{\beta L/2} \right] v_f + E_m v_m \quad (6.24)$$

Note that the assumption of equal strains in fiber and matrix here does not violate the original assumptions about the displacements  $u$  and  $v$  being different, because  $v$  is the displacement in a piece of unreinforced matrix material. The term inside the brackets represents the effect of fiber length on the composite modulus.

The parameter  $\beta$  in the above equations and the interfacial shear stress,  $\tau$ , can be determined by considering the shear strain in the matrix, as shown by Kelly [7]. The results are

$$\beta^2 = \frac{2\pi G_m}{A_f E_{fl} \ln(D/d)} \quad (6.25)$$

and

$$\tau = \frac{d E_{fl} e \beta}{4} \left[ \frac{\sinh[\beta(0.5L - x)]}{\cosh(0.5\beta L)} \right] \quad (6.26)$$

where  $G_m$  is the matrix shear modulus and  $D$  is the outside diameter of the RVE, as shown in Figure 6.2. The predicted variations of the fiber stress and the interfacial shear stress from the Cox model when the fiber length  $L < L_i$  are shown schematically in Figure 6.9. Notice the difference between these stress distributions and the ones from the Kelly-Tyson model in Figure 6.6.

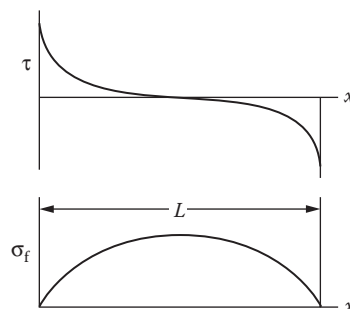


**FIGURE 6.9**

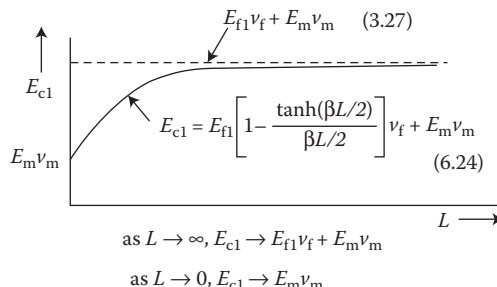
Variation of interfacial shear stress,  $\tau$ , and fiber normal stress,  $\sigma_f$ , with distance along the fiber according to the Cox model.

For the Cox stresses evaluated at the midpoint of the fiber ( $x = L/2$ ), as  $L \rightarrow L_i$ , the term in brackets in Equation 6.21 approaches the value 1.0, whereas the term in brackets in Equation 6.26 approaches zero.

Figure 6.10 graphically shows how the longitudinal modulus  $E_{cl}$  in Equation 6.24 varies with fiber length  $L$ . As we might expect,  $E_{cl}$  increases with increasing fiber length. Note that as the fiber length  $L \rightarrow \infty$ ,  $E_{cl} \rightarrow E_{f1}v_f + E_m v_m$ , the rule of mixtures value for a continuous fiber composite, and that as  $L \rightarrow 0$ ,  $E_{cl} \rightarrow E_m v_m$ , which represents the matrix contribution only.

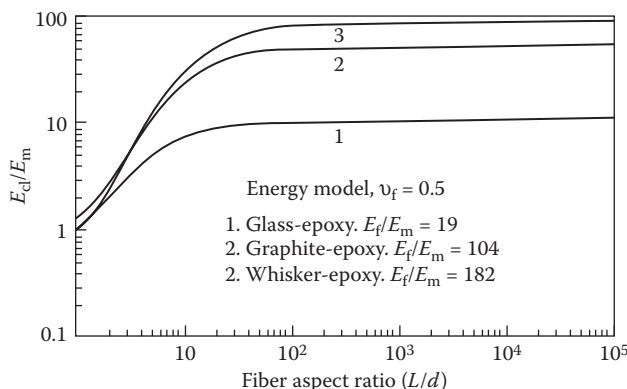
Another variation on the Cox model was developed by Gibson et al. [9], who used the Cox stresses,  $\sigma_f$  and  $\tau$ , in a strain energy method similar to that outlined in Equations 3.28 and 3.29. The longitudinal modulus calculated by the energy method was found to agree closely with Equation 6.24, and the predicted variation of  $E_{cl}$  with fiber aspect ratio,  $L/d$ , is shown for several composites in Figure 6.11. It is also interesting to see that the fiber length does not have to be very large relative to the fiber diameter to bring the modulus  $E_{cl}$  very close to the limiting value for a continuous fiber composite, as given by the rule of mixtures. For all practical purposes, Equation 6.24 predicts that the aligned discontinuous fiber composites of the types shown in Figure 6.11 have the longitudinal modulus of a continuous fiber composite if the fiber aspect ratio  $L/d > 100$ .

Although the Kelly-Tyson model and the Cox model both provide valuable insight into the concepts of load transfer, fiber length effects, and strength and modulus analysis, neither model accurately predicts the stress distributions. For example, more recent results from finite element analyses [10,11] and experimental photoelasticity [7,12,13] indicate that both the magnitude and the rate of change of the interfacial shear stresses near the end of the fiber are much higher than those predicted by the Kelly-Tyson or Cox models. A typical comparison of predicted shear stress distributions along the fiber from FEA and from the Cox model is shown in Figure 6.12. The finite element predictions of Sun and Wu [11] also showed good agreement with experimental photoelasticity results. FEAs have also been used to study the effects of different fiber end shapes on the stress distributions [10,11].



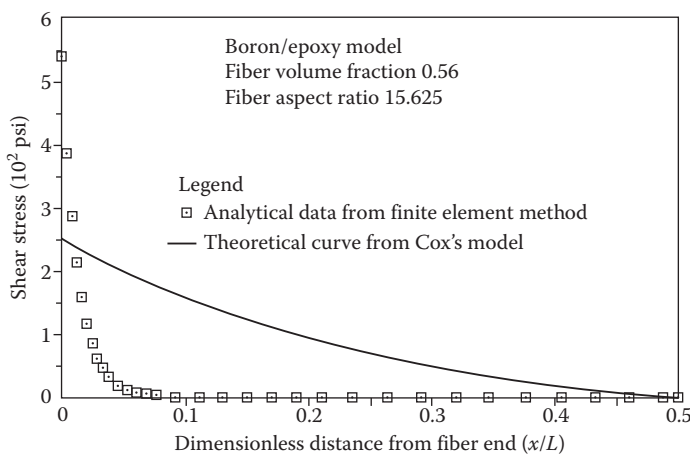
**FIGURE 6.10**

Variation of longitudinal modulus  $E_{cl}$  with fiber length  $L$  according to Equation 6.24.

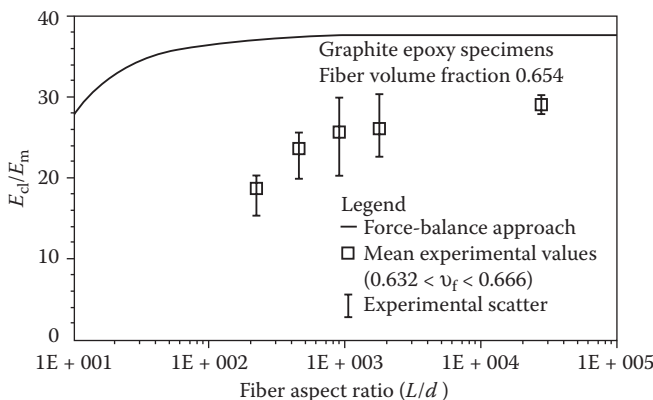
**FIGURE 6.11**

Variation of modulus ratio,  $E_{cl}/E_m$ , with fiber aspect ratio,  $L/d$ , for several composites. (From Gibson, R. F., Chaturvedi, S. K., and Sun, C. T. 1982. *Journal of Materials Science*, 17, 3499–3509. Reprinted with permission from Chapman & Hall.)

It is important to remember that both the Kelly-Tyson and the Cox models were derived for the RVE in Figure 6.2b, which does not include matrix material at the ends of the fiber. One result is that the actual modulus values are lower than predicted by Equation 6.24. For example, the experimental results of Suarez et al. [14] on aligned discontinuous graphite/epoxy composites having various fiber aspect ratios,  $L/d$ , are shown in Figure 6.13. The experimental modulus data at different fiber aspect ratios in Figure 6.13 were

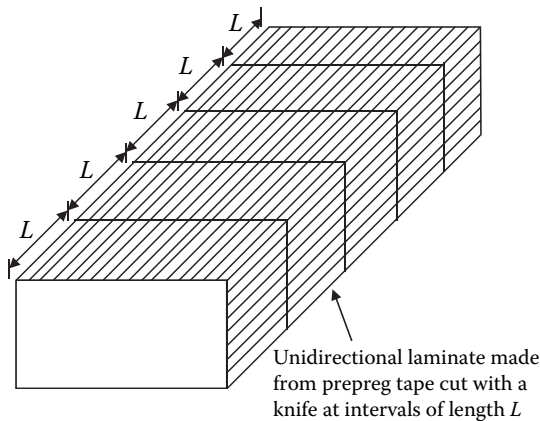
**FIGURE 6.12**

Predicted shear stress distributions along the fiber from FEA and the Cox model. (From Hwang, S. J. 1985. Finite element modeling of damping in discontinuous fiber composites. MS thesis, University of Idaho, Moscow, ID. With permission.)

**FIGURE 6.13**

Comparison of measured and predicted (Cox model) longitudinal moduli of aligned discontinuous fiber graphite/epoxy for various fiber aspect ratios.  $(L/d)_{\text{eff}} = L/d$ . (From Suarez, S. A. et al. 1986. *Experimental Mechanics*, 26(2), 175–184. With permission.)

obtained from the test specimens shown schematically in Figure 6.14, which were manufactured using a conventional unidirectional prepreg tape that had been cut at intervals of length  $L$  before being processed with a standard autoclave-style cure cycle. The measured moduli are seen to be well below the predicted curve from the Cox model. In order to shift the predicted curve to match the experimental results better, Suarez et al. introduced the concept of an “effective fiber aspect ratio,”  $(L/d)_{\text{eff}}$ , which would account for the fact that the reinforcement was not a single fiber but, rather, a bundle of fibers having an aspect ratio lower than that of a single fiber.

**FIGURE 6.14**

Aligned discontinuous fiber composite test specimen fabricated from a unidirectional prepreg tape cut at intervals of length  $L$  before curing.

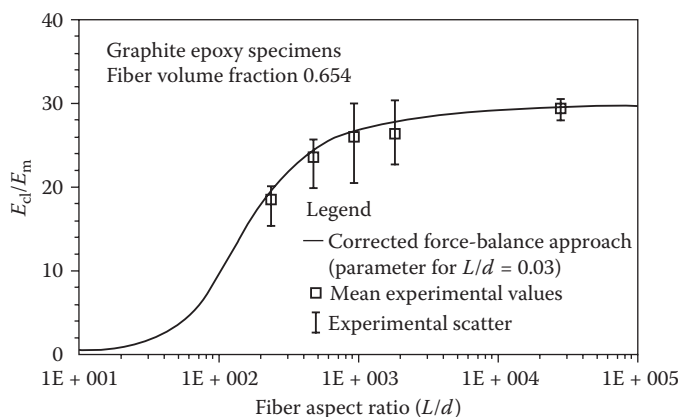
The effective fiber aspect ratio is defined as

$$\left(\frac{L}{d}\right)_{\text{eff}} = Z \left(\frac{L}{d}\right) \quad (6.27)$$

where  $Z$  is a curve-fitting parameter that accomplishes a horizontal shift of the curve of  $E_{cl}$  versus  $L/d$ . Before the horizontal shift, the predicted curve was shifted vertically by using a reduced fiber modulus to account for possible degradation of fiber properties or fiber misalignment during fabrication. The results of vertical and horizontal shifting of the graphite/epoxy curve of Figure 6.13 are shown in Figure 6.15, and the agreement is very good. Similar results were reported for aramid/epoxy and boron/epoxy. This approach did not take into account the matrix material between the fiber ends, however.

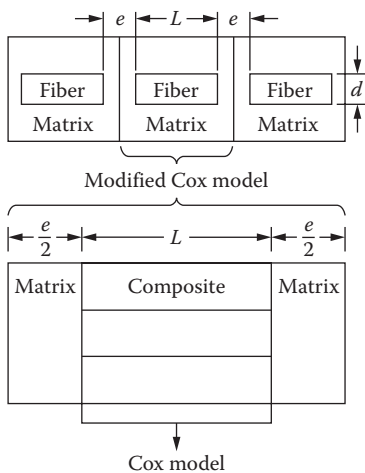
Hwang and Gibson [15] studied the effect of the fiber end gap on the composite modulus by using both FEA and a modified Cox model. The modified Cox model consists of the Cox model (Figure 6.2b) with one piece of matrix material attached on each end, as shown schematically in Figure 6.16. Following the development of Equation 3.36 for the series arrangement of elements under longitudinal stress, with the assumption of equal stresses in each element, the modified Cox modulus is

$$\frac{1}{E_{Mcl}} = \frac{v_{cl}}{E_{cl}} + \frac{v_m}{E_m} = \frac{L/(L+e)}{E_{cl}} + \frac{e/(L+e)}{E_m} \quad (6.28)$$



**FIGURE 6.15**

Comparison of measured and predicted (Cox model corrected for fiber aspect ratio) longitudinal moduli of aligned discontinuous fiber graphite/epoxy for various fiber aspect ratios.  $(L/d)_{\text{eff}} = 0.03$   $L/d$ . (From Suarez, S. A. et al. 1986. *Experimental Mechanics*, 26(2), 175–184. With permission.)

**FIGURE 6.16**

Modified Cox model including matrix material at ends of fiber. (From Hwang, S. J. and Gibson, R. F. 1987. *Journal of Engineering Materials and Technology*, 109, 47–52. Reprinted with permission from ASME.)

where

$E_{\text{Mcl}}$  = longitudinal modulus of the modified Cox model

$v_{\text{cl}}$  = volume fraction of the Cox model in the modified Cox model

$L$  = length of the Cox model

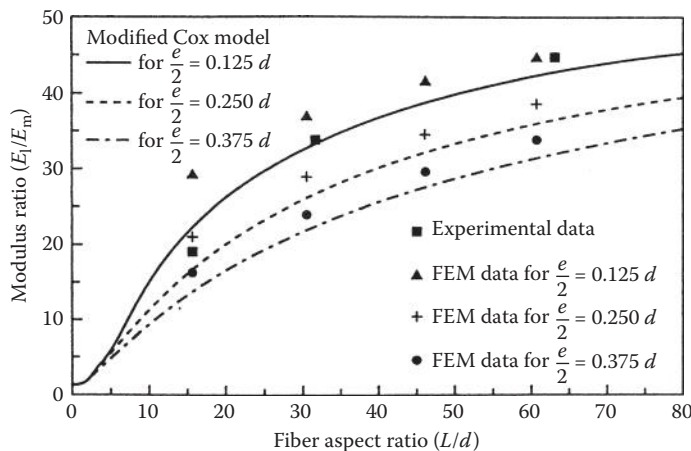
$e$  = distance between fiber ends in the modified Cox model

$L + e$  = length of the modified Cox model

Figure 6.17 shows a comparison of predictions from a finite element model and the modified Cox model, with experimental data for boron/epoxy. Micromechanical predictions using the finite element method (FEM) in Figure 6.17 were obtained using quarter domain models from RVEs of discontinuous aligned composites, as shown schematically in Figure 6.18. The moduli of the finite element models having different fiber aspect ratios,  $L/d$ , and abutting fiber end separations,  $e$ , were calculated using an equation similar to Equation 3.62 and a procedure similar to that described in the discussion of Equation 3.62. The modified Cox model shows good agreement with both the FEA and experimental data.

Halpin [16] has proposed a modification of the Halpin-Tsai equations (recall Section 3.5) as another approach to estimate the longitudinal modulus of the aligned discontinuous fiber composite. The proposed equations are

$$\frac{E_1}{E_m} = \frac{1 + \xi \eta v_f}{1 - \eta v_f} \quad (6.29)$$

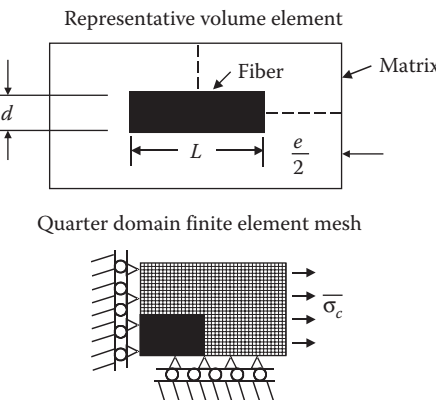
**FIGURE 6.17**

Comparison of predictions from the modified Cox model and FEA with experimental data for boron/epoxy-aligned discontinuous fiber composite at different fiber aspect ratios. (From Hwang, S. J. and Gibson, R. F. 1987. *Journal of Engineering Materials and Technology*, 109, 47–52. Reprinted with permission from ASME.)

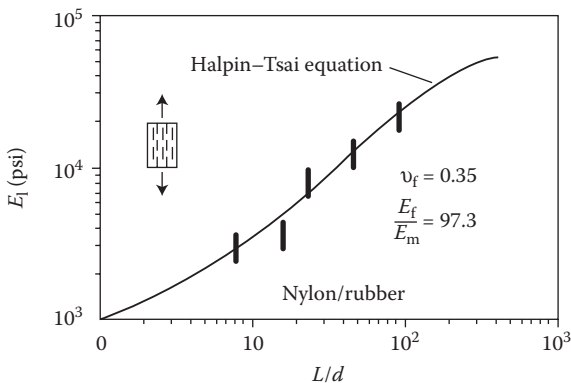
where

$$\eta = \frac{(E_{f1}/E_m) - 1}{(E_{f1}/E_m) + \xi} \quad (6.30)$$

and the suggested value of the curve-fitting parameter is  $\xi = 2L/d$ . Figure 6.19 shows that the predictions from these equations give good agreement with experimental data. Halpin also concluded that  $E_2$ ,  $G_{12}$ , and  $v_{12}$  are not significantly affected by the fiber length [16]. Thus, Equations 3.63 and 3.64

**FIGURE 6.18**

Quarter domain finite element model from RVE of discontinuous aligned fiber composite.

**FIGURE 6.19**

Dependence of longitudinal modulus on fiber aspect ratio for aligned discontinuous fiber nylon/rubber composite. Predictions from Halpin-Tsai equations are compared with experimental results. (From Halpin, J. C. 1969. *Journal of Composite Materials*, 3, 732–734. Reprinted with permission from Technomic Publishing Co.)

for  $E_2$  in the continuous fiber case can also be used for the discontinuous fiber case. Similar equations can be used for  $G_{12}$ , as described in Section 3.5, and Equation 3.45 can be used for  $v_{12}$ .

Other micromechanics equations for predicting stiffness of unidirectional short-fiber composites are summarized in the review article by Tucker and Liang [17].

### Example 6.3

For the differential element in Figure 6.4 and the stress distributions given in Example 6.1, find the corresponding equation for the longitudinal composite modulus  $E_{c1}$ . Assume that the fiber and matrix materials are linear elastic and that the fiber length  $L$  is less than the ineffective length  $L_i$ .

### SOLUTION

This derivation follows that of Equation 6.24, with different stress distributions along the fiber. In this case, the average fiber stress is given by

$$\bar{\sigma}_{f1} = \frac{\int_0^{L/2} \sigma_{f1} dx}{L/2} = \frac{\int_0^{L/2} \frac{4\tau_{\max}}{d} \left( x - \frac{x^2}{L} \right) dx}{L/2} = \frac{2\tau_{\max}L}{3d}$$

The rule of mixtures for longitudinal composite stress is

$$\bar{\sigma}_{c1} = \bar{\sigma}_{f1}v_f + \bar{\sigma}_m v_m = \frac{2\tau_{\max}L}{3d} v_f + \bar{\sigma}_m v_m$$

Assuming that the applied composite stress produces equal strains,  $e$ , in the composite, fiber and matrix, dividing both sides of the above equation by  $e$ , and applying Hooke's law for composite and matrix materials, we get

$$E_{cl} = \frac{2\tau_{max}L}{3de} v_f + E_m v_m$$

So for this model, the longitudinal composite modulus  $E_{cl}$  increases linearly with increasing fiber length  $L$ , starting at  $E_m v_m$  when  $L = 0$ .

### Example 6.4

The RVE for an aligned discontinuous fiber composite is shown in Figure 6.16. Assume that the composite part of the RVE has length  $L$  and longitudinal CTE  $\alpha_c$ , while the matrix material has total length  $e$  and longitudinal CTE  $\alpha_m$ . Develop a micromechanical equation for predicting the effective longitudinal thermal expansion coefficient,  $\alpha_{eff}$ , for the RVE, which has a total length  $L + e$ .

### SOLUTION

The overall thermal deformation of the RVE along the fiber direction due to a temperature change  $\Delta T$  is given by

$$\delta_{total} = \alpha_{eff}(L + e)\Delta T$$

But for the series arrangement of the composite and matrix, geometric compatibility requires the total thermal expansion to be

$$\delta_{total} = \delta_c + \delta_m = \alpha_c L \Delta T + \alpha_m e \Delta T$$

where

$\delta_c$  = thermal deformation of the composite part

$\delta_m$  = thermal deformation of the matrix part

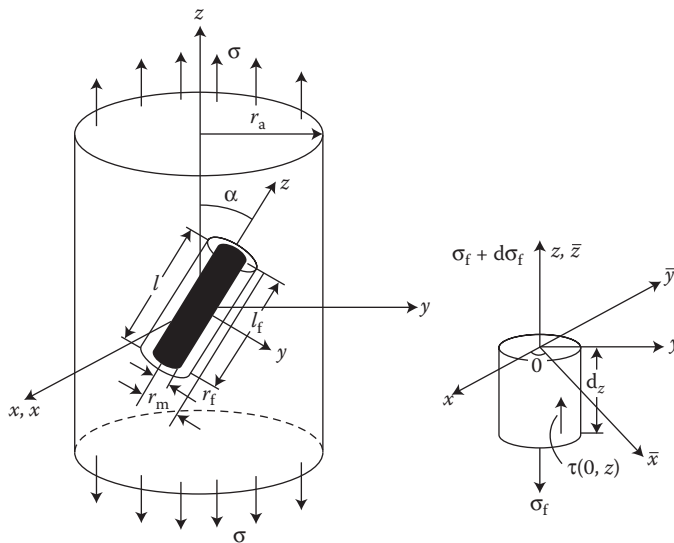
Equating the above two expressions for the total thermal deformation and solving for  $\alpha_{eff}$ , it is seen that the effective thermal expansion coefficient for the RVE is

$$\alpha_{eff} = \frac{\alpha_c L + \alpha_m e}{L + e}$$

## 6.3 Off Axis-Aligned Discontinuous Fibers

### 6.3.1 Stress and Strength Analysis

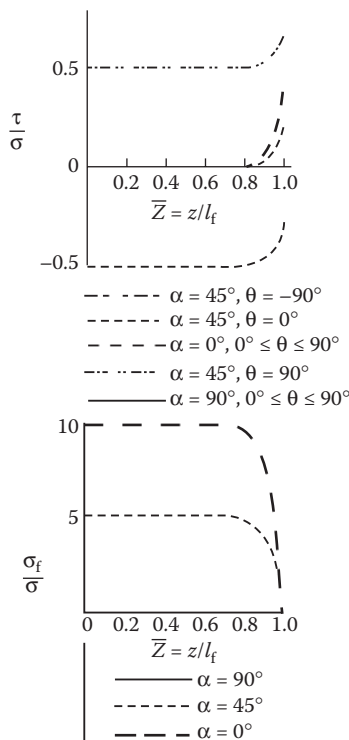
The generally orthotropic aligned discontinuous fiber composite can be conveniently analyzed by using the RVE shown in Figure 6.20, where the

**FIGURE 6.20**

RVE for an off-axis short-fiber composite. (From Chon, C. T. and Sun, C. T. 1980. *Journal of Materials Science*, 15, 931–938. Reprinted with permission from Chapman & Hall.)

short fiber is oriented at an angle with the loading axis. Chon and Sun [18] used this RVE to develop a generalized shear-lag analysis of the off-axis short-fiber composite. Only the key results will be summarized here as the equations are quite lengthy. The predicted variations of the interfacial shear stress and the fiber stress with the distance along the fiber for various angles are shown in Figure 6.21. Note that the results from the Cox model (recall Figure 6.9) are recovered for the case of fiber orientation  $\alpha = 0^\circ$ , and that the stress distribution curves are just shifted up or down as the angle  $\alpha$  changes. Maximum values of shear stresses and fiber stresses normalized to the applied composite stress are shown for various angles  $\alpha$  in Figure 6.22. It is seen that the maximum interfacial shear stress,  $\tau_{\max}$ , occurs at some off-axis angle, that  $\tau_{\max}$  decreases with increasing  $E_f/G_m$ , and that the angle corresponding to  $\tau_{\max}$  increases with increasing  $E_f/G_m$ . Thus, the maximum interfacial shear stresses according to the Kelly-Tyson and Cox models are only maximum values in the case of  $\alpha = 0$ . On the basis of these results, Chon and Sun suggest that if fiber failure is the composite failure mode, the matrix should be modified to reduce the ratio of  $E_f/G_m$ , but if failure is due to interfacial shear,  $E_f/G_m$  should be increased. In more recent work, FEAs of off-axis short-fiber composites, including the effects of fiber angle and fiber end geometry, were conducted by Sun and Wu [11].

Calculation of the off-axis strength of an aligned discontinuous fiber composite can be accomplished by considering the off-axis uniaxial loading

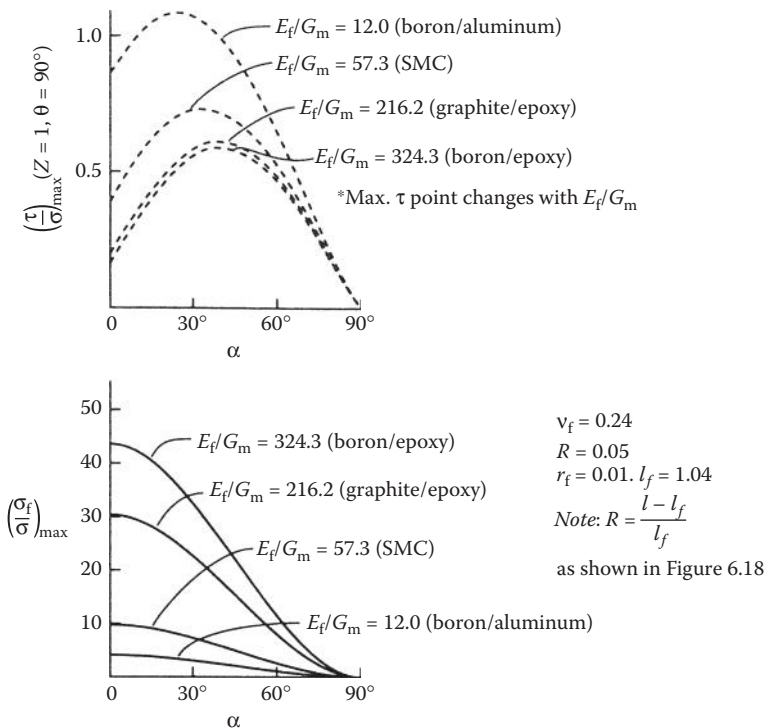
**FIGURE 6.21**

Variation of interfacial shear stress and fiber normal stress along the fiber for the Chon–Sun model at various off-axis angles. (From Chon, C. T. and Sun, C. T. 1980. *Journal of Materials Science*, 15, 931–938. Reprinted with permission from Chapman & Hall.)

situation in Figure 4.5, where the fibers are discontinuous. For example, if the corresponding off-axis stress state described in Equations 4.3 is substituted in the Tsai–Hill criterion (Equation 4.14), the result for the off-axis strength is

$$\sigma_x = \left[ \frac{\cos^4 \theta}{s_L^2} + \left( \frac{1}{s_{LT}^2} - \frac{1}{s_L^2} \right) \sin^2 \theta \cos^2 \theta + \frac{\sin^4 \theta}{s_T^2} \right]^{-1/2} \quad (6.31)$$

In the evaluation of such equations for discontinuous fiber composites, it is often assumed that only the longitudinal strength,  $s_L$ , depends on fiber length, and that the other strengths are essentially independent of fiber length. In this case, depending on whether the fiber length is less than or greater than the critical length, either Equation 6.14 or Equation 6.15 can be

**FIGURE 6.22**

Variation of maximum interfacial shear stress and maximum fiber stress with off-axis angle from the Chon-Sun model. (From Chon, C. T. and Sun, C. T. 1980. *Journal of Materials Science*, 15, 931–938. Reprinted with permission from Chapman & Hall.)

used to estimate  $s_L^{(+)}$ , while the other strengths can be estimated using the micromechanical models for continuous fiber composites described in Section 4.3.

### 6.3.2 Modulus Analysis

Elastic constants for the off-axis-aligned discontinuous fiber composite may be estimated by using equations developed earlier in this chapter and in Chapters 2 and 3. Following the procedure outlined by Sun et al. [19] and Suarez et al. [14], the Cox model (Equation 6.24) is used to find the longitudinal modulus along the 1-direction. The transverse modulus,  $E_2$ , the in-plane shear modulus,  $G_{12}$ , and the major Poisson's ratio,  $v_{12}$ , are assumed to be independent of fiber length [16,17] and are calculated using the micromechanics equations developed in Chapter 3. The off-axis modulus of elasticity,  $E_v$ , is then found by substituting the Cox modulus,  $E_{cl}$ , for  $E_1$  in the transformation equation (the first of Equation 2.40), along with the calculated values of  $E_2$ ,

$E_{12}$ ,  $v_{12}$ , and  $\theta$ . The other off-axis properties  $E_y$ ,  $G_{xy}$ , and  $v_{xy}$  are found by using a similar approach. The resulting set of equations is of the form

$$\begin{aligned} E_x &= f_1(E_{c1}, E_2, G_{12}, v_{12}, \theta) \\ E_y &= f_2(E_{c1}, E_2, G_{12}, v_{12}, \theta) \\ G_{xy} &= f_3(E_{c1}, E_2, G_{12}, v_{12}, \theta) \\ v_{xy} &= f_4(E_{c1}, E_2, G_{12}, v_{12}, \theta) \end{aligned} \quad (6.32)$$

A comparison of the predicted off-axis modulus,  $E_x$ , for graphite/epoxy with experimental values for various angles,  $\theta$ , is shown in Figure 6.23. It should be mentioned that the good agreement between theory and experiment seen in Figure 6.23 was not possible as long as the fibers were assumed to be isotropic. Once the orthotropic nature of the graphite fibers was taken into account (i.e.,  $E_{f1} \gg E_{f2}$ ), the agreement between theory and experiment improved significantly. The same analysis was used to generate a tridimensional plot of the off-axis modulus,  $E_x$ , versus the fiber aspect ratio and the fiber orientation, as shown in Figure 6.24. Due to the assumption that  $E_2$ ,  $G_{12}$ , and  $v_{12}$  are independent of the fiber aspect ratio,  $L/d$  has little effect on the calculated  $E_x$  for fiber orientations other than those near  $\theta = 0^\circ$ . As shown in the previous section, the fiber length required to attain the maximum composite stiffness at  $\theta = 0^\circ$  is quite small. Thus, the relatively low stiffness of practical short-fiber composites is more likely to be caused by the off-axis orientation of the fibers than by the short length of the fibers. Another important factor that should not be overlooked is the fiber volume fraction. In most short-fiber composites, the maximum fiber volume fraction is quite low due to processing limitations. That is, the viscosity of the fiber/resin

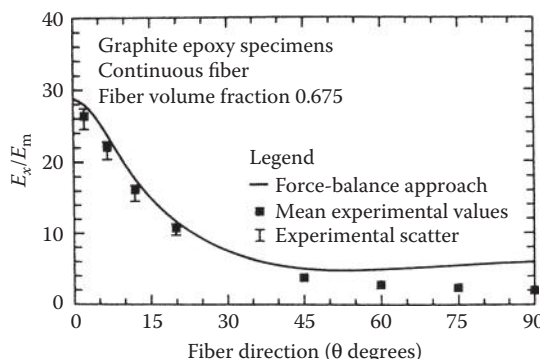
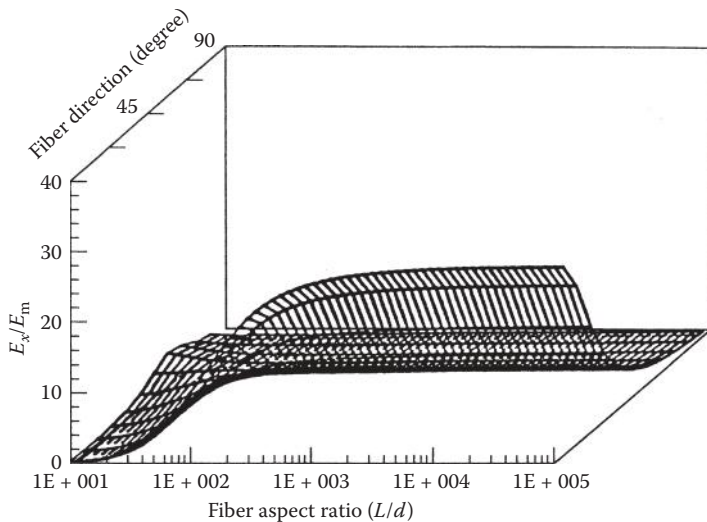


FIGURE 6.23

Comparison of predicted and measured off-axis modulus ratio,  $E_x/E_m$ , for graphite/epoxy. (From Suarez, S. A. et al. 1986. *Experimental Mechanics*, 26(2), 175–184. With permission.)

**FIGURE 6.24**

Tridimensional plot of  $E_x/E_m$  as a function of fiber aspect ratio and fiber orientation for graphite/epoxy. (From Suarez, S. A. et al. 1986. *Experimental Mechanics*, 26(2), 175–184. With permission.)

mixture must be kept below a certain limit for proper flow during the molding process. All these conclusions have important implications for the behavior of randomly oriented short-fiber composites, which are discussed in Section 6.4.

### Example 6.5

Set up the equations for predicting the off-axis tensile strength of an aligned discontinuous fiber composite based on the Maximum Strain criterion.

### SOLUTION

Refer to the solution for Example 4.4, which is for an off-axis continuous fiber composite. Based on the Maximum Strain criterion, the off-axis tensile strength is given by

$$\sigma_x = S_L^{(+)} / (\cos^2 \theta - v_{12} \sin^2 \theta) \text{ for longitudinal tensile failure when } 0 \leq \theta \leq \theta_1$$

$$\sigma_x = S_{LT} / (\sin \theta \cos \theta) \text{ for in-plane shear failure when } \theta_1 \leq \theta \leq \theta_2$$

$$\sigma_x = S_T^{(+)} / (\sin^2 \theta - v_{21} \cos^2 \theta) \text{ for transverse tensile failure when } \theta_2 \leq \theta \leq \pi/2$$

where  $\theta_1$  is the solution of

$$\frac{S_L^{(+)}}{\cos^2 \theta_1 - v_{12} \sin^2 \theta_1} = \frac{S_{LT}}{\sin \theta_1 \cos \theta_1}$$

and  $\theta_2$  is the solution of

$$\frac{S_{LT}}{\sin \theta_2 \cos \theta_2} = \frac{S_T^{(+)}}{\sin^2 \theta_2 - v_{21} \cos^2 \theta_2}$$

For the discontinuous aligned fiber composite,  $s_L^{(+)}$  is found by using either Equation 6.14 or Equation 6.15, depending on whether the fiber length is less than or greater than the critical length. The other strengths  $S_{LT}$  and  $s_T^{(+)}$  are assumed to be independent of fiber length, and are calculated from the corresponding micro-mechanics equations for strengths of continuous fiber composites in Section 4.3.

## 6.4 Randomly Oriented Discontinuous Fibers

If the fiber orientation in a composite is truly random in a 3D sense, the composite exhibits 3D isotropy. Such a situation is likely to exist when the fiber length,  $L$ , is much less than the thickness of the part,  $t$ , as shown in Figure 6.25a. Composites with low aspect ratio reinforcement such as whiskers, microfibers, and nanotubes generally fall into this category. However, in many short-fiber composite parts (e.g., panels made from sheet-molding compounds or resin transfer moldings), the fiber length is much greater than the thickness of the part, as shown in Figure 6.25b. In this case, fiber orientation in the thickness direction is not possible, and the material exhibits 2D isotropy or planar isotropy. The analysis of both types of materials will be discussed here, but the emphasis will be on the 2D case.

### 6.4.1 Stress and Strength Analysis

The use of geometric averaging techniques for analyzing randomly oriented fiber composites has been introduced in Example 2.6, and models for predicting strength and modulus of such composites are typically based on

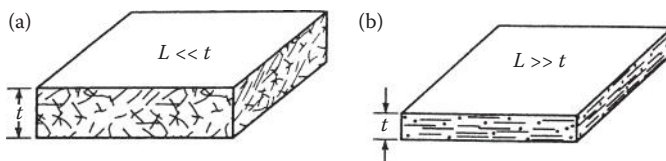


**FIGURE 6.25**

3D and 2D random orientations of fibers. (a) Fiber length is less than thickness of part, so fibers are randomly oriented in three dimensions. (b) Fiber length is greater than thickness of part, so fibers are randomly oriented in only two dimensions.

averaging. For example, Baxter [20] developed a model for predicting the strength of randomly oriented fiber-reinforced metal matrix composites by averaging the Tsai–Hill equation for off-axis strength (Equation 6.31) as

$$\tilde{\sigma}_x = \frac{\int_0^\pi \sigma_x d\theta}{\pi} = \frac{\int_0^{\pi/2} \sigma_x d\theta}{\pi/2} \quad (6.33)$$

Numerical integration was employed, since the integral could not be evaluated in closed form. The model was used to establish upper and lower limits of composite strength. The composite longitudinal strength was estimated from Equation 6.14 or Equation 6.15, and the other strengths in Equation 6.31 were estimated according to the most likely failure modes.

Lees [21] assumed that the angular dependence of the failure stress,  $\sigma_x$ , for such a material under uniaxial off-axis loading could be described by using the Maximum Stress Criterion. Lees also assumed that there are three failure mechanisms according to the Maximum Stress Criterion, each operating over a range of angles as follows [recall Equations 4.3 for uniaxial off-axis loading]:

$$\text{for } 0 \leq \theta \leq \theta_1, \quad \sigma_x = \frac{s_L^{(+)}}{\cos^2 \theta} \text{ (longitudinal tensile failure)}$$

$$\text{for } \theta_1 \leq \theta \leq \theta_2, \quad \sigma_x = \frac{s_{LT}}{\sin \theta \cos \theta} \text{ (interfacial shear failure)}$$

$$\text{for } \theta_2 \leq \theta \leq \frac{\pi}{2}, \quad \sigma_x = \frac{s_T^{(+)}}{\sin^2 \theta} \text{ (transverse tensile failure)}$$

where

$$\cot \theta_1 = \frac{s_L^{(+)}}{s_{LT}} \quad \text{and} \quad \tan \theta_2 = \frac{s_T^{(+)}}{s_{LT}}$$

With regard to the randomly oriented fiber composite, Lees assumed that the average strength over all angles is given by

$$\tilde{\sigma}_x = \frac{2}{\pi} \left\{ \int_0^{\theta_1} \frac{s_L^{(+)}}{\cos^2 \theta} d\theta + \int_{\theta_1}^{\theta_2} \frac{s_{LT}}{\sin \theta \cos \theta} d\theta + \int_{\theta_2}^{\pi/2} \frac{s_T^{(+)}}{\sin^2 \theta} d\theta \right\} \quad (6.34)$$

After integrating and using Equation 4.24 for  $s_L^{(+)}$  for continuous fibers, and then making some simplifying approximations, Lees found that

$$\tilde{\sigma}_x \approx \frac{2s_{LT}}{\pi} \left[ 1 + \frac{s_T^{(+)}}{s_{mf1}} + \ln \frac{s_T^{(+)s_{mf1}}}{s_{LT}^2} \right] \quad (6.35)$$

where  $s_{\text{mfl}}$  is the matrix stress corresponding to the fiber failure strain. The same approach was later taken by Chen [22], who included a strength efficiency factor,  $\psi$ , to account for discontinuous fibers and obtained the equation

$$\tilde{\sigma}_x = \frac{2s_{\text{LT}}}{\pi} \left[ 2 + \ln \frac{\psi s_L^{(+)} s_T^{(+)}}{s_{\text{LT}}^2} \right] \quad (6.36)$$

Lees and Chen both reported reasonable agreement of their predictions with experimental data. Although Lees [21] and Chen [22] did not propose the use of equations like Equations 6.14 and 6.15 to estimate the effects of fiber length on  $s_L^{(+)}$  in the above equations, it seems consistent with the approach of Baxter [20] and others.

Another approach suggested by Halpin and Kardos [23] is based on the assumption that the strength of a randomly oriented fiber composite is the same as the strength of a quasi-isotropic laminate of the same material. Quasi-isotropic laminates, which are laminates of certain stacking sequences that behave in a planar isotropic manner, will be discussed in Chapter 7 on laminates. Halpin and Kardos [23] reported that the quasi-isotropic laminate model with the Maximum Strain Criterion for lamina failure gave good agreement with experimental data for a glass–epoxy composite.

#### 6.4.2 Modulus Analysis

One major conclusion from Section 6.3.2 was that fiber orientation is more important than fiber length in the determination of off-axis elastic constants of unidirectional composites. Further support for this conclusion is provided by the observation that continuous fiber models give reasonably accurate predictions of elastic properties of randomly oriented fiber-reinforced composites. The concept of averaging the elastic constants over all possible orientations by integration was apparently introduced by Cox [2], who modeled paper as a planar mat of continuous fibers without matrix material. The Cox formulas for the averaged isotropic elastic constants of random arrays of fibers are given here for later reference, but they are not considered to be accurate enough for design use. For the 2D case,

$$\tilde{E} = \frac{E_f v_f}{3}, \quad \tilde{G} = \frac{E_f v_f}{8}, \quad \tilde{v} = \frac{1}{3} \quad (6.37)$$

and for the 3D case,

$$\tilde{E} = \frac{E_f v_f}{6}, \quad \tilde{G} = \frac{E_f v_f}{15}, \quad \tilde{v} = \frac{1}{4} \quad (6.38)$$

where

$\tilde{E}$  = averaged Young's modulus for the randomly oriented fiber composite

$\tilde{G}$  = averaged shear modulus for the randomly oriented fiber composite

$\tilde{\nu}$  = averaged Poisson's ratio for the randomly oriented fiber composite

Nielsen and Chen [24] used the averaging concept, along with micromechanics equations and transformation equations for a unidirectional continuous fiber-reinforced lamina, to analyze a planar isotropic composite. The geometrically averaged Young's modulus, which is assumed to be the same as the in-plane Young's modulus of the isotropic composite, is given by

$$\tilde{E} = \frac{\int_0^\pi E_x d\theta}{\int_0^\pi d\theta} \quad (6.39)$$

where the off-axis Young's modulus,  $E_x$ , is defined by the first of Equations 2.40, and the angle  $\theta$  is defined in Figure 2.11. Nielsen and Chen used a set of micromechanics equations for a unidirectional continuous fiber composite to calculate  $E_1$ ,  $E_2$ ,  $G_{12}$ , and  $\nu_{12}$ . Figure 6.26 shows that the averaged modulus for the randomly oriented fiber composite is much lower than the corresponding longitudinal modulus,  $E_1$ , for most practical composites. Since the analysis is based on a continuous fiber model, the predicted reduction in modulus is due to fiber orientation, and not to fiber length. The equation that Nielsen and Chen used for  $E_2$  was known to give values lower than measured values, and so the predictions of Equation 6.39 were also lower than the corresponding experimental values.

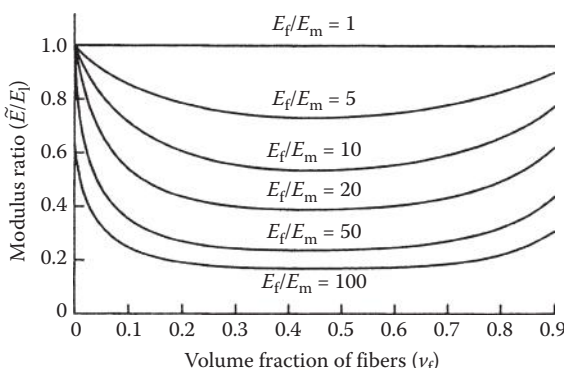


FIGURE 6.26

Dependence of modulus ratio,  $\tilde{E}/E_1$ , on fiber volume fraction for several values of  $E_f/E_m$  from Nielsen-Chen model. (From Nielsen, L. E. and Chen, P. E. 1968. *Journal of Materials*, 3(2), 352–358. Copyright ASTM. Reprinted with permission.)

The evaluation of Equation 6.39 requires the integration of the expression for  $E_x$  given by Equation 2.40, which is quite cumbersome. The integration is much simpler if the invariant forms of the transformed lamina stiffnesses are used. For example, the averaged value of the transformed lamina stiffness  $\bar{Q}_{11}$  is given by

$$\tilde{Q}_{11} = \frac{\int_0^\pi \bar{Q}_{11} d\theta}{\int_0^\pi d\theta} = \frac{\int_0^\pi [U_1 + U_2 \cos \theta + U_3 \cos 4\theta] d\theta}{\pi} = U_1 \quad (6.40)$$

Similarly,

$$\tilde{Q}_{22} = U_1, \quad \tilde{Q}_{12} = \tilde{Q}_{21} = U_4, \quad \tilde{Q}_{66} = \frac{(U_1 - U_4)}{2}, \quad \tilde{Q}_{16} = \tilde{Q}_{26} = 0$$

and the stress-strain relations for any set of axes  $x, y$  in the plane are

$$\begin{Bmatrix} \sigma_x \\ \sigma_y \\ \tau_{xy} \end{Bmatrix} = \begin{Bmatrix} U_1 & U_4 & 0 \\ U_4 & U_1 & 0 \\ 0 & 0 & (U_1 - U_4)/2 \end{Bmatrix} \begin{Bmatrix} \epsilon_x \\ \epsilon_y \\ \gamma_{xy} \end{Bmatrix} \quad (6.41)$$

Since this is an isotropic material, we can write

$$\begin{aligned} \tilde{Q}_{11} &= U_1 = \frac{\tilde{E}}{1 - \tilde{v}^2} = \tilde{Q}_{22} \\ \tilde{Q}_{12} &= U_4 = \frac{\tilde{v}\tilde{E}}{1 - \tilde{v}^2} \\ \tilde{Q}_{66} &= \tilde{G} = \frac{\tilde{E}}{2(1 + \tilde{v})} = \frac{U_1 - U_4}{2} \end{aligned} \quad (6.42)$$

Tsai and Pagano [25] and Halpin and Pagano [26] have obtained the same results by using invariant concepts along with quasi-isotropic laminate theory, which will be discussed in Chapter 7. Solving these equations for the isotropic engineering constants, we get

$$\begin{aligned} \tilde{E} &= \frac{(U_1 - U_4)(U_1 + U_4)}{U_1} \\ \tilde{G} &= \frac{U_1 - U_4}{2} \\ \tilde{v} &= \frac{U_4}{U_1} \end{aligned} \quad (6.43)$$

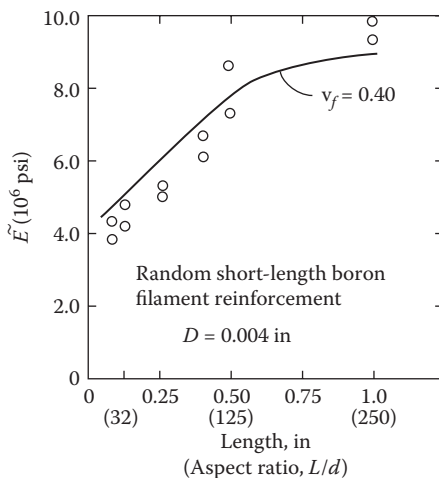
Using the equations relating the invariants in Equations 6.43 to the engineering constants  $E_1$ ,  $E_2$ ,  $G_{12}$ , and  $v_{12}$  for the orthotropic lamina (recall Equations 2.45 and 2.27), Tsai and Pagano [25] also developed the following approximate expressions:

$$\tilde{E} = \frac{3}{8}E_1 + \frac{5}{8}E_2, \quad \tilde{G} = \frac{1}{8}E_1 + \frac{1}{4}E_2 \quad (6.44)$$

These equations, along with the Halpin–Tsai equations for  $E_1$  and  $E_2$ , were used to estimate the elastic moduli of randomly oriented boron fiber-reinforced epoxy, and the results compare favorably with experimental results (Figure 6.27). Manera [27] also got good agreement with experimental results by using Equations 6.43 with a different set of micromechanics equations for  $E_1$ ,  $E_2$ ,  $G_{12}$ , and  $v_{12}$ .

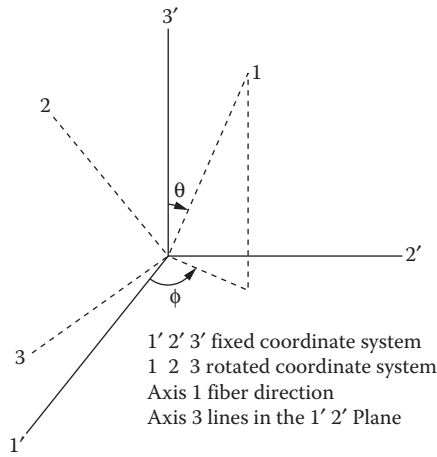
Christensen and Waals [28] also used the averaging approach to find the isotropic elastic constants for continuous fiber composites with 2D and 3D random fiber orientation. This appears to be the first published report of the analysis of a composite with 3D oriented fibers, although Cox [2] derived Equations 6.38 with regard to the case of fibers without matrix material. Only the 3D analysis of Christensen and Waals is summarized here, since the 2D analysis is quite similar to those that have already been discussed.

For the 3D Christensen–Waals analysis, the spherical coordinate system shown in Figure 6.28 is used. An orthotropic, transversely isotropic composite with fibers oriented along the 1 direction is subjected to an arbitrary normal



**FIGURE 6.27**

Dependence of Young's modulus of randomly oriented short-fiber boron/epoxy composite on fiber aspect ratio. Comparison of predictions from Halpin–Tsai equations and invariant expressions with experimental data. (From Halpin, J. C. and Pagano, N. J. 1969. *Journal of Composite Materials*, 3, 720–724. Reprinted with permission from Technomic Publishing Co.)

**FIGURE 6.28**

Spherical coordinates for 3D Christensen–Waals analysis. (From Christensen, R. M. and Waals, F. M. 1972. *Journal of Composite Materials*, 6, 518–532. Reprinted with permission of Technomic Publishing Co.)

strain such as  $\epsilon'_{33}$  along the  $3'$  direction. For the purpose of the analysis, the  $3$  axis is taken to be in the  $1'2'$  plane. The basic premise of the solution is that the resulting ratio of stress to strain  $\sigma'_{ij}/\epsilon'_{33}$  ( $i, j = 1, 2, 3$ ) for a random orientation of fibers can be found by calculating the average value of  $\sigma'_{ij}/\epsilon'_{33}$  over all possible orientations of the fiber direction ( $1$  axis) relative to the fixed  $x'_i$  axes. Using the 3D stress–strain relationships for a generally orthotropic, transversely isotropic material (i.e., the stiffness matrix of Equation 2.17 transformed to an arbitrary  $1'2'3'$  off-axis coordinate system), it can be shown that

$$\frac{\sigma'_{33}}{\epsilon'_{33}} = C_{11}\lambda_{31}^4 + (2C_{12} + 4C_{66})\lambda_{31}^2\lambda_{32}^2 + C_{22}\lambda_{32}^4 \quad (6.45)$$

and that

$$\begin{aligned} \frac{\sigma'_{22}}{\epsilon'_{33}} &= C_{11}\lambda_{31}^2\lambda_{21}^2 + C_{12}\left(\lambda_{32}^2\lambda_{21}^2 + \lambda_{31}^2\lambda_{22}^2 + \lambda_{31}^2\lambda_{23}^2\right) \\ &\quad + C_{22}\lambda_{32}^2\lambda_{22}^2 + 4C_{66}\lambda_{31}\lambda_{32}\lambda_{21}\lambda_{22} + C_{23}\lambda_{32}^2\lambda_{23}^2 \end{aligned} \quad (6.46)$$

where the direction cosines  $\lambda_{ij}$  are given by

$$\lambda_{ij} = \begin{bmatrix} \sin \theta \cos \phi & -\cos \theta \cos \phi & \sin \phi \\ \sin \theta \sin \phi & -\cos \theta \sin \phi & -\cos \phi \\ \cos \theta & \sin \theta & 0 \end{bmatrix} \quad (6.47)$$

Averaging over all possible orientations of the fiber direction, we have

$$\left. \frac{\sigma'_{ij}}{\epsilon'_{33}} \right|_{\text{Random}} = \frac{\int_0^\pi \int_0^\pi (\sigma'_{ij}/\epsilon'_{33}) \sin \theta d\theta d\phi}{\int_0^\pi \int_0^\pi \sin \theta d\theta d\phi} \quad (6.48)$$

After substituting Equation 6.45 into Equation 6.48, we get

$$\left. \frac{\sigma'_{33}}{\epsilon'_{33}} \right|_{\text{Random}} = \frac{1}{15} (3C_{11} + 4C_{12} + 8C_{22} + 8C_{23}) \quad (6.49)$$

For an equivalent homogeneous isotropic material, the corresponding ratio of stress to strain is

$$\frac{\sigma'_{33}}{\epsilon'_{33}} = \frac{\tilde{E}(1 - \tilde{\nu})}{(1 + \tilde{\nu})(1 - 2\tilde{\nu})} \quad (6.50)$$

Similarly, after substituting Equation 6.46 into Equation 6.48, we get

$$\left. \frac{\sigma'_{22}}{\epsilon'_{33}} \right|_{\text{Random}} = \frac{1}{15} (C_{11} + 8C_{12} + C_{22} - 4C_{66} + 5C_{23}) \quad (6.51)$$

and the corresponding ratio of stress to strain for an equivalent homogeneous isotropic material is

$$\frac{\sigma'_{22}}{\epsilon'_{33}} = \frac{\tilde{\nu}\tilde{E}}{(1 + \tilde{\nu})(1 - 2\tilde{\nu})} \quad (6.52)$$

Equating the ratio in Equation 6.49 to that in Equation 6.50, then equating the ratio in Equation 6.51 to that in Equation 6.52, and solving the two resulting equations simultaneously for the effective isotropic engineering constants, Christensen and Waals found that

$$\tilde{E} = \frac{\left[ E_1 + (4v_{12}^2 + 8v_{12} + 4)K_{23} \right] \left[ E_1 + (4v_{12}^2 - 4v_{12} + 1)K_{23} + 6(G_{12} + G_{23}) \right]}{3 \left[ 2E_1 + (8v_{12}^2 + 12v_{12} + 7)K_{23} + 2(G_{12} + G_{23}) \right]} \quad (6.53)$$

and

$$\tilde{\nu} = \frac{E_1 + (4v_{12}^2 + 16v_{12} + 6)K_{23} - 4(G_{12} + G_{23})}{4E_1 + (16v_{12}^2 + 24v_{12} + 14)K_{23} + 4(G_{12} + G_{23})} \quad (6.54)$$

where  $K_{23}$  is the plane strain bulk modulus for dilatation in the 2–3 plane with  $\epsilon_{11} = 0$ , and the other properties are defined in Chapter 2. Christensen and Waals used the previously developed micromechanics equations by Hashin [29,30] and Hill [31] to calculate the five independent engineering constants  $E_1$ ,  $v_{12}$ ,  $G_{12}$ ,  $G_{23}$ , and  $K_{23}$ , which appear in Equations 6.53 and 6.54. Predictions from Equation 6.53 for a glass–epoxy composite are shown in Figure 6.29, along with the rule of mixtures prediction from Equation 3.23 and the Cox prediction from Equation 6.38. The prediction from the Cox model is well below that of the Christensen–Waals model, and the rule of mixtures prediction is much too high.

Using the same averaging technique, Christensen and Waals also developed a set of equations analogous to Equations 6.53 and 6.54 for the 2D case. The results are [23]:

$$\tilde{E} = \frac{1}{u_1} (u_1^2 - u_2^2) \quad (6.55)$$

and

$$\tilde{v} = \frac{u_2}{u_1} \quad (6.56)$$

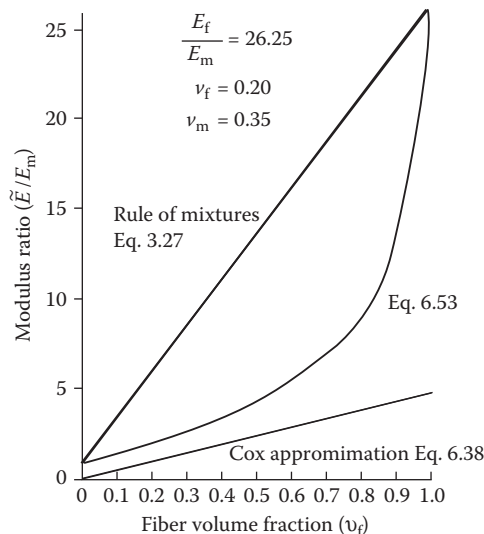


**FIGURE 6.29**

Comparison of Christensen–Waals 3D analysis for Young's modulus of randomly oriented fiber composite with rule of mixtures and Cox approximation for a glass/epoxy composite. (From Christensen, R. M. and Waals, F. M. 1972. *Journal of Composite Materials*, 6, 518–532. Reprinted with permission from Technomic Publishing Co.)

where

$$\begin{aligned} u_1 &= \frac{3}{8}E_1 + \frac{G_{12}}{2} + \frac{(3 + 2v_{12} + 3v_{12}^2)G_{23}K_{23}}{2(G_{23} + K_{23})} \\ u_2 &= \frac{1}{8}E_1 - \frac{G_{12}}{2} + \frac{(1 + 6v_{12} + v_{12}^2)G_{23}K_{23}}{2(G_{23} + K_{23})} \end{aligned} \quad (6.57)$$

The results from Equations 6.55 through 6.57 for a glass-polystyrene composite are shown in Figure 6.30. The Christensen-Waals model is seen to give much better agreement with the measurements than either the Cox model or the rule of mixtures, although none of the models takes into account the fiber length. Chang and Weng [32] also obtained good agreement with experimental results for glass/polyester sheet-molding compounds by using Equations 6.55 through 6.57. Christensen later presented simplified versions of these equations based on an asymptotic expansion [33,34].

Weng and Sun [35] used the Christensen-Waals equations along with micro-mechanics equations, which were modified to account for the effect of fiber length. The effect of fiber length was modeled by using a so-called "fictitious fiber," which included the effect of matrix material at the ends of the fiber in the RVE shown in Figure 6.2a. The effects of varying stresses along the fiber were not accounted for; however, as it was assumed that the stresses were equal in the fiber and matrix portions of the fictitious fiber. The equation for the effective modulus of the fictitious fiber is analogous to Equation 6.28 for

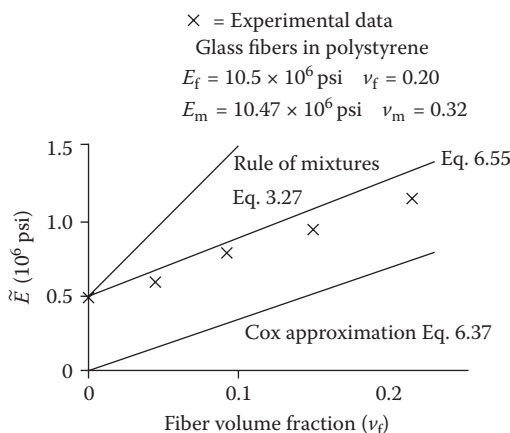


**FIGURE 6.30**

Comparison of Christensen-Waals 2D analysis for Young's modulus of randomly oriented fiber composite with rule of mixtures and Cox approximation for a glass/polystyrene composite. (From Christensen, R. M. and Waals, F. M. 1972. *Journal of Composite Materials*, 6, 518–532. Reprinted with permission from Technomic Publishing Co.)

the modified Cox model, except that the stress distribution along the fiber is assumed to be uniform. Figure 6.31 shows a comparison of the predictions of the modified Christensen–Waals theory with the original Christensen–Waals theory, the rule of mixtures, the Halpin–Tsai equations, and experimental data. For the glass/polyester sheet-molding compound material used, the effect of fiber length is apparently not very great, as the predictions of modified and original Christensen–Waals theories are almost the same. Both theories give predictions that are in good agreement with the experimental data.

The effects of fiber length and nonuniform stress distribution along the discontinuous fiber were accounted for by Sun et al. [36], who developed equations for the elastic moduli of 2D randomly oriented, short-fiber composites as part of a study of vibration damping properties. A modified Cox model was used to determine  $E_1$ , while the other lamina properties were assumed to be independent of fiber length. The modified Cox model in this case is of the form

$$E_{MC1} = E_{f1} \left[ \frac{1 - \tanh(\beta L/2)}{\beta L/2} \right] v_f \alpha + E_m v_m \gamma \quad (6.58)$$

where  $\alpha$  and  $\gamma$  are strain magnification factors, which are determined from an FEA. The modified Cox model for  $E_1$ , along with the rule of mixtures

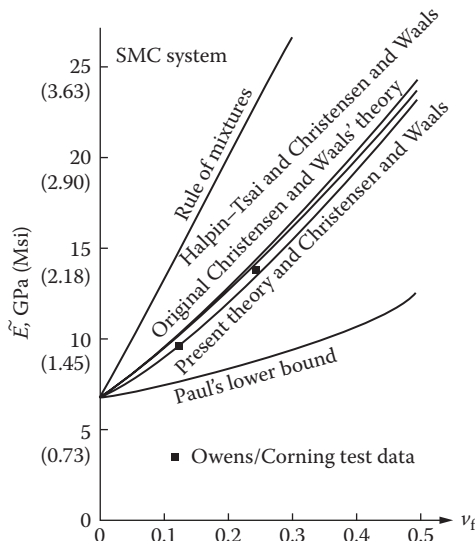


**FIGURE 6.31**

Comparison of various theories for prediction of Young's modulus of randomly oriented chopped glass/polyester sheet molding compound. (From Weng, G. J. and Sun, C. T. 1979. In Tsai, S. W., ed., *Composite Materials: Testing and Design (Fifth Conference)*, ASTM STP 674. American Society for Testing and Materials, Philadelphia, PA, pp. 149–162. Copyright ASTM. Reprinted with permission.)

(Equation 3.45) for  $v_{12}$  and the Halpin-Tsai equations (Equations 3.63 and 3.64) for  $E_2$  and  $G_{12}$ , are used in transformation equations of the form described in Equations 6.32, which are then used in Equations 6.43 to determine the averaged isotropic engineering constants for the randomly oriented fiber composite. A tridimensional plot of the Young's modulus versus the fiber aspect ratio,  $L/d$ , and the ratio  $E_f/E_m$  is shown in Figure 6.32. It is seen that high  $E_f/E_m$  and high  $L/d$  are required in order to have a high composite modulus. As with the aligned discontinuous case, the fiber aspect ratio required to attain maximum stiffness for given fiber and matrix materials is quite low.

### Example 6.6

A carbon–epoxy composite with randomly oriented short fibers is made of the same constituent materials with the same fiber volume fraction as the material described in Examples 3.1, 3.5, and 4.5. Assuming that the in-plane shear strength  $s_{LT} = 60$  MPa, and that the fiber length is much greater than the thickness of the material, estimate the Young's modulus, shear modulus, Poisson's ratio, and tensile strength of this composite.

### SOLUTION

From Equations 6.44, the Young's modulus is approximately

$$\tilde{E} = \frac{3}{8} E_1 + \frac{5}{8} E_2 = \frac{3}{8}(113) + \frac{5}{8}(5.65) = 45.9 \text{ GPa}$$

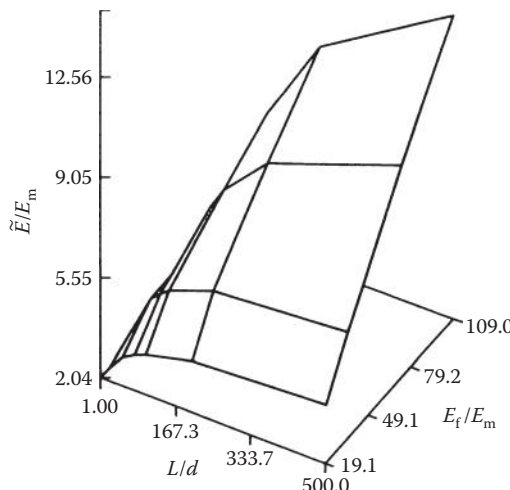


**FIGURE 6.32**

Tridimensional plot of  $\tilde{E}/E_m$  as a function of  $L/d$  and  $E_f/E_m$  for a randomly oriented short-fiber composite. (From Sun, C. T., Wu, J. K., and Gibson, R. F. 1985. *Journal of Reinforced Plastics and Composites*, 4, 262–272. Reprinted with permission from Technomic Publishing Co.)

and the shear modulus is approximately

$$\tilde{G} = \frac{1}{8}E_1 + \frac{1}{4}E_2 = \frac{1}{8}(113) + \frac{1}{4}(5.65) = 15.54 \text{ GPa}$$

which means that Poisson's ratio is

$$\tilde{\nu} = \frac{\tilde{E}}{2\tilde{G}} - 1 = \frac{45.9}{2(15.54)} - 1 = 0.47$$

From Equation 6.35, the tensile strength is approximately

$$\tilde{\sigma}_x = \frac{2s_{LT}}{\pi} \left[ 1 + \frac{s_{Tf}^{(+)}}{s_{mf1}} + \ln \frac{s_{Tf}^{(+)} s_{mf1}}{s_{LT}^2} \right] = \frac{2(60)}{\pi} \left[ 1 + \frac{66.9}{37.95} + \ln \frac{66.9(37.95)}{(60)^2} \right] = 92.2 \text{ MPa}$$

Note that the isotropic Young's modulus for the randomly oriented composite is much greater than the transverse modulus but less than half the longitudinal modulus of the corresponding orthotropic lamina. Likewise, the isotropic strength is greater than the orthotropic transverse strength but well below the orthotropic longitudinal strength. It is also important to remember that these predictions are based on randomly oriented continuous fibers, so that the differences between the isotropic properties and the orthotropic properties are due to fiber orientation, and not to fiber length.

### Example 6.7

Determine the Young's modulus of a randomly oriented fiber composite if the unidirectional form of the composite has an off-axis Young's modulus that can be described by an equation of the form

$$E_x(\theta) = E_2 + (E_1 - E_2) \left[ 1 - \left( \frac{2\theta}{\pi} \right)^{1/3} \right]$$

where  $\theta$  is the fiber angle in radians and  $E_1$  and  $E_2$  are the longitudinal and transverse Young's moduli, respectively, of the unidirectional composite.

### SOLUTION

The Young's modulus of the randomly oriented fiber composite, averaged over all angles, is

$$\tilde{E} = \frac{2}{\pi} \int_0^{\pi/2} E_x(\theta) d\theta = \frac{2}{\pi} \int_0^{\pi/2} \left\{ E_2 + (E_1 - E_2) \left[ 1 - \left( \frac{2\theta}{\pi} \right)^{1/3} \right] \right\} d\theta = 0.25E_1 + 0.75E_2$$

If, say,  $E_2 = 0.1E_1$  for carbon/epoxy composite, then

$$\tilde{E} = 0.25E_1 + 0.75(0.1E_1) = 0.325E_1 \text{ or } 3.25E_2$$

These results again reflect the magnitude of the reduction in stiffness that can be expected because of fiber orientation effects alone, since the fiber length has not been considered in this analysis.

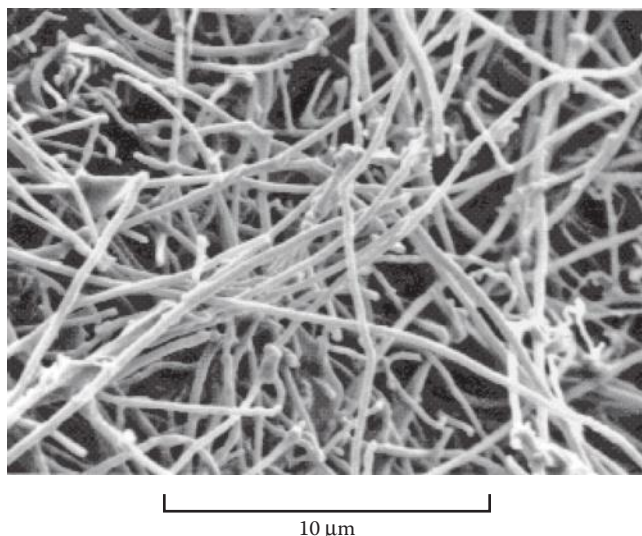
---

## 6.5 Nanofibers and Nanotubes

The development of nanofibers and nanotubes has played a major role in the recent nanotechnology revolution, and the use of these materials as reinforcements in composites has received particular attention. With dimensions in the nanometer range, nanofibers have solid cylindrical shapes and nanotubes have hollow tubular geometries. Although aspect ratios  $L/d$  may range up into thousands, they are both generally considered to be discontinuous in nature, and so it is particularly appropriate to discuss them in this chapter. There has been intense interest in CNTs since they were discovered in 1991 by Iijima [37], and the number of publications on CNTs and CNT-reinforced composite materials has grown very quickly since that time. Several review articles on the mechanical behavior of CNTs have appeared [38,39], and a special issue of a leading composites journal was dedicated to modeling and characterization of nanostructured materials [40]. CNTs are available in single-wall (SWNT) or multiwalled (MWNT) configurations, and the geometrical arrangement of carbon atoms in the nanotubes can be described as being either zigzag or armchair [38,39].

Microscopic images of carbon nanofibers (CNFs) and CNTs in various polymer matrices are shown in Figure 6.33 from Ref. [41] and Figure 6.34 from Ref. [42], respectively, while typical geometrical and mechanical properties of nanofibers and nanotubes are listed in Table 6.1, which is partially taken from Ref. [43].

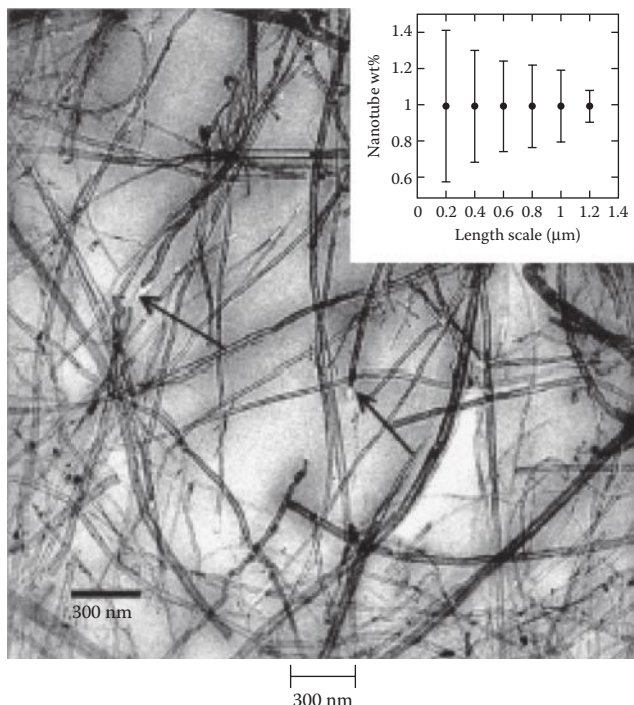
From Figures 6.33 and 6.34 and Table 6.1, it is clear that two key geometrical features must be accounted for in the development of micromechanical models for nanocomposites reinforced with nanofibers and/or nanotubes. Due to their microscopic dimensions by comparison with typical thicknesses of composite structures, nanofibers or nanotubes will almost certainly have random orientations in all three dimensions within the composite as in Figure 6.25a, and so the resulting nanocomposite will be macroscopically isotropic. Nanofibers and nanotubes exhibit significant waviness, but all the previously discussed micromechanics models as in Figures 6.2, 6.16, and 6.18 have been based on the assumption of straight fiber reinforcement.

**FIGURE 6.33**

Scanning electron microscope (SEM) image of vapor-grown CNFs in a polypropylene matrix. (From Tibbetts, G. G. and McHugh, J. J. 1999. *Journal of Materials Research*, 14(7), 2871–2880. With permission.)

### 6.5.1 Stress and Strength Analysis

Models for predicting the strength of nanocomposites with randomly oriented nanofibers or nanotubes are not as well developed as those for predicting elastic modulus. Tibbetts and McHugh [41] presented experimental and analytical results for randomly oriented CNF-reinforced polypropylene and nylon composites. Strength predictions were based on the averaging method of Baxter [20], which was described in Section 6.4.1. Nanofibers were assumed to have lengths less than the critical length, so Equation 6.14 was used to estimate the longitudinal composite strength as input to the Tsai–Hill equation (Equation 6.31) before performing the averaging in Equation 6.33, but the effect of nanofiber waviness was not considered. The authors concluded that the experimental results for as-grown nanofibers were generally disappointing due to inadequate infiltration of the fiber clumps by the matrix resin during the injection molding of the specimens, but ball milling of the nanofibers reduced the size of the clumps, resulting in significant improvement in the properties, as did etching of the surfaces of the nanofibers. Experimental strength data generally fell between the predictions of 1D and 3D models based on Baxter's approach, but since nanofiber waviness was not included in the models, it is difficult to draw conclusions from comparisons of predictions with measurements.

**FIGURE 6.34**

Transmission electron microscope image of MWNTs in a polystyrene matrix. (Reprinted with permission from [Qian, D. et al. Load transfer and deformation mechanisms in carbon nanotube-polystyrene composites. *Applied Physics Letters*, 76(20), 2868–2870.] Copyright [2000], American Institute of Physics.)

### 6.5.2 Modulus Analysis

Micromechanics models for the elastic moduli of nanocomposites, which include the effects of both 3D random orientation and waviness of the reinforcement, have been developed by Fisher et al. [44–46] and by Anumandla and Gibson [47,48]. The approach of Fisher et al. [44–46] is based on 3D finite

**TABLE 6.1**

Geometrical and Mechanical Properties of Typical CNFs and Nanotubes

Material	Diameter (nm)	Length (nm)	Young's Modulus (GPa)	Tensile Strength (GPa)
Vapor-grown CNFs	100–200 <sup>a</sup>	30,000–100,000 <sup>a</sup>	400–600 <sup>a</sup>	2.7–7.0 <sup>a</sup>
SWNT	~1.3 <sup>b</sup>	500–40,000 <sup>b</sup>	320–1470 <sup>c</sup>	13–52 <sup>c</sup>

<sup>a</sup> Nanofiber geometrical and mechanical properties from Applied Sciences, Inc., Cedarville, OH.

<sup>b</sup> Nanotube geometrical properties from Helix Material Solutions, Inc., Richardson, TX.

<sup>c</sup> Nanotube mechanical properties from Yu, M.-F., Files, B., Arepalli, S., and Ruoff, R. S. 2000. *Physical Review Letters*, 84(24), 5552–5555. With permission.

element models, whereas the model of Anumandla and Gibson [47,48] is an approximate closed-form solution. Only the latter approach is summarized in the following.

The Anumandla–Gibson approach [47,48] consists of a combination of the waviness models of Chan and Wang [49] and Hsiao and Daniel [50] for locally orthotropic materials, the Chamis micromechanics equations ([14] of Chapter 3) for predicting the elastic constants of the locally orthotropic material, and the Christensen–Waals model [28], which accounts for the 3D random orientation of the fibers (or in this case, nanotubes). The wavy fiber-reinforced composite is divided into segments along its length, each of which is locally orthotropic but with off-axis orientation. The strains are averaged over one wavelength along the loading direction for uniaxial loading, and the effective Young's modulus is determined from the ratio of applied stress to resulting average strains. The RVEs are shown in Figure 6.35, where the waviness and orientation of the nanotube are accounted for in RVE1, and the overall length of RVE2 includes the matrix material between fibers.

The nanotube waviness is characterized by the waviness factor,

$$w = \frac{A}{L_{NT}} \quad (6.59)$$

where  $A$  is the amplitude of the waviness,  $L_{NT}$  is the nanotube length, and coordinates  $x$  and  $z$ , describing the waviness, are defined in Figure 6.35 and Equation 6.60:

$$z = A \sin\left(\frac{2\pi x}{L_{NT}}\right) \quad (6.60)$$

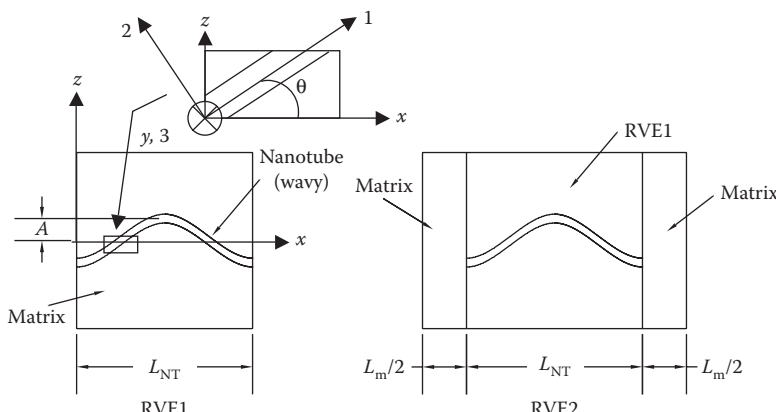


**FIGURE 6.35**

RVEs for Anumandla–Gibson model. (From Anumandla, V. and Gibson, R. F. 2006. *Composites Part A: Applied Science and Manufacturing* 37(12), 2178–2185. With permission.)

The effective Young's modulus,  $E_x$ , of RVE1, with uniform waviness of the embedded nanotube, is assumed to be the same as that of an element in a locally orthotropic lamina containing wavy fibers as described by Hsiao and Daniel [50]. Following this approach, the transformed compliances of an off-axis orthotropic lamina are averaged over one wavelength of fiber waviness, and the definition of an effective Young's modulus is used to find [50]

$$E_x = \frac{\sigma_x}{\bar{\epsilon}_x} = \frac{1}{S_{11}I_1 + (2S_{12} + S_{66})I_3 + S_{22}I_5} = E_{\text{RVE1}} \quad (6.61)$$

where  $\sigma_x$  is the applied uniaxial stress,  $\bar{\epsilon}_x$  is the resulting average strain,  $S_{11}$ ,  $S_{12}$ ,  $S_{22}$ , and  $S_{66}$  are the locally orthotropic compliances referred to as the principal material coordinates, and  $I_1$ ,  $I_3$ , and  $I_5$  are functions that depend only on the waviness factor. The locally orthotropic compliances are estimated from micromechanics using the Chamis equations ([14] of Chapter 3). The effective elastic modulus  $\tilde{E}$  ( $= E_{3D-\text{RVE1}}$ ) for the 3D random orientation of the nanotubes is assumed to be the same as the modulus for a fiber-reinforced composite containing fibers that are randomly oriented in all three dimensions as given by Christensen and Waals [28]. For the purpose of the present discussion, the Christensen–Waals analysis described in Section 6.4. is modified by replacing the (1,2,3), and (1',2',3') coordinate systems in Figure 6.28 by the  $(x,y,z)$  and  $(x',y',z')$  coordinate systems, respectively. Then according to the modified Christensen–Waals analysis, an orthotropic, transversely isotropic composite with nanotube waviness along the  $x$ -direction is subjected to an arbitrary normal strain such as  $\epsilon'_{zz}$  along the  $z'$ -direction (the  $z$ -axis is taken to be in the  $x'y'$ -plane for the purpose of the analysis). The resulting ratio of stress to strain,  $\sigma'_{ij}/\epsilon'_{zz}$  ( $i, j = x, y, z$ ), for random orientation of fibers is found by calculating the average value of  $\sigma'_{ij}/\epsilon'_{zz}$  over all possible orientations of the nanotube waviness direction ( $x$ -axis) relative to the fixed  $x'_i$ -axis. Equation 6.62 indicates the averaging over all possible orientations of the wavy nanotube

$$\left. \frac{\sigma'_{ij}}{\epsilon'_{zz}} \right|_{\text{Random}} = \frac{\int_0^\pi \int_0^\pi \frac{\sigma'_{ij}}{\epsilon'_{zz}} \sin \theta d\theta d\phi}{\int_0^\pi \int_0^\pi \sin \theta d\theta d\phi} = \frac{1}{2\pi} \int_0^\pi \int_0^\pi \frac{\sigma'_{ij}}{\epsilon'_{zz}} \sin \theta d\theta d\phi \quad (6.62)$$

where the angles  $\theta$  and  $\phi$  are defined in Figure 6.28. The equations resulting from Equation 6.62 on substituting the 3D stress–strain relationships for a generally orthotropic transversely isotropic material and solving simultaneously with the stress–strain relations for an equivalent homogenous isotropic

material yield the effective composite elastic modulus  $\tilde{E}$  ( $= E_{3D\text{-RVE}1}$ ) for the 3D random orientation of the nanotube as

$$\begin{aligned}\tilde{E} &= \frac{\left[ E_x + (4v_{xz}^2 + 8v_{xz} + 4)K_{zy} \right] \left[ E_x + (4v_{xz}^2 - 4v_{xz} + 1)K_{zy} + 6(G_{xz} + G_{zy}) \right]}{3 \left[ 2E_x + (8v_{xz}^2 + 12v_{xz} + 7)K_{zy} + 2(G_{xz} + G_{zy}) \right]} \\ &= E_{3D\text{-RVE}1}\end{aligned}\quad (6.63)$$

where  $E_x$  ( $= E_{RVE1}$ ) is the effective elastic modulus of RVE1 according to Equation 6.61,  $K_{zy}$  is the plane bulk modulus for dilatation in the  $y$ - $z$ -plane with  $\epsilon_{xx} = 0$ , and all other properties in Equation 6.63 are for RVE1 in accordance with those defined in Ref. [50]. Note that Equation 6.63 is the same as Equation 6.53, except for the substitution of coordinates described above. An expression for the effective elastic modulus of RVE2 with 3D random orientation of nanotubes,  $E_{3D\text{-RVE}2}$ , is approximated by means of another inverse rule of mixtures for the series arrangement in RVE2 (Figure 6.35) as

$$\frac{1}{E_{3D\text{-RVE}2}} = \frac{1}{E_{3D\text{-RVE}1}} \left( \frac{L_{NT}}{L_m + L_{NT}} \right) + \frac{1}{E_m} \left( \frac{L_m}{L_m + L_{NT}} \right) \quad (6.64)$$

where  $E_{3D\text{-RVE}1}$  is the effective elastic modulus of RVE1 for 3D random orientation of the nanotubes according to Equation 6.63.

Figure 6.36 shows a comparison of the predictions of  $E_{3D\text{-RVE}2}$  from Equation 6.64 with experimental results on multiwalled nanotube (MWNT)/

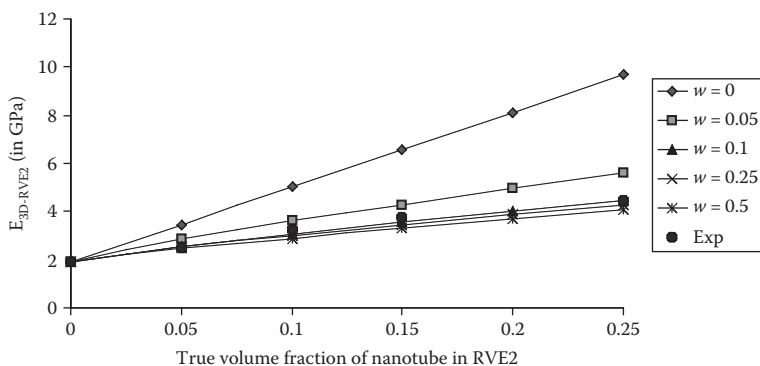
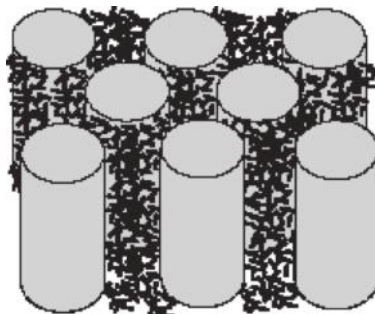


**FIGURE 6.36**

Comparison of experimental modulus data for MWNT/polystyrene composite. (From Andrews et al. 2002. *Micromolecular Materials Engineering*, 287(6), 395–403. With micromechanics predictions from Equation 6.64; Reprinted from *Composites Part A: Applied Science and Manufacturing*, 37(12), Anumandla, V. and Gibson, R. F., A comprehensive closed form micromechanics model for estimating the elastic modulus of nanotube-reinforced composites, 2178–2185, Copyright (2006), with permission from Elsevier.)

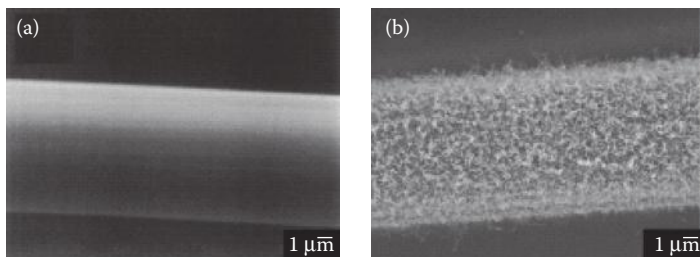
polystyrene composites published by Andrews et al. [51]. In the predictions, the modulus of the polystyrene matrix was assumed to be 1.9 GPa, the local modulus of the nanotube was assumed to be 1 TPa, and the nanotube volume fraction in RVE2 was varied by assuming  $L_{NT}/L_m$  ratios of 0, 1, 2, 3, 4, and 5. It is seen that if waviness is neglected (i.e.,  $w = 0$ ), Equation 6.64 significantly overpredicts the experimental data, but as waviness increases, the predicted modulus is reduced accordingly. For waviness factors lying within the range of 0.075–0.25, the predictions are in best agreement with the published experimental results. These values of waviness seem quite reasonable in view of microscopic images such as the one in Figure 6.34.

Nanofibers and nanotubes can be used not only as the principal reinforcement in composites, but as a third phase in composites consisting of conventional fiber reinforcement. Such a nanocomposite matrix material can improve the matrix-dominated properties of a conventional continuous fiber composite, such as compressive strength. A nanocomposite matrix material typically has a higher modulus than the plain polymer matrix, thus increasing the lateral support for the continuous fibers, increasing the buckling load, and improving the compressive strength of the conventional composite. For example, Vlasveld et al. [52] developed hybrid composites consisting of conventional glass or carbon fibers (CFs) in a nanocomposite matrix (Figure 6.37), where the nanocomposite matrix was made of polyamide 6 polymer reinforced with synthetic mica-layered silica nanoparticles. The nanocomposite matrix led to significant increases in flexural strength, which was dominated by fiber microbuckling on the compression side of the specimens. The effect was particularly significant at elevated temperatures. Thostenson et al. [53] developed a hybrid multiscale composite by growing CNTs directly on the surfaces of conventional CFs, which were then combined with a conventional epoxy matrix. Figure 6.38 shows micrographs of the CF before and after nanotube growth.



**FIGURE 6.37**

Nanoparticle reinforcement of the matrix in a conventional continuous fiber composite. (Reprinted from *Polymer*, 46, Vlasveld, D. P. N., Bersee, H. E. N., and Picken, S. J., Nanocomposite matrix for increased fibre composite strength, 10269–10278, Copyright (2005), with permission from Elsevier.)

**FIGURE 6.38**

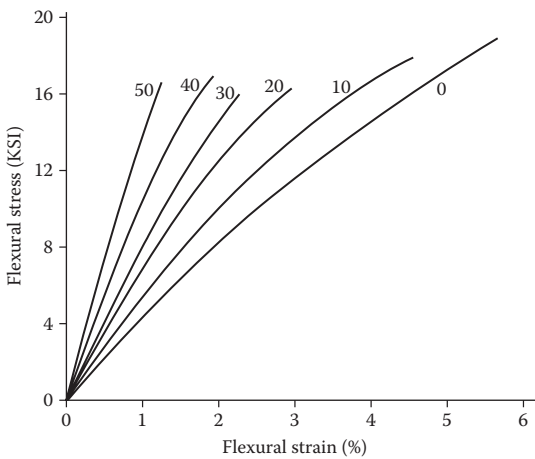
SEM micrographs of CFs (a) before and (b) after CNT growth on the fiber surface. (Reprinted with permission from [Thostenson, E. T. et al. Carbon nanotube/carbon fiber hybrid multiscale composite. *Journal of Applied Physics*, 91(9), 6034–6037] Copyright [2002], American Institute of Physics.)

## 6.6 Particulates

Particulate-reinforced composites (Figure 6.1d) are typically less expensive and more quickly processed than fiber-reinforced composites, but due to their relatively low mechanical properties, they are used mainly in nonstructural applications. In fact, particles are often used as nonstructural fillers rather than as reinforcements. However, as shown later in Section 6.7, nanometer (nm)-scale particles, or nanoparticles, are increasingly used to enhance the properties of conventional fiber-reinforced composites in a new class of composites known as hybrid multiscale composites.

This section mainly deals with conventional micron ( $\mu\text{m}$ )-scale particulate reinforcements in polymer matrix materials. Typically, as shown in Figure 6.39, when the volume fraction of conventional micron-scale particles is increased, the composite modulus increases, but both the corresponding elongation and strength of the composite decrease. In Figure 6.39, Sahu and Broutman [54] show experimental stress-strain curves from flexural tests of  $30\ \mu\text{m}$  diameter spherical glass bead-reinforced epoxy composites of various bead volume fractions, where the glass beads have been treated with a coupling agent to promote interfacial adhesion. In the same paper, it was shown that when the glass beads were treated with a commercial mold release to prevent interfacial adhesion, the composite modulus did not change much with increasing bead volume fraction, but the elongation and strength both decreased significantly.

This section briefly summarizes several analytical approaches to predicting the strength and modulus of conventional particle-reinforced composites as functions of the particle volume fraction. Particle-reinforced composites are assumed to be isotropic. Accordingly, each composite is assumed to have a single composite strength and a single composite Young's modulus.

**FIGURE 6.39**

Flexural stress–strain curves for glass bead-reinforced epoxy composites of various bead volume fractions. (Sahu, S. and Broutman, L. J., Mechanical properties of particulate composites. *Polymer Engineering and Science*, 1972, 12(2), 91–100. Copyright Wiley-VCH Verlag GmbH & Co. KGaA. Reproduced with permission.)

### 6.6.1 Stress and Strength Analysis

As seen in Figure 6.39, the presence of particles in a polymer matrix material typically reduces the elongation and strength of the matrix material. An important contributing factor to this phenomenon is the stress and strain concentration in the matrix around the particles. So one approximate analytical approach is analogous to the model for the transverse strength of a fiber-reinforced composite, as discussed in Section 4.3.2 (see Figure 4.16 and Equations 4.35 through 4.39). There are two problems with this approach, however. One problem is that the analysis in Section 4.3.2 is a 2D analysis, whereas the particulate composite contains 3D particles such as spheres. The second problem is that Equations 4.35 through 4.39 are based on linear elastic behavior, but as shown in Figure 6.39, the stress–strain behavior of particulate composites is typically nonlinear. In order to avoid these problems, several publications have presented semiempirical equations for estimating the strength of particulate composites. For example, Nicolais and Narkis [55] suggested that the yield strength of a spherical particle-reinforced composite with no adhesion between particles and matrix can be adequately predicted by

$$S_{yc} = S_{ym}(1 - 1.21v_p^{2/3}) \quad (6.65)$$

where  $S_{ym}$  is the yield strength of the matrix material and  $v_p$  is the volume fraction of particles. The coefficient 1.21 and the exponent 2/3 for  $v_p$  were selected so as to insure that  $S_{yc}$  decreases with increasing  $v_p$ , that  $S_{yc} = S_{ym}$  when  $v_p = 0$ , and that  $S_{yc} = 0$  when  $v_p = 0.74$ . The particle volume fraction  $v_p = 0.74$  corresponds to the maximum packing fraction for spherical particles of the

same size in a hexagonal close-packed arrangement, in which case the particles are all in direct contact with each other [56]. Subsequently, Liang and Li [57] and Liang [58] have suggested that Equation 6.65 can be modified to include particle/matrix interfacial adhesion by adding a term to account for the interfacial bonding angle,  $\theta$ , which characterizes interfacial adhesion as in

$$S_{yc} = S_{ym}(1 - 1.21 \sin^2 \theta v_p^{2/3}) \quad (6.66)$$

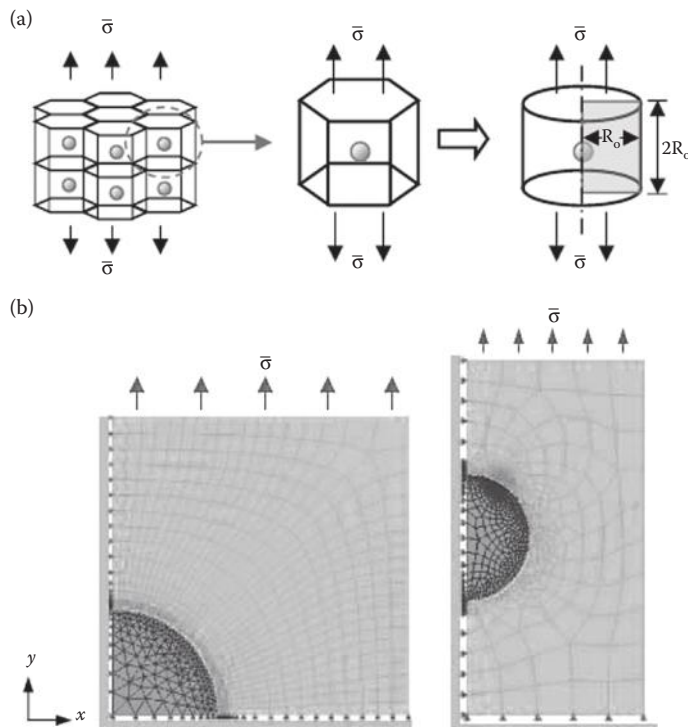
where  $\theta = 0^\circ$  corresponds to good adhesion and  $\theta = 90^\circ$  corresponds to poor bonding. The best fits to experimental data for different composites were found to be  $\theta = 70^\circ$  for solid spherical glass beads in polypropylene [57] and  $\theta = 40^\circ$  for hollow glass beads in polypropylene [58]. The glass beads were surface treated with a silane coupling agent in both cases to promote adhesion.

Finite element micromechanics models have been employed to predict the strength of particle-reinforced composites. For example, Sahu and Broutman [54] used a quarter domain model with an embedded spherical particle based on axisymmetric ring elements in combination with the von Mises failure criterion (recall Equation 4.40) to predict failure of the matrix. Due to stress concentration around the particle, the predicted failure occurred at the particle/matrix interface, but a detailed study of the effects of interface bonding on the composite strength was not conducted. More recently, Cho et al. [59] used axisymmetric finite element models (Figure 6.40) of spherical particle-reinforced composites and fracture mechanics to study the effects of the interface debonding angle and particle size on composite fracture behavior.

Related work has been done on the effects of particle shape [60], particle size [59,61] and particle agglomeration [61]. As previously shown in Figure 1.3, the surface area-to-volume ratio is greatest when the particle aspect ratio is either large (fiber) or small (platelet), so a spherical particle is at a comparative disadvantage with regard to the interfacial area available for stress transfer per unit volume. Tensile strength improves as the particle size is reduced, and this has motivated recent studies of the strength of nanocomposites [59]. However, an important limitation on the use of nanoparticles for strengthening composites is that particle agglomeration during processing becomes more of a problem as the particle volume fraction is increased, and agglomeration tends to reduce the composite strength [61].

### 6.6.2 Modulus Analysis

As shown in Figure 6.39, the Young's modulus of a particle-reinforced composite increases with increasing particle volume fraction, assuming that the particle modulus is greater than the matrix modulus. There are obvious geometric similarities between a plane passing through a particle-reinforced composite (Figure 6.1d) and a plane passing through the transverse direction in a unidirectional fiber-reinforced composite (Figure 4.16a), so it is not surprising that analytical models for the Young's modulus of a

**FIGURE 6.40**

Finite element models for spherical particle-reinforced composite. (a) Development of axisymmetric RVE and (b) finite element models of RVE with half and full axisymmetric planes. (Reprinted from *Composites Science and Technology*, 66, Cho, J., Joshi, M. S., and Sun, C. T., Effect of inclusion size on mechanical properties of polymeric composites with micro and nano particles, 1941–1952. Copyright (2006), with permission from Elsevier.)

particle composite,  $E_c$ , are often similar to models for the transverse Young's modulus of a unidirectional fiber composite,  $E_2$ . Recall from Section 3.2.2 that the most widely used semiempirical model for  $E_2$  is based on the Halpin-Tsai equations (Equations 3.63 and 3.64). Katz and Milewski [56] and Nielsen and Landel [61] suggested the following generalizations of the Halpin-Tsai equations for the Young's modulus of a particulate composite

$$\frac{E_c}{E_m} = \frac{1 + ABv_p}{1 - B\psi v_p} \quad (6.67)$$

where

$$A = k_E - 1 \quad B = \frac{(E_p/E_m) - 1}{(E_p/E_m) + A} \quad \psi = 1 + \left( \frac{1 - v_{p\max}}{v_{p\max}^2} \right) v_p$$

$E_c$  is the Young's modulus of the composite

$E_p$  is the Young's modulus of the particle

$E_m$  is the Young's modulus of the matrix

$k_E$  is the Einstein coefficient

$v_p$  is the particle volume fraction

$v_{p\max}$  is the maximum particle packing fraction

It was also suggested that, with the appropriate substitutions of input properties, equations of the same form can be used to estimate the shear modulus or the bulk modulus. Recall from Chapter 3 that Paul ([29] in Chapter 3) used variational methods to derive the upper and lower bounds on the moduli of a particle composite or the transverse moduli of a fiber composite. The upper bound turned out to be the rule of mixtures (Equation 3.27) and the lower bound turned out to be the inverse rule of mixtures (Equation 3.40). Richard [62] measured the Young's moduli of glass microsphere-reinforced polyester composites having various particle volume fractions, and the results are compared here with analytical predictions from Equations 3.27, 3.40, and 6.67 in Figure 6.41. The predicted values in all three equations were based on input moduli  $E_p = 10.2 \times 10^6$  psi,  $E_m = 0.25 \times 10^6$  psi [62], Einstein coefficient  $k_E = 2.5$ , and maximum particle packing fraction  $v_{p\max} = 0.6$  for randomly loose packed spheres [56]. It is seen in Figure 6.41 that the experimental values agree closely with the predicted values from the Halpin-Tsai equations, but are well below the predicted upper bound, and slightly above the predicted lower bound. The Halpin-Tsai prediction is fairly sensitive to the assumed value of  $v_{p\max}$ , which in turn depends on the particle shape and packing arrangement [56,61]. It is important to note that little improvement is seen in the composite modulus for  $v_p$  less than about 0.2.

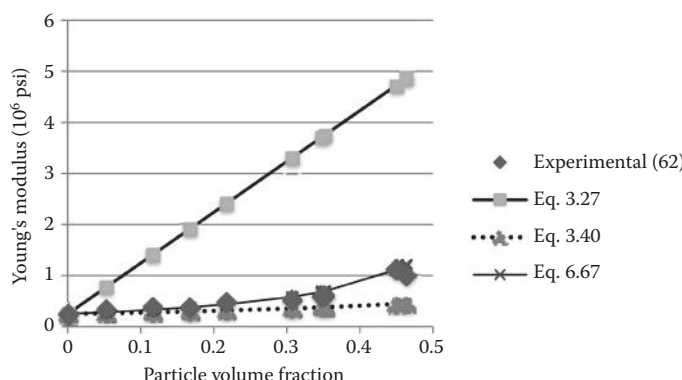


**FIGURE 6.41**

Comparison of predicted and measured values of Young's modulus for glass microsphere-reinforced polyester composites of various particle volume fractions.

Recent research has shown that as the particle size is reduced to the nanometer range, unexpected improvements in the composite modulus may occur. For example, Cho et al. [59] have shown experimentally that the Young's modulus of a particulate composite is essentially independent of particle size if the particle is of micron or larger size, but if the particle size is reduced to the nanometer range, the Young's modulus increases with decreasing particle size. Later, Cho and Sun [63] employed molecular dynamics simulations to show that this phenomenon could be explained by the creation of a layer of dense polymer matrix material around the nanoparticle if the strength of the polymer–nanoparticle interaction is greater than or equal to that of the polymer–polymer interaction. Finite element micromechanics models such as the ones illustrated in Figure 6.40 have also been used to study the dependence of the Young's modulus on the particle size. For example, Boutaleb et al. [64] used finite element models to show that the development of a particle/matrix interphase region around the nanoparticle may be responsible for the improved modulus of the nanocomposite. Further research on this important phenomenon is warranted.

### Example 6.8

A particle-reinforced composite has its reinforcement in a simple cubic array of spherical particles as shown in Figure 6.42. Determine (a) the relationship between the particle center-to-center spacing,  $s$ , the particle diameter,  $d$ , and the particle volume fraction,  $v_p$ , (b) the maximum particle packing fraction,  $v_{p\max}$ , and (c) the yield strength and the Young's modulus for a composite having the maximum particle volume fraction  $v_p = v_{p\max}$  and constituent material properties  $E_p = 10.2 \times 10^6$  psi,  $E_m = 0.25 \times 10^6$  psi,  $S_{ym} = 5 \times 10^3$  psi and bonding angle  $\theta = 45^\circ$ .

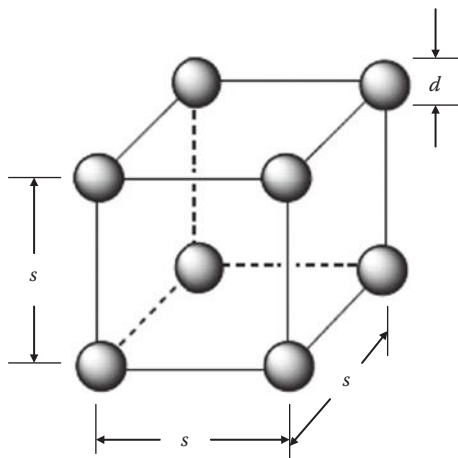


**FIGURE 6.42**  
Simple cubic array of spherical particles.

### SOLUTION

- Following the analogous derivation for the square packing array of fibers in Section 3.1, the volume of a spherical particle is  $V_p = (\pi/6)d^3$ . The volume of the eight corners of the spherical particles that are enclosed in the cube having sides of equal length  $s$  is then  $V_p = (V_p/8)8 = V_p$  and the particle volume fraction in the cube is  $v_p = V_p/s^3 = (\pi/6)(d/s)^3$ .
- The maximum particle packing fraction is equal to  $v_p$  when  $s = d$ , or  $v_{p\max} = \pi/6 = 0.5236$ .
- When the particle volume fraction  $v_p = 0.5236$ , the yield strength is  $S_{yc} = S_{ym}(1 - 1.21 \sin^2 \theta v_p^{2/3}) = 5000(1 - 1.21(\sin^2 45^\circ)0.5236^{2/3}) = 3034$  psi and the Young's modulus is found from

$$A = k_E - 1 = 2.5 - 1 = 1.5, B = \frac{(E_p/E_m) - 1}{(E_p/E_m) + A} = \frac{(10.2/0.25) - 1}{(10.2/0.25) + 1.5} = 0.9409$$

$$\Psi = 1 + \left( \frac{1 - v_{p\max}}{v_{p\max}^2} \right) v_p = 1 + \left( \frac{1 - 0.5236}{0.5236^2} \right) 0.5236 = 1.9098$$

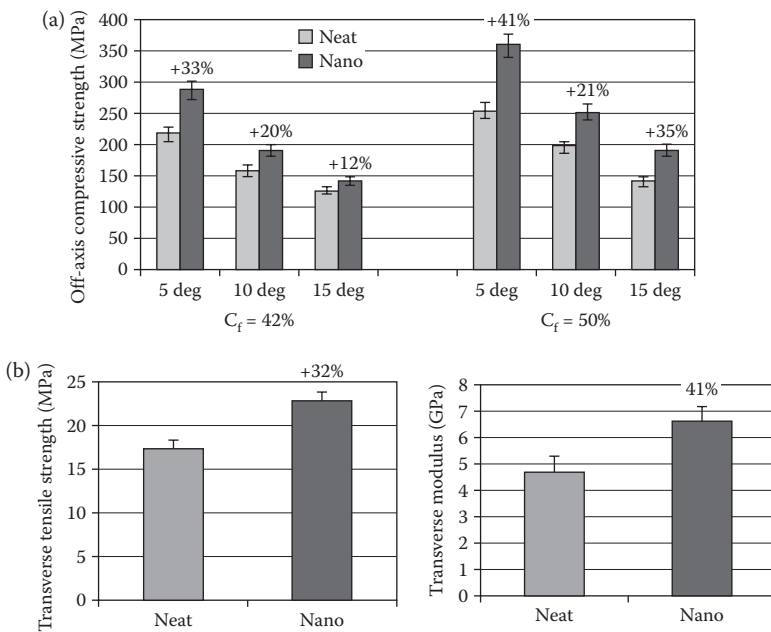
$$\frac{E_c}{E_m} = \frac{1 + ABv_p}{1 - B\Psi v_p} = \frac{1 + 1.5(0.9409)(0.5236)}{1 - 0.9409(1.9098)(0.5236)} = 29.4$$

$$E_c = 29.4 E_m = 29.4(0.25 \times 10^6) = 7.35 \times 10^6 \text{ psi}$$

## 6.7 Hybrid Multiscale Reinforcements

Recent research has shown that significant improvements of multiple properties in conventional composites can be achieved by using new hybrid multiscale reinforcements which incorporate nanoscale reinforcements as well as conventional micron-scale fiber or particle reinforcements (Figure 6.1e). For example, while fiber-dominated properties (i.e., longitudinal tensile strength and elastic modulus) of conventional unidirectional polymer composites with micron size fiber reinforcements are excellent, the corresponding matrix-dominated transverse tensile strength, transverse modulus and longitudinal compressive strength properties are often poor. However, these traditionally poor properties can be significantly improved by (a) replacing the neat resin polymer matrix with a nanocomposite matrix (see Figure 6.37), and/or by (b) growing nanoreinforcements like CNTs on the surface of the fibers (see Figure 6.38).

In one example of approach (a), Uddin and Sun [65] reported that when a silica nanoparticle-enhanced epoxy was used as the matrix material in a unidirectional E-glass/epoxy composite, the off-axis compressive strength

**FIGURE 6.43**

Improvement of mechanical properties of conventional unidirectional E-glass/epoxy composites by using silica nanoparticle-enhanced epoxy matrix. (a) Off-axis compressive strength and (b) transverse tensile strength and transverse modulus. (Reprinted from *Composites Science and Technology*, 68(7–8), Uddin, M. F. and Sun, C. T., Improved dispersion and mechanical properties of hybrid nanocomposites, 1637–1643. Copyright (2008), with permission from Elsevier.)

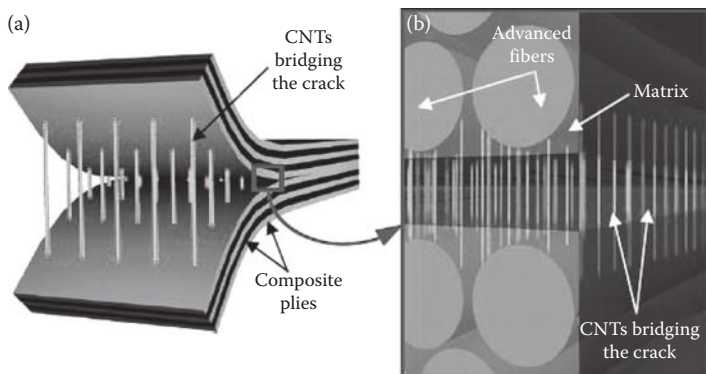
(Figure 6.43a) and the transverse tensile strength and transverse modulus (Figure 6.43b) were all simultaneously and significantly improved in comparison with the composites having a neat epoxy matrix.

Minimization of particle agglomeration and resulting improved dispersion of silica nanoparticles in the epoxy matrix due to the use of a sol-gel process based on the use of organosilicasol (colloidal silica in organic solvent) is believed to be the primary reason for these improvements. More recent research by the same authors extended the approach to hybrid multi-scale composites containing not only the silica nanoparticles from the sol-gel process but alumina nanoparticles and CNFs in an epoxy matrix [66]. It was shown that simultaneous improvements of at least 30% in modulus, strength, and strain at break are possible with several types of these hybrid nanocomposites. Similarly, Liu et al. [67] and Zhang et al. [68] found that Young's modulus, tensile strength and fracture toughness of epoxy all simultaneously improved with the addition of sol-gel-formed nanosilica particles, and that the dispersion of the particles was excellent. Manjunatha et al. [69] observed that the addition of 10 wt% sol-gel-formed nanosilica to the epoxy matrix resulted in simultaneous improvements of 4.4% in tensile strength, 7.4% in

tensile modulus and a factor of 2–3 in tensile fatigue life of a glass fabric-reinforced epoxy composite. The presence of the nanoparticles was believed to suppress matrix cracking and reduce delamination growth rate, thus improving the fatigue life.

Since hybrid multiscale composites typically have reinforcement sizes ranging from the micron scale to the nanoscale, it is essential to understand the effects of particle size on the resulting composite properties. As previously mentioned, important observations regarding such effects were reported by Cho et al. [59], who measured modulus and strength of vinyl ester polymer matrix composites containing spherical alumina particles or glass beads, with particle sizes ranging from 0.5 mm down to 15 nm. It was found that the Young's modulus was not affected by varying particle sizes in the micron range, but as the particle size was reduced in the nanorange, the Young's modulus increased with decreasing particle size. The tensile strength increased with decreasing particle sizes in both micron and nanoranges as long as particle agglomeration was avoided. Cho and Sun [63] later used molecular dynamics simulation to show that if the polymer-nanoparticle interaction strength is greater than the polymer-polymer interaction strength, the polymer density near the polymer-nanoparticle interface and the Young's modulus of the nanocomposite both increase significantly with reduced particle size. More research is needed about particle size effects on both structural and nonstructural properties of nanocomposites and hybrid multiscale composites. This is particularly true for analytical modeling, since most of the publications to date involve experimental work.

Approach (b) which involves the growth of nanotubes on the surfaces of micron-sized fibers has also been the subject of numerous investigations. Thostenson et al. [53] grew CNTs on the surface of CFs using chemical vapor deposition (CVD), and then conducted single fiber fragmentation tests of the modified CFs in an epoxy matrix to determine the fiber/matrix interfacial shear strength. It was found that the interfacial shear strength of the modified CFs was 15% greater than that of the baseline CFs. Veedu et al. [70] also used CVD to grow aligned CNT forests perpendicular to the surface of 2D woven SiC fabric cloth consisting of micron-sized SiC fibers. The fabrics were then infiltrated with epoxy resin and stacked to form a 3D composite. Compared with the baseline composite, the 3D composite was found to exhibit simultaneous and significant improvements in the flexural modulus, the flexural strength, the flexural toughness, the CTE, the thermal conductivity, and the electrical conductivity. This is a true multifunctional composite combining structural and nonstructural functions. Further studies and applications of aligned CNT forests to conventional fiber composites have been reported by Wardle and his colleagues [71–75], who focused on the use of the aligned CNT forests to improve interlaminar strength and toughness. These are major concerns about conventional composite laminates because of the weak matrix resin-rich regions that exist between the composite laminae. As shown in Figure 6.44, vertically aligned CNT forests can bridge and

**FIGURE 6.44**

Use of aligned CNT forests to strengthen interlaminar region in conventional fiber-reinforced composite laminates. (a) Vertically aligned CNTs placed between two plies of a laminated composite and (b) close-up of the crack, showing vertically aligned CNTs bridging the crack between the two plies. (Reprinted from *Composites Part A: Applied Science and Manufacturing*, 39, Garcia, E. J., Wardle, B. L., and Hart, A. J., Joining prepreg composite interfaces with aligned carbon nanotubes, 1065–1070. Copyright (2008), with permission from Elsevier.)

strengthen this interlaminar region [72]. The so-called “fuzzy fiber” (CNTs grown on CFs) concept applied to composite laminates can provide both interlaminar and intralaminar reinforcement.

As indicated earlier in Section 1.4, hybrid multiscale reinforcements have not only resulted in significant and simultaneous improvements in many structural properties, but they have also opened up many new possibilities for the development of multifunctional composites. Among the most important nonstructural functions made possible by hybrid multiscale reinforcements are electrical and thermal conductivity, sensing and actuation, energy harvesting/storage, self-healing capability, electromagnetic interference shielding, recyclability, and biodegradability. Recent publications related to the mechanics of multifunctional composite materials and structures have been reviewed by Gibson [76].

Finally, since nanoparticles or other nanoreinforcements play such an important role in hybrid multiscale composites, it is appropriate to mention an experimental observation that has important implications for analytical modeling of the behavior of these materials. In some cases, a so-called “interphase” region develops at the reinforcement/matrix interface (see Figure 3.22) due to either a chemical reaction between the materials or partial immobilization of the polymer matrix due to mechanical interactions with the reinforcements at the interface. The presence of this interphase region essentially enlarges the region of influence of the reinforcement, leading to an “effective volume fraction” of reinforcement that is larger than the actual volume fraction of reinforcement. There is experimental evidence that this effect is greater for nanoreinforcements than for microreinforcements. For

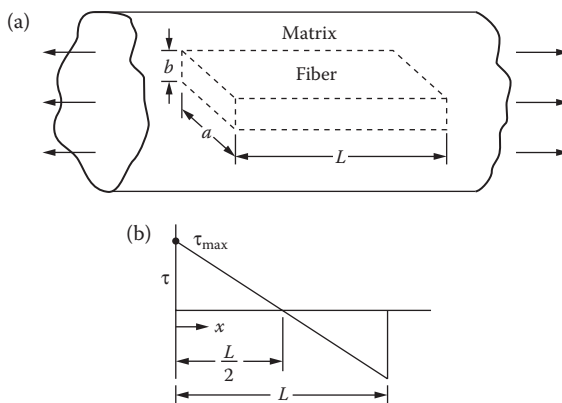
example, for a spherical particle and its interphase having the dimensions shown in Figure 3.22, it can be shown that the ratio of the effective particle volume fraction to the actual particle volume fraction is given by

$$\frac{v_{\text{eff}}}{v_{\text{act}}} = \left(1 + \frac{\Delta R}{R}\right)^3 \quad (6.68)$$

where  $R = d_f/2$  is the particle radius and  $\Delta R = (d_i - d_f)/2$  is the interphase thickness. Experimental evidence suggests that, as the particle radius  $R$  is reduced, the ratio  $\Delta R/R$  increases, causing a corresponding increase in the ratio  $v_{\text{eff}}/v_{\text{act}}$ . For example, Zhang et al. [77] have reported that for nanosilica/epoxy,  $\Delta R/R$  was in the range 0.22–0.84, which is much larger than the corresponding range of 0.02–0.07 for similar microparticle-filled composites. This obviously has important implications for accurate prediction of nanocomposite properties, and the reader is encouraged to consult current journal publications for further developments.

## PROBLEMS

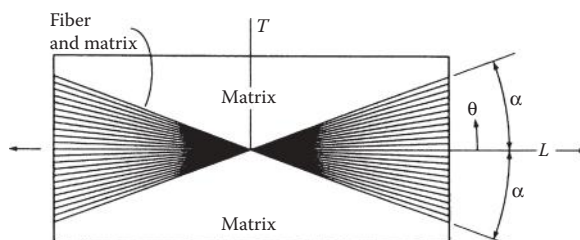
1. A short-fiber composite is to be modeled using the RVE in Figure 6.2b. Assuming that the matrix is rigid-plastic in shear but that both the fiber and matrix are elastic in extension, develop an equation for the longitudinal modulus of the RVE. What values of the longitudinal modulus does the model give as the fiber length becomes—very large or very small?
2. Using the result from Problem 6.1, develop an expression for the longitudinal modulus of the RVE shown in Figure 6.2a that includes the effect of the matrix material at the fiber ends.
3. A carbon/epoxy single fiber test specimen is subjected to a uniaxial tensile stress that is increased until the fiber breaks up into pieces having a length of 0.625 mm. If the fiber has a diameter of 0.01 mm, a longitudinal modulus of 240 GPa, and an ultimate tensile strength of 2.5 GPa, what is the interfacial shear strength of the specimen? If the composite longitudinal modulus is 80 GPa, what applied composite stress is required to produce the condition above?
4. A linear elastic fiber of rectangular cross-section is embedded in a linear elastic matrix material, and the composite is subjected to a uniaxial stress as shown in Figure 6.45a. The interfacial shear stress distribution along the fiber is to be approximated by a linear function, as shown in Figure 6.45b. Determine the fiber length,  $L$ , that is required to develop the ultimate tensile stress,  $s_u^{(+)}$ , at the midpoint of the fiber. Neglect the stress transmitted across the ends of the fiber.
5. A short-fiber composite is made from boron fibers of length 0.125 in. (3.175 mm) and diameter 0.0056 in. (0.142 mm) randomly oriented in a HM epoxy matrix with a fiber volume fraction of 0.4. Using the fiber and matrix properties in Table 3.1 and Table 3.2,

**FIGURE 6.45**

(a) Fiber with rectangular cross section embedded in matrix. (b) Interfacial shear stress distribution along the fiber shown in (a).

respectively, estimate the modulus of elasticity for the composite. Compare the modulus for the randomly oriented short-fiber composite with the longitudinal and transverse moduli of an orthotropically aligned discontinuous fiber lamina of the same material.

6. Express the isotropic moduli  $\tilde{E}$  and  $\tilde{G}$  of a randomly oriented fiber composite in Equations 6.43 in terms of the orthotropic lamina stiffnesses  $Q_{ij}$ .
7. Determine the isotropic moduli  $\tilde{E}$  and  $\tilde{G}$  for a composite consisting of randomly oriented T300 CFs in a 934 epoxy matrix if the fibers are long enough to be considered continuous. Use the properties in Table 2.2. Compare the values of  $\tilde{E}$  and  $\tilde{G}$  calculated from the invariant expressions (Equations 6.43) with those calculated from the approximate expressions in Equations 6.44.
8. In order to reduce material costs, a composite panel is to be made by placing fibers in the matrix material in an X-pattern of  $\pm\alpha$  as shown in Figure 6.46, instead of randomly distributing the fibers over all angles. The X-pattern composite is to be designed so that it has at least 90% of the stiffness of the randomly oriented fiber composite

**FIGURE 6.46**

Composite panel with fibers arranged in X-pattern.

along the longitudinal ( $L$ ) axis. From tensile tests of a *unidirectional* composite consisting of the same fiber and matrix materials and the same fiber volume fraction, it is found that the off-axis Young's modulus of the composite can be described by the equation

$$E_x(\theta) = 100 - 90\sin\theta \text{ (GPa)} \quad (0 \leq \theta \leq \pi/2)$$

whereas the Young's modulus of the matrix material is  $E_m = 3.5$  GPa. Determine the angle  $\alpha$  in Figure 6.46 such that the longitudinal Young's modulus of the X-pattern composite is equal to 90% of the Young's modulus of the randomly oriented fiber composite.

9. Determine the CTE for a randomly oriented fiber composite in terms of the longitudinal and transverse coefficients of thermal expansion  $\alpha_1$  and  $\alpha_2$  of the corresponding unidirectional composite lamina.
10. Using micromechanics and the Tsai–Hill criterion, set up the equation for the averaged isotropic tensile strength for a randomly oriented short-fiber composite. The equation should be in terms of fiber and matrix properties and volume fractions and the angle  $\theta$ .
11. The RVE for an aligned discontinuous fiber composite without matrix material at its ends is shown in Figure 6.4. Assume that when the RVE is loaded along the fiber direction, the interfacial shear stress distribution is given by

$$\tau = \frac{2\tau_{\max}}{L} \left( \frac{L}{2} - x \right)$$

and the fiber tensile stress is given by

$$\sigma_f = \frac{4\sigma_{f\max}x(L-x)}{L^2}$$

where  $L$  = fiber length,  $x$  = distance from the left end of RVE,  $\tau_{\max}$  = maximum interfacial shear stress, and  $\sigma_{f\max}$  = maximum fiber tensile normal stress.

- a. Sketch the distributions of  $\tau$  and  $\sigma_f$  along the length of the fiber.
- b. Neglecting the stress transmitted across the ends of the fiber, derive the relationship between  $\tau_{\max}$  and  $\sigma_{f\max}$ .
- c. If the interfacial shear strength is about the same as the fiber tensile strength, and the fiber aspect ratio  $L/d$  is very large (say  $L/d > 1000$ ), will the most likely mode of failure be interfacial shear failure or fiber tensile failure?
12. For the RVE in Figure 6.4, assume that the fiber length is greater than the ineffective length, and that the distribution of the fiber tensile normal stress is given by

$$\sigma_f = \frac{4\sigma_{f\max}x(L_i-x)}{L_i^2} \quad \text{for } 0 \leq x \leq \frac{L_i}{2}$$

$$\sigma_f = \sigma_{f\max} \quad \text{for } \frac{L_i}{2} \leq x \leq \frac{L}{2}$$

- a. Determine the expression for the fiber/matrix interfacial stress,  $\tau$ , and plot its distribution along the fiber length.
- b. Determine the magnitude and location of the maximum interfacial shear stress,  $\tau_{\max}$ , and show it on the shear stress distribution from part (a).
13. Using the Maximum Strain Criterion and the appropriate micromechanics equations, set up the equation for predicting the averaged isotropic strength of a randomly oriented short-fiber-reinforced composite. You may assume that the matrix failure strain is greater than the fiber failure strain. Your answer should be given in terms of the appropriate fiber and matrix properties and volume fractions and trigonometric functions of the fiber orientation angle  $\theta$ . It is not necessary to solve the equation.
14. The off-axis Young's modulus for a particular unidirectional fiber-reinforced orthotropic composite lamina is given by

$$E_x = E_1 - (E_1 - E_2) \sin \theta$$

where  $\theta$  is the lamina orientation in radians,  $E_1$  is the longitudinal Young's modulus of the lamina, and  $E_2$  is the transverse Young's modulus of the lamina. (a) For the material described above, find the equation for the Young's modulus of the composite if the fibers are randomly oriented with respect to  $\theta$ . Express your answer in terms of  $E_1$  and  $E_2$ . Derive your own equation and do not use the Tsai-Pagano equation (Equation 6.44). (b) For the equation derived in part (a), what would be the appropriate micromechanics equations to use in the derived equation if the fibers are continuous? (c) for the equation derived in part (a), what would be the appropriate micromechanics equations to use in the derived equation if the fibers are discontinuous?

15. Set up the equations for predicting the averaged isotropic shear modulus of a randomly oriented short-fiber composite. Your answer should be in terms of the fiber and matrix properties and volume fractions and trigonometric functions of the fiber orientation angle,  $\theta$ . It is not necessary to solve the equation.
16. Using the Tsai-Hill criterion and the appropriate micromechanics equations, set up the equation for predicting the averaged isotropic shear strength for a randomly oriented short-fiber composite. Your answer should be in terms of the fiber and matrix properties and volume fractions and trigonometric functions of the fiber orientation angle,  $\theta$ . It is not necessary to solve the equation.

## References

1. Kelly, A. and Tyson, W. R. 1965. Tensile properties of fibre reinforced metals: Copper/tungsten and copper/molybdenum. *Journal of the Mechanics and Physics of Solids*, 13, 329–350.

2. Cox, H. L. 1952. The elasticity and strength of paper and other fibrous materials. *British Journal of Applied Physics*, 3, 72–79.
3. Rosen, B. W. 1987. Composite materials analysis and design, in Reinhart, T. J., ed., *Engineered Materials Handbook*, Vol. 1, *Composites*, Sec. 4, pp. 173–281. ASM International, Materials Park, OH.
4. Agarwal, B. D. and Broutman, L. J. 1990. *Analysis and Performance of Fiber Composites*, 2nd edn. John Wiley & Sons Inc., New York, NY.
5. Drzal, L. T., Rich, M. J., and Lloyd, P. F. 1982. Adhesion of graphite fibers to epoxy matrices: I. The role of fiber surface treatment. *Journal of Adhesion*, 16, 1–30.
6. Drzal, L. T., Rich, M. J., Koenig, M. F., and Lloyd, P. F. 1983. Adhesion of graphite fibers to epoxy matrices: II. The effect of fiber finish. *Journal of Adhesion*, 16, 133–152.
7. Kelly, A. 1973. *Strong Solids*, 2nd edn. Clarendon Press, Oxford.
8. Rosen, B. W. 1965. Mechanics of composite strengthening, in Bush, S. H., ed., *Fiber Composite Materials*, Chap. 3, pp. 37–75. American Society for Metals, Metals Park, OH.
9. Gibson, R. F., Chaturvedi, S. K., and Sun, C. T. 1982. Complex moduli of aligned discontinuous fibre reinforced polymer composites. *Journal of Materials Science*, 17, 3499–3509.
10. Hwang, S. J. 1985. Finite element modeling of damping in discontinuous fiber composites. MS Thesis, University of Idaho, Moscow, ID.
11. Sun, C. T. and Wu, J. K. 1984. Stress distribution of aligned short fiber composites under axial load. *Journal of Reinforced Plastics and Composites*, 3, 130–144.
12. Tyson, W. R. and Davies, G. J. 1965. A photoelastic study of the shear stress associated with the transfer of stress during fiber reinforcement. *British Journal of Applied Physics*, 16, 199–205.
13. MacLaughlin, T. F. 1968. A photoelastic analysis of fiber discontinuities in composite materials. *Journal of Composite Materials*, 2(1), 44–45.
14. Suarez, S. A., Gibson, R. F., Sun, C. T., and Chaturvedi, S. K. 1986. The influence of fiber length and fiber orientation on damping and stiffness of polymer composite materials. *Experimental Mechanics*, 26(2), 175–184.
15. Hwang, S. J. and Gibson, R. F. 1987. Micromechanical modeling of damping in discontinuous fiber composites using a strain energy/finite element approach. *Journal of Engineering Materials and Technology*, 109, 47–52.
16. Halpin, J. C. 1969. Stiffness and expansion estimates for oriented short fiber composites. *Journal of Composite Materials*, 3, 732–734.
17. Tucker, C. L. and Liang, E. 1999. Stiffness predictions for unidirectional short fiber composites: Review and evaluation. *Composites Science and Technology*, 59(5), 655–671.
18. Chon, C. T. and Sun, C. T. 1980. Stress distribution along a short fiber in fiber reinforced plastics. *Journal of Materials Science*, 15, 931–938.
19. Sun, C. T., Gibson, R. F., and Chaturvedi, S. K. 1985. Internal damping of polymer matrix composites under off-axis loading. *Journal of Materials Science*, 20, 2575–2585.
20. Baxter, W. J. 1992. The strength of metal matrix composites reinforced with randomly oriented discontinuous fibers. *Metallurgical Transactions A*, 23A, 3045–3053.
21. Lees, J. K. 1968. A study of the tensile strength of short fiber reinforced plastics. *Polymer Engineering and Science*, 8(3), 195–201.

22. Chen, P. E. 1971. Strength properties of discontinuous fiber composites. *Polymer Engineering and Science*, 11(1), 51–55.
23. Halpin, J. C. and Kardos, J. L. 1978. Strength of discontinuous reinforced composites: I. Fiber reinforced composites. *Polymer Engineering and Science*, 18(6), 496–504.
24. Nielsen, L. E. and Chen, P. E. 1968. Young's modulus of composites filled with randomly oriented fibers. *Journal of Materials*, 3(2), 352–358.
25. Tsai, S. W. and Pagano, N. J. 1968. Invariant properties of composite materials, in Tsai, S. W., Halpin, J. C., and Pagano, N. J., eds., *Composite Materials Workshop*, pp. 233–252. Technomic Publishing Co., Lancaster, PA.
26. Halpin, J. C. and Pagano, N. J. 1969. The laminate approximation for randomly oriented fibrous composites. *Journal of Composite Materials*, 3, 720–724.
27. Manera, M. 1977. Elastic properties of randomly oriented short fiber-glass composites. *Journal of Composite Materials*, 11, 235–247.
28. Christensen, R. M. and Waals, F. M. 1972. Effective stiffness of randomly oriented fibre composites. *Journal of Composite Materials*, 6, 518–532.
29. Hashin, Z. 1965. On elastic behavior of fibre reinforced materials of arbitrary transverse phase geometry. *Journal of the Mechanics and Physics of Solids*, 13, 119–134.
30. Hashin, Z. 1966. Viscoelastic fiber reinforced materials. *AIAA Journal*, 4, 1411–1417.
31. Hill, R. 1964. Theory of mechanical properties of fiber-strengthened materials: I. Elastic behavior. *Journal of the Mechanics and Physics of Solids*, 12, 199–212.
32. Chang, D. C. and Weng, G. J. 1979. Elastic moduli of randomly oriented chopped fibre composites with filled resin. *Journal of Materials Science*, 14, 2183–2190.
33. Christensen, R. M. 1976. Asymptotic modulus results for composites containing randomly oriented fibers. *International Journal of Solids and Structures*, 12, 537–544.
34. Christensen, R. M. 1979. *Mechanics of Composite Materials*. John Wiley & Sons, New York, NY.
35. Weng, G. J. and Sun, C. T. 1979. Effects of fiber length on elastic moduli of randomly oriented chopped fiber composites, in Tsai, S. W., ed., *Composite Materials: Testing and Design (Fifth Conference)*, ASTM STP 674. American Society for Testing and Materials, Philadelphia, PA, pp. 149–162.
36. Sun, C. T., Wu, J. K., and Gibson, R. F. 1985. Prediction of material damping in randomly oriented short fiber polymer matrix composites. *Journal of Reinforced Plastics and Composites*, 4, 262–272.
37. Iijima, S. 1991. Helical microtubules of graphitic carbon. *Nature*, 354, 56–58.
38. Qian, D., Wagner, J. G., Liu, W. K., Yu, M. F., and Ruoff, R. S. 2002. Mechanics of carbon nanotubes. *Applied Mechanics Reviews*, 55(6), 495–533.
39. Thostenson, E. T., Ren, Z., and Chou, T. W. 2001. Advances in the science and technology of carbon nanotubes and their composites: A review. *Composites Science and Technology*, 61(13), 1899–1912.
40. Gates, T. S., ed. 2003. Modeling and characterization of nanostructured materials. *Composites Science and Technology (Special Issue)*, 63(11), 1497–1724.
41. Tibbetts, G. G. and McHugh, J. J. 1999. Mechanical properties of vapor-grown carbon fiber composites with thermoplastic matrices. *Journal of Materials Research*, 14(7), 2871–2880.
42. Qian, D., Dickey, E. C., Andrews, R., and Rantell, T. 2000. Load transfer and deformation mechanisms in carbon nanotube–polystyrene composites. *Applied Physics Letters*, 76 (20), 2868–2870.

43. Yu, M.-F., Files, B., Arepalli, S., and Ruoff, R. S. 2000. Tensile loading of ropes of single wall carbon nanotubes and their mechanical properties. *Physical Review Letters*, 84(24), 5552–5555.
44. Fisher, F. T. 2002. Nanomechanics of carbon nanotube-reinforced polymers. PhD thesis, Department of Mechanical Engineering, Northwestern University.
45. Fisher, F. T., Bradshaw, R. D., and Brinson, L. C. 2003. Fiber waviness in nanotube-reinforced polymer composites—I: Modulus predictions using effective nanotube properties. *Composites Science and Technology*, 63(11), 1689–1703.
46. Bradshaw, R. D., Fisher, F. T., and Brinson, L. C. 2003. Fiber waviness in nanotube-reinforced polymer composites—II: Modeling via numerical approximation of the dilute strain concentration tensor. *Composites Science and Technology*, 63(11), 1705–1722.
47. Anumandla, V. 2004. A comprehensive closed form micromechanics model for estimating the elastic modulus of nanotube-reinforced composites. MS Thesis, Department of Mechanical Engineering, Wayne State University.
48. Anumandla, V. and Gibson, R. F. 2006. A comprehensive closed form micromechanics model for estimating the elastic modulus of nanotube-reinforced composites. *Composites Part A: Applied Science and Manufacturing*, 37(12), 2178–2185.
49. Chan, W. S. and Wang, J. S. 1994. Influence of fiber waviness on the structural response of composite laminates. *Journal of Thermoplastic Composite Materials*, 7(3), 243–260.
50. Hsiao, H. M. and Daniel, I. M. 1996. Elastic properties of composites with fiber waviness. *Composites Part A: Applied Science and Manufacturing*, 27(10), 931–941.
51. Andrews, R., Jacques, D., Minot, M., and Ratnelli, T. 2002. Fabrication of carbon multiwall nanotube/polymer composites by shear mixing. *Micromolecular Materials Engineering*, 287(6), 395–403.
52. Vlasveld, D. P. N., Bersee, H. E. N., and Picken, S. J. 2005. Nanocomposite matrix for increased fibre composite strength. *Polymer*, 46, 10269–10278.
53. Thostenson, E. T., Li, W. Z., Wang, D. Z., Ren, Z. F., and Chou, T. W. 2002. Carbon nanotube/carbon fiber hybrid multiscale composite. *Journal of Applied Physics*, 91(9), 6034–6037.
54. Sahu, S. and Broutman, L. J. 1972. Mechanical properties of particulate composites. *Polymer Engineering and Science*, 12(2), 91–100.
55. Nicolais, L. and Narkis, M. 1971. Stress-strain behavior of styrene-acrylonitrile/glass bead composites in the glassy region. *Polymer Engineering and Science*, 11(3), 194–199.
56. Katz, H. S. and Milewski, J. V., eds. 1978. *Handbook of Fillers and Reinforcements for Plastics*. Van Nostrand Reinhold Co., New York, NY.
57. Liang, J. Z. and Li, R. K. Y. 1998. Mechanical properties and morphology of glass bead-filled polypropylene composites. *Polymer Composites*, 19(6), 698–703.
58. Liang, J. Z. 2007. Tensile properties of hollow glass bead-filled polypropylene composites. *Journal of Applied Polymer Science*, 104, 1697–1701.
59. Cho, J., Joshi, M. S., and Sun, C. T. 2006. Effect of inclusion size on mechanical properties of polymeric composites with micro and nano particles. *Composites Science and Technology*, 66, 1941–1952.
60. Nicolais, L. and Nicodemo, L. 1974. The effect of particle shape on tensile properties of glassy thermoplastic composites. *International Journal of Polymeric Materials*, 3(3), 229–243.

61. Nielsen, L. E. and Landel, R. F. 1994. *Mechanical Properties of Polymers and Polymer Composites*, 2nd edn. Marcel Dekker Inc., New York, NY.
62. Richard, T. G. 1975. The mechanical behavior of a solid microsphere filled composite. *Journal of Composite Materials*, 9, 108–113.
63. Cho, J. and Sun, C. T. 2007. A molecular dynamics simulation study of inclusion size effect on polymeric composites. *Computational Materials Science*, 41, 54–62.
64. Boutaleb, S., Zairi, F., Mesbah, A., Nait-Abdelaziz, M., Gloaguen, J. M., Boukharouba, T., and Lefebvre, J. M. 2009. Micromechanics-based modeling of stiffness and yield stress for silica/polymer nanocomposites. *International Journal of Solids and Structures*, 46, 1716–1726.
65. Uddin, M. F. and Sun, C. T. 2008. Strength of unidirectional glass/epoxy composite with silica nanoparticle-enhanced matrix. *Composites Science and Technology*, 68, 1637–1643.
66. Uddin, M. F. and Sun, C. T. 2010. Improved dispersion and mechanical properties of hybrid nanocomposites. *Composites Science and Technology*, 70, 223–230.
67. Liu, S., Zhang, H., Zhang, Z., Zhang, T., and Sprenger, S. 2008. Tailoring the mechanical properties of epoxy resin by various nanoparticles. *Polymers and Polymer Composites*, 16(8), 471–477.
68. Zhang, H., Tang, L.-C., Zhang Z., Friedrich, K., and Sprenger, S. 2008. Fracture behavior of *in situ* nanoparticle-filled epoxy at different temperatures. *Polymer*, 49, 3816–3825.
69. Manjunatha, C. M., Taylor, A. C., and Kinloch, A. J. 2009. The effect of rubber micro-particles and silica nano-particles on the tensile fatigue behavior of a glass fibre epoxy composite. *Journal of Materials Science*, 44, 342–345.
70. Veedu, V. P., Cao, A., Li, X., Ma, K., Soldano, C., Kar, S., Ajayan, P. M., and Ghasemi-Nejhad, M. N. 2006. Multifunctional composites using reinforced laminae with carbon nanotube forests. *Nature Materials*, 5, 457–462.
71. Garcia, E. J., Hart, A. J., and Wardle, B. L. 2008. Long carbon nanotubes grown on the surface of fibers for hybrid composites. *AIAA Journal*, 46(6), 1405–1412.
72. Garcia, E. J., Wardle, B. L., and Hart, A. J. 2008. Joining prepreg composite interfaces with aligned carbon nanotubes. *Composites Part A: Applied Science and Manufacturing*, 39, 1065–1070.
73. Garcia, E. J., Wardle, B. L., Hart, A. J., and Yamamoto, N. 2008. Fabrication and multifunctional properties of a hybrid laminate with aligned carbon nanotubes grown *in situ*. *Composites Science and Technology*, 68, 2034–2041.
74. Blanco, J., Garcia, E. J., Guzman de Viloria, R., and Wardle, B. L. 2009. Limitations of Mode I interlaminar toughening of composites reinforced with aligned carbon nanotubes. *Journal of Composite Materials*, 43, 825–841.
75. Wick, S., Guzman de Viloria, R., and Wardle, B. L. 2010. Interlaminar and intra-laminar reinforcement of composite laminates with aligned carbon nanotubes. *Composites Science and Technology*, 70, 20–28.
76. Gibson, R. F. 2010. A review of recent research on mechanics of multifunctional composite materials and structures. *Composite Structures*, 92, 2793–2810.
77. Zhang, H., Zhang, Z., Friedrich, K., and Eger, C. 2006. Property improvements of *in-situ* epoxy nanocomposites with reduced interparticle distance at high nanosilica content. *Acta Materialia*, 54, 1833–1842.

# 7

---

## *Analysis of Laminates*

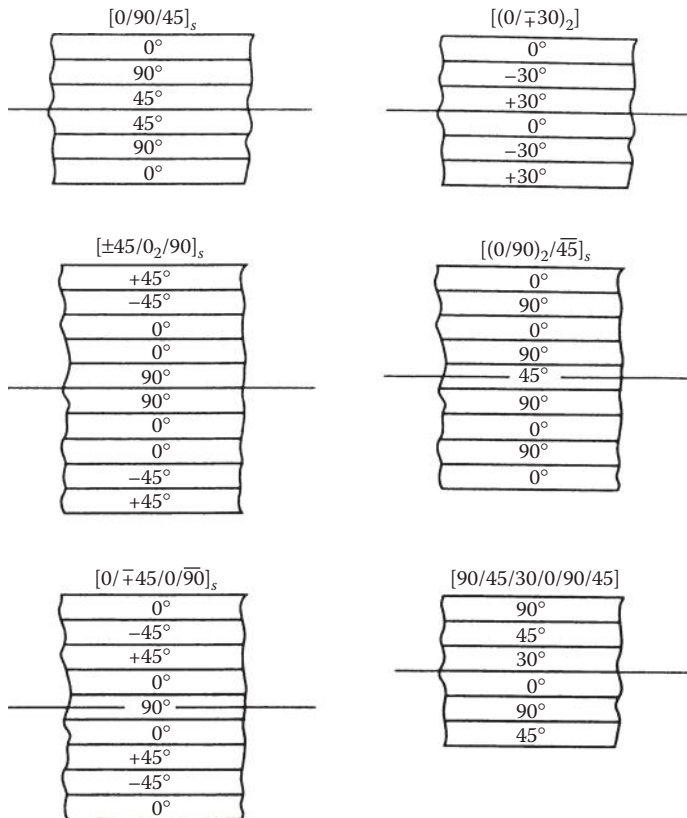
---

### 7.1 Introduction

While an understanding of lamina mechanical behavior is essential to the development of theories for the analysis of composite structures, the unidirectional lamina alone is generally not very useful as a structural element because of its poor transverse properties. Composite structures are more likely to be in the form of laminates consisting of multiple laminae or plies oriented in the desired directions and bonded together in a structural unit. The virtually limitless combinations of ply materials, ply orientations, and ply-stacking sequences offered by laminated construction considerably enhance the design flexibility inherent in composite structures.

In this chapter, the analysis of laminates will be introduced by considering a simplified theory of laminated beams in pure flexure, and then the effects of the transverse shear force will be treated separately. This will be followed by a discussion of the more general classical lamination theory (CLT), which makes it possible to analyze the complex coupling effects that may occur in laminates. Other aspects of laminate analysis, such as prediction of thermal and residual stresses, interlaminar stresses, and laminate strength are also discussed.

Owing to the need for adequate description of many possible combinations of ply orientations and stacking sequences in laminates, a laminate orientation code has evolved in the composites literature. The basis of the code is that ply angles, separated by slashes, are listed in order from the top surface to the bottom surface and enclosed in square brackets, as shown by the examples in Figure 7.1. Note that symmetric laminates can be described by listing only the ply angles for the top half of the laminate and by using the subscript "s" outside the brackets, and that adjacent plies having the same orientations can be described by using a numerical subscript on the appropriate ply angle. In the case of symmetric laminates having an odd number of plies, the center ply angle is denoted by an overbar. Sets of ply angles that are repeated in the laminate are identified by enclosing the set of angles in parentheses. The examples shown in Figure 7.1 are for laminates consisting of plies of the same material. For hybrid laminates having plies of different materials, additional subscripts on the ply angles may be used to identify the ply material.

**FIGURE 7.1**

Examples of laminate stacking sequences and the corresponding laminate orientation codes.

## 7.2 Theory of Laminated Beams

### 7.2.1 Flexural Stresses and Deflections

For the purpose of analysis, the simplest laminated structure is a laminated beam that is subjected to pure bending. A theory of laminated beams in pure flexure can be developed from the Bernoulli–Euler theory of elementary mechanics of materials. Although the application of this theory is quite restricted, it yields considerable insight into the analysis of laminated structures and provides a natural introduction to the more general CLT, which is described in the next section. The theory described here is based on the analysis of Pagano [1].

A section of a rectangular laminated beam of depth  $h$  and width  $b$  is shown in Figure 7.2 before and after the application of a bending moment  $M$ . The assumptions used in developing the analysis are as follows:

1. Plane sections that are initially normal to the longitudinal axis of the beam remain plane and normal during flexure.
2. The beam has both geometric and material property symmetry about the neutral surface (i.e., the plies are symmetrically arranged about the  $xy$  plane).
3. Each ply is linearly elastic with no shear coupling (i.e., ply orientations are either  $0^\circ$  or  $90^\circ$ ).
4. The plies are perfectly bonded together, so that no slip occurs at ply interfaces.
5. The only stress components present are  $\sigma_x$  and  $\tau_{xz}$ .

As a result of Assumption 1, the longitudinal normal strain at a distance  $z$  from the neutral surface is given by the familiar equation

$$\epsilon_x = \frac{(\rho + z)\phi - \rho\phi}{\rho\phi} = \frac{z}{\rho} \quad (7.1)$$

where  $\rho$  is the radius of curvature of the neutral surface during flexure,  $\phi$  the angle defined in Figure 7.2, and  $z$  the distance from neutral surface defined by the  $xy$  plane.

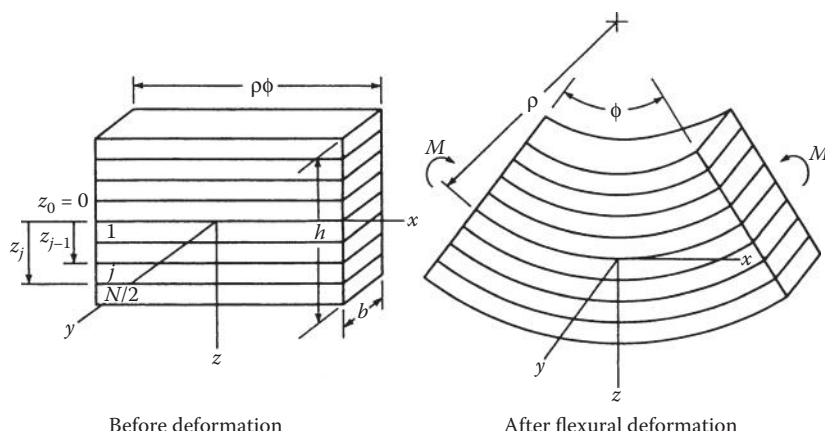


**FIGURE 7.2**

An element of a laminated beam before and after the application of a bending moment.

From Assumption 3, the longitudinal stress in the  $j$ th ply is given by

$$(\sigma_x)_j = (E_x)_j (\epsilon_x)_j \quad (7.2)$$

where  $(E_x)_j$  is the Young's modulus of  $j$ th ply along the  $x$  direction and  $(\epsilon_x)_j$  is the longitudinal strain in the  $j$ th ply along the  $x$  direction. From Equations 7.1 and 7.2, the longitudinal stress is seen to be

$$(\sigma_x)_j = (E_x)_j \frac{z}{\rho} \quad (7.3)$$

Static equilibrium requires that the applied bending moment  $M$  must be related to the longitudinal stresses by

$$M = 2 \int_0^{h/2} \sigma_x z b dz \quad (7.4)$$

where the symmetry Assumption 2 has been used. Substitution of Equation 7.3 into Equation 7.4 gives

$$M = \frac{2b}{3\rho} \sum_{j=1}^{N/2} (E_x)_j (z_j^3 - z_{j-1}^3) \quad (7.5)$$

where  $N$  is the total number of plies and  $z_j$  is the distance from the neutral surface to the outside of the  $j$ th ply. For an even number of plies of uniform thickness  $z_j = jh/N$  and Equation 7.5 becomes

$$M = \frac{2bh^3}{3\rho N^3} \sum_{j=1}^{N/2} (E_x)_j (3j^2 - 3j + 1) \quad (7.6)$$

Equation 7.6 can also be used for an odd number of plies if we simply divide each ply into two identical plies having half the thickness of the original ply, so that the total number of plies is now even.

Recall from mechanics of materials that for a homogeneous, isotropic beam, the moment-curvature relation is given by

$$M = \frac{E_f I_{yy}}{\rho} = \frac{E_f b h^3}{12\rho} \quad (7.7)$$

where  $I_{yy} = \int z^2 dA = bh^3/12$  is the moment of inertia of the cross section about the neutral axis ( $y$  axis),  $A$  the cross-sectional area, and  $E_f$  the effective flexural modulus of the beam (which is same as Young's modulus of the beam

material for a homogeneous, isotropic beam). Note that the subscript "f" here denotes "flexural" and not "fiber."

Combining Equation 7.5 and Equation 7.7, we find that the effective flexural modulus of the laminated beam can be expressed as

$$E_f = \frac{8}{h^3} \sum_{j=1}^{N/2} (E_x)_j (z_j^3 - z_{j-1}^3) \quad (7.8)$$

or for an even number of uniform thickness plies we can combine Equation 7.6 and Equation 7.7 to get

$$E_f = \frac{8}{N^3} \sum_{j=1}^{N/2} (E_x)_j (3j^2 - 3j + 1) \quad (7.9)$$

Thus, the flexural modulus of the laminated beam, unlike the Young's modulus of the homogeneous isotropic beam, depends on the ply-stacking sequence and the ply moduli. That is, if the properties do not change through the thickness of a beam, the flexural modulus is the same as the Young's modulus.

The flexural deflections of laminated beams can now be calculated by using the flexural modulus in place of the Young's modulus in the beam deflection equations from elementary mechanics of materials. For example, the differential equation for the transverse flexural deflection,  $w_f$ , of a laminated beam would be of the form

$$E_f I_{yy} \frac{d^2 w_f}{dx^2} = M \quad (7.10)$$

and the maximum flexural deflection,  $w_{f\max}$ , at the tip of the laminated cantilever beam in Figure 7.3 would be given by the familiar equation

$$w_{f\max} = \frac{PL^3}{3E_f I_{yy}} \quad \text{at } x = L \quad (7.11)$$

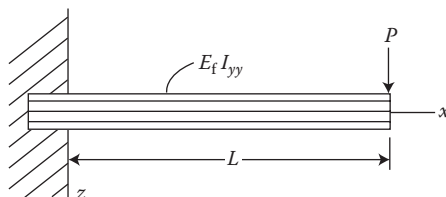


**FIGURE 7.3**  
Cantilevered laminated beam under a concentrated tip load.

where  $P$  is the applied tip load and  $L$  is the beam length. If the beam is loaded as a column in axial compression, the Euler buckling load,  $P_{\text{cr}}$ , for a laminated beam can be estimated by the formula

$$P_{\text{cr}} = \frac{\pi^2 E_f I_{yy}}{L_e^2} \quad (7.12)$$

where  $L_e$  is the effective length that includes the effect of end conditions. Similarly, other beam equations involving the Young's modulus can now be modified for use with laminated beams.

An alternative expression for the stress in the  $j$ th ply can be obtained by combining Equation 7.3 and Equation 7.7 and by eliminating the radius of curvature:

$$(\sigma_x)_j = \frac{M}{E_f I_{yy}} (E_x)_j z = \frac{Mz}{I_{yy}} \left[ \frac{(E_x)_j}{E_f} \right] \quad (7.13)$$

Thus, the term in square brackets can be thought of as a correction term, which when multiplied by the familiar homogeneous isotropic beam stress,  $Mz/I_{yy}$  gives the stress in the  $j$ th ply of the laminated beam. Another important observation is that the maximum stress in the laminated beam does not always occur on the outer surface as it does in the homogeneous, isotropic beam. At each section in a laminated beam, the ratio  $M/E_f I_{yy}$  is constant, and the remaining term  $(E_x)_j z$  determines the maximum stress. The maximum stress in the laminated beam therefore occurs in the ply having the greatest product of modulus  $(E_x)_j$  and distance from the neutral axis,  $z$ . For the homogeneous isotropic beam, the stress at a given point in the cross section depends only on the distance  $z$ , and the maximum stress occurs at the outer surface where  $z$  is the greatest. The stress distributions in homogeneous isotropic beams and laminated beams are compared schematically in Figure 7.4.

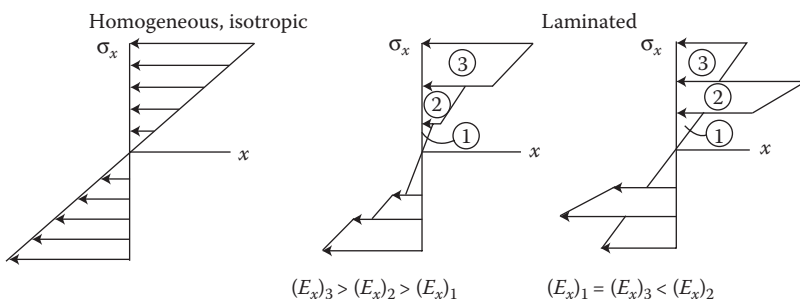


**FIGURE 7.4**

Stress distributions in homogeneous, isotropic beams and in laminated beams.

Failure of laminated beams can be estimated by using the stress from Equation 7.13 in one of the failure criteria that was discussed in Chapter 4. For example, if the  $j$ th ply is a longitudinal ( $0^\circ$ ) ply in compression, failure in this ply according to the maximum stress criterion will occur when  $(\sigma_{x \max})_j = s_L^{(-)}$ , where  $(\sigma_{x \max})_j$  is the maximum stress in the  $j$ th ply at  $z = z_j$ . From Equation 7.13, the applied bending moment that would cause this condition is

$$M_{\max} = \frac{E_f I_{yy} s_L^{(-)}}{(E_1)_j z_j} \quad (7.14)$$

where  $(E_1)_j$  is the longitudinal modulus of the  $j$ th ply. Similarly, for a transverse ( $90^\circ$ ) ply in tension the maximum bending moment is

$$M_{\max} = \frac{E_f I_{yy} s_T^{(+)}}{(E_2)_j z_j} \quad (7.15)$$

Laminate failure would therefore occur when the bending moment reaches the value that would cause first ply failure. This value can be determined by applying the failure criterion to each ply until the lowest  $M_{\max}$  is found. The internal bending moment can be related to the external applied loads by the equations of static equilibrium, so that the applied loads corresponding to first ply failure can also be determined. Since the maximum stress does not necessarily occur on the outer surface, first ply failure may occur in an interior ply. One of the difficulties encountered in inspection for ply failure in laminates is that only failures on the outer surfaces can be observed with the naked eye. Interior ply failures can only be detected by methods such as ultrasonic or x-ray inspection.

### Example 7.1

Determine the flexural and Young's moduli of E-glass/epoxy laminated beams having stacking sequences of  $[0/90/0]_s$  and  $[90/0/90]_s$ . The ply moduli are  $E_1 = 5 \times 10^6$  psi (34.48 GPa) and  $E_2 = 1.5 \times 10^6$  psi (10.34 GPa), and the plies all have the same thickness.

### SOLUTION

The total number of plies is  $N = 6$  in each case, and only the stacking sequences are different. Since the ply thicknesses are all the same, we can use Equation 7.9 for the flexural modulus in both cases. For the  $[0/90/0]_s$  beam

$$E_f = \frac{8}{N^3} \sum_{j=1}^{N/2} (E_x)_j (3j^2 - 3j + 1)$$

or

$$E_f = \frac{8}{(6)^3} \{5[3(1)^2 - 3 + 1] + 1.5[3(2)^2 - 3(2) + 1] + 5[3(3)^2 - 3(3) + 1]\} \times 10^6 \text{ psi}$$

$$= 4.09 \times 10^6 \text{ psi} (28.2 \text{ GPa})$$

The Young's modulus, or extensional modulus, can be estimated by using the rule of mixtures

$$E_x = E_1 v_1 + E_2 v_2$$

where  $v_1$  = volume fraction of longitudinal ( $0^\circ$ ) plies and  $v_2$  = volume fraction of transverse ( $90^\circ$ ) plies. Therefore,

$$E_x = \left[ 5\left(\frac{4}{6}\right) + 1.5\left(\frac{2}{6}\right) \right] \times 10^6 \text{ psi} = 3.83 \times 10^6 \text{ psi} (26.4 \text{ GPa})$$

For the [90/0/90]<sub>s</sub> beam

$$E_f = \frac{8}{(6)^3} \{1.5(1) + 5(7) + 1.5(19)\} \times 10^6 \text{ psi} = 2.4 \times 10^6 \text{ psi} (16.55 \text{ GPa})$$

and

$$E_x = \left[ 1.5\left(\frac{4}{6}\right) + 5\left(\frac{2}{6}\right) \right] \times 10^6 \text{ psi} = 2.66 \times 10^6 \text{ psi} (18.34 \text{ GPa})$$

Note that the flexural modulus depends on the stacking sequence and is not the same as the Young's modulus. The Young's modulus does not depend on the stacking sequence (i.e., the rule of mixtures gives the same result regardless of the ply-stacking sequence, as long as the number of longitudinal and transverse plies remains unchanged).

## 7.2.2 Shear Stresses and Deflections

In most practical cases, the applied loads on a beam would be such that not only bending moments but also transverse shear forces would be developed. These transverse shear forces cause corresponding transverse shear stresses and deflections. In laminated beams, the transverse shear stresses are often referred to as interlaminar shear stresses. Pagano [1] has also developed a mechanics of materials approach for estimating interlaminar shear stresses, as summarized here. Recall from the mechanics of materials [2] that the bending moment,  $M$ , is related to the transverse shear force,  $V$ , by the equation

$$\frac{dM}{dx} = V \quad (7.16)$$

Thus, the presence of the shear force implies that the bending moment must change along the length of the beam (the  $x$  direction). From Equation 7.13, we see that if the bending moment changes with respect to  $x$ , so, too, must the normal stresses,  $\sigma_x$ . This means that the normal stresses acting on the two faces of the  $j$ th ply in a differential element must be different, as shown in Figure 7.5. Since the element cannot be in static equilibrium under these normal stresses alone, the interlaminar shear stress,  $(\tau_{xz})_k$ , must act at the inner edge of the  $k$ th ply, as shown in Figure 7.5.

From static equilibrium of the element with respect to the forces along the  $x$  direction,

$$(\tau_{xz})_k \, dx + \sum_{j=k}^{N/2} \int_{z_{j-1}}^{z_j} (\sigma_x)_j \, dz - \sum_{j=k}^{N/2} \int_{z_{j-1}}^{z_j} \left[ (\sigma_x)_j + \frac{d(\sigma_x)_j}{dx} \, dx \right] dz = 0 \quad (7.17)$$

or

$$(\tau_{xz})_k = \sum_{j=k}^{N/2} \int_{z_{j-1}}^{z_j} \frac{d(\sigma_x)_j}{dx} \, dz \quad (7.18)$$

Substituting Equations 7.13 and 7.16 into Equation 7.18 and integrating, we find that the interlaminar stress at the inner edge of the  $k$ th ply is

$$(\tau_{xz})_k = \frac{V}{E_f I_{yy}} \sum_{j=k}^{N/2} \int_{z_{j-1}}^{z_j} (E_x)_j z \, dz \quad (7.19)$$

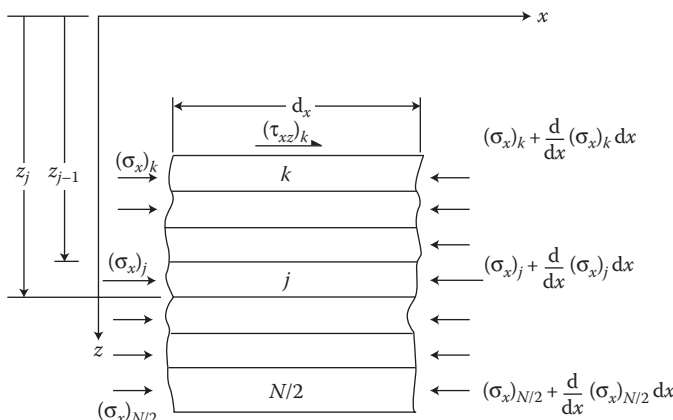


**FIGURE 7.5**

Differential element of a laminated beam showing interlaminar shear stress that is necessary for static equilibrium when the bending moment varies along the length.

For a rectangular beam having an even number of plies of uniform thickness,  $z_j = jh/N$ , and Equation 7.19 reduces to

$$(\tau_{xz})_k = \frac{3V}{2bh} \left[ \frac{S}{E_f} \right] \quad (7.20)$$

where

$$S = \frac{4}{N^2} \sum_{j=k}^{N/2} (E_x)_j (2j - 1) \quad (7.21)$$

Equation 7.20 is seen to be similar to the “mechanics of materials” equation for transverse shear stress in a homogeneous isotropic beam, which is

$$\tau_{xz} = \frac{3V}{2bh} \left[ 1 - 4 \left( \frac{z}{h} \right)^2 \right] \quad (7.22)$$

Thus, the transverse shear stress is given by

$$\tau_{xz} = \frac{3V}{2bh} \beta \quad (7.23)$$

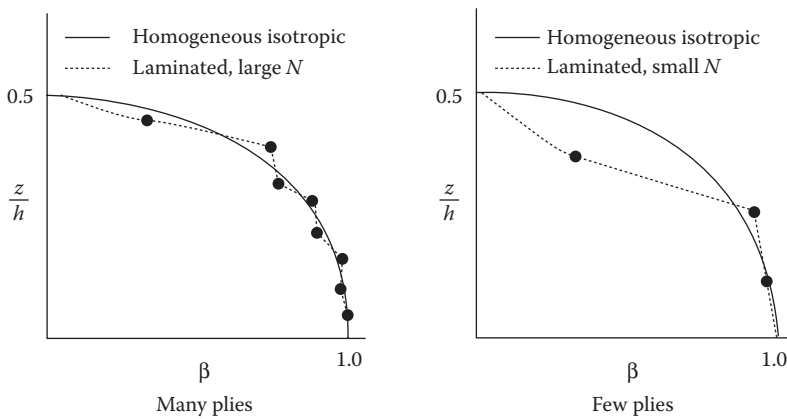
where

$$\beta = \begin{cases} 1 - 4 \left( \frac{z}{h} \right)^2 & \text{for a homogeneous isotropic beam} \\ \frac{S}{E_f} & \text{for a laminated beam} \end{cases}$$

The shear stress distribution, as governed by the variation of the factor  $\beta$ , is shown for both types of beams in Figure 7.6. As the number of plies increases, the shear stress distribution for the laminated beam can be expected to approach the parabolic distribution described by Equation 7.22. For a small number of plies, however, the laminated beam shear stress distribution departs significantly from the parabolic distribution.

Interlaminar stresses are responsible for an important failure mode in composites known as delamination. Recall that the failure criteria discussed in Chapter 4 were based only on in-plane stresses in the lamina. Both normal and shear components of the interlaminar stresses in laminated plates along with failure criteria, which include the interlaminar stresses, will be discussed later.

Equation 7.10 is the differential equation for the flexural deflection,  $w_f$ , of laminated beams due to the bending moment,  $M$ . The corresponding

**FIGURE 7.6**

Variation of shear stress, as governed by the factor  $\beta$ , across half the beam thickness for homogeneous, isotropic beams and for laminated beams. Results are given for laminated beams with a small number of plies and a large number of plies.

differential equation for the shear deflection,  $w_s$ , of a laminated beam due to the shear force  $V$  is approximately

$$\frac{dw_s}{dx} = \frac{V}{AG_t} \quad (7.24)$$

where  $A$  is the cross-sectional area of the beam, and  $G_t$  is the effective transverse (or through-the-thickness) shear modulus of the beam. The total deflection of the beam is then

$$w = w_f + w_s \quad (7.25)$$

For the cantilever beam in Figure 7.3, the maximum shear deflection,  $w_{s\max}$ , at  $x = L$  is given by

$$w_{s\max} = \frac{PL}{AG_t} \quad (7.26)$$

For more detailed discussions and derivations of these equations, see Example 7.3. Note that, while  $w_{f\max}$  in Equation 7.10 is proportional to  $L^3$ ,  $w_{s\max}$  in Equation 7.26 is proportional to  $L$ , and so for long beams, the flexural deflection is typically much greater than the shear deflection. However, due to the relatively low effective shear modulus  $G_t$  for some laminates, the shear deflection may be significant, especially for short beams. As will be shown later in Section 7.11.1,  $G_t$  may be particularly low in sandwich beams due to the low shear modulus of the foam or honeycomb core material.

### Example 7.2

For the [90/0/90]<sub>s</sub>, E-glass/epoxy beam described in Example 7.1, sketch the distribution of normal and shear stresses through the thickness of the beam. Assume a ply thickness of 0.01 in. (0.254 mm).

#### SOLUTION

The normal stress is given by Equation 7.13, but the ratio  $M/E_f I_{yy}$  is constant for a given cross section, and the stress distribution across the thickness is governed by the product  $(E_x)z$ . Thus, the stress distribution can be determined to within a constant  $K_1 = M/E_f I_{yy}$  by finding the corresponding variation of  $(E_x)z$ .

For the outer surface of ply number 3 (the outer transverse ply), the ply modulus is  $(E_x)_3 = E_2 = 1.5 \times 10^6$  psi,  $z = 0.03$  in. and the stress is  $\sigma_x = K_1(1.5 \times 10^6)(0.03) = 4.5 \times 10^4 K_1$ .

For the inner surface of ply number 3,  $z = 0.02$  in. and the stress is  $\sigma_x = K_1(1.5 \times 10^6)(0.02) = 3.0 \times 10^4 K_1$ .

Similarly, for the outer surface of ply number 2, the stress is  $\sigma_x = K_1(5 \times 10^6)(0.02) = 10 \times 10^4 K_1$ .

For the inner surface of ply number 2,  $\sigma_x = K_1(5 \times 10^6)(0.01) = 5 \times 10^4 K_1$ .

For the outer surface of ply number 1,  $\sigma_x = K_1(1.5 \times 10^6)(0.01) = 1.5 \times 10^4 K_1$ .

For the inner surface of ply number 1 (on the neutral surface),  $\sigma_x = 0$ .

The predicted distribution of  $\sigma_x$  across the thickness is plotted in Figure 7.7a. It is seen that the maximum normal stress occurs not on the outer surface as in a homogeneous isotropic beam but, rather, at the outer edge of ply number 2.

The interlaminar shear stress at the inner surface of the  $k$ th ply for a beam with an even number of uniform thickness plies is given by Equations 7.20 and 7.21. For a given cross section, however, the ratio  $3V/2bhE_f$  can be set equal to a constant,  $K_2$ , and the shear stress can be written as  $(\tau_{xz})_k = K_2 S$ , where  $S$  is defined by Equation 7.21. The shear stress distribution can then be determined to within a constant  $K_2$  by finding the variation of  $S$  across the thickness.

From Equation 7.20 and Equation 7.21,

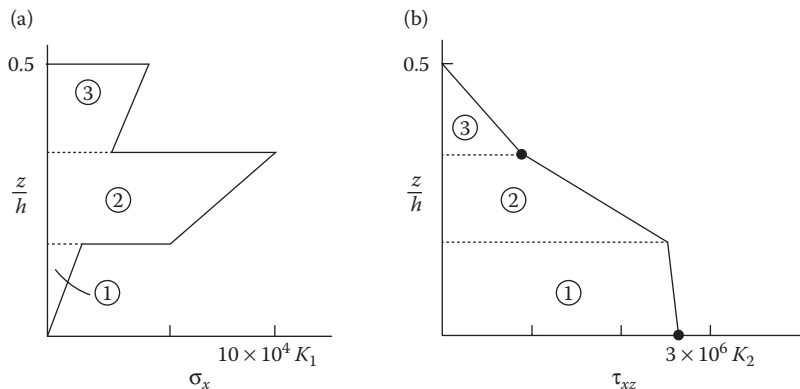
$$(\tau_{xz})_k = \frac{3V}{2bh} \left[ \frac{S}{E_f} \right] = K_2 S$$

where

$$S = \frac{4}{N^2} \sum_{j=k}^{N/2} (E_x)_j (2j - 1)$$

for  $k = 1$

$$\begin{aligned} S &= \frac{4}{(6)^2} [1.5[2(1) - 1] + 5[2(2) - 1] + 1.5[2(3) - 1]] \times 10^6 \\ &= 2.66 \times 10^6 \text{ psi (18.34 GPa)} \end{aligned}$$

**FIGURE 7.7**

Stress distributions for the beam described in Example 7.2. (a) Normal stresses and (b) shear stresses.

for  $k = 2$

$$\begin{aligned} S &= \frac{4}{(6)^2} \{5[2(2) - 1] + 1.5[2(3) - 1]\} \times 10^6 \\ &= 2.5 \times 10^6 \text{ psi (17.24 GPa)} \end{aligned}$$

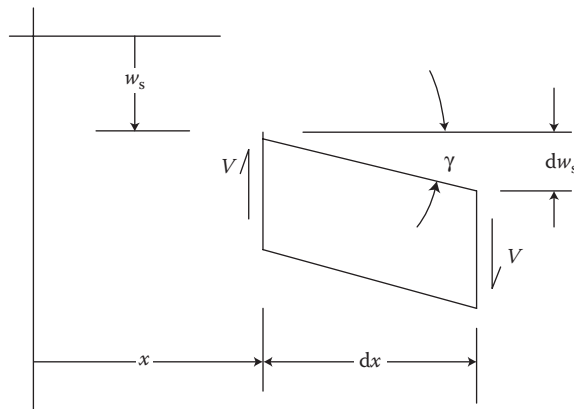
for  $k = 3$

$$\begin{aligned} S &= \frac{4}{(6)^2} \{1.5[2(3) - 1]\} \times 10^6 \\ &= 0.833 \times 10^6 \text{ psi (5.74 GPa)} \end{aligned}$$

Finally, for  $k = 4$ , Equation 7.20 gives the shear stress at the inner surface of an “imaginary ply” whose inner surface is the same as the outer surface of ply number 3 or the outer surface of the laminate. Since there is no material in this “imaginary ply,”  $S = 0$  and the shear stress must be zero on the outer surface. This also satisfies the boundary condition that the outer surface must be stress free. The predicted distribution of  $\tau_{xz}$  across the thickness is plotted in Figure 7.7b. As with the shear stress in a homogeneous isotropic beam, the maximum shear stress occurs on the neutral surface and the shear stress at the outer surface is zero. The deviation from the parabolic distribution is substantial, however, because of the small number of plies.

### Example 7.3

Derive the differential equation (7.24) for the shear deflection of a laminated beam due to the shear force,  $V$ , and then apply it to find Equation 7.26, the maximum shear deflection for the cantilever beam in Figure 7.3.

**FIGURE 7.8**

Differential element of deformed beam loaded in transverse shear.

### SOLUTION

A differential element of a deformed beam loaded in transverse shear is shown in Figure 7.8. For small deformations, the average shear strain,  $\gamma$ , is approximated by  $\gamma \approx \tan \gamma = dw_s/dx = \bar{\tau}/G_t$  where  $\bar{\tau}$  is the average transverse shear stress, which is approximately equal to  $V/A$ ,  $A$  is the cross-sectional area of the beam, and  $G_t$  is the effective transverse shear modulus of the beam. The result is Equation 7.24,

$$\frac{dw_s}{dx} = \frac{V}{AG_t}$$

Separating variables and integrating both sides of the equation along the length of the cantilever beam in Figure 7.3, we find that

$$\int_0^{w_{s\max}} dw_s = \frac{1}{AG_t} \int_0^L V dx$$

For the cantilever beam with load  $P$  at  $x = L$ , the shear force is a constant  $V = P$  along the entire length of the beam, which leads to Equation 7.26:

$$w_{s\max} = \frac{PL}{AG_t}$$

### 7.3 Theory of Laminated Plates with Coupling

While the simplified theory of laminated beams in pure flexure is useful and instructive, it is restricted to symmetric laminates without coupling that are

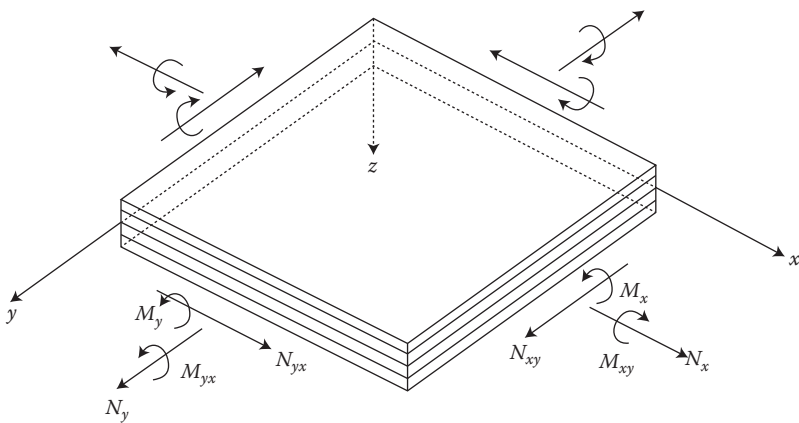
subjected to a single bending moment. In this section, we will discuss the more general CLT, which does not have these restrictions. Using this theory, we can analyze nonsymmetric laminates whose arbitrarily oriented plies may have various coupling effects that may lead to complex combinations of extensional, flexural, and torsional deformations. In addition, in-plane loading due to shear and axial forces and both bending and twisting moments are included. The most important limitation of the CLT is that each ply is assumed to be in a state of plane stress and that interlaminar stresses are neglected.

What is now referred to as the CLT has apparently evolved from work in the 1950s and 1960s by investigators such as Smith [3], Pister and Dong [4], Reissner and Stavsky [5], Stavsky [6], Lekhnitskii [7], and Stavsky and Hoff [8]. The major difference between this theory and the classical theory of homogeneous, isotropic plates [9] is in the form of the lamina stress-strain relationships. Other elements of the theory such as the deformation hypothesis, the equilibrium equations (Appendix B), and the strain-displacement relationships (Appendix C) are the same as those used in the classical plate theory [9].

Although the laminate is made up of multiple laminae, it is assumed that the individual laminae are perfectly bonded together so as to behave as a unitary, nonhomogeneous anisotropic plate. Interfacial slip is not allowed, and the interfacial bonds are not allowed to deform in shear, which means that displacements across lamina interfaces are assumed to be continuous. These assumptions mean that the deformation hypothesis from the classical homogeneous plate theory can be used for the laminated plate. The laminate force-deformation equations resulting from this deformation hypothesis are now derived following the procedure outlined by Whitney [10]. Although Whitney has presented a general analysis including the equations of motion, only the static analysis will be considered here.

Figure 7.9 defines the coordinate system to be used in developing the laminated plate analysis. The  $xyz$  coordinate system is assumed to have its origin on the middle surface of the plate, so that the middle surface lies in the  $xy$  plane. The displacements at a point in the  $x$ ,  $y$ , and  $z$  directions are  $u$ ,  $v$ , and  $w$ , respectively. The basic assumptions relevant to the present static analysis are [10]:

1. The plate consists of orthotropic laminae bonded together, with the principal material axes of the orthotropic laminae oriented along arbitrary directions with respect to the  $xy$  axes.
2. The thickness of the plate,  $t$ , is much smaller than the lengths along the plate edges,  $a$  and  $b$ .
3. The displacements  $u$ ,  $v$ , and  $w$  are small compared with the plate thickness.
4. The in-plane strains  $\epsilon_x$ ,  $\epsilon_y$ , and  $\gamma_{xy}$  are small compared with unity.
5. Transverse shear strains  $\gamma_{xz}$  and  $\gamma_{yz}$  are negligible.

**FIGURE 7.9**

Coordinate system and stress resultants for laminated plate.

6. Tangential displacements  $u$  and  $v$  are linear functions of the  $z$  coordinate.
7. The transverse normal strain  $\epsilon_z$  is negligible.
8. Each ply obeys Hooke's law.
9. The plate thickness  $t$  is constant.
10. Transverse shear stresses  $\tau_{xz}$  and  $\tau_{yz}$  vanish on the plate surfaces defined by  $z = \pm t/2$ .

Assumption 5 is a result of the assumed state of plane stress in each ply, whereas Assumptions 5 and 6 together define the Kirchhoff deformation hypothesis that normals to the middle surface remain straight and normal during deformation. According to Assumptions 6 and 7, the displacements can be expressed as

$$\begin{aligned} u &= u^0(x, y) + zF_1(x, y) \\ v &= v^0(x, y) + zF_2(x, y) \\ w &= w^0(x, y) = w(x, y) \end{aligned} \quad (7.27)$$

where  $u^0$  and  $v^0$  are the tangential displacements of the middle surface along the  $x$  and  $y$  directions, respectively. Due to Assumption 7, the transverse displacement at the middle surface,  $w^0(x, y)$ , is the same as the transverse displacement of any point having the same  $x$  and  $y$  coordinates, and so  $w^0(x, y) = w(x, y)$ . At this point it is appropriate to mention that to account for possible warping of the cross section of the laminate and resulting transverse

shear deformations, it is necessary to use a so-called higher-order lamination theory. For example, Christensen [11] describes one such theory, which is based on the assumption that the displacements are *nonlinear* functions of the  $z$  coordinate as follows:

$$\begin{aligned} u &= u^0(x, y) + z\psi_x(x, y) + z^2\zeta_x(x, y) + z^3\phi_x(x, y) \\ v &= v^0(x, y) + z\psi_y(x, y) + z^2\zeta_y(x, y) + z^3\phi_y(x, y) \\ w &= w^0(x, y) + z\psi_z(x, y) + z^2\zeta_z(x, y) \end{aligned} \quad (7.28)$$

Such a theory is beyond the scope of this book, however, and we will only develop the CLT based on Equation 7.27. Substituting Equations 7.27 in the strain–displacement equations (Appendix C) for the transverse shear strains and using Assumption 5, we find that

$$\begin{aligned} \gamma_{xz} &= \frac{\partial u}{\partial z} + \frac{\partial w}{\partial x} = F_1(x, y) + \frac{\partial w}{\partial x} = 0 \\ \gamma_{yz} &= \frac{\partial v}{\partial z} + \frac{\partial w}{\partial y} = F_2(x, y) + \frac{\partial w}{\partial y} = 0 \end{aligned} \quad (7.29)$$

and that

$$F_1(x, y) = -\frac{\partial w}{\partial x}, \quad F_2(x, y) = -\frac{\partial w}{\partial y} \quad (7.30)$$

Substituting Equations 7.27 and Equations 7.30 in the strain–displacement relations for the in-plane strains (Appendix C), we find that

$$\begin{aligned} \varepsilon_x &= \frac{\partial u}{\partial x} = \varepsilon_x^0 + z\kappa_x \\ \varepsilon_y &= \frac{\partial v}{\partial y} = \varepsilon_y^0 + z\kappa_y \\ \gamma_{xy} &= \frac{\partial u}{\partial y} + \frac{\partial v}{\partial x} = \gamma_{xy}^0 + z\kappa_{xy} \end{aligned} \quad (7.31)$$

where the strains on the middle surface are

$$\varepsilon_x^0 = \frac{\partial u^0}{\partial x}, \quad \varepsilon_y^0 = \frac{\partial v^0}{\partial y}, \quad \gamma_{xy}^0 = \frac{\partial u^0}{\partial y} + \frac{\partial v^0}{\partial x} \quad (7.32)$$

and the curvatures of the middle surface are

$$\kappa_x = -\frac{\partial^2 w}{\partial x^2}, \quad \kappa_y = -\frac{\partial^2 w}{\partial y^2}, \quad \kappa_{xy} = -2 \frac{\partial^2 w}{\partial x \partial y} \quad (7.33)$$

where  $\kappa_x$  is a bending curvature associated with bending of the middle surface in the  $xz$  plane,  $\kappa_y$  is a bending curvature associated with bending of the middle surface in the  $yz$  plane, and  $\kappa_{xy}$  is a twisting curvature associated with out-of-plane twisting of the middle surface, which lies in the  $xy$  plane before deformation.

Since Equations 7.31 give the strains at any distance  $z$  from the middle surface, the stresses along arbitrary  $xy$  axes in the  $k$ th lamina of a laminate may be found by substituting Equations 7.31 into the lamina stress-strain relationships from Equations 2.35 as follows:

$$\begin{Bmatrix} \sigma_x \\ \sigma_y \\ \tau_{xy} \end{Bmatrix}_{\kappa} = \begin{bmatrix} \bar{Q}_{11} & \bar{Q}_{12} & \bar{Q}_{16} \\ \bar{Q}_{12} & \bar{Q}_{22} & \bar{Q}_{26} \\ \bar{Q}_{16} & \bar{Q}_{26} & \bar{Q}_{66} \end{bmatrix}_k \begin{Bmatrix} \epsilon_x^0 + z\kappa_x \\ \epsilon_y^0 + z\kappa_y \\ \gamma_{xy}^0 + z\kappa_{xy} \end{Bmatrix} \quad (7.34)$$

where the subscript  $k$  refers to the  $k$ th lamina. Comparing the laminated plate stresses in Equations 7.34 with the laminated beam stress given by Equation 7.3, we notice several differences. The laminated beam analysis only gives the uniaxial stress,  $\sigma_x$ , due to the bending curvature, whereas the laminated plate analysis gives the 2-D lamina stresses  $\sigma_x$ ,  $\sigma_y$ , and  $\tau_{xy}$  due to bending and twisting curvatures and to the midplane biaxial extension and shear. In addition, the laminated plate analysis includes the stresses due to shear coupling, as discussed in Chapter 2.

In the laminated beam analysis, Equation 7.3 for lamina stress is seen to be of limited practical use because the curvature is not generally known and is difficult to measure. Thus, the lamina stress was related to the applied bending moment by using the static equilibrium relationship in Equation 7.4. The result was that a more useful equation for stress, Equation 7.13, was developed. The bending moment can be related to the loads on the structure by additional static equilibrium equations. Similarly, in the laminated plate analysis, the midplane strains and curvatures in Equations 7.34 must be related to applied forces and moments by static equilibrium equations to make these equations more useful. In the laminated plate analysis, however, it is convenient to use forces and moments per unit length rather than forces and moments. The forces and moments per unit length shown in Figure 7.9 are also referred to as stress resultants.

For example, the force per unit length,  $N_x$ , is given by

$$N_x = \int_{-t/2}^{t/2} \sigma_x dz = \sum_{k=1}^N \left\{ \int_{z_{k-1}}^{z_k} (\sigma_x)_k dz \right\} \quad (7.35)$$

and the moment per unit length,  $M_x$ , is given by

$$M_x = \int_{-t/2}^{t/2} \sigma_x z dz = \sum_{k=1}^N \left\{ \int_{z_{k-1}}^{z_k} (\sigma_x)_k z dz \right\} \quad (7.36)$$

where  $t$  is the laminate thickness,  $(\sigma_x)_k$  the stress in the  $k$ th lamina,  $z_{k-1}$  the distance from middle surface to inner surface of the  $k$ th lamina, and  $z_k$  the corresponding distance from middle surface to outer surface of the  $k$ th lamina, as shown in Figure 7.10.

Substituting the lamina stress-strain relationships from Equations 7.34 into Equations 7.35 and 7.36, respectively, we find that

$$N_x = \sum_{k=1}^N \int_{z_{k-1}}^{z_k} \left\{ (\bar{Q}_{11})_k (\varepsilon_x^0 + z \kappa_x) + (\bar{Q}_{12})_k (\varepsilon_y^0 + z \kappa_y) + (\bar{Q}_{16})_k (\gamma_{xy}^0 + z \kappa_{xy}) \right\} dz \quad (7.37)$$

and

$$M_x = \sum_{k=1}^N \int_{z_{k-1}}^{z_k} \left\{ (\bar{Q}_{11})_k (\varepsilon_x^0 + z \kappa_x) + (\bar{Q}_{12})_k (\varepsilon_y^0 + z \kappa_y) + (\bar{Q}_{16})_k (\gamma_{xy}^0 + z \kappa_{xy}) \right\} z dz \quad (7.38)$$

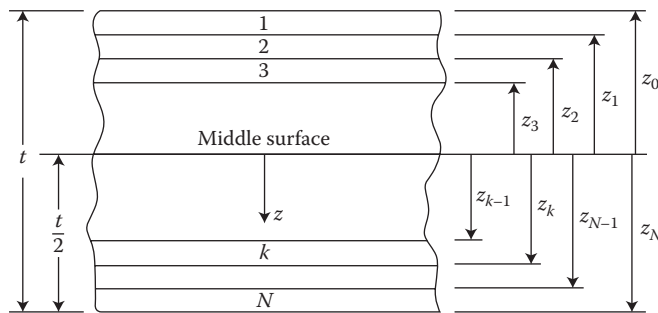


**FIGURE 7.10**

Laminated plate geometry and ply numbering system. *Caution:* The ply numbering system here is different from that used in Figure 7.2 for the laminated beam analysis.

Combining terms and rearranging Equation 7.37 and Equation 7.38, we find that

$$N_x = A_{11}\varepsilon_x^0 + A_{12}\varepsilon_y^0 + A_{16}\gamma_{xy}^0 + B_{11}\kappa_x + B_{12}\kappa_y + B_{16}\kappa_{xy} \quad (7.39)$$

and

$$M_x = B_{11}\varepsilon_x^0 + B_{12}\varepsilon_y^0 + B_{16}\gamma_{xy}^0 + D_{11}\kappa_x + D_{12}\kappa_y + D_{16}\kappa_{xy} \quad (7.40)$$

where the laminate extensional stiffnesses are given by

$$A_{ij} = \int_{-t/2}^{t/2} (\bar{Q}_{ij})_k dz = \sum_{k=1}^N (\bar{Q}_{ij})_k (z_k - z_{k-1}) \quad (7.41)$$

The laminate-coupling stiffnesses are given by

$$B_{ij} = \int_{-t/2}^{t/2} (\bar{Q}_{ij})_k z dz = \frac{1}{2} \sum_{k=1}^N (\bar{Q}_{ij})_k (z_k^2 - z_{k-1}^2) \quad (7.42)$$

and the laminate-bending stiffnesses are given by

$$D_{ij} = \int_{-t/2}^{t/2} (\bar{Q}_{ij})_k z^2 dz = \frac{1}{3} \sum_{k=1}^N (\bar{Q}_{ij})_k (z_k^3 - z_{k-1}^3) \quad (7.43)$$

where the subscripts  $i, j = 1, 2$ , or 6. The other stress resultants can be written in similar form, and the complete set of equations can be expressed in matrix form as

$$\begin{Bmatrix} N_x \\ N_y \\ N_{xy} \\ M_x \\ M_y \\ M_{xy} \end{Bmatrix} = \begin{bmatrix} A_{11} & A_{12} & A_{16} & B_{11} & B_{12} & B_{16} \\ A_{12} & A_{22} & A_{26} & B_{12} & B_{22} & B_{26} \\ A_{16} & A_{26} & A_{66} & B_{16} & B_{26} & B_{66} \\ B_{11} & B_{12} & B_{16} & D_{11} & D_{12} & D_{16} \\ B_{12} & B_{22} & B_{26} & D_{12} & D_{22} & D_{26} \\ B_{16} & B_{26} & B_{66} & D_{16} & D_{26} & D_{66} \end{bmatrix} \begin{Bmatrix} \varepsilon_x^0 \\ \varepsilon_y^0 \\ \gamma_{xy}^0 \\ \kappa_x \\ \kappa_y \\ \kappa_{xy} \end{Bmatrix} \quad (7.44)$$

or in partitioned form as

$$\begin{Bmatrix} N \\ M \end{Bmatrix} = \begin{bmatrix} A & | & B \\ B & | & D \end{bmatrix} \begin{Bmatrix} \varepsilon^0 \\ \kappa \end{Bmatrix} \quad (7.45)$$

$$N_x = \underbrace{A_{11}\epsilon_x^0 + A_{12}\epsilon_y^0}_{\text{Stretching of middle surface}} + \underbrace{A_{16}\gamma_{xy}^0}_{\text{Shearing of middle surface}} + \underbrace{B_{11}\kappa_x + B_{12}\kappa_y}_{\text{Bending along } x \text{ and } y \text{ directions}} + \underbrace{B_{16}\kappa_{xy}}_{\text{Twisting of } xy \text{ plane}}$$

*Note:* If  $B_{11} = B_{12} = B_{16} = 0$ , no bending or twisting and if  $A_{16} = 0$ , pure stretching of middle surface

**FIGURE 7.11**

Illustration of decomposition of coupling effects in a general laminate loaded by a single force per unit length  $N_x$ .

From Equations 7.45, we can see that the extensional stiffness matrix  $[A]$  relates the in-plane forces  $\{N\}$  to the midplane strains  $\{\epsilon^0\}$ , and the bending stiffness matrix  $[D]$  relates the moments  $\{M\}$  to the curvatures  $\{\kappa\}$ . The coupling stiffness matrix  $[B]$  couples the in-plane forces  $\{N\}$  with the curvatures  $\{\kappa\}$  and the moments  $\{M\}$  with the midplane strains  $\{\epsilon^0\}$ . A laminate having nonzero  $B_{ij}$  will bend or twist under in-plane loads. Such a laminate will also exhibit midplane stretching under bending and twisting moment loading. It can be easily shown that laminate geometric and material property symmetry with respect to the middle surface leads to the condition that all  $B_{ij} = 0$  and that asymmetry about the middle surface leads to nonzero  $B_{ij}$ .

The decomposition of typical force and moment terms in Equations 7.44 is illustrated in Figures 7.11 and 7.12, respectively. Note in Figure 7.11 that the corresponding force-deformation relationship for a homogeneous isotropic plate would only include the first two terms and no coupling terms of any kind, whereas in Figure 7.12, the corresponding moment-curvature relationship for a homogeneous isotropic plate would only include the fourth and fifth terms and no coupling terms of any kind.

$$M_x = \underbrace{B_{11}\epsilon_x^0 + B_{12}\epsilon_y^0}_{\text{Stretching of middle surface}} + \underbrace{B_{16}\gamma_{xy}^0}_{\text{Shearing of middle surface}} + \underbrace{D_{11}\kappa_x + D_{12}\kappa_y + D_{16}\kappa_{xy}}_{\text{Bending along } x \text{ and } y \text{ axes}} + \underbrace{B_{16}\kappa_{xy}}_{\text{Twisting of } xy \text{ plane}}$$

*Note:* If  $B_{11} = B_{12} = B_{16} = 0$ , no stretching or shearing and if  $D_{16} = 0$ , pure bending

*Conclusion:* Major simplifications possible if  $B_{ij} = 0$

**FIGURE 7.12**

Illustration of decomposition of coupling effects in a general laminate loaded by a single bending moment per unit length  $M_x$ .

*Example: Expanding expression for  $N_x$*

$$N_x = A_{11} \frac{0}{x} + A_{12} \frac{0}{y} + A_{16} \frac{\gamma_{xy}^0}{x} + \underbrace{B_{11} \frac{x}{x} + B_{12} \frac{y}{y} + B_{16} \frac{x}{x}}$$

$A_{16} \gamma_{xy}^0$  term due to coupling at lamina level since

$$A_{16} = \sum_{k=1}^N (\bar{Q}_{16})_k (z_k - z_{k-1})$$

and  $\bar{Q}_{16}$  is due to shear coupling in off-axis lamina ( $\bar{Q}_{16} = 0$  for  $0^\circ$  or  $90^\circ$  lamina)

$B_{11} x$   $B_{12} y$  terms cause coupling at the laminate level even though lamina coupling terms such as  $Q_{16}$  and  $Q_{26}$  may not be present.  $B_{ij}$  terms present due to nonsymmetrical arrangement of plies about middle surface.

**FIGURE 7.13**

Illustration of the difference between lamina level coupling and laminate level coupling in a general laminate loaded by a single force per unit length  $N_x$ .

It is now clear that there may be coupling effects at both the lamina level and the laminate level, but the two types of coupling are not necessarily related. Lamina shear coupling is a result of anisotropic material behavior and the presence of 16 and 26 terms in the lamina stiffness or compliance matrices (recall Section 2.6). This type of coupling at the lamina level also leads to coupling at the laminate level due to terms such as  $A_{16}$ ,  $A_{26}$ ,  $D_{16}$ , and  $D_{26}$ . On the other hand, the  $B_{ij}$ -type coupling at the laminate level is due to geometric and/or material property asymmetry with respect to the middle surface and is unrelated to material anisotropy. For example, it is possible for a laminate to have nonzero  $B_{ij}$  even with isotropic laminae if they are stacked in nonsymmetrical fashion, but the isotropic lamina properties lead to the condition  $A_{16} = A_{26} = D_{16} = D_{26} = 0$ . Figure 7.13 illustrates the two different types of coupling that appear in one specific laminate force-deformation equation. In the next section, the nature of the stiffness matrices for several special types of laminates will be summarized.

## 7.4 Stiffness Characteristics of Selected Laminate Configurations

As shown in the previous section, the number of nonzero terms in the laminate stiffness matrices is reduced for certain laminate configurations. Symmetry or antisymmetry of geometric and material properties about the middle surface, ply orientations, and ply-stacking sequences are all factors that govern the form of the laminate stiffness matrices. It is particularly important to be able to understand the effects of these factors on the

type of coupling that may exist in the stiffness matrices of commonly used laminates.

Before beginning the discussion of special laminate configurations, it is useful to define several terms that are associated with special ply orientations. Although these ply orientations, by themselves, do not necessarily produce simplifications in the stiffness matrices, they are often used in combination with other terms to describe special laminates that do have simplified stiffness matrices. “Angle-ply” laminates have lamina orientations of either  $+θ$  or  $-θ$ , where  $0^\circ \leq θ \leq 90^\circ$ . Depending on ply-stacking sequences, angle-ply laminates may be symmetric, antisymmetric, or asymmetric with respect to the middle surface. “Cross-ply” laminates consist of plies oriented at either  $θ = 0^\circ$  or  $θ = 90^\circ$ . A balanced cross-ply laminate has equal numbers of  $0^\circ$  and  $90^\circ$  plies. Depending on the ply arrangement, cross-ply laminates may be either symmetric or asymmetric with respect to the middle surface, but not antisymmetric. Since all plies in a cross-ply laminate behave as specially orthotropic laminae, such a laminate will always have  $A_{16} = A_{26} = D_{16} = D_{26} = 0$ . However, since all plies in an angle-ply laminate behave as generally orthotropic laminae, the 16 and 26 terms may not vanish.

#### 7.4.1 Specially Orthotropic Laminates

One of the simplest possible laminates is the specially orthotropic laminate, which is nothing more than a specially orthotropic lamina (Figure 2.5, where the laminate is aligned with the principal 1,2,3 axes) of thickness  $t$ . The multilayered laminate would typically be thicker than a single lamina. From Equations 7.41 through 7.43, the laminate stiffnesses for this configuration are

$$\begin{aligned} A_{11} &= Q_{11}t, \quad A_{12} = Q_{12}t, \quad A_{22} = Q_{22}t, \quad A_{66} = Q_{66}t, \quad A_{16} = A_{26} = 0 \\ D_{11} &= \frac{Q_{11}t^3}{12}, \quad D_{12} = \frac{Q_{12}t^3}{12}, \quad D_{22} = \frac{Q_{22}t^3}{12}, \quad D_{66} = \frac{Q_{66}t^3}{12}, \quad D_{16} = D_{26} = 0 \\ \text{all } B_{ij} &= 0 \end{aligned} \tag{7.46}$$

where the lamina stiffnesses,  $Q_{ij}$ , were defined in Section 2.5. Note that, since there are no off-axis laminae,  $A_{16} = A_{26} = D_{16} = D_{26} = 0$ , and due to symmetry of the laminate about the middle surface, all  $B_{ij} = 0$ .

#### 7.4.2 Generally Orthotropic Laminates

The generally orthotropic laminate is simply an off-axis version of the specially orthotropic laminate, or a generally orthotropic lamina (Figure 2.5, where the laminate is aligned with the nonprincipal  $x,y,z$  axes) of thickness  $t$ .

From Equations 7.41 through 7.43, the laminate stiffnesses for this configuration are

$$\begin{aligned} A_{11} &= \bar{Q}_{11}t, A_{12} = \bar{Q}_{12}t, A_{22} = \bar{Q}_{22}t, \bar{A}_{66} = \bar{Q}_{66}t, A_{16} = \bar{Q}_{16}t, A_{26} = \bar{Q}_{26}t \\ D_{11} &= \frac{\bar{Q}_{11}t^3}{12}, D_{12} = \frac{\bar{Q}_{12}t^3}{12}, D_{22} = \frac{\bar{Q}_{22}t^3}{12}, D_{66} = \frac{\bar{Q}_{66}t^3}{12}, D_{16} = \frac{\bar{Q}_{16}t^3}{12}, D_{26} = \frac{\bar{Q}_{26}t^3}{12} \\ \text{all } B_{ij} &= 0 \end{aligned} \quad (7.47)$$

where the transformed, or off-axis lamina stiffnesses,  $\bar{Q}_{ij}$ , were defined in Section 2.6. In this case, due to the off-axis orientation, the 16 and 26 stiffness terms are no longer equal to zero, but since the laminate is symmetric about the middle surface, the coupling stiffnesses  $B_{ij} = 0$  as with the specially orthotropic laminate.

#### 7.4.3 Symmetric Laminates

A symmetric laminate has both geometric and material property symmetry about the middle surface. That is, the ply material, ply orientation, and ply thickness at a positive distance  $z$  from the middle surface are identical to the corresponding values at an equal negative distance  $z$  from the middle surface. Examples of symmetric angle-ply and cross-ply laminates are shown in Figure 7.14a and b, respectively. Such a symmetry condition when substituted in Equation 7.42 leads to the major simplification that all  $B_{ij} = 0$ . This means that bending-stretching coupling will not be present in such laminates. Consequently, in-plane loads will not generate bending and twisting curvatures that cause out-of-plane warping, and bending or twisting moments will not produce an extension of the middle surface. This can be particularly important in structures that are subjected to changes in

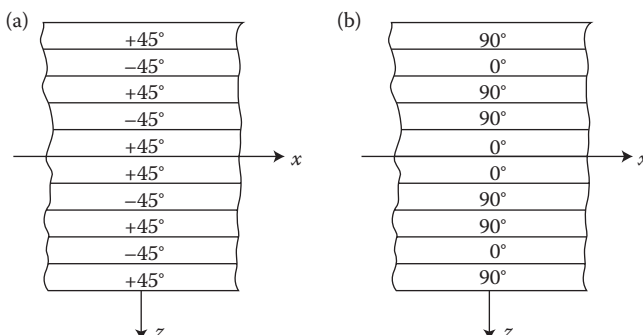


**FIGURE 7.14**

Examples of symmetric laminates. Ply orientations and material properties are symmetric about middle surface. (a) Symmetric angle-ply and (b) symmetric cross-ply.

environmental conditions, where the resulting hygrothermal forces would lead to undesirable warping in nonsymmetric laminates.

### Example 7.4

Determine the stiffness matrix for a  $[+45/-45/-45/+45]$  symmetric angle-ply laminate consisting of 0.25 mm-thick unidirectional AS/3501 carbon/epoxy laminae. An exploded view of the laminate is shown in Figure 7.15.

### SOLUTION

From Table 2.2, the lamina engineering constants are

$$E_1 = 138 \text{ GPa} \quad E_2 = 9 \text{ GPa} \quad G_{12} = 6.9 \text{ GPa} \quad v_{12} = 0.3$$

$$\text{and } v_{21} = v_{12} \frac{E_2}{E_1} = 0.3 \frac{9.0}{138.0} = 0.0196$$

Substitution of the above engineering constants in Equations 2.27 yields the components of the lamina stiffness matrix associated with the principal material axes:

$$[Q] = \begin{bmatrix} 138.8 & 2.72 & 0 \\ 2.72 & 9.05 & 0 \\ 0 & 0 & 6.9 \end{bmatrix} \text{ GPa}$$

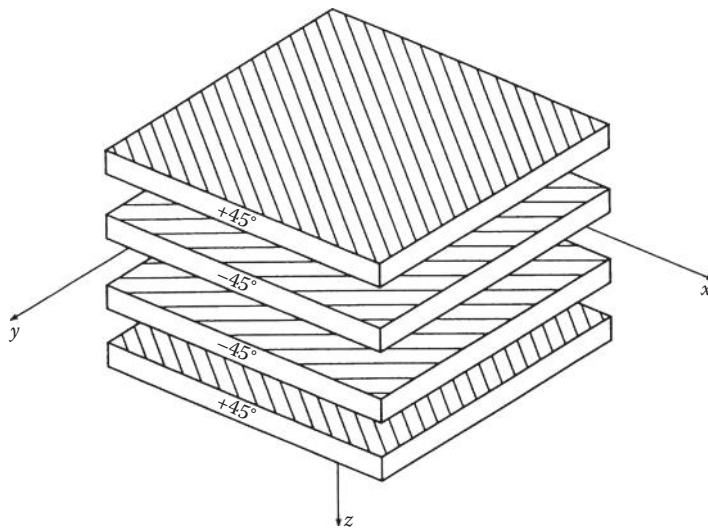


**FIGURE 7.15**

Exploded view of  $[+45/-45/-45/+45]$  symmetric laminate.

The transformed lamina stiffness matrices for the  $+45^\circ$  and  $-45^\circ$  plies are then found by substituting the above stiffnesses in Equations 2.36 or Equations 2.44 and Equations 2.45. For the  $+45^\circ$  plies,

$$[\bar{Q}]_{+45^\circ} = \begin{bmatrix} 45.22 & 31.42 & 32.44 \\ 31.42 & 45.22 & 32.44 \\ 32.44 & 32.44 & 35.6 \end{bmatrix} \text{GPa}$$

For the  $-45^\circ$  plies,

$$[\bar{Q}]_{-45^\circ} = \begin{bmatrix} 45.22 & 31.42 & -32.44 \\ 31.42 & 45.22 & -32.44 \\ -32.44 & -32.44 & 35.6 \end{bmatrix} \text{GPa}$$

Note that the only difference between the stiffness matrices for the plies is that the shear coupling terms (i.e., the terms with subscripts 16 and 26) for the  $-45^\circ$  ply have the opposite sign from the corresponding terms for  $+45^\circ$  ply. Before calculating the laminate stiffnesses, we must determine distances from the middle surface on the various ply interfaces according to Figure 7.10. The distances are  $z_0 = -0.50$  mm,  $z_1 = -0.25$  mm,  $z_2 = 0$ ,  $z_3 = 0.25$  mm, and  $z_4 = 0.5$  mm. The laminate extensional stiffnesses are then found by substituting these distances along with the lamina stiffness in Equations 7.41:

$$[A] = \begin{bmatrix} 45.22 & 31.42 & 0 \\ 31.42 & 45.22 & 0 \\ 0 & 0 & 35.6 \end{bmatrix} \text{GPa-mm}$$

Similarly, the laminate-coupling stiffnesses are found from Equation 7.42:

$$[B] = \begin{bmatrix} 0 & 0 & 0 \\ 0 & 0 & 0 \\ 0 & 0 & 0 \end{bmatrix} \text{GPa-mm}^2$$

and the laminate-bending stiffnesses are found from Equations 7.43:

$$[D] = \begin{bmatrix} 3.77 & 2.62 & 2.03 \\ 2.62 & 3.77 & 2.03 \\ 2.03 & 2.03 & 2.97 \end{bmatrix} \text{GPa-mm}^3$$

#### 7.4.4 Antisymmetric Laminates

An antisymmetric laminate has plies of identical material and thickness at equal positive and negative distances from the middle surface, but the ply orientations are antisymmetric with respect to the middle surface. That is,

the ply orientation at a positive distance  $z$  is  $+θ$ , if the ply orientation at an equal negative distance  $z$  is  $-θ$ . Examples of antisymmetric angle-ply laminates are shown in Figure 7.16. Note that the antisymmetric definition has no meaning for a cross-ply laminate, which must be either symmetric or non-symmetric. It can be shown that by substituting the antisymmetric condition into Equations 7.41 and 7.43, the coupling terms  $A_{16} = A_{26} = D_{16} = D_{26} = 0$ . From Equations 7.42, it can also be shown that  $B_{11} = B_{12} = B_{22} = B_{66} = 0$  for the anti-symmetric angle-ply laminate.

### Example 7.5

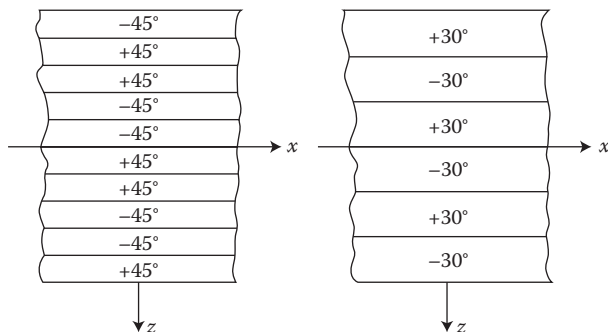
Determine the stiffness matrix for a  $[-45/+45/-45/+45]$  antisymmetric angle-ply laminate consisting of the same 0.25 mm thick unidirectional AS/3501 carbon/epoxy laminae that were used in Example 7.4. An exploded view of the laminate is shown in Figure 7.17.

### SOLUTION

Since the lamina orientations are still  $+45^\circ$  and  $-45^\circ$ , the lamina stiffnesses are the same as those calculated in Example 7.4. The distances  $z_k$  are also the same as those shown in Example 7.4, since the ply thicknesses and the number of plies are the same. Laminate extensional stiffnesses are then found by substituting these values, along with the antisymmetric stacking sequence, in Equations 7.41:

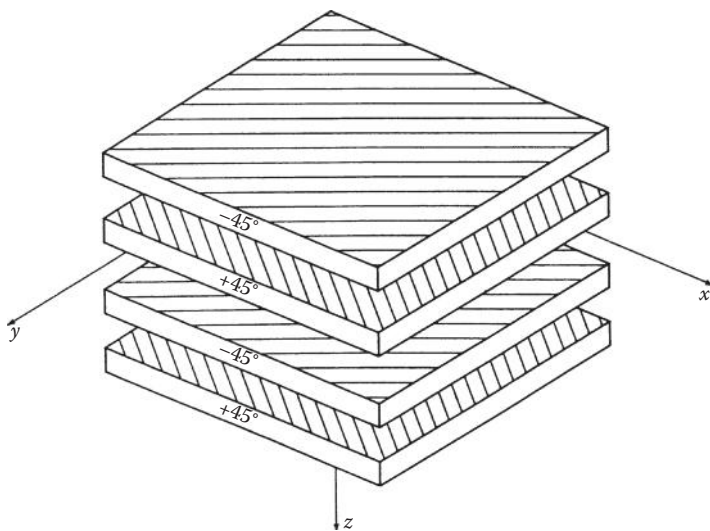
$$[A] = \begin{bmatrix} 45.22 & 31.42 & 0 \\ 31.42 & 45.22 & 0 \\ 0 & 0 & 35.6 \end{bmatrix} \text{ GPa-mm}$$

Note that these results are identical to those in Example 7.4 because we still have two plies at  $+45^\circ$  and two plies at  $-45^\circ$ . Thus, the stacking sequence has



**FIGURE 7.16**

Examples of antisymmetric angle-ply laminates. Although ply orientations are antisymmetric about middle surface, the material distribution is symmetric

**FIGURE 7.17**

Exploded view of  $[−45/+45/−45/+45]$  antisymmetric laminate.

no effect on  $[A]$  as long as the number of plies at a given orientation remains the same. The laminate-coupling stiffnesses are found from Equations 7.42:

$$[B] = \begin{bmatrix} 0 & 0 & 4.055 \\ 0 & 0 & 4.055 \\ 4.055 & 4.055 & 0 \end{bmatrix} \text{ GPa-mm}^2$$

Note that due to the antisymmetry,  $B_{11} = B_{22} = B_{12} = B_{66} = 0$  but  $B_{16}$  and  $B_{26}$  have nonzero values; this is true in general for antisymmetric angle-ply laminates. Thus, the antisymmetric laminate has extension-twisting and bending-shearing coupling, but the symmetric laminate does not. The laminate-bending stiffnesses are found from Equation 7.43:

$$[D] = \begin{bmatrix} 3.77 & 2.62 & 0 \\ 2.62 & 3.77 & 0 \\ 0 & 0 & 2.97 \end{bmatrix} \text{ GPa-mm}^3$$

Note that  $D_{11}$ ,  $D_{22}$ ,  $D_{12}$ , and  $D_{66}$  are the same as the corresponding values in Example 7.4, but we now have  $D_{16} = D_{26} = 0$ . Thus, bending-twisting coupling is present in symmetric angle-ply laminates, but not in antisymmetric angle-ply laminates.

#### 7.4.5 Quasi-Isotropic Laminates

Although it may seem unlikely, it is possible to use orthotropic laminae to construct a laminate that exhibits some elements of isotropic behavior. For

example, if a laminate consists of three or more identical orthotropic laminae (i.e., all have the same material and geometric properties) that are oriented at the same angle relative to adjacent laminae, the extensional stiffness matrix  $[A]$  will be isotropic, but the other stiffness matrices  $[B]$  and  $[D]$  will not necessarily have isotropic form. Such a laminate is called a quasi-isotropic or planar isotropic laminate, and the angle between adjacent laminae must be  $\pi/N$ , where  $N$  is the total number of laminae. For example, [60/0/-60] and [90/45/0/-45] laminates are quasi-isotropic.

Recall that in Section 6.4 it was mentioned that randomly oriented fiber composites could be modeled as planar isotropic or quasi-isotropic laminates. Now it is clear that although a randomly oriented fiber composite must theoretically have an infinite number of fiber orientations to be isotropic, the in-plane behavior of such materials can be modeled by using a quasi-isotropic laminate having only three laminae, as in the [60/0/-60] laminate.

Recall also that the stress-strain relationships for an isotropic lamina are given by Equation 2.26, with the additional requirements that  $Q_{11} = Q_{22}$ ,  $Q_{66} = (Q_{11} - Q_{12})/2$ , and  $Q_{16} = Q_{26} = 0$ . Similarly, the extensional force-deformation relationships for the quasi-isotropic laminate are given by

$$\begin{Bmatrix} N_x \\ N_x \\ N_{xy} \end{Bmatrix} = \begin{bmatrix} A_{11} & A_{12} & 0 \\ A_{12} & A_{11} & 0 \\ 0 & 0 & (A_{11} - A_{12})/2 \end{bmatrix} \begin{Bmatrix} \varepsilon_x^0 \\ e_y^0 \\ \gamma_{xy}^0 \end{Bmatrix} \quad (7.48)$$

In general, such simplifications are not possible for the  $[B]$  and  $[D]$  matrices, as can be shown by calculating the stiffness matrices for quasi-isotropic laminates such as [60/0/-60] or [90/45/0/-45].

In Section 6.4, it was shown that the invariants could be useful in the development of the stress-strain relationships and equations for the engineering constants of a planar isotropic, randomly oriented fiber composite. Similarly, the invariants can be used in the study of quasi-isotropic laminates. For example, by substituting the lamina stiffnesses in terms of invariants from Equations 2.44 in Equations 7.41 for the laminate extensional stiffnesses, we find that

$$\begin{aligned} A_{11} &= A_{22} = U_1 t \\ A_{12} &= U_4 t \\ A_{66} &= \frac{(U_1 - U_4)t}{2} \end{aligned} \quad (7.49)$$

Using developments similar to those in Section 6.4, we can show that the effective extensional engineering constants for quasi-isotropic laminates are given by Equations 6.43.

### Example 7.6

Determine the stiffness matrices and engineering constants for a quasi-isotropic [60/0/-60] laminate consisting of the same laminae that were described in Example 7.4. Figure 7.18 shows an exploded view of the laminate.

### SOLUTION

The required lamina stiffnesses are the  $Q_{ij}$  in Example 7.4 and the appropriate transformed stiffnesses for  $60^\circ$  and  $-60^\circ$  from Equations 2.36 or Equations 2.44 and Equations 2.45. Substituting these stiffnesses in Equations 7.41, we find that the laminate extensional stiffnesses are

$$[A] = \begin{bmatrix} 44.68 & 12.80 & 0 \\ 12.80 & 44.68 & 0 \\ 0 & 0 & 15.94 \end{bmatrix} \text{GPa-mm}$$

It is easily shown that this matrix is of the isotropic form shown in Equations 7.48. The laminate-coupling stiffnesses from Equations 7.42 are

$$[B] = \begin{bmatrix} 0 & 0 & -1.96 \\ 0 & 0 & -5.06 \\ -1.96 & -5.06 & 0 \end{bmatrix} \text{GPa-mm}^2$$

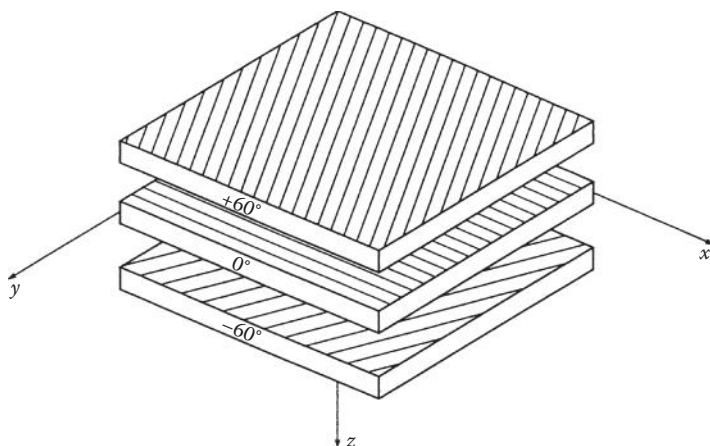


**FIGURE 7.18**  
Exploded view of [+60/0/-60] quasi-isotropic laminate.

and the bending stiffnesses from Equations 7.43 are

$$[D] = \begin{bmatrix} 0.856 & 0.824 & 0 \\ 0.824 & 2.88 & 0 \\ 0 & 0 & 0.972 \end{bmatrix} \text{GPa-mm}^3$$

It is seen that the matrices  $[B]$  and  $[D]$  do not have the isotropic form of Equations 7.48. It can also be shown that by changing the lamina orientations while maintaining equal angles between adjacent laminae (e.g., [75/15/-45], [30/-30/-90], or [0/-60/-120]), the  $A_{ij}$  remain unchanged but the  $B_{ij}$  and  $D_{ij}$  do not. Thus, the laminate is isotropic with respect to in-plane behavior only.

The engineering constants for the laminate may be found by using the invariants. By substituting the  $Q_{ij}$  from Example 7.4 in Equation 2.45, we find that

$$U_1 = 59.57 \text{ GPa} \quad \text{and} \quad U_4 = 17.07 \text{ GPa}$$

Substituting these results in Equations 6.43, we find that the engineering constants are

$$\tilde{E} = 54.68 \text{ GPa}, \quad \tilde{G} = 21.25 \text{ GPa}, \quad \text{and} \quad \tilde{\nu} = 0.287$$

Note that the  $A_{ij}$  can also be found by using the invariants  $U_1$  and  $U_4$ , along with the laminate thickness,  $t$ , in Equations 7.49.

### Example 7.7

A laminate has the stiffnesses shown below. (a) if this laminate is loaded in such a way that the midplane strain  $\epsilon_x^0 = 0.001 \text{ mm/mm}$  and all other strains and curvatures are equal to zero, determine all of the forces and moments per unit length acting on the laminate, (b) if this laminate is loaded in such a way that the bending curvature  $\kappa_x = 0.01 \text{ mm}^{-1}$  and all other strains and curvatures are equal to zero, determine all of the forces and moments per unit length acting on the laminate.

$$[A] = \begin{bmatrix} 22.61 & 15.71 & 0 \\ 15.71 & 22.61 & 0 \\ 0 & 0 & 17.8 \end{bmatrix} \text{GPa mm}$$

$$[B] = \begin{bmatrix} 0 & 0 & -2.027 \\ 0 & 0 & -2.027 \\ -2.027 & -2.027 & 0 \end{bmatrix} \text{GPa mm}^2$$

$$[D] = \begin{bmatrix} 0.471 & 0.327 & 0 \\ 0.327 & 0.471 & 0 \\ 0 & 0 & 0.371 \end{bmatrix} \text{GPa mm}^3$$

### SOLUTION

a.  $N_x = A_{11}\epsilon_x^0 = (22.61)(0.001) = 0.02261 \text{ GPa mm}$

$$N_y = A_{12}\epsilon_x^0 = (15.71)(0.001) = 0.01571 \text{ GPa mm}$$

$$N_{xy} = A_{16}\epsilon_x^0 = 0$$

$$M_x = B_{11}\epsilon_x^0 = 0$$

$$M_y = B_{12}\epsilon_x^0 = 0$$

$$M_{xy} = B_{16}\epsilon_x^0 = (-2.027)(0.001) = -0.002027 \text{ GPa mm}^2$$

b.  $N_x = B_{11}\kappa_x = 0$

$$N_y = B_{12}\kappa_x = 0$$

$$N_{xy} = B_{16}\kappa_x = (-2.027)(0.01) = -0.02027 \text{ GPa mm}$$

$$M_x = D_{11}\kappa_x = (0.471)(0.01) = 0.00471 \text{ GPa mm}^2$$

$$M_y = D_{12}\kappa_x = (0.327)(0.01) = 0.00327 \text{ GPa mm}^2$$

$$M_{xy} = D_{16}\kappa_x = 0$$

## 7.5 Derivation and Use of Laminate Compliances

Since the applied loads are generally known rather than the deformations, it is often necessary to use the inverted form of the laminate force–deformation relationships shown in Equation 7.44 and Equation 7.45. The use of the inverted equations means that we must deal with the laminate compliance matrix instead of the laminate stiffness matrix. In this section, the inverted equations are derived and used to calculate the lamina stresses and strains due to known laminate loads. The inverted equations are also used in the derivation of the laminate engineering constants and in the comparison of predicted and measured laminate compliances.

### 7.5.1 Inversion of Laminate Force–Deformation Equations

The general laminate force–deformation equations shown in Equations 7.45 can be expressed as

$$\begin{Bmatrix} N \\ M \end{Bmatrix} = \begin{bmatrix} A & | & B \\ B & | & D \end{bmatrix} \begin{Bmatrix} \epsilon^0 \\ \kappa \end{Bmatrix} = [E] \begin{Bmatrix} \epsilon^0 \\ \kappa \end{Bmatrix} \quad (7.50)$$

where the  $A_{ij}$ ,  $B_{ij}$  and  $D_{ij}$  make up the laminate stiffness matrix,  $[E]$ . The fully inverted form of this equation can be obtained directly by premultiplying both sides of the equation by the compliance matrix, which is the inverse of the stiffness matrix (see Appendix A)

$$\begin{Bmatrix} \epsilon^0 \\ \kappa \end{Bmatrix} = \begin{bmatrix} A & | & B \\ B & | & D \end{bmatrix}^{-1} \begin{Bmatrix} N \\ M \end{Bmatrix} = [E]^{-1} \begin{Bmatrix} N \\ M \end{Bmatrix} \quad (7.51)$$

Alternatively, Equations 7.51 are derived below by the inversion of subdivided smaller matrices, as shown by Halpin [12].

From Equations 7.50, the in-plane forces per unit length are

$$\{N\} = [A]\{\epsilon^0\} + [B]\{\kappa\} \quad (7.52)$$

whereas the moments per unit length are

$$\{M\} = [B]\{\epsilon^0\} + [D]\{\kappa\} \quad (7.53)$$

The midplane strains may be obtained from Equations 7.52 as

$$\{\epsilon^0\} = [A]^{-1}\{N\} - [A]^{-1}[B]\{\kappa\} \quad (7.54)$$

Substitution of these strains in Equations 7.53 gives

$$\{M\} = [B][A]^{-1}\{N\} - [B][A]^{-1}[B]\{\kappa\} + [D]\{\kappa\} \quad (7.55)$$

Equations 7.54 and 7.55 can be combined to give a partially inverted form of Equations 7.50 as follows:

$$\begin{Bmatrix} \epsilon^0 \\ M \end{Bmatrix} = \begin{bmatrix} A^* & | & B^* \\ C^* & | & D^* \end{bmatrix} \begin{Bmatrix} N \\ \kappa \end{Bmatrix} \quad (7.56)$$

where

$$\begin{aligned}[A^*] &= [A]^{-1} \\ [B^*] &= -[A]^{-1}[B] \\ [C^*] &= [B][A]^{-1} \\ [D^*] &= [D] - [B][A]^{-1}[B]\end{aligned}$$

Inverting the last set of partitioned Equations 7.56 to solve for the curvatures, we find that

$$\{\kappa\} = [D^*]^{-1}\{M\} - [D^*]^{-1}[C^*]\{N\} \quad (7.57)$$

Now substituting Equations 7.57 into Equations 7.54, we have

$$\{\epsilon^0\} = ([A^*] - [B^*][D^*]^{-1}[C^*])\{N\} + [B^*][D^*]^{-1}\{M\} \quad (7.58)$$

Equations 7.57 and 7.58 can now be combined in partitioned matrix form to give

$$\begin{Bmatrix} \epsilon^0 \\ \kappa \end{Bmatrix} = \begin{bmatrix} A' & | & B' \\ \hline C' & + & C' \end{bmatrix} \begin{Bmatrix} N \\ M \end{Bmatrix} \quad (7.59)$$

where

$$\begin{aligned}[A'] &= [A^*] - [B^*][D^*]^{-1}[C^*] \\ [B'] &= [B^*][D^*]^{-1} \\ [C'] &= -[D^*]^{-1}[C^*] = [B']^T \\ [D'] &= [D^*]^{-1}\end{aligned}$$

and the compliance matrix is

$$\begin{bmatrix} A' & | & B' \\ \hline C' & + & D' \end{bmatrix} = [E]^{-1} \quad (7.60)$$

Since the stiffness matrix  $[E]$  is symmetric, the compliance matrix must also be symmetric.

### 7.5.2 Determination of Lamina Stresses and Strains

Now that we have the inverted laminate force-deformation relationships in Equations 7.59, the calculation of lamina stresses and strains from known

laminate forces and moments is a straightforward procedure. For a laminate at constant temperature and moisture content, the stresses in the  $k$ th lamina are given by Equations 7.34, which can be written in abbreviated matrix notation as

$$\{\sigma\}_k = [\bar{Q}]_k(\{\epsilon^0\} + z\{\kappa\}) \quad (7.61)$$

where the midplane strains  $\{\epsilon^0\}$  and curvatures  $\{\kappa\}$  are given in terms of laminate forces and moments by Equations 7.59. The lamina stresses from Equations 7.61 can then be used in conjunction with a lamina strength criterion to check each lamina against failure. The analysis of hygrothermal stresses will be discussed later in Section 7.6, and laminate strength analysis will be presented in Section 7.8.

### Example 7.8

The symmetric angle-ply laminate described in Example 7.4 is subjected to a single uniaxial force per unit length  $N_x = 50 \text{ MPamm}$ . Determine the resulting stresses associated with the  $x$  and  $y$  axes in each lamina.

#### SOLUTION

Owing to symmetry,  $[B] = 0$  and  $[A'] = [A^*] = [A]^{-1}$ . Since  $\{M\} = 0$  here,

$$\{\epsilon^0\} = [A']\{N\} = [A]^{-1}\{N\}$$

Using the inverse of the  $[A]$  matrix from Example 7.4, we find that

$$\begin{Bmatrix} \epsilon_x^0 \\ \epsilon_y^0 \\ \gamma_{xy}^0 \end{Bmatrix} = \begin{bmatrix} 0.04276 & -0.0297 & 0 \\ -0.0297 & 0.04276 & 0 \\ 0 & 0 & 0.02809 \end{bmatrix} \begin{Bmatrix} 50 \\ 0 \\ 0 \end{Bmatrix} \times (10^{-3}) = \begin{Bmatrix} 0.002138 \\ -0.001485 \\ 0 \end{Bmatrix}$$

where  $(\text{GPa mm})^{-1} = 10^{-3} (\text{MPa mm})^{-1}$ . Substituting the above strains and the lamina stiffnesses from Example 7.4 in Equations 7.61, we find that the stresses in the  $+45^\circ$  plies are

$$\begin{Bmatrix} \sigma_x \\ \sigma_y \\ \tau_{xy} \end{Bmatrix} = \begin{bmatrix} 45.22 & 31.42 & 32.44 \\ 31.42 & 45.22 & 32.44 \\ 32.44 & 32.44 & 35.6 \end{bmatrix} \begin{Bmatrix} 0.002138 \\ -0.001485 \\ 0 \end{Bmatrix} \times 10^3 = \begin{Bmatrix} 50 \\ 0 \\ 21.2 \end{Bmatrix} \text{ MPa}$$

where  $10^3 \text{ MPa} = \text{GPa}$ . Similarly, the stresses in the  $-45^\circ$  plies are

$$\begin{Bmatrix} \sigma_x \\ \sigma_y \\ \tau_{xy} \end{Bmatrix} = \begin{bmatrix} 45.22 & 31.42 & -32.44 \\ 31.42 & 45.22 & -32.44 \\ -32.44 & -32.44 & 35.6 \end{bmatrix} \begin{Bmatrix} 0.002138 \\ -0.001485 \\ 0 \end{Bmatrix} \times 10^3 = \begin{Bmatrix} 50 \\ 0 \\ -21.2 \end{Bmatrix} \text{ MPa}$$

Note that since the curvatures vanish for this problem, the stresses do not depend on the distance  $z$ .

### Example 7.9

The antisymmetric angle-ply laminate described in Example 7.5 is subjected to a single uniaxial force per unit length  $N_x = 50 \text{ MPa-mm}$ . Determine the resulting stresses associated with the  $x$  and  $y$  axes in each lamina.

### SOLUTION

Since this laminate is not symmetric, we must invert the full stiffness matrix as in Equation 7.51 or Equation 7.59. Forming the full stiffness matrix from the  $[A]$ ,  $[B]$ , and  $[D]$  matrices in Example 7.5 and inverting, we find the resulting mid plane strains and curvatures to be

$$\begin{Bmatrix} \epsilon_x^0 \\ \epsilon_y^0 \\ \gamma_{xy}^0 \\ \kappa_x \\ \kappa_y \\ \kappa_{xy} \end{Bmatrix} = \begin{bmatrix} 0.04386 & -0.02861 & 0 & 0 & 0 & -0.02083 \\ -0.02861 & 0.04386 & 0 & 0 & 0 & -0.02083 \\ 0 & 0 & 0.03284 & -0.02083 & -0.02083 & 0 \\ 0 & 0 & -0.02083 & 0.52625 & 0.34331 & 0 \\ 0 & 0 & -0.02083 & -0.34331 & 0.52625 & 0 \\ -0.02083 & -0.02083 & 0 & 0 & 0 & 0.39356 \end{bmatrix} \times \begin{Bmatrix} 50 \\ 0 \\ 0 \\ 0 \\ 0 \\ 0 \end{Bmatrix} \times 10^{-3} = \begin{Bmatrix} 0.002193 \text{ mm/mm} \\ -0.001430 \text{ mm/mm} \\ 0 \text{ mm/mm} \\ 0 \text{ mm}^{-1} \\ 0 \text{ mm}^{-1} \\ -0.001042 \text{ mm}^{-1} \end{Bmatrix}$$

where again the factor of  $10^{-3}$  has been introduced for dimensional consistency. Due to the curvatures, the total strains and stresses now depend on the distance  $z$  (unlike Example 7.8). For example, at the top surface of the #1 ply ( $-45^\circ$ ),  $z = -0.5 \text{ mm}$  and the resulting total strains are

$$\epsilon_x = \epsilon_x^0 + z\kappa_x = 0.002193 + (-0.5)(0) = 0.002193 \text{ mm/mm}$$

$$\epsilon_y = \epsilon_y^0 + z\kappa_y = -0.00143 + (-0.5)(0) = -0.00143 \text{ mm/mm}$$

$$\gamma_{xy} = \gamma_{xy}^0 + z\kappa_{xy} = 0 + (-0.5)(-0.001042) = 0.000521 \text{ mm/mm}$$

Similarly, at the bottom surface of the #1 ply ( $-45^\circ$ ), or at the top surface of the #2 ply ( $+45^\circ$ ),  $z = -0.25$  mm and the strains are

$$\epsilon_x = 0.002193 + (-0.25)(0) = 0.002193 \text{ mm/mm}$$

$$\epsilon_y = -0.00143 + (-0.25)(0) = -0.00143 \text{ mm/mm}$$

$$\gamma_{xy} = 0 + (-0.25)(-0.001042) = 0.000261 \text{ mm/mm}$$

At the top surface of the #3 ply ( $-45^\circ$ ), or at the bottom surface of the #2 ply,  $z = 0$  and the strains are

$$\epsilon_x = 0.002193 \text{ mm/mm}$$

$$\epsilon_y = -0.00143 \text{ mm/mm}$$

$$\gamma_{xy} = 0$$

At the top surface of the #4 ply ( $+45^\circ$ ), or at the bottom surface of the #3 ply ( $-45^\circ$ ),  $z = 0.25$  mm and

$$\epsilon_x = 0.002193 \text{ mm/mm}$$

$$\epsilon_y = -0.00143 \text{ mm/mm}$$

$$\gamma_{xy} = -0.000261 \text{ mm/mm}$$

Finally, at the bottom of the #4 ply ( $+45^\circ$ ),  $z = +0.5$  mm and

$$\epsilon_x = 0.002193 \text{ mm/mm}$$

$$\epsilon_y = -0.00143 \text{ mm/mm}$$

$$\gamma_{xy} = -0.000521 \text{ mm/mm}$$

The stresses at the top surface of the #1 ply ( $-45^\circ$ ) are then

$$\begin{aligned} \begin{Bmatrix} \sigma_x \\ \sigma_y \\ \tau_{xy} \end{Bmatrix} &= \begin{bmatrix} 45.22 & 31.42 & -32.44 \\ 31.42 & 45.22 & -32.44 \\ -32.44 & -32.44 & 35.6 \end{bmatrix} \begin{Bmatrix} 0.002193 \\ -0.001430 \\ 0.000521 \end{Bmatrix} \times 10^3 \\ &= \begin{Bmatrix} 37.3 \\ -12.7 \\ -6.2 \end{Bmatrix} \text{ MPa} \end{aligned}$$

where again  $10^3 \text{ MPa} = \text{GPa}$ . Similar calculations for the other plies yield the values shown in the following table:

Location	$\sigma_x$ (MPa)	$\sigma_y$ (MPa)	$\tau_{xy}$ (MPa)
#1 Top	37.3	-12.7	-6.2
#1 Bottom	45.8	-4.2	-15.5
#2 Top	62.7	12.7	34.0
#2 Bottom	54.2	4.2	24.7
#3 Top	54.2	4.2	-24.7
#3 Bottom	62.7	12.7	-34.0
#4 Top	45.8	-4.2	15.5
#4 Bottom	37.3	-12.7	6.2

Thus, the stress distribution across the thickness of the antisymmetric laminate is quite complex, even for simple uniaxial loading. This is typical for laminates that exhibit coupling.

### 7.5.3 Determination of Laminate Engineering Constants

It is sometimes more convenient to use effective laminate engineering constants rather than the laminate stiffnesses defined in Equations 7.41 through 7.43. These effective laminate engineering constants may be derived by using laminate compliances. For example, the force–deformation relationships for a symmetric laminate under in-plane loads only are given by

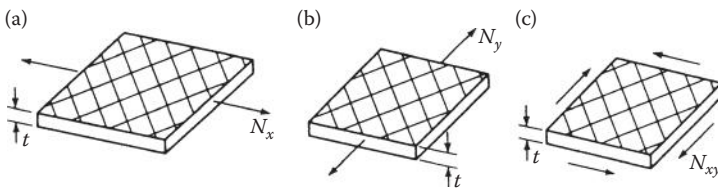
$$\begin{Bmatrix} N_x \\ N_y \\ N_{xy} \end{Bmatrix} = \begin{bmatrix} A_{11} & A_{12} & A_{16} \\ A_{12} & A_{22} & A_{26} \\ A_{16} & A_{26} & A_{66} \end{bmatrix} \begin{Bmatrix} \varepsilon_x^0 \\ \varepsilon_y^0 \\ \gamma_{xy}^0 \end{Bmatrix} \quad (7.62)$$

and the corresponding inverted force–deformation relationships are

$$\begin{Bmatrix} \varepsilon_x^0 \\ \varepsilon_y^0 \\ \gamma_{xy}^0 \end{Bmatrix} = \begin{bmatrix} A'_{11} & A'_{12} & A'_{16} \\ A'_{12} & A'_{22} & A'_{26} \\ A'_{16} & A'_{26} & A'_{66} \end{bmatrix} \begin{Bmatrix} N_x \\ N_y \\ N_{xy} \end{Bmatrix} \quad (7.63)$$

The effective longitudinal Young's modulus of the laminate,  $E_x$ , governs the response of the laminate under the single axial load per unit length  $N_x$  with  $N_y = N_{xy} = 0$  (Figure 7.19a) and is defined as

$$E_x = \frac{\sigma_x}{\varepsilon_x^0} = \frac{N_x/t}{A'_{11}N_x} = \frac{1}{tA'_{11}} \quad (7.64)$$

**FIGURE 7.19**

In-plane loading of symmetric laminate for defining the in-plane laminate engineering constants. (a) Applied axial load  $N_x$ , (b) applied axial load  $N_y$ , and (c) applied shear load  $N_{xy}$ .

The effective transverse Young's modulus of the laminate,  $E_y$ , governs the response of the laminate under the single axial load per unit length  $N_y$  with  $N_x = N_{xy} = 0$  (Figure 7.19b) and is defined as

$$E_y = \frac{\sigma_y}{\epsilon_y^0} = \frac{N_y/t}{A'_{22}N_y} = \frac{1}{tA'_{22}} \quad (7.65)$$

The effective laminate in-plane shear modulus,  $G_{xy}$ , governs the laminate response under the pure shear load per unit length  $N_{xy}$  with  $N_x = N_y = 0$  (Figure 7.19c) and is defined as

$$G_{xy} = \frac{\tau_{xy}}{\gamma_{xy}^0} = \frac{N_{xy}/t}{A'_{66}N_{xy}} = \frac{1}{tA'_{66}} \quad (7.66)$$

Similarly, the effective laminate longitudinal Poisson's ratio is

$$\nu_{xy} = -\frac{A'_{12}}{A'_{11}} \quad (7.67)$$

and the effective laminate shear coupling ratios analogous to those given in Equation 2.41 and Equation 2.42 for the orthotropic lamina are

$$\eta_{x,xy} = \frac{A'_{16}}{A'_{11}} \quad \text{and} \quad \eta_{xy,y} = \frac{A'_{26}}{A'_{66}} \quad (7.68)$$

Using similar derivations, the effective laminate flexural moduli may be expressed in terms of the flexural compliances. For the symmetric laminate subjected to bending only, the laminate moment-curvature relationships are given by

$$\begin{Bmatrix} M_x \\ M_y \\ M_{xy} \end{Bmatrix} = \begin{bmatrix} D_{11} & D_{12} & D_{16} \\ D_{12} & D_{22} & D_{26} \\ D_{16} & D_{26} & D_{66} \end{bmatrix} \begin{Bmatrix} \kappa_x \\ \kappa_y \\ \kappa_{xy} \end{Bmatrix} \quad (7.69)$$

and the inverted forms are given by

$$\begin{Bmatrix} \kappa_x \\ \kappa_y \\ \kappa_{xy} \end{Bmatrix} = \begin{bmatrix} D'_{11} & D'_{12} & D'_{16} \\ D'_{12} & D'_{22} & D'_{26} \\ D'_{16} & D'_{26} & D'_{66} \end{bmatrix} \begin{Bmatrix} M_x \\ M_y \\ M_{xy} \end{Bmatrix} \quad (7.70)$$

Thus, when the laminate is subjected to a pure bending moment per unit length  $M_x$  with  $M_y = M_{xy} = 0$  (Figure 7.20a), the resulting curvature is

$$\kappa_x = D'_{11}M_x = D'_{11} \frac{M}{b} = \frac{1}{\rho_x} \quad (7.71)$$

where  $M$  is the total bending moment, which is  $M_x b$ ,  $b$  the laminate width, and the radius of curvature  $\rho_x = 1/\kappa_x$ .

For an equivalent homogeneous beam, the moment-curvature relationship is

$$\frac{M}{E_{fx}I_{yy}} = \frac{1}{\rho_x} \quad (7.72)$$

where  $I_{yy}$  is the second moment of inertia of the beam about the neutral axis, which is  $bt^3/12$ , and  $E_{fx}$  the flexural modulus of the beam along the  $x$  direction.

Recall that the flexural modulus was also defined by Equations 7.8 and 7.9 according to laminated beam theory. Combining Equations 7.71 and 7.72, we find that the flexural modulus is related to the laminate compliance  $D'_{11}$ , by the equation

$$E_{fx} = \frac{12}{t^3 D'_{11}} \quad (7.73)$$

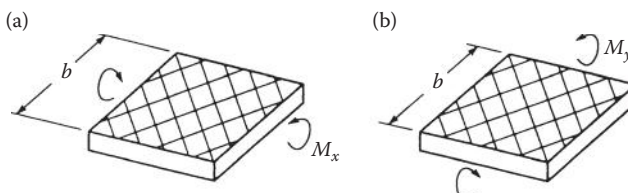


**FIGURE 7.20**

Bending moment leading of symmetric laminate for defining the laminate flexural moduli. (a) Applied bending moment  $M_x$  and (b) applied bending moment  $M_y$ .

Similarly, the flexural modulus along the  $y$  direction (Figure 7.20b) is found to be

$$E_{fy} = \frac{12}{t^3 D'_{22}} \quad (7.74)$$

Although the laminate stiffnesses  $A_{ij}$ ,  $B_{ij}$ , and  $D_{ij}$  are meaningful parameters for all laminate configurations, the engineering constants may not be. Clearly, the use of effective engineering constants must be restricted to those cases where the deformations are similar to the deformations associated with the engineering constant being used. That is, in the above examples for symmetric laminates the  $B_{ij} = 0$  and warping under in-plane loads or mid-plane extension under bending or twisting moments will not occur, so the deformations of the laminate under load would be similar to those for the equivalent homogeneous material. However, the use of engineering constants for the antisymmetric laminate may not be appropriate because of the complex deformations due to coupling effects.

### Example 7.10

For the symmetric laminate described in Examples 7.4 and 7.8, determine the effective Young's moduli, in-plane shear modulus, longitudinal Poisson's ratio, and shear-coupling ratios associated with the  $x$  and  $y$  axes.

#### SOLUTION

The effective longitudinal Young's modulus is given by Equation 7.64

$$E_x = \frac{1}{tA'_{11}} = \frac{1}{(1)(0.04276)} = 23.4 \text{ GPa}$$

Note that due to the  $\pm 45^\circ$  ply orientations for this laminate,  $E_x = E_y$ . The effective in-plane shear modulus is given by Equation 7.66:

$$G_{xy} = \frac{1}{tA'_{66}} = \frac{1}{(1)(0.02809)} = 35.6 \text{ GPa}$$

The effective longitudinal Poisson's ratio is given by Equation 7.67:

$$\nu_{xy} = -\frac{A'_{12}}{A'_{11}} = -\frac{-0.0297}{0.04276} = 0.694$$

Since  $A_{16} = A_{26} = 0$  for this laminate, it is seen from Equations 7.68 that the effective shear-coupling ratios  $\eta_{x,xy} = \eta_{xy,y} = 0$ . Due to the complex coupling effects acting in the antisymmetric laminate of Examples 7.5 and 7.9, the use of engineering constants for such a laminate would be questionable.

### 7.5.4 Comparison of Measured and Predicted Compliances

Experimental verification of the laminate theory can be done by applying known loads to laminate and by measuring resulting deformations and then comparing measured deformations with those predicted from the laminate theory. Alternatively, the compliances that are formed from ratios of strains to loads or ratios of curvature to moments for certain simple loading conditions can be experimentally determined and compared with predicted values. The latter approach has been used by Tsai [13] who reported results for cross-ply and angle-ply glass/epoxy laminates. Only the results for the angle-ply laminates will be discussed here.

In order to determine the compliances of the laminates under various loads, electrical resistance strain gage rosettes with gages oriented at  $0^\circ$  ( $x$  direction),  $45^\circ$ , and  $90^\circ$  ( $y$  direction) were attached on both sides of the test specimens (Figure 7.21). From Equations 7.31, the measured normal strains on the upper surface (where  $z = -t/2$ ) are related to the corresponding midplane strains and curvatures by

$$\epsilon_x^U = \epsilon_x^0 - \frac{t}{2} \kappa_x \quad (7.75)$$

$$\epsilon_y^U = \epsilon_y^0 - \frac{t}{2} k_y \quad (7.76)$$

where  $\epsilon_x^U$  is the measured normal strain along the  $x$  direction on upper surface and  $\epsilon_y^U$  the measured normal strain along  $y$  direction on upper surface.

Similarly, the normal strains on the lower surface (where  $z = t/2$ ) are given by

$$\epsilon_x^L = \epsilon_x^0 + \frac{t}{2} \kappa_x \quad (7.77)$$

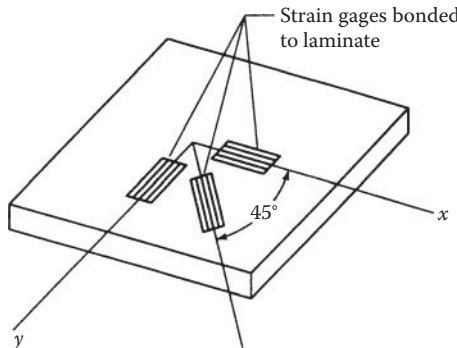


**FIGURE 7.21**  
Strain gage rosette bonded to upper surface of laminate.

$$\varepsilon_y^L = \varepsilon_y^0 + \frac{t}{2} \kappa_y \quad (7.78)$$

where  $\varepsilon_x^L$  is the measured normal strain along the  $x$  direction on the lower surface and  $\varepsilon_y^L$  the measured normal strain along the  $y$  direction on the lower surface.

Equations 7.75 and 7.77 can be solved simultaneously for the midplane strain,  $\varepsilon_x^0$  and curvature,  $\kappa_x$ , whereas  $\varepsilon_y^0$  and  $\kappa_y$  can be determined from Equations 7.76 and 7.78. Although the surface shear strains  $\gamma_{xy}^U$  and  $\gamma_{xy}^L$  are not measured directly like the normal strains, they can be determined from the measured strains along  $0^\circ$ ,  $45^\circ$ , and  $90^\circ$  and the strain transformation relationships similar to Equations 2.33. For example, from Equation 2.33, the measured normal strain along the  $45^\circ$  direction on the upper surface,  $\varepsilon_{45}^U$ , is related to the corresponding strains along the  $x$  and  $y$  axes by

$$\varepsilon_{45}^U = \varepsilon_x^U \cos^2 \theta + \varepsilon_y^U \sin^2 \theta + \gamma_{xy}^U \sin \theta \cos \theta \quad (7.79)$$

and substituting  $\theta = 45^\circ$  and solving for  $\gamma_{xy}^U$ , we find that

$$\gamma_{xy}^U = 2\varepsilon_{45}^U - (\varepsilon_x^U + \varepsilon_y^U) \quad (7.80)$$

Thus, the shear strain is related to the measured strains on the right-hand side of Equation 7.80. Similarly, for the lower surface

$$\gamma_{xy}^L = 2\varepsilon_{45}^L - (\varepsilon_x^L + \varepsilon_y^L) \quad (7.81)$$

Now the last part of Equations 7.31 is used to relate the surface shear strains to the midplane shear strains and twisting curvatures:

$$\gamma_{xy}^U = \gamma_{xy}^0 - \frac{t}{2} \kappa_{xy} \quad (7.82)$$

$$\gamma_{xy}^L = \gamma_{xy}^0 + \frac{t}{2} \kappa_{xy} \quad (7.83)$$

These equations can be solved simultaneously for  $\gamma_{xy}^0$  and  $\kappa_{xy}$ , so that all midplane strains and curvatures can be determined from the six measured surface strains. For known loading conditions, the compliances can then be found.

For a uniaxial loading-test of such a strain-gaged specimen with  $N_x \neq 0$  and  $N_y = N_{xy} = M_x = M_y = M_{xy} = 0$  (Figure 7.19a), Equations 7.59 can be used to

determine six compliances from known loads, midplane strains, and curvatures as follows:

$$\begin{aligned} A'_{11} &= \frac{\epsilon_x^0}{N_x}, & B'_{11} &= \frac{\kappa_x}{N_x} \\ A'_{12} &= \frac{\epsilon_y^0}{N_x}, & B'_{12} &= \frac{\kappa_y}{N_x} \\ A'_{16} &= \frac{\gamma_{xy}^0}{N_x}, & B'_{16} &= \frac{\kappa_{xy}}{N_x} \end{aligned} \quad (7.84)$$

Similar data from a pure flexure test, with  $M_x \neq 0$  and  $N_x = N_y = N_{xy} = M_y = M_{xy} = 0$  (Figure 7.20a) can be used to find the six compliances:

$$\begin{aligned} B'_{11} &= \frac{\epsilon_x^0}{M_x}, & D'_{11} &= \frac{\kappa_x}{M_x} \\ B'_{12} &= \frac{\epsilon_y^0}{M_x}, & D'_{12} &= \frac{\kappa_y}{M_x} \\ B'_{16} &= \frac{\gamma_{xy}^0}{M_x}, & D'_{16} &= \frac{\kappa_{xy}}{M_x} \end{aligned} \quad (7.85)$$

All compliances can be determined from such tests. In addition, some compliances can be determined from more than one test (e.g., the  $B_{ij}$  in the above tests). A comparison of measured and predicted compliances of angle-ply glass/epoxy laminates having either two or three plies of various lamination angles is shown in Figure 7.22 from Tsai [13]. Predicted compliances were determined by using measured lamina properties as follows [13]:

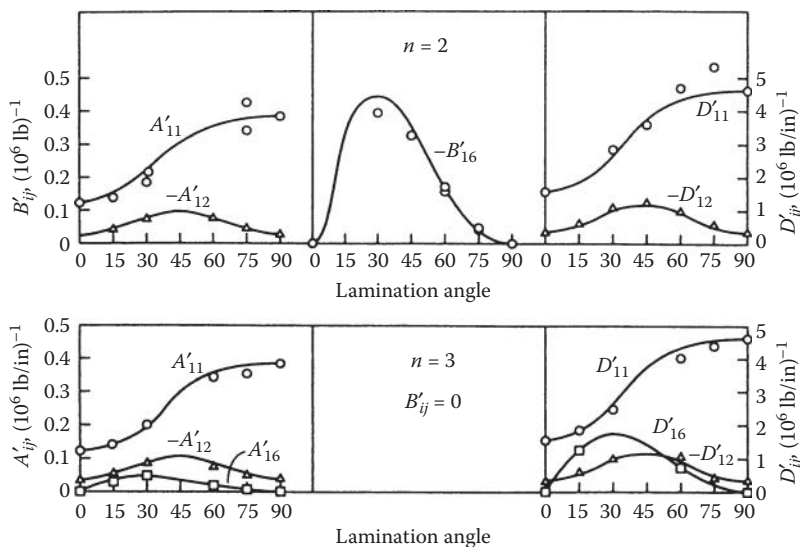
$$E_1 = 7.8 \times 10^6 \text{ psi} \quad (53.8 \text{ MPa})$$

$$E_2 = 2.6 \times 10^6 \text{ psi} \quad (17.9 \text{ MPa})$$

$$G_{12} = 1.25 \times 10^6 \text{ psi} \quad (8.6 \text{ MPa})$$

$$v_{12} = 0.25$$

The agreement between measured and predicted values in Figure 7.22 is quite favorable, which means that the laminate theory must be reasonably accurate. It is interesting to note that the predicted  $B_{ij}$ -type coupling occurs for the two-ply antisymmetric laminate but not for the three-ply symmetric laminate. Note also that the predicted  $A_{16}$ ,  $A_{26}$ ,  $D_{16}$ , and  $D_{26}$ -type coupling occurs for the three-ply laminate but not for the two-ply laminate.

**FIGURE 7.22**

Measured and predicted compliances for glass/epoxy angle-ply laminates for various lamination angles. (Adapted from Tsai, S. W. 1964. *Structural Behavior of Composite Materials*. NASA CR-71.)

## 7.6 Hygrothermal Effects in Laminates

The analysis of hygrothermal behavior of the lamina in Chapter 5 can now be extended to laminates. If we again restrict the discussion to polymer matrix composites, the two main effects of changes in the hygrothermal environment on laminate behavior are degradation of properties and changes in the stress and strain distributions. In this section, the analysis of both these effects along with the prediction of laminate hygrothermal expansion coefficients will be discussed. The basic assumption in all these discussions is that of linearity. That is, we assume that mechanical and hygrothermal effects can be treated separately and then combined using superposition. Coupling between the effects is ignored, as this would lead to nonlinear equations. Another key assumption used here is that temperature and moisture distributions in the laminate are uniform. That is, the temperature and moisture concentration are assumed to be the same for each ply in the laminate.

### 7.6.1 Hygrothermal Degradation of Laminates

The analysis of hygrothermal degradation in laminates involves the combination of the lamina degradation analysis in Section 5.2, with the laminate analysis described earlier in this chapter. For example, given a combination

of temperature and moisture, Equation 5.7 can be used to estimate the degraded matrix property, which is then substituted in the appropriate micromechanics equations to estimate the degraded lamina properties such as  $E_1$ ,  $E_2$ ,  $G_{12}$ , and  $\nu_{12}$ . The degraded lamina properties are then used in Equations 7.41 through 7.43 to find the corresponding degraded laminate stiffnesses. Hygrothermal properties such as the coefficients of thermal expansion and hygroscopic expansion can also be degraded using empirical equations such as Equation 5.41. These properties would then be used to estimate hygrothermal stresses, as shown in the next section.

### 7.6.2 Hygrothermal Stresses in Laminates

In Section 5.3, the analysis of hygrothermal stresses in an isolated lamina due to temperature and moisture was developed. We now consider the corresponding lamina stresses due to interaction with other laminae in the laminate. Hygrothermal stresses are not only generated during the use of composite materials in various environmental conditions, but also are generated during fabrication. The hygrothermal stresses induced by fabrication are usually referred to as residual stresses. Composites are processed or cured at elevated temperatures and then cooled to room temperature. Due to differences between fiber and matrix coefficient of thermal expansions (CTEs) in the lamina and differences between lamina CTEs in the laminate, residual stresses of fabrication may occur at both the micromechanical and the macromechanical levels. One particularly important result of residual stresses is that in nonsymmetric laminates the  $B_{ij}$ -type coupling can cause residual warping of the cured laminate.

In Section 7.5.2, the lamina stresses without hygrothermal effects were found by using Equations 7.61. As shown in Section 5.3, however, when changes in temperature and moisture concentration occur, the total strains in the  $k$ th lamina are given by

$$\{\varepsilon\}_k = [\bar{S}]_k \{\sigma\}_k + \{\alpha\}_k \Delta T + \{\beta\}_k c \quad (7.86)$$

and the resulting stresses are given by

$$\{\sigma\}_k = [\bar{Q}]_k (\{\varepsilon\}_k - \{\alpha\}_k \Delta T - \{\beta\}_k c) \quad (7.87)$$

where the subscript  $k$  refers to the  $k$ th lamina. As shown in Section 5.3, if the lamina is completely restrained by adjacent laminae, the total strains  $\{\varepsilon\}_k = 0$  and the resulting hygrothermal stresses are given by

$$\{\sigma\}_k = [\bar{Q}]_k (-\{\alpha\}_k \Delta T - \{\beta\}_k c) \quad (7.88)$$

In a laminate, however, the total lamina strains generally do not vanish, but are instead given by

$$\{\epsilon\}_k = \{\epsilon^0\} + z\{\kappa\} \quad (7.89)$$

and the resulting stresses, including hygrothermal effects, are given by

$$\{\sigma\}_k = [\bar{Q}]_k (\{\epsilon^0\} + z\{\kappa\} - \{\alpha\}_k \Delta T - \{\beta\}_k c) \quad (7.90)$$

Following the procedure outlined in Equations 7.35 through 7.45, the resultant laminate forces per unit length are found by integrating Equation 7.90 through the thickness of the laminate:

$$\begin{aligned} \{N\} &= \int \{\sigma\}_k dz = \int [\bar{Q}]_k (\{\epsilon^0\} + z\{\kappa\} - \{\alpha\}_k \Delta T - \{\beta\}_k c) dz \\ &= [A]\{\epsilon^0\} + [B]\{\kappa\} - \{N^T\} - \{N^M\} \end{aligned} \quad (7.91)$$

where the thermal forces due to temperature change are given by

$$\{N^T\} = \int [\bar{Q}]_k \{\alpha\}_k \Delta T dz = (\Delta T) \sum_{k=1}^N [\bar{Q}]_k \{\alpha\}_k (z_k - z_{k-1}) \quad (7.92)$$

and the hygroscopic forces due to moisture are given by

$$\{N^M\} = \int [\bar{Q}]_k \{\beta\}_k c dz = (c) \sum_{k=1}^N [\bar{Q}]_k \{\beta\}_k (z_k - z_{k-1}) \quad (7.93)$$

Similarly, the resultant moments per unit length are

$$\begin{aligned} \{M\} &= \int \{\sigma\}_k z dz = \int [\bar{Q}]_k (\{\epsilon^0\} + z\{\kappa\} - \{\alpha\}_k \Delta T - \{\beta\}_k c) z dz \\ &= [B]\{\epsilon^0\} + [D]\{\kappa\} - \{M^T\} - \{M^M\} \end{aligned} \quad (7.94)$$

where the thermal moments due to temperature changes are

$$\{M^T\} = \int [\bar{Q}]_k \{\alpha\}_k \Delta T z dz = \frac{\Delta T}{2} \sum_{k=1}^N [\bar{Q}]_k \{\alpha\}_k (z_k^2 - z_{k-1}^2) \quad (7.95)$$

and the hygroscopic moments due to moisture are given by

$$\{M^M\} = \int [\bar{Q}]_k \{\beta\}_k cz dz = \frac{c}{2} \sum_{k=1}^N [\bar{Q}]_k \{\beta\}_k (z_k^2 - z_{k-1}^2) \quad (7.96)$$

Rearranging Equations 7.91 and 7.94, we find that

$$\{N\} + \{N^T\} + \{N^M\} = [A]\{\varepsilon^0\} + [B]\{\kappa\} \quad (7.97)$$

and

$$\{M\} + \{M^T\} + \{M^M\} = [B]\{\varepsilon^0\} + [D]\{\kappa\} \quad (7.98)$$

or

$$\begin{Bmatrix} N^E \\ M^E \end{Bmatrix} = \begin{bmatrix} A & | & B \\ \hline B & | & D \end{bmatrix} \begin{Bmatrix} \varepsilon^0 \\ \kappa \end{Bmatrix} \quad (7.99)$$

where the total effective forces (mechanical plus hygrothermal) are

$$\{N^E\} = \{N\} + \{N^T\} + \{N^M\} \quad (7.100)$$

and the total effective moments (mechanical plus hygrothermal) are

$$\{M^E\} = \{M\} + \{M^T\} + \{M^M\} \quad (7.101)$$

Alternatively, the inverted forms of Equations 7.99 are given by

$$\begin{Bmatrix} \varepsilon^0 \\ \kappa \end{Bmatrix} = \begin{bmatrix} A' & | & B' \\ \hline C' & | & D' \end{bmatrix} \begin{Bmatrix} N^E \\ M^E \end{Bmatrix} \quad (7.102)$$

Thus, the lamina stresses for combined mechanical and hygrothermal loading are determined by using a procedure similar to that outlined in Section 7.5.2. That is, the midplane strains and curvatures are determined from the total effective forces and moments according to Equations 7.102; then the lamina stresses are determined from Equations 7.90.

### Example 7.11

The antisymmetric angle-ply laminate described in Example 7.5 is heated from 20°C (68°F) to 100°C (212°F). Assuming that the lamina properties do not change over this temperature range, determine the hygrothermal stresses.

### SOLUTION

From Table 5.3, the lamina CTEs associated with the principal material axes are

$$\alpha_1 = 0.88 \times 10^{-6}/^\circ\text{C}, \quad \alpha_2 = 31.0 \times 10^{-6}/^\circ\text{C}$$

The CTEs associated with the  $+45^\circ$  and  $-45^\circ$  lamina orientations are found by using the transformations in Equations 5.22:

$$\begin{aligned} \left\{ \begin{array}{c} \alpha_x \\ \alpha_y \\ \alpha_{xy}/2 \end{array} \right\}_{+45^\circ} &= \begin{bmatrix} 0.5 & 0.5 & -1.0 \\ 0.5 & 0.5 & 1.0 \\ 0.5 & -0.5 & 0 \end{bmatrix} \begin{Bmatrix} 0.88 \\ 31.0 \\ 0 \end{Bmatrix} \times 10^{-6} = \begin{Bmatrix} 15.94 \\ 15.94 \\ -15.06 \end{Bmatrix} \times 10^{-6}/^\circ\text{C} \\ \left\{ \begin{array}{c} \alpha_x \\ \alpha_y \\ \alpha_{xy}/2 \end{array} \right\}_{-45^\circ} &= \begin{bmatrix} 0.5 & 0.5 & 1.0 \\ 0.5 & 0.5 & -1.0 \\ -0.5 & 0.5 & 0 \end{bmatrix} \begin{Bmatrix} 0.88 \\ 31.0 \\ 0 \end{Bmatrix} \times 10^{-6} = \begin{Bmatrix} 15.94 \\ 15.94 \\ 15.06 \end{Bmatrix} \times 10^{-6}/^\circ\text{C} \end{aligned}$$

Next, the thermal forces due to temperature change are found by substituting the above values and the lamina stiffnesses from Example 7.4 into Equation 7.92. Note also that the third element in column vector  $\{\alpha\}_k$  in Equation 7.92 is  $\alpha_{xy}$ , not  $\alpha_{xy}/2$  as in the above transformations. Since  $z_k - z_{k-1} = t/4$  for all laminae,

$$\{N^T\} = ([\bar{Q}]_{+45^\circ}\{\alpha\}_{+45^\circ} + [\bar{Q}]_{-45^\circ}\{\alpha\}_{-45^\circ})2(\Delta T)\left(\frac{t}{4}\right)$$

or

$$\begin{aligned} \begin{Bmatrix} N_x^T \\ N_y^T \\ N_{xy}^T \end{Bmatrix} &= \begin{bmatrix} 45.22 & 31.42 & 32.44 \\ 31.42 & 45.22 & 32.44 \\ 32.44 & 32.44 & 35.6 \end{bmatrix} \begin{Bmatrix} 15.94 \\ 15.94 \\ -30.12 \end{Bmatrix} (10^{-6})(2)(80)(0.25) \\ &\quad + \begin{bmatrix} 45.22 & 31.42 & -32.44 \\ 31.42 & 45.22 & -32.44 \\ -32.44 & -32.44 & 35.6 \end{bmatrix} \begin{Bmatrix} 15.94 \\ 15.94 \\ 30.12 \end{Bmatrix} (10^{-6})(2)(80)(0.25) \\ &= \begin{Bmatrix} 1.956 \\ 1.956 \\ 0 \end{Bmatrix} \times 10^{-2} \text{ GPa mm} \end{aligned}$$

Similarly, the thermal moments are found from Equations 7.95 as

$$\begin{aligned} \{M^T\} &= \left( [\bar{Q}]_{-45^\circ}\{\alpha\}_{-45^\circ}(z_1^2 - z_0^2) + [\bar{Q}]_{+45^\circ}\{\alpha\}_{+45^\circ}(z_2^2 - z_1^2) \right. \\ &\quad \left. + [\bar{Q}]_{-45^\circ}\{\alpha\}_{-45^\circ}(z_3^2 - z_2^2) + [\bar{Q}]_{+45^\circ}\{\alpha\}_{+45^\circ}(z_4^2 - z_3^2) \right) \frac{\Delta T}{2} \end{aligned}$$

or

$$\begin{Bmatrix} M_x^T \\ M_y^T \\ M_{xy}^T \end{Bmatrix} = \begin{Bmatrix} 0 \\ 0 \\ -3.81 \end{Bmatrix} \times 10^{-4} \text{ GPa mm}^2$$

From Equations 7.100 and 7.101, we have  $\{N^E\} = \{N^T\}$  and  $\{M^E\} = \{M^T\}$ . Using these results along with the compliances from Example 7.9 in Equation 7.102, we find that the midplane strains and curvatures are

$$\begin{Bmatrix} \epsilon_x^0 \\ \epsilon_y^0 \\ \gamma_{xy}^0 \\ \kappa_x \\ \kappa_y \\ \kappa_{xy} \end{Bmatrix} = \begin{Bmatrix} 3.06 \text{ mm/mm} \\ 3.06 \text{ mm/mm} \\ 0 \text{ mm/mm} \\ 0 \text{ mm}^{-1} \\ 0 \text{ mm}^{-1} \\ -9.65 \text{ mm}^{-1} \end{Bmatrix} \times 10^{-4}$$

Note that the thermal twisting moment,  $M_{xy}^T$ , causes a corresponding twisting curvature,  $\kappa_{xy}$ , which means that the laminate will warp under the temperature change. Stresses along the  $x$  and  $y$  axes are now found by substituting the above midplane strains and curvatures, along with the lamina stiffnesses from Example 7.4, in Equation 7.90. Stresses at the top and bottom of each ply are given in the following table:

Location	$\sigma_x(\text{MPa})$	$\sigma_y(\text{MPa})$	$\tau_{xy}(\text{MPa})$
#1 Top	-11.8	-11.8	-5.7
#1 Bottom	-3.9	-3.9	-14.3
#2 Top	11.8	11.8	31.6
#2 Bottom	3.9	3.9	23.0
#3 Top	3.9	3.9	-23.0
#3 Bottom	11.8	11.8	-31.6
#4 Top	-3.9	-3.9	14.3
#4 Bottom	-11.8	-11.8	5.7

As with Example 7.9, the stress distribution is quite complex because of the coupling effect.

### 7.6.3 Laminate Hygrothermal Expansion Coefficients

The effective hygrothermal expansion coefficients for the laminate can be calculated directly by combining the definitions of the coefficients with the

appropriate laminate equations. For example, the effective CTE of a laminate along the  $x$  direction is

$$\alpha_x = \frac{\epsilon_x^0}{\Delta T} \quad (7.103)$$

For a symmetric laminate with  $B_{ij} = 0$ , the midplane strain along the  $x$  direction due to a temperature change  $\Delta T$  only is given by the first of Equation 7.102:

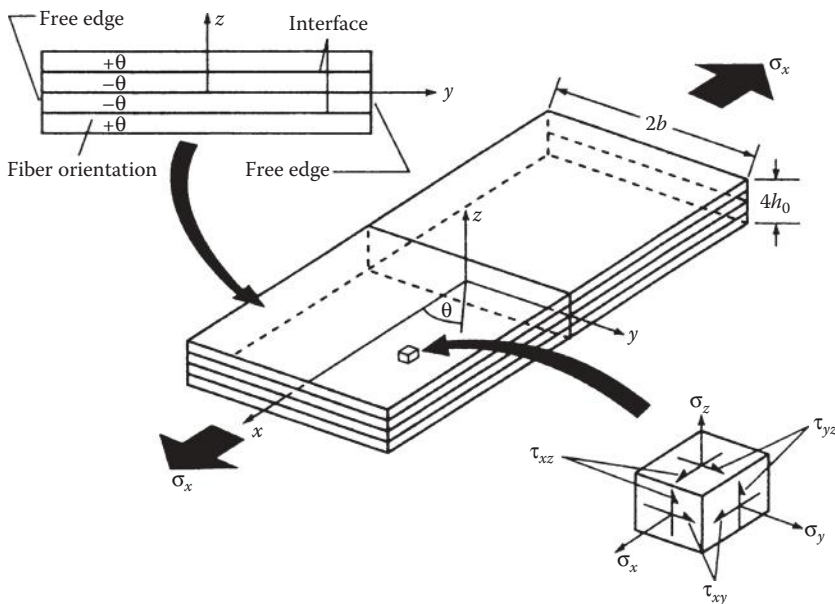
$$\epsilon_x^0 = A'_{11}N_x^T + A'_{12}N_y^T + A'_{16}N_{xy}^T \quad (7.104)$$

The desired thermal expansion coefficient,  $\alpha_x$ , is then found by substituting the thermal forces from Equation 7.92 in Equation 7.104 and then by substituting the result in Equation 7.103. It is important to note that this procedure effectively relates the laminate CTE to lamina CTEs, lamina stiffnesses, laminate compliances, and laminate geometry. The temperature change,  $\Delta T$ , will cancel out since it appears in both the numerator and the denominator. Similar results can be obtained for other thermal and hygroscopic expansion coefficients. As with the effective laminate engineering constants, it is appropriate to restrict the use of the effective hygrothermal expansion coefficients to those cases where the deformations are similar to the deformations associated with the particular coefficient being used. For example, it is probably not a good practice to use such coefficients to describe the hygrothermal behavior of a laminate that exhibits significant warping due to coupling effects.

## 7.7 Interlaminar Stresses

One of the key limitations of the CLT is that each ply is assumed to be in plane stress in the  $xy$  plane (Figure 7.9), and that interlaminar stresses associated with the  $z$  axis are neglected. Such interlaminar stresses can cause delamination or separation of the laminae, which is a failure mode that we have not previously considered. In this section, 3-D stress analyses that yield the interlaminar stresses will be discussed, and the resulting interlaminar stresses will be used later in a laminate strength analysis.

A state of plane stress actually does exist in the laminae of a laminate in regions sufficiently far away from geometric discontinuities such as free edges. A 3-D elasticity solution by Pipes and Pagano [14] has shown, however, that even in a laminate under simple uniaxial loading (Figure 7.23), there is a “boundary layer” region along the free edges where a 3-D state of

**FIGURE 7.23**

Pipes and Pagano model for analysis of interlaminar stresses in a laminate under uniaxial extension. (From Pipes, R. B. and Pagano, N. J. 1970. *Journal of Composite Materials*, 4, 538–548. With permission.)

stress exists, and that the boundary layer thickness is roughly equal to the laminate thickness.

The behavior of interlaminar stresses near a free edge in a laminate will be demonstrated here by using the three stress equilibrium equations from the theory of elasticity (Appendix B):

$$\frac{\partial \sigma_x}{\partial x} + \frac{\partial \tau_{xy}}{\partial y} + \frac{\partial \tau_{xz}}{\partial z} = 0 \quad (7.105)$$

$$\frac{\partial \tau_{yx}}{\partial x} + \frac{\partial \sigma_y}{\partial y} + \frac{\partial \tau_{yz}}{\partial z} = 0 \quad (7.106)$$

$$\frac{\partial \tau_{zx}}{\partial x} + \frac{\partial \tau_{zy}}{\partial y} + \frac{\partial \sigma_z}{\partial z} = 0 \quad (7.107)$$

For the uniaxially loaded laminate in Figure 7.23, we now consider a region near the free edges, where  $y = \pm b$ , and assume that the stresses do not vary

along the loading direction (the  $x$  axis). It follows that  $\partial\sigma_x/\partial x = 0$  and from Equation 7.105, the interlaminar shear stress,  $\tau_{xz}(z)$ , is given by

$$\tau_{xz}(z) = - \int_{-t/2}^z \frac{\partial\tau_{xy}}{\partial y} dz \quad (7.108)$$

We now assume that the in-plane shear stress  $\tau_{xy}$  has a constant value given by the CLT in the interior regions of the laminae. As we move along the  $y$  direction toward a free edge, however,  $\tau_{xy}$  must decrease to zero at the stress-free surfaces where  $y = \pm b$ . Thus, as  $y \rightarrow \pm b$ ,  $|\partial\tau_{xy}/\partial y|$  must increase. It follows from Equation 7.108 that  $\tau_{xz}$  must increase from zero in the interior region to a very large value as  $y \rightarrow \pm b$ , as shown in Figure 7.24. The region where these rapid changes take place is referred to as the interlaminar stress boundary layer region, as shown in Figure 7.24. From Equations 7.106 and 7.107, respectively, the other interlaminar stresses as

$$\tau_{yz}(z) = - \int_{-t/2}^z \frac{\partial\sigma_y}{\partial y} dz \quad (7.109)$$

$$\sigma_z(z) = - \int_{-t/2}^z \frac{\partial\tau_{yz}}{\partial y} dz \quad (7.110)$$

Pipes and Pagano [14] used a finite difference numerical scheme to solve the three governing field equations that are generated by combining the full 3D

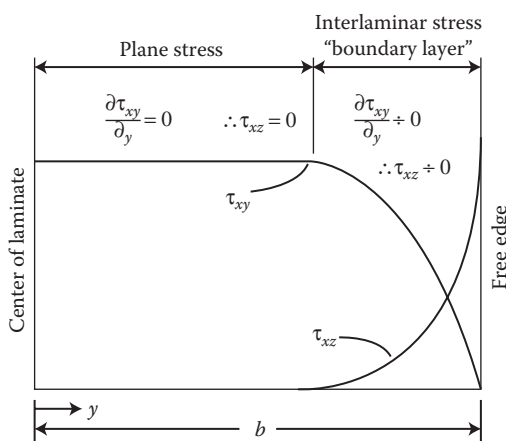


**FIGURE 7.24**

Schematic representation of in-plane shear stress and interlaminar shear stress distributions at the ply interface.

stress equilibrium equations (Appendix B, and Equations 7.105 through 7.107), the full 3D off-axis lamina stress-strain relationships (Equations 7.111),

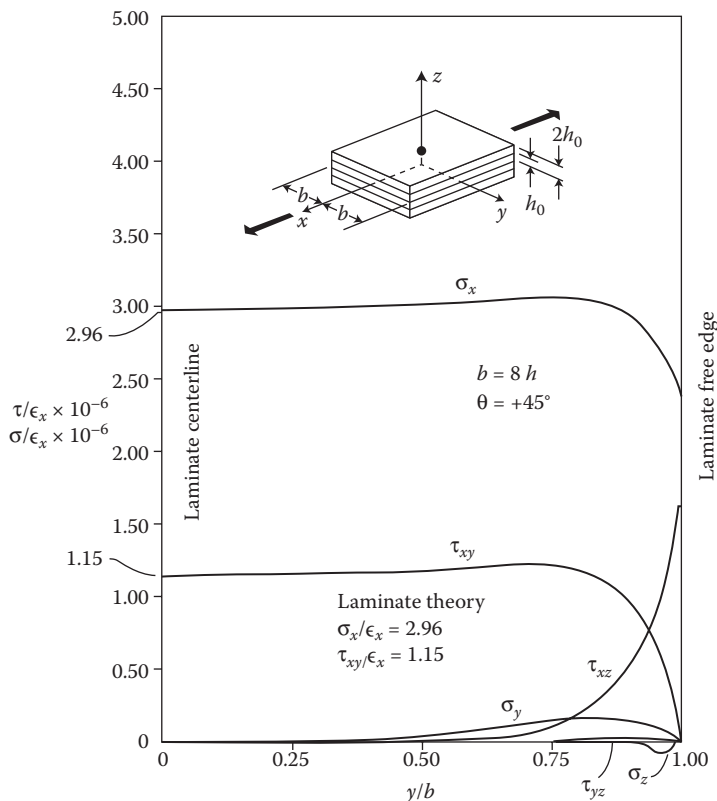
$$\begin{Bmatrix} \sigma_x \\ \sigma_y \\ \sigma_z \\ \tau_{yz} \\ \tau_{xz} \\ \tau_{xy} \end{Bmatrix} = \begin{bmatrix} C_{11} & C_{12} & C_{13} & 0 & 0 & C_{16} \\ C_{12} & C_{22} & C_{23} & 0 & 0 & C_{26} \\ C_{13} & C_{23} & C_{33} & 0 & 0 & C_{36} \\ 0 & 0 & 0 & C_{44} & C_{45} & 0 \\ 0 & 0 & 0 & C_{45} & C_{55} & 0 \\ C_{16} & C_{26} & C_{36} & 0 & 0 & C_{66} \end{bmatrix} \begin{Bmatrix} \epsilon_x \\ \epsilon_y \\ \epsilon_z \\ \gamma_{yz} \\ \gamma_{xz} \\ \gamma_{xy} \end{Bmatrix} \quad (7.111)$$

And the full 3D strain-displacement relations (Appendix C and Equations 7.112).

$$\begin{aligned} \epsilon_x &= \frac{\partial u}{\partial x}, \quad \epsilon_y = \frac{\partial v}{\partial y}, \quad \epsilon_z = \frac{\partial w}{\partial z} \\ \gamma_{yz} &= \frac{\partial v}{\partial z} + \frac{\partial w}{\partial y}, \quad \gamma_{xz} = \frac{\partial u}{\partial z} + \frac{\partial w}{\partial x}, \quad \gamma_{xy} = \frac{\partial u}{\partial y} + \frac{\partial v}{\partial x} \end{aligned} \quad (7.112)$$

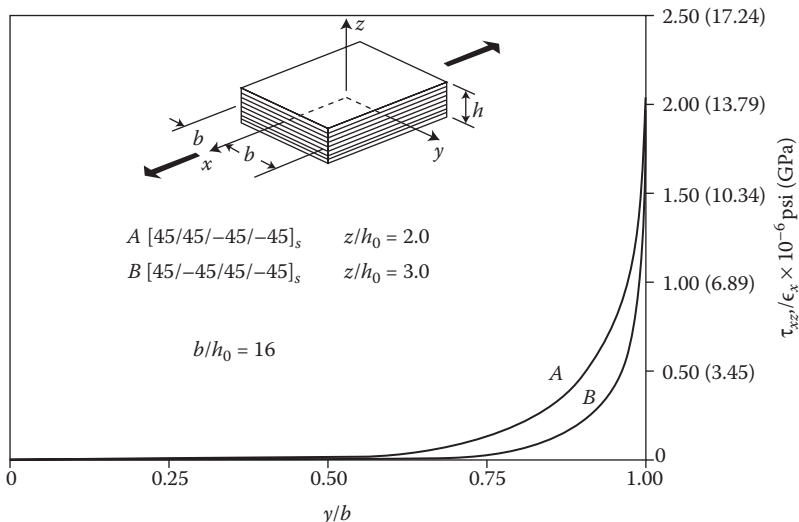
The equations were solved subject to stress-free boundary conditions along the free edges of a four-layer  $\pm 45^\circ$  graphite/epoxy laminate under uniform axial strain,  $\epsilon_x$ . Figure 7.25 shows the complete stress results obtained by Pipes and Pagano [14]. It is important to note that the in-plane stresses  $\sigma_x$  and  $\tau_{xy}$  from the 3-D analysis agree with those predicted by the CLT in the central portion of the laminate, but both stresses drop in the boundary layer region near the free edge. On the other hand, the interlaminar stresses  $\sigma_z$ ,  $\tau_{xz}$ , and  $\tau_{yz}$  are all equal to zero in the central portion of the laminate but change rapidly near the free edge. The shear stress  $\tau_{xz}$  is the largest of the interlaminar stresses, as it appeared to grow without bound at  $y/b = 1.0$ . Pipes and Pagano suspected that a singularity for this stress component exists at the free edge, but it was not possible to prove the existence of such a singularity with the approximate finite difference solution. Analytical proof of the existence of these singularities was published later by Wang and Choi [15,16].

The numerical results of Pipes and Pagano [14] for a variety of laminate cross-sectional aspect ratios led to the conclusion that the boundary layer region of 3-D stresses extends inward approximately one laminate thickness from the free edge. This conclusion was later verified experimentally by Pipes and Daniel [17] who used a Moiré technique to measure displacements along the  $x$  direction on the surface of the laminate. The measured surface displacement profiles, which also clearly indicated the presence of the boundary layer, agreed closely with those predicted by the Pipes and Pagano analysis.

**FIGURE 7.25**

Distribution of all stresses from Pipes and Pagano analysis. (From Pipes, R. B. and Pagano, N. J. 1970. *Journal of Composite Materials*, 4, 538–548. With permission.)

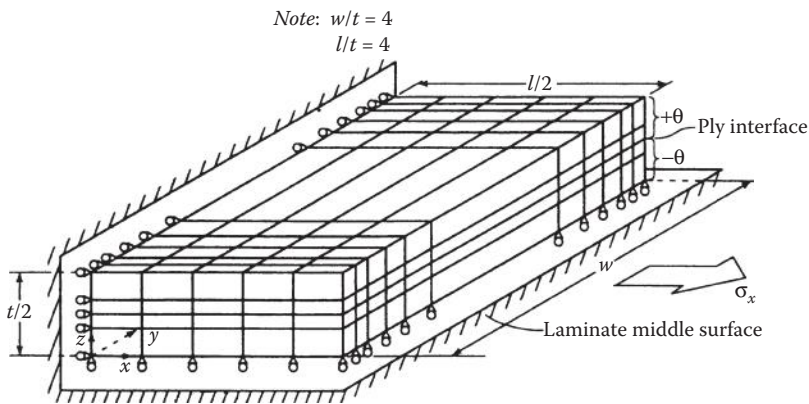
It has been shown both analytically and experimentally that the laminate stacking sequence influences interlaminar stresses and, consequently, delamination in laminates. Pipes and Pagano [18] used an approximate elasticity solution to study the effect of the stacking sequence on the interlaminar shear stress in  $\pm 45^\circ$  laminates, as shown in Figure 7.26. It is clear from Figure 7.26 that when layers having the same orientation are stacked together (which increases the apparent layer thickness), the interlaminar shear stress,  $\tau_{xz}$  is higher than for the case where layers of opposite orientation are stacked together. In a separate paper, Pagano and Pipes [19] showed that a change in the stacking sequence can actually cause the interlaminar normal stress,  $\sigma_z$ , to change from tensile to compressive. Since tensile interlaminar normal stresses would tend to cause separation of the plies, while compressive interlaminar normal stresses would tend to keep the plies together, stacking sequences that produce the former stress state should have lower strengths than those producing the latter stress state. Experimental results such as

**FIGURE 7.26**

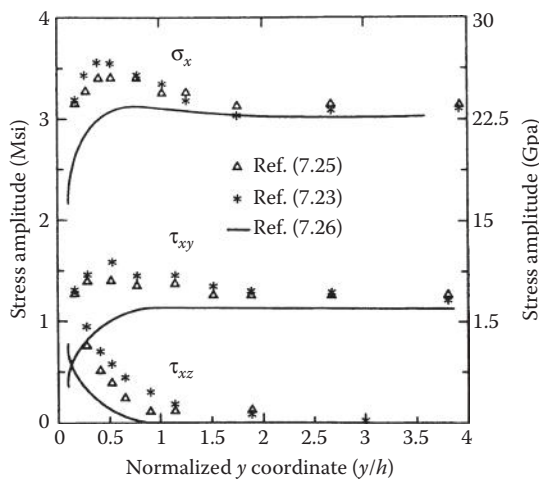
Effect of stacking sequence on interlaminar shear stress. (From Pipes, R. B. and Pagano, N. J. 1974. *Journal of Applied Mechanics*, 41, Series E (3), 668–672. Reprinted by permission of The American Society of Mechanical Engineers.)

those by Whitney and Browning [20] and Whitney and Kim [21] seem to support this conclusion. Ply orientation also has a strong effect on interlaminar stresses, as shown by Pipes and Pagano [14].

Since the publication of the Pipes and Pagano solution, a number of investigators have used other methods to study the “free-edge” interlaminar stress phenomenon. Rybicki [22], Wang and Crossman [23], Herakovich [24], and Hwang and Gibson [25] all used 3-D finite element analyses to investigate interlaminar stresses. The quarter-domain finite element model used by Hwang and Gibson [25] for the analysis of the original Pipes and Pagano [14] laminate is shown in Figure 7.27. Finite element stress distributions near the free edge from Wang and Crossman [23] and Hwang and Gibson [25] are compared with those from an empirical solution derived from the theory of elasticity by Hwang [26] in Figure 7.28. The empirical elasticity solution by Hwang [26] is based on a similar solution by Whitney [27], which, in turn, is an attempt to fit the finite difference results of Pipes and Pagano [14] with relatively simple empirical equations that satisfy the stress equilibrium equations (Equations 7.105 through 7.107) and the free-edge boundary conditions. Thus, the empirical results shown by the solid curve in Figure 7.28 should be very close to the original Pipes and Pagano results. Although the stress distributions from the two finite element models show good agreement with each other, both sets of stresses are seen to be greater than those from the empirical solution near the free edge. Improved approximate polynomial solutions have been proposed by Conti and De Paulis [28].

**FIGURE 7.27**

Quarter domain finite element model of laminate used by Hwang and Gibson to analyze the Pipes–Pagano problem. (From Hwang, S. J. and Gibson, R. F. 1992. *Composite Structures*, 20, 29–35. Reprinted by permission of Elsevier Publishers, Ltd.)

**FIGURE 7.28**

Comparison of stress distributions near the free edge. (From Hwang, S. J. and Gibson, R. F. 1992. *Composite Structures*, 20, 29–35. Reprinted by permission of Elsevier Publishers, Ltd.)

## 7.8 Laminate Strength Analysis

Recall that in Section 4.2, we discussed several multiaxial strength criteria for estimating the strength of individual laminae under in-plane stresses. Such strength criteria can also be used on a ply-by-ply basis for a laminate to

determine which ply fails first under in-plane loads. In Section 7.7, however, we have seen that interlaminar stresses in laminates also have to be taken into account because they may lead to a different mode of failure known as delamination. This section deals with the analysis of both first ply failure due to in-plane stresses and delamination due to interlaminar stresses. The mechanical behavior of the laminate after first ply failure and subsequent ply failures is also discussed.

### 7.8.1 First Ply Failure and Subsequent Ply Failures Due to In-Plane Stresses

The prediction of first ply failure due to in-plane stresses is a straightforward application of the appropriate multiaxial lamina strength criterion in combination with the lamina stress analysis from the CLT. The loads corresponding to first ply failure are not necessarily the laminate failure loads, however, since a laminate generally has plies at several orientations. That is, there will usually be a sequence of ply failures at different loads culminating in ultimate laminate failure when all plies have failed. Thus, the ultimate load-carrying capacity of the laminate may be significantly higher than the first ply failure load, and prediction of laminate failure based on first ply failure may be too conservative.

In the analysis of first ply failure and subsequent ply failures, the stiffness matrices for the failed plies and the corresponding laminate stiffness matrix must be modified after each ply failure to reflect the effects of those failures. Figure 7.29 shows an idealized piecewise linear laminate load-deformation

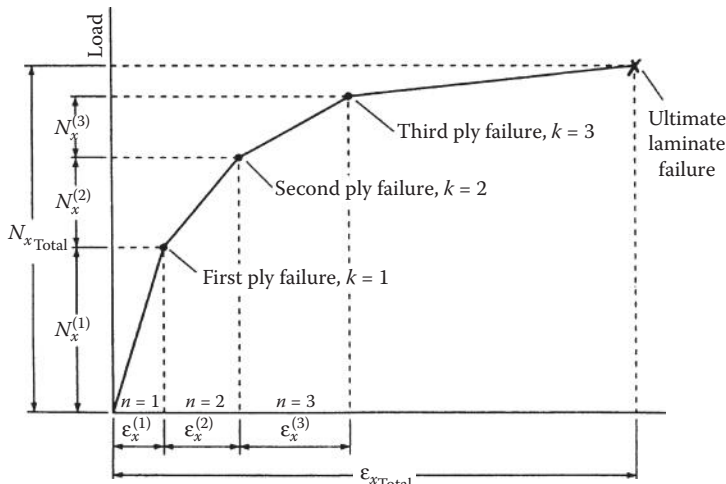


**FIGURE 7.29**

Idealized load-strain curve for uniaxially loaded laminate showing multiple sequential ply failures leading up to ultimate laminate failure.

curve with several “knees” due to ply failures. The total forces and moments at the  $k$ th knee in the curve are related to the corresponding forces and moments for the  $n$ th section of such a curve (where  $n \leq k$ ) by the summation

$$\begin{Bmatrix} N \\ M \end{Bmatrix}_{\text{Total}} = \sum_{n=1}^k \begin{Bmatrix} N^{(n)} \\ M^{(n)} \end{Bmatrix} \quad (7.113)$$

where the superscript  $(n)$  on a parameter denotes the particular value of that parameter associated with the  $n$ th section. The corresponding midplane strains and curvatures are given by

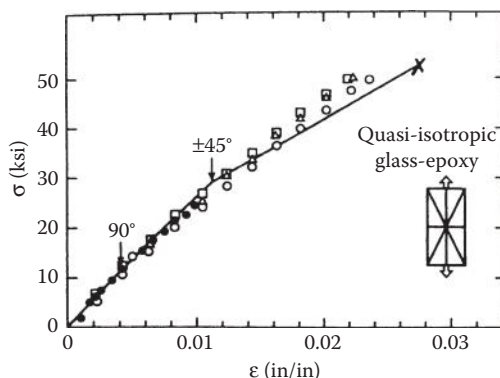
$$\begin{Bmatrix} \epsilon^0 \\ \kappa \end{Bmatrix}_{\text{Total}} = \sum_{n=1}^k \begin{Bmatrix} \epsilon^{0(n)} \\ \kappa^{(n)} \end{Bmatrix} \quad (7.114)$$

Using the piecewise linear assumption, the load–deformation relationship for the  $n$ th section can be approximated by modifying Equations 7.45 as

$$\begin{Bmatrix} N^{(n)} \\ M^{(\bar{n})} \end{Bmatrix} = \begin{bmatrix} A^{(n)} & | & B^{(n)} \\ \hline B^{(\bar{n})} & | & D^{(\bar{n})} \end{bmatrix} \begin{Bmatrix} \epsilon^{0(n)} \\ \kappa^{(\bar{n})} \end{Bmatrix} \quad (7.115)$$

where the  $[A^{(n)}]$ ,  $[B^{(n)}]$ , and  $[D^{(\bar{n})}]$  are the modified stiffness matrices after the  $(n - 1)$ th ply failure. But the calculation of these modified laminate stiffnesses requires that we know the modified ply stiffnesses,  $[Q^{(n)}]$ , and before we can modify the ply stiffness matrices, we must know the type of failure. That is, if the ply failure is caused by the in-plane shear stress exceeding the shear strength, the shear modulus and the transverse modulus of that ply may be severely degraded by longitudinal cracks, but the longitudinal modulus may not be affected significantly by these cracks. Alternatively, all the ply stiffnesses for the failed ply could be equated to zero or some very small number in the calculation of the degraded laminate stiffnesses.

Halpin [12] has used a procedure similar to the one outlined above to analyze the uniaxial stress–strain response of a  $[0/\pm 45/90]_s$  glass/epoxy laminate. The maximum strain criterion was used to predict ply failure, and the ply stiffnesses of the failed plies were set equal to zero. The predicted stress–strain curve shows good agreement with the corresponding experimental data, as shown in Figure 7.30. Notice that the curve has two “knees”—the first one at the strain corresponding to failure of the  $90^\circ$  plies and the second one at the strain corresponding to failure of the  $\pm 45^\circ$  plies. The knee for the  $\pm 45^\circ$  ply failure is more distinct than the one for the  $90^\circ$  ply failure, because the laminate has twice as many  $\pm 45^\circ$  plies as it does  $90^\circ$  plies. Ultimate laminate failure occurs at the longitudinal failure strain for the  $0^\circ$  plies. It is also interesting to note that the experimental data do not show as much of a change in slope at the knees as the theoretical curve does. This may be due

**FIGURE 7.30**

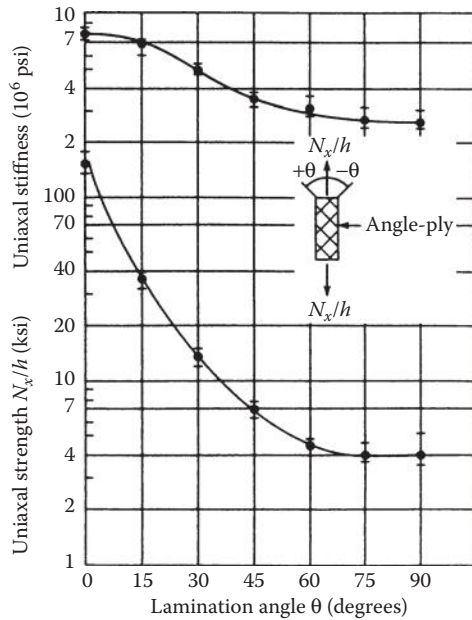
Comparison of predicted and measured stress–strain response of  $[0/\pm 45/90]_s$  glass/epoxy laminate. (From Halpin, J. C. 1984. *Primer on Composite Materials: Analysis*. Technomic Publishing Co., Lancaster, PA. With permission.)

to the fact that actual ply failure occurs gradually over a finite strain range, whereas instantaneous ply failure at a single strain level is assumed in the analysis. The same reasoning may explain the absence of jumps in the stress–strain curve after ply failure [29]. A horizontal jump would be predicted if the test data were taken under load-control, whereas a vertical jump would be predicted for a displacement-control test. Hahn and Tsai [29] have observed that the knee in the stress–strain curve for cross-ply laminates is quite obvious if the  $90^\circ$  plies are all stacked adjacent to each other, but the knee is not so obvious if the  $0^\circ$  and  $90^\circ$  plies are arranged in an alternating  $0^\circ/90^\circ$  sequence. Restraint of the failed  $90^\circ$  plies by the remaining  $0^\circ$  plies was thought to be more effective in the alternating  $0^\circ/90^\circ$  sequence, making the failure of the  $90^\circ$  plies more gradual.

The in-plane strength of  $\pm\theta$  angle-ply laminates may also be analyzed using a multiaxial lamina strength criterion and the CLT, but the piecewise linear approximation of the stress–strain curve may not be needed. This is because if the lamina tensile and compressive strengths are equal, all plies fail simultaneously in the angle-ply laminate, and the stress–strain curve does not have the characteristic knees shown in Figures 7.29 and 7.30. Tsai [30] has used the Tsai–Hill Criterion to predict the strength of glass–epoxy angle-ply laminates as a function of the lamination angle  $\theta$ , and the predictions are seen to agree well with experimental data in Figure 7.31. The predicted laminate stiffness  $A_{11}$  also shows good agreement with the prediction from the CLT in Figure 7.31.

### Example 7.12

A  $[90/0/90]_s$  laminate consisting of the AS/3501 laminae described in Example 7.4 is subjected to tensile uniaxial loading along the  $x$  direction. Using the Maximum

**FIGURE 7.31**

Comparison of predicted and measured uniaxial strength and stiffness of glass/epoxy angle-ply laminates. (From Tsai, S. W. 1965. *Strength Characteristics of Composite Materials*, NASA CR-224.)

Strain Criterion, find the loads corresponding to first ply failure and subsequent ply failures; then plot the load-strain curve up to failure.

### SOLUTION

The failure strains are found by substituting the data from Tables 2.2 and 4.1 in Equation 4.1:

$$e_L^{(+)} = \frac{s_L^{(+)}}{E_1} = \frac{1448}{138 \times 10^3} = 0.0105$$

$$e_T^{(+)} = \frac{s_T^{(+)}}{E_2} = \frac{48.3}{9 \times 10^3} = 0.0054$$

Using these results in the Maximum Strain Criterion, we see that first ply failure occurs at a strain  $\epsilon_x = e_T^{(+)} = 0.0054$ . In order to find the corresponding load  $N_x$  at first ply failure, it is necessary to find the initial laminate stiffness matrix  $[A^{(1)}$ . From Example 7.4, the lamina stiffness matrix for the  $0^\circ$  plies is given by

$$[\bar{Q}]_{0^\circ} = [Q] = \begin{bmatrix} 138.8 & 2.72 & 0 \\ 2.72 & 9.05 & 0 \\ 0 & 0 & 6.9 \end{bmatrix} \text{ GPa}$$

The stiffness matrix for the 90° plies is formed by simply interchanging the 11 and 22 terms in the stiffness matrix for the 0° plies:

$$[\bar{Q}]_{90^\circ} = \begin{bmatrix} 9.05 & 2.72 & 0 \\ 2.72 & 138.8 & 0 \\ 0 & 0 & 6.9 \end{bmatrix} \text{ GPa}$$

For the first section of the load-strain curve, the laminate stiffness matrix is therefore

$$[A^{(1)}] = [\bar{Q}]_{0^\circ}(2)(0.25) + [\bar{Q}]_{90^\circ}(4)(0.25) = 0.5[\bar{Q}]_{0^\circ} + [\bar{Q}]_{90^\circ}$$

or

$$[A^{(1)}] = \begin{bmatrix} 78.45 & 4.08 & 0 \\ 4.08 & 143.3 & 0 \\ 0 & 0 & 10.35 \end{bmatrix} \text{ GPa mm}$$

At first ply failure, the laminate load-deformation equations can be written as

$$\begin{Bmatrix} N_x^{(1)} \\ 0 \\ 0 \end{Bmatrix} = \begin{bmatrix} 78.45 & 4.08 & 0 \\ 4.08 & 143.3 & 0 \\ 0 & 0 & 10.35 \end{bmatrix} \begin{Bmatrix} 0.0054 \\ \epsilon_y^{(1)} \\ \gamma_{xy}^{(1)} \end{Bmatrix}$$

These equations can be solved simultaneously to get the following values of loads and strains at first ply failure:

$$N_x^{(1)} = 0.423 \text{ GPa mm}; \quad \epsilon_y^{(1)} = -0.000154; \quad \gamma_{xy}^{(1)} = 0$$

We will now demonstrate two different approaches for modifying the laminate stiffness matrix after first ply failure.

- a. In the first approach, we simply set all ply stiffnesses equal to zero for the failed 90° plies. The adjusted laminate stiffness matrix is then

$$[A^{(2)}] = 0.5[\bar{Q}]_{0^\circ} = \begin{bmatrix} 69.4 & 1.36 & 0 \\ 1.36 & 4.52 & 0 \\ 0 & 0 & 3.45 \end{bmatrix} \text{ GPa mm}$$

Now the 0° ply failure and the ultimate laminate failure occurs at a strain level  $\epsilon_x = \epsilon_l^{(+)} = 0.0105$ , which means that the strain increment for the second section of the load-strain curve is

$$\epsilon_x^{(2)} = \epsilon_l^{(+)} - \epsilon_x^{(1)} = 0.0105 - 0.0054 = 0.0051$$

The load-deformation equations describing the second section of the load-strain curve are

$$\begin{Bmatrix} N_x^{(2)} \\ 0 \\ 0 \end{Bmatrix} = \begin{bmatrix} 69.4 & 1.36 & 0 \\ 1.36 & 4.52 & 0 \\ 0 & 0 & 3.45 \end{bmatrix} \begin{Bmatrix} 0.0051 \\ \epsilon_y^{(2)} \\ \gamma_{xy}^{(2)} \end{Bmatrix}$$

and the simultaneous solution of these equations yields the results

$$N_x^{(2)} = 0.352 \text{ GPa mm}; \quad \epsilon_y^{(2)} = -0.00153; \quad \gamma_{xy}^{(2)} = 0$$

The total laminate failure load is then

$$N_{x\text{Total}} = N_x^{(1)} + N_x^{(2)} = 0.423 + 0.352 = 0.775 \text{ GPa mm}$$

and the load-strain curve is shown as curve (a) in Figure 7.32.

- b. In the second approach, we set only  $E_2 = G_{12} = v_{21} = 0$  for the failed  $90^\circ$  plies, but we assume that  $E_1$ , for the  $90^\circ$  plies is not affected by the transverse failure. According to these assumptions,

$$[\bar{Q}_{22}]_{90^\circ} = E_1 = 138 \text{ GPa}; \quad [\bar{Q}_{11}]_{90^\circ} = [\bar{Q}_{12}]_{90^\circ} = [\bar{Q}_{66}]_{90^\circ} = 0$$

and the adjusted laminate stiffness matrix is

$$[A^{(2)}] = \begin{bmatrix} 69.4 & 1.36 & 0 \\ 1.36 & 142.52 & 0 \\ 0 & 0 & 3.45 \end{bmatrix} \text{ GPa mm}$$

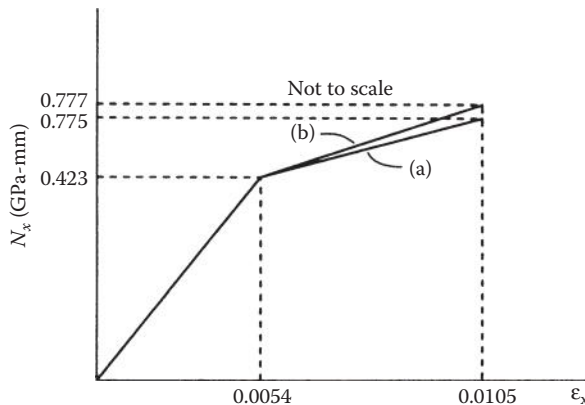


**FIGURE 7.32**

Predicted load-strain curves for Example 7.12.

The laminate load–deformation equations for the second section are

$$\begin{Bmatrix} N_x^{(2)} \\ 0 \\ 0 \end{Bmatrix} = \begin{bmatrix} 69.4 & 1.36 & 0 \\ 1.36 & 142.52 & 0 \\ 0 & 0 & 3.45 \end{bmatrix} \begin{Bmatrix} 0.0051 \\ \epsilon_y^{(2)} \\ \gamma_{xy}^{(2)} \end{Bmatrix}$$

and the resulting loads and strains for the second section are

$$N_x^{(2)} = 0.354 \text{ GPa mm}; \quad \epsilon_y^{(2)} = -0.0000487; \quad \gamma_{xy}^{(2)} = 0$$

The total load at laminate failure is

$$N_{x\text{Total}} = 0.423 + 0.354 = 0.777 \text{ GPa mm}$$

and the load–strain curve is shown as curve (b) in Figure 7.32. It is interesting to note that although the assumptions regarding degradation of the failed plies are quite different for curves (a) and (b), the predicted load–strain curves for the two approaches are virtually the same. In general, differences in predictions from the two approaches would depend on ply properties and stacking sequences. It is also interesting to note that we might intuitively expect approach (a) to be more conservative than approach (b) and this turns out to be the case.

### Example 7.13

Repeat Example 7.12 using the Maximum Stress Criterion.

#### SOLUTION

From Example 7.12, the load–strain relationship for the first increment is

$$\begin{Bmatrix} N_x^{(1)} \\ 0 \\ 0 \end{Bmatrix} = [A^{(1)}] \begin{Bmatrix} \epsilon_x^{(1)} \\ \epsilon_y^{(1)} \\ \gamma_{xy}^{(1)} \end{Bmatrix} = \begin{bmatrix} 78.45 & 4.08 & 0 \\ 4.08 & 143.3 & 0 \\ 0 & 0 & 10.35 \end{bmatrix} \begin{Bmatrix} \epsilon_x^{(1)} \\ \epsilon_y^{(1)} \\ \gamma_{xy}^{(1)} \end{Bmatrix} \text{ GPa mm}$$

Note that, unlike Example 7.12 where, according to the Maximum Strain Criterion, the first ply failure strain along the  $x$  direction was known to be the transverse tensile failure strain in the  $90^\circ$  plies, we do not know the corresponding strains here, and we must find them using the Maximum Stress Criterion. Expanding the above equation,

$$N_x^{(1)} = 78.45\epsilon_x^{(1)} + 4.08\epsilon_y^{(1)}$$

$$0 = 4.08\epsilon_x^{(1)} + 143.3\epsilon_y^{(1)}$$

$$0 = 10.35\gamma_{xy}^{(1)}$$

Solving these equations simultaneously,

$$\epsilon_y^{(1)} = -0.0285\epsilon_x^{(1)}$$

$$\gamma_{xy}^{(1)} = 0$$

$$N_x^{(1)} = 78.33\epsilon_x^{(1)}$$

So for the first ply failure of the 90° plies, the stresses along the x and y axes are

$$\begin{aligned} \left\{ \begin{array}{l} \sigma_x^{(1)} \\ \sigma_y^{(1)} \\ \tau_{xy}^{(1)} \end{array} \right\}_{90^\circ} &= [\bar{Q}]_{90^\circ} \begin{Bmatrix} \epsilon_x^{(1)} \\ -0.0285\epsilon_x^{(1)} \\ 0 \end{Bmatrix} = \begin{bmatrix} 9.05 & 2.72 & 0 \\ 2.72 & 138.8 & 0 \\ 0 & 0 & 6.9 \end{bmatrix} \begin{Bmatrix} \epsilon_x^{(1)} \\ -0.0285\epsilon_x^{(1)} \\ 0 \end{Bmatrix} \\ &= \begin{Bmatrix} 8.972\epsilon_x^{(1)} \\ -1.2358\epsilon_x^{(1)} \\ 0 \end{Bmatrix} \text{GPa} \end{aligned}$$

The corresponding stresses in the 90° plies along the principal material axes are

$$\begin{aligned} \left\{ \begin{array}{l} \sigma_1^{(1)} \\ \sigma_2^{(1)} \\ \tau_{12}^{(1)} \end{array} \right\}_{90^\circ} &= [T]_{90^\circ} \begin{Bmatrix} 8.972\epsilon_x^{(1)} \\ -1.2358\epsilon_x^{(1)} \\ 0 \end{Bmatrix} = \begin{bmatrix} 0 & 1 & 0 \\ 1 & 0 & 0 \\ 0 & 0 & -1 \end{bmatrix} \begin{Bmatrix} 8.972\epsilon_x^{(1)} \\ -1.2358\epsilon_x^{(1)} \\ 0 \end{Bmatrix} = \begin{Bmatrix} -1.2358\epsilon_x^{(1)} \\ 8.972\epsilon_x^{(1)} \\ 0 \end{Bmatrix} \text{GPa} \end{aligned}$$

Applying the Maximum Stress Criterion for the 90° plies, we find that

$$\sigma_1^{(1)} = -1.2358\epsilon_x^{(1)} = S_l^{(+)} = 1448 \text{ MPa} = 1.448 \text{ GPa} \quad \text{or} \quad \epsilon_x^{(1)} = -1.17$$

$$\sigma_2^{(1)} = 8.972\epsilon_x^{(1)} = S_l^{(+)} = 48.3 \text{ MPa} = 0.0483 \text{ GPa} \quad \text{or} \quad \epsilon_x^{(1)} = 0.00538$$

Choosing the smallest of these failure strains, we find that for first ply failure, we have

$$\epsilon_x^{(1)} = 0.00538$$

$$\epsilon_y^{(1)} = -0.0285\epsilon_x^{(1)} = -0.0285(0.00538) = -0.000153$$

$$N_x^{(1)} = 78.33\epsilon_x^{(1)} = 78.33(0.00538) = 0.4216 \text{ GPa mm}$$

The corresponding stresses in the  $0^\circ$  plies at first ply failure are

$$\begin{aligned} \begin{Bmatrix} \sigma_x^{(1)} \\ \sigma_y^{(1)} \\ \tau_{xy}^{(1)} \end{Bmatrix}_{0^\circ} &= [\bar{Q}]_{0^\circ} \begin{Bmatrix} \epsilon_x^{(1)} \\ \epsilon_y^{(1)} \\ \gamma_{xy}^{(1)} \end{Bmatrix} = \begin{bmatrix} 138.8 & 2.72 & 0 \\ 2.72 & 9.05 & 0 \\ 0 & 0 & 6.9 \end{bmatrix} \begin{Bmatrix} 0.00538 \\ -0.0001533 \\ 0 \end{Bmatrix} = \begin{Bmatrix} 0.746 \\ 0.0132 \\ 0 \end{Bmatrix} \text{GPa} \\ &= \begin{Bmatrix} \sigma_1^{(1)} \\ \sigma_2^{(1)} \\ \tau_{12}^{(1)} \end{Bmatrix}_{0^\circ} \end{aligned}$$

For the second increment after first ply failure, setting all the ply stiffnesses equal to zero for the failed  $90^\circ$  plies and using the corresponding degraded laminate stiffness matrix from Example 7.10, we find that

$$\begin{Bmatrix} N_x^{(2)} \\ 0 \\ 0 \end{Bmatrix} = [A^{(2)}] \begin{Bmatrix} \epsilon_x^{(2)} \\ \epsilon_y^{(2)} \\ \gamma_{xy}^{(2)} \end{Bmatrix} = \begin{bmatrix} 69.4 & 1.36 & 0 \\ 1.36 & 4.52 & 0 \\ 0 & 0 & 3.45 \end{bmatrix} \begin{Bmatrix} \epsilon_x^{(2)} \\ \epsilon_y^{(2)} \\ \gamma_{xy}^{(2)} \end{Bmatrix} \text{GPa mm}$$

Solving these equations simultaneously,

$$\epsilon_y^{(2)} = -0.3\epsilon_x^{(2)}$$

$$N_x^{(2)} = 68.992\epsilon_x^{(2)}$$

$$\gamma_{xy}^{(2)} = 0$$

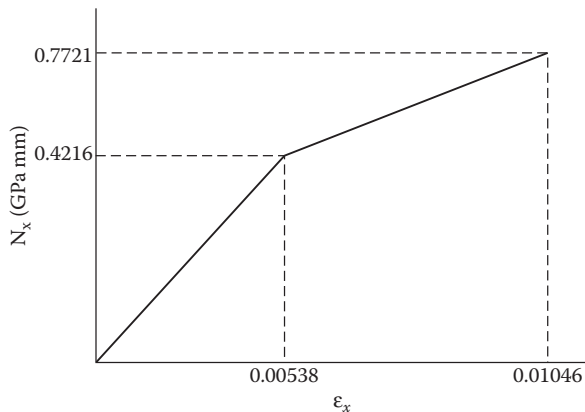
The incremental stresses for the  $0^\circ$  plies are then

$$\begin{aligned} \begin{Bmatrix} \sigma_x^{(2)} \\ \sigma_y^{(2)} \\ \tau_{xy}^{(2)} \end{Bmatrix}_{0^\circ} &= [\bar{Q}]_{0^\circ} \begin{Bmatrix} \epsilon_x^{(2)} \\ \epsilon_y^{(2)} \\ \gamma_{xy}^{(2)} \end{Bmatrix} = \begin{bmatrix} 138.8 & 2.72 & 0 \\ 2.72 & 9.05 & 0 \\ 0 & 0 & 6.9 \end{bmatrix} \begin{Bmatrix} \epsilon_x^{(2)} \\ -0.3\epsilon_x^{(2)} \\ 0 \end{Bmatrix} = \begin{Bmatrix} 137.98\epsilon_x^{(2)} \\ 0.005\epsilon_x^{(2)} \\ 0 \end{Bmatrix} \text{GPa} \\ &= \begin{Bmatrix} \sigma_1^{(2)} \\ \sigma_2^{(2)} \\ \tau_{12}^{(2)} \end{Bmatrix}_{0^\circ} \end{aligned}$$

Substituting the total stresses in the  $0^\circ$  plies at the end of the second increment in the Maximum Stress Criterion,

$$(\sigma_1)_{\text{total}} = \sigma_1^{(1)} + \sigma_1^{(2)} = 0.746 + 137.98\epsilon_x^{(2)} = S_L^{(+)} = 1.448 \text{ GPa} \quad \text{or} \quad \epsilon_x^{(2)} = 0.00508$$

$$(\sigma_2)_{\text{total}} = \sigma_2^{(1)} + \sigma_2^{(2)} = 0.0132 + 0.005\epsilon_x^{(2)} = S_T^{(+)} = 0.0483 \text{ GPa} \quad \text{or} \quad \epsilon_x^{(2)} = 7.02$$

**FIGURE 7.33**

Predicted load-strain curve for Example 7.13.

Choosing the smallest of the incremental strains to cause failure of the  $0^\circ$  plies,

$$\epsilon_x^{(2)} = 0.00508$$

$$N_x^{(2)} = 68.992(0.00508) = 0.3505 \text{ GPa mm}$$

The total loads and strains at final failure are then

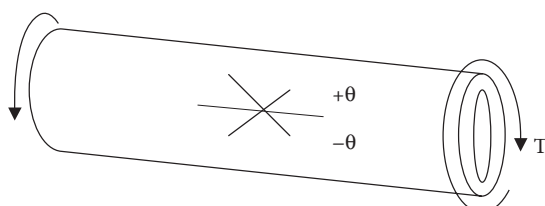
$$(N_x)_{\text{total}} = N_x^{(1)} + N_x^{(2)} = 0.4216 + 0.3505 = 0.7721 \text{ GPa mm}$$

$$(\epsilon_x)_{\text{total}} = \epsilon_x^{(1)} + \epsilon_x^{(2)} = 0.00538 + 0.00508 = 0.01046$$

The resulting load strain plot in Figure 7.33 is seen to be quite similar to the corresponding plots for the Maximum Strain Criterion in Figure 7.32, but this is not necessarily the case in general.

### Example 7.14

The composite power transmission shaft shown in Figure 7.34 has mean radius  $R=50$  mm and wall thickness  $t=1$  mm. The material is filament wound

**FIGURE 7.34**

Composite shaft for Example 7.14.

AS/3501 carbon/epoxy, and the wall of the shaft has a symmetric angle-ply [+45°/−45°/−45°/+45°] lay-up sequence (same as material in Example 7.4) for maximum torsional stiffness. Determine the largest torque  $T$  that can be transmitted by the shaft without failure according to the Maximum Stress Criterion.

### SOLUTION

From mechanics of materials, the torsional shear stress in a thin-walled tube is approximately

$$\tau_{xy} = \frac{T}{2\pi R^2 t}$$

where  $T$  = torque in N m,  $R$  = mean wall radius in m, and  $t$  = wall thickness in m. For the laminate analysis, the loads per unit length acting on an element of the tube wall are therefore

$$N_{xy} = \tau_{xy}t = \frac{T}{2\pi R^2} = \frac{T}{2\pi(0.05)^2} = 63.66 T \frac{N}{m} = 63.66(10^{-6})T \text{ GPa mm}$$

$$N_x = N_y = M_x = M_y = M_{xy} = 0$$

As in Example 7.8, we can take advantage of the symmetry of the laminate and invert the  $[A]$  matrix to solve for the strains in terms of the loads as

$$\begin{aligned} \begin{Bmatrix} \varepsilon_x^0 \\ \varepsilon_y^0 \\ \gamma_{xy}^0 \end{Bmatrix} &= [A'] \begin{Bmatrix} 0 \\ 0 \\ N_{xy} \end{Bmatrix} = \begin{bmatrix} 0.04276 & -0.0297 & 0 \\ -0.0297 & 0.04276 & 0 \\ 0 & 0 & 0.02809 \end{bmatrix} \begin{Bmatrix} 0 \\ 0 \\ 63.66(10^{-6})T \end{Bmatrix} \\ &= \begin{Bmatrix} 0 \\ 0 \\ 1.788(10^{-6})T \end{Bmatrix} \end{aligned}$$

Using the lamina stiffness matrices from Example 7.4, the corresponding stresses in the +45° plies along the  $x$  and  $y$  axes are

$$\begin{aligned} \begin{Bmatrix} \sigma_x \\ \sigma_y \\ \tau_{xy} \end{Bmatrix}_{+45^\circ} &= [\bar{Q}]_{+45^\circ} \begin{Bmatrix} \varepsilon_x^0 \\ \varepsilon_y^0 \\ \gamma_{xy}^0 \end{Bmatrix} = \begin{bmatrix} 45.22 & 31.42 & 32.44 \\ 31.42 & 45.22 & 32.44 \\ 32.44 & 32.44 & 35.6 \end{bmatrix} \begin{Bmatrix} 0 \\ 0 \\ 1.788(10^{-6})T \end{Bmatrix} \\ &= \begin{Bmatrix} 58.0T \\ 58.0T \\ 63.65T \end{Bmatrix} (10^{-6}) \text{ GPa} = \begin{Bmatrix} 0.058T \\ 0.058T \\ 0.06365T \end{Bmatrix} \text{ MPa} \end{aligned}$$

Similarly, for the  $-45^\circ$  plies,

$$\begin{aligned} \begin{Bmatrix} \sigma_x \\ \sigma_y \\ \tau_{xy} \end{Bmatrix}_{-45^\circ} &= [\bar{Q}]_{-45^\circ} \begin{Bmatrix} \varepsilon_x^0 \\ \varepsilon_y^0 \\ \gamma_{xy}^0 \end{Bmatrix} = \begin{bmatrix} 45.22 & 31.42 & -32.44 \\ 31.42 & 45.22 & -32.44 \\ -32.44 & -32.44 & 35.6 \end{bmatrix} \begin{Bmatrix} 0 \\ 0 \\ 1.788(10^{-6})T \end{Bmatrix} \\ &= \begin{Bmatrix} -58.0T \\ -58.0T \\ 63.65T \end{Bmatrix} (10^{-6}) \text{ GPa} = \begin{Bmatrix} -0.058T \\ -0.058T \\ 0.06365T \end{Bmatrix} \text{ MPa} \end{aligned}$$

In order to use the Maximum Stress Criterion, the stresses must be transformed to the principal material axes. Accordingly, for the  $+45^\circ$  plies,

$$\begin{Bmatrix} \sigma_1 \\ \sigma_2 \\ \tau_{12} \end{Bmatrix}_{+45^\circ} = [T]_{+45^\circ} \begin{Bmatrix} \sigma_x \\ \sigma_y \\ \tau_{xy} \end{Bmatrix} = \begin{bmatrix} 0.5 & 0.5 & 1.0 \\ 0.5 & 0.5 & -1.0 \\ -0.5 & 0.5 & 0 \end{bmatrix} \begin{Bmatrix} 0.058T \\ 0.058T \\ 0.06365T \end{Bmatrix} = \begin{Bmatrix} 0.12165T \\ -0.00565T \\ (0)T \end{Bmatrix} \text{ MPa}$$

Note that it is important to distinguish here between the stress transformation matrix,  $[T]$ , and the applied torque,  $T$ . Similarly, for the  $-45^\circ$  plies,

$$\begin{Bmatrix} \sigma_1 \\ \sigma_2 \\ \tau_{12} \end{Bmatrix}_{-45^\circ} = [T]_{-45^\circ} \begin{Bmatrix} \sigma_x \\ \sigma_y \\ \tau_{xy} \end{Bmatrix} = \begin{bmatrix} 0.5 & 0.5 & -1.0 \\ 0.5 & 0.5 & 1.0 \\ 0.5 & -0.5 & 0 \end{bmatrix} \begin{Bmatrix} -0.058T \\ -0.058T \\ 0.06365T \end{Bmatrix} = \begin{Bmatrix} -0.12165T \\ 0.00565T \\ (0)T \end{Bmatrix} \text{ MPa}$$

Applying the Maximum Stress Criterion for the  $+45^\circ$  plies and using the strength data for AS/3501 from Table 4.1,

$$\sigma_1 = 0.12165T = S_L^{(+)} = 1448 \text{ MPa} \quad \text{and} \quad T = 11,903 \text{ N m}$$

$$\sigma_2 = -0.00565T = -S_T^{(-)} = -248 \text{ MPa} \quad \text{and} \quad T = 43,894 \text{ N m}$$

$$\tau_{12} = 0(T) = S_{LT} = 62.1 \text{ MPa} \quad \text{and} \quad T = \infty$$

Similarly, for the  $-45^\circ$  plies,

$$\sigma_1 = -0.12165T = -S_L^{(-)} = -1172 \text{ MPa} \quad \text{and} \quad T = 9,634 \text{ N m}$$

$$\sigma_2 = 0.00565T = S_T^{(+)} = 48.3 \text{ MPa} \quad \text{and} \quad T = 8,549 \text{ N m}$$

$$\tau_{12} = 0(T) = S_{LT} = 62.1 \text{ MPa} \quad \text{and} \quad T = \infty$$

Note that, since the shear stress is zero along the 1,2 axes and the resulting torque needed to cause shear failure is infinite, failure due to shear is not possible. Of the remaining values, it is seen that the value of  $T = 8549$  N m for transverse tensile failure in the  $-45^\circ$  plies is the smallest, and so this would be the largest torque that could be transmitted without failure. It is also important to note that,

if the strengths were the same in tension and compression, all plies would fail simultaneously, but as the strengths are different in tension and compression, this is not the case here.

### 7.8.2 Delamination Due to Interlaminar Stresses

Delamination due to interlaminar stresses can reduce the failure stress of the laminate below that predicted by the in-plane failure criteria discussed in the previous section. Failure by delamination is not necessarily the same as the initiation of delamination, however. The initiation of delamination is generally followed by stable delamination growth, which eventually leads to unstable growth and ultimate failure. The onset of delamination can be predicted by using either mechanics of materials approaches or fracture mechanics approaches. Fracture mechanics is also the preferred analytical treatment for delamination growth and failure. In this section, we will discuss mechanics of materials approaches to the prediction of delamination initiation, and fracture mechanics will be covered in Chapter 9.

The average stress criterion of Kim and Soni [31] was one of the first mechanics of materials approaches to the prediction of the onset of delamination. This criterion is based on the premise that delamination will begin once the average value of the interlaminar tensile normal stress,  $\bar{\sigma}_z$ , near the free edge reaches the interlaminar tensile strength,  $s_z^{(+)}$ . A similar criterion for failure of notched laminates had been proposed previously by Whitney and Nuismer [32]. In the Kim–Soni Criterion, the averaging is done over a critical length,  $b_0$ , as shown in Equation 7.116 and Figure 7.35:

$$\bar{\sigma}_z = \frac{1}{b_0} \int_{b-b_0}^b \sigma_z(y, 0) dy = s_z^{(+)} \quad (7.116)$$

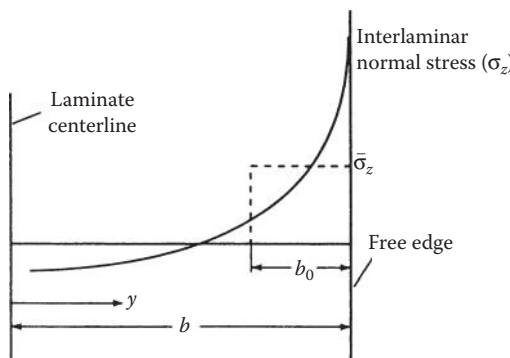


**FIGURE 7.35**

Graphical interpretation of average interlaminar normal stress near free edge according to the Kim–Soni Criterion.

The distance  $b$  was the half-width of the laminate, as shown in Figure 7.23, and the critical length  $b_0$  is assumed to be equal to one-ply thickness. Due to the difficulty of measuring  $s_z^{(+)}$ , Kim and Soni assumed that  $s_z^{(+)} = s_T^{(+)}$ . Although this criterion provided reasonably accurate predictions of the onset of delamination in composites where the tensile normal stress,  $\sigma_z$ , was the dominant interlaminar stress, a more general criterion was needed for cases where delamination may be affected by interlaminar shear stresses as well.

The need for a more general criterion for predicting the onset of delamination was recognized by Brewer and Lagace [33], who proposed the Quadratic Delamination Criterion:

$$\left(\frac{\bar{\sigma}_{xz}}{s_{xz}}\right)^2 + \left(\frac{\bar{\sigma}_{yz}}{s_{yz}}\right)^2 + \left(\frac{\bar{\sigma}_z^t}{s_z^{(+)}}\right)^2 + \left(\frac{\bar{\sigma}_z^c}{s_z^{(-)}}\right)^2 = 1 \quad (7.117)$$

where  $\bar{\sigma}_{xz}$  and  $\bar{\sigma}_{yz}$  are the average interlaminar shear stresses,  $\bar{\sigma}_z^t$  and  $\bar{\sigma}_z^c$  the average interlaminar tensile and compressive normal stresses, respectively,  $S_{xz}$  and  $S_{yz}$  the interlaminar shear strengths, and  $s_z^{(+)}$  and  $s_z^{(-)}$  the interlaminar tensile and compressive strengths, respectively.

Each of the average stress components in this case is defined as

$$\bar{\sigma}_{ij} = \frac{1}{\lambda_{avg}} \int_0^{\lambda_{avg}} \sigma_{ij} d\lambda \quad (7.118)$$

where  $\lambda$  is the distance from some reference point (in this case the free edge),  $\lambda_{avg}$  is the averaging dimension,  $\sigma_{ij}$  is the stress component  $\sigma_{xz}$ ,  $\sigma_{yz}$ ,  $\sigma_z^t$ , or  $\sigma_z^c$  and the overbar denotes its average value.

Brewer and Lagace found that for the  $[\pm 15_n]_s$ ,  $[\pm 15_n/0_n]_s$ , and  $[0_n/\pm 15_n]_s$  AS1/3501-6 carbon/epoxy laminates tested the second and fourth terms in Equation 7.117 were negligible, so that the Quadratic Delamination Criterion took on the simplified form

$$\left(\frac{\bar{\sigma}_{xz}}{s_{xz}}\right)^2 + \left(\frac{\bar{\sigma}_z^t}{s_z^{(+)}}\right)^2 = 1 \quad (7.119)$$

Transverse isotropy was assumed, so that  $s_z^{(+)} = s_T^{(+)} = 53.9$  MPa. The parameters  $\lambda_{avg}$  and  $s_{xz}$  were used as curve-fitting parameters to obtain the best agreement with experimental data. In the corresponding experiments, laminate specimens were tested under displacement control, and an instantaneous drop in the tensile load at delamination onset was observed. The "best-fit" parameters for all laminate configurations tested were  $\lambda_{avg} = 0.178$  mm and  $s_{xz} = 105$  MPa. Further support for the validity of the Quadratic Delamination Criterion and the assumption of transverse isotropy was discovered with the observation that the best-fit value of  $s_{xz}$  was the same as

$s_{LT}$ , the in-plane shear strength of this material. Although the value of  $\lambda_{avg}$  was not assumed to be equal to the ply thickness as in the Kim–Soni analysis, the best-fit value of 0.178 mm was of the same order as the ply thickness. A comparison of the measured and predicted delamination onset stresses for various normalized ply thicknesses,  $n$ , are shown for the  $[\pm 15]_s$  laminate in Figure 7.35. Specimens were made by stacking single plies of the same orientation together to form a ply with greater effective thickness, and the value of  $n$  is this effective ply thickness divided by the single ply thickness. Also shown in Figure 7.36 are the predictions from a fracture mechanics approach, which will be discussed later.

Catastrophic failure of laminated structures is not the only undesirable result of delamination. The reduction in stiffness of a laminate during delamination growth may make the structure unsafe even if fracture does not occur. Conversely, stiffness loss can be used to characterize the growth of delamination. Thus, analytical models are needed for estimating this stiffness loss during delamination.

O'Brien [34] has developed an analysis of stiffness reduction in symmetric laminates during delamination based on a simple “rule of mixtures” and the CLT. Recall from Equation 7.64 that the effective longitudinal Young's modulus of a symmetric laminate is given by

$$E_x = \frac{1}{tA'_{11}} \quad (7.120)$$

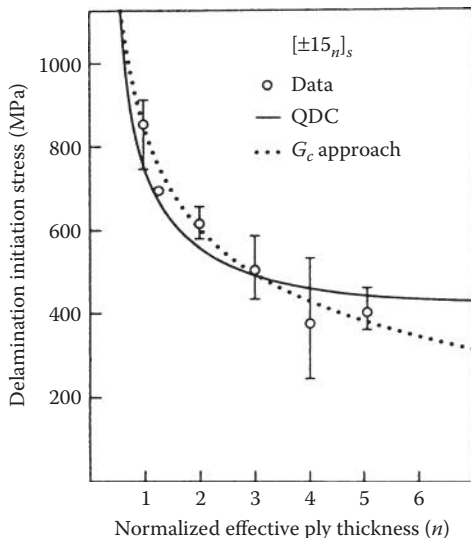


**FIGURE 7.36**

Predicted and measured delamination initiation stresses for  $[\pm 15]_s$  laminates. (From Brewer, J. C. and Lagace, P. A. 1988. *Journal of Composite Materials*, 22, 1141–1155. With permission.)

This equation was used by O'Brien to model the stiffness of the laminate without delaminations, as shown in Figure 7.37a. The corresponding stiffness of a laminate, which has been totally delaminated along one or more interfaces (Figure 7.37b), but whose sublaminates must still have the same longitudinal strain, is given by the rule of mixtures formula

$$E_{\text{td}} = \frac{\sum_{i=1}^m E_{xi} t_i}{t} \quad (7.121)$$

where  $E_{\text{td}}$  is the longitudinal Young's modulus of a laminate totally delaminated along one or more interfaces,  $E_{xi}$  the longitudinal Young's modulus of  $i$ th sublamine formed by the delamination,  $t_i$  the thickness of the  $i$ th sublamine, and  $m$  the number of sublaminates formed by the delamination.

The longitudinal Young's modulus of a laminate that has been partially delaminated along the same interfaces (Figure 7.37c) is given by the rule of mixtures formula

$$E = (E_{\text{td}} - E_x) \frac{a}{b} + E_x \quad (7.122)$$

where  $E$  is the longitudinal Young's modulus of a laminate partially delaminated along one or more interfaces,  $a$  the distance that delamination extends in from the free edge, and  $b$  the half-width of the laminate.

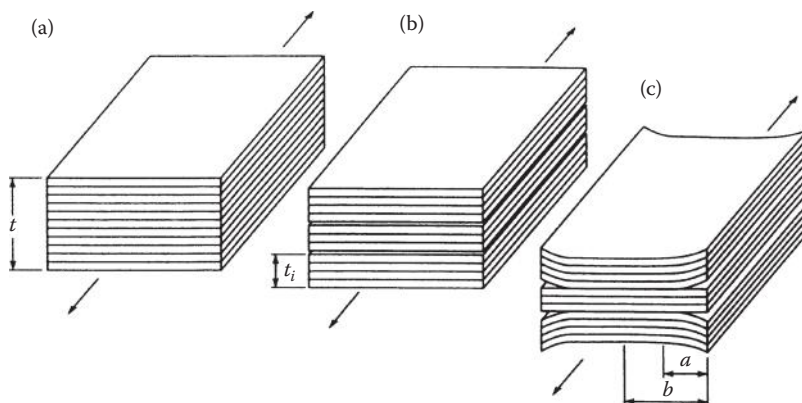


**FIGURE 7.37**

Rule of mixtures analysis of stiffness loss due to delamination. (a) Laminated, (b) totally delaminated, and (c) partially delaminated. (From O'Brien, T. K. 1982. In: Reifsnider, K. L. ed., *Damage in Composite Materials*. ASTM STP 775, pp. 140–167. American Society for Testing and Materials, Philadelphia, PA. Copyright ASTM. With permission.)

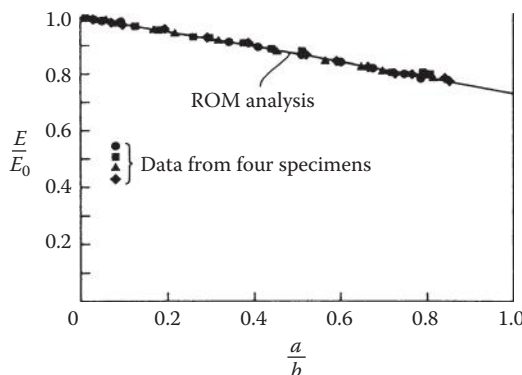
A more general form of Equation 7.122 is given by Equation 7.123:

$$E = (E_{\text{td}} - E_x) \frac{A_d}{A_t} + E_x \quad (7.123)$$

where  $A_d$  is the delaminated area and  $A_t$  total interfacial area.

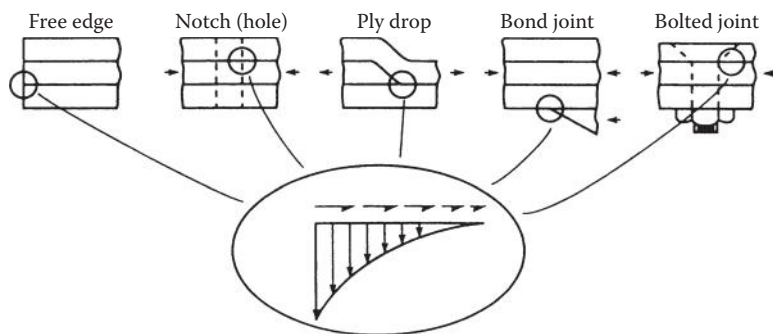
The predicted values of  $E$  normalized to the initial modulus,  $E_0$ , are compared with measured values of  $E/E_0$  for various delamination sizes in  $[\pm 30/\pm 30/90/90]_s$  graphite/epoxy laminates in Figure 7.38, and the agreement is seen to be excellent. As shown in Figure 7.38, complete delamination of this laminate would result in a 25.8% reduction in the laminate stiffness. Such a loss of stiffness would lead to an undesirable increase in the deflection of the structure under load.

In this section, we have only been concerned with delamination near free edges in laminates, but interlaminar stresses and delamination may occur at other discontinuities such as holes, ply drops, and joints (see Figure 7.39 from Ref. [35]). Low-velocity impact (e.g., dropping a wrench) on a composite structure may cause internal delaminations that may reduce the in-plane compressive strength (Figure 7.40). The so-called “compression after impact” (CAI) problem is of considerable interest, and CAI testing will be discussed later in Chapter 10. The analysis of delamination under such complex states of stress generally requires the use of fracture mechanics and finite element numerical approaches, some of which are discussed in Chapter 9. The reader is also encouraged to refer to numerous analytical and experimental studies in several recent books [35–37].

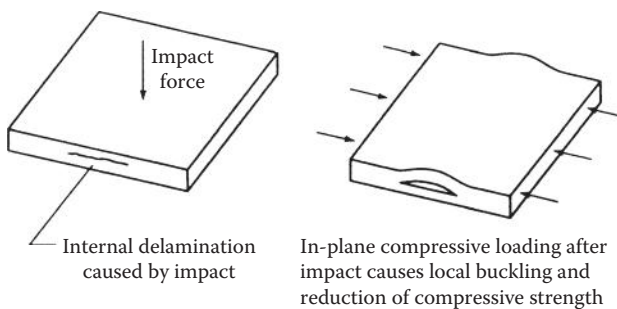


**FIGURE 7.38**

Predicted and measured laminate stiffness as a function of delamination size. (From O’Brien, T. K. 1982. In: Reifsnider, K.L. ed., *Damage in Composite Materials*. ASTM STP 775, pp. 140–167. American Society for Testing and Materials, Philadelphia, PA. Copyright ASTM. Reprinted with permission.)

**FIGURE 7.39**

Interlaminar stresses occur at a variety of discontinuities in composite structures. (From Newaz, G. M. ed. 1991. *Delamination in Advanced Composites*. Technomic Publishing Co., Lancaster, PA. With permission.)

**FIGURE 7.40**

Reduction of in-plane compressive strength of laminate after transverse impact.

There is obviously a lot of interest in the improvement of delamination resistance in laminates, and a number of such approaches will be discussed later in Chapter 9.

## 7.9 Deflection and Buckling of Laminates

This section is concerned with the analysis of transverse deflections of laminates under transverse loading and the prediction of laminate buckling forces. Transverse deflections of laminates due to bending are generally much larger than in-plane deflections, because flexural stiffnesses are lower than extensional stiffnesses. Thus, transverse deflections are an important design consideration, and developments of analytical models for predicting such deflections are of interest. Buckling of laminates is an

instability that is characterized by excessive transverse deflections under in-plane compressive or shear forces. The general equilibrium equations governing transverse deflections involve both in-plane and out-of-plane forces, but the coupling between in-plane forces and transverse deflections is usually taken into account only for the buckling analysis or for large deflection analysis. In the analysis of small transverse deflections alone, the out-of-plane forces are the most important because the laminate is normally designed in such a way that the in-plane forces are less than the corresponding buckling loads. Only a brief introduction to deflection and buckling is given here. For more detailed coverage of these subjects, the reader is referred to the works of Whitney [10], Lekhnitskii [7], Vinson and Sierakowski [38], and Liessa [39].

### 7.9.1 Analysis of Small Transverse Deflections

The analysis of transverse deflections of laminated plates has its basis in the CLT, which was outlined in Section 7.3 and in the differential equations of equilibrium. In order to develop the differential equations governing plate deflections, it is convenient to use an infinitesimal element, as shown in Figure 7.41a–c from Halpin [12]. The in-plane stress resultants and moment resultants are shown in Figure 7.41a, the moment resultants are shown in Figure 7.41b, and the transverse shear stress resultants are shown

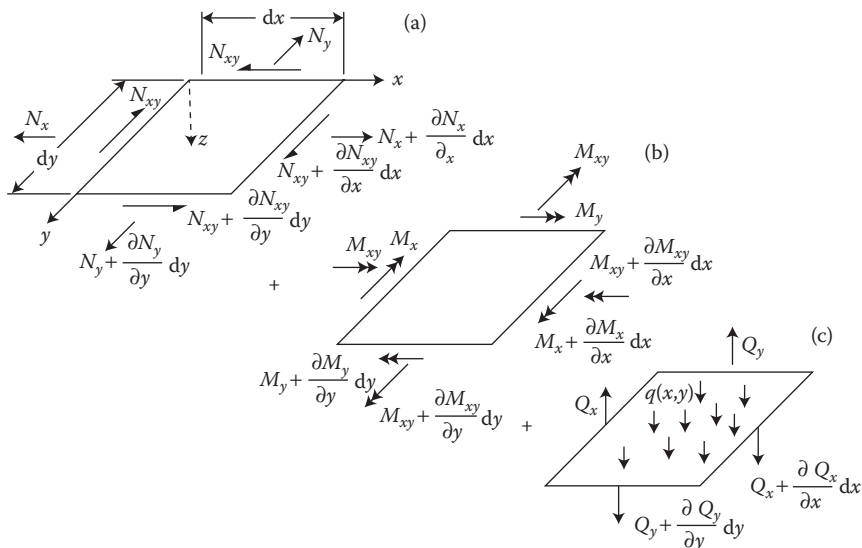


**FIGURE 7.41**

Stress resultants and external loads acting on laminate. (a) In-plane stress resultants, (b) moment resultants, and (c) transverse loads and shear stress resultants. (From Halpin, J. C. 1984. *Primer on Composite Materials: Analysis*. Technomic Publishing Co., Lancaster, PA. With permission.)

in Figure 7.41c. Transverse shear stress resultants were not considered in Section 7.3, but they must be considered here in the transverse deflection analysis. In these diagrams, it is assumed that the transverse deflections are small, so that the out-of-plane components of the in-plane resultants  $N_x$ ,  $N_y$ , and  $N_{xy}$  are negligible. However, these out-of-plane components will be considered in the next section on buckling analysis because of the large transverse deflections associated with buckling. Along with the stress and moment resultants such as those defined previously in Figure 7.9 and in Equations 7.35 and 7.36, the transverse shear stress resultants  $Q_x$  and  $Q_y$  are similarly defined as

$$Q_x = \int_{-t/2}^{t/2} \tau_{xz} dz \quad (7.124)$$

and

$$Q_y = \int_{-t/2}^{t/2} \tau_{yz} dz \quad (7.125)$$

Also included in Figure 7.41 is a distributed transverse load  $q(x,y)$ . Following the derivation by Halpin [12] for static equilibrium according to Newton's second law, the summation of forces along the  $x$  direction must be

$$N_x dy + \frac{\partial N_x}{\partial x} dx dy + N_{xy} dx + \frac{\partial N_{xy}}{\partial y} dx dy - N_x dy - N_{xy} dx = 0 \quad (7.126)$$

Equation 7.126 may be simplified as

$$\frac{\partial N_x}{\partial x} + \frac{\partial N_{xy}}{\partial y} = 0 \quad (7.127)$$

The summation of forces along the  $y$  direction yields

$$N_y dx + \frac{\partial N_y}{\partial y} dx dy + N_{xy} dy + \frac{\partial N_{xy}}{\partial x} dx dy - N_y dx - N_{xy} dy = 0 \quad (7.128)$$

or

$$\frac{\partial N_y}{\partial y} + \frac{\partial N_{xy}}{\partial x} = 0 \quad (7.129)$$

The summation of forces along the  $z$  direction gives

$$Q_x \, dy + \frac{\partial Q_x}{\partial x} \, dx \, dy + Q_y \, dx + \frac{\partial Q_y}{\partial y} \, dy \, dx - Q_x \, dy - Q_y \, dx + q(x, y) \, dx \, dy = 0 \quad (7.130)$$

or

$$\frac{\partial Q_x}{\partial x} + \frac{\partial Q_y}{\partial y} + q(x, y) = 0 \quad (7.131)$$

The summation of moments about the  $x$ -axis yields

$$\begin{aligned} & -M_y \, dx - \frac{\partial M_y}{\partial y} \, dy \, dx - M_{xy} \, dy - \frac{\partial M_{xy}}{\partial x} \, dx \, dy + Q_y \, dx \, dy \\ & + \frac{\partial Q_y}{\partial y} \, dy \, dx \, dy + q(x, y) \, dx \, dy \frac{dy}{2} + Q_x \, dy \frac{dy}{2} \\ & + \frac{\partial Q_x}{\partial x} \, dx \, dy \frac{dy}{2} + M_y \, dx + M_{xy} \, dy - Q_x \, dy \frac{dy}{2} = 0 \end{aligned} \quad (7.132)$$

Simplifying and neglecting products of differentials, we get

$$\frac{\partial M_y}{\partial y} + -\frac{\partial M_{xy}}{\partial x} = Q_y \quad (7.133)$$

A similar summation of moments about the  $y$ -axis gives

$$\frac{\partial M_x}{\partial x} + \frac{\partial M_{xy}}{\partial y} = Q_x \quad (7.134)$$

Substitution of Equations 7.133 and 7.134 into Equation 7.131 yields

$$\frac{\partial^2 M_x}{\partial x^2} + 2 \frac{\partial^2 M_{xy}}{\partial x \, \partial y} + \frac{\partial^2 M_y}{\partial y^2} + q(x, y) = 0 \quad (7.135)$$

Equations 7.127, 7.129, and 7.135 are the differential equations of equilibrium of the plate in terms of stress and moment resultants. The corresponding equilibrium equations in terms of displacements can be derived by substituting the laminate force-deformation equation (7.44), the strain-displacement relations (7.32), and the curvature-displacement equations

(7.33) in Equations 7.12, 7.129, and 7.135. The resulting set of coupled partial differential equations in the displacements  $u^0$ ,  $v^0$ , and  $w$  are

$$\begin{aligned} A_{11} \frac{\partial^2 u^0}{\partial x^2} + 2A_{16} \frac{\partial^2 u^0}{\partial x \partial y} + A_{66} \frac{\partial^2 u^0}{\partial y^2} + A_{16} \frac{\partial^2 v^0}{\partial x^2} + (A_{12} + A_{66}) \frac{\partial^2 v^0}{\partial x \partial y} \\ + A_{26} \frac{\partial^2 v^0}{\partial y^2} - B_{11} \frac{\partial^3 w}{\partial x^3} - 3B_{16} \frac{\partial^3 w}{\partial x^2 \partial y} \\ - (B_{12} + 2B_{66}) \frac{\partial^3 w}{\partial x \partial y^2} - B_{26} \frac{\partial^3 w}{\partial y^3} = 0 \end{aligned} \quad (7.136)$$

$$\begin{aligned} A_{16} \frac{\partial^2 u^0}{\partial x^2} + (A_{12} + A_{66}) \frac{\partial^2 u^0}{\partial x \partial y} + A_{26} \frac{\partial^2 u^0}{\partial y^2} + A_{66} \frac{\partial^2 v^0}{\partial x^2} \\ + 2A_{26} \frac{\partial^2 v^0}{\partial x \partial y} + A_{22} \frac{\partial^2 v^0}{\partial y^2} - B_{16} \frac{\partial^3 w}{\partial x^3} - (B_{12} + 2B_{66}) \frac{\partial^3 w}{\partial x^2 \partial y} \\ - 3B_{26} \frac{\partial^3 w}{\partial x \partial y^2} - B_{22} \frac{\partial^3 w}{\partial y^3} = 0 \end{aligned} \quad (7.137)$$

$$\begin{aligned} D_{11} \frac{\partial^4 w}{\partial x^4} + 4D_{16} \frac{\partial^4 w}{\partial x^3 \partial y} + 2(D_{12} + 2D_{66}) \frac{\partial^4 w}{\partial x^2 \partial y^2} + 4D_{26} \frac{\partial^4 w}{\partial x \partial y^3} \\ + D_{22} \frac{\partial^4 w}{\partial y^4} - B_{11} \frac{\partial^3 u^0}{\partial x^3} - 3B_{16} \frac{\partial^3 u^0}{\partial x^2 \partial y} - (B_{12} + 2B_{66}) \frac{\partial^3 u^0}{\partial x \partial y^2} \\ - B_{26} \frac{\partial^3 u^0}{\partial y^3} - B_{16} \frac{\partial^3 v^0}{\partial x^3} - (B_{12} + 2B_{66}) \frac{\partial^3 v^0}{\partial x^2 \partial y} - 3B_{26} \frac{\partial^3 v^0}{\partial x \partial y^2} \\ - B_{22} \frac{\partial^3 v^0}{\partial y^3} = q(x, y) \end{aligned} \quad (7.138)$$

Note that the in-plane displacements  $u^0$  and  $v^0$  are coupled with the transverse displacements,  $w$ , when the coupling stiffnesses,  $B_{ij}$ , are present. For symmetric laminates with  $B_{ij} = 0$ , Equation 7.138 alone becomes the governing equation for transverse displacements. These governing partial differential equations must be solved subject to the appropriate boundary conditions. In the general case, when the in-plane displacements are coupled with the transverse displacements, the boundary conditions must be a combination of boundary conditions for a planar theory of elasticity problem and boundary conditions for a plate-bending problem [10]. In this section, however, we will restrict the discussion to bending of symmetric laminated plates. That is, we will only consider transverse displacements according to Equation 7.138 with all  $B_{ij} = 0$ .

Let us now consider the case of transverse deflection of the rectangular, specially orthotropic plate, which is simply supported on all edges and loaded with a distributed load,  $q(x, y)$ , as shown in Figure 7.42. For a specially orthotropic plate all  $B_{ij} = 0$ ,  $A_{16} = A_{26} = D_{16} = D_{26} = 0$  and Equation 7.138 becomes

$$D_{11} \frac{\partial^4 w}{\partial x^4} + 2(D_{12} + 2D_{66}) \frac{\partial^4 w}{\partial x^2 \partial y^2} + D_{22} \frac{\partial^4 w}{\partial y^4} = q(x, y) \quad (7.139)$$

For the simply supported boundary condition, the transverse displacements and bending moments must vanish at the edges. In order to use the bending moment boundary conditions to solve the differential equation for displacements, however, the bending moments must be expressed in terms of displacements. Such expressions can be obtained from Equations 7.33 and 7.44 for the specially orthotropic plate as follows:

$$M_x = D_{11}\kappa_x + D_{12}\kappa_y = -D_{11} \frac{\partial^2 w}{\partial x^2} - D_{12} \frac{\partial^2 w}{\partial y^2} \quad (7.140)$$

and

$$M_y = D_{12}\kappa_x + D_{22}\kappa_y = -D_{12} \frac{\partial^2 w}{\partial x^2} - D_{22} \frac{\partial^2 w}{\partial y^2} \quad (7.141)$$

Thus, along  $x = 0$  and  $x = a$ ,

$$w = 0$$

and

$$M_x = -D_{11} \frac{\partial^2 w}{\partial x^2} - D_{12} \frac{\partial^2 w}{\partial y^2} = 0 \quad (7.142)$$

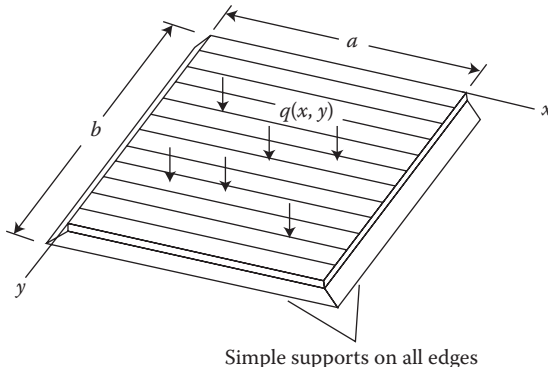


**FIGURE 7.42**

Simply supported, specially orthotropic plate with distributed loading.

and along  $y = 0$  and  $y = b$

$$w = 0$$

and

$$M_y = -D_{12} \frac{\partial^2 w}{\partial x^2} - D_{22} \frac{\partial^2 w}{\partial y^2} = 0 \quad (7.143)$$

Several approaches to the solution of such problems have been proposed [10,38]. This simplest method involves the use of double Fourier sine series to represent both the load  $q(x, y)$  and the displacements  $w(x, y)$ . If the load can be represented as

$$q(x, y) = \sum_{m=1}^{\infty} \sum_{n=1}^{\infty} q_{mn} \sin \frac{m\pi x}{a} \sin \frac{n\pi y}{b} \quad (7.144)$$

then it can be shown that the differential equation and the boundary conditions are satisfied by solutions of the form

$$w(x, y) = \sum_{m=1}^{\infty} \sum_{n=1}^{\infty} w_{mn} \sin \frac{m\pi x}{a} \sin \frac{n\pi y}{b} \quad (7.145)$$

Substitution of Equations 7.145 and 7.144 into Equation 7.139 yields the displacement coefficients

$$w_{mn} = \frac{a^4 q_{mn}}{\pi^4 [D_{11}m^4 + 2(D_{12} + 2D_{66})(mnR)^2 + D_{22}(nR)^4]} \quad (7.146)$$

where the plate aspect ratio  $R = a/b$  [10]. The Fourier coefficients  $q_{mn}$  can be found for the particular assumed load distribution [9,10]. For the uniform load  $q(x, y) = q_0$ , a constant, it can be shown that the Fourier coefficients are

$$q_{mn} = \frac{16q_0}{\pi^2 mn} \quad \text{for } m, n = 1, 3, 5, \dots \quad (7.147)$$

$$\text{and } q_{mn} = 0 \quad \text{for } m, n = 2, 4, 6, \dots$$

Displacements  $w(x, y)$  for the uniformly loaded, simply supported plate may now be found by substituting Equations 7.146 and 7.147 into Equation 7.145. Moment resultants may be found by substituting these equations into Equation 7.33 and then substituting the result into Equation 7.44. Finally,

lamina stresses may be found by combining Equations 7.33, 7.34, 7.145, 7.146, and 7.147.

For boundary conditions such as clamped edges or free edges, exact series solutions similar to Equation 7.145 are generally not possible. For such cases, approximate solutions must be derived using approaches such as the Rayleigh–Ritz method or the Galerkin method. For a detailed discussion of these methods and other boundary conditions, the reader is referred to the book by Whitney [10].

### 7.9.2 Buckling Analysis

In the derivations of Equations 7.127, 7.129, and 7.131, the coupling between the in-plane forces  $N_x$ ,  $N_y$ , and  $N_{xy}$  and the out-of-plane deflections,  $w$ , was ignored because of the assumption of small displacements. In order to develop the equations to predict buckling under in-plane loads, however, this coupling must be considered due to the large deflections associated with buckling. Such equations can be derived by assuming the differential element of Figure 7.41a to be oriented in a general out-of-plane position, as shown in Figure 7.43. Using Figure 7.43, and taking into account the vertical components of the in-plane forces, the summation of forces in the  $z$  direction now becomes

$$\frac{\partial Q_x}{\partial x} + \frac{\partial Q_y}{\partial y} + q(x, y) + N_x \frac{\partial^2 w}{\partial x^2} + 2N_{xy} \frac{\partial^2 w}{\partial x \partial y} + N_y \frac{\partial^2 w}{\partial y^2} = 0 \quad (7.148)$$

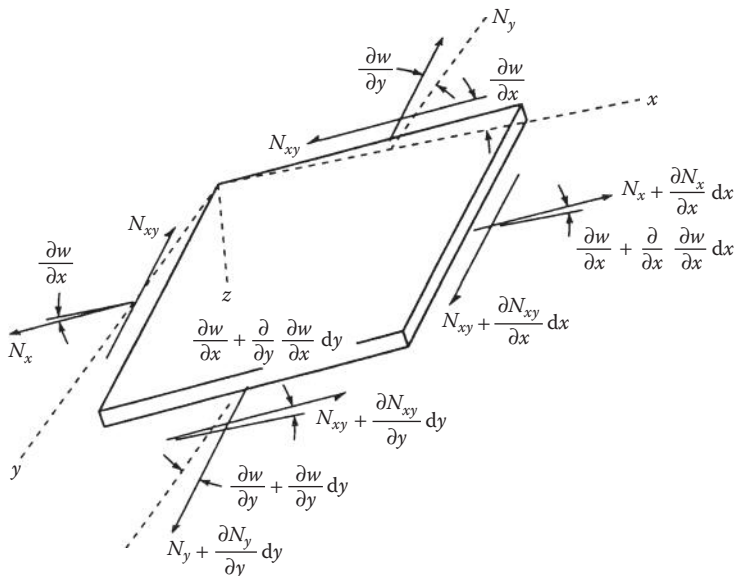


**FIGURE 7.43**

Differential element of laminate in out-of-plane position for buckling analysis.

Note that Equation 7.148 consists of the terms from Equation 7.131 plus the terms involving the in-plane forces. Combining Equations 7.148, 7.133, and 7.134, we find that

$$\frac{\partial^2 M_x}{\partial x^2} + 2 \frac{\partial^2 M_{xy}}{\partial x \partial y} + \frac{\partial^2 M_y}{\partial y^2} + N_x \frac{\partial^2 w}{\partial x^2} + 2N_{xy} \frac{\partial^2 w}{\partial x \partial y} + N_y \frac{\partial^2 w}{\partial y^2} + q(x, y) = 0 \quad (7.149)$$

Equation 7.149 consists of all the terms in Equation 7.135 plus the terms involving the in-plane forces. Substitution of Equations 7.148, 7.32, and 7.33 into Equation 7.149 yields the equation

$$\begin{aligned} D_{11} \frac{\partial^4 w}{\partial x^4} + 4D_{16} \frac{\partial^4 w}{\partial x^3 \partial y} + 2(D_{12} + 2D_{66}) \frac{\partial^4 w}{\partial x^2 \partial y^2} + 4D_{26} \frac{\partial^4 w}{\partial x \partial y^3} \\ + D_{22} \frac{\partial^4 w}{\partial y^4} - B_{11} \frac{\partial^3 u^0}{\partial x^3} - 3B_{16} \frac{\partial^3 u^0}{\partial x^2 \partial y} - (B_{12} + 2B_{66}) \frac{\partial^3 u^0}{\partial x \partial y^2} \\ - B_{26} \frac{\partial^3 u^0}{\partial y^3} - B_{16} \frac{\partial^3 v^0}{\partial x^3} - (B_{12} + 2B_{66}) \frac{\partial^3 v^0}{\partial x^2 \partial y} - 3B_{26} \frac{\partial^3 v^0}{\partial x \partial y^2} \\ - B_{22} \frac{\partial^3 v^0}{\partial y^3} = q(x, y) + N_x \frac{\partial^2 w}{\partial x^2} + 2N_{xy} \frac{\partial^2 w}{\partial x \partial y} + N_y \frac{\partial^2 w}{\partial y^2} \end{aligned} \quad (7.150)$$

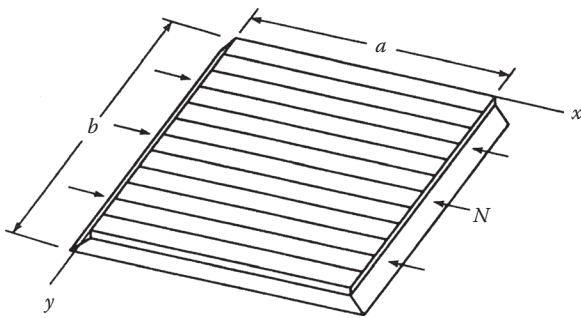
Note that Equation 7.150 consists of the terms in Equation 7.138 and the additional terms due to the in-plane forces.

We now consider the case of buckling of a rectangular, simply supported, specially orthotropic plate under a single compressive axial load,  $N_x = -N$ , as shown in Figure 7.44. In this case, the loads  $N_y = N_{xy} = q(x, y) = 0$ , all  $B_{ij} = 0$ , the stiffnesses  $A_{16} = A_{26} = D_{16} = D_{26} = 0$  and Equation 7.150 becomes

$$D_{11} \frac{\partial^4 w}{\partial x^4} + 2(D_{12} + 2D_{66}) \frac{\partial^4 w}{\partial x^2 \partial y^2} + D_{22} \frac{\partial^4 w}{\partial y^4} = -N \frac{\partial^2 w}{\partial x^2} \quad (7.151)$$

For the simply supported boundary condition described previously by Equations 7.142 and 7.143, we may assume a solution of the form

$$w(x, y) = \sum_{m=1}^{\infty} \sum_{n=1}^{\infty} w_{mn} \sin \frac{m\pi x}{a} \sin \frac{n\pi y}{b} \quad (7.152)$$

**FIGURE 7.44**

Simply supported, specially orthotropic plate under compressive uniaxial in-plane loading.

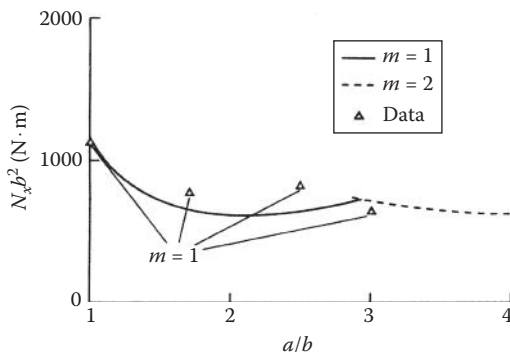
The mode shape for a particular buckling mode is described by the subscripts  $m$  and  $n$ , since  $m$  is the number of half-sine waves along the  $x$  direction and  $n$  is the number of half-sine waves along the  $y$  direction. Substitution of this solution in the governing differential equation (7.151) leads to the equation

$$w_{mn}\pi^2 \left[ (D_{11}m^4 + 2(D_{12} + 2D_{66})(mnR)^2 + D_{22}(nR)^4) \right] = w_{mn}Na^2m^2 \quad (7.153)$$

where again  $R = a/b$ . This equation has the trivial solution  $w_{mn} = 0$ , which is of no interest. For nontrivial solutions, the critical buckling load must be

$$N_{cr} = \frac{\pi^2}{a^2m^2} \left[ (D_{11}m^4 + 2(D_{12} + 2D_{66})(mnR)^2 + D_{22}(nR)^4) \right] \quad (7.154)$$

where the smallest buckling load occurs for  $n = 1$ , and the lowest value of the load corresponding to a particular value of  $m$  can only be determined if the  $D_{ij}$  and the plate dimensions  $a$  and  $b$  are known. As shown in Figure 7.45, Hatcher and Tuttle [40] have compared experimentally determined buckling loads for simply supported, specially orthotropic graphite/epoxy panels with predicted buckling loads from Equation 7.154. The value  $n = 1$  is used for all predicted curves, and the curves for  $m = 1$  and  $m = 2$  are shown. Measurement of critical buckling loads is shown schematically in Figures 7.46 and 7.47, where the compressive axial load on the laminate is increased until the lateral deflection starts to increase dramatically and the instability known as buckling soon follows. Although the predictions are reasonably accurate for this case, it was found that the agreement for some other laminate configurations was not quite as good. Difficulties in simulating the simply supported boundary conditions and in measuring the critical buckling loads, along with other problems such as the existence of imperfections in the test panels, were cited as possible reasons for the disagreement.

**FIGURE 7.45**

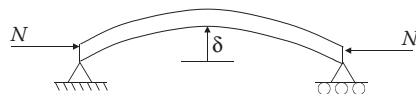
Comparison of predicted and measured normalized buckling load,  $N_x b^2$ , vs. plate aspect ratio,  $a/b$ , for  $[0_1]$  graphite/epoxy laminates. (From Hatcher, D. and Tuttle, M. 1991. *Recent Advances in Structural Mechanics*, PVP-Vol. 225/NE-Vol. 7, pp. 21–26. American Society of Mechanical Engineers, New York. Reprinted by permission of The American Society of Mechanical Engineers.)

Other types of buckling can occur in laminates in addition to buckling under in-plane axial loads. For example, if the critical in-plane shear load is exceeded, shear buckling can occur as shown in Figure 7.48.

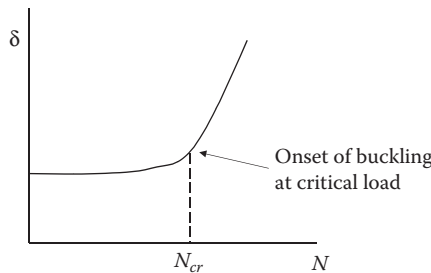
For laminates other than specially orthotropic and boundary conditions other than simply supported, closed-form solutions similar to Equation 7.154 are generally not possible, and approximate methods such as Rayleigh–Ritz or Galerkin must be used. Exceptions include the antisymmetric cross-ply and antisymmetric angle-ply laminates, which do admit closed-form solutions [41].

## 7.10 Selection of Laminate Designs

When designing with conventional isotropic materials, the problem of material selection is usually solved by simply looking up the appropriate properties of candidate materials in a handbook. The selection of a composite laminate design can be a formidable task, however, due to the large number of available fiber and matrix materials and the endless variety of laminate configurations. The major differences between the analysis of laminates and the design of laminates are best explained by giving examples. A typical

**FIGURE 7.46**

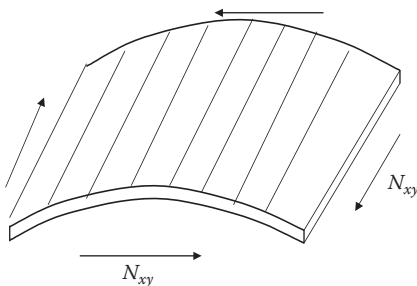
Measurement of critical axial buckling load for laminate.

**FIGURE 7.47**

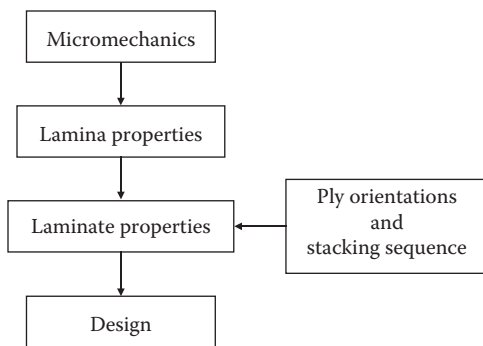
Variation of lateral deflection with in-plane axial load during buckling test.

analysis problem would be given a composite laminate and allowable ply stresses, determine the loads that it will support, or given the laminate, loads, and properties, determine the resulting stresses and strains. Either way, the analysis problem has a unique solution. A typical design problem would be, given a set of loads and other design constraints, select the materials and laminate configuration to withstand the loads. As opposed to the analysis problem, the design problem may have an infinite number of solutions. Depending on the number of constraints, it may be possible to reduce the number of feasible designs or to even optimize the design. A general flow chart showing the laminate design sequence is shown in Figure 7.49. Depending on the degree of design flexibility desired and the availability of measured lamina level properties, the laminate design may begin either with micromechanics modeling at the fiber/matrix level or directly from measured lamina properties.

Obviously, the nature of the applied loads must be known in order to start the design process. Uniaxial loading on a unidirectional laminate is clearly the simplest case to deal with, but, unfortunately, most practical loading situations are multiaxial, and this requires the design of a multidirectional laminate. For example, if the loading is biaxial as shown in Figure 7.50a, only a

**FIGURE 7.48**

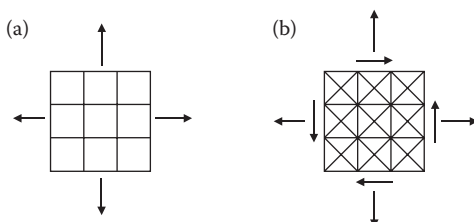
Buckling due to in-plane shear loads.



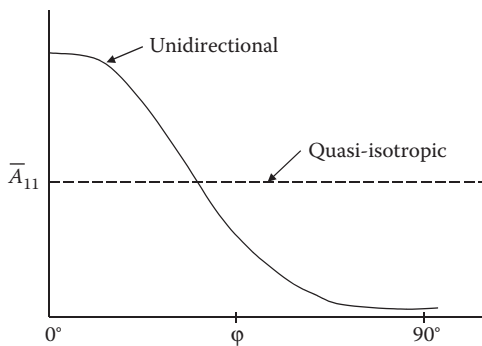
**FIGURE 7.49**  
Flow chart for laminate analysis.

crossply [0/90] laminate may be needed. However, if shear loads are present as in Figure 7.50b, some angle plies will be required as well. In the beginning stages of a design, it may be helpful to establish some practical bounds on the laminate properties based on knowledge of the mechanical behavior of certain special types of laminates. For example, Figure 7.51 shows the variation of the in-plane laminate stiffness,  $\bar{A}_{11}$ , with  $\phi$ , the orientation of the laminate with respect to the loading direction, for both unidirectional and quasi-isotropic laminates. The unidirectional laminate stiffness for  $\phi = 0$  may be considered to represent the practical upper bound on laminate stiffness, and the quasi-isotropic laminate may be considered to represent the practical lower bound on laminate extensional stiffness.

An essential component of any design problem is the identification all of the possible failure modes. Whether intentional or not, if a particular failure mode is overlooked in the design process, that failure mode is the one that will most likely come back to haunt the designer. A list of the major design criteria for composite laminates and the associated failure modes are provided in Table 7.1. It is beyond the scope of this book to cover the analytical tools needed for all these design criteria, and the focus here is on strength, stiffness, stability, hygrothermal effects, and creep.



**FIGURE 7.50**  
Lamina orientations to resist different loading conditions. (a) Cross plies required to resist biaxial different loading conditions and (b) angle plies required to resist shear loads.

**FIGURE 7.51**

Variation of laminate extensional stiffness with laminate orientation for unidirectional and quasi-isotropic laminates.

In order to use the laminate analysis equations that were derived and discussed earlier in this chapter, extensive matrix algebra is obviously required. In addition, proper evaluation of laminate designs requires numerous repetitive calculations resulting from changes in loading conditions, material properties, and laminate geometry. These computational requirements are ideally suited for solutions by digital computers, and a variety of software packages for laminate analysis now exist. A list of some of the available software packages is given in Table 7.2. Most of these programs have been developed for use on microcomputers, and many of them will do both micromechanical analysis of laminae and laminate analysis according to the CLT. The two basic approaches used in many of these programs are (1) stress and strain analysis for prescribed loads, and (2) first ply failure analysis and ultimate laminate failure analysis according to one of the multiaxial lamina strength criteria that were discussed in Chapter 4. In addition, some of the programs will do specialized tasks such as deflection and buckling analyses, interlaminar stress calculations, effective property calculations, and hygrothermal and

**TABLE 7.1**

Design Criteria for Composite Laminates and the Associated Failure Modes

Design Criteria	Associated Failure Modes
Strength	Fracture (either partial or complete)
Stiffness	Excessive deformation
Stability	Buckling
Hygrothermal effects	Property degradation, expansion and contraction, residual stresses
Life or durability	Fatigue, creep
Weight	Heavier than conventional design
Cost	Not affordable
Manufacturability	Impractical to build, warping due to residual stresses

**TABLE 7.2**

## Composite Analysis Software

Software	Company	Address
Helius: CompositePro	Firehole Technologies	210 South 3rd St., Suite 202, Laramie, WY 82070; web address: <a href="http://www.fireholetech.com">http://www.fireholetech.com</a>
MicMac, Super MicMac/FEA	Think Composites	101 Alma Street, #703, Palo Alto, CA 94301, web address: <a href="http://www.thinkcomposites.com/">http://www.thinkcomposites.com/</a>
FiberSim	Vistagy, Inc.	200 Fifth Avenue, 5 <sup>th</sup> Floor, Waltham, MA 02451, web address: <a href="http://www.vistagy.com">http://www.vistagy.com</a>
HyperSizer	Collier Research	45 Diamond Hill Road, Hampton, VA 23666, web address: <a href="http://www.hypersizer.com">http://www.hypersizer.com</a>
Lamona	AdTech Systems Research, Inc.	1342 N. Fairfield Road, Beavercreek, OH 45432-2698, web address: <a href="http://www.adtech25.com/">http://www.adtech25.com/</a>
LAP	Anaglyph Ltd.	Suite 33, 10 Barley Mow Passage, London W4 4PH, United Kingdom, web address: <a href="http://www.anaglyph.co.uk/">http://www.anaglyph.co.uk/</a>
The Laminator	RegSoft.com	<a href="http://www.thelaminator.net/">http://www.thelaminator.net/</a>

transport property calculations. Such programs are indispensable in design and analysis because hand calculations are not only too time consuming, but the possibilities for errors in such hand calculations are endless.

For composite structures having complex geometries the preferred analytical tool is the finite element method. The use of the finite element method in micromechanical analysis has already been discussed in Chapter 3. Macromechanical finite element analysis of laminated structures is also widely used, and most of the popular finite element codes have special elements such as orthotropic 3-D solid elements, orthotropic 2- and 3-D shell elements, and orthotropic axisymmetric solid elements [42].

Although computer software gives the designer great flexibility in the selection of materials and laminate geometries, graphical representations that show the range of properties that can be attained with different laminate configurations are also helpful. One type of graphical representation, known as a carpet plot, is particularly useful. For example, if the ply orientations in a laminate are restricted to certain angles such as  $0^\circ$ ,  $\pm 45^\circ$ , and  $90^\circ$ , then a carpet plot can be generated, which shows how a given laminate property depends on the percentages of the plies at the various orientations. The carpet plots in Figure 7.52 from ref. [43] show how  $E_x$ ,  $G_{xy}$ ,  $v_{xy}$ , and  $\alpha_x$  for  $[0_i/\pm 45_j/90_k]$  Kevlar®/epoxy laminates vary with the percentages of the plies at the three angles. In this case,  $i$  is the number of  $0^\circ$  plies,  $j$  is the number of  $\pm 45^\circ$  plies, and  $k$  is the number of  $90^\circ$  plies. Therefore, the percentage of  $0^\circ$  plies is  $i/(i + j + k)$ , the percentage of  $\pm 45^\circ$  plies is  $j/(i + j + k)$ , and the percentage of  $90^\circ$  plies is  $k/(i + j + k)$ .

For example, the various ply combinations that will give a certain value of longitudinal modulus,  $E_x$ , can be determined by drawing a horizontal line in Figure 7.52a at the value of  $E_x$  and then reading off the percentage of the plies at the three angles corresponding to a particular point on the line. Obviously, there are many possible combinations that will give the same value of  $E_x$ , and the design flexibility inherent in composite construction is again demonstrated. Carpet plots for laminate strength are also widely used. Since there would normally be more than one design constraint, an iterative approach involving the repeated use of carpet plots for several different properties may

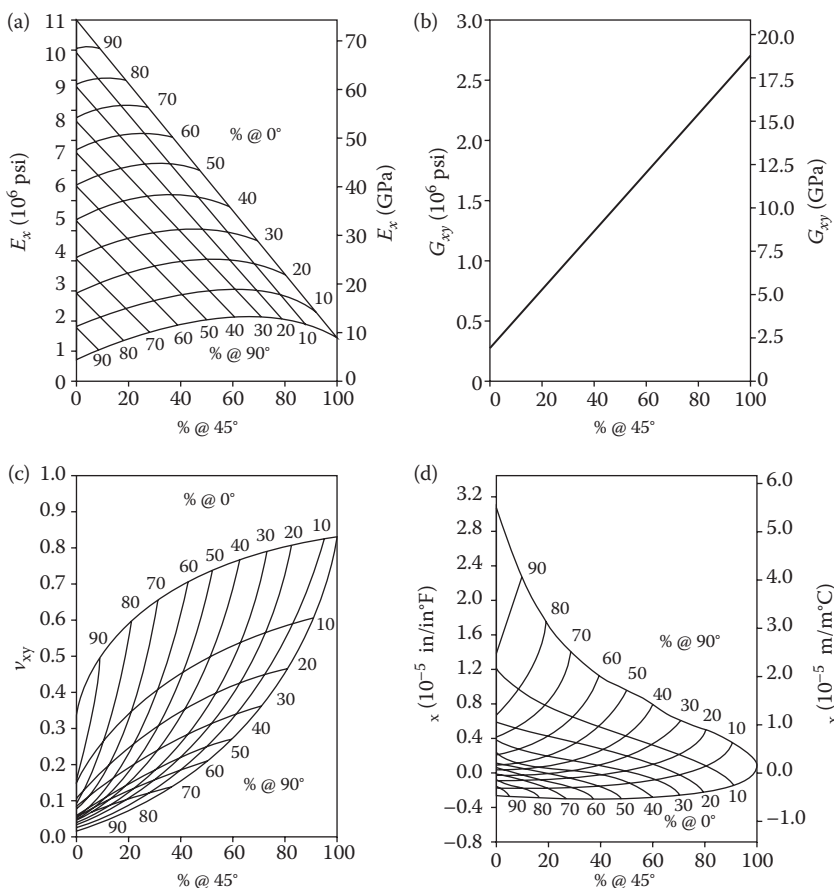


**FIGURE 7.52**

Carpet plots for [0<sub>i</sub>/±45<sub>j</sub>/90<sub>k</sub>] Kevlar®/epoxy laminates. (a) Axial modulus of elasticity,  $E_x$ , (b) shear modulus,  $G_{xy}$ , (c) poisson's ratio,  $\nu_{xy}$ , and (d) linear coefficient of thermal expansion,  $\alpha_x$ . (From Peters, S. T., Humphrey, W. D., and Foral, R. F. 1991. *Filament Winding Composite Structure Fabrication*, pp. 5–45. Society for Advancement of Materials and Process Engineering, Covina, CA. Reprinted by permission of The Society for the Advancement of Material and Process Engineering.)

be needed for the selection of the required ply combinations. Carpet plots can be quickly generated using the output of laminate analysis software.

While composite analysis software packages and carpet plots are very convenient and efficient design tools for dealing with micromechanics analysis and laminate analysis using CLT, they generally do not include consideration of interlaminar stresses or other "secondary stresses." Indeed, the secondary stresses are often neglected in the design process, which tends to focus on the "primary" in-plane stresses that are directly associated with the loading. As seen in Section 7.7, the interlaminar stresses often develop near free edges such as bolt holes or other discontinuities. An example of this is shown in Figure 7.53, where the transverse interlaminar stresses around the bolt holes in the composite link may lead to failure before the primary axial stresses do. Thus, the maximum applied axial load on the link may be limited by the secondary stresses more than by the primary axial stresses. There are other secondary stresses besides interlaminar stresses that may limit the applied loading on the composite more than the primary stresses do. For example, in the filament wound, composite cylindrical pressure vessel shown in Figure 7.54, axial bending stresses in the composite cylinder may be generated due to rotational deformation of the lip of the metal end cap as the cylinder is internally pressurized. Since the fibers in such a filament wound vessel are oriented primarily in the circumferential or "hoop" direction, the axial direction in the cylinder corresponds to the transverse direction in the composite. As shown in Chapter 4, the transverse tensile strength is generally the lowest of all the composite strengths, so the secondary bending stresses rather than the hoop stresses may limit the internal pressure that the cylinder can withstand.

A number of available handbooks and design guides are useful in the design of composite laminates and structures. These books contain not only the necessary analytical tools, but also the material property data that is required for the use of the tools. Among the recent composites handbooks are those edited by Kelly and Zweben [44], Mallick [45], Harper [46], and Donaldson and Miracle [47]. Of particular note is the five volume series *Composite Materials Handbook*, MIL-HDBK-17 [48], which is sponsored by the U.S. Department of Defense, and is available online.

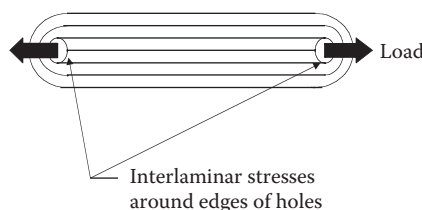


**FIGURE 7.53**  
Interlaminar stresses in axially loaded composite link.

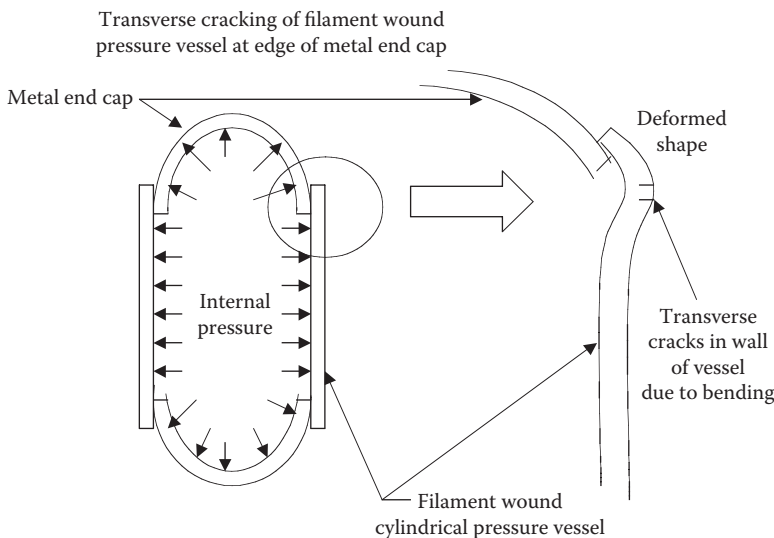


**FIGURE 7.54**  
Axial bending stresses in filament wound composite cylinder caused by metal end cap.

### Example 7.15

Using the carpet plots for Kevlar®/epoxy laminates in Figure 7.52a, specify the required percentages of plies at  $0^\circ$ ,  $45^\circ$ , and  $90^\circ$  if the longitudinal modulus of the laminate is to be  $E_x = 30$  GPa.

### SOLUTION

The reader should be able to use Figure 7.52a to verify that a Kevlar®/epoxy laminate with a longitudinal modulus of  $E_x = 30$  GPa can be obtained with the following ply combinations; (1) 35% at  $0^\circ$ , 0% at  $45^\circ$ , and 65% at  $90^\circ$ ; (2) 30% at  $0^\circ$ , 30% at  $45^\circ$ , and 40% at  $90^\circ$ ; and (3) 30% at  $0^\circ$ , 60% at  $45^\circ$ , and 10% at  $90^\circ$ . These are only three of many possible combinations that will give the same result. Additional design constraints may also be taken into account with other carpet plots. For example, if a shear modulus,  $G_{xy}$ , of at least 5.0 GPa is needed, Figure 7.52b indicates that the laminate should have at least 20% of its plies at  $45^\circ$ . Thus, laminates (2) and (3) above both satisfy the constraints on  $E_x$  and  $G_{xy}$ , but laminate (1) does not.

### Example 7.16

An existing power transmission shaft consists of a hollow composite tube as shown in Figure 7.34, and the tube wall is a filament wound quasi-isotropic  $[60/0/-60]_s$  laminate of thickness  $t$ . A new shaft of the same wall thickness  $t$  is to be designed from the same lamina material, but the new laminate is to have a shear stiffness greater than that of the existing shaft. Over what range of angles  $\theta$  will a  $[+\theta/-\theta/-\theta]$ , angle-ply laminate achieve this design objective?

### SOLUTION

The shear stiffness of the new angle-ply laminate is

$$(A_{66})_{ap} = \int_{-t/2}^{t/2} \bar{Q}_{66} dz = (\bar{Q}_{66})_{+\theta} \frac{t}{3} + (\bar{Q}_{66})_{-\theta} \frac{2t}{3}$$

Recalling that the lamina stiffnesses can be expressed in terms of invariants as

$$\bar{Q}_{66} = \frac{U_1 - U_4}{2} - U_3 \cos 4\theta$$

and that  $\cos 4\theta = \cos(-4\theta)$ , the new laminate stiffness can be written as

$$\begin{aligned} (A_{66})_{ap} &= \left[ \frac{U_1 - U_4}{2} - U_3 \cos 4\theta \right] \frac{t}{3} + \left[ \frac{U_1 - U_4}{2} - U_3 \cos(-4\theta) \right] \frac{2t}{3} \\ &= \frac{U_1 - U_4}{2} t - U_3 t \cos 4\theta \end{aligned}$$

The shear stiffness of a quasi-isotropic laminate is

$$(A_{66})_{Qi} = \frac{U_1 - U_4}{2} t$$

Therefore, the shear stiffness of the new laminate can be expressed as

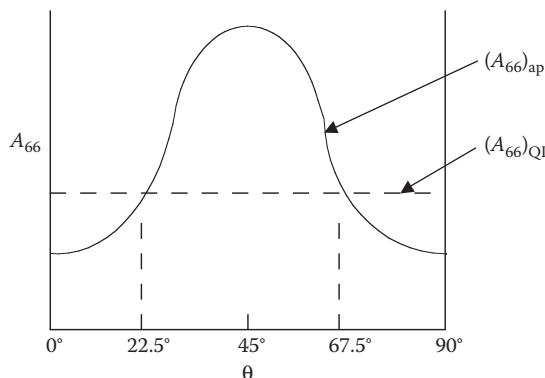
$$(A_{66})_{ap} = (A_{66})_{Qi} - U_3 t \cos 4\theta$$

The variations of  $(A_{66})_{ap}$  and  $(A_{66})_{Qi}$  with  $\theta$  are shown in Figure 7.55, where it can be seen that

$$(A_{66})_{ap} > (A_{66})_{Qi} \quad \text{for angles } \theta \text{ in the range } 22.5^\circ \leq \theta \leq 67.5^\circ.$$

## 7.11 Application of Laminate Analysis to Composite Structures

Composite structures often consist of components in the form of beams, plates, shells, sandwich panels, and grids, and for detailed coverage of the mechanics of composite structures, the reader is referred to books by Vinson and Sierakowski [49], Kollar and Springer [50], and Sun [51]. The purpose of this section is to show how the previously described CLT can be applied to composite structures that are not usually thought of as being laminates. More specifically, the application of CLT to composite sandwich structures and composite grid structures will be discussed briefly. Applications of laminated beam theory to the analysis of sandwich beams will also be given.

**FIGURE 7.55**

Variation of laminate shear stiffness with ply orientation for angle ply and quasi-isotropic laminates.

Detailed discussion of these structures is beyond the scope of this book, as both types of structures have been the subject of numerous books and journal articles, some of which are referred to here.

### 7.11.1 Composite Sandwich Structures

Composite sandwich structures such as the one shown in Figure 1.5 are widely used in aerospace and marine applications due to the extremely high flexural stiffness-to-weight ratios and flexural strength-to-weight ratios that can be achieved with such structures. The mechanical behavior of composite sandwich structures has been described in detail by Vinson [52]. As shown in Figure 1.5, composite sandwich structures consist of two composite face sheets adhesively bonded on both sides of a lightweight foam or honeycomb core. The equivalent laminate stiffnesses of composite sandwich panels can be found directly from CLT. As shown in Figures 1.5 and 7.56, such structures are typically symmetric with respect to the middle surface, and so the corresponding coupling stiffnesses \$B\_{ij} = 0\$. The equivalent laminate extensional stiffnesses for the symmetric sandwich structure geometry in Figure 7.56 are given by substitution in Equation 7.41, as shown by Vinson [52]:

$$\begin{aligned}
 A_{ij} &= \sum_{k=1}^3 [\bar{Q}_{ij}]_k (z_k - z_{k-1}) \\
 &= [\bar{Q}_{ij}]_f \left( -\frac{h_c}{2} - \left( \frac{h_c}{2} - t_f \right) \right) + [\bar{Q}_{ij}]_c \left( \frac{h_c}{2} - \left( -\frac{h_c}{2} \right) \right) + [\bar{Q}_{ij}]_f \left( \left( \frac{h_c}{2} + t_f \right) - \frac{h_c}{2} \right) \\
 &= [\bar{Q}_{ij}]_f (2t_f) + [\bar{Q}_{ij}]_c h_c
 \end{aligned} \tag{7.155}$$

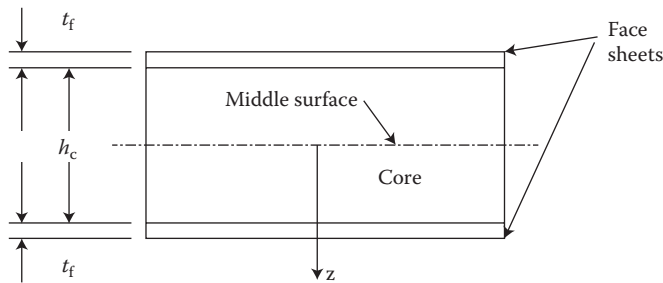


**FIGURE 7.56**  
Geometry of composite sandwich structure for laminate analysis.

where facing properties are denoted by the subscript  $f$  and core properties are denoted by the subscript  $c$ . Similarly, Equation 7.42 leads to  $B_{ij} = 0$ , and Equation 7.43 gives the following equivalent laminate flexural stiffnesses, as shown by Vinson [52]:

$$\begin{aligned}
 D_{ij} &= \frac{1}{3} \sum_{k=1}^3 [\bar{Q}_{ij}]_k (z_k^3 - z_{k-1}^3) \\
 &= \frac{1}{3} [\bar{Q}_{ij}]_f \left( \left( -\frac{h_c}{2} \right)^3 - \left( -\frac{h_c}{2} - t_f \right)^3 \right) + \frac{1}{3} [\bar{Q}_{ij}]_c \left( \left( \frac{h_c}{2} \right)^3 - \left( -\frac{h_c}{2} \right)^3 \right) \\
 &\quad + \frac{1}{3} [\bar{Q}_{ij}]_f \left( \left( \frac{h_c}{2} + t_f \right)^3 - \left( \frac{h_c}{2} \right)^3 \right)
 \end{aligned} \tag{7.156}$$

Once the equivalent laminate stiffnesses are known, the stresses and deformations can be predicted using the approaches outlined earlier in this chapter. However, there are some corrections to laminate analysis that may be required for use on sandwich structures. For example, one of the assumptions of CLT was that the transverse shear strains  $\gamma_{xz}$  and  $\gamma_{yz}$  are negligible. This may not be the case in sandwich structures, because the core is often made of foam or honeycomb material that has a low shear modulus. If the transverse shear strains are to be considered, the transverse shear stress resultants  $Q_x$  and  $Q_y$  in Figure 7.41 would be related to the transverse shear strains  $\gamma_{xz}$  and  $\gamma_{yz}$  by a transverse shear stiffness matrix, there will be additional strain–displacement equations to supplement equation 7.32, and the governing partial differential equations (Equations 7.136 through 7.138) will include additional transverse shear terms [50,52]. The importance of shear deflections in sandwich structures can be demonstrated by using the laminated beam theory from Section 7.2 to compare flexural deflections and shear deflections of sandwich beams, as shown in the following example.

### Example 7.17

A sandwich beam is loaded in 4-point flexure, as shown in Figure 7.57, along with the shear force and bending moment diagrams. The overall dimensions of the beam are  $s = 120$  mm,  $d = 41.6$  mm,  $h_c = 12.7$  mm,  $t_f = 0.711$  mm, and  $b = 25.4$  mm. The fibers in the unidirectional carbon/epoxy face sheets are aligned with the beam axis, the longitudinal Young's modulus of the face sheets is  $E_{fs} = 139.4$  GPa, and the shear modulus is  $G_{fs} = 3.36$  GPa. The isotropic foam core material has a Young's modulus  $E_c = 0.092$  GPa and a shear modulus  $G_c = 0.035$  GPa. Compare the beam deflections (displacements) due to flexure and shear at the loading points (i.e., at  $x = d$ ).

### SOLUTION

Since the sandwich beam to be analyzed here is symmetric about its middle surface and there are no coupling effects, a simple laminated beam analysis can be used. It can be shown using mechanics of materials beam theory (e.g., Popov [53]) that the solution to Equation 7.10 for the loading point flexural deflection at  $x = d$  is  $w_f = (Pd^2/12E_f I_{yy})(3L - 4d)$  where the Young's modulus from beam theory has been replaced with the flexural modulus,  $E_f$ , for a laminated beam,  $I_{yy}$  is the moment of inertia of the cross-section, and the support span  $L = s + 2d$ . The flexural modulus from Equation 7.8 and Figure 7.2 is

$$E_f = \frac{8}{h^3} \sum_{j=1}^{N/2} (E_x)_j (z_j^3 - z_{j-1}^3)$$

$$= \frac{8}{(14.122)^3} [0.092(6.35^3 - 0) + 139.4(7.061^3 - 6.35^3)] = 38.08 \text{ GPa}$$

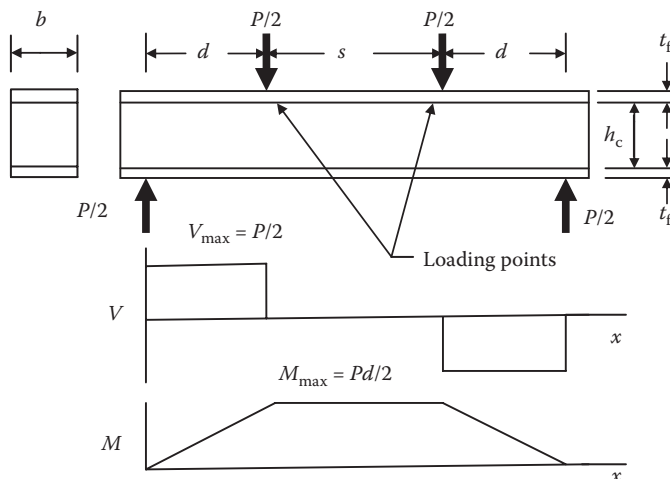


**FIGURE 7.57**

Sandwich beam in 4-point flexural loading, along with corresponding shear force and bending moment diagrams.

Therefore, the flexural deflection at the loading point is

$$w_f = \frac{P(41.6)^2}{12(38.08 \times 10^9)(25.4)(14.122)^3/12} (3(203.2) - 4(41.6))(10^6)$$

$$= 2.82 \times 10^{-4} P \quad \text{where } P \text{ is in N and } w_f \text{ is in mm}$$

The shear deflection at  $x = d$  is found by separating variables and integrating Equation 7.24 as

$$\int_0^{w_s} dw_s = \frac{1}{AG_t} \int_0^d V dx$$

As shown in Figure 7.57, the shear force  $V = P/2$ , a constant, in  $0 \leq x \leq d$ , so that the shear deflection at  $x = d$  is

$$w_s = \frac{Pd}{2AG_t}$$

where the effective transverse shear modulus for the sandwich can be approximated by Equation 3.47 as

$$\frac{1}{G_t} = \frac{v_{fs}}{G_{fs}} + \frac{v_c}{G_c}$$

The volume fraction of face sheets is

$$v_{fs} = 2t_f/(h_c + 2t_f) = 2(0.711)/14.122 = 0.1$$

and the volume fraction of core material is

$$v_c = h_c/(h_c + 2t_f) = 12.7/14.122 = 0.9.$$

Assuming that the face sheets are specially orthotropic and transversely isotropic,

$$G_t = \frac{1}{(0.1/3.36) + (0.9/0.035)} = 0.0388 \text{ GPa}$$

and the loading point shear deflection is

$$w_s = \frac{P(41.6)(10^6)}{2(14.122)(25.4)(0.0388 \times 10^9)} = 1.495 \times 10^{-3} P$$

where  $P$  is in  $N$  and  $w_s$  is in  $\text{mm}$ .

The total loading point deflection is then

$$w = w_f + w_s = 2.82 \times 10^{-4} P + 1.495 \times 10^{-3} P = 0.001777 P$$

The fraction of the total deflection due to flexure is

$$\frac{w_f}{w} = \frac{0.000282P}{0.001777P} = 0.1587$$

while the fraction of the total deflection due to shear is

$$\frac{w_s}{w} = \frac{0.001495 P}{0.001777 P} = 0.8446$$

The fraction of total deflection due to shear is so large because the ratio  $w_s/w_f$  is proportional to  $E_f/G_v$ , which can be very large for such beams. In this case, the effective transverse shear modulus,  $G_v$ , is typically dominated by the low shear modulus of the core,  $G_c$ , and the high volume fraction of the core,  $v_c$ . That is,  $v_c/G_c \gg v_{fs}/G_{fs}$  in the above equation for  $G_v$ . It is clear that predicted deflections that do not include the shear component would be significantly in error. While shear deflection is typically important for sandwich structures, it is less likely to be important for conventional composite laminates, where the composite laminae would typically have much higher transverse shear moduli and much lower core volume fractions than would a foam core sandwich beam.

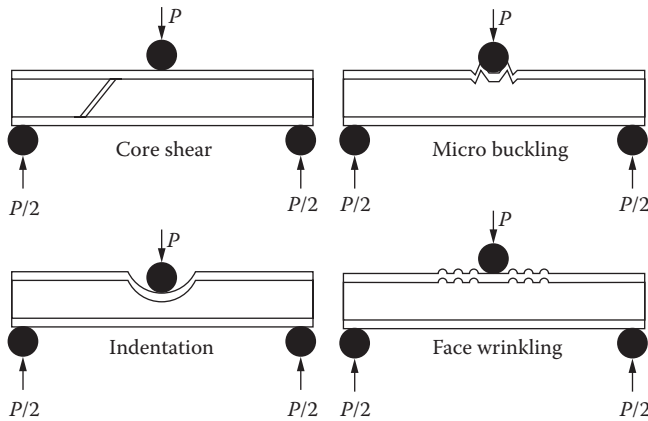
The application of laminate analysis in the prediction of strength in composite sandwich structures is significantly limited by the existence of important failure modes in sandwich structures that are not present in composite laminates. Laminate failure modes would only be relevant for the face sheets in the sandwich, but other possible failure modes are due to the core or core/face sheet interactions. For example, Steeves and Fleck [54] have investigated the failure modes in foam-cored composite sandwich beams under three-point flexure, and the observed failure modes are summarized in Figure 7.58. The failure load,  $P$ , can be estimated from simple mechanics of materials formulas for each of the failure modes once the beam parameters and dimensions are known. The lowest of the predicted failure loads would govern the design of the sandwich structure. In Figure 7.59, the midpoint of the beam deflects by a transverse displacement  $u$  due to the applied load  $P$  of the mid-roller.  $L$  is the beam length between the supports,  $H$  is the overhang at each end,  $b$  is the width of the beam,  $c$  is the core thickness, and  $t_f$  is the face sheet thickness. The relevant mechanical properties of the isotropic core are the Young's modulus  $E_c$ , shear modulus  $G_c$ , compressive strength  $\sigma_c$ , and shear strength  $\tau_c$ . For the face sheets, the relevant properties are the axial compressive strength,  $\sigma_f$ , the Young's modulus,  $E_f$ , and the distance between the centroids of the face sheets,  $d = c + t_f$ .

According to Zenkert [55], the predicted collapse load for face yielding or microbuckling is given as

$$P = \frac{4\sigma_f b t_f d}{L} \quad (7.157)$$

whereas the corresponding critical load for core shear failure can be estimated as

$$P = 2\tau_c b d \quad (7.158)$$

**FIGURE 7.58**

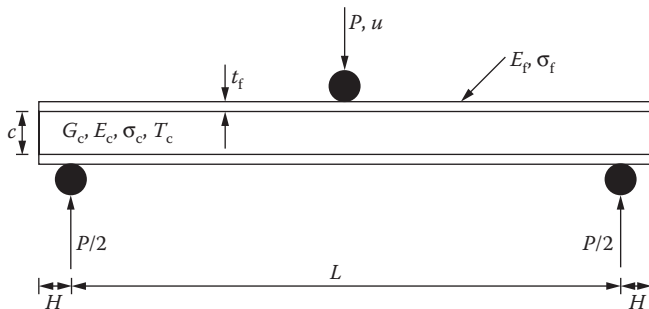
Failure modes of a sandwich beam in three-point bending. (Reprinted from *International Journal of Mechanical Sciences*, 46, Steeves, C. A. and Fleck, N. A. Collapse mechanisms of sandwich beams with composite faces and a foam core, loaded in three-point bending. Part II: Experimental investigation and numerical modeling. 585–608. Copyright (2004), with permission from Elsevier.)

and the load required to produce face sheet wrinkling is

$$P = \frac{2bt_f d}{L} \sqrt[3]{E_f E_c G_c} \quad (7.159)$$

Steeves and Fleck [56] have suggested that the load required for indentation failure is

$$P = bt_f \left( \frac{\pi^2 \sigma_c^2 E_f d}{3L} \right)^{1/3} \quad (7.160)$$

**FIGURE 7.59**

Geometry of a sandwich beam in three-point bending. (Reprinted from *International Journal of Mechanical Sciences*, 46, Steeves, C. A. and Fleck, N. A. Collapse mechanisms of sandwich beams with composite faces and a foam core, loaded in three-point bending. Part II: Experimental investigation and numerical modeling. 585–608. Copyright (2004), with permission from Elsevier.)

### Example 7.18

For the sandwich beam in 4-point flexure described in Example 7.17, use the Maximum Stress criterion and laminated beam theory to determine the applied load  $P$  that would cause core shear failure if the core shear strength is  $\tau_c = 1.3$  MPa.

### SOLUTION

Since Equation 7.158 only applies to 3-point flexure of a sandwich beam, a new equation must be developed here. As shown in Figure 7.6, the maximum transverse shear stress occurs at the middle surface where  $z = 0$ . From Equation 7.19, the shear stress is

$$(\tau_{xz})_k = \frac{V}{E_f I_{yy}} \sum_{j=k}^{N/2} \int_{z_{j-1}}^{z_j} (E_x)_j z dz = \frac{V}{2E_f I_{yy}} \sum_{j=k}^{N/2} (E_x)_j (z_j^2 - z_{j-1}^2)$$

Failure would occur when this shear stress is equal to the shear strength at the middle surface  $z = 0$  in the region  $0 \leq x \leq d$  where the maximum shear force  $V_{\max} = P/2$ . Substituting these conditions in the above equation, along with the value of  $E_f$  from Example 7.17,

$$1.3 = \frac{3P[0.092(6.35^2 - 0) + 139.4(7.061^2 - 6.35^2)]}{38.08(25.4)(14.122)^3}$$

and solving for the failure load, we find that  $P = 885.6$  N. Note that this problem only involves core shear failure, and that a complete failure analysis would include investigation of other possible failure modes such as those described in Figure 7.58.

There are many other aspects of composite sandwich structures that are not necessarily relevant to laminate analysis. For more detailed studies on composite sandwich structures, the reader is encouraged to explore the publications referred to earlier in this section.

#### 7.11.2 Composite Grid Structures

Grid-stiffened geodesic structural configurations date back to the 1920s [57] when they were first used in aircraft construction with a metal grid and fabric skin. The structures of these aircraft were known for their excellent tolerance to battle damage. Along with the maturation of composite technology, there has been increasing interest in composite grid structures for the last several decades. The most common grid structures are the orthogrid, with the ribs oriented at  $0^\circ$  or  $90^\circ$  (Figure 7.60) and the isogrid, with the ribs oriented at  $0^\circ$  and  $\pm 60^\circ$  (Figure 7.61). Composite grid structures are a promising concept for applications in plate or shell-like components of systems such as spacecraft, aircraft, automobile, containers, bridges, ships, and propellers. These structures have several advantages over traditional construction methods that use panels, sandwich cores, or expensive framework. As the ribs of the grids are made of unidirectional continuous fiber-reinforced composites, they are

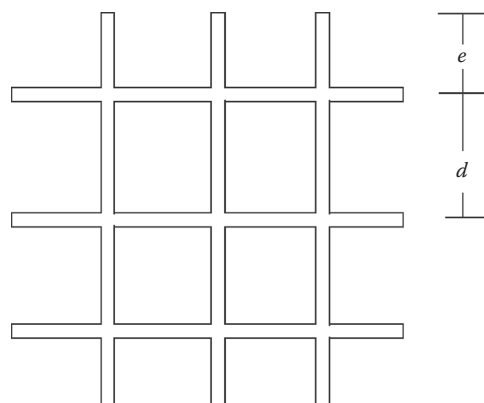


**FIGURE 7.60**  
Orthogrid structure.

strong, tough, damage tolerant, and do not delaminate. As grids are open structures, they are easy to inspect and repair. With such processes as automated fiber placement and pultrusion, the potential also exists for completely automating the grid fabrication process and reducing the processing cost.

The use of laminate analysis in modeling the mechanical behavior of grid structures is based on the concept of replacing the grid with a laminated plate having equivalent stiffnesses, as described by Chen and Tsai [58] and Huybrechts and Tsai [59]. The grid structure can be considered as a combination of sets of parallel ribs. The equivalent axial, flexural and torsional stiffnesses of each family of parallel ribs can be calculated separately, and then the overall stiffnesses of the grid structure are obtained by the principle of

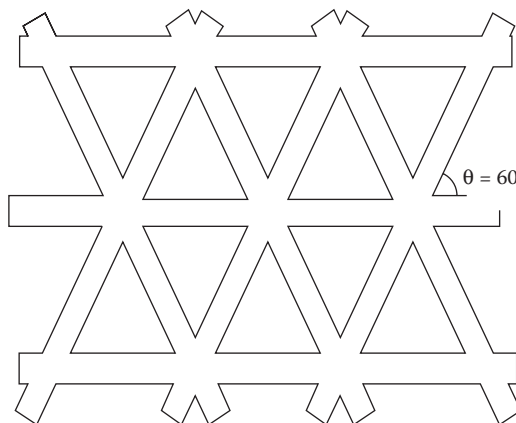


**FIGURE 7.61**  
Isogrid structure.

superposition. Following the analysis by Chen and Tsai [58], consider the family of  $N$  parallel ribs in Figure 7.62, each of which has center-to-center spacing  $d$  (Figure 7.60), cross-sectional area  $A$ , and longitudinal modulus  $E_x$ . The direction of the local  $(x,y,z)$  coordinate axes are along and perpendicular to the ribs. Let  $\theta$  be the angle between the local and global axes (1,2,3). It should be noted that the normal strain along the  $y$  direction,  $\epsilon_y$ , the shear strains  $\gamma_{xy}$  and  $\gamma_{yz}$ , and the curvature  $\kappa_y$  in the ribs were not considered. If all  $N$  ribs are identical, static equilibrium and geometric compatibility requirements lead to the following equation relating the force per unit length along the  $x$  direction to the corresponding strain  $\epsilon_x$  [58],

$$N_x = \frac{AE_x\epsilon_x}{d} \quad (7.161)$$

In this case, the force per unit length is based on the effective width  $(N - 1)d + 2e$  for the parallel family of ribs, where the distance  $e$  in Figure 7.60 approaches  $d/2$ . Thus, the corresponding effective width becomes approximately  $Nd$ . Transforming both the force per unit length and the strain to the global coordinates and factoring out the resulting extensional stiffnesses  $A_{ij}$  for an equivalent flat laminated plate,

$$[A] = \frac{E_x A}{d} \begin{bmatrix} m^4 & m^2 n^2 & m^3 n \\ m^2 n^2 & n^4 & mn^3 \\ m^3 n & mn^3 & m^2 n^2 \end{bmatrix} = \begin{bmatrix} A_{11} & A_{12} & A_{16} \\ A_{21} & A_{22} & A_{26} \\ A_{16} & A_{26} & A_{66} \end{bmatrix} \quad (7.162)$$

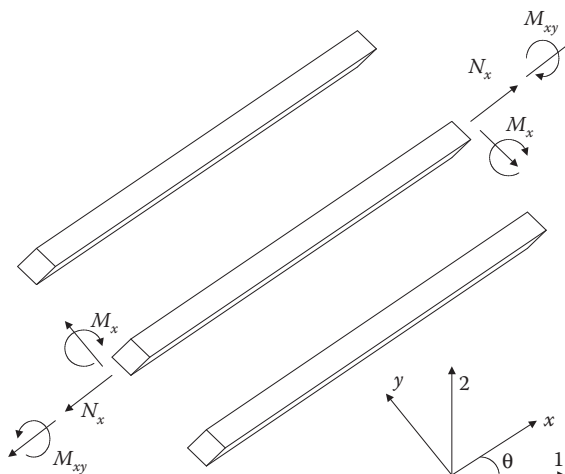


**FIGURE 7.62**  
Family of parallel ribs for modeling of grid structure.

where  $m = \cos \theta$  and  $n = \sin \theta$ . Applying a similar approach for bending of the parallel family of ribs, the flexural stiffness matrix for an equivalent flat laminated plate is found to be

$$[D] = \frac{1}{d} \begin{bmatrix} E_x I m^4 + G J m^2 n^2 & E_x I m^2 n^2 + G J m^2 n^2 & E_x I m^3 n - \frac{G J m n (m^2 - n^2)}{2} \\ E_x I m^2 n^2 - G J m^2 n^2 & E_x I n^4 + G J m^2 n^2 & E_x I m^3 n + \frac{G J m n (m^2 - n^2)}{2} \\ E_x I m^3 n - G J m^3 n & E_x I m^3 n + G J m^3 n & E_x I m^2 n^2 + \frac{G J m^2 (m^2 - n^2)}{2} \\ E_x I m^3 n + G J m n^3 & E_x I m^3 n - G J m n^3 & E_x I m^2 n^2 - \frac{G J n^2 (m^2 - n^2)}{2} \end{bmatrix}$$

$$= \begin{bmatrix} D_{11} & D_{12} & D_{16} \\ D_{21} & D_{22} & D_{26} \\ D_{16} & D_{26} & D_{66} \end{bmatrix} \quad (7.163)$$

where

$$J = \frac{h w^3}{16} \left[ \frac{16}{3} - 3.36 \frac{w}{h} \left( 1 - \frac{w^4}{12 h^4} \right) \right] \quad (7.164)$$

and  $E_x$  and  $G$  are longitudinal and shear modulus of the rib, respectively;  $h$  is rib height, and  $I$  and  $J$  are the moment of inertia with respect to the midplane and the torsional constant of the rib cross section, respectively.

For the orthogrid case, the  $[D]$  matrix becomes a  $3 \times 3$  symmetric matrix with  $D_{16}$ , and  $D_{26}$  equal to zero. The  $A_{66}$  term for the orthogrid must be taken into account because the bending and shear effects of ribs tangential to the midplane cannot be neglected and it becomes as [58].

$$A_{66} = \frac{1}{a_{66}} \quad (7.165)$$

where

$$a_{66} = \frac{1}{12} \frac{d_{90}^2 d_0}{E_x I_0^t} + \frac{1}{12} \frac{d_{90} d_0^2}{E_x I_{90}^t} + \frac{d_0}{\kappa G A_0} + \frac{d_{90}}{\kappa G A_{90}} \quad (7.166)$$

$G$  is the shear modulus of the ribs,  $d_0$  and  $d_{90}$  are horizontal and vertical spacing of ribs, and  $\kappa$  is the shear correction factor, which is taken as 5/6.

The total stiffnesses for the grid can be obtained from superposition by summing up the stiffnesses of each parallel family of ribs taking into account the orientation of each family of ribs. For example, the  $[A]$  and  $[D]$  matrices for the orthogrid with two families of identical ribs at  $\theta = 0^\circ$  and  $90^\circ$  are

$$[A]_{\text{orthogrid}} = \begin{bmatrix} \frac{E_x A}{d} & 0 & 0 \\ 0 & \frac{E_x A}{d} & 0 \\ 0 & 0 & A_{66} \end{bmatrix} \quad (7.167)$$

$$[D]_{\text{orthogrid}} = \frac{1}{d} \begin{bmatrix} E_x I & 0 & 0 \\ 0 & E_x I & 0 \\ 0 & 0 & \frac{GJ}{2} \end{bmatrix} \quad (7.168)$$

Similarly, for the isogrid with three parallel families of identical ribs at  $\theta = 0^\circ$ ,  $60^\circ$ , and  $-60^\circ$ ,

$$[A]_{\text{isogrid}} = \frac{\sqrt{3} E_x A}{4d} \begin{bmatrix} 3 & 1 & 0 \\ 1 & 3 & 0 \\ 0 & 0 & 1 \end{bmatrix} \quad (7.169)$$

$$[D]_{\text{isogrid}} = \frac{\sqrt{3} E_x I}{4d} \begin{bmatrix} 3 + \tau & 1 + \tau & 0 \\ 1 + \tau & 3 + \tau & 0 \\ 0 & 0 & 1 + \tau \end{bmatrix} \quad (7.170)$$

where

$$\tau = \frac{GJ}{E_x I}$$

$$I = \frac{1}{12} wh^3$$

and

$$J = \frac{hw^3}{16} \left[ \frac{16}{3} - 3.36 \frac{w}{h} \left( 1 - \frac{w^4}{12h^4} \right) \right] \quad (7.171)$$

and  $h$  is rib height,  $d$  is the length of each side of the equilateral triangles in the isogrid, and  $I$  and  $J$  are the moment of inertia with respect to the mid-plane and torsional constant of the rib cross section, respectively. All the above equations apply to the case of the grid alone, but the method can also be applied to the case where the ribs are attached to a composite laminate skin on one or both sides [58].

### PROBLEMS

1. A laminated [0/90/0/90]<sub>s</sub> carbon/epoxy beam is 1 mm thick, is 20 mm wide, and has 0.125 mm-thick plies. The lamina properties are  
 $E_1 = 180 \text{ GPa}$     $s_L^{(+)} = 1700 \text{ MPa}$   
 $E_2 = 10 \text{ GPa}$     $s_L^{(-)} = 1400 \text{ MPa}$   
 $G_{12} = 7 \text{ GPa}$     $s_T^{(+)} = 40 \text{ MPa}$   
 $v_{12} = 0.28$     $s_T^{(-)} = 230 \text{ MPa}$ 
  - a. Determine the flexural modulus for the beam.
  - b. How could the flexural modulus be improved without changing the ply materials, the number of plies, or the ply orientations?
  - c. Using the Maximum Stress Criterion for each ply, determine the magnitude of the maximum allowable bending moment that the beam can withstand. Which ply fails first?
  - d. What type of analysis would be required if the ply orientations are [+45/90/ - 45/0]<sub>s</sub>?
2. The laminated beam shown in Figure 7.63 is made up of two outer plies of material "A" having Young's modulus  $E_A$ , two inner plies of material "B" having Young's modulus  $E_B$ , and a honeycomb core of negligible stiffness. Materials A and B are isotropic, but they have different thicknesses. The laminate is symmetric about the middle surface. Find the expression for the flexural modulus in terms of the given properties and the dimensions shown in Figure 7.63.
3. A thin-walled composite tube having an outside diameter of 48 mm is made by securely bonding an aluminum tube inside a steel tube, as shown in Figure 7.64. Determine the maximum allowable bending moment,  $M$ , that the composite tube can withstand without exceeding the yield stress of either the steel or the aluminum. The tube properties are:

	Steel	Aluminum
Young's modulus (GPa)	200	78
Yield stress (MPa)	259	98
Wall thickness (mm)	3	6

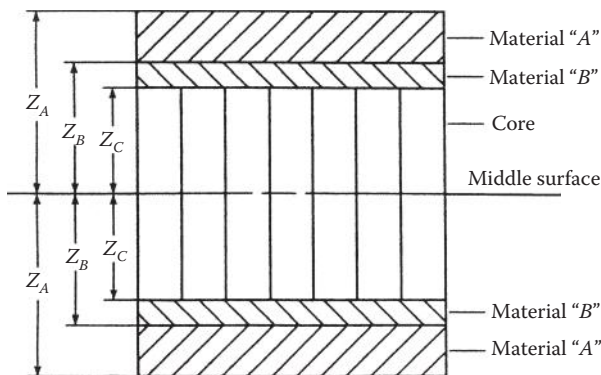


**FIGURE 7.63**  
Laminated beam for problem 2.

4. Determine the stiffness matrix for a  $[+45/-45]$  antisymmetric laminate consisting of 0.25 mm-thick unidirectional AS/3501 carbon/epoxy plies.
5. Show that for symmetric laminates the coupling stiffnesses,  $B_{ij}$ , must all be equal to zero.
6. By expanding the  $[A]$  matrix in terms of ply stiffnesses show that a "balanced" cross-ply laminate having equal numbers of  $0^\circ$  and  $90^\circ$  plies is not necessarily quasi-isotropic.
7. A  $[-60/0/60]$  laminate and a  $[0/45/90]$  laminate both consist of 1.0 mm-thick plies having the following properties:  $E_1 = 181$  GPa,  $E_2 = 10.3$  GPa,  $G_{12} = 7.17$  GPa,  $\nu_{12} = 0.28$ . Plot the  $A_{ij}$  for both laminates as a function of the orientation to determine which, if any, of the laminates is quasi-isotropic.
8. The  $[+45/-45]$  laminate described in problem 4 is subjected to a uniaxial force per unit length  $N_x = 30$  MPa mm. Find the resulting stresses and strains in each ply along the  $x$  and  $y$  directions.
9. A  $[0/90]_s$  laminate is subjected to a single bending moment per unit length,  $M_x$ . If the laminate is unconstrained, so that bending

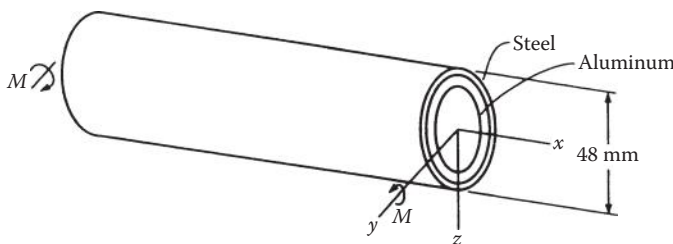


**FIGURE 7.64**  
Composite tube for Problem 3.

along both the  $x$  and the  $y$  directions occurs freely, determine the ply stresses,  $(\sigma_x)_k$ , in terms of the moment,  $M_x$ , the bending stiffnesses,  $D_{ij}$ , the ply stiffnesses,  $Q_{ij}$ , and the distance from the middle surface,  $z$ . Determine the ply stresses  $(\sigma_x)_k$  in terms of  $M_x$ ,  $z$ , and a numerical coefficient if the properties are  $E_1 = 129$  GPa,  $E_2 = 12.8$  GPa,  $G_{12} = 4.6$  GPa,  $v_{12} = 0.313$ , and  $t = 1$  mm.

10. The laminate described in problem 9 is subjected to a single bending moment per unit length,  $M_x$ , and the two edges on which  $M_x$  acts are fixed so that bending along the  $x$  direction occurs freely but bending along the  $y$  direction is prevented. That is, the longitudinal curvature is unconstrained (i.e.,  $\kappa_x \neq 0$ ), but the transverse curvature is constrained (i.e.,  $\kappa_y = 0$ ). Determine the ply stresses  $(\sigma_x)_k$  as in problem 9 (give equations and numerical results) and compare with the results of problem 9.
11. A  $[90/0/90]_s$  laminate is fabricated from laminae consisting of isotropic fibers ( $E_f = 220$  GPa,  $v_f = 0.25$ ) embedded in an isotropic matrix ( $E_m = 3.6$  GPa,  $v_m = 0.4$ ). Each lamina is 0.25 mm thick, and the 0.01 mm diameter fibers have been precoated with a 0.00125 mm thick sizing, which is the same as the matrix material. The precoated fibers are arranged in the closest possible packing array in the matrix. Using both micromechanics and laminate analysis, find the laminate engineering constants  $E_x$ ,  $E_y$ ,  $G_{xy}$ , and  $v_{xy}$ . The laminate  $x$ -axis is parallel to the  $0^\circ$  lamina orientation.
12. An antisymmetric angle-ply  $[+0/-\theta]$  laminate is to be made of carbon/epoxy and designed to have a laminate CTE,  $\alpha_x$ , as close to zero as possible. Determine the ply orientation  $\theta$  needed to meet this requirement. The lamina properties are as follows:

$$E_1 = 138 \text{ GPa}, \text{ laminate thickness} = 0.125 \text{ mm}$$

$$E_2 = 8.96 \text{ GPa} \quad \alpha_1 = -0.3 \times 10^{-6} \text{ m/m/K}$$

$$G_{12} = 7.1 \text{ GPa} \quad \alpha_2 = 28.1 \times 10^{-6} \text{ m/m/K}$$

$$v_{12} = 0.3$$

This problem requires extensive calculations, and the use of a computer is recommended.

13. Repeat problem 12 for a Kevlar®/epoxy composite having lamina properties as follows:

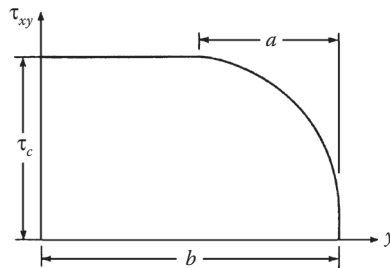
$$E_1 = 76 \text{ GPa} \quad \text{lamina thickness} = 0.125 \text{ mm}$$

$$E_2 = 5.5 \text{ GPa} \quad \alpha_1 = -4.0 \times 10^{-6} \text{ m/m/K}$$

$$G_{12} = 2.3 \text{ GPa} \quad \alpha_2 = 79.0 \times 10^{-6} \text{ m/m/K}$$

$$v_{12} = 0.34$$

14. The distribution of the in-plane shear stress,  $\tau_{xy}$ , along the  $y$  direction at a particular distance  $z$  from the middle surface of a uniaxially loaded laminate is idealized, as shown in Figure 7.65. The interlaminar stress boundary layer region is assumed to extend inward from the free edge at  $y = b$  by a distance "a," the in-plane shear stress  $\tau_{xy} = \tau_c$  in the region  $0 \leq y \leq (b-a)$  is assumed to be the shear stress from the CLT, and the in-plane shear stress in the boundary layer region  $(b-a) \leq y \leq b$  is assumed to be of the form

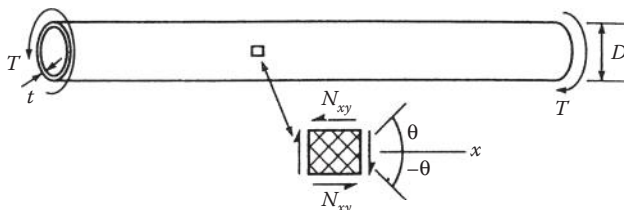
**FIGURE 7.65**

In-plane shear stress distribution for Problem 14.

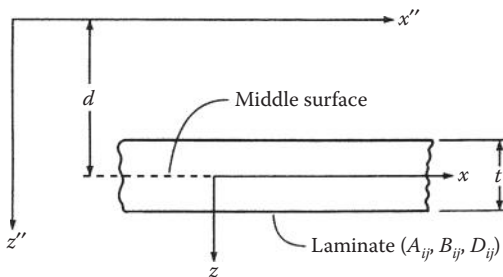
$$\tau_{xy} = \frac{\tau_c}{a^2}(y - b)(b - 2a - y)$$

For the same location, determine the distribution of the interlaminar shear stress,  $\tau_{xz}$  along the  $y$  direction.

15. A filament-wound composite drive shaft for a helicopter transmits a torque  $T$  that generates shear loading of the shaft material, as shown in Figure 7.66. The shaft is to be designed as a hollow tube with a two-ply  $[+\theta/-\theta]$  laminated wall. If the outside diameter, the length, and the material density are fixed, use invariants to determine the angle  $\theta$ , which should be used to maximize the shear stiffness-to-weight ratio,  $A_{66}/W$ , where  $A_{66}$  is the laminate shear stiffness and  $W$  is the shaft weight. It may be assumed that the shaft diameter,  $D$ , is much greater than the wall thickness,  $t$ .
16. Develop a "parallel axis theorem" for the effective laminate stiffnesses  $A''_{ij}$ ,  $B''_{ij}$ , and  $D''_{ij}$  associated with the  $(x'',z'')$  axes, which are parallel to the original  $(x,z)$  axes, as shown in Figure 7.67. Express the new  $A''_{ij}$ ,  $B''_{ij}$ , and  $D''_{ij}$  in terms of the original  $A_{ij}$ ,  $B_{ij}$ , and  $D_{ij}$  for the  $(x,z)$  axes and the distance  $d$  between the parallel axes, where  $z'' = z + d$ .
17. A  $[0/90/0]_s$  laminate consisting of AS/3501 carbon/epoxy laminae is subjected to uniaxial loading along the  $x$  direction. Use the Maximum Strain Criterion to find the loads corresponding to first

**FIGURE 7.66**

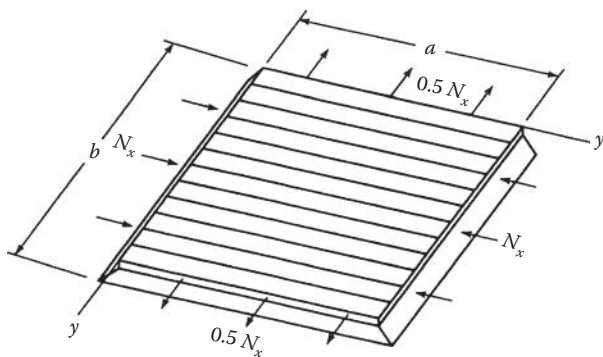
Filament wound shaft for Problem 15.

**FIGURE 7.67**

Laminate with parallel axes for Problem 16.

ply failure and ultimate laminate failure; then plot the load-strain curve up to failure. Compare these results with those of Example 7.12 and discuss any differences.

18. Prove that for the specially orthotropic plate shown in Figure 7.42 under the loading described by Equation 7.144, the solution given by Equation 7.146 satisfies the differential equation (7.139) and the boundary conditions in Equations 7.142 and 7.143.
19. Find expressions for the moments  $M_x$ ,  $M_y$ , and  $M_{xy}$  and the stresses  $(\sigma_x)_k$ ,  $(\sigma_y)_k$ , and  $(\tau_{xy})_k$  in the  $k$ th ply of the uniformly loaded, specially orthotropic laminate with simply supported edges shown in Figure 7.42.
20. Derive the differential equation and the boundary conditions governing the small transverse deflections of a simply supported, rectangular, symmetric angle-ply laminate that is subjected to distributed loading. If the loading is described by Equation 7.144, does a solution of the form given in Equation 7.145 satisfy this differential equation and boundary conditions? Why?
21. Derive the coupled differential equations and the boundary conditions governing the small transverse deflections of a simply supported, rectangular, antisymmetric angle-ply laminate that is subjected to distributed loading. Propose solutions for the displacements  $u$ ,  $v$ , and  $w$  that satisfy the differential equations and boundary conditions.
22. A simply supported, specially orthotropic plate is subjected to an in-plane compressive load per unit length  $N_x$  and an in-plane tensile load per unit length  $N_y = -0.5 N_x$ , as shown in Figure 7.68. Derive the expression for the critical buckling load.
23. Derive the differential equation and the boundary conditions governing the buckling of a simply supported, rectangular, symmetric angle-ply laminate that is subjected to a uniaxial in-plane load,  $N_x$ . Does a solution of the form given in Equation 7.152 satisfy this differential equation and boundary conditions? Why?
24. Using the carpet plots of Figure 7.52, select the percentages of  $0^\circ$ ,  $\pm 45^\circ$ , and  $90^\circ$  plies that are needed in a  $[0/\pm 45/90]$  laminate if the longitudinal modulus,  $E_x$ , is to be at least 20 GPa, the in-plane shear

**FIGURE 7.68**

Simply supported, specially orthotropic plate under in-plane loads for Problem 22.

modulus,  $G_{xy}$ , is to be at least 10 GPa, and the longitudinal CTE,  $\alpha_x$ , is equal to zero.

25. A symmetric [0/90/0] laminate is 0.75 mm thick and its full compliance matrix is given below.

$$\begin{bmatrix} A & B \\ B & D \end{bmatrix}^{-1} = \begin{bmatrix} A' & B' \\ B' & D' \end{bmatrix}$$

$$= \begin{bmatrix} 0.014 & -7.235 \times 10^{-4} & 0 & 0 & 0 & 0 \\ -7.235 \times 10^{-4} & 0.026 & 0 & 0 & 0 & 0 \\ 0 & 0 & 0.188 & 0 & 0 & 0 \\ 0 & 0 & 0 & 0.213 & -0.042 & 0 \\ 0 & 0 & 0 & -0.042 & 2.066 & 0 \\ 0 & 0 & 0 & 0 & 0 & 4.016 \end{bmatrix}$$

where the units of the matrix are

$$\begin{bmatrix} A' & B' \\ B' & D' \end{bmatrix} = \begin{bmatrix} [\text{GPa mm}]^{-1} & [\text{GPa mm}^2]^{-1} \\ [\text{GPa mm}^2]^{-1} & [\text{GPa mm}^3]^{-1} \end{bmatrix}$$

Determine the following effective engineering constants for the laminate, giving both magnitude and units; (a) the effective longitudinal Young's modulus,  $E_x$ , (b) the effective transverse Young's modulus,  $E_y$ , (c) the effective in-plane shear modulus,  $G_{xy}$ , (d) the effective longitudinal Poisson's ratio,  $\nu_{xy}$ , and (e) the effective flexural modulus,  $E_{fx}$ .

26. The laminate described in problem 25 has laminae that are 0.25 mm thick and the stiffness matrix associated with the  $0^\circ$  lamina is given by

$$[Q] = \begin{bmatrix} 138.8 & 2.7 & 0 \\ 2.7 & 8.965 & 0 \\ 0 & 0 & 7.1 \end{bmatrix} \text{ GPa}$$

If a single bending moment per unit length  $M_x = 0.1 \text{ GPa mm}^2$  is applied to the laminate, (a) determine the stresses associated with the  $x$  and  $y$  axes on the top surface of the laminate and (b) determine the stresses associated with the  $x$  and  $y$  axes on the middle surface of the laminate.

27. The sensing element in many thermostats is a bimetallic strip (Figure 7.69), which is a nonsymmetric laminate consisting of two plies made from different metals. If the strip is subjected to a temperature change  $\Delta T$ , the differential thermal expansion of the two plies causes a corresponding change in the radius of curvature of the strip,  $\rho_x$ , and this motion activates the temperature control system. In the strip shown in Figure 7.69, ply #1 is aluminum, ply #2 is steel, both plies are isotropic, and each ply is 0.005-in. thick. It has been determined that the effects of  $B_{ij}$ -type coupling on the thermal response of the strip can be neglected. Find the relationship between the temperature change  $\Delta T$  and the radius of curvature,  $\rho_x$ . Recall that the curvature  $\kappa_x = 1/\rho_x$ . The required properties are given below.

Ply thermal expansion coefficients:

Aluminum:  $\alpha_{\text{Al}} = 12.5 \times 10^{-6}/^\circ\text{F}$

Steel:  $\alpha_{\text{St}} = 6.6 \times 10^{-6}/^\circ\text{F}$

Laminate-bending compliances:

$$[D'] = \begin{bmatrix} 0.739 & -0.227 & 0 \\ -0.227 & 0.739 & 0 \\ 0 & 0 & 1.928 \end{bmatrix} (\text{psi} - \text{in.}^3)^{-1}$$

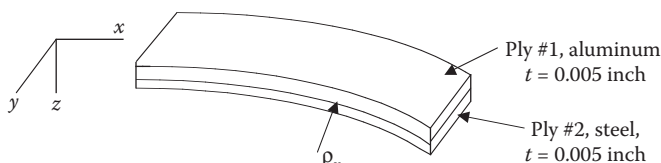


**FIGURE 7.69**  
Bimetallic strip for Problem 27.

Ply stiffness matrices:

$$[Q]_{st} = \begin{bmatrix} 32.817 & 9.615 & 0 \\ 9.615 & 32.817 & 0 \\ 0 & 0 & 11.6 \end{bmatrix} 10^6 \text{ psi}$$

$$[Q]_{AI} = \begin{bmatrix} 11.11 & 3.51 & 0 \\ 3.51 & 11.11 & 0 \\ 0 & 0 & 3.8 \end{bmatrix} 10^6 \text{ psi}$$

28. The plate in Figure 7.70 has edge dimensions  $a$  and  $b$  and is made from a [90/0/90]<sub>s</sub> symmetric cross-ply laminate. The plate is simply supported on all edges and is subjected to a single in-plane shear load  $N_{xy}$  along its edges as shown. Answer the following questions below in terms of variables, not numerical values. Do not try to solve the equations, just set them up: (a) write the differential equation governing the buckling behavior of the plate, (b) write the boundary conditions for the plate, and (c) is a solution of the form shown in Equation 7.152 in the textbook possible for this problem? If so, why? If not, why not?
29. The nonsymmetrically laminated beam shown in Figure 7.71 consists of a substrate material having Young's modulus  $E_S$  and a coating material having Young's modulus  $E_C$ , and both materials are linear elastic, isotropic, and homogeneous. Using a modified laminated beam theory, derive the equation for the flexural modulus  $E_f$  for the beam. Your answer should be in terms of the given parameters. Hint: Assumption #2 for laminated beam theory in Section 7.2 is violated here, so how must the derivation of the flexural modulus in Section 7.2 be modified?
30. Solve Example 7.14 using the Tsai–Hill Criterion instead of the Maximum Stress Criterion. That is, determine the largest torque  $T$  that can be transmitted by the shaft without failure according

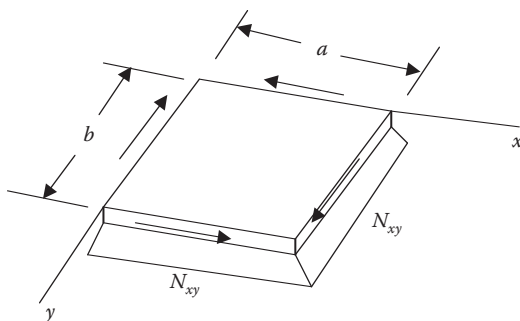


**FIGURE 7.70**

Simply supported laminated plate under in-plane shear loads for Problem 28.

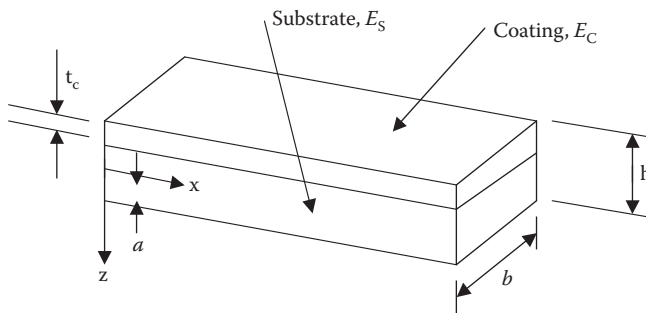


**FIGURE 7.71**  
Nonsymmetriesically laminated beam for Problem 29.

to the Tsai–Hill Criterion. Also indicate which plies fail first (i.e., the  $+45^\circ$  or the  $-45^\circ$  plies) according to the Tsai–Hill Criterion. You may use any relevant results from Examples 7.14 and 7.4 without repeating their derivations, but you must clearly explain your analysis procedure.

31. Repeat Problem 30 for a  $0^\circ$  unidirectional AS/3501 carbon/epoxy composite shaft which has the same total wall thickness  $t = 1$  mm and mean radius  $R = 50$  mm. That is, find the largest torque  $T$  that can be transmitted by the shaft according to the Tsai–Hill Criterion. You may use any relevant results from Examples 7.14 and 7.4 without repeating their derivations, but you must clearly explain your analysis procedure. Compare and discuss the results of this problem with those of Problem 30.

## References

1. Pagano, N. J. 1967. Analysis of the flexure test of bidirectional composites. *Journal of Composite Materials*, 1, 336–342.
2. Higdon, A., Ohlsen, E. H., Stiles, W. B., Weese, J. A., and Riley, W. F. 1976. *Mechanics of Materials*, 3d ed. John Wiley & Sons, New York.
3. Smith, C. B. 1953. Some new types of orthotropic plates laminated of orthotropic material. *Journal of Applied Mechanics*, 20, 286–288.
4. Pister, K. S. and Dong, S. B. 1959. Elastic bending of layered plates, in *Proceedings of the American Society of Civil Engineers (Journal of Engineering Mechanics Division)*, 85, EM4, 1–10.
5. Reissner, E. and Stavsky, Y. 1961. Bending and stretching of certain types of heterogeneous aeolotropic elastic plates. *Journal of Applied Mechanics*, 28, 402–408.
6. Stavsky, Y. 1964. On the general theory of heterogeneous aeolotropic plates. *Aeronautical Quarterly*, 15, 29–38.

7. Lekhnitskii, S. G. 1968. *Anisotropic Plates* (translation from the 2d Russian ed.) in Tsai, S. W. and Cheron, T. eds. Gordon and Breach Science Publishers, New York.
8. Stavsky, Y. and Hoff, N. J. 1969. Mechanics of composite structures, in Dietz, A. G. H. ed., *Composite Engineering Laminates*. MIT Press, Cambridge, MA.
9. Timoshenko, S. A. and Woinowsky-Krieger, S. 1959. *Theory of Plates and Shells*, 2nd ed. McGraw-Hill, Inc., New York.
10. Whitney, J. M. 1987. *Structural Analysis of Laminated Plates*. Technomic Publishing Co., Inc., Lancaster, PA.
11. Christensen, R. M. 1979. *Mechanics of Composite Materials*. John Wiley & Sons, Inc., New York.
12. Halpin, J. C. 1984. *Primer on Composite Materials: Analysis*. Technomic Publishing Co. Lancaster, PA.
13. Tsai, S. W. 1964. *Structural Behavior of Composite Materials*. NASA CR-71.
14. Pipes, R. B. and Pagano, N. J. 1970. Interlaminar stresses in composite laminates under uniform axial extension. *Journal of Composite Materials*, 4, 538–548.
15. Wang, S. S. and Choi, I. 1982. Boundary layer effects in composite laminates. Part 1: Free edge singularities. *Journal of Applied Mechanics*, 49, 541–548.
16. Wang, S. S. and Choi, I. 1982. Boundary layer effects in composite laminates. Part 2: Free edge solutions and basic characteristics. *Journal of Applied Mechanics*, 49, 549–560.
17. Pipes, R. B. and Daniel, I. M. 1971. Moiré analysis of the interlaminar shear edge effect in laminated composites. *Journal of Composite Materials*, 5, 255–259.
18. Pipes, R. B. and Pagano, N. J. 1974. Interlaminar stresses in composite laminates—An approximate elasticity solution. *Journal of Applied Mechanics*, 41, Series E (3), 668–672.
19. Pagano, N. J. and Pipes, R. B. 1971. The influence of stacking sequence on laminate strength. *Journal of Composite Materials*, 5(1), 50–57.
20. Whitney, J. M. and Browning, C. E. 1972. Free-edge delamination of tensile coupons. *Journal of Composite Materials*, 6(2), 300–303.
21. Whitney, J. M. and Kim, R. Y. 1977. Effect of stacking sequence on the notched strength of laminated composites. *Composite Materials: Testing and Design (Fourth Conference)*, ASTM STP 617, pp. 229–242. American Society for Testing and Materials, Philadelphia, PA.
22. Rybicki, E. F. 1971. Approximate three-dimensional solutions for symmetric laminates under in-plane loading. *Journal of Composite Materials*, 5(3), 354–360.
23. Wang, A. S. D. and Crossman, F. W. 1977. Some new results on edge effect in symmetric composite laminates. *Journal of Composite Materials*, 11, 92–106.
24. Herakovich, C. T. 1981. On the relationship between engineering properties and delamination of composite materials. *Journal of Composite Materials*, 15, 336–348.
25. Hwang, S. J. and Gibson, R. F. 1992. Contribution of interlaminar stresses to damping in thick composites under uniaxial extension. *Composite Structures*, 20, 29–35.
26. Hwang, S. J. 1988. Characterization of the effects of three dimensional states of stress on damping of laminated composites. PhD dissertation, Mechanical Engineering Department, University of Idaho.
27. Whitney, J. M. 1973. Free edge effects in the characterization of composite materials. *Analysis of the Test Methods for High Modulus Fibers and Composites*, ASTM STP 521, pp. 167–180. American Society for Testing and Materials, Philadelphia, PA.

28. Conti, P. and De Paulis, A. 1985. A simple model to simulate the interlaminar stresses generated near the free edge of a composite laminate, in Johnson, W.S. ed. *Delamination and Debonding of Materials*, ASTM STP 876, pp. 35–51. American Society for Testing and Materials, Philadelphia, PA.
29. Hahn, H. T. and Tsai, S. W. 1974. On the behavior of composite laminates after initial failures. *Journal of Composite Materials*, 8(3), 288–305.
30. Tsai, S. W. 1965. *Strength Characteristics of Composite Materials*. NASA CR-224.
31. Kim, R. Y. and Soni, S. R. 1984. Experimental and analytical studies on the onset of delamination in laminated composites. *Journal of Composite Materials*, 18, 70–80.
32. Whitney, J. M. and Nuismer, R. J. 1974. Stress fracture criteria for laminated composites containing stress concentrations. *Journal of Composite Materials*, 8, 253–265.
33. Brewer, J. C. and Lagace, P. A. 1988. Quadratic stress criterion for initiation of delamination. *Journal of Composite Materials*, 22, 1141–1155.
34. O'Brien, T. K. 1982. Characterization of delamination onset and growth in a composite laminate, in Reifsnider, K.L. ed. *Damage in Composite Materials*, ASTM STP 775, pp. 140–167. American Society for Testing and Materials, Philadelphia, PA.
35. Newaz, G. M. ed., 1991. *Delamination in Advanced Composites*. Technomic Publishing Co., Lancaster, PA.
36. Johnson, W. S. ed. 1985. *Delamination and Debonding of Materials*. ASTM STP 876, American Society for Testing and Materials, Philadelphia, PA.
37. Pagano, N. J. ed. 1989. *Interlaminar Response of Composite Laminates*, Vol. 5, *Composite Laminates Series*, Pipes, R. B. (series ed.). Elsevier Science Publishers, Amsterdam.
38. Vinson, J. R. and Sierakowski, R. L. 1986. *The Behavior of Structures Composed of Composite Materials*. Martinus Mijhoff Publishers, Dordrecht, The Netherlands.
39. Leissa, A. W. 1985. *Buckling of Laminated Composite Plates and Shell Panels*. AFWAL-TR-85-3069, Air Force Wright Aeronautical Laboratories, Wright-Patterson Air Force Base, OH.
40. Hatcher, D. and Tuttle, M. 1991. Measurement of critical buckling loads and mode shapes of composite panels, in Chung, H. H. and Kwon, Y. W. eds. *Recent Advances in Structural Mechanics*, PVP-Vol. 225/NE-Vol. 7, pp. 21–26. American Society of Mechanical Engineers, New York.
41. Jones, R. M. 1975. *Mechanics of Composite Materials*, pp. 264–270. Hemisphere Publishing Co., New York.
42. Dopek, R. K. 1987. Numerical design and analysis of structures, in Reinhart, T.J. ed. *Engineered Materials Handbook*, Vol. 1, *Composites*, pp. 463–478. ASM International, Materials Park, OH.
43. Peters, S. T., Humphrey, W. D., and Foral, R. F. 1991. *Filament Winding Composite Structure Fabrication*, pp. 5–45. Society for Advancement of Materials and Process Engineering, Covina, CA.
44. Kelly, A. and Zweber, C. eds. 2000. *Comprehensive Composite Materials*, Vols. 1–6. Elsevier, Amsterdam.
45. Mallick, P. K. ed. 1997. *Composites Engineering Handbook*. Marcel Dekker, Inc., New York.
46. Harper, C. A., ed. 2002. *Handbook of Plastics, Elastomers and Composites*. McGraw-Hill Co., New York.

47. Donaldson, S. L. and Miracle, D. B. eds. 2001. *ASM Handbook, Composites*, Vol. 21. ASM International, Materials Park, OH.
48. U.S. Department of Defense, 2002. *MIL-HDBK-17, Composite Materials Handbook*, Vols. 1–5. Available online at [http://www.everyspec.com/MIL-HDBK/MIL-HDBK+\(0001+ - + 0099\)/](http://www.everyspec.com/MIL-HDBK/MIL-HDBK+(0001+ - + 0099)/).
49. Vinson, J. R. and Sierakowski, R. L. 2002. *The Behavior of Structures Composed of Composite Materials*, 2nd ed. Kluwer Academic Publishers, Dordrecht, The Netherlands.
50. Kollar, L. P. and Springer, G. S. 2003. *Mechanics of Composite Structures*. Cambridge University Press, Cambridge.
51. Sun, C. T. 1998. *Mechanics of Aircraft Structures*. John Wiley & Sons, Inc., New York.
52. Vinson, J. R. 1999. *The Behavior of Sandwich Structures of Isotropic and Composite Materials*. CRC Press, Boca Raton, FL.
53. Popov, E. P., 1999. *Engineering Mechanics of Solids*. Prentice-Hall, Upper Saddle River, NJ.
54. Steeves, C. A. and Fleck, N. A. 2004. Collapse mechanisms of sandwich beams with composite faces and a foam core, loaded in three-point bending. Part II: Experimental investigation and numerical modeling. *International Journal of Mechanical Sciences*, 46, 585–608.
55. Zenkert, D. 1995. *An Introduction to Sandwich Construction*. Chameleon, London.
56. Steeves, C. A. and Fleck, N. A. 2004. Collapse mechanisms of sandwich beams with composite faces and a foam core, loaded in three-point bending. Part I: Analytical models and minimum weight design. *International Journal of Mechanical Sciences*, 46, 561–583.
57. Rehfield, L. W. 1999. A brief history of analysis methodology for grid-stiffened geodesic composite structures. *Proc. 44th International SAMPE Symposium*, CD-ROM.
58. Chen, H. J. and Tsai, S. W. 1996. Analysis and optimum design of composite grid structures. *Journal of Composite Materials*, 30(4), 503–534.
59. Huybrechts, S. and Tsai, S. W. 1996. Analysis and behavior of grid structures. *Composites Science and Technology*, 56(9), 1001–1015.

# 8

---

## *Analysis of Viscoelastic and Dynamic Behavior*

---

### 8.1 Introduction

In the analyses of Chapters 1 through 7, it has been assumed that the applied loads are static in nature and that the composite and its constituents exhibit time-independent linear elastic behavior. However, composite structures are often subjected to dynamic loading caused by vibration or wave propagation. In addition, many composites exhibit time-dependent viscoelastic behavior under load; this is particularly true for composites having polymeric constituents. This chapter contains the basic information needed for the analysis of both viscoelastic and dynamic behavior of composites and their constituents.

The word “viscoelastic” has evolved as a way of describing materials that exhibit characteristics of both viscous fluids and elastic solids. Polymeric materials, which are known to be viscoelastic, may behave like fluids or solids, depending on the timescale and/or the temperature. For example, polycarbonate, a thermoplastic polymer, is a liquid during molding at processing temperatures, but is a glassy solid at service (ambient) temperatures. It will deform like a rubber at temperatures just above the glass transition temperature,  $T_g$ . At temperatures below  $T_g$ , however, it will deform just as much, and in the same way if the test time is long enough.

We know that ideal Hookean elastic solids are capable of energy storage under load, but not energy dissipation, whereas ideal Newtonian fluids under nonhydrostatic stresses are capable of energy dissipation, but not energy storage. Viscoelastic materials, however, are capable of both storage and dissipation of energy under load. Another characteristic of viscoelastic materials is memory. Perfectly elastic solids are said to have only “simple memory” because they remember only the unstrained state and the current strains depend only on the current stresses. Viscoelastic materials have what is often referred to as “fading memory” because they remember the past in such a way that the current strains depend more strongly on the recent stress–time history than on the more distant stress–time history.

There are four important physical manifestations of viscoelastic behavior in structural materials, as illustrated by the various conditions of the uniaxially loaded viscoelastic rod in Figure 8.1. First, if the rod is subjected to a constant stress, the resulting strain will exhibit time-dependent “creep,” as shown in Figure 8.1a. The time-dependent creep strains are superimposed on the initial elastic strains. Second, if the rod is subjected to a constant strain or displacement, the resulting stress will exhibit time-dependent “relaxation,” as shown in Figure 8.1b. That is, the stress relaxes from the initial elastic stress. Third, if the bar is subjected to oscillatory loading, the resulting stress-strain curve will describe a “hysteresis loop,” as shown in Figure 8.1c. The area enclosed by the hysteresis loop is a measure of the damping, or dissipation, of energy in the material. Fourth, if the bar is loaded at various strain rates, the stress-strain curves will exhibit strain-rate dependence, as shown in Figure 8.1d. That is, the stress corresponding to a given strain depends on the rate of straining. An ideal elastic material exhibits none of the above characteristics.

All structural materials exhibit some degree of viscoelasticity, and the extent of such behavior often depends on environmental conditions such as temperature. For example, while a structural steel or aluminum material may

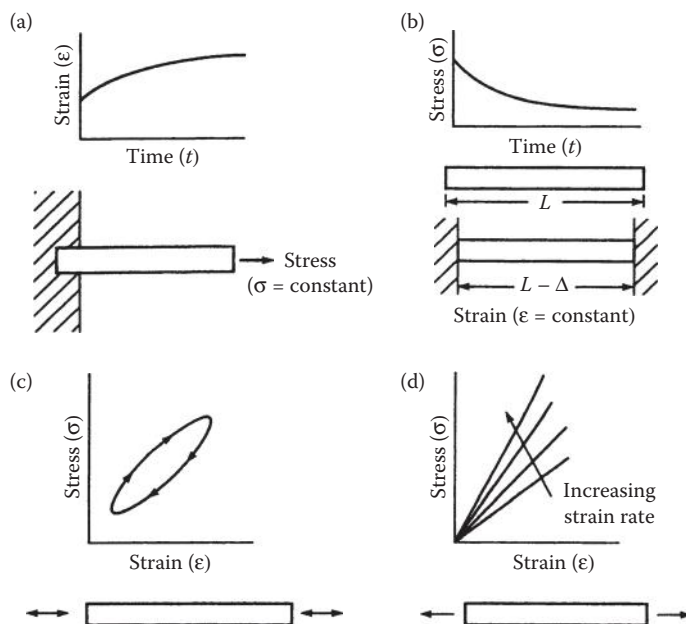


**FIGURE 8.1**

Physical manifestations of viscoelastic behavior in structural materials, as demonstrated by various types of loading applied to a viscoelastic rod. (a) Creep under constant stress, (b) relaxation under constant strain, (c) Hysteresis loop due to cyclic stress, and (d) strain rate dependence of stress-strain curve.

be essentially elastic at room temperature, viscoelastic effects become apparent at elevated temperatures approaching half the melting temperature. Polymeric materials are viscoelastic at room temperature, and the viscoelastic effects become stronger as the temperature approaches the glass transition temperature. Recall from Chapter 5 that the glass transition region (Figure 5.1) is a region of transition between glassy behavior and rubbery behavior and a region characterized by the onset of pronounced viscoelastic behavior.

Polymers with amorphous microstructures tend to be more viscoelastic than those with crystalline microstructures. As shown in Figure 8.2, amorphous microstructures consist of 3D arrangements of randomly entangled long-chain polymer molecules that are often characterized by analogy to a "bowl of spaghetti." On the other hand, crystalline microstructures consist of regular, ordered crystalline arrays of atoms (Figure 8.2). Some polymers have both amorphous and crystalline components in their microstructures, and some polymers are purely amorphous. For example, a semicrystalline polymer may consist of crystalline "islands" in an amorphous "sea," and the degree of crystallinity typically depends on the rates of heating and cooling during processing.

On the basis of the previous discussion, we conclude that viscoelastic behavior of composite materials is typically more significant for composites having one or more polymeric constituents. Viscoelastic effects in polymer matrix composites are most pronounced in matrix-dominated response to off-axis or shear loading. Viscoelastic deformations and plastic deformations are similar in that both are driven by shear stresses. Indeed, elements of the theory of plasticity are often borrowed for use in the theory of viscoelasticity. For example, it is sometimes assumed in viscoelasticity analysis that the dilatational response to hydrostatic stresses is elastic, but that the distortional response to shear stresses is viscoelastic.

This chapter concerns the development of stress-strain relationships for linear viscoelastic materials and their composites. These stress-strain relationships take on special forms for creep, relaxation, and sinusoidal

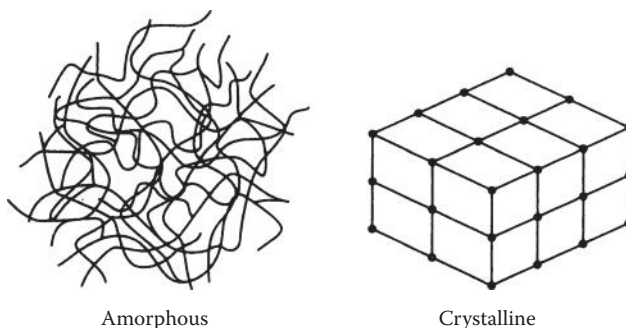


**FIGURE 8.2**  
Amorphous and crystalline microstructures in polymers.

oscillation. Following the use of certain integral transforms, the viscoelastic stress-strain relationships turn out to be analogous to Hookean elastic stress-strain relationships, leading to the so-called Elastic-Viscoelastic Correspondence Principle.

Dynamic loading is usually categorized as being either impulsive or oscillatory. Dynamic response consists of either a propagating wave or a vibration, depending on the elapsed time and the relative magnitudes of the wavelength of the response and the characteristic structural dimension. Both types of excitation usually cause wave propagation initially. Wave propagation will continue if the response wavelength is much shorter than the characteristic structural dimension, otherwise standing waves (i.e., vibrations) will be set up as the waves begin to reflect back from the boundaries. Wave propagation in composites may involve complex reflection and/or refraction effects at fiber-matrix interfaces or ply interfaces, complicating matters further.

The dynamic response of composites may also be complicated by their anisotropic behavior. For example, the speed of a propagating wave in an isotropic material is independent of orientation, whereas the wave speed in an anisotropic composite depends on the direction of propagation. Anisotropic coupling effects often lead to complex waves or modes of vibration. For example, an isotropic beam subjected to an oscillatory bending moment will respond in pure flexural modes of vibration, but a nonsymmetric laminate may respond in a coupled bending-twisting mode or some other complex mode. In this chapter, however, the focus is on the analyses for vibrations and wave propagation in specially orthotropic composites or laminates without coupling.

Damping, which is one of the manifestations of viscoelastic behavior, is obviously important for noise and vibration control. Composites generally have better damping than conventional metallic structural materials, especially if the composite has one or more polymeric constituents. It will be shown that the complex modulus notation and the Elastic-Viscoelastic Correspondence Principle from viscoelasticity theory are particularly useful in the development of analytical models for predicting the damping behavior of composites.

Finally, it will be shown that the effective modulus theory, which was introduced in Chapters 2 and 3, is indispensable in both viscoelastic and dynamic analyses of composites. Under certain restrictions, the concept of an effective modulus or effective compliance will be used to extend various viscoelastic analyses and dynamic analyses of homogeneous materials to the corresponding analyses of heterogeneous composites.

---

## 8.2 Linear Viscoelastic Behavior of Composites

A linear elastic solid exhibits a linearity between stress and strain, and this linear relationship is independent of time. A linear viscoelastic solid also

exhibits a linearity between stress and strain, but the linear relationship depends on the time history of the input. The mathematical criteria for linear viscoelastic behavior are similar to those for the linear behavior of any system. Following the notation of Schapery [1], the criteria can be stated as follows:

Let the response  $R$  to an input  $I$  be written as  $R = R\{I\}$ , where  $R\{I\}$  denotes that the current value of  $R$  is a function of the time history of the input  $I$ . For linear viscoelastic behavior, the response  $R\{I\}$  must satisfy both the following conditions:

1. *Proportionality*: that is,  $R\{cI\} = cR\{I\}$ , where  $c$  is a constant.
2. *Superposition*: that is,  $R\{I_a + I_b\} = R\{I_a\} + R\{I_b\}$ , where  $I_a$  and  $I_b$  may be the same or different time histories.

Any response not satisfying these criteria would be a nonlinear response. These criteria form the basis of the stress-strain relationship known as the Boltzmann superposition integral, which is developed in Section 8.2.1.

Before getting into the analytical modeling of linear viscoelastic behavior, however, it is instructive to briefly discuss a phenomenological approach to verification of linear viscoelastic behavior. Probably the most widely used method of characterizing viscoelastic behavior is the tensile creep test described in Figures 8.1a and 8.3, which involves the application of a constant tensile stress to a specimen and measurement of the resulting time-dependent strain. The strain versus time curves are known as creep curves, and, as shown in Figure 8.3, the total strain at any time is the sum of the initial elastic strain,  $\varepsilon_0$ , and the time-dependent creep strain,  $\varepsilon(t)$ . At this point,

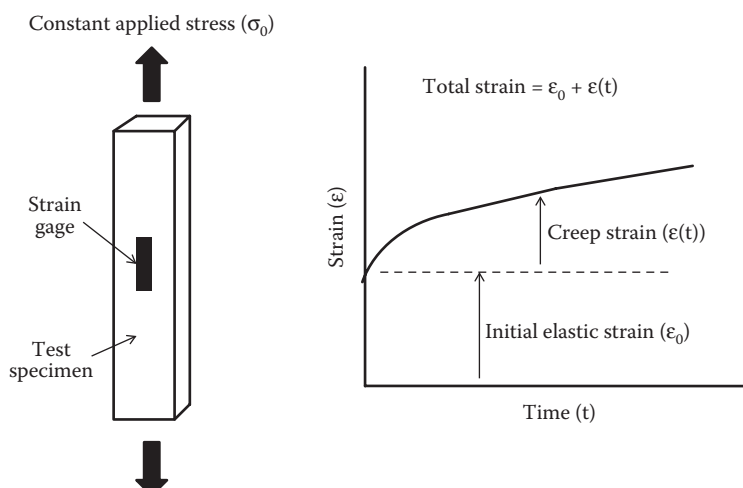


**FIGURE 8.3**  
Tensile creep test of a viscoelastic specimen under constant stress.

we focus on isotropic viscoelastic materials, and more details on creep tests of anisotropic composites will be presented in Chapter 10.

If a number of creep curves are generated at different stress levels as shown schematically in Figure 8.4a, these creep curves can be used to plot stress-strain curves at different times. For example, by taking the ratio of stress to strain at each stress level corresponding to time  $t_1$  in Figure 8.4a, we can plot the so-called *isochronous stress-strain curve* at time  $t = t_1$ , as shown in Figure 8.4b. The slope of the isochronous stress-strain curve is  $E(t)$ , the time-dependent Young's modulus at time  $t$ . When  $t = 0$ , the value of  $E(t)$  corresponds to the elastic Young's modulus, and  $E(t)$  typically decreases from this value as time increases. Thus, from a set of creep curves at different stress levels as in Figure 8.4a, a family of isochronous stress-strain curves at different times can be developed for design use. The creep compliance for a constant stress  $\sigma$  is

$$S(t) = \frac{\epsilon(t)}{\sigma} \approx \frac{1}{E(t)} \quad (8.1)$$

And obviously  $S(t)$  increases with time. Phenomenologically speaking, a material is linear viscoelastic within the range of stresses and times for which its isochronous stress-strain curves are linear. There are always limits on the ranges of stress and time within which a material will continue to behave in a linear viscoelastic manner. For example, if the stress level becomes high enough, the isochronous stress-strain curve will become nonlinear, and this means that the material becomes nonlinear viscoelastic. In this book, it is always assumed that the viscoelastic materials being discussed are linear viscoelastic.

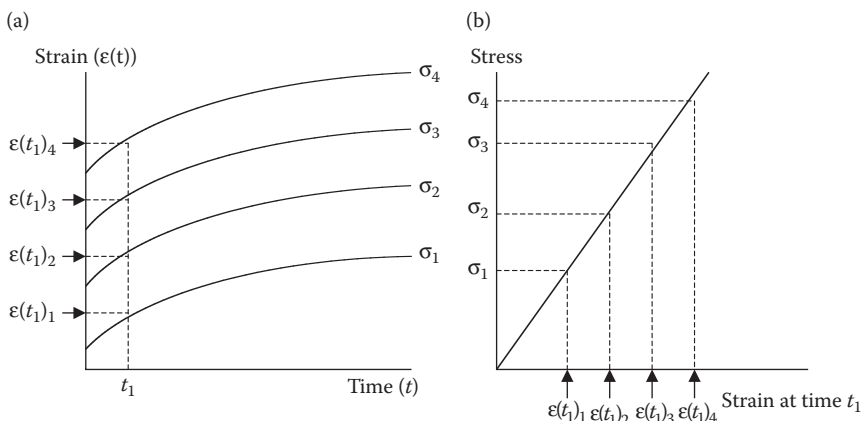


**FIGURE 8.4**

Illustration of creep curves at constant stress and corresponding isochronous stress-strain curves. (a) Creep curves at constant stress where  $\sigma_4 > \sigma_3 > \sigma_2 > \sigma_1$  and (b) isochronous stress-strain curve at time  $t = t_1$ .

Typically, the creep compliance for linear viscoelastic creep curves such as those shown in Figure 8.4a can be described empirically using a power-law expression of the form

$$S(t) = S_0 + S_1 t^n \quad (8.2)$$

where  $S_0$  is the initial elastic compliance and  $S_1$  and  $n$  are empirically determined parameters. It has been shown experimentally by Beckwith [2] that for linear viscoelastic polymer matrix composites, the creep exponent  $n$  depends only on the polymer matrix, and indeed that  $n$  is the same for the composite and the polymer matrix material. Since creep experiments are generally conducted over several decades, it is often convenient to use log-log scales to plot creep compliance data. A power law plotted on a log-log scale becomes a straight line, and this provides another way to check for linear viscoelastic behavior. For example, moving  $S_0$  to the left-hand side of Equation 8.2 and taking the log of both sides of the resulting equation yields

$$\log[S(t) - S_0] = \log S_1 + n \log t \quad (8.3)$$

which is the equation for a straight line on a log-log plot of  $\log[S(t) - S_0]$  versus  $\log t$  with slope  $n$  and vertical axis intercept  $\log S_1$ , as shown in Figure 8.5.

### 8.2.1 Boltzmann Superposition Integrals for Creep and Relaxation

The stress-strain relationships for a linear viscoelastic material can be developed by using the Boltzmann Superposition Principle [3]. If the material is at a constant temperature and is “nonaging,” then the response at any time  $t$  due to an input at time  $t = \tau$  is a function of the input and the elapsed time  $(t - \tau)$  only. Aging is a time-dependent change in the material, which is

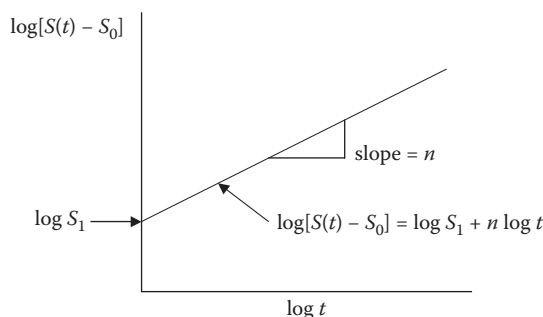


**FIGURE 8.5**  
Illustration of log creep compliance versus log time plot.

different from viscoelastic creep or relaxation. Both temperature and aging effects are considered in Section 8.2.6.

Consider the 1D isothermal loading of a nonaging, isotropic, homogeneous linear viscoelastic material by the stresses  $\Delta\sigma_1$ ,  $\Delta\sigma_2$ , and  $\Delta\sigma_3$  at times  $\tau_1$ ,  $\tau_2$ , and  $\tau_3$ , respectively, as shown in Figure 8.6. According to the Boltzmann Superposition Principle, the strain response is linearly proportional to the input stress, but the proportionality factor is a function of the elapsed time since the application of the input stress. Thus, for the stress–time history in Figure 8.6, the total strain response at any time  $t > \tau_3$  is given by

$$\varepsilon(t) = \Delta\sigma_1 S(t - \tau_1) + \Delta\sigma_2 S(t - \tau_2) + \Delta\sigma_3 S(t - \tau_3) \quad (8.4)$$

where  $S(t)$  is the creep compliance, which is zero for  $t < 0$ . For input stresses having arbitrary time histories, Equation 8.4 can be generalized as the Boltzmann superposition integral or hereditary law:

$$\varepsilon(t) = \int_{-\infty}^t S(t - \tau) \frac{d\sigma(\tau)}{d\tau} d\tau \quad (8.5)$$

Alternatively, the stress resulting from arbitrary strain inputs may be given by

$$\sigma(t) = \int_{-\infty}^t C(t - \tau) \frac{d\varepsilon(\tau)}{d\tau} d\tau \quad (8.6)$$

where  $C(t)$  is the relaxation modulus, which is zero for  $t < 0$ .

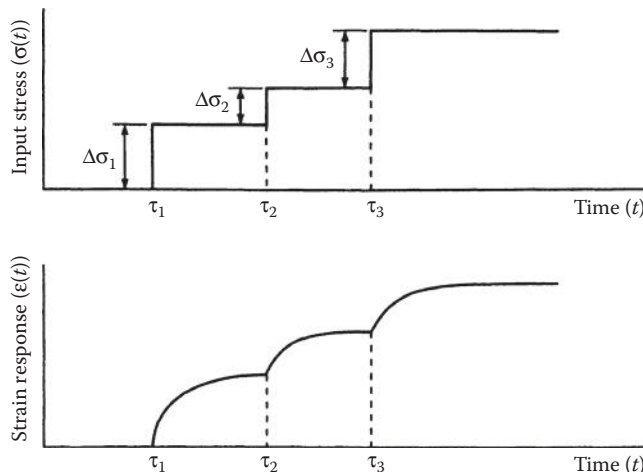


**FIGURE 8.6**

Input stress and strain response in 1D loading of a linear viscoelastic material for illustration of the Boltzmann Superposition Principle.

Equation 8.5 can be extended to the more general case of a homogeneous, anisotropic, linear viscoelastic material with multiaxial inputs and responses by using the contracted notation and writing

$$\varepsilon_i(t) = \int_{-\infty}^t S_{ij}(t-\tau) \frac{d\sigma_j(\tau)}{d\tau} d\tau \quad (8.7)$$

where

$$i, j = 1, 2, \dots, 6$$

$S_{ij}(t)$  = creep compliances

For the specific case of the homogeneous, linear viscoelastic, specially orthotropic lamina in plane stress, Equation 8.7 becomes

$$\begin{aligned} \varepsilon_1(t) &= \int_{-\infty}^t S_{11}(t-\tau) \frac{d\sigma_1(\tau)}{d\tau} d\tau + \int_{-\infty}^t S_{12}(t-\tau) \frac{d\sigma_2(\tau)}{d\tau} d\tau \\ \varepsilon_2(t) &= \int_{-\infty}^t S_{12}(t-\tau) \frac{d\sigma_1(\tau)}{d\tau} d\tau + \int_{-\infty}^t S_{22}(t-\tau) \frac{d\sigma_2(\tau)}{d\tau} d\tau \\ \gamma_{12}(t) &= \int_{-\infty}^t S_{66}(t-\tau) \frac{d\tau_{12}(\tau)}{d\tau} d\tau \end{aligned} \quad (8.8)$$

Similarly, Equation 8.6 can be generalized to the form

$$\sigma_i(t) = \int_{-\infty}^t C_{ij}(t-\tau) \frac{d\varepsilon_j(\tau)}{d\tau} d\tau \quad (8.9)$$

where the  $C_{ij}(t)$  are the relaxation moduli. Note that Equations 8.7 and 8.9 are analogous to the generalized Hooke's law for linear elastic materials given by Equations 2.5 and 2.3, respectively, and that Equations 8.8 are analogous to the Hooke's law for the specially orthotropic lamina given by Equation 2.24. Thus, the creep compliances,  $S_{ij}(t)$ , for the viscoelastic material are analogous to the elastic compliances,  $S_{ij}$ , and the viscoelastic relaxation moduli,  $C_{ij}(t)$ , are analogous to the elastic stiffnesses,  $C_{ij}$ .

In order to apply the stress-strain relationships in Equations 8.7 through 8.9 to *heterogeneous*, anisotropic, linear viscoelastic composites, we again make use of the "effective modulus theory" that was introduced in Chapters 2 and 3. Recall that in order to apply the stress-strain relationships at a point in a homogeneous material (i.e., Equations 2.3 and 2.5) to the case of a heterogeneous composite, we replaced the stresses and strains at a point with the volume-averaged stresses and strains (Equations 2.7 and 2.8) and

also replaced the elastic moduli of the heterogeneous composite by effective moduli of an equivalent homogeneous material (Equations 2.9 and 2.10). Recall also that the criterion for the use of the effective modulus theory was that the scale of the inhomogeneity,  $d$ , had to be much smaller than the characteristic structural dimension,  $L$ , over which the averaging is done (Figure 8.7). However, since this chapter also deals with dynamic behavior, it is appropriate to add another criterion related to dynamic effects. That is, the scale of the inhomogeneity,  $d$ , must also be much smaller than the characteristic wavelength,  $\lambda$ , of the dynamic stress distribution (Figure 8.7). Thus, the criteria for the use of the effective modulus theory in dynamic loading of viscoelastic composites are  $d \ll L$  and  $d \ll \lambda$ . Practically speaking, the second criterion becomes important only when dealing with the propagation of high-frequency waves having very short wavelengths. On the other hand, the wavelengths associated with typical mechanical vibrations will almost always be sufficiently large so as to satisfy  $d \ll \lambda$ . The book by Christensen [4] provides a more detailed discussion on the effective modulus theory.

Thus, Equations 8.7 through 8.9 are valid for heterogeneous, anisotropic, linear viscoelastic composites if at an arbitrary time,  $t$ , we simply replace the stresses and strains at a point with the volume-averaged stresses and strains, replace the creep compliances with the effective creep compliances, and replace the relaxation moduli with the effective relaxation moduli. Thus, the effective creep compliance matrix for the specially orthotropic lamina in plane stress is given by

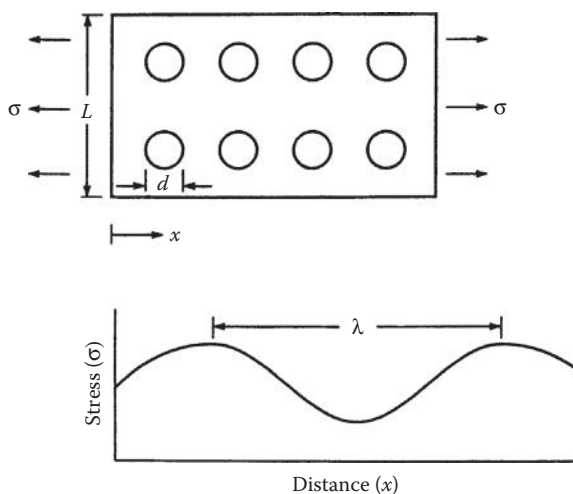


**FIGURE 8.7**

Critical dimensions which are used in the criteria for the application of the effective modulus theory.

$$S_{ij}(t) = \begin{bmatrix} S_{11}(t) & S_{12}(t) & 0 \\ S_{21}(t) & S_{22}(t) & 0 \\ 0 & 0 & S_{66}(t) \end{bmatrix} \quad (8.10)$$

Note the close resemblance of this creep compliance matrix to the corresponding elastic compliance matrix in Equation 2.24. For the generally orthotropic lamina, we have

$$\bar{S}_{ij}(t) = \begin{bmatrix} \bar{S}_{11}(t) & \bar{S}_{12}(t) & \bar{S}_{16}(t) \\ \bar{S}_{21}(t) & \bar{S}_{22}(t) & \bar{S}_{26}(t) \\ \bar{S}_{16}(t) & \bar{S}_{26}(t) & \bar{S}_{66}(t) \end{bmatrix} \quad (8.11)$$

where the  $\bar{S}_{ij}(t)$  are the transformed effective creep compliances. Note the close resemblance of this matrix to the corresponding transformed elastic compliance matrix in Equation 2.37. Halpin and Pagano [5] have shown that  $\bar{S}_{ij}(t)$  are related to  $S_{ij}(t)$  by the transformations

$$\begin{aligned} \bar{S}_{11}(t) &= S_{11}(t)c^4 + [2S_{12}(t) + S_{66}(t)]c^2s^2 + S_{22}(t)s^4 \\ \bar{S}_{12}(t) &= S_{12}(t)(s^4 + c^4) + [S_{11}(t) - S_{22}(t) - S_{66}(t)]s^2c^2 \\ \bar{S}_{22}(t) &= S_{11}(t)s^4 + [2S_{12}(t) + S_{66}(t)]s^2c^2 + S_{22}(t)c^4 \\ \bar{S}_{66}(t) &= 2[2S_{11}(t) + 2S_{22}(t) - 4S_{12}(t) - S_{66}(t)]c^2s^2 + S_{66}(t)(s^4 + c^4) \\ \bar{S}_{16}(t) &= [2S_{11}(t) - 2S_{12}(t) - S_{66}(t)]sc^3 - [2S_{22}(t) - 2S_{12}(t) - S_{66}(t)]s^3c \\ \bar{S}_{26}(t) &= [2S_{11}(t) - 2S_{12}(t) - S_{66}(t)]s^3c - [2S_{22}(t) - 2S_{12}(t) - S_{66}(t)]sc^3 \end{aligned} \quad (8.12)$$

where  $s = \sin \theta$ ,  $c = \cos \theta$ , and the angle  $\theta$  has been defined in Figure 2.11. Note that these equations are entirely analogous to the corresponding elastic compliance transformations in Equation 2.38. Further justification for such direct correspondence between elastic and viscoelastic equations is provided by the Elastic–Viscoelastic Correspondence Principle, which is discussed later in Section 8.2.5.

Recall that for the elastic case, strain energy considerations led to the symmetry conditions  $S_{ij} = S_{ji}$  and  $C_{ij} = C_{ji}$ . For the viscoelastic case, Schapery [1] has used thermodynamic arguments to show that if  $S_{ij}(t) = S_{ji}(t)$  for the constituent materials, then the same is true for the composite. Halpin and Pagano [5] and others have presented experimental evidence that for transversely isotropic composites under plane stress,  $S_{12}(t) = S_{21}(t)$ . In both elastic and viscoelastic cases, further reductions in the number of independent moduli or

compliances depend on material property symmetry and the coordinate system used.

### Example 8.1

A specially orthotropic, linear viscoelastic composite lamina is subjected to the shear stress–time history shown in Figure 8.8. If the effective shear creep compliance is given by

$$S_{66}(t) = A + Bt, \quad t \geq 0; \quad S_{66}(t) = 0, \quad t < 0$$

where A and B are material constants and t is time. Find the expressions for the creep strain at  $t < T_0$  and  $t > T_0$ .

### SOLUTION

The creep strain is given by Equation 8.7:

$$\varepsilon_i(t) = \int_{-\infty}^t S_{ij}(t - \tau) \frac{d\sigma_j(\tau)}{d\tau} d\tau$$

which, for the case of  $t < T_0$ , reduces to

$$\varepsilon_6(t) = \gamma_{12}(t) = \int_0^t [A + B(t - \tau)] \frac{\tau_{\max}}{T_0} d\tau = \frac{A\tau_{\max}}{T_0} t + \frac{B\tau_{\max}}{2T_0} t^2$$

For  $t > T_0$ , we have

$$\varepsilon_6(t) = \gamma_{12}(t) = \int_0^{T_0} [A + B(t - \tau)] \frac{\tau_{\max}}{T_0} d\tau + \int_{T_0}^t (0) d\tau = A\tau_{\max} + B\tau_{\max}t - \frac{B\tau_{\max}T_0}{2}$$

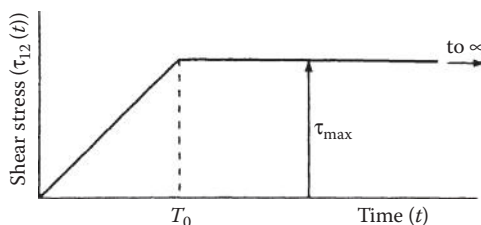


**FIGURE 8.8**  
Shear stress time history for Example 8.1.

### 8.2.2 Differential Equations and Spring–Dashpot Models

Although the Boltzmann superposition integral is a valid mathematical expression of the stress–strain relationship for a linear viscoelastic material, it does not lend itself easily to the use of physical models that help us to understand viscoelastic behavior better. In this section, Laplace transforms will be used to convert the Boltzmann superposition integral to an ordinary differential equation involving time derivatives of stress and strain. Physical models for viscoelastic behavior can be easily interpreted by using differential equations.

The Laplace transform,  $\mathcal{L}[f(t)]$  or  $\bar{f}(s)$ , of a function  $f(t)$  is defined by

$$\mathcal{L}[f(t)] = \bar{f}(s) = \int_0^\infty f(t)e^{-st}dt \quad (8.13)$$

where  $s$  is the Laplace parameter. For purposes of illustration, we now take the Laplace transform of the 1D Boltzmann superposition integral given by Equation 8.6. The Laplace transform of both sides of the equation is given by

$$\mathcal{L}[\sigma(t)] = \bar{\sigma}(s) = \mathcal{L}\left[\int_{-\infty}^t C(t-\tau) \frac{d\varepsilon(\tau)}{dt} d\tau\right] \quad (8.14)$$

Noting that the right-hand side of Equation 8.14 is in the form of a convolution integral [6], we can also write

$$\bar{C}(s) \frac{d\bar{\varepsilon}(s)}{dt} = \mathcal{L}\left[\int_{-\infty}^t C(t-\tau) \frac{d\varepsilon(\tau)}{dt} d\tau\right] \quad (8.15)$$

Taking the inverse Laplace transform of Equation 8.15, we find that

$$\mathcal{L}^{-1}\left[\bar{C}(s) \frac{d\bar{\varepsilon}(s)}{dt}\right] = \int_{-\infty}^t C(t-\tau) \frac{d\varepsilon(\tau)}{dt} d\tau \quad (8.16)$$

Thus, Equation 8.14 can be written as

$$\bar{\sigma}(s) = \mathcal{L}\left[\mathcal{L}^{-1}\left(\bar{C}(s) \frac{d\bar{\varepsilon}(s)}{dt}\right)\right] = \bar{C}(s) \frac{d\bar{\varepsilon}(s)}{dt} \quad (8.17)$$

But from the properties of Laplace transforms of derivatives [6],

$$\mathcal{L}\left[\frac{d\varepsilon(\tau)}{d\tau}\right] = \frac{d\bar{\varepsilon}(s)}{dt} = s\bar{\varepsilon}(s) - \varepsilon(0) \quad (8.18)$$

where  $\varepsilon(0)$  is the initial strain. If we neglect the initial conditions, Equation 8.17 becomes

$$\bar{\sigma}(s) = s\bar{C}(s)\bar{\varepsilon}(s) \quad (8.19)$$

If we perform similar operations on Equation 8.5, we find that

$$\bar{\varepsilon}(s) = s\bar{S}(s)\bar{\sigma}(s) \quad (8.20)$$

Note that Equations 8.19 and 8.20 are now of the same form as Hooke's law for linear elastic materials, except that the Laplace transforms of the stresses and strains are linearly related, and the proportionality constants are the Laplace transform of the creep compliance and the Laplace transform of the relaxation modulus. This is another example of the correspondence between the equations for elastic and viscoelastic materials and is another building block in the Elastic–Viscoelastic Correspondence Principle, which will be discussed in Section 8.2.5. Note also that according to Equations 8.19 and 8.20, the Laplace transform of the creep compliance and the Laplace transform of the relaxation modulus must be related by

$$\bar{S}(s) = \frac{1}{s^2\bar{C}(s)} \quad (8.21)$$

However, the corresponding time-domain properties are not mathematically related by a simple inverse relationship. That is, in general,

$$S(t) \neq \frac{1}{C(t)} \quad (8.22)$$

However, a usually good approximation is

$$S(t) \approx \frac{1}{C(t)} \quad (8.23)$$

and it can be shown by using the Initial Value Theorem and the Final Value Theorem of Laplace transforms (see Problem 2) that for short times or for long times, the mathematically exact relationship is

$$S(t) = \frac{1}{C(t)}, \quad \text{when } t \rightarrow 0 \text{ or when } t \rightarrow \infty \quad (8.24)$$

The coefficient term in Equation 8.20 can also be written as a ratio of two polynomials in the Laplace parameter  $s$  as follows:

$$\bar{\epsilon}(s) = s\bar{S}(s)\bar{\sigma}(s) = \frac{Q(s)}{P(s)}\bar{\sigma}(s) \quad (8.25)$$

where

$$P(s) = a_0 + a_1s + a_2s^2 + \cdots + a_ns^n$$

$$Q(s) = b_0 + b_1s + b_2s^2 + \cdots + b_ns^n$$

Thus, we can write

$$P(s)\bar{\epsilon}(s) = Q(s)\bar{\sigma}(s) \quad (8.26)$$

But if we neglect the initial conditions, the Laplace transform of the  $n$ th derivative of a function  $f(t)$  is

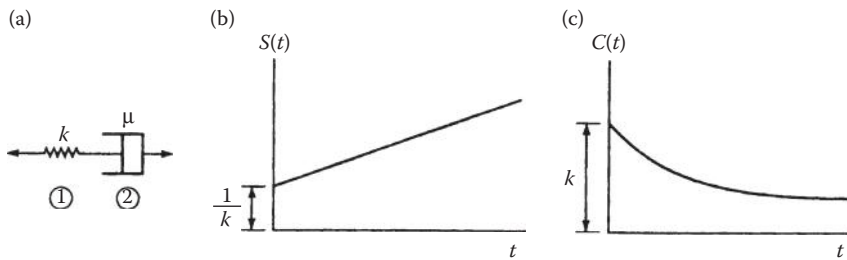
$$\mathcal{L}\left[\frac{d^n f(t)}{dt^n}\right] = s^n \bar{f}(s) \quad (8.27)$$

Making use of Equation 8.27 and taking the inverse Laplace transform of Equation 8.26, we find that

$$a_n \frac{d^n \epsilon}{dt^n} + \cdots + a_2 \frac{d^2 \epsilon}{dt^2} + a_1 \frac{d \epsilon}{dt} + a_0 \epsilon = b_0 \sigma + b_1 \frac{d \sigma}{dt} + b_2 \frac{d^2 \sigma}{dt^2} + \cdots + b_n \frac{d^n \sigma}{dt^n} \quad (8.28)$$

Thus, linear viscoelastic behavior may also be described by an ordinary differential equation as well as by the Boltzmann superposition integral. Note that the linear elastic material described by Hooke's law is a special case of Equation 8.28 when all time derivatives of stress and strain vanish (i.e.,  $a_0\epsilon = b_0\sigma$ ). Recall that one of the physical manifestations of viscoelastic behavior is the dependence of stress on strain rate; such strain rate effects can be modeled with Equation 8.28. We now consider several simple physical models of linear viscoelastic behavior that include various time derivatives of stress and strain.

As shown in Figures 8.9 through 8.11, useful physical models can be constructed from simple elements such as the elastic spring and the viscous dashpot, where the spring of modulus  $k$  is assumed to follow Hooke's law and the dashpot is assumed to be filled with a Newtonian fluid of viscosity  $\mu$ . Thus, the stress-strain relationship for the elastic spring element is of the

**FIGURE 8.9**

Maxwell model, with corresponding creep and relaxation curves. (a) Spring–dashpot arrangement, (b) creep compliance vs. time, and (c) relaxation modulus vs. time.

form  $\varepsilon = \sigma/k$ , whereas the corresponding equation for the viscous dashpot is  $d\varepsilon/dt = \sigma/\mu$ .

The Maxwell model consists of a spring and a dashpot in series, as shown in Figure 8.9a. The total strain across a model of unit length must equal the sum of the strains in the spring and the dashpot, so that

$$\varepsilon = \varepsilon_1 + \varepsilon_2 \quad (8.29)$$

and the strain rate across the model is then

$$\frac{d\varepsilon}{dt} = \frac{d\varepsilon_1}{dt} + \frac{d\varepsilon_2}{dt} = \frac{1}{k} \frac{d\sigma}{dt} + \frac{\sigma}{\mu} \quad (8.30)$$

Note that Equation 8.30 is just a special case of Equation 8.28, with only first derivatives of stress and strain. For creep at constant stress  $\sigma = \sigma_0$ , Equation 8.30 reduces to

$$\frac{d\varepsilon}{dt} = \frac{\sigma_0}{\mu} \quad (8.31)$$

Integrating Equation 8.31 once, we find that

$$\varepsilon(t) = \frac{\sigma_0}{\mu} t + C_1 \quad (8.32)$$

where the constant of integration,  $C_1$ , is found from the initial condition  $\varepsilon(0) = C_1 = \sigma_0/k$ . Thus, the creep strain for the Maxwell model is given by

$$\varepsilon(t) = \frac{\sigma_0}{\mu} t + \frac{\sigma_0}{k} \quad (8.33)$$

and the corresponding creep compliance is given by

$$S(t) = \frac{\epsilon(t)}{\sigma_0} = \frac{t}{\mu} + \frac{1}{k} \quad (8.34)$$

A plot of the creep compliance versus time according to Equation 8.34 is shown in Figure 8.9b. The type of creep behavior that is actually observed in experiments is more like that shown in Figure 8.6, however. Thus, the Maxwell model does not adequately describe creep.

For relaxation at constant strain  $\epsilon = \epsilon_0$ , the Maxwell model stress-strain relationship in Equation 8.30 becomes

$$0 = \frac{1}{k} \frac{d\sigma}{dt} + \frac{\sigma}{\mu} \quad (8.35)$$

Integrating Equation 8.35 once, we find

$$\ln \sigma = -\frac{k}{\mu} t + C_2 \quad (8.36)$$

where the constant of integration,  $C_2$ , is found from the initial condition  $\sigma(0) = \sigma_0$ . The resulting stress relaxation function is

$$\sigma(t) = \sigma_0 e^{-kt/\mu} = \sigma_0 e^{-t/\lambda} \quad (8.37)$$

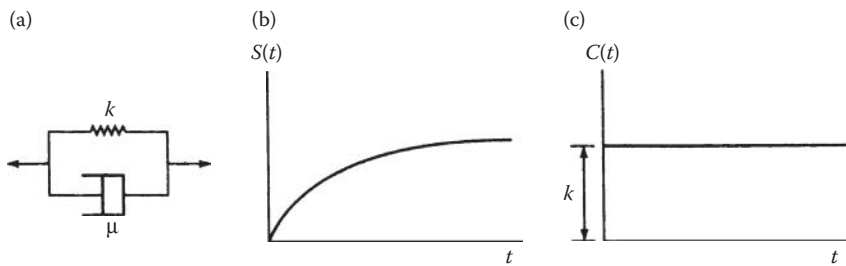
where  $\lambda = \mu/k$  is the relaxation time, or the time required for the stress to relax to  $1/e$ , or 37% of its initial value. The relaxation time is therefore a measure of the internal timescale of the material. The corresponding relaxation modulus is

$$C(t) = \frac{\sigma(t)}{\epsilon_0} = \frac{\sigma_0}{\epsilon_0} e^{-t/\lambda} = k e^{-t/\lambda} \quad (8.38)$$

Figure 8.9c shows the relaxation modulus versus time from Equation 8.38, which is in general agreement with the type of relaxation observed experimentally. Thus, the Maxwell model appears to describe adequately the relaxation phenomenon, but not the creep response.

Figure 8.10a shows the Kelvin–Voigt model, which consists of a spring and a dashpot in parallel. Using the appropriate equations for a parallel arrangement and following a procedure similar to the one just outlined, it can be shown that the differential equation describing the behavior of the Kelvin–Voigt model is given by

$$\sigma = k\epsilon + \mu \frac{d\epsilon}{dt} \quad (8.39)$$

**FIGURE 8.10**

Kelvin–Voigt model, with corresponding creep and relaxation curves. (a) Spring–dashpot arrangement, (b) creep compliance vs. time, and (c) relaxation modulus vs. time.

Equation 8.39 is seen to be another special case of Equation 8.28, with only first derivatives of strain. It can also be shown that the creep compliance for the Kelvin–Voigt model is given by

$$S(t) = \frac{1}{k} [1 - e^{-t/\rho}] \quad (8.40)$$

where  $\rho = \mu/k$  is now referred to as the retardation time. Similarly, the relaxation modulus is given by

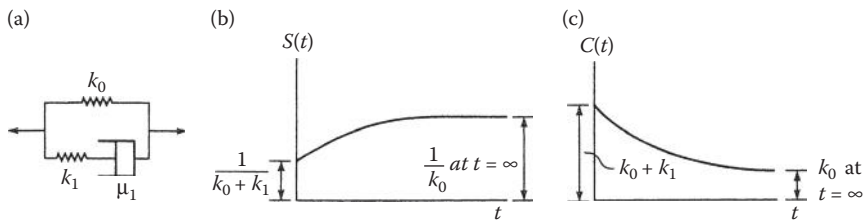
$$C(t) = k \quad (8.41)$$

Equations 8.40 and 8.41 are plotted in Figures 8.10b and c, respectively. The creep compliance curve agrees with experimental observation, except that the initial elastic response is missing. On the other hand, the relaxation modulus has not been observed to be constant, as shown in Figure 8.10c. Thus, like the Maxwell model, the Kelvin–Voigt model does not adequately describe all features of experimentally observed creep and relaxation.

One obvious way to improve the spring–dashpot model is to add more elements. One such improved model, shown in Figure 8.11a, is referred to as the standard linear solid or Zener model. It can be shown that the differential equation for the Zener model is given by

$$\sigma + \frac{\mu_1}{k_1} \frac{d\sigma}{dt} = k_0 \epsilon + \frac{\mu_1}{k_1} (k_0 + k_1) \frac{d\epsilon}{dt} \quad (8.42)$$

where parameters  $k_0$ ,  $k_1$ , and  $\mu_1$  are defined in Figure 8.11a. Equation 8.42 is obviously another special case of the general differential Equation 8.28. It is also interesting to note that the Zener model shown in Figure 8.11a is just a

**FIGURE 8.11**

Standard linear solid or Zener model, with corresponding creep and relaxation curves. (a) Spring–dashpot arrangement, (b) creep compliance vs. time, and (c) relaxation modulus vs. time.

Maxwell model in parallel with a spring. The creep compliance for the Zener model is given by

$$S(t) = \frac{1}{k_0} \left[ 1 - \frac{k_1}{k_0 + k_1} e^{-t/\rho_1} \right] \quad (8.43)$$

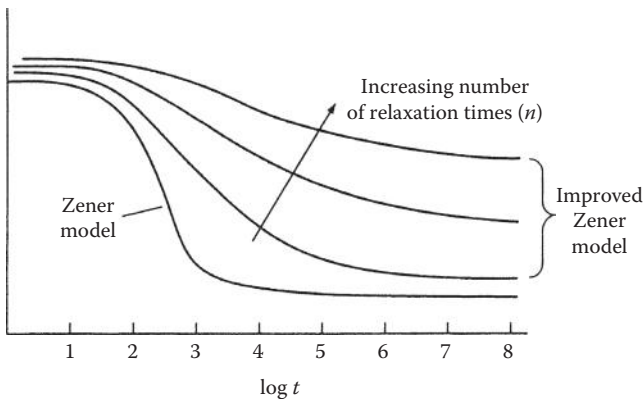
where  $\rho_1 = (\mu_1/k_0 k_1)(k_0 + k_1)$  is the retardation time.

As shown in Figure 8.11b, the shape of the creep compliance curve from Equation 8.43 matches the expected shape based on experimental observations. The relaxation modulus for the Zener model is given by

$$C(t) = k_0 + k_1 e^{-t/\lambda_1} \quad (8.44)$$

where  $\lambda_1 = \mu_1/k_1$  is the relaxation time. Note that  $\lambda_1$  is just the relaxation time for the Maxwell model consisting of  $\mu_1$  and  $k_1$ . Figure 8.11c shows the predicted relaxation modulus curve from Equation 8.44, and, again, the general shape of the curve appears to be similar to what is experimentally observed.

Although the Zener model is the simplest spring–dashpot model that correctly describes all expected features of experimentally observed creep and relaxation behavior in linear viscoelastic materials, it still is not completely adequate. This remaining inadequacy is best described by plotting the relaxation modulus versus the logarithm of time, as shown in Figure 8.12. Practically speaking, complete relaxation for the Zener model occurs in less than a decade in time, but relaxation for real polymers happens over a much longer timescale. For example, the glass-to-rubber transition, which is only one of several regions of polymer viscoelastic behavior, takes about six to eight decades in time to complete [7]. This extended relaxation period for polymers is due to the existence of a distribution of relaxation times. By using an improved Zener model such as the parallel arrangement shown in Figure 8.13, we can introduce such a distribution of relaxation times,  $\lambda_i$ , that makes it possible to extend the range of relaxation to more realistic values. This form of the improved Zener model consists of  $n$  Maxwell elements in parallel

**FIGURE 8.12**

Effect of increasing number of relaxation times on relaxation curve of the Zener model.

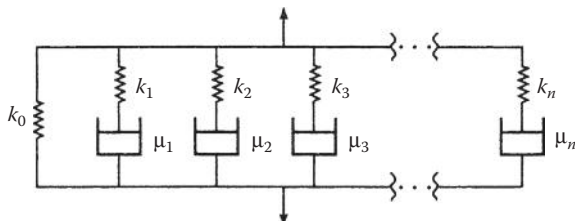
with the elastic spring,  $k_0$ . It can be easily shown that the relaxation modulus for this improved Zener model is given by

$$C(t) = k_0 + \sum_{i=1}^n k_i e^{-t/\lambda_i} \quad (8.45)$$

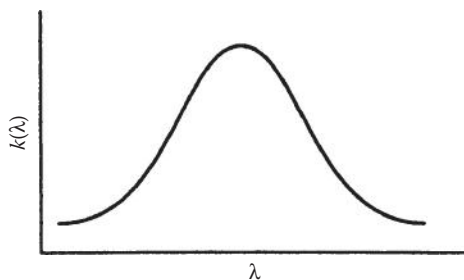
where  $\lambda_i = \mu_i/k_i$  is the relaxation time for the  $i$ th Maxwell element.

As shown in Figure 8.12, the effect of increasing  $n$  and the corresponding number of relaxation times is to broaden the range of relaxation. The number of relaxation times needed to describe adequately the viscoelastic behavior of a particular material must be determined experimentally. For an infinite number of elements in the improved Zener model of Figure 8.13 and a continuous distribution of relaxation times, the relaxation modulus can be expressed as [8]

$$C(t) = k_0 + \int_0^\infty k(\lambda) e^{-t/\lambda} d\lambda \quad (8.46)$$

**FIGURE 8.13**

Improved Zener model, parallel arrangement.

**FIGURE 8.14**

Continuous distribution of relaxation times, or relaxation spectrum  $k(\lambda)$ , for improved Zener model of Figure 8.13, with an infinite number of elements.

where  $k(\lambda)$  is the distribution of relaxation times, or the relaxation spectrum, which is shown schematically in Figure 8.14.

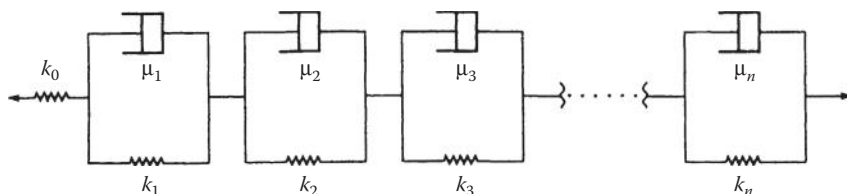
By considering an alternative form of an improved Zener model consisting of a spring in series with  $n$  Kelvin–Voigt elements, as shown in Figure 8.15, it can be shown that the corresponding creep compliance expression is

$$S(t) = \frac{1}{k_0} + \sum_{i=1}^n \frac{1}{k_i} [1 - e^{-t/\rho_i}] \quad (8.47)$$

where  $\rho_i = \mu_i/k_i$  is the retardation time for the  $i$ th Kelvin–Voigt element.

Although the above equations have been derived on the basis of simple spring–dashpot models, the generalized relaxation modulus and creep compliance expressions for anisotropic linear viscoelastic composites have the same forms as Equations 8.45 and 8.47, respectively. According to Schapery [1], if the elastic moduli are positive definite (i.e., always either positive or equal to zero), it can be shown using thermodynamic theory that the generalized expressions corresponding to Equations 8.45 and 8.47 are, respectively,

$$C_{ij}(t) = \sum_{m=1}^n C_{ij}^{(m)} e^{-t/\lambda_m} + C_{ij} \quad (8.48)$$

**FIGURE 8.15**

Improved Zener model, series arrangement.

and

$$S_{ij}(t) = \sum_{m=1}^n S_{ij}^{(m)} [1 - e^{-t/\rho_m}] + S_{ij} \quad (8.49)$$

where

$$i, j = 1, 2, \dots, 6$$

$C_{ij}$ ,  $S_{ij}$  = elastic moduli and compliances, respectively

$\lambda_m$ ,  $\rho_m$  = relaxation times and retardation times, respectively

$C_{ij}^{(m)}$ ,  $S_{ij}^{(m)}$  = coefficients corresponding to  $\lambda_m$  and  $\rho_m$ , respectively

As with the simple spring–dashpot models, the numerical values of the parameters on the right-hand side of Equations 8.48 and 8.49 must be determined experimentally.

The relaxation times and retardation times are strongly dependent on temperature, and such temperature dependence is the basis of the time-temperature superposition (TTS) method, which will be discussed later. It is assumed here that the materials are “thermorheologically simple.” That is, all the relaxation times,  $\lambda_i$ , and the retardation times,  $\rho_i$ , are assumed to have the same temperature dependence. A similar argument holds for the effect of aging, which will also be discussed later.

### Example 8.2

For the problem in Example 8.1, the effective shear compliance is to be approximated by a Kelvin–Voigt model of the form

$$S_{66}(t) = \begin{cases} \frac{1}{k}(1 - e^{-t/\lambda}), & \text{when } t \geq 0 \\ 0, & \text{when } t < 0 \end{cases}$$

Determine the creep strain at  $t < T_0$  and  $t > T_0$ .

### SOLUTION

For the case of  $t < T_0$ , Equation 8.7 reduces to

$$\gamma_{12}(t) = \int_0^t \frac{1}{k} [1 - e^{-(t-\tau)/\lambda}] \frac{\tau_{\max}}{T_0} d\tau = \frac{\tau_{\max}}{kT_0} [t - \lambda(1 - e^{-t/\lambda})]$$

and for  $t > T_0$ , we have

$$\gamma_{12}(t) = \int_0^{T_0} \frac{1}{k} [1 - e^{-(t-\tau)/\lambda}] \frac{\tau_{\max}}{T_0} d\tau + (0) = \frac{\tau_{\max}}{kT_0} \left[ T_0 - \lambda e^{-t/\lambda} (e^{T_0/\lambda} - 1) \right]$$

### 8.2.3 Quasielastic Analysis

From the previous section, it should be clear that the generalized Boltzmann superposition integrals in Equations 8.7 and 8.9 can be Laplace transformed to yield equations of the form

$$\bar{\epsilon}_i(s) = s \bar{S}_{ij}(s) \bar{\sigma}_j(s) \quad (8.50)$$

and

$$\bar{\sigma}_i(s) = s \bar{C}_{ij}(s) \bar{\epsilon}_j(s) \quad (8.51)$$

These equations are of the same form as the corresponding elastic stress-strain relationships and are presumably easier to work with than the integral equations. In a practical analysis or design problem involving the use of these equations, however, the problem solution in the Laplace domain would then have to be inverse transformed to get the desired time-domain result, and this can present difficulties. Schapery [1] has presented several approximate methods for performing such inversions. If the input stresses or strains are constant, however, there is no need for inverse transforms and the time-domain equations turn out to be very simple. Schapery refers to this as a "quasielastic analysis," and the equations used in such an analysis will be developed in the remainder of this section.

Consider a generalized creep problem with time-varying stresses  $\sigma_j(t)$  given by

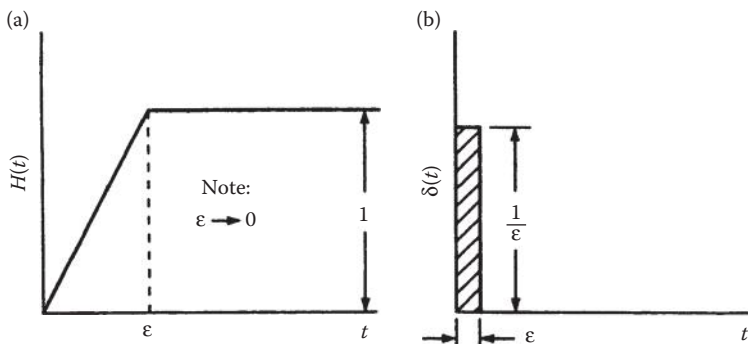
$$\sigma_j(t) = \sigma'_j H(t) \quad (8.52)$$

where  $j = 1, 2, \dots, 6$ ,  $\sigma'_j$  are constant stresses, and  $H(t)$  is the unit step function, or Heaviside function, shown in Figure 8.16a and defined as follows [3]:

$$\lim_{\varepsilon \rightarrow 0} H(t) = \begin{cases} 0 & \text{for } t \leq 0 \\ t/\varepsilon & \text{for } 0 \leq t \leq \varepsilon \\ 1 & \text{for } t \geq \varepsilon \end{cases} \quad (8.53)$$

The unit step function can be easily shifted along the time axis by an amount  $\xi$  by writing the function as  $H(t - \xi)$ . Substituting the stresses from Equation 8.52 into the Boltzmann superposition integral, Equation 8.7, we find that the resulting strains are given by

$$\epsilon_i(t) = \int_{-\infty}^t S_{ij}(t - \tau) \sigma'_j \frac{dH(\tau)}{d\tau} d\tau \quad (8.54)$$

**FIGURE 8.16**

Unit step function and Dirac delta function. (a) Unit step function and (b) Dirac delta function.

but according to Equation 8.53, the derivative of the step function must be

$$\frac{dH(t)}{dt} = \delta(t) = \begin{cases} 0 & \text{for } t \leq 0 \\ 1/\varepsilon & \text{for } 0 < t \leq \varepsilon \\ 0 & \text{for } t \geq \varepsilon \end{cases} \quad (8.55)$$

where the parameter  $\varepsilon$  can be made arbitrarily small, the derivative in Equation 8.55 is taken before  $\varepsilon \rightarrow 0$ , and  $\delta(t)$  is the Dirac delta function shown in Figure 8.16b. Thus, the integral in Equation 8.54 can be written as

$$\varepsilon_i(t) = \left\{ \int_{-\infty}^t S_{ij}(t - \tau) \delta(\tau) d\tau \right\} \sigma'_j \quad (8.56)$$

where the constants  $\sigma'_j$  have been moved outside the integral. According to the properties of convolution integrals [6], we can also write

$$\varepsilon_i(t) = \left\{ \int_{-\infty}^t S_{ij}(\tau) \delta(t - \tau) d\tau \right\} \sigma'_j \quad (8.57)$$

This integral can be broken down and rewritten as follows:

$$\varepsilon_i(t) = \left\{ \int_{-\infty}^{t-\varepsilon} (0) d\tau + \int_{t-\varepsilon}^t S_{ij}(\tau) \delta(t - \tau) d\tau \right\} \sigma'_j \quad (8.58)$$

where  $S_{ij}(\tau)$  evaluated over the interval  $t - \varepsilon \leq \tau \leq t$  can be approximated as  $S_{ij}(t)$  since  $\varepsilon$  is very small.  $S_{ij}(t)$  can now be moved outside the integral, leaving the integral of the Dirac delta function, which is defined as [6]

$$\int_{t-\varepsilon}^t \delta(t - \tau) d\tau = 1 \quad (8.59)$$

Thus, the final result is

$$\varepsilon_i(t) = S_{ij}(t)\sigma'_j \quad (8.60)$$

The form of this equation suggests that we can solve for creep strains under constant stresses,  $\sigma'_j$ , by simply replacing the elastic compliances,  $S_{ij}$ , in Hooke's law (Equation 2.5) with the corresponding viscoelastic creep compliances,  $S_{ij}(t)$ . Similarly, it can be shown that if the constant strain inputs

$$\varepsilon_j(t) = \varepsilon'_j H(t) \quad (8.61)$$

are substituted into Equation 8.9, the resulting stresses must be

$$\sigma_i(t) = C_{ij}(t)\varepsilon'_j \quad (8.62)$$

Thus, the stress relaxation under constant strains can be found by replacing the elastic moduli,  $C_{ij}$ , in Hooke's law (Equation 2.3) with the corresponding viscoelastic relaxation moduli,  $C_{ij}(t)$ . Equations 8.60 and 8.62 form the basis of the so-called "quasielastic analysis" and obviously eliminate the need for Laplace transform analysis in the stress-strain relationships. It should be emphasized again, however, that Equations 8.60 and 8.62 are only valid for constant or near-constant inputs. Such equations give additional hints of a direct correspondence between the equations for linear elastic systems and those for linear viscoelastic systems, and this correspondence will be discussed in more detail later.

The quasielastic approach has been successfully used in a number of practical applications such as micromechanical modeling of creep in polymer composites [9], prediction of creep in rotating viscoelastic disks [10], analysis of creep in prestressed composite connectors [11], and modeling of creep in prestressed polymer composite lubricators [12]. Many of these applications involve finite element implementations of the quasielastic approach, where finite element models are employed to solve a series of elastic problems, and the time dependence is accounted for by using different elastic moduli at each time step.

### Example 8.3

The filament wound pressure vessel described in Example 2.4 is constructed of a viscoelastic composite having creep compliances that can be modeled by using one-term series representations of the form shown in Equation 8.49. Assuming that

the internal pressure,  $p$ , is constant, determine the creep strains along the principal material directions in the wall of the vessel.

### SOLUTION

Since the internal pressure,  $p$ , is constant, the stresses in the wall of the vessel are all constants, and we can use a quasielastic analysis to predict the creep strains. From Equation 8.60, we find that the creep strains along the principal material directions are given by

$$\varepsilon_1(t) = S_{11}(t)\sigma_1 + S_{12}(t)\sigma_2$$

$$\varepsilon_2(t) = S_{12}(t)\sigma_1 + S_{22}(t)\sigma_2$$

and

$$\varepsilon_6(t) = \gamma_{12}(t) = S_{66}(t)\tau_{12}$$

From Example 2.4, stresses along the principal material directions were found to be

$$\sigma_1 = 20.5p \text{ MPa}$$

$$\sigma_2 = 17.0p \text{ MPa}$$

$$\sigma_6 = \sigma_{12} = \tau_{12} = 6.0p \text{ MPa}$$

Substituting these stresses and the creep compliances from Equation 8.49 into the above expressions for the strains, we find that

$$\varepsilon_1(t) = (S_{11}^{(1)}[1 - e^{-t/p}] + S_{11})(20.5p) + (S_{12}^{(1)}[1 - e^{-t/p}] + S_{12})(17.0p)$$

$$\varepsilon_2(t) = (S_{12}^{(1)}[1 - e^{-t/p}] + S_{12})(20.5p) + (S_{22}^{(1)}[1 - e^{-t/p}] + S_{22})(17.0p)$$

$$\gamma_{12}(t) = (S_{66}^{(1)}[1 - e^{-t/p}] + S_{66})(6.0p)$$

#### 8.2.4 Sinusoidal Oscillations and Complex Modulus Notation

In the previous section, it was shown that when the inputs are constant, the Boltzmann superposition integrals are reduced to simple algebraic equations that resemble the linear elastic Hooke's law. In this section, an analogous simplification will be demonstrated for the case of stresses or strains that vary sinusoidally with time. The results will make it much easier to analyze sinusoidal vibrations of viscoelastic composites. The general procedure here follows that presented by Fung [3].

Consider the case where the stresses vary sinusoidally with frequency  $\omega$ . Using the contracted notation and complex exponentials, such stresses can be written as

$$\tilde{\sigma}_n(t) = A_n e^{i\omega t} \quad (8.63)$$

where

$$n = 1, 2, \dots, 6$$

$i$  = imaginary operator, is  $\sqrt{-1}$

$A_n$  = complex stress amplitudes

$\sim$  = superscript denoting a sinusoidally varying quantity

Substituting Equation 8.63 into Equation 8.7, we find that the resulting sinusoidally varying strains are given by

$$\tilde{\varepsilon}_m(t) = \int_{-\infty}^t S_{mn}(t - \tau) i\omega A_n e^{i\omega\tau} d\tau \quad (8.64)$$

where  $m, n = 1, 2, \dots, 6$ .

It is now convenient to define a new variable  $\xi = t - \tau$ , so that

$$\tilde{\varepsilon}_m(t) = \int_0^\infty S_{mn}(\xi) e^{-i\omega\xi} i\omega A_n e^{i\omega t} d\xi \quad (8.65)$$

The terms not involving functions of  $\xi$  may be moved outside the integral, and since  $S_{mn}(t) = 0$  for  $t < 0$ , the lower limit on the integral can be changed to  $-\infty$ , so that

$$\tilde{\varepsilon}_m(t) = i\omega A_n e^{i\omega t} \int_{-\infty}^\infty S_{mn}(\xi) e^{-i\omega\xi} d\xi \quad (8.66)$$

The integral in Equation 8.66 is just the Fourier transform of the creep compliances,  $\mathcal{F}[S_{mn}(\xi)]$ , or  $S_{mn}(\omega)$ , which is written as

$$\mathcal{F}[S_{mn}(\xi)] = S_{mn}(\omega) = \int_{-\infty}^\infty S_{mn}(\xi) e^{-i\omega\xi} d\xi \quad (8.67)$$

Thus, the stress-strain relationship reduces to

$$\tilde{\varepsilon}_m(t) = i\omega S_{mn}(\omega) A_n e^{i\omega t} = i\omega S_{mn}(\omega) \tilde{\sigma}_n(t) \quad (8.68)$$

In order to get this equation to resemble Hooke's law more closely, we simply define the frequency-domain complex compliances as follows:

$$S_{mn}^*(\omega) = i\omega S_{mn}(\omega) \quad (8.69)$$

so that Equation 8.68 becomes

$$\tilde{\epsilon}_m(t) = S_{mn}^*(\omega) \tilde{\sigma}_n(t) \quad (8.70)$$

Thus, in linear viscoelastic materials, the sinusoidally varying stresses are related to the sinusoidally varying strains by complex compliances in the same way that static stresses and strains are related by elastic compliances in the linear elastic material. In addition, the time-domain creep compliances are related to frequency-domain complex compliances by Fourier transforms. It is important to note, however, that the complex compliance is not simply equal to the Fourier transform of the corresponding creep compliance. According to Equation 8.69, the complex compliance,  $S_{mn}^*(\omega)$ , is equal to a factor of  $i\omega$  times  $S_{mn}(\omega)$ , and  $S_{mn}(\omega)$  is the Fourier transform of the creep compliance  $S_{mn}(t)$ .

Alternatively, if we substitute sinusoidally varying strains into Equation 8.9, we find that the sinusoidally varying stresses are

$$\tilde{\sigma}_m(t) = C_{mn}^*(\omega) \tilde{\epsilon}_n(t) \quad (8.71)$$

where the complex moduli are defined by

$$C_{mn}^*(\omega) = i\omega C_{mn}(\omega) \quad (8.72)$$

and the  $C_{mn}(\omega)$  are the Fourier transforms of the corresponding relaxation moduli,  $C_{mn}(t)$ . Alternatively, Equations 8.70 and 8.71 may be written in matrix form as

$$\{\tilde{\epsilon}(t)\} = [S^*(\omega)]\{\tilde{\sigma}(t)\} \quad (8.73)$$

and

$$\{\tilde{\sigma}(t)\} = [C^*(\omega)]\{\tilde{\epsilon}(t)\} \quad (8.74)$$

respectively, where the complex compliance matrix and the complex modulus matrix must be related by  $[S^*(\omega)] = [C^*(\omega)]^{-1}$ .

The complex modulus notation not only has a mathematical basis in viscoelasticity theory, but it also has a straightforward physical interpretation. Since the complex modulus is a complex variable, we can write it in terms of its real and imaginary parts as follows:

$$C_{mn}^*(\omega) = C'_{mn}(\omega) + iC''_{mn}(\omega) = C'_{mn}(\omega)[1 + i\eta_{mn}(\omega)] = |C_{mn}^*(\omega)| e^{-i\delta_{mn}(\omega)} \quad (8.75)$$

(no summation on  $m$  and  $n$  in Equation 8.75), where

$C'_{mn}(\omega)$  = storage modulus

$C''_{mn}(\omega)$  = loss modulus

$\eta_{mn}(\omega)$  = loss factor =  $\tan[\delta_{mn}(\omega)] = (C''_{mn}(\omega)/C'_{mn}(\omega))$

$\delta_{mn}(\omega)$  = phase lag between  $\tilde{\sigma}_m(t)$  and  $\tilde{\varepsilon}_n(t)$

Thus, the real part of the complex modulus is associated with elastic energy storage, whereas the imaginary part is associated with energy dissipation, or damping. A physical interpretation of the 1D forms of these equations may be given with the aid of the rotating vector diagram in Figure 8.17. The stress and strain vectors are both assumed to be rotating with angular velocity  $\omega$ , and the physical oscillation is generated by either the horizontal or the vertical projection of the vectors. The complex exponential representations of the rotating stress and strain vectors in the diagram are

$$\tilde{\sigma}(t) = \sigma e^{i(\omega t + \delta)} \quad \text{and} \quad \tilde{\varepsilon}(t) = \varepsilon e^{i\omega t} \quad (8.76)$$

so that the 1D complex modulus is defined as

$$\begin{aligned} C^*(\omega) &= \frac{\tilde{\sigma}(t)}{\tilde{\varepsilon}(t)} = \frac{\sigma e^{i\delta}}{\varepsilon} = \frac{\sigma}{\varepsilon} (\cos \delta + i \sin \delta) = \frac{\sigma'}{\varepsilon} + i \frac{\sigma''}{\varepsilon} \\ &= C'(\omega) + iC''(\omega) = C'(\omega)[1 + i\eta(\omega)] \end{aligned} \quad (8.77)$$

It is seen that the strain lags the stress by the phase angle  $\delta$ ; the storage modulus,  $C'(\omega)$ , is the in-phase component of the stress,  $\sigma'$ , divided by the strain,  $\varepsilon$ ; the loss modulus,  $C''(\omega)$ , is the out-of-phase component of stress,  $\sigma''$ , divided by the strain,  $\varepsilon$ ; and the loss factor,  $\eta(\omega)$ , is the tangent of the phase angle  $\delta$ . Experimental determination of the complex modulus involves the

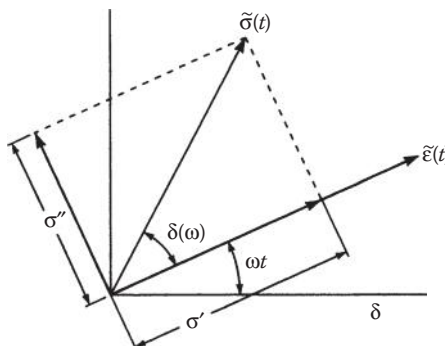


**FIGURE 8.17**

Rotating vector diagram for physical interpretation of the complex modulus.

measurement of the storage modulus,  $C'(\omega)$ , and the loss factor,  $\eta(\omega)$ , as a function of frequency,  $\omega$ ; several techniques for doing this will be described in Chapter 10.

The inverse Fourier transform of the parameter  $S_{mn}(\omega)$  is the creep compliance  $S_{mn}(t)$ , as given by

$$\mathcal{F}^{-1}[S_{mn}(\omega)] = S_{mn}(t) = \frac{1}{2\pi} \int_{-\infty}^{\infty} S(\omega) e^{i\omega t} d\omega \quad (8.78)$$

where  $\mathcal{F}^{-1}$  is the inverse Fourier transform operator. Equations 8.67 and 8.78 form the so-called Fourier transform pair, which makes it possible to transform back and forth between the time domain and the frequency domain [13]. Since experimental frequency data are usually expressed in units of cycles per second, or Hertz, it is convenient to define the frequency as  $f = \omega/2\pi$  (Hz), so that the Fourier transform pair now becomes symmetric in form:

$$\mathcal{F}[S_{mn}(t)] = S_{mn}(f) = \int_{-\infty}^{\infty} S_{mn}(t) e^{-i2\pi ft} dt \quad (8.79)$$

and

$$\mathcal{F}^{-1}[S_{mn}(f)] = S_{mn}(t) = \int_{-\infty}^{\infty} S_{mn}(f) e^{i2\pi ft} df \quad (8.80)$$

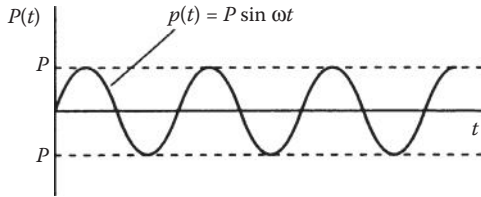
It can be shown that the time-domain relaxation modulus and the corresponding frequency-domain complex modulus are related by a similar Fourier transform pair. As a further indication of the usefulness of such equations, inverse Fourier transforms have been used to estimate time-domain creep behavior of composites from frequency-domain complex modulus data obtained from vibration tests of the same materials [14].

### Example 8.4

The composite pressure vessel described in Examples 2.4 and 8.3 has an internal pressure  $p$  that varies sinusoidally with time, as shown in Figure 8.18. If the complex compliances of the composite material are given by

$$S_{mn}^*(\omega) = S'_{mn}(\omega) + iS''_{mn}(\omega)$$

determine all the time-dependent strains associated with the principal material axes.

**FIGURE 8.18**

Sinusoidally varying pressure for Example 8.4.

**SOLUTION**

From Example 2.4 and Figure 8.18, the stresses along the 12 directions are

$$\tilde{\sigma}_1(t) = 20.5p = 20.5P \sin \omega t \text{ (MPa)}$$

$$\tilde{\sigma}_2(t) = 17.0p = 17.0P \sin \omega t \text{ (MPa)}$$

$$\tilde{\sigma}_6(t) = \tilde{\tau}_{12}(t) = 6.0p = 6.0P \sin \omega t \text{ (MPa)}$$

The corresponding strains from Equation 8.70 are

$$\begin{aligned}\tilde{\epsilon}_1(t) &= S_{11}^*(\omega)\tilde{\sigma}_1(t) + S_{12}^*(\omega)\tilde{\sigma}_2(t) + (0)\tilde{\sigma}_6(t) \\ &= [S'_{11}(\omega) + iS''_{11}(\omega)]20.5P \sin \omega t + [S'_{12}(\omega) + iS''_{12}(\omega)]17.0P \sin \omega t\end{aligned}$$

$$\begin{aligned}\tilde{\epsilon}_2(t) &= S_{12}^*(\omega)\tilde{\sigma}_1(t) + S_{22}^*(\omega)\tilde{\sigma}_2(t) + (0)\tilde{\sigma}_6(t) \\ &= [S'_{12}(\omega) + iS''_{12}(\omega)]20.5P \sin \omega t + [S'_{22}(\omega) + iS''_{22}(\omega)]17.0P \sin \omega t\end{aligned}$$

$$\begin{aligned}\tilde{\epsilon}_6(t) &= \tilde{\gamma}_{12}^*(t) = S_{66}^*(\omega)\tilde{\sigma}_6(t) = S_{66}^*(\omega)\tilde{\tau}_{12}(t) \\ &= [S'_{66}(\omega) + iS''_{66}(\omega)]6.0P \sin \omega t\end{aligned}$$

**Example 8.5**

Derive the equation for the complex modulus of the Kelvin–Voigt spring–dashpot model described in Figure 8.10.

**SOLUTION**

The differential equation for the Kelvin–Voigt model is given by Equation 8.39 as

$$\sigma = k\epsilon + \mu \frac{d\epsilon}{dt}$$

For sinusoidally varying stress and strain, the stress–strain relationship can be expressed as

$$\tilde{\sigma}(t) = \sigma e^{i\omega t} = [E^*(\omega)]\tilde{\epsilon}(t) \quad \text{or} \quad \tilde{\epsilon}(t) = \frac{\sigma e^{i\omega t}}{E^*(\omega)}$$

where  $E^*(\omega)$  is the complex modulus and  $\omega$  is the frequency. Substituting this stress-strain relationship into the differential equation for the Kelvin–Voigt model, we find that

$$\sigma e^{i\omega t} = k \frac{\sigma e^{i\omega t}}{E^*(\omega)} + \mu \frac{i\omega \sigma e^{i\omega t}}{E^*(\omega)}$$

Solving for the complex modulus, we get

$$E^*(\omega) = k + i\omega\mu$$

Note that the creep compliance, the relaxation modulus, and the complex modulus are all expressed in terms of the Kelvin–Voigt model parameters  $k$  and  $\mu$ . Similar relationships can be derived for the other spring–dashpot models.

### 8.2.5 Elastic–Viscoelastic Correspondence Principle

In the previous sections, we have seen a number of examples where the form of the stress–strain relationships for linear viscoelastic materials is the same as that for linear elastic materials. Such analogies between the equations for elastic and viscoelastic analysis have led to the formal recognition of an “Elastic–Viscoelastic Correspondence Principle.” The correspondence principle for isotropic materials was apparently introduced by Lee [15], whereas the application to anisotropic materials was proposed by Biot [16]. The specific application of the correspondence principle to the viscoelastic analysis of anisotropic composites has been discussed in detail by Schapery [1,17] and Christensen [6].

A summary of the correspondences between elastic and viscoelastic stress–strain relationships is given in Table 8.1. The implication of this table is that if we have the necessary equations for a linear elastic solution to a problem, we simply make the corresponding substitutions in the equations to get the corresponding linear viscoelastic solution. Although Table 8.1 is only concerned with the correspondences in the stress–strain relationships, there are obviously other equations involved in a complete solution to an elasticity problem. The correspondences in the equilibrium equations, the strain–displacement relations, the boundary conditions, and the variational methods of elastic analysis are beyond the scope of this book, but detailed discussions of these are given by Schapery [1,17] and Christensen [4,6].

One of the most important implications of the correspondence principle is that analytical models for predicting elastic properties of composites at both the micromechanical and the macromechanical levels can be easily converted for prediction of the corresponding viscoelastic properties. For example, the rule of mixtures for predicting the longitudinal modulus of a unidirectional composite can now be converted for viscoelastic relaxation problems by rewriting Equation 3.27 as

$$E_1(t) = E_{f1}(t)v_f + E_m(t)v_m \quad (8.81)$$

**TABLE 8.1**

Elastic–Viscoelastic Correspondence in Stress–Strain Relationships

Material and Input	Stresses	Strains	Properties	Equation
<i>Linear Elastic</i>				
Input stresses	$\sigma_j$	$\epsilon_i$	$S_{ij}$	(2.5)
Input strains	$\sigma_i$	$\epsilon_j$	$C_{ij}$	(2.3)
<i>Linear Viscoelastic</i>				
Generalized creep	$\bar{\sigma}_j(s)$	$\bar{\epsilon}_i(s)$	$s\bar{S}_{ij}(s)$	(8.50)
Constant stress creep	$\bar{\sigma}'_j$	$\epsilon_i(t)$	$S_{ij}(t)$	(8.60)
Generalized relaxation	$\bar{\sigma}_i(s)$	$\bar{\epsilon}_j(s)$	$s\bar{C}_{ij}(s)$	(8.51)
Constant strain relaxation	$\sigma_i(t)$	$\epsilon'_j$	$C_{ij}(t)$	(8.62)
Sinusoidal stress input	$\tilde{\sigma}_j(t)$	$\tilde{\epsilon}_i(t)$	$S_{ij}^*(\omega)$	(8.70)
Sinusoidal strain input	$\tilde{\sigma}_i(t)$	$\tilde{\epsilon}_j(t)$	$C_{ij}^*(\omega)$	(8.71)

Note:  $i, j = 1, 2, \dots, 6$ .

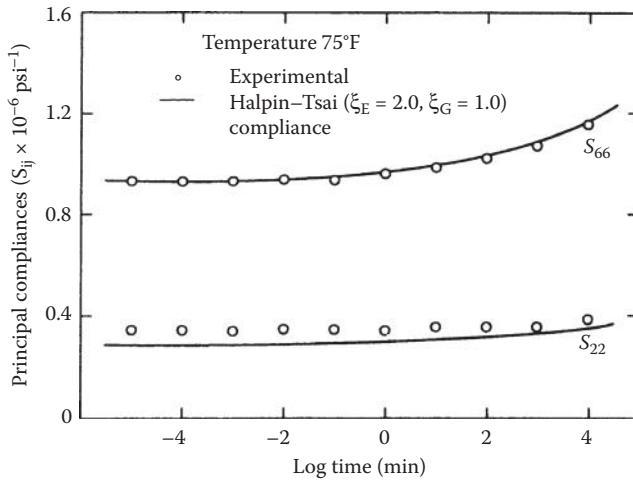
where

 $E_1(t)$  = longitudinal relaxation modulus of composite $E_{f1}(t)$  = longitudinal relaxation modulus of fiber $E_m(t)$  = relaxation modulus of isotropic matrix $v_f$  = fiber volume fraction $v_m$  = matrix volume fraction

The relative viscoelasticity of fiber and matrix materials may make further simplification possible. In most polymer matrix composites, the time dependency of the matrix material would be much more significant than that of the fiber, so the fiber modulus could be assumed to be elastic, and the time dependency of  $E_1(t)$  would be governed by  $E_m(t)$  alone. The results of a similar analysis of the creep compliances  $S_{22}(t)$  and  $S_{66}(t)$  for a glass–epoxy composite are shown in Figure 8.19 from ref. [18]. From these results, it appears that the compliances can be accurately predicted by using the viscoelastic properties of the epoxy matrix in the corresponding viscoelastic forms of the Halpin–Tsai equations (3.63 and 3.64).

And as mentioned earlier, Beckwith [2] showed experimentally that the creep exponent  $n$ , which governs the time dependency in the power-law expression (Equation 8.2), depends only on the polymer matrix.

Similarly, Wen et al. [9] modeled transverse creep compliances of thermoplastic polymer matrix composites by applying the correspondence principle to both the Tsai–Hahn equation (3.66) and finite element micromechanical

**FIGURE 8.19**

Measured and predicted creep compliances for glass–epoxy composite. (From Beckwith, S. W. 1974. *Viscoelastic characterization of a nonlinear glass–epoxy composite including the effects of damage*. PhD Dissertation, Texas A&M University, College Station, TX. With permission.)

models, and agreement with experimental results was shown to be excellent. Gibson et al. [11–12] applied the correspondence principle and finite element models to predict creep in prestressed viscoelastic composite connectors [11], and prestressed viscoelastic composite timing devices for extended interval lubricators [12].

At the macromechanical level, equations such as laminate force–deformation relationships can be converted to viscoelastic form using the correspondence principle. For example, the creep strains in a symmetric laminate under constant in-plane loading can be analyzed by employing the correspondence principle and a quasielastic analysis to rewrite equation 7.63 as

$$\begin{Bmatrix} \varepsilon_x^0(t) \\ \varepsilon_y^0(t) \\ \gamma_{xy}^0(t) \end{Bmatrix} = \begin{bmatrix} A'_{11}(t) & A'_{12}(t) & A'_{16}(t) \\ A'_{12}(t) & A'_{22}(t) & A'_{26}(t) \\ A'_{16}(t) & A'_{26}(t) & A'_{66}(t) \end{bmatrix} \begin{Bmatrix} N_x \\ N_y \\ N_{xy} \end{Bmatrix} \quad (8.82)$$

where

$A'_{ij}(t)$  = laminate creep compliances

$N_x, N_y, N_{xy}$  = constant loads

Sims and Halpin [19] have used these equations, along with uniaxial creep tests, to determine the creep compliances of glass/epoxy laminates for

comparison with predictions. For example, the compliance  $A'_{11}(t)$  was determined by applying a constant load  $N_x$  and by measuring the creep strain,  $\varepsilon_x^0(t)$ , and then using the equation

$$A'_{11}(t) = \frac{\varepsilon_x^0(t)}{N_x} \quad (8.83)$$

These measured values were compared with predicted values from a combined micromechanics–macromechanics analysis that was based on the use of the correspondence principle, the Halpin–Tsai equations, and CLT. The agreement between measurements and predictions was excellent, as shown in Figure 8.20.

When the correspondence principle is used for problems involving sinusoidally varying stresses and strains in viscoelastic composites, we must be particularly careful to make sure that the criteria for using the effective modulus theory are met. These restrictions are discussed in more detail, and applications of the correspondence principle to the prediction of complex moduli of particle and fiber composites are given in papers by Hashin [20, 21]. For example, assuming that these criteria have been met, micromechanics equations such as Equation 3.27 can be modified for the case of sinusoidal oscillations as

$$E_1^*(\omega) = E_{f1}^*(\omega)v_f + E_m^*(\omega)v_m \quad (8.84)$$

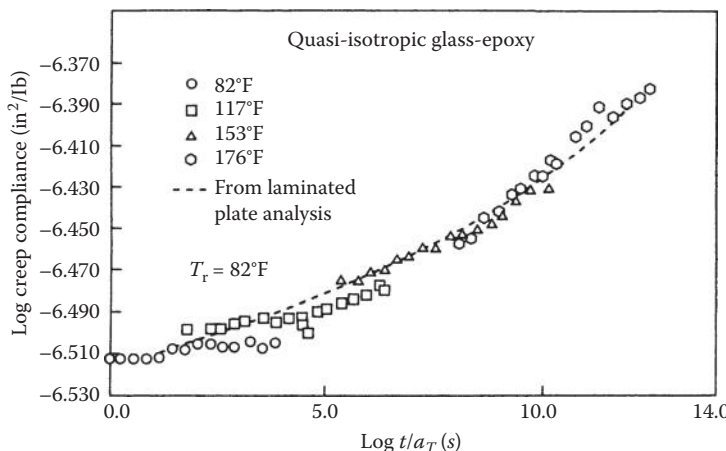


**FIGURE 8.20**

Predicted and measured creep compliance for a quasi-isotropic glass/epoxy laminate. (Reprinted from Sims, D. F. and Halpin, J. C. 1974. *Composite Materials: Testing and Design (Third Conference)*, ASTM 546. American Society for Testing and Materials, Philadelphia, PA, pp. 46–66. Copyright ASTM. With permission.)

where

$E_1^*(\omega)$  = longitudinal complex modulus of composite

$E_{fl}^*(\omega)$  = longitudinal complex modulus of fiber

$E_m^*(\omega)$  = complex modulus of isotropic matrix

By setting the real parts of both sides of Equation 8.84 equal, we find the composite longitudinal storage modulus to be

$$E'_1(\omega) = E'_{fl}(\omega)v_f + E'_m(\omega)v_m \quad (8.85)$$

where

$E'_1(\omega)$  = longitudinal storage modulus of composite

$E'_{fl}(\omega)$  = longitudinal storage modulus of fiber

$E'(\omega)$  = storage modulus of isotropic matrix

Similarly, by setting the imaginary parts of both sides of Equation 8.84 equal, we find that the composite longitudinal loss modulus is

$$E''_1(\omega) = E''_{fl}(\omega)v_f + E''_m(\omega)v_m \quad (8.86)$$

where

$E''_1(\omega)$  = longitudinal loss modulus of composite

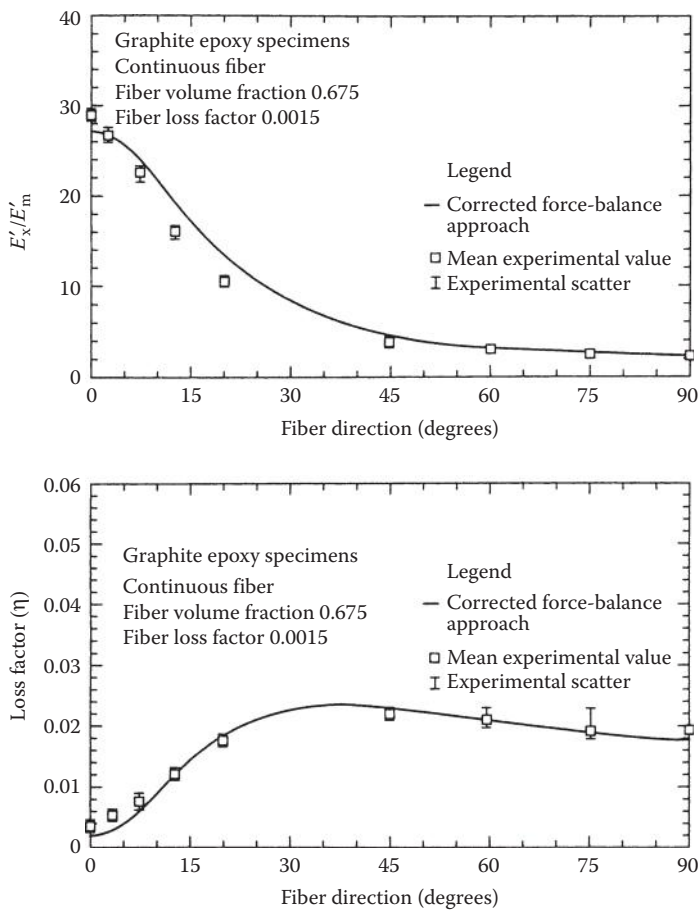
$E''_{fl}(\omega)$  = longitudinal loss modulus of fiber

$E''_m(\omega)$  = loss modulus of isotropic matrix

The composite longitudinal loss factor is found by dividing Equation 8.86 by Equation 8.85:

$$\eta_1(\omega) = \frac{E''_1(\omega)}{E'_1(\omega)} = \frac{E''_{fl}(\omega)v_f + E''_m(\omega)v_m}{E'_{fl}(\omega)v_f + E'_m(\omega)v_m} \quad (8.87)$$

The complex forms of the other lamina properties can be determined in a similar fashion. In studies of the complex moduli of aligned discontinuous fiber composites, Suarez et al. [22] used the complex forms of Equations 6.24, 3.45 and 3.63 to determine  $E_1^*(\omega)$ ,  $v_{12}^*(\omega)$ ,  $E_2^*(\omega)$ , and  $G_{12}^*(\omega)$ . These properties were then substituted into the complex form of Equation 2.40 to obtain the off-axis complex modulus,  $E_x^*(\omega)$ . The predicted off-axis storage moduli and loss factors for various fiber orientations are compared with experimental data for a continuous fiber graphite–epoxy composite in Figure 8.21, and the agreement is seen to be quite reasonable. Similar results were obtained for discontinuous fiber composites, but the fiber length effect is dominated by the fiber orientation effect, except for fiber orientations of  $\theta \approx 0^\circ$ . It is also interesting to note that there is an optimum fiber orientation for maximizing the loss factor. Thus damping is another design variable in composite structures.

**FIGURE 8.21**

Predicted and measured off-axis storage modulus ratio,  $E'_x/E'_m$  and loss factor,  $\eta'$ , of graphite/epoxy for various fiber orientations. (From Suarez, S. A. et al. 1986. *Experimental Mechanics*, 26(2), 175–184. With permission.)

For oscillatory loading of symmetric viscoelastic laminates, Equation 7.63 can be rewritten, so that the sinusoidally varying strains are related to the sinusoidally varying loads by

$$\begin{Bmatrix} \tilde{\epsilon}_x^0(t) \\ \tilde{\epsilon}_y^0(t) \\ \tilde{\gamma}_{xy}^0(t) \end{Bmatrix} = \begin{bmatrix} A_{11}^{*}(\omega) & A_{12}^{*}(\omega) & A_{16}^{*}(\omega) \\ A_{12}^{*}(\omega) & A_{22}^{*}(\omega) & A_{26}^{*}(\omega) \\ A_{16}^{*}(\omega) & A_{26}^{*}(\omega) & A_{66}^{*}(\omega) \end{bmatrix} \begin{Bmatrix} \tilde{N}_x(t) \\ \tilde{N}_y(t) \\ \tilde{N}_{xy}(t) \end{Bmatrix} \quad (8.88)$$

where  $A_{ij}^{**}(\omega)$  are the laminate complex extensional compliances. The laminate stiffnesses can also be written in complex form (i.e., the  $A_{ij}^*(\omega)$ ,  $B_{ij}^*(\omega)$ , and  $D_{ij}^*(\omega)$ ), and the resulting equations have been used by Sun et al. [23] and others in studies of damping in laminates. Damping in composites will be discussed in more detail later in this chapter.

### Example 8.6

Using the Elastic–Viscoelastic Correspondence Principle, set up a micromechanics model for predicting the transverse creep compliance,  $S_{22}(t)$ , of a unidirectional composite which consists of linear elastic isotropic fibers in a linear viscoelastic isotropic polymer matrix.

#### SOLUTION

One approach is to start with a micromechanics equation for the transverse elastic modulus such as the semiempirical Tsai–Hahn equation (3.66)

$$\frac{1}{E_2} = \frac{1}{v_f + \eta_2 v_m} \left[ \frac{v_f}{E_f} + \frac{\eta_2 v_m}{E_m} \right]$$

Converting this equation to compliances,

$$S_{22} = \frac{1}{v_f + \eta_2 v_m} [S_f v_f + \eta_2 v_m S_m]$$

where  $S_f = 1/E_f$ ,  $S_m = 1/E_m$ , and  $S_{22} = 1/E_2$  are the elastic compliances of fiber, matrix, and transverse composite materials, respectively. Now using the correspondence principle and the assumption that the fibers are elastic while the matrix is viscoelastic, the equation for the transverse creep compliance of the composite is

$$S_{22}(t) = \frac{1}{v_f + \eta_2 v_m} [S_f v_f + \eta_2 v_m S_m(t)]$$

where  $S_m(t)$  is the creep compliance of the viscoelastic matrix material, which would need to be measured in a creep test of the pure matrix material. Creep testing will be discussed in more detail in Chapter 10.

#### 8.2.6 Temperature and Aging Effects

In the previous sections of this chapter the effects of temperature and aging on viscoelastic behavior have not been taken into account. We now consider these effects, as well as the corresponding methods of analysis. It is convenient to discuss first the effects of temperature. In Section 8.2.2, a thermorheologically simple material was defined as having relaxation times,  $\lambda_i$ , and

retardation times,  $\rho_i$ , which all have the same temperature dependence. Considering only the temperature dependence, the relaxation times at different temperatures can then be related by the equation

$$\lambda_i(T) = a_T \lambda_i(T_r) \quad (8.89)$$

where

$\lambda_i(T)$  =  $i$ th relaxation time at temperature  $T$

$\lambda_i(T_r)$  =  $i$ th relaxation time at reference temperature,  $T_r$

$a_T$  = temperature-dependent shift factor

A similar equation can be used to express the temperature dependence of the retardation times. The effect of increasing temperature is to reduce the relaxation and retardation times and to speed up the relaxation and creep processes. This “speeding up” of the viscoelastic response can also be thought of as a process operating in “reduced time” [24]. For the purpose of illustration, we now consider the effect of the temperature-dependent relaxation times on the relaxation modulus by using the Zener single-relaxation model in Figure 8.11. The relaxation modulus at time  $t$  and temperature  $T$  is determined by modifying Equation 8.44 as

$$C(t, T) = k_0 + k_1 e^{-t/\lambda_1(T)} \quad (8.90)$$

whereas the relaxation modulus at time  $t$  and reference temperature  $T_r$  is

$$C(t, T_r) = k_0 + k_1 e^{-t/\lambda_1(T_r)} \quad (8.91)$$

If we let the time at the reference temperature  $T_r$  be the “reduced time,”

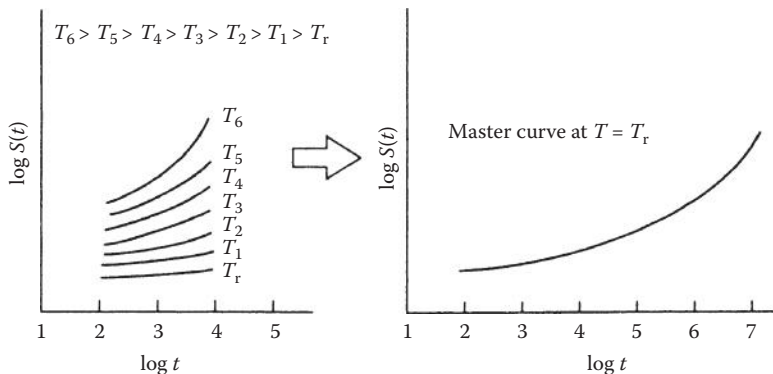
$$\xi = \frac{t}{a_T} \quad (8.92)$$

then Equation 8.91 becomes

$$C(\xi, T_r) = k_0 + k_1 e^{-t/a_T \lambda_1(T_r)} = k_0 + k_1 e^{-t/\lambda_1(T)} = C(t, T) \quad (8.93)$$

Thus, the effect of changing temperature on the relaxation modulus is the same as the effect of a corresponding change in the timescale, and this is the basis of the well-known TTS Principle, or the method of reduced variables [25].

One of the most useful applications of TTS is to extend the time range of short-term creep or relaxation test data by taking such data at various temperatures and then shifting the data along the time axis to form a “master curve” at a reference temperature, as shown in Figure 8.22. However, the

**FIGURE 8.22**

Shifting of creep data at various temperatures to generate a master curve at a reference temperature.

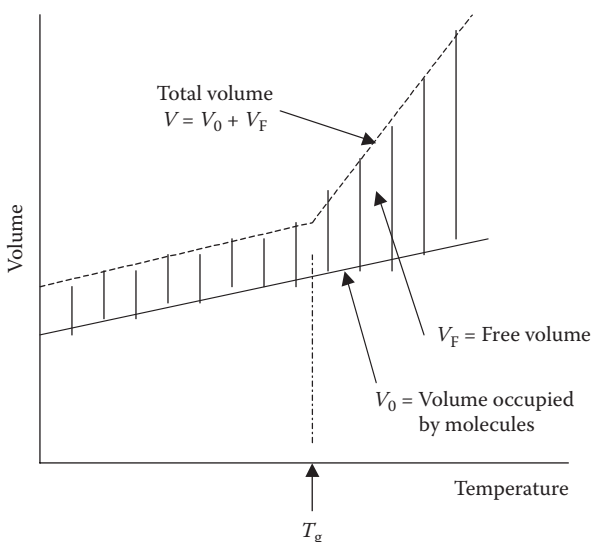
usefulness of the method depends on the ability to determine the shift factor,  $a_T$ . When the temperature,  $T$ , is greater than the glass transition temperature,  $T_g$ , the shift factor can be determined empirically with the well-known Williams–Landel–Ferry (WLF) equation [25]:

$$\log a_T = \frac{-c_1(T - T_r)}{c_2 + (T - T_r)} \quad (8.94)$$

where  $c_1$  and  $c_2$  are material constants that must be determined from the experimental data. It has been found that when  $T_r$  is approximately 50°C above  $T_g$ , the values  $c_1 = 8.86$  and  $c_2 = 101.6\text{K}$  are valid for a variety of polymers.

TTS has been successfully applied to many polymers at temperatures above  $T_g$ , but it is a different matter below the glass transition. Although TTS has been shown to be suitable for short-term creep or relaxation data at those temperatures, it does not produce valid results when applied to long-term test data. The reason is that a process called “physical aging” occurs in a polymer below  $T_g$ , and this aging process changes the viscoelastic response of the material during a long-term creep test. In a short-term test, because the test duration is much less than the aging time, no significant aging occurs during the test. Physical aging in polymers is associated with a slow loss of free volume that has been trapped in the polymer microstructure after quenching below  $T_g$  [26]. As shown in Figure 8.23, as the temperature of a polymer increases, its total volume consists of  $V_0$ , the volume occupied by the polymer molecules, and  $V_F$ , the so-called free volume between the molecules.

Below the glass transition temperature  $T_g$ , most of the total volume is occupied by the molecules, but as the temperature increases above  $T_g$ ,  $V_F$  increases

**FIGURE 8.23**

Polymer volume expansion with increasing temperature, showing how free volume increases sharply above the glass transition temperature.

much faster than  $V_0$ . The polymer is usually processed in its molten form at temperatures above  $T_g$ ; then when it is cooled or quenched to room temperature after molding, a significant amount of free volume is “locked in.” This is a thermodynamically unstable condition, and as a result, the polymer will slowly give up free volume with time, to approach a more stable thermodynamic condition. As the polymer gives up free volume, the polymer chain mobility decreases and the relaxation times increase, thus reducing the speed of the relaxation or creep [7]. Pioneering work on aging of polymers has been done by Struik [26, 27], and more recent work has been reported by Janas and McCullough [28] and Ogale and McCullough [29]. Still more recently, Sullivan [30] has shown that physical aging significantly affects the creep behavior of polymer matrix composites.

Since aging time,  $t_a$ , and temperature,  $T$ , both affect the relaxation times, Sullivan [30] has suggested that a new shift factor,  $a(T, t_a)$ , be defined by modifying Equation 8.89 as

$$a = a(T, t_a) = \frac{\lambda_i(T, t_a)}{\lambda_i(T_r, t_{ar})} \quad (8.95)$$

where

$\lambda_i(T, t_a)$  =  $i$ th relaxation time at temperature  $T$  and aging time  $t_a$

$\lambda_i(T_r, t_{ar})$  =  $i$ th relaxation time at reference temperature  $T_r$  and reference aging time  $t_{ar}$

Struik [26] proposes that the TTS relationship for creep compliance be modified to include aging time effects by writing

$$S(t, T, t_a) = B(T)S(at, T_r, t_{ar}) \quad (8.96)$$

where

$B(T)$  = temperature-dependent vertical shift factor

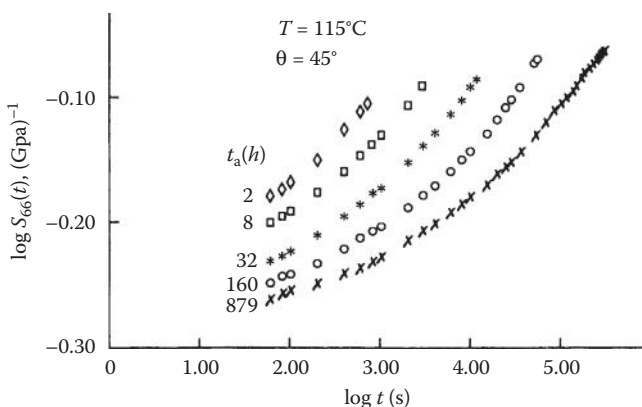
$S(t, T, t_a)$  = creep compliance at time  $t$ , temperature  $T$ , and aging time  $t_a$

$S(at, T_r, t_{ar})$  = creep compliance at shifted time  $at$ , reference temperature  $T_r$ , and reference aging time  $t_{ar}$

Note that Equation 8.96 is analogous to the TTS relationship for relaxation in Equation 8.93, and a modified equation similar to Equation 8.96 can be written for relaxation. This new shift factor may be related to  $\bar{a}_r$ , the temperature shift factor below  $T_g$ , and  $a_{ta}$ , the shift factor for aging time, by the equation [30]

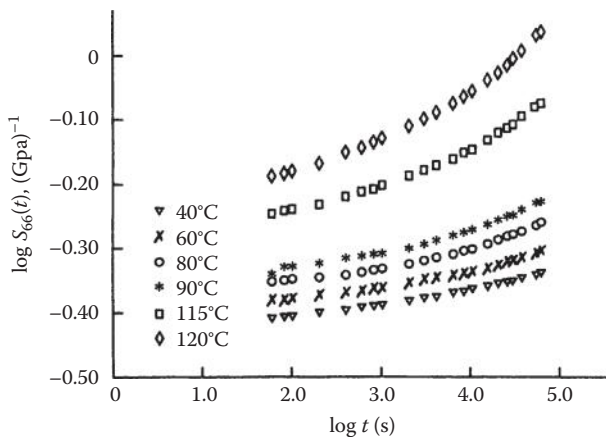
$$\log a = \log \bar{a}_r + \log a_{ta} \quad (8.97)$$

Figure 8.24 shows Sullivan's data on the effect of aging time on the shear creep compliance  $S_{66}(t)$  of a glass-vinyl ester composite [30]. Clearly, the creep rate decreases with increased aging time, indicating an increase in the relaxation times and a slowing of the creep process. Support for the conclusion that TTS works well for short-term creep at constant age is provided by additional data from Sullivan [30] in Figures 8.25 and 8.26. Figure 8.25 shows the short-term (or momentary) creep at various temperatures and "constant age,"



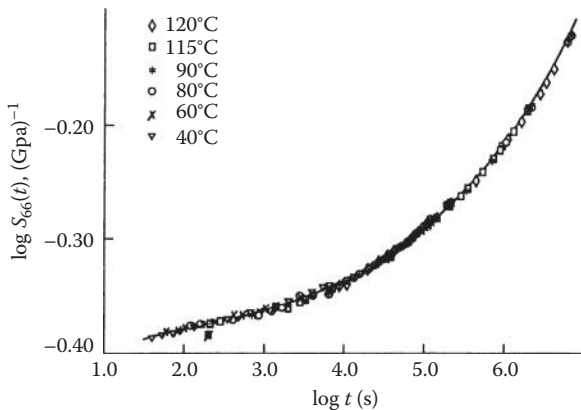
**FIGURE 8.24**

Effect of aging time,  $t_a$ , on shear creep compliance of 45° off-axis glass-vinyl ester composite at a test temperature of 115°C. (Reprinted from Sullivan, J. L. 1990. *Composites Science and Technology*, 39, 207–232. With permission from Elsevier Science Publishers, Ltd.)

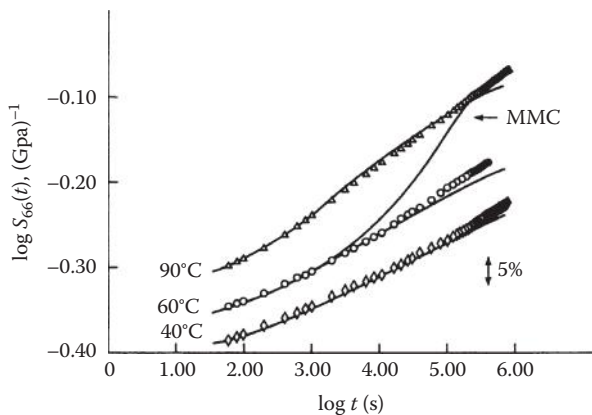
**FIGURE 8.25**

Momentary shear creep compliance data for glass–vinyl ester composite at various temperatures and constant aging time,  $t_a = 166$  h. (Reprinted from Sullivan, J. L. 1990. *Composites Science and Technology*, 39, 207–232. With permission from Elsevier Science Publishers, Ltd.)

where the creep testing time is limited to no more than 10% of the aging time used in preconditioning the specimens. Figure 8.26 shows the corresponding momentary master curve at a reference temperature of 60°C. Both horizontal and vertical shifting of the momentary creep data were necessary to obtain the master curve [30]. The difference between long-term creep curves and the master curve from momentary creep data is shown in Figure 8.27. Again, the conclusion is that aging slows down the creep process and that TTS does not work for long-term creep. Also shown in Figure 8.27 are predicted long-term

**FIGURE 8.26**

Momentary master curve for glass–vinyl ester composite at  $t_a = 166$  h,  $T_r = 60^\circ\text{C}$ , based on the test data from Figure 8.25. (Reprinted from Sullivan, J. L. 1990. *Composites Science and Technology*, 39, 207–232. With permission from Elsevier Science Publishers, Ltd.)

**FIGURE 8.27**

Long-term shear creep compliance and a momentary master curve for glass–vinyl ester composite,  $t_a = 1$  h. Also shown are predicted curves from the effective time theory, which is not discussed here. (Reprinted from Sullivan, J. L. 1990. *Composites Science and Technology*, 39, 207–232. With permission from Elsevier Science Publishers, Ltd.)

creep curves based on effective time theory [30], which is not discussed here.

In conclusion, the reader is encouraged to refer to journal review articles for more information on various aspects of viscoelastic behavior of composites. For example, Schapery [1] has summarized the theoretical approaches to modeling of viscoelastic behavior of composites, and Scott et al. [31] have published a useful review of the technical literature on creep of fiber-reinforced composites.

### Example 8.7

The momentary master curve for the shear creep compliance,  $S_{66}(t)$ , of a unidirectional glass–vinyl ester composite at a reference temperature of 60°C and a reference aging time of 166 h is shown on a log–log scale in Figure 8.26. (a) Neglecting aging effects, determine the time required to reach compliance of 0.63 GPa<sup>-1</sup> at a temperature of 60°C, and (b) neglecting vertical shifting, estimate the time required to reach the same compliance of 0.63 GPa<sup>-1</sup> at a temperature of 100°C. From experimental data, it is known that for this material, the WLF parameters are  $c_1 = -1.01$  and  $c_2 = -89.2$ .

### SOLUTION

- From Figure 8.26, at a value of  $\log S_{66}(t) = \log(0.63) = 0.2$ , the corresponding value from the curve is  $\log t = 6$ , and so  $t = 10^6$  s at  $T = 60^\circ\text{C}$ .
- From Equation 8.96, we have

$$S_{66}(t, T, t_a) = B(T)S_{66}(at, T_r, t_{ar})$$

Since we neglect vertical shifting,  $B(t) = 1$ . Since the data are for a constant aging time, we have  $a = a_T$  and Equation 8.96 becomes

$$S_{66}(t, T) = S_{66}(at, T_r) = S_{66}(a_T t, T_r)$$

where the shift factor,  $a_T$ , is found from the WLF equation

$$\log a_T = \frac{-c_1(T - T_r)}{c_2 + (T - T_r)} = \frac{-(-1.01)(100 - 60)}{-89.2 + (100 - 60)} = -0.8211$$

or  $a_T = 0.151$ , which means that  $a_T t = 0.151(10^6) = 1.51 \times 10^5$  s. Thus, the creep compliance curve at 100°C is shifted to the left of the curve at the reference temperature of 60°C, and it takes only 15% as much time to reach the compliance of 0.63 GPa<sup>-1</sup> at 100°C as it does at 60°C.

### 8.3 Dynamic Behavior of Composites

In this section, the basic concepts of dynamic behavior of composites will be introduced by discussing wave propagation, vibration, and damping of specially orthotropic composites without coupling. Only 1D wave propagation without dispersion, reflection, or refraction will be considered, as 3D wave propagation, wave dispersion, and reflection/refraction effects are beyond the scope of this book. For detailed discussions on these topics, the reader is referred to publications by Christensen [4], Hearmon [32], Achenbach [33], Ross and Sierakowski [34], and Moon [35]. Longitudinal vibrations of composite bars and flexural vibrations of composite beams and plates without coupling will also be considered. Vibrations of laminates with coupling and laminated plate boundary conditions other than the simply supported ones will not be emphasized. These topics are discussed in detail in books by Whitney [36], Vinson and Sierakowski [37], and Sierakowski and Chaturvedi [38]. The use of the Elastic–Viscoelastic Correspondence Principle and a strain energy method to analyze damping in composites will also be discussed.

The basic premise of all analyses presented in this section is that the criteria for valid use of the effective modulus theory have been met. That is, the scale of the inhomogeneity,  $d$ , is assumed to be much smaller than the characteristic structural dimension,  $L$ , and the characteristic wavelength of the dynamic stress distribution,  $\lambda$  ( $d \ll L$  and  $d \ll \lambda$  in Figure 8.7). Thus, all heterogeneous composite material properties are assumed to be effective properties of equivalent homogeneous materials. If the wavelength is not long in comparison with the scale of the inhomogeneity in the material, the wave shape is distorted as it travels through the material, and this is referred to as dispersion. Dispersion in composites has been discussed in several previous publications [4,33,35,38].

### 8.3.1 Longitudinal Wave Propagation and Vibrations in Specially Orthotropic Composite Bars

As will be shown in any book on vibrations [39], longitudinal wave propagation and vibration in a homogeneous, isotropic, linear elastic bar (Figure 8.28) are governed by the 1D wave equation

$$\frac{\partial}{\partial x} \left( AE \frac{\partial u}{\partial x} \right) = \rho A \frac{\partial^2 u}{\partial t^2} \quad (8.98)$$

where

$x$  = distance from the end of the bar

$t$  = time

$u = u(x,t)$  is the longitudinal displacement of a cross section in the bar at a distance  $x$  and time  $t$

$A = A(x)$  is the cross-sectional area of the bar

$\rho$  = mass density of the bar

$E = E(x)$  is the modulus of elasticity of the bar

It is assumed that the displacement  $u(x,t)$  is uniform across a given cross section. Using effective modulus theory for a heterogeneous, specially orthotropic, linear elastic composite bar, we simply replace the properties  $\rho$  and  $E$  with the corresponding effective properties of an equivalent homogeneous material. The effective modulus  $E$  then depends on the orientation of fibers relative to the axis of the bar. For fibers oriented along the  $x$ -direction,  $E = E_1$ ; for fibers oriented along the transverse direction,  $E = E_2$ ; and for a specially orthotropic laminate, we use the effective laminate engineering constant  $E = E_x$ . For laminates with coupling, the analysis is much more difficult, as shown in Section 8.3.3. If the area and the modulus are not functions of position,  $x$ , Equation 8.98 reduces to

$$c^2 \frac{\partial^2 u}{\partial x^2} = \frac{\partial^2 u}{\partial t^2} \quad (8.99)$$

where  $c = \sqrt{E/\rho}$  is the wave speed.

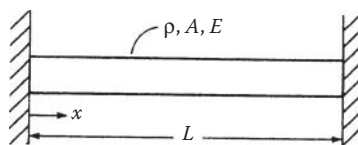


**FIGURE 8.28**

Bar of density  $\rho$ , cross-sectional area  $A$ , modulus  $E$ , and length  $L$ , fixed on both ends.

The most common solutions to the 1D wave equation are of the d'Alembert type or the separation of variables type. The d'Alembert solution is of the form

$$u(x,t) = p(x + ct) + q(x - ct) \quad (8.100)$$

The function  $p(x + ct)$  represents a wave traveling to the left with velocity  $c$ . That is, a point located at  $\xi = x + ct$  moves to the left with velocity  $c$  if  $\xi$  is a constant, since  $x = \xi - ct$ . Similarly,  $q(x - ct)$  represents a wave traveling to the right with velocity  $c$ . For a sine wave, we have

$$u(x,t) = A \sin \frac{2\pi}{\lambda} (x + ct) + A \sin \frac{2\pi}{\lambda} (x - ct) \quad (8.101)$$

where  $\lambda$  is the wavelength. Note that this is the wavelength that must be greater than the scale of the inhomogeneity,  $d$ , in order for the effective modulus theory to be valid. Alternatively, we can write Equation 8.101 as

$$u(x,t) = A \sin(2\pi kx + \omega t) + A \sin(2\pi kx - \omega t) \quad (8.102)$$

where

$k = 1/\lambda$  = wave number = the number of wavelengths per unit distance  
 $\omega = 2\pi c/\lambda$  = frequency of the wave

Using trigonometric identities, we find that

$$u(x,t) = 2A \sin 2\pi kx \cos \omega t \quad (8.103)$$

which represents a standing wave of profile  $2A \sin 2\pi kx$ , which oscillates with frequency  $\omega$ . Generally, the combined wave motion in opposite directions is caused by reflections from the boundaries. Thus, wave propagation without reflection will not lead to a standing wave (or vibration).

A separation of variables solution is found by letting

$$u(x,t) = U(x)F(t) \quad (8.104)$$

where  $U(x)$  is a function of  $x$  alone and  $F(t)$  is a function of  $t$  alone. Substituting this solution into Equation 8.99 and separating variables, we obtain

$$c^2 \frac{1}{U} \frac{d^2 U}{dx^2} = \frac{1}{F} \frac{d^2 F}{dt^2} \quad (8.105)$$

The left-hand side of Equation 8.105 is a function of  $x$  alone and the right-hand side is a function of  $t$  alone; therefore, each side must be equal to a

constant. If we let this constant be, say,  $-\omega^2$ , then Equation 8.105 gives the two ordinary differential equations,

$$\frac{d^2F}{dt^2} + \omega^2 F = 0 \quad (8.106a)$$

$$\frac{d^2U}{dx^2} + \left(\frac{\omega}{c}\right)^2 U = 0 \quad (8.106b)$$

and the solutions to these equations are of the form

$$F(t) = A_1 \sin \omega t + B_1 \cos \omega t \quad (8.107)$$

$$U(x) = A_2 \sin\left(\frac{\omega}{c}\right)x + B_2 \cos\left(\frac{\omega}{c}\right)x \quad (8.108)$$

where  $A_1$  and  $B_1$  depend on the initial conditions, and  $A_2$  and  $B_2$  depend on the boundary conditions. For a bar that is fixed at both ends (Figure 8.28), the substitution of the boundary conditions  $u(0,t) = u(L,t) = 0$  leads to the conclusion that  $B_2 = 0$  and

$$\sin\left(\frac{\omega}{c}\right)L = 0 \quad (8.109)$$

Equation 8.109 is the eigenvalue equation, which has an infinite number of solutions,  $\omega_n$ , such that

$$\frac{\omega_n L}{c} = n\pi \quad (8.110)$$

where

$n$  = mode number = 1, 2, 3, ...,  $\infty$

$\omega_n$  = eigenvalues, or natural frequencies (rad/s) =  $2\pi f_n$

$f_n$  = natural frequencies (Hz)

Thus,

$$f_n = \frac{nc}{2L} = \frac{n}{2L} \left(\frac{E}{\rho}\right)^{1/2} \quad (8.111)$$

For the  $n$ th mode of vibration, the displacements are then

$$u_n(x,t) = (A' \sin \omega_n t + B' \cos \omega_n t) \sin\left(\frac{n\pi x}{L}\right) \quad (8.112)$$

where  $A' = A_1 A_2$  and  $B' = B_1 A_2$ . The mode shape for the  $n$ th mode is given by the eigenfunction

$$U_n(x) = \sin\left(\frac{n\pi x}{L}\right) \quad (8.113)$$

and the general solution is the superposition of all modal responses

$$u(x,t) = \sum_{n=1}^{\infty} (A' \sin \omega_n t + B' \cos \omega_n t) \sin\left(\frac{n\pi x}{L}\right) \quad (8.114)$$

Mode shapes, natural frequencies, and wavelengths for the first three modes of the fixed-fixed bar are shown in Figure 8.29. An important point is that as the mode number increases, the wavelength decreases and the use of effective modulus theory becomes more questionable. In general, the wavelengths associated with typical mechanical vibration frequencies of structures in the audio frequency range will satisfy the effective modulus criterion  $d \ll \lambda$ . However, the wavelengths associated with ultrasonic wave propagation may be short enough to cause concern about the use of effective modulus theory.

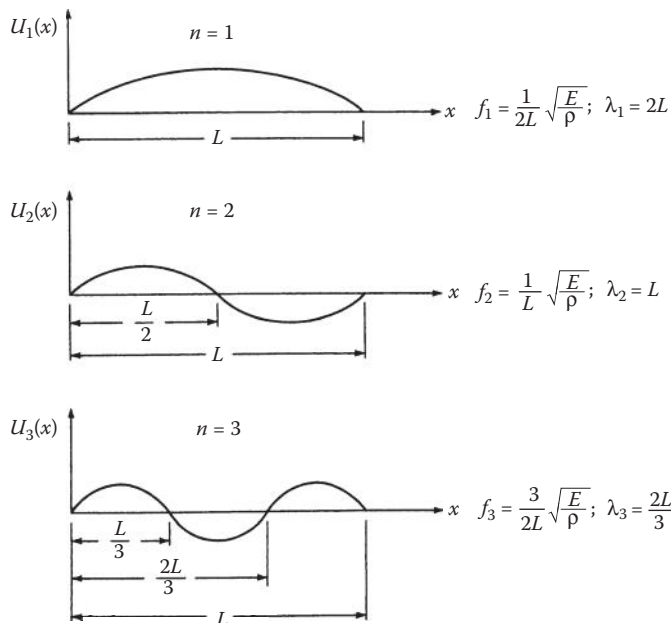


**FIGURE 8.29**

Mode shapes, natural frequencies, and wavelengths for the first three modes of longitudinal vibration of a bar with both ends fixed (Figure 8.28).

Validation of the application of effective modulus theory to the 1D wave equation has been demonstrated. For example, a comparison of measured and predicted wave speeds in unidirectional stainless-steel filament-reinforced epoxy rods was reported by Ross and Sierakowski [34] and Sierakowski and Chaturvedi [38]. Figure 8.30 shows drawings of the (a) longitudinal and (b) transverse composite rod specimens. Stress waves in the specimens were induced by using a gas gun to propel short epoxy striker rods against one end of the specimens, and strain gages separated by known distances were used to measure the wave speeds. Stress wavelengths were much greater than the diameters of the filaments, so the use of effective modulus theory was valid. The predicted longitudinal wave speeds,  $c_1$ , were calculated from the 1D wave speed equation, the rule of mixtures for the longitudinal modulus, and the corresponding rule of mixtures for composite density as

$$c_1 = \sqrt{\frac{E_1}{\rho_c}} = \sqrt{\frac{E_f v_f + E_m v_m}{\rho_f v_f + \rho_m v_m}} \quad (8.115)$$

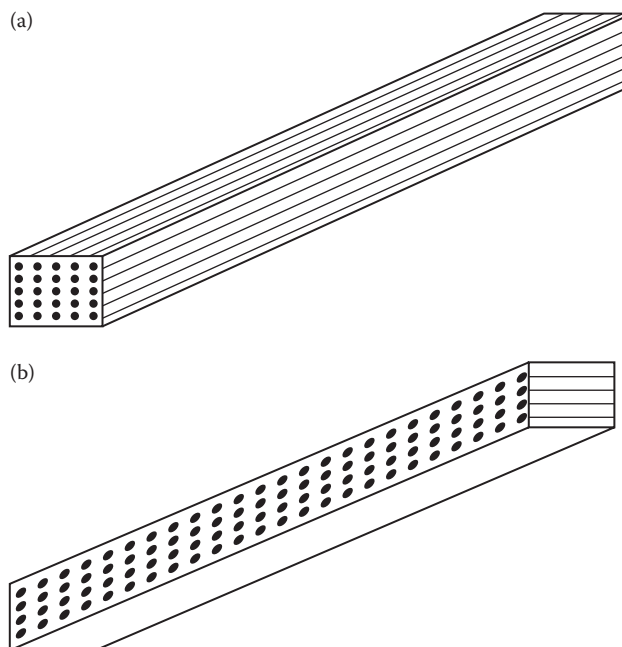


**FIGURE 8.30**

Unidirectional composite rods with longitudinal (a) and transverse (b) filaments. (From Sierakowski, R. L. and Chaturvedi, S. K., 1997, *Dynamic Loading and Characterization of Fiber-Reinforced Composites*, John Wiley & Sons, Inc. With permission.)

while the transverse wave speeds,  $c_2$ , were calculated from the 1D wave speed equation, the semiempirical Halpin-Tsai equations for transverse modulus and the rule of mixtures for composite density as

$$c_2 = \sqrt{\frac{E_2}{\rho_c}} = \sqrt{\frac{E_m(1 + \xi\eta v_f)}{(1 - \eta v_f)(\rho_f v_f + \rho_m v_m)}} \quad (8.116)$$

where

$$\eta = \frac{(E_f/E_m) - 1}{(E_f/E_m) + \xi} \quad (8.117)$$

and the Halpin-Tsai parameter was assumed to be  $\xi = 2$  as mentioned in Section 3.5. Measured and predicted wave speeds for composites having several fiber volume fractions and fiber diameters show good agreement, as shown in Figure 8.31.

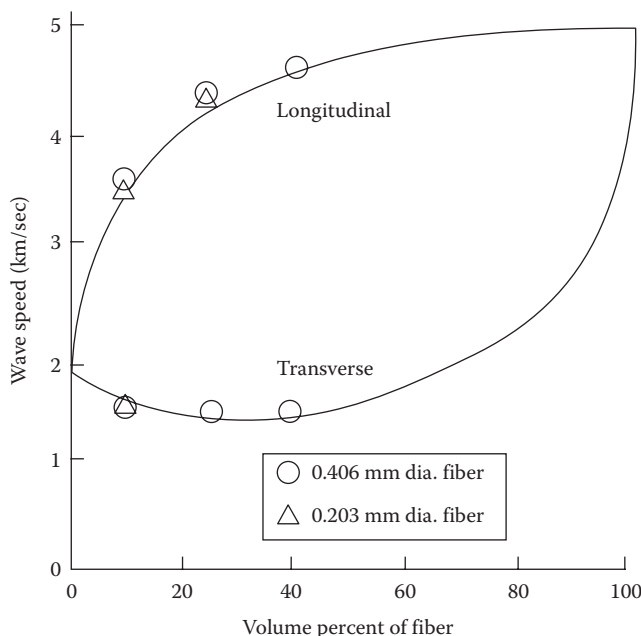


**FIGURE 8.31**

Comparison of predicted and measured longitudinal and transverse wave speeds for stainless-steel filament reinforced epoxy rods. (From Sierakowski, R. L. and Chaturvedi, S. K., 1997, *Dynamic Loading and Characterization of Fiber-Reinforced Composites*, John Wiley & Sons, Inc. With permission.)

The equations developed in this section are instructive not only from the point of view of the limitations of effective modulus theory, but for material characterization as well. The two basic approaches to measurement of dynamic mechanical properties of materials involve the use of either wave propagation experiments or vibration experiments. Assuming that the criteria for the use of effective modulus theory have been met, the effective modulus of a specially orthotropic composite can be determined by measuring the longitudinal wave speed,  $c$ , in a specimen of density,  $\rho$ , and then solving for  $E = c^2\rho$ . Alternatively, the  $n$ th mode natural frequency,  $f_n$ , can be measured in a vibration experiment, and the effective modulus can be found from an equation such as Equation 8.111. Dynamic mechanical testing of composites will be discussed in more detail in Chapter 10.

Finally, the equations presented here can be modified for linear viscoelastic composites in sinusoidal vibration by using the Elastic Viscoelastic Correspondence Principle. This means that the effective modulus  $E$  will be replaced by the complex modulus  $E^*(\omega)$ . Alternatively, the stress-strain relationship used in deriving the equation of motion could be an equation of the form shown in Equation 8.28 or a special case of that equation.

### 8.3.2 Flexural Vibration of Composite Beams

Transverse, or flexural, motion of a homogeneous, isotropic, linear elastic beam (Figure 8.32) without shear or rotary inertia effects is described by the well-known Bernoulli–Euler equation

$$-\frac{\partial^2}{\partial x^2} \left( EI \frac{\partial^2 w}{\partial x^2} \right) = \rho A \frac{\partial^2 w}{\partial t^2} \quad (8.118)$$

where

$I$  = area moment of inertia of the cross section about the centroidal axis of the beam

$w = w(x, t)$  is the transverse displacement of the centroidal axis of the beam

$x, t, \rho, A$ , and  $E$  are as defined in Equation 8.98

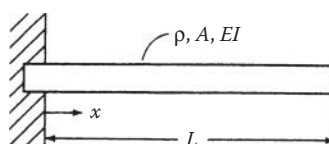


**FIGURE 8.32**  
Cantilever beam for the Bernoulli–Euler beam theory.

If the beam is such that  $EI$  is constant along the length, Equation 8.118 reduces to

$$EI \left( \frac{\partial^4 w}{\partial x^4} \right) + \rho A \frac{\partial^2 w}{\partial t^2} = 0 \quad (8.119)$$

Assuming that the criteria for the use of effective modulus theory have been met, these equations can be used for specially orthotropic composites or laminates without coupling if the modulus  $E$  is replaced by the effective flexural modulus  $E_f$ . Recall that, depending on the laminate configuration,  $E_f$  may be found from equations such as Equation 7.8, 7.9, Equation 7.73, or Equation 7.74. For laminates with coupling, the equations of motion based on the CLT will be developed in the next section.

As an example of a solution of the Bernoulli–Euler equation, consider a separation of variables solution for harmonic free vibration:

$$w(x,t) = W(x)e^{i\omega t} \quad (8.120)$$

where  $\omega$  is the frequency and  $W(x)$  is the mode shape function. Substituting this solution into Equation 8.119 yields

$$\frac{d^4 W(x)}{dx^4} - k^4 W(x) = 0 \quad (8.121)$$

where  $k = (\omega^2 \rho A / EI)^{1/4}$ .

The solution for Equation 8.121 is of the form

$$W(x) = C_1 \sin kx + C_2 \cos kx + C_3 \sinh kx + C_4 \cosh kx \quad (8.122)$$

where the constants  $C_1$ ,  $C_2$ ,  $C_3$ , and  $C_4$  depend on the boundary conditions. For example, for a cantilever beam (Figure 8.32), the four boundary conditions yield the following relationships:

$$W(x) = 0 \quad \text{when } x = 0; \quad \text{therefore, } C_2 = -C_4$$

$$\frac{dW(x)}{dx} = 0 \quad \text{when } w = 0; \quad \text{therefore, } C_1 = -C_3$$

$$\frac{d^2W(x)}{dx^2} = 0 \quad \text{when } x = L$$

Therefore,  $C_1(\sin kL + \sinh kL) + C_2(\cos kL + \cosh kL) = 0$ .

$$\frac{d^3W(x)}{dx^3} = 0 \quad \text{when } x = L$$

Therefore,  $C_1(\cos kL + \cosh kL) + C_2(\sin kL - \sinh kL) = 0$ .

For nontrivial solutions  $C_1$  and  $C_2$  in the last two equations, the determinant of the coefficients must be equal to zero and

$$\cos kL \cosh kL + 1 = 0 \quad (8.123)$$

This is the eigenvalue equation for the cantilever beam, which has an infinite number of solutions,  $k_nL$ . The subscript  $n$  refers to the mode number. The eigenvalues for the first three modes are

$$k_1L = 1.875, \quad k_2L = 4.694, \quad k_3L = 7.855 \quad (8.124)$$

Substituting the eigenvalues in the definition of  $k$  (see Equation 8.121 and rearranging), then using the relationship  $\omega = 2\pi f$ , we have the frequency equation

$$f_n = \frac{(k_nL)^2}{2\pi L^2} \left( \frac{EI}{\rho A} \right)^{1/2} \quad (8.125)$$

The mode shape function for the  $n$ th mode is then

$$W_n(x) = C_2[\cos k_nx - \cosh k_nx + \sigma_n(\sin k_nx - \sinh k_nx)] \quad (8.126)$$

where

$$\sigma_n = \frac{\sin k_nL - \sinh k_nL}{\cos k_nL + \cosh k_nL}$$

The mode shapes and frequencies for the first three modes of the cantilever beam are shown in Figure 8.33. The effect of increasing the mode number and the corresponding reduction in wavelength is again apparent.

If transverse shear and rotary inertia effects are included in the derivation of the equation of motion for transverse vibration of a beam, the result is the well-known Timoshenko beam equation [40]:

$$EI \left( \frac{\partial^4 w}{\partial x^4} \right) + \rho A \frac{\partial^2 w}{\partial t^2} + \frac{J\rho}{FG} \frac{\partial^4 w}{\partial t^4} - \left( J + \frac{EI\rho}{FG} \right) \frac{\partial^2 w}{\partial x^2 \partial t^2} = 0 \quad (8.127)$$

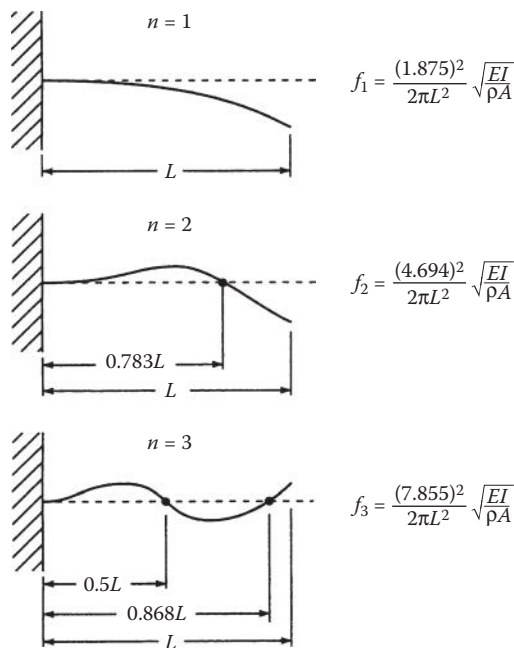
where

$J$  = rotary inertia per unit length

$F$  = shape factor for the cross section

$G$  = shear modulus

This equation can also be used for specially orthotropic composites and laminates without coupling by replacing  $E$  and  $G$  with the effective flexural

**FIGURE 8.33**

Mode shapes and natural frequencies for the first three modes of flexural vibration of the cantilever beam in Figure 8.32.

modulus,  $E_f$ , and the effective through-the-thickness shear modulus, respectively, for the composite. For example, for a unidirectional, transversely isotropic composite with the fibers along the beam axis, the appropriate shear modulus to use is  $G = G_{13} = G_{12}$ . If the fibers are oriented in the transverse direction,  $G = G_{23}$ . Both shear and rotary inertia effects become more important as the mode number increases, and both effects reduce the natural frequencies below the Bernoulli–Euler values. The beam length-to-thickness ratio,  $L/h$ , is an important factor in the determination of the shear effect, with decreasing  $L/h$  generating increased shear effects. It appears that for highly anisotropic composite beams, shear effects may be significant unless  $L/h$  is greater than about 100 [41]. The transverse shear effect is also strongly dependent on the ratio  $E/G$ , which is much greater for composite beams than for isotropic beams. For a typical isotropic metal  $E/G \approx 2.6$ , but for composites such as unidirectional carbon/epoxy,  $E_1/G_{12} \approx 20$  or higher. Sandwich beams with foam or honeycomb cores have even higher  $E/G$  ratios due to the low shear stiffness and high volume fraction of the core and are very susceptible to transverse shear effects.

As in the previous section, the equations developed here can be used in dynamic mechanical testing to determine the effective moduli of a composite specimen. The equations can also be converted to linear viscoelastic form

by replacing the elastic moduli with the corresponding complex moduli, or by deriving the equation of motion from a viscoelastic stress-strain relationship. More sophisticated analytical models for vibrating composite beams, including various effects such as viscoelastic behavior, transverse shear, and bending-twisting coupling, have been developed [36–38,42–44], but these are beyond the scope of this book.

### Example 8.8

For a symmetric laminated beam having a rectangular cross section of width  $b$  and thickness  $h$ , determine (a) the equation of motion for free vibration and (b) the natural frequencies. Assume that the criteria for use of the effective modulus theory have been met.

#### SOLUTION

- Substituting the flexural modulus,  $E_{\text{fx}}$ , from Equation 7.73 into the expression for  $EI$ , we find that

$$EI = E_{\text{fx}}I = \frac{12}{h^3 D'_{11}} \frac{bh^3}{12} = \frac{b}{D'_{11}}$$

(Note that  $h$  is used to denote thickness and  $t$  is used for time.) Thus, the Bernoulli-Euler beam equation (8.111) becomes

$$\frac{b}{D'_{11}} \frac{\partial^4 w}{\partial x^4} + \rho A \frac{\partial^2 w}{\partial x^2} = 0$$

- The natural frequencies are then found from Equation 8.125:

$$f_n = \frac{(k_n L)^2}{2\pi L^2} \left( \frac{b}{D'_{11}\rho A} \right)^{1/2}$$

where the eigenvalues,  $k_n$ , depend on the boundary conditions.

#### 8.3.3 Transverse Vibration of Laminated Plates

Although the equations for vibration of composite beams in the previous section are useful, they are limited to laminates without coupling. The more general equations of motion for transverse vibration of a laminated plate can be derived by modifying the static equilibrium equations that were developed for the analysis of static deflections of laminated plates in Section 7.9. For example, according to Newton's second law, Equation 7.126 must now be

modified, so that the summation of forces along the  $x$ -direction in Figure 7.41 is given by

$$N_x \, dy + \frac{\partial N_x}{\partial x} \, dx \, dy + N_{xy} \, dx + \frac{\partial N_{xy}}{\partial y} \, dx \, dy - N_x \, dy - N_{xy} \, dx = \rho_0 \, dx \, dy \frac{\partial^2 u^0}{\partial t^2} \quad (8.128)$$

where

$\rho_0$  = mass per unit area of laminate (equal to  $\rho h$ )

$\rho$  = mass density of laminate is the mass per unit volume

$h$  = thickness of laminate (since  $t$  is used for time here)

$u^0 = u^0(x, y, t)$  is the middle surface displacement in the  $x$ -direction

Equation 8.128 may be simplified as

$$\frac{\partial N_x}{\partial x} + \frac{\partial N_{xy}}{\partial y} = \rho_0 \frac{\partial^2 u^0}{\partial t^2} \quad (8.129)$$

Similarly, the summation of forces along the  $y$ -direction yields

$$N_x \, dx + \frac{\partial N_x}{\partial y} \, dx \, dy + N_{xy} \, dy + \frac{\partial N_{xy}}{\partial x} \, dx \, dy - N_y \, dx - N_{xy} \, dy = \rho_0 \, dx \, dy \frac{\partial^2 v^0}{\partial t^2} \quad (8.130)$$

or

$$\frac{\partial N_y}{\partial y} + \frac{\partial N_{xy}}{\partial x} = \rho_0 \frac{\partial^2 v^0}{\partial t^2} \quad (8.131)$$

where  $v_0 = v_0(x, y, t)$  is the middle surface displacement in the  $y$ -direction. The summation of forces along the  $z$ -direction gives

$$Q_x \, dy + \frac{\partial Q_x}{\partial x} \, dx \, dy + Q_y \, dx + \frac{\partial Q_y}{\partial y} \, dx \, dy - Q_x \, dy - Q_y \, dx + q(x, y) = \rho_0 \frac{\partial^2 w}{\partial t^2} \quad (8.132)$$

or

$$\frac{\partial Q_x}{\partial x} + \frac{\partial Q_y}{\partial y} + q(x, y) = \rho_0 \frac{\partial^2 w}{\partial t^2} \quad (8.133)$$

where  $w = w(x, y, t)$  is the displacement in the  $z$ -direction.

For moment equilibrium we consider the moments about the  $x$ -axis and the  $y$ -axis while neglecting rotary inertia. Thus, the summation of moments about the  $x$ -axis gives

$$\begin{aligned} -M_y \, dx - \frac{\partial M_y}{\partial y} \, dy \, dx - M_{xy} \, dy - \frac{\partial M_{xy}}{\partial x} \, dx \, dy + Q_y \, dx \, dy \\ + \frac{\partial Q_y}{\partial y} \, dy \, dx \, dy + q(x, y) \, dx \, dy \, dy / 2 + Q_x \, dy \, dy / 2 \\ + \frac{\partial Q_x}{\partial x} \, dx \, dy \, dy / 2 + M_y \, dx + M_{xy} \, dy - Q_x \, dy \, dy / 2 = 0 \end{aligned} \quad (8.134)$$

Simplifying and neglecting products of differentials, we get

$$\frac{\partial M_y}{\partial y} + \frac{\partial M_{xy}}{\partial x} = Q_y \quad (8.135)$$

A similar summation of moments about the  $y$ -axis gives

$$\frac{\partial M_x}{\partial x} + \frac{\partial M_{xy}}{\partial y} = Q_x \quad (8.136)$$

Substitution of Equations 8.135 and 8.136 into Equation 8.133 yields

$$\frac{\partial^2 M_x}{\partial x^2} + 2 \frac{\partial^2 M_{xy}}{\partial x \partial y} + \frac{\partial^2 M_y}{\partial y^2} + q(x, y) = \rho_0 \frac{\partial^2 w}{\partial t^2} \quad (8.137)$$

Equations 8.129, 8.131, and 8.137 are differential equations of motion of the plate in terms of stress and moment resultants. The corresponding equations of motion in terms of displacements can be derived by substituting the laminate force-deformation equation (7.44), the strain-displacement relations (7.32), and the curvature-displacement Equation 7.33 into Equations 8.129, 8.133, and 8.137. The resulting equations are

$$\begin{aligned} A_{11} \frac{\partial^2 u^0}{\partial x^2} + 2A_{16} \frac{\partial^2 u^0}{\partial x \partial y} + A_{66} \frac{\partial^2 u^0}{\partial y^2} + A_{16} \frac{\partial^2 v^0}{\partial x^2} + (A_{12} + A_{66}) \frac{\partial^2 v^0}{\partial x \partial y} + A_{26} \frac{\partial^2 v^0}{\partial y^2} \\ - B_{11} \frac{\partial^3 w}{\partial x^3} - 3B_{16} \frac{\partial^3 w}{\partial x^2 \partial y} - (B_{12} + 2B_{66}) \frac{\partial^3 w}{\partial x \partial y^2} - B_{26} \frac{\partial^3 w}{\partial y^3} = \rho_0 \frac{\partial^2 u^0}{\partial t^2} \end{aligned} \quad (8.138)$$

$$\begin{aligned}
& A_{16} \frac{\partial^2 u^0}{\partial x^2} + (A_{12} + A_{66}) \frac{\partial^2 u^0}{\partial x \partial y} + A_{26} \frac{\partial^2 u^0}{\partial y^2} + A_{66} \frac{\partial^2 v^0}{\partial x^2} + 2A_{26} \frac{\partial^2 v^0}{\partial x \partial y} + A_{22} \frac{\partial^2 v^0}{\partial y^2} \\
& - B_{16} \frac{\partial^3 w}{\partial x^3} - (B_{12} + 2B_{66}) \frac{\partial^3 w}{\partial x^2 \partial y} - 3B_{26} \frac{\partial^3 w}{\partial x \partial y^2} - B_{22} \frac{\partial^3 w}{\partial y^3} = \rho_0 \frac{\partial^3 v^0}{\partial t^2}
\end{aligned} \tag{8.139}$$

$$\begin{aligned}
& D_{11} \frac{\partial^4 w}{\partial x^4} + 4D_{16} \frac{\partial^4 w}{\partial x^3 \partial y} + 2(D_{12} + 2D_{66}) \frac{\partial^4 w}{\partial x^2 \partial y^2} + 4D_{26} \frac{\partial^4 w}{\partial x \partial y^3} + D_{22} \frac{\partial^4 w}{\partial y^4} \\
& - B_{11} \frac{\partial^3 u^0}{\partial x^3} - 3B_{16} \frac{\partial^3 u^0}{\partial x^2 \partial y} - (B_{12} + 2B_{66}) \frac{\partial^3 u^0}{\partial x \partial y^2} - B_{26} \frac{\partial^3 u^0}{\partial y^3} - B_{16} \frac{\partial^3 v^0}{\partial x^3} \\
& + (B_{12} + 2B_{66}) \frac{\partial^3 v^0}{\partial x^2 \partial y} - 3B_{26} \frac{\partial^3 v^0}{\partial x \partial y^2} - B_{22} \frac{\partial^3 v^0}{\partial y^3} + \rho_0 \frac{\partial^2 w}{\partial t^2} = q(x, y)
\end{aligned} \tag{8.140}$$

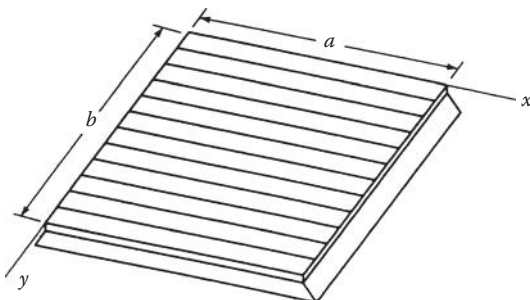
As with the static case in Section 7.9, the in-plane displacements  $u^0$  and  $v^0$  are coupled with the transverse displacements  $w$  when the  $B_{ij}$  are present. For symmetric laminates with  $B_{ij} = 0$ , Equation 8.140 alone becomes the governing equation for transverse displacements. These governing partial differential equations must be solved subject to the appropriate boundary conditions. As in the static case, when the in-plane displacements are coupled with the transverse displacements, the boundary conditions must be a combination of boundary conditions for a planar theory of elasticity problem and boundary conditions for a plate-bending problem. In this section we focus on transverse vibrations according to Equation 8.140 with all  $B_{ij} = 0$  and the transverse distributed load  $q(x, y) = 0$ . An example of coupling effects will be given in Example 8.10.

Let us now consider the case of free transverse vibration of the rectangular, specially orthotropic plate that is simply supported on all edges, as shown in Figure 8.34. The discussion here follows the analysis of Whitney [36]. For a specially orthotropic plate, all  $B_{ij} = 0$ ,  $A_{16} = A_{26} = D_{16} = D_{26} = 0$  and Equation 8.140 becomes

$$D_{11} \frac{\partial^4 w}{\partial x^4} + 2(D_{12} + 2D_{66}) \frac{\partial^4 w}{\partial x^2 \partial y^2} + D_{22} \frac{\partial^4 w}{\partial y^4} + \rho_0 \frac{\partial^2 w}{\partial t^2} = 0 \tag{8.141}$$

For free harmonic vibration at frequency  $\omega$ , we can assume that

$$w(x, y, t) = W(x, y) e^{i\omega t} \tag{8.142}$$

**FIGURE 8.34**

Simply supported, specially orthotropic plate for free transverse vibration analysis.

where  $W(x,y)$  is a mode shape function. Substituting Equation 8.142 into Equation 8.141, we have

$$D_{11} \frac{\partial^4 W}{\partial x^4} + 2(D_{12} + 2D_{66}) \frac{\partial^4 W}{\partial x^2 \partial y^2} + D_{22} \frac{\partial^4 W}{\partial y^4} - \rho_0 \omega^2 W = 0 \quad (8.143)$$

For the simply supported boundary condition, the transverse displacements and bending moments must vanish at the edges as in the static case. Thus, from Equations 7.142 and 7.143, we have, again, along  $x = 0$  and  $x = a$ ,

$$W(x,y) = 0$$

and

$$M_x = -D_{11} \frac{\partial^2 W}{\partial x^2} - D_{12} \frac{\partial^2 W}{\partial y^2} = 0 \quad (8.144)$$

and along  $y = 0$  and  $y = b$ ,

$$W(x,y) = 0$$

and

$$M_y = -D_{12} \frac{\partial^2 W}{\partial x^2} - D_{22} \frac{\partial^2 W}{\partial y^2} = 0 \quad (8.145)$$

It can be shown that the equation of motion and the boundary conditions are satisfied by solutions of the form

$$W(x,y) = A_{mn} \sin\left(\frac{m\pi x}{a}\right) \sin\left(\frac{n\pi y}{b}\right) \quad (8.146)$$

where  $m$  and  $n$  are mode indices that refer to the number of half wavelengths along the  $x$ - and  $y$ -directions, respectively, for mode  $mn$ , and  $a$  and  $b$  are the plate dimensions along the  $x$ - and  $y$ -directions, respectively. Substitution of Equation 8.146 into Equation 8.143 yields the frequency equation:

$$\omega_{mn}^2 = \frac{\pi^4}{\rho_0 a^4} \left[ D_{11} m^4 + 2(D_{12} + 2D_{66})(mnR)^2 + D_{22}(nR)^4 \right] \quad (8.147)$$

where the plate aspect ratio  $R = a/b$ , and  $\omega_{mn}$  is the natural frequency for mode  $mn$  [36]. For the fundamental mode, where  $m = n = 1$ , the natural frequency is given by

$$\omega_{11}^2 = \frac{\pi^4}{\rho_0} \left[ \frac{D_{11}}{a^4} + \frac{(2D_{12} + 2D_{66})}{a^2 b^2} + \frac{D_{22}}{b^4} \right] \quad (8.148)$$

and the mode shape function is given by

$$W(x, y) = \sin\left(\frac{\pi x}{a}\right) \sin\left(\frac{\pi y}{b}\right) \quad (8.149)$$

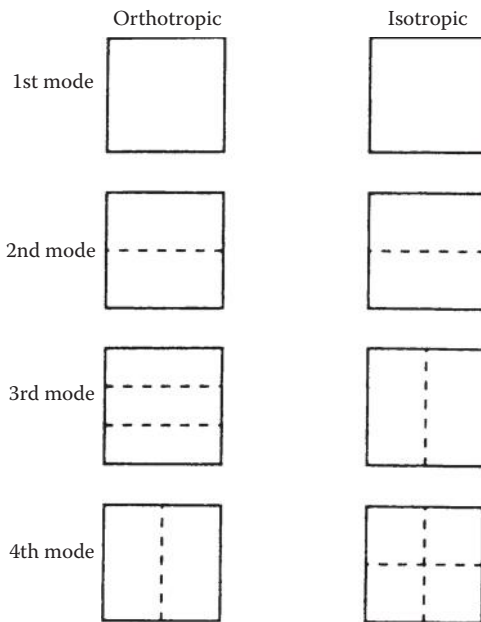
We now consider numerical results given by Whitney [36] for frequencies and mode shapes of two square plates. One plate is orthotropic with  $D_{11}/D_{22} = 10$  and  $(D_{12} + 2D_{66})/D_{22} = 1$ ; the other is isotropic with  $D_{11}/D_{22} = 1$  and  $(D_{12} + 2D_{66})/D_{22} = 1$ . The four lowest natural frequencies for the two plates are compared in Table 8.2 and the corresponding mode shapes are compared in Figure 8.35. The dotted lines in Figure 8.35 denote the nodal lines of zero displacement for a particular mode. It is interesting to note that, in order of increasing frequency, the sequence of mode numbers is different for the

**TABLE 8.2**

Predicted Natural Frequencies for the First Four Modes of Simply Supported Plates Made of Specially Orthotropic and Isotropic Materials

Mode	Orthotropic, $w = kp^2/b^2 \sqrt{D_{22}/r_0}$			Isotropic, $w = kp^2/b^2 \sqrt{D/r_0}$		
	$m$	$n$	$k$	$m$	$n$	$k$
1st	1	1	3.62	1	1	2.0
2nd	1	2	5.68	1	2	5.0
3rd	1	3	10.45	2	1	5.0
4th	2	1	13.0	2	2	8.0

Source: From Whitney, J. M. 1987. *Structural Analysis of Laminated Anisotropic Plates*. Technomic Publishing Co., Lancaster, PA. With permission.

**FIGURE 8.35**

Mode shapes for the first four modes of simply supported plates made of specially orthotropic and isotropic materials. (From Whitney, J. M. 1987. *Structural Analysis of Laminated Anisotropic Plates*. Technomic Publishing Co., Lancaster, PA. With permission.)

isotropic and orthotropic plates. Due to the high stiffness of the orthotropic plate along the  $x$ -direction, its frequencies are higher than the corresponding isotropic plate frequencies. It is also interesting to note that for the isotropic plate  $\omega_{12} = \omega_{21}$ , but for the orthotropic plate  $\omega_{21} > \omega_{12}$ .

As with the static case, it is generally not possible to find exact mode shape functions similar to those given by Equation 8.146 for boundary conditions such as clamped edges or free edges. For such cases, approximate solutions must be derived using approaches such as the Rayleigh–Ritz method or the Galerkin method. For more detailed discussions of these methods, the reader is referred to books by Whitney [36] and Vinson and Sierakowski [37].

The equation of motion for a specially orthotropic, laminated beam is found by reducing Equation 8.141 to the 1D form

$$D_{11} \frac{\partial^4 w}{\partial x^4} + \rho_0 \frac{\partial^2 w}{\partial t^2} = 0 \quad (8.150)$$

If we substitute  $\rho_0 = \rho h$ , and if we multiply Equation 8.150 by the beam width,  $b$ , we have

$$bD_{11} \frac{\partial^4 w}{\partial x^4} + \rho b h \frac{\partial^2 w}{\partial t^2} = 0 \quad (8.151)$$

For the 1D case,  $D_{11} = 1/D'_{11}$  and since  $bh = A$ , we have

$$\frac{b}{D'_{11}} \frac{\partial^4 w}{\partial x^4} + \rho A \frac{\partial^2 w}{\partial t^2} = 0 \quad (8.152)$$

which is the same as the equation that was derived from the beam theory earlier in Example 8.8.

### Example 8.9

A unidirectional AS/3501 carbon–epoxy plate is simply supported on all four edges. The plate is 300 mm × 300 mm square, 2 mm thick, and has a mass density of 1.6 mg/mm<sup>3</sup>. Determine the frequency of the fundamental mode of the plate.

#### SOLUTION

Using the lamina stiffnesses,  $Q_{ij}$ , from Example 7.4 and the thickness of 2 mm in Equation 7.43 for a laminate consisting of a single orthotropic lamina, we find the laminate bending stiffnesses to be

$$\begin{aligned} D_{11} &= 92.53 \text{ GPa mm}^3, & D_{12} &= 1.813 \text{ GPa mm}^3 \\ D_{11} &= 6.03 \text{ GPa mm}^3, & D_{66} &= 4.6 \text{ GPa mm}^3 \end{aligned}$$

The mass per unit area is

$$\rho_0 = \rho h = (1.6 \text{ mg/mm}^3)(2 \text{ mm}) = 3.2 \text{ mg/mm}^2 = 0.0032 \text{ g/mm}^2$$

The fundamental frequency is then found from Equation 8.148 as

$$\omega_{11}^2 = \frac{\pi^4}{(0.0032)(300)^4} [92.53 + 2(1.813 + 2(4.6)) + 6.03](10^9) = 4.53(10^5) \text{ rad}^2/\text{s}^2$$

or

$$\omega_{11} = 673 \text{ rad/s}$$

(Note: GPa mm<sup>3</sup> = 10<sup>9</sup> g mm<sup>2</sup>/s<sup>2</sup> in the above equation.)

### Example 8.10

Investigate the effects of coupling on the flexural vibration frequencies of a non-symmetrically laminated [0/90] cross-ply composite beam that is simply supported on each end. The beam has length  $L$  and the  $x$ -axis is parallel to the longitudinal axis of the beam.

### SOLUTION

Since the plies are all oriented at either 0° or 90°, there is no shear coupling, and  $A_{16} = A_{26} = B_{16} = B_{26} = D_{16} = D_{26} = 0$ . In addition, for a 1D beam oriented along the x-direction, all terms in the equations of motion (Equations 8.138 through 8.140) involving  $v^0$  and  $y$ , and derivatives in  $y$  may be neglected. Finally, we neglect the longitudinal inertia term on the right-hand side of Equation 8.138, and the transverse loading term  $q(x,y)$  on the right-hand side of Equation 8.140. With these simplifications, Equation 8.139 becomes identically zero on both sides, while Equation 8.138 and Equation 8.140 reduce to the coupled partial differential equations, respectively,

$$A_{11} \frac{\partial^2 u^0}{\partial x^2} - B_{11} \frac{\partial^3 w}{\partial x^3} = 0$$

and

$$D_{11} \frac{\partial^4 w}{\partial x^4} - B_{11} \frac{\partial^3 u^0}{\partial x^3} = -\rho_0 \frac{\partial^2 w}{\partial t^2}$$

For free harmonic vibration at frequency,  $\omega$ , we can assume separation of variables solutions of the form

$$u^0(x,t) = U(x)e^{i\omega t}$$

and

$$w(x,t) = W(x)e^{i\omega t}$$

where  $U(x)$ ,  $W(x)$  are mode shape functions. Substitution of these assumed shape functions into the two equations of motion above yields the ordinary differential equations

$$A_{11} \frac{d^2 U}{dx^2} - B_{11} \frac{d^3 W}{dx^3} = 0$$

and

$$D_{11} \frac{d^4 W}{dx^4} - B_{11} \frac{d^3 U}{dx^3} = \rho_0 \omega^2 W$$

For the simple supports at  $x = 0$  and  $x = L$ , the boundary conditions are given by specifying that the transverse displacement  $W(x)$  and the bending moment per unit length  $M_x(x)$  must both vanish at  $x = 0$  and  $x = L$ . Therefore

$$W(0) = 0$$

$$W(L) = 0$$

$$M_x(0) = B_{11} \frac{dU}{dx}(0) - D_{11} \frac{d^2 W}{dx^2}(0) = 0$$

$$M_x(L) = B_{11} \frac{dU}{dx}(L) - D_{11} \frac{d^2 W}{dx^2}(L) = 0$$

where the equations for the bending moment per unit length,  $M_x(x)$ , are found by substituting the simplifications listed above in Equations 7.32 through 7.44, and evaluating the resulting expressions at  $x = 0$  and  $x = L$ . It can be shown by substitution that the boundary conditions are all satisfied by mode shape functions of the form

$$U(x) = U_0 \cos\left(\frac{n\pi x}{L}\right)$$

$$W(x) = W_0 \sin\left(\frac{n\pi x}{L}\right)$$

where  $n = 1, 2, 3, \dots$ , is the mode number. It can also be shown that these functions satisfy the in-plane boundary conditions  $N_x(0) = N_x(L) = N_{xy}(0) = N_{xy}(L) = 0$ .

Substitution of these mode shape functions in the two differential equations yields the algebraic equations,

$$\begin{bmatrix} A_{11} \left(\frac{n\pi}{L}\right)^2 & -B_{11} \left(\frac{n\pi}{L}\right)^3 \\ -B_{11} \left(\frac{n\pi}{L}\right)^3 & D_{11} \left(\frac{n\pi}{L}\right)^4 - \rho_0 \omega_n^2 \end{bmatrix} \begin{Bmatrix} U_0 \\ W_0 \end{Bmatrix} = \begin{Bmatrix} 0 \\ 0 \end{Bmatrix}$$

where  $\omega = \omega_n$  for vibration in mode  $n$ . For nontrivial solutions of the displacements, the determinant of the coefficient matrix must be equal to zero, and this yields the frequency equation for mode  $n$ :

$$\omega_n^2 = \frac{1}{\rho_0} \left(\frac{n\pi}{L}\right)^4 \left(D_{11} - \frac{B_{11}^2}{A_{11}}\right)$$

It is easily shown from the definitions of the laminate stiffnesses that for this [0/90] laminate,  $A_{11}$ ,  $B_{11}^2$ , and  $D_{11}$  are all positive, and that as a result, the bending-extension coupling term  $B_{11}^2/A_{11}$  causes the frequencies to be reduced below those of a symmetrically laminated beam that has the  $n$ th mode frequency,

$$\omega_n^2 = \left(\frac{n\pi}{L}\right)^4 \frac{D_{11}}{\rho_0}$$

Similarly, Jones [45] has shown that, for antisymmetric cross-ply laminated plates of various aspect ratios and various numbers of plies, bending-extension coupling always reduces the frequencies. However, it was found that the frequency reduction is greatest for the case of only two plies (i.e., [0/90]), and that the coupling effect was reduced as the number of plies was increased. Similar results have been found for antisymmetric angle-ply laminates.

### 8.3.4 Analysis of Damping in Composites

Damping is simply the dissipation of energy during dynamic deformation. As structures and machines are pushed to higher and higher levels of precision and performance, and as the control of noise and vibration becomes more of a societal concern, it becomes essential to take damping into account in the design process. In conventional metallic structures, it is commonly accepted that much of the damping comes from friction in structural joints or from add-on surface damping treatments because the damping in the metal itself is typically very low. On the other hand, polymer composites have generated increased interest in the development of highly damped, lightweight, structural composites because of their good damping characteristics and the inherent design flexibility, which allows trade-offs between such properties as damping and stiffness. The purpose of this section is to give a brief overview of the analysis of linear viscoelastic damping in composites. Dynamic mechanical testing of composites, which includes experimental determination of damping, will be discussed in Chapter 10. More detailed treatments of damping in composites are presented in publications by Gibson [46–48], Bert [49], Adams [50], Chaturvedi [51], Kinra and Wolfenden [52], and Sun and Lu [53].

As described in Section 8.1, damping is one of the important physical manifestations of viscoelastic behavior in dynamically loaded structural materials, and the stress-strain hysteresis loop in Figure 8.1c is typical of damped response under cyclic loading. Viscoelastic behavior of fiber and/or matrix materials is not the only mechanism for structural damping in composite materials although it does appear to be the dominant mechanism in undamaged polymer composites vibrating at small amplitudes. Other damping mechanisms include thermoelastic damping due to cyclic heat flow, coulomb friction due to slip in unbonded regions of the fiber–matrix interface, and energy dissipation at sites of cracks and/or delaminations [46]. Thermoelastic damping is generally more important for metal composites than for polymer composites. Damping due to poor interface bonding, cracks, and/or delaminations cannot be relied upon in the design of structures, but the measurement of such damping may be the basis of a valuable nondestructive evaluation methodology [47].

In order to understand linear viscoelastic damping better, it is important to recognize the relationship between the timescale of the applied deformation and the internal timescale of the material. The timescale for cyclic deformation is determined by the oscillation frequency,  $\omega$ . Recall that the relaxation times,  $\lambda_i$ , or retardation times,  $\rho_i$ , are measures of the internal timescale of the material. We will now use the Zener single relaxation model to illustrate how damping depends on the relationship between these two timescales.

For sinusoidal oscillation of the Zener single relaxation model (Figure 8.11a), we can write

$$\sigma = \sigma_0 e^{i\omega t} = (E' + iE'')\epsilon \quad (8.153)$$

where

$\sigma$  = stress

$\sigma_0$  = stress amplitude

$\epsilon$  = strain

$\omega$  = frequency

$E'$  = storage modulus is  $E'(\omega)$

$E''$  = loss modulus is  $E''(\omega)$

$i$  = imaginary operator, which is  $\sqrt{-1}$

Substituting Equation 8.153 into the stress-strain relationship for the Zener model (Equation 8.42) and separating into real and imaginary parts, we find that

$$E' = E'(\omega) = \frac{k_0 + (k_0 + k_1)\omega^2\lambda_1^2}{1 + \omega^2\lambda_1^2} \quad (8.154)$$

$$E'' = E''(\omega) = \frac{\omega\lambda_1 k_1}{1 + \omega^2\lambda_1^2} \quad (8.155)$$

and

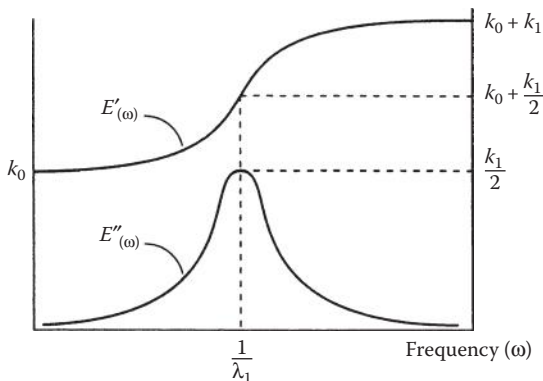
$$\eta = \eta(\omega) = \frac{E''(\omega)}{E'(\omega)} = \frac{\omega\lambda_1 k_1}{k_0 + (k_0 + k_1)\omega^2\lambda_1^2} \quad (8.156)$$

where

$\lambda_1 = \mu_1/k_1$  is the relaxation time from Equation 8.44

$\eta = \eta(\omega)$  is the loss factor

The variations of  $E'$  and  $E''$  with frequency  $\omega$  are shown schematically in Figure 8.36. Note that when the frequency is the reciprocal of the relaxation time,  $\omega = 1/\lambda_1$ , the loss modulus peaks and the storage modulus passes through a transition region. Such damping peaks in the frequency domain are often referred to as "relaxation peaks." The loss factor has a peak at a different frequency, not shown in Figure 8.36 because the relative position of that peak depends on the numerical values of the parameters. But the important point is that the dissipation of energy, whether characterized by the loss modulus or the loss factor, is maximized when the timescale of the deformation is the same as the internal timescale of the material. If the two timescales are substantially different, the energy dissipation is reduced. For example, note in Figure 8.36 that  $E'' \rightarrow 0$  as  $\omega \rightarrow 0$  and as  $\omega \rightarrow \infty$ . This behavior is typical for viscoelastic materials, but, as mentioned earlier, the actual transitions occur over a wider range (in this case a wider frequency range) than the single relaxation model produces. Thus, as before, an improved Zener model (Figure 8.13 or Figure 8.16) with a distribution of relaxation

**FIGURE 8.36**

Variation of storage modulus,  $E'(\omega)$ , and loss modulus,  $E''(\omega)$ , with frequency for the Zener single relaxation model.

times makes it possible to extend the range of the relaxation to approximate the actual behavior better.

Analytical models have been developed for predicting damping in composites at both the micromechanical and macromechanical levels. Only in certain special cases, such as thermoelastic damping [54] or dislocation damping [55] in metals, can the damping be predicted from first principles without knowledge of constituent material damping properties. (These damping mechanisms are not discussed here.) If the damping mechanism is of the linear viscoelastic type, there are two basic approaches to the development of analytical models, both of which are based on the existence of experimental damping data for constituent materials. The two approaches are as follows:

1. The use of the Elastic–Viscoelastic Correspondence Principle in combination with elastic solutions from the mechanics of materials, elasticity theory, or numerical simulations.
2. The use of a strain energy formulation that relates the total damping in the structure to the damping of each element and the fraction of the total strain energy stored in that element.

The basis of the first approach is that linear elastostatic analyses can be converted to vibratory linear viscoelastic analyses by replacing static stresses and strains with the corresponding vibratory stresses and strains, and by replacing the elastic moduli or compliances with the corresponding complex moduli or compliances, respectively. According to this procedure, the elastostatic stress–strain relationships in Equation 2.5 would be converted to the viscoelastic vibratory equations (8.70), and Equation 2.3 would be converted to Equation 8.71, as described in Section 8.2.5. The use of this approach to

derive the micromechanics equation for the longitudinal loss factor of a unidirectional composite (Equation 8.87) has already been demonstrated. The same approach has been used to derive micromechanics equations for the prediction of damping in aligned discontinuous fiber composites having various fiber aspect ratios and fiber orientations [22, 56] in randomly oriented short fiber composites [57], in metal matrix and ceramic matrix composites at elevated temperatures [58], in hybrid composites with coated fibers [59], and in woven fiber-reinforced composites [60].

The correspondence principle has also been used in combination with the CLT to develop equations for the laminate loss factors [23]. For example, the extensional loss factors for a laminate can be expressed in terms of the real and imaginary parts of the corresponding laminate extensional stiffnesses:

$$\eta_{ij}^{(A)} = \frac{A''_{ij}}{A'_{ij}} \quad (8.157)$$

Similar equations can be used to describe laminate coupling and flexural loss factors [23]. The major limitation of such analyses is that the CLT neglects interlaminar stresses, so that interlaminar damping is not included. As shown later in this section, a more general 3D analysis including interlaminar damping may be developed by using a strain energy method.

Although sinusoidally varying stresses and strains were assumed in the development of the complex modulus notation in Section 8.2.4, it has been shown that as long as the stiffness and damping show some frequency dependence, the complex modulus notation is also valid for the more general nonsinusoidal case [61]. Anomalous analytical results such as noncausal response can occur if the components of the complex modulus are independent of frequency. Composite materials (particularly polymer composites) generally have frequency-dependent complex moduli, however.

The second approach involves the use of a strain–energy relationship that was first presented in 1962 by Ungar and Kerwin [62]. Ungar and Kerwin found that for an arbitrary system of linear viscoelastic elements, the system loss factor can be expressed as a summation of the products of the individual element loss factors and the fraction of the total strain energy stored in each element:

$$\eta = \frac{\sum_{i=1}^n \eta_i W_i}{\sum_{i=1}^n W_i} \quad (8.158)$$

where

$\eta_i$  = loss factor for the  $i$ th element in the system

$W_i$  = strain energy stored in the  $i$ th element at maximum vibratory displacement

$n$  = total number of elements in the system

When applying this equation to composite damping analysis, the composite becomes the “system,” and the nature of the elements depends on whether the analysis is micromechanical or macromechanical. For example, this equation has been used in combination with mechanics of materials solutions for the strain energy of aligned discontinuous fiber composites [63]. In this analysis, the damping in the fiber was neglected (i.e., the fiber loss factor  $\eta_f = 0$ ), so that the longitudinal loss factor of the aligned discontinuous fiber composite was approximated by the following form of Equation 8.158:

$$\eta_l = \frac{\eta_m W_m}{W_f + W_m} \quad (8.159)$$

where

$\eta_m$  = matrix loss factor

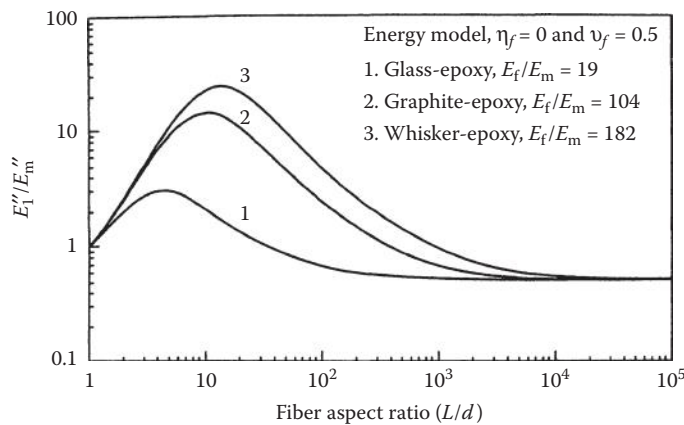
$W_m$  = strain energy in the matrix at maximum vibratory displacement

$W_f$  = strain energy in the fiber at maximum vibratory displacement

The strain energy terms  $W_f$  and  $W_m$  were determined from mechanics of materials by using the stress distributions from the Cox model (Equations 6.21 and 6.26). The longitudinal storage modulus,  $E'_1$ , was also determined from the Cox model (Equation 6.24), and the loss modulus was found from  $E''_1 = E'_1 \eta_l$ . Figure 8.37 shows the variation of the predicted ratio  $E''_1/E''_m$  with fiber length-to-diameter ratio,  $L/d$ , for several fiber–matrix combinations [63]. It is seen that each composite has an optimum  $L/d$  where the ratio  $E''_1/E''_m$  is maximized, and that both the peak value of  $E''_1/E''_m$  and the optimum  $L/d$  shift to higher values as the modulus ratio  $E_f/E_m$  increases. This means that the damping, which is primarily due to interfacial shear deformation, is increased when the mismatch between the fiber and the matrix stiffnesses (as determined by  $E_f/E_m$ ) is increased.

The Ungar–Kerwin equation is ideally suited for finite element implementation in the analysis of complex structures. In the finite element implementation, the element index “ $i$ ” in Equation 8.158 refers to the element number,  $n$  refers to the total number of finite elements, and the strain energy terms,  $W_i$ , are determined from the FEA. It appears that the equation was first implemented in the finite element form in the so-called “modal strain energy” approach for the analysis of modal damping in complex structures [64]. The strain energy/finite element approach has also been used in numerous composite analysis applications at both the micromechanical level [59,60,65,66] and the laminate level [67–69]. For example, in studies of the fiber–matrix interphase, the finite element models shown in Figure 8.38 were used in conjunction with the equation

$$\eta = \frac{\eta_f W_f + \eta_m W_m + \eta_i W_i}{W_f + W_m + W_i} \quad (8.160)$$

**FIGURE 8.37**

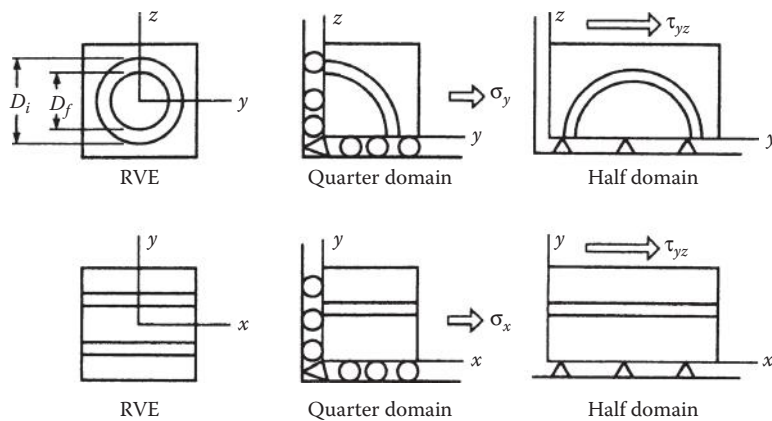
Variation of loss modulus ratio,  $E''_f / E''_m$ , with fiber aspect ratio,  $L/d$ , for several aligned discontinuous fiber composite systems. (Reprinted from Gibson, R. F., Chaturvedi, S. K., and Sun, C. T. 1982. *Journal of Materials Science*, 17, 3499–3509. With permission from Chapman & Hall.)

where

$\eta_f$  = fiber loss factor

$\eta_i$  = interphase loss factor

$W_i$  = strain energy in the interphase region at maximum vibratory displacement.

**FIGURE 8.38**

Models used for strain energy/FEA of effect of interphase on damping or unidirectional graphite/epoxy under different loading conditions. (Reprinted from Gibson, R. F., Hwang, S. J., and Kwak, H. 1991. *How Concept Becomes Reality—Proceedings of 36th International SAMPE Symposium*, Vol. 1. With permission from the Society for the Advancement of Material and Process Engineering, Covina, CA, pp. 592–606.)

Typical results for four different loading conditions are shown in Figure 8.39. It appears that the in-plane shear loss factor,  $\eta_{xy}$ , is the most sensitive of the four loss factors to the size of the interphase region.

Three-dimensional FEA has been used in conjunction with the Ungar-Kerwin equation to study interlaminar damping and the effects of coupling on damping in laminates [67–69]. In these studies, the laminate loss factor was modeled using the equation

$$\eta = \sum_{k=1}^N [\eta_x^{(k)} W_x^{(k)} + \eta_y^{(k)} W_y^{(k)} + \eta_{xy}^{(k)} W_{xy}^{(k)} + \eta_z^{(k)} W_z^{(k)} + \eta_{yz}^{(k)} W_{yz}^{(k)} + \eta_{xz}^{(k)} W_{xz}^{(k)}] / W_t \quad (8.161)$$

where

$k$  = lamina number

$N$  = total number of laminae

$W_t$  = total strain energy stored in laminate at maximum vibratory displacement:

$$W_t = \sum_{k=1}^N [W_x^{(k)} + W_y^{(k)} + W_{xy}^{(k)} + W_z^{(k)} + W_{yz}^{(k)} + W_{xz}^{(k)}]$$

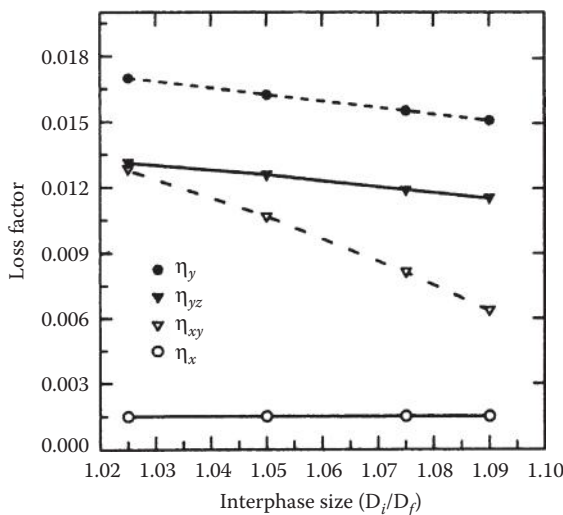


**FIGURE 8.39**

Predicted effect of interphase size on loss factor for material and loading conditions described in Figure 8.38 (Reprinted from Gibson, R. F., Hwang, S. J., and Kwak, H. 1991. *How Concept Becomes Reality—Proceedings of 36th International SAMPE Symposium*, Vol. 1. With permission from the Society for the Advancement of Material and Process Engineering, Covina, CA, pp. 592–606.)

$x, y, z$  = global laminate coordinates

$\eta_x^{(k)}, \eta_y^{(k)}, \eta_{xy}^{(k)}$  = in-plane loss factors for the  $k$ th lamina

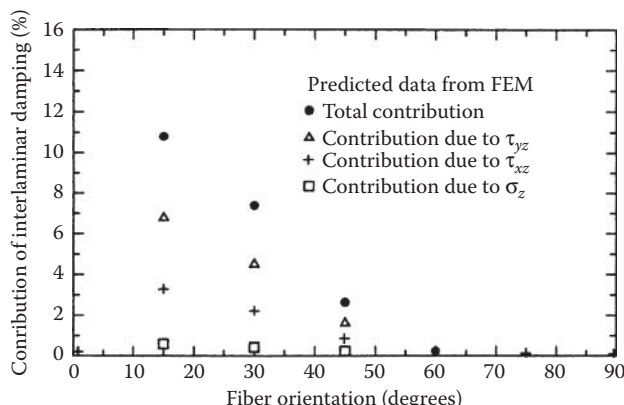
$\eta_z^{(k)}, \eta_{yz}^{(k)}, \eta_{xz}^{(k)}$  = out-of-plane loss factors for the  $k$ th lamina

$W_x^{(k)}, W_y^{(k)}, W_{xy}^{(k)}$  = in-plane strain energy terms for the  $k$ th lamina

$W_z^{(k)}, W_{yz}^{(k)}, W_{xz}^{(k)}$  = out-of-plane strain energy terms for the  $k$ th lamina

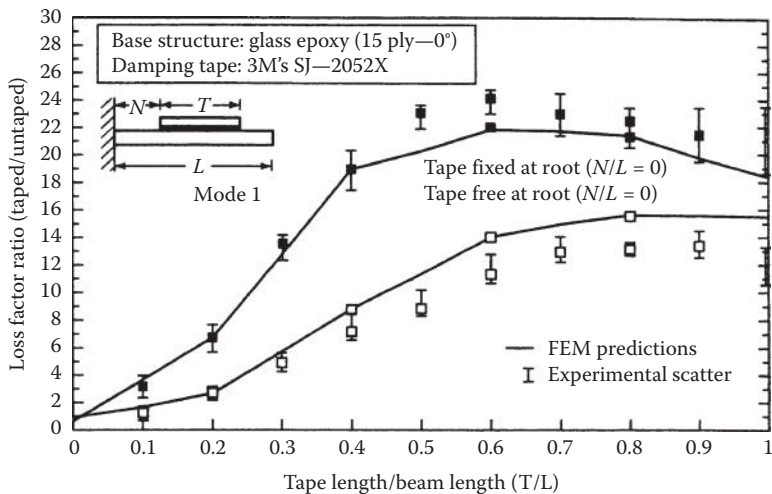
Thus, the decomposition of the total damping into contributions associated with each stress component is a relatively simple task with the strain energy approach. For example, Figure 8.40 shows the contribution of the different components of interlaminar damping as a function of fiber orientation for angle-ply graphite laminates under uniaxial extension [67]. The finite element model for this work was shown in Figure 7.27. It is seen that the interlaminar damping is maximized at a particular fiber orientation, and that the interlaminar shear stress,  $\tau_{yz}$ , is the most significant contributor to interlaminar damping in this case. A similar approach was used to study damping in composite beams with constrained viscoelastic layer damping treatments, and Figure 8.41 shows the effect of constrained viscoelastic layer (damping tape) length on damping for a glass/epoxy beam [70]. In this case, damping is seen to be strongly dependent on the ratio of damping tape length to beam length and the tape end fixity condition.

A review of the applications of the strain energy method for studying various aspects of damping in composite materials and structures has been published by Hwang and Gibson [71]. At the structural level, this method has been used to predict damping in composite grid structures [72], curvilinear laminates and composite shell structures [73], and composite sandwich



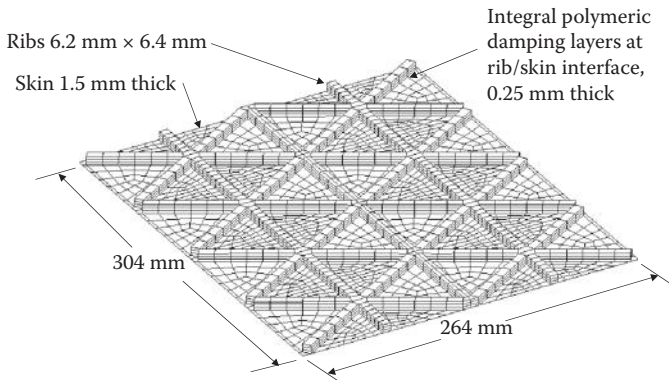
**FIGURE 8.40**

Contribution of different components of interlaminar damping for various fiber orientations for  $[\pm\theta]_s$  graphite/epoxy laminates (with laminate width/thickness = 4 and length/thickness = 6) under uniaxial loading. (Reprinted from Hwang, S. J. and Gibson, R. F. 1991. *Composites Science and Technology*, 41, 379–393. With permission from Elsevier Science Publishers, Ltd.)

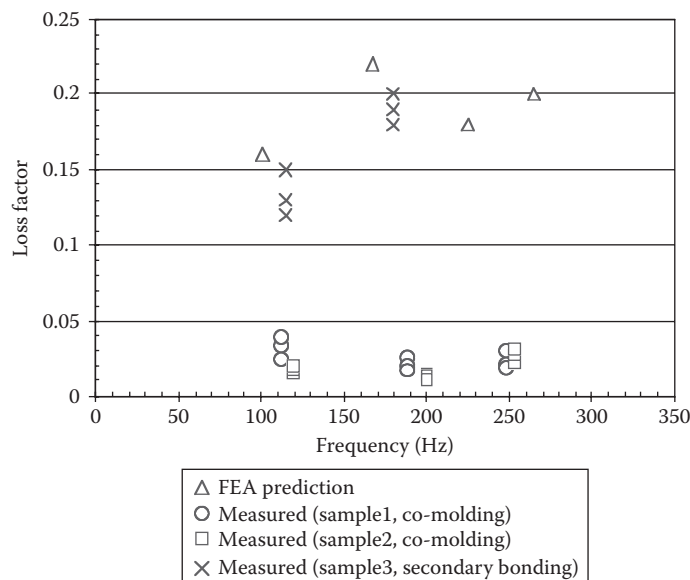
**FIGURE 8.41**

Measured and predicted damping for unidirectional glass/epoxy beam with constrained viscoelastic layer damping tapes of different lengths and tape end fixity conditions. (From Mantena, P. R., Gibson, R. F., and Hwang, S. J. 1991. *AIAA Journal*, 29(10), 1678–1685. Copyright AIAA, 1990. With permission.)

structures [74]. For example, Chen and Gibson [72] used a finite element implementation of the strain energy approach to study integral passive damping in composite isogrid structures. Figure 8.42 shows a typical 3D finite element model for the composite isogrid structure, which has an integral layer of polymeric damping material at the rib–skin interface. Figure 8.43 shows that the

**FIGURE 8.42**

Finite element model for analysis of vibration and damping in composite isogrid structure with integral passive damping. (From Chen, Y. and Gibson, R. F. 2003. *Mechanics of Advanced Materials and Structures*, 10(2), 127–143. With permission.)

**FIGURE 8.43**

Comparison of predicted and measured damping loss factors in composite isogrid structures with and without integral passive damping. (From Chen, Y. and Gibson, R. F. 2003. *Mechanics of Advanced Materials and Structures*, 10(2), 127–143. With permission.)

predicted and measured damping can be increased significantly by using the integral damping layer. Further discussions on the experimental aspects of this work can be found in Chapter 10.

Although the loss factor is a convenient measure of damping because of its connection with the complex modulus notation, it is not the only parameter used to describe damping. For materials with small damping ( $\eta \ll 1$ ), other measures of damping that appear in the literature are related to the loss factor as follows [49]:

$$\eta = \frac{\Psi}{2\pi} = \frac{\Delta}{\pi} = 2\zeta = \frac{1}{Q} \quad (8.162)$$

where

$\Psi$  = specific damping capacity

$\Delta$  = logarithmic decrement

$\zeta$  = damping ratio, or damping factor

$Q$  = quality factor

Most of these parameters are associated with the damping of a single-degree-of-freedom (SDOF) vibration model and are used to obtain damping from vibration test data. Such tests will be discussed in more detail in Chapter 10.

In summary, damping has become an important consideration in the design of dynamically loaded composite materials and structures. As a result, there is increased interest in the prediction of damping in composites. Several analytical methods for making such predictions have been reviewed, and sample results have been presented. Because of the design flexibility that is inherent in composite materials, the potential for improvement and optimization of damping appears to be much greater than that for conventional structural materials.

### Example 8.11

The constituent materials in a unidirectional carbon/epoxy material have the following dynamic mechanical properties at a certain frequency:

$$E'_f = 220 \text{ GPa} (32 \times 10^6 \text{ psi}); \quad \eta_{f1} = 0.002; \quad v_f = 0.6$$

$$E'_m = 3.45 \text{ GPa} (0.5 \times 10^6 \text{ psi}); \quad \eta_{m1} = 0.02; \quad v_m = 0.4$$

Determine the composite longitudinal loss factor and the percentage of the total longitudinal damping due to each constituent.

### SOLUTION

Substituting the above data into Equation 8.87 from the Elastic Viscoelastic Correspondence Principle, or using the strain energy approach and Equation 8.158, we find that the composite longitudinal loss factor is

$$\begin{aligned} \eta_l &= \frac{E''_f v_f + E''_m v_m}{E'_f v_f + E'_m v_m} = \frac{\eta_{f1} E'_f v_f + \eta_{m1} E'_m v_m}{E'_f v_f + E'_m v_m} = \frac{0.002(220)(0.6) + 0.02(3.45)(0.4)}{220(0.6) + 3.45(0.4)} \\ &= 0.001979 + 0.000207 = 0.002186 \end{aligned}$$

Thus, the fiber contributes  $(0.001979/0.002186) \times 100 = 90.5\%$  of the damping and the matrix contributes the remaining 9.5%. Even though the matrix has a greater loss factor than the fiber, most of the strain energy is stored in the fiber, and this is why the fiber contributes more to the total composite damping. This is not true for the off-axis case, however, as the strain energy in the matrix becomes more significant. For example, the composite transverse loss factor is dominated by the matrix contribution.

### Example 8.12

A [0/90/0]<sub>s</sub> symmetric laminated beam consists of six plies of equal thickness and the plies have the following complex Young's moduli at a certain frequency:

For the 0° plies:

$$E_1^* = E'_1 + iE''_1 = [(5 \times 10^6) + i(5 \times 10^3)] \text{ psi}$$

For the 90° plies

$$E_2^* = E'_2 + iE''_2 = [(1.5 \times 10^6) + i(1.5 \times 10^4)] \text{ psi}$$

Find the flexural loss factor,  $\eta_f$ , for the beam, assuming that the complex moduli for the plies and the laminate are all determined at the same frequency. Note that the subscript f here refers to flexural, not fiber.

### SOLUTION

The equation for the complex flexural modulus of the laminated beam is found by applying the Elastic–Viscoelastic Correspondence Principle to the equation for the elastic flexural modulus. The elastic flexural modulus of a laminated beam having an even number of equal thickness plies is given by Equation 7.9;

$$E_f = \frac{8}{N^3} \sum_{j=1}^{N/2} (E_x)_j (3j^2 - 3j + 1)$$

The corresponding equation for the complex flexural modulus is

$$E_f^* = \frac{8}{N^3} \sum_{j=1}^{N/2} (E_x^*)_j (3j^2 - 3j + 1)$$

Substituting into the complex moduli of the plies,  $E_x^*$ , and the associated ply numbers,  $j$ , we find that

$$\begin{aligned} E_f^* &= \frac{8}{(6)^3} [(5 \times 10^6) + i(5 \times 10^3)] (3(1)^2 - 3(1) + 1) \\ &\quad + \frac{8}{(6)^3} [(1.5 \times 10^6) + i(1.5 \times 10^4)] (3(2)^2 - 3(2) + 1) \\ &\quad + \frac{8}{(6)^3} [(5 \times 10^6) + i(5 \times 10^3)] (3(3)^2 - 3(3) + 1) \end{aligned}$$

or

$$E_f^* = E'_f + iE''_f = (4.088 \times 10^6) + i(7.585 \times 10^3) \text{ psi}$$

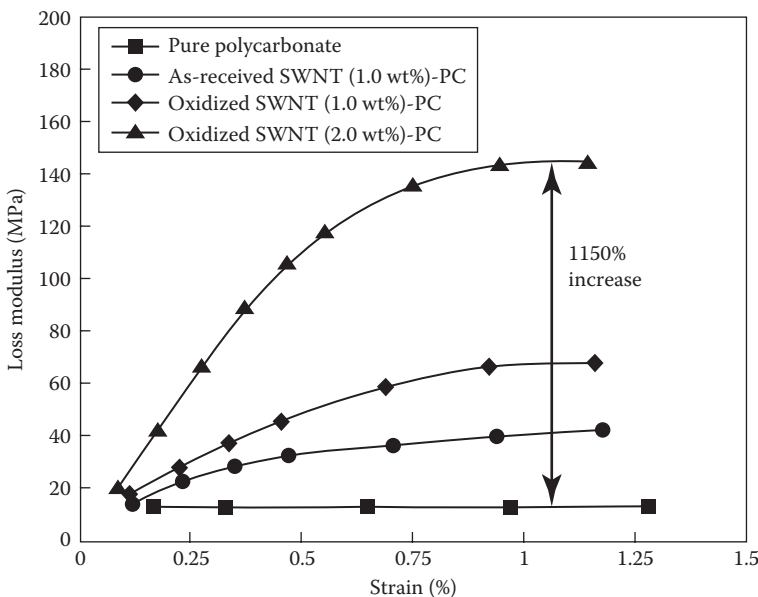
Setting the real parts of both sides of the equation equal, the flexural storage modulus is  $E'_f = 4.088 \times 10^6$  psi. Setting the imaginary parts of both sides of the equation equal, the flexural loss modulus is  $E''_f = 7.585 \times 10^3$  psi. Finally, the flexural loss factor is given by

$$\eta_f = \frac{E''_f}{E'_f} = \frac{7.585 \times 10^3}{4.088 \times 10^6} = 0.00185$$

## 8.4 Nanoenhancement of Viscoelastic and Dynamic Properties

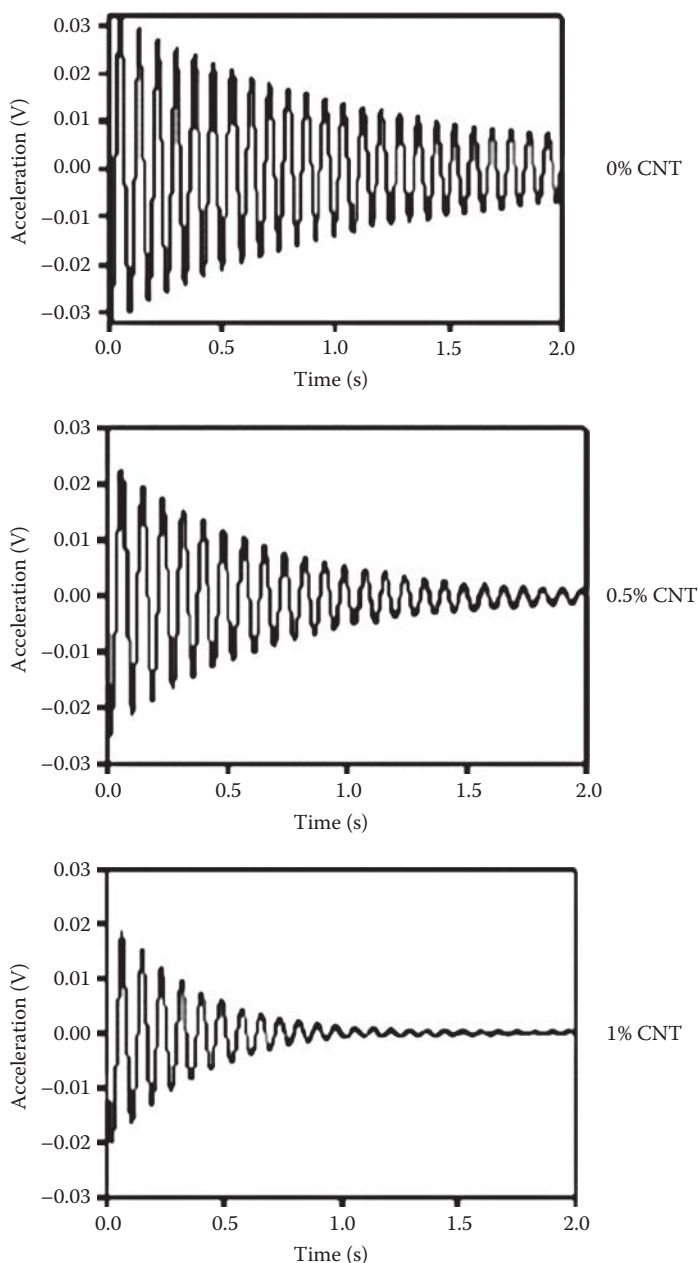
As part of the nanotechnology revolution, the study of vibration and damping in nanocomposites has been the subject of numerous investigations in recent years. A review of the literature on vibrations of CNTs and their composites has been published by Gibson et al. [75]. Several papers have reported significant increases in internal damping of polymer nanocomposites when very small amounts of CNTs are used as reinforcement. For example, as shown in Figure 8.44, increases in the loss modulus of more than 1000% were reported by Koratkar et al. [76] for SWNT–polycarbonate nanocomposites containing up to 2% by weight SWNTs. It was shown that the increase in damping was primarily due to frictional sliding at the nanotube–polymer interfaces as the strain level increases. This points out an advantage of nano-fillers in that they present a very large interfacial contact area with the matrix material by comparison with conventional reinforcements.

Zhou et al. [77] fabricated and tested SWNT/epoxy beams with varying amounts of SWNT reinforcement and developed a “stick-slip” micromechanical model that captured the observed trends in the damping. The increased damping effect (i.e., more rapid free vibration decay) with increased CNT content is clearly shown in Figure 8.45. Another key conclusion from



**FIGURE 8.44**

Variation of loss modulus with increasing strain for SWNT–polycarbonate nanocomposite. (Reprinted with permission from [Koratkar, N. A. et al. *Applied Physics Letters*, 87, 063102.] Copyright (2005), American Institute of Physics.)

**FIGURE 8.45**

Free vibration decay curves for SWNT-epoxy nanocomposite beams having different amounts of SWNT reinforcement. (Reprinted from *Composites Science and Technology*, 64, Zhou, X., Shin, E., Wang, K. W., and Bakis, C. E., Interfacial damping characteristics of carbon nanotube composites, 2425–2437. Copyright (2004), with permission from Elsevier.)

the analytical model developed here was that the size and specific surface area of filler materials are extremely important factors that affect damping in composites, and that the very large interfacial contact area of nanotubes is a definite advantage when it comes to damping.

Rajoria and Jalili [78] generated a large amount of experimental data on damping of CNT-epoxy–steel sandwich beams having various weight percentages of CNTs. As shown in Figure 8.46, beams containing MWNT reinforcement had greater damping than those containing either SWNT reinforcement or conventional CF reinforcement. In addition, the frequency dependence of CNT-reinforced beams was more pronounced than that of the other beams, and it appears that once the weight percentage of either SWNTs or MWNTs reaches 5%, there is no further improvement in damping. Up to 700% improvement in damping for 5% MWNT-reinforced beams was reported. On the other hand, corresponding changes in the storage modulus were found to be much less pronounced.

Most of the studies of damping in nanocomposites so far have been of an experimental nature, and there is a need for more analytical work. For example, the analytical predictions of Gibson et al. [63] in Figure 8.37 show that there is an optimum fiber aspect ratio for maximizing the loss modulus of a discontinuous-aligned fiber composite, and that the optimum loss modulus increases with increasing fiber/matrix stiffness mismatch, as quantified by the ratio  $E_f/E_m$ . The maximum ratio  $E_f/E_m = 182$  shown in Figure 8.37 is for a

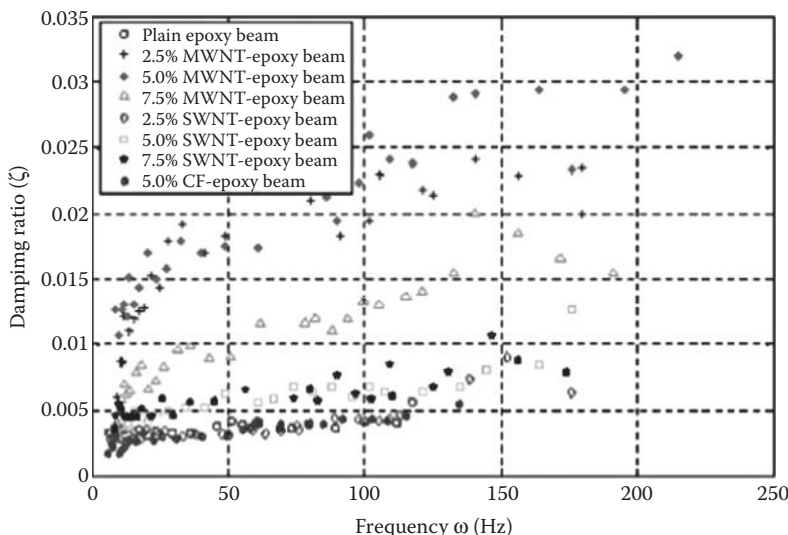


**FIGURE 8.46**

Measured frequency dependence of damping ratio for various composite beams. (Reprinted from *Composites Science and Technology*, 65, Rajoria, H. and Jalili, N. Passive vibration damping enhancement using carbon nanotube–epoxy reinforced composites, 2079–2093. Copyright (2005), with permission from Elsevier.)

whisker–epoxy composite, but the corresponding  $E_f/E_m$  ratio for a CNT nanocomposite should be at least 500 or so, and the optimum loss modulus should be much greater than those shown in Figure 8.37. This model is for a discontinuous-aligned fiber composite, however, and such models need to be revised to include the waviness and 3D orientation of nanotubes or nanofibers.

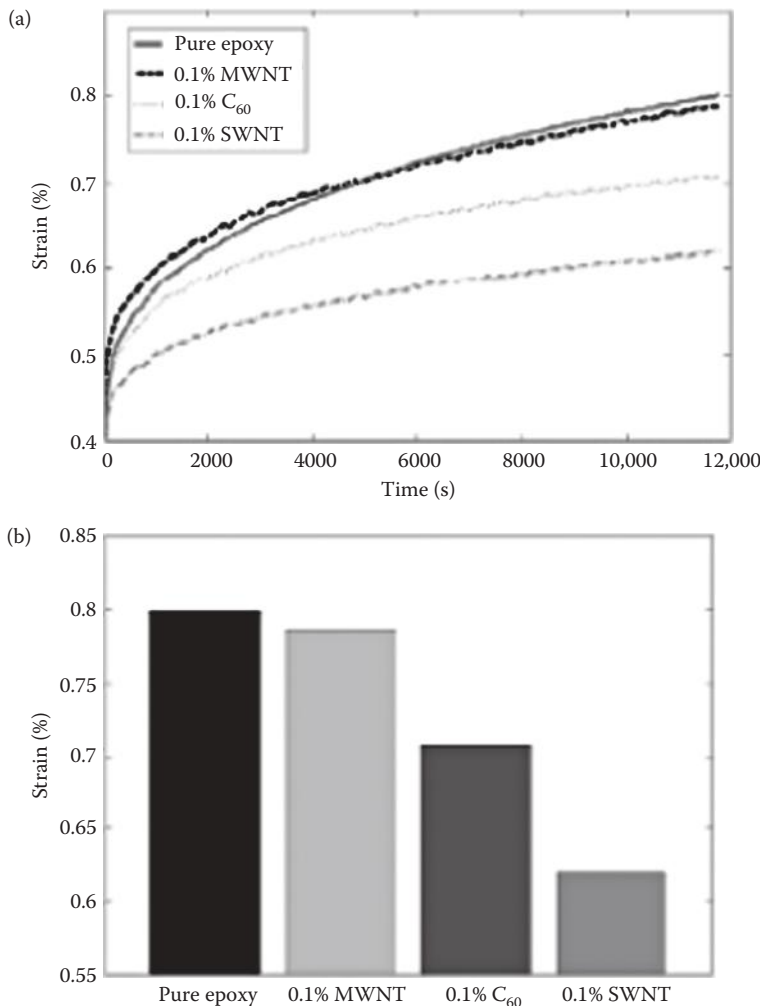
Another example of the nanoenhancement of viscoelastic behavior is the use of nanoreinforcements to improve creep resistance in polymers and polymer composites. For example, as shown in Figure 8.47, Zhang et al. [79] demonstrated that the tensile creep strain of epoxy is markedly reduced by adding only 0.1 wt% of well-dispersed SWNTs. It is believed that the reason for the improved creep performance is that the SWNTs limit the time-dependent, load-induced reorientation of the polymer chains. In this case, the SWNTs were more effective than either MWNTs or  $C_{60}$  fullerene nanoparticles in reducing creep. However, it was found that for SWNT weight fractions greater than about 0.1 wt%, the creep response deteriorated significantly due to poor dispersion of the SWNTs. Numerous other examples of improved creep performance of polymers due to the addition of small amounts of nanofillers have been reported in the literature. For example, Yang et al. [80] studied creep of  $TiO_2$  nanoparticle-enhanced polypropylene (PP), Zhou, et al. [81] characterized creep of  $SiO_2$  nanoparticle-enhanced PP, and Varela-Rizo, et al. [82] conducted creep tests of polymethylmethacrylate (PMMA) reinforced with either chopped CFs, MWNTs, or CNFs. As with the dynamic properties of nanocomposites, much of the research on creep of nanocomposites has been experimental, and there is a need for more analytical modeling work.

## PROBLEMS

- For a linear viscoelastic material, the creep response under a constant stress is followed by a “recovery response” after the stress is removed at some time,  $t_0$ . Using the Boltzmann Superposition Principle, find an expression for the uniaxial recovery compliance,  $R(t)$ , for times  $t > t_0$  in terms of the creep compliance,  $S(t)$ , the time of stress removal,  $t_0$ , and the time,  $t$ .
- In general, the creep compliances,  $S_{ij}(t)$ , and the relaxation moduli,  $C_{ij}(t)$ , are not related by a simple inverse relationship. Show that only when  $t \rightarrow 0$  and when  $t \rightarrow \infty$ , can we say that

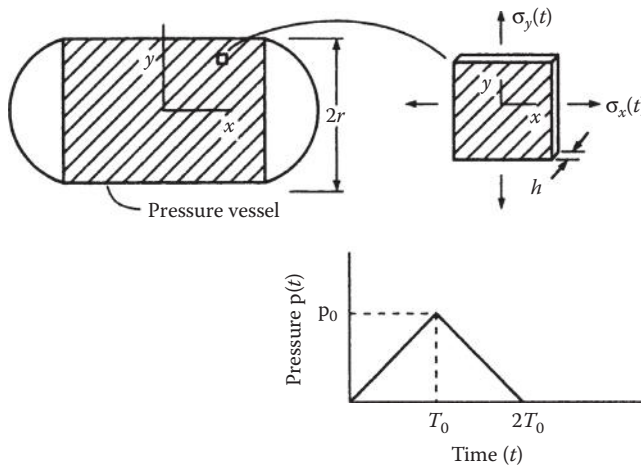
$$[C_{ij}(t)] = [S_{ij}(t)] - 1$$

- The shear creep compliance,  $S_{66}(t)$ , for a unidirectional viscoelastic composite is given by  $S_{66}(t) = \gamma_{12}(t)/\tau_{12}$ , where  $\gamma_{12}(t)$  is the time-dependent shear creep strain and  $\tau_{12}$  is the constant shear stress. If  $S_{66}(t)$  can be approximated by a power law as  $S_{66}(t) = at^b$ , where  $a$  and  $b$  are material constants and  $t$  is time, determine the “constant loading rate compliance”  $U_{66}(t) = \gamma_{12}(t)/\tau_{12}(t)$ , where the shear stress is due to a constant loading rate, so that  $\tau_{12}(t) = Kt$ , where  $K$  is a constant.

**FIGURE 8.47**

Effect of nanofillers on the creep response of epoxy composites. (a) Creep strain versus time for pure epoxy sample and epoxy nanocomposite samples with 0.1 wt% of SWNT, MWNT, and C<sub>60</sub> additives. Creep tests were performed at room temperature at an applied stress of 10 MPa. (b) Measured creep strain after 3 h of continuous testing for the pure epoxy and nanocomposite samples. (From Zhang, W. et al. 2007. *Nanotechnology*, 18, 185703. With permission.)

4. The time-dependent axial stress,  $\sigma_x(t)$ , and the time-dependent circumferential stress,  $\sigma_y(t)$ , in the wall of the filament-wound, thin-walled composite pressure vessel shown in Figure 8.48 are caused by the internal pressure  $p(t)$ , where  $t$  is time. The required dimensions of the vessel are the wall thickness  $h$  and the mean radius  $r$ .

**FIGURE 8.48**

State of stress in composite pressure vessel and variation of internal pressure with time for Problem 4.

Note that  $x$  and  $y$  are not the principal material axes, but, rather, are the longitudinal and transverse axes for the vessel. The variation of  $p(t)$  with time is also shown in Figure 8.48. If the creep compliances associated with the  $x$  and  $y$  axes are given in contracted notation by

$$\bar{S}_{ij}(t) = \bar{E}_{ij} + \bar{F}_{ij}t, \quad i, j = 1, 2, \dots, 6$$

where  $\bar{E}_{ij}$  and  $\bar{F}_{ij}$  are material constants, determine all the time-dependent strains along the  $x$  and  $y$  axes for  $t > 2T_0$ . Answers should be given in terms of  $p_0$ ,  $r$ ,  $h$ ,  $T_0$ ,  $t$ , and the individual  $\bar{E}_{ij}$  and  $\bar{F}_{ij}$ .

5. A linear viscoelastic, orthotropic lamina has principal creep compliances given in contracted notation by

$$S_{ij}(t) + E_{ij} + F_{ij}t, \quad i, j = 1, 2, \dots, 6$$

where  $E_{ij}$  and  $F_{ij}$  are material constants and  $t$  is time. The lamina is subjected to plane stress with constant stresses

$$\sigma_i(t) = \sigma'_i H(t), \quad i, j = 1, 2, \dots, 6$$

where  $\sigma'_i$  are constants and  $H(t)$  is the unit step function. If the failure strains for pure longitudinal, transverse, and shear loading of the lamina are  $e_L$ ,  $e_T$ , and  $e_{LT}$ , respectively, find the expressions for the time to failure for each of the three strains.

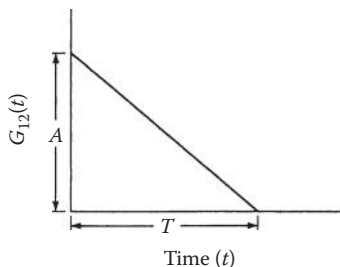
6. Derive the equations for the stress-strain relationship, the creep compliance, and the relaxation modulus for the Kelvin-Voigt model.

7. Derive the equations for the stress-strain relationship, the creep compliance, and the relaxation modulus for the Zener model.
8. Derive Equation 8.45.
9. Derive Equation 8.47.
10. The shear relaxation modulus,  $G_{12}(t)$ , for an orthotropic lamina is idealized, as shown in Figure 8.49. Find the corresponding equations for the shear storage modulus,  $G'_{12}(\omega)$ , and the shear loss modulus,  $G''_{12}(\omega)$ , and draw sketches of both parts of the complex modulus in the frequency domain.
11. For the Maxwell model in Figure 8.9, express the storage modulus,  $E'(\omega)$ , the loss modulus,  $E''(\omega)$ , and the loss factor,  $\eta(\omega)$ , in terms of the parameters  $\mu$  and  $k$  and the frequency  $\omega$ . Sketch the variation of  $E'(\omega)$ ,  $E''(\omega)$ , and  $\eta(\omega)$  in the frequency domain. It is not necessary to use Fourier transforms here.
12. Derive Equations 8.154 and 8.155.
13. The composite pressure vessel in Problem 4 is subjected to an internal pressure that varies sinusoidally with time according to the relationship  $p(t) = P_0 \sin t$ , and the principal complex compliances are given by

$$S_{mn}^*(\omega) = S'_{mn}(\omega) + iS''_{mn}(\omega), \quad m, n = 1, 2, \dots, 6$$

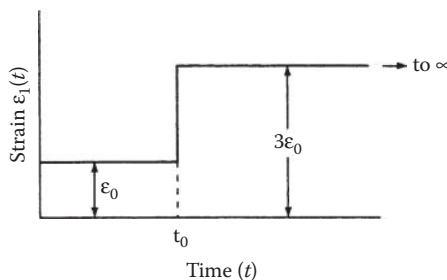
where  $\omega$  is the frequency. Determine all the time-dependent strains associated with the  $x$  and  $y$  axes in terms of  $P_0$ ,  $r$ ,  $h$ ,  $\omega$ , and the individual  $S'_{mn}(\omega)$  and  $S''_{mn}(\omega)$ .

14. The polymer matrix material in a linear viscoelastic, unidirectional composite material has a relaxation modulus that can be characterized by the Maxwell model in Figure 8.9. The fibers are assumed to be linear elastic. If the composite longitudinal strain-time history is as shown in Figure 8.50, express the composite longitudinal stress as a function of time.
15. The matrix material in a linear viscoelastic, unidirectional composite material is to be modeled by using a Maxwell model having parameters  $k_m$  and  $\mu_m$ , while the fiber is to be modeled by using a Kelvin-Voigt model having parameters  $k_f$  and  $\mu_f$ .



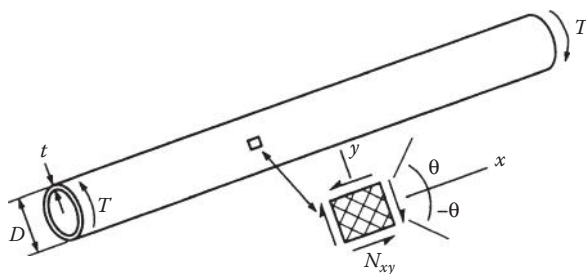
**FIGURE 8.49**

Variation of shear relaxation modulus,  $G_{12}(t)$ , with time for Problem 10.

**FIGURE 8.50**

Composite longitudinal strain–time history for Problem 14.

- Determine the complex extensional moduli of fiber and matrix materials in terms of the Maxwell and Kelvin–Voigt parameters and the frequency,  $\omega$ .
- Determine the complex longitudinal modulus of the unidirectional composite. Assume that fiber and matrix materials are isotropic. It is not necessary to use the Fourier transforms.
- The dynamic mechanical behavior of an isotropic polymer matrix material may be characterized by two independent complex moduli such as the complex extensional modulus,  $E^*(\omega)$ , and the complex shear modulus,  $G^*(\omega)$ . Based on experimental evidence, however, the imaginary parts of  $E^*(\omega)$  and  $G^*(\omega)$  are not independent, because the material can be assumed to be viscoelastic in shear but elastic in dilatation (i.e., the shear modulus,  $G^*(\omega)$ , is complex and frequency dependent, but the bulk modulus,  $k$ , is real and frequency independent). Use this simplifying assumption to develop an expression for the shear loss factor,  $\eta_G(\omega)$ , in terms of the extensional loss factor,  $\eta_E(\omega)$ , the extensional storage modulus,  $E'(\omega)$ , and the bulk modulus,  $k$ . Assume all loss factors  $\ll 1$ .
- A drive shaft in the shape of a hollow tube and made of a linear viscoelastic angle-ply laminate is subjected to a torque,  $T$ , as shown in Figure 8.51. Develop an analytical model for predicting the vibratory shear deformation in the shaft from the vibratory

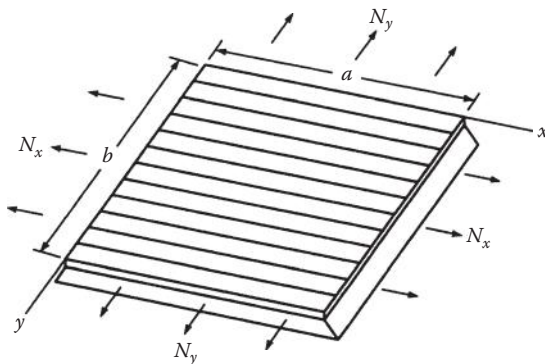
**FIGURE 8.51**

Composite drive under applied torque for Problem 17.

shear force,  $\bar{N}_{xy}(t)$ , when the torque  $T$  varies sinusoidally with time. The input to the model should include the properties and volume fractions of fiber and matrix materials, lamina orientations, and lamina-stacking sequences. That is, the model should include both micromechanical and macromechanical components. No calculations are necessary, but the key equations should be described, all parameters should be defined, and key assumptions should be delineated.

18. Longitudinal vibration of an isotropic, particle-reinforced composite bar may be modeled by using the 1D wave equation (Equation 8.99) if the material is linear elastic. Derive the equation of motion for longitudinal vibration of the bar if it can be assumed to be a Kelvin–Voigt linear viscoelastic material having the stress–strain relationship given by Equation 8.39.
19. Find the separation of variables solution for the longitudinal displacement,  $u(x,t)$ , of the equation derived in Problem 18. Leave the answer in terms of constants, which must be determined from the boundary conditions and the initial conditions.
20. Derive the equation of motion for free transverse vibration of a simply supported, specially orthotropic plate that is subjected to in-plane loads per unit length  $N_x$  and  $N_y$ , as shown in Figure 8.52.
21. For the plate described in Problem 20, find the equations for the plate natural frequencies and determine the effects of positive (tensile) and negative (compressive) in-plane loads  $N_x$  and  $N_y$  on the natural frequencies.
22. If the plate described in Problem 20 is clamped on all edges, investigate solutions of the form

$$W(x,y) = A_{mn} \left( 1 - \cos\left(\frac{2\pi x}{a}\right) \right) \left( 1 - \cos\left(\frac{2\pi y}{b}\right) \right)$$

**FIGURE 8.52**

Simply supported, specially orthotropic plate under in-plane loads for Problem 20.

Does this solution satisfy the boundary conditions? Can it be used to find the natural frequencies? Explain your answers.

23. The isochronous stress-strain curves for an epoxy material at different times are shown in Figure 8.53. This material is used as the matrix in a unidirectional E-glass–epoxy composite having a fiber volume fraction of 0.6. Using micromechanics and the Elastic–Viscoelastic Correspondence Principle, determine the longitudinal relaxation modulus  $E_1(t)$  for the composite at  $t = 1$  h and  $t = 10,000$  h. Note that the strain in Figure 8.53 is given in percent strain (e.g., a percent strain value of 1.5 corresponds to a strain of 0.015). Elastic properties of fibers are given in Table 1.1.
24. Part of the required input to the viscoelastic option in some finite element codes is a table showing the time-dependent, isotropic shear modulus  $G(t)$  at different times  $t$ . Explain how you would generate such a table from tensile isochronous stress–strain curves such as the ones in Figure 8.53. Include the key equations and a list of assumptions in your explanation.
25. For the Maxwell model shown in Figure 8.9, it can be shown that the complex modulus is given by

$$E^*(\omega) = E'(\omega)[1 + i\eta(\omega)]$$

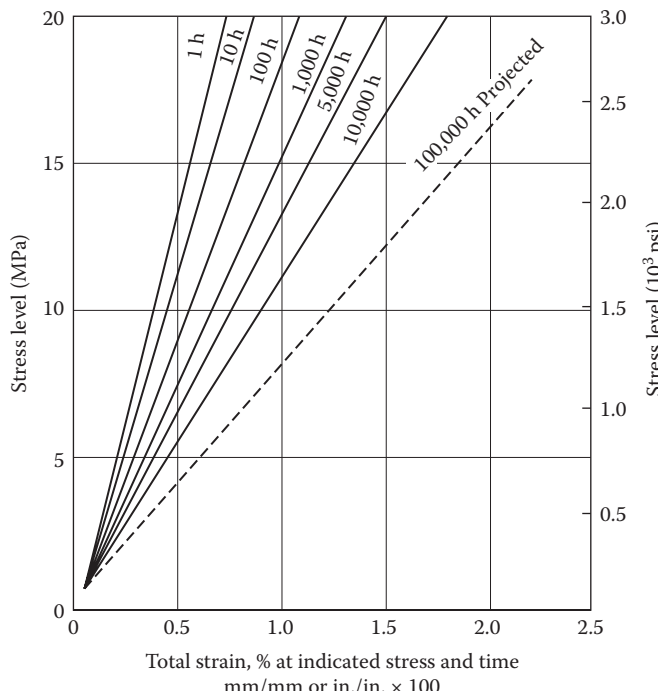


**FIGURE 8.53**  
Isochronous stress–strain curves for epoxy matrix material in Problem 23.

where the frequency-dependent storage modulus is given by

$$E'(\omega) = \frac{k\omega^2\lambda^2}{1 + \omega^2\lambda^2}$$

and the frequency-dependent loss factor is given by

$$\eta(\omega) = \frac{1}{\omega\lambda}$$

where  $\omega$  is the frequency and  $\lambda = \mu/k$  is the relaxation time. Let us assume that the Maxwell model adequately describes the viscoelastic behavior of a particular material. Explain how you would use the Maxwell model and frequency-domain vibration test data to indirectly determine the numerical value of the relaxation modulus  $C(t)$  for this material.

26. A thin-walled cylindrical pressure vessel has mean diameter  $d = 18$  in. and wall thickness  $h = 0.25$  in. The vessel is made of filament-wound unidirectional composite material with all fibers oriented in the circumferential, or hoop, direction. The internal pressure in the vessel can be assumed to be constant. From creep tests of specimens of the unidirectional composite material, it is found that the principal creep compliances can be described by the following power-law expressions:

$$S_{11}(t) = 0.121 + 0.0003t^{0.19}$$

$$S_{12}(t) = -0.0315 + 0.004t^{0.19}$$

$$S_{22}(t) = 0.3115 + 0.0025t^{0.19}$$

$$S_{66}(t) = 0.839 + 0.003t^{0.19}$$

where  $t$  is the time in minutes and all compliances are given in units of  $(\times 10^{-6} \text{ psi}^{-1})$ . The ultimate failure strains for the material are found to be as follows.

$$e_L^{(+)} = 0.0194, \quad e_T^{(+)} = 0.00125, \quad e_{LT} = 0.010$$

- a. According to the Maximum Strain Criterion, what is the allowable internal pressure in the vessel, if it is to be designed to last for at least 20 years under constant pressure?
  - b. How would you change the design of the vessel so as to increase the allowable internal pressure, while maintaining the 20-year design life?
27. For the nonsymmetrical laminated beam of Problem 29 in Chapter 7, determine the effects of  $B_{ij}$ -type coupling on the flexural vibration frequencies.

28. If the complex moduli of the 0° and 90° plies in a laminated beam are the same as those described in Example 8.12, but the laminate has a stacking sequence of [90/0/90]s instead of [0/90/0]s, determine the corresponding flexural loss factor. Compare and contrast these results with those of Example 8.12.

---

## References

1. Schapery, R. A. 1974. Viscoelastic behavior and analysis of composite materials, in Sendeckyj, G. P. ed., *Composite Materials*, Vol. 2, *Mechanics of Composite Materials*, pp. 85–168. Academic Press, New York, NY.
2. Beckwith, S. W. 1984. Viscoelastic creep behavior of filament-wound case materials. *Journal of Spacecraft and Rockets*, 21(6), 546–552.
3. Fung, Y. C. 1979. *Foundations of Solid Mechanics*. Prentice-Hall, Inc., Englewood Cliffs, NJ.
4. Christensen, R. M. 1979. *Mechanics of Composite Materials*. John Wiley & Sons, New York, NY.
5. Halpin, J. C. and Pagano, N. J. 1968. Observations on linear anisotropic viscoelasticity. *Journal of Composite Materials*, 2(1), 68–80.
6. Christensen, R. M. 1982. *Theory of Viscoelasticity: An Introduction*, 2nd edn. Academic Press, New York, NY.
7. Sullivan, J. L. 1992. Polymer viscoelasticity. Unpublished notes, Ford Motor Co., Dearborn, MI.
8. McCrum, N. G., Buckley, C. P., and Bucknall, C. B. 1988. *Principles of Polymer Engineering*. Oxford University Press, Oxford.
9. Wen, Y. F., Gibson, R. F., and Sullivan, J. L. 1997. Prediction of momentary transverse creep behavior of thermoplastic polymer matrix composites using micro-mechanical models. *Journal of Composite Materials*, 31(21), 2124–2145.
10. Gibson, R. F. 1979. Measurement of creep in rotating viscoelastic disks. *Experimental Mechanics*, 19(10), 378–383.
11. Gibson, R. F., Baxi, J., Bettinger, D., Stoll, F., and Johnson, V. 1999. Simulation of assembly and operation of pre-stressed, heat-shrinkable structural composite connectors, *Proceedings of ASME Noise Control and Acoustics Division*, NCA Vol. 26. American Society of Mechanical Engineers, New York, NY, pp. 319–332.
12. Gibson, R. F., Younus, M., Kumar, P., Stoll, F., and Bettinger, D. 1998. Viscoelastic behavior of extended interval lubricator cartridges made from nylon and glass/nylon composites, *Proceedings of 43rd International SAMPE Symposium & Exhibition*. Society for the Advancement of Material and Process Engineering, Covina, CA, pp. 2144–2157.
13. Bracewell, R. N. 1978. *The Fourier Transform and Its Application*, 2nd edn. McGraw-Hill, Inc., New York, NY.
14. Gibson, R. F., Hwang, S. J., and Sheppard, C. H. 1990. Characterization of creep in polymer composites by the use of frequency-time transformations. *Journal of Composite Materials*, 24, 441–453.
15. Lee, E. H. 1955. Stress analysis in viscoelastic bodies. *Quarterly of Applied Mathematics*, 13, 183–190.

16. Biot, M. A. 1958. Linear thermodynamics and the mechanics of solids, *Proceedings of the Third U.S. National Congress of Applied Mechanics*. The National Academies, Washington, DC, pp. 1–18.
17. Schapery, R. A. 1967. Stress analysis of viscoelastic composite materials. *Journal of Composite Materials*, 1, 228–267.
18. Beckwith, S. W. 1974. *Viscoelastic characterization of a nonlinear glass/epoxy composite including the effects of damage*. PhD dissertation, Texas A&M University, College Station, TX.
19. Sims, D. F. and Halpin, J. C. 1974. Methods for determining the elastic and viscoelastic response of composite materials, *Composite Materials: Testing and Design (Third Conference)*, ASTM STP 546. American Society for Testing and Materials, Philadelphia, PA, pp. 46–66.
20. Hashin, Z. 1970. Complex moduli of viscoelastic composites. I: General theory and application to particulate composites. *International Journal of Solids and Structures*, 6, 539–552.
21. Hashin, Z. 1970. Complex moduli of viscoelastic composites. ii: Fiber reinforced materials. *International Journal of Solids and Structures*, 6, 797–807.
22. Suarez, S. A., Gibson, R. F., Sun, C. T., and Chaturvedi, S. K. 1986. The influence of fiber length and fiber orientation on damping and stiffness of polymer composite materials. *Experimental Mechanics*, 26(2), 175–184.
23. Sun, C. T., Wu, J. K., and Gibson, R. F. 1987. Prediction of material damping of laminated polymer matrix composites. *Journal of Materials Science*, 22, 1006–1012.
24. Findley, W. N., Lai, J. S., and Onaran, K. 1976. *Creep and Relaxation of Nonlinear Viscoelastic Materials*. Dover Publications, New York, NY.
25. Ferry, J. D. 1970. *Viscoelastic Properties of Polymers*, 2nd edn. John Wiley & Sons, New York, NY.
26. Struik, L. C. E. 1977. Physical aging in plastics and other glassy materials. *Polymer Engineering and Science*, 17, 165–173.
27. Struik, L. C. E. 1978. *Physical Aging in Amorphous Polymers and Other Materials*. Elsevier, Amsterdam.
28. Janas, V. F. and McCullough, R. L. 1987. The effects of physical aging on the viscoelastic behavior of a thermoset polyester. *Composites Science and Technology*, 30, 99–118.
29. Ogale, A. A. and McCullough, R. L. 1987. Physical aging of polyether ether ketone. *Composites Science and Technology*, 30, 137–148.
30. Sullivan, J. L. 1990. Creep and physical aging of composites. *Composites Science and Technology*, 39, 207–232.
31. Scott, D. W., Lai, J. S., and Zureick, A.-H. 1995. Creep behavior of fiber-reinforced polymeric composites: A review of the technical literature. *Journal of Reinforced Plastics and Composites*, 14, 588–617.
32. Hearmon, R. F. S. 1961. *An Introduction to Applied Anisotropic Elasticity*. Oxford University Press, Oxford.
33. Achenbach, J. D. 1974. Waves and vibrations in directionally reinforced composites, in Sendeckyj, G. P. ed., *Composite Materials*, Vol. 2, *Mechanics of Composite Materials*. Academic Press, New York, NY.
34. Ross, C. A. and Sierakowski, R. L. 1975. Elastic waves in fiber reinforced materials. *The Shock and Vibration Digest*, 7(1), 1–12.
35. Moon, F. C. 1974. Wave propagation and impact in composite materials, in Chamis, C. C. ed., *Composite Materials*, Vol. 7. Academic Press, New York, NY.

36. Whitney, J. M. 1987. *Structural Analysis of Laminated Anisotropic Plates*. Technomic Publishing Co., Lancaster, PA.
37. Vinson, J. R. and Sierakowski, R. L. 1986. *The Behavior of Structures Composed of Composite Materials*. Martinus Nijhoff Publishers, Dordrecht, The Netherlands.
38. Sierakowski, R. L. and Chaturvedi, S. K. 1997. *Dynamic Loading and Characterization of Fiber-Reinforced Composites*. John Wiley & Sons, Inc., New York, NY.
39. Meirovitch, L. 1986. *Elements of Vibration Analysis*, 2nd edn. McGraw-Hill, Inc., New York, NY.
40. Timoshenko, S. P., Young, D. H., and Weaver, W., Jr. 1974. *Vibration Problems in Engineering*. John Wiley & Sons, New York, NY.
41. Dudek, T. J. 1970. Young's and shear moduli of unidirectional composites by a resonant beam method. *Journal of Composite Materials*, 4, 232–241.
42. Ni, R. G. and Adams, R. D. 1984. The damping and dynamic moduli of symmetric laminated beams—Theoretical and experimental results. *Journal of Composite Materials*, 18, 104–121.
43. Huang, T. C. and Huang, C. C. 1971. Free vibrations of viscoelastic Timoshenko beam. *Journal of Applied Mechanics*, 38, Series E(2), 515–521.
44. Nakao, T., Okano, T., and Asano, I. 1985. Theoretical and experimental analysis of flexural vibration of the viscoelastic Timoshenko beam. *Journal of Applied Mechanics*, 52(3), 728–731.
45. Jones, R. M. 1973. Buckling and vibration of unsymmetrically laminated cross-ply rectangular plates. *AIAA Journal*, 11(12), 1626–1632.
46. Gibson, R. F. 1992. Damping characteristics of composite materials and structures. *Journal of Engineering Materials and Performance*, 1(1), 11–20.
47. Gibson, R. F. 1987. Dynamic mechanical properties of advanced composite materials and structures: A review. *The Shock and Vibration Digest*, 19(7), 13–22.
48. Gibson, R. F. 1990. Dynamic mechanical properties of advanced composite materials and structures: A review of recent research. *The Shock and Vibration Digest*, 22(8), 3–12.
49. Bert, C. W. 1980. Composite materials: A survey of the damping capacity of fiber reinforced composites, in Torvik, P. J. ed., *Damping Applications for Vibration Control*, AMD Vol. 38, pp. 53–63. American Society of Mechanical Engineers, New York, NY.
50. Adams, R. D. 1987. Damping properties analysis of composites, in Reinhart, T. J. ed., *Engineered Materials Handbook*, Vol. 1, *Composites*, pp. 206–217. ASM International, Materials Park, OH.
51. Chaturvedi, S. K. 1989. Damping of polymer matrix composite materials, in Lee, S. ed., *Encyclopedia of Composites*. VCH Publishing Co., New York, NY.
52. Kinra, V. K. and Wolfenden, A. eds. 1992. *M3D: Mechanics and Mechanisms of Material Damping*, ASTM STP 1169. American Society for Testing and Materials, Philadelphia, PA.
53. Sun, C. T. and Lu, Y. P. 1995. *Vibration Damping of Structural Elements*. Prentice-Hall, Englewood Cliffs, NJ.
54. Zener, C. 1948. *Elasticity and Anelasticity of Metals*. The University of Chicago Press, Chicago, IL.
55. Granato, A. V. and Lucke, K. 1956. Application of dislocation theory to internal friction phenomena at high frequencies. *Journal of Applied Physics*, 27(7), 789–805.

56. Sun, C. T., Chaturvedi, S. K., and Gibson, R. F. 1985. Internal material damping of polymer matrix composites under off-axis loading. *Journal of Materials Science*, 20, 2575–2585.
57. Sun, C. T., Wu, J. K., and Gibson, R. F. 1985. Prediction of material damping in randomly oriented short fiber polymer matrix composites. *Journal of Reinforced, Plastics and Composites*, 4, 262–272.
58. Pant, R. H. and Gibson, R. F. 1996. Analysis and testing of dynamic micromechanical behavior of composite materials at elevated temperatures. *Journal of Engineering Materials and Technology*, 118, 554–560.
59. Finegan, I. C. and Gibson, R. F. 2000. Analytical modeling of damping at micro-mechanical level in polymer composites reinforced with coated fibers. *Composites Science and Technology*, 60, 1077–1084.
60. Guan, H. and Gibson, R. F. 2001. Micromechanical models for damping in woven fabric-reinforced polymer matrix composites. *Journal of Composite Materials*, 35(16), 1417–1434.
61. Nashif, A. D., Jones, D. I. G., and Henderson, J. P. 1985. *Vibration Damping*. John Wiley & Sons, New York, NY.
62. Ungar, E. E. and Kerwin, E. M., Jr. 1962. Loss factors of viscoelastic systems in terms of strain energy. *Journal of the Acoustical Society of America*, 34(2), 954–958.
63. Gibson, R. F., Chaturvedi, S. K., and Sun, C. T. 1982. Complex moduli of aligned discontinuous fiber reinforced polymer composites. *Journal of Materials Science*, 17, 3499–3509.
64. Johnson, C. D. and Kienholz, D. A. 1982. Finite element prediction of damping in structures with constrained viscoelastic layers. *AIAA Journal*, 20(9), 1284–1290.
65. Hwang, S. J. and Gibson, R. F. 1987. Micromechanical modeling of damping in discontinuous fiber composites using a strain energy/finite element approach. *Journal of Engineering Materials and Technology*, 109, 47–52.
66. Gibson, R. F., Hwang, S. J., and Kwak, H. 1991. Micromechanical modeling of damping in composites including interphase effects, in *How Concept Becomes Reality—Proceedings of 36th International SAMPE Symposium*, vol. 1. Society for the Advancement of Material and Process Engineering, Covina, CA, pp. 592–606.
67. Hwang, S. J. and Gibson, R. F. 1991. The effects of 3-D states of stress on damping of laminated composites. *Composites Science and Technology*, 41, 379–393.
68. Hwang, S. J. and Gibson, R. F. 1992. Contribution of interlaminar stresses to damping in thick laminated composites under uniaxial extension. *Composite Structures*, 20, 29–35.
69. Hwang, S. J., Gibson, R. F., and Singh, J. 1992. Decomposition of coupling effects on damping of laminated composites under flexural vibration. *Composites Science and Technology*, 43, 159–169.
70. Mantena, P. R., Gibson, R. F., and Hwang, S. J. 1991. Optimal constrained viscoelastic tape lengths for maximizing damping in laminated composites. *AIAA Journal*, 29(10), 1678–1685.
71. Hwang, S. J. and Gibson, R. F. 1992. The use of strain energy-based finite element techniques in the analysis of various aspects of damping of composite materials and structures. *Journal of Composite Materials*, 26(17), 2585–2605.
72. Chen, Y. and Gibson, R. F. 2003. Analytical and experimental studies of composite isogrid structures with integral passive damping. *Mechanics of Advanced Materials and Structures*, 10(2), 127–143.

73. Plagianakos, T. S. and Saravacos, D. S. 2003. Mechanics and finite elements for the damped dynamic characteristics of curvilinear laminates and composite shell structures. *Journal of Sound and Vibration*, 263(2), 399–414.
74. Li, Z. and Crocker, M. J. 2005. A review on vibration damping in sandwich composite structures. *International Journal of Acoustics and Vibration*, 10(4), 159–169.
75. Gibson, R. F., Ayorinde, E. O., and Wen, Y. F. 2007. Vibrations of carbon nanotubes and their composites: A review. *Composites Science and Technology*, 67(1), 1–28.
76. Koratkar, N. A., Suhr, J., Joshi, A., Kane, R. S., Schadler, L. S., Ajayan, P. M., and Bartolucci, S. 2005. Characterizing energy dissipation in single-walled carbon nanotube polycarbonate composites. *Applied Physics Letters*, 87, 063102.
77. Zhou, X., Shin, E., Wang, K. W., and Bakis, C. E. 2004. Interfacial damping characteristics of carbon nanotube composites. *Composites Science and Technology*, 64, 2425–2437.
78. Rajoria, H. and Jalili, N. 2005. Passive vibration damping enhancement using carbon nanotube–epoxy reinforced composites. *Composites Science and Technology*, 65, 2079–2093.
79. Zhang, W., Joshi, A., Wang, Z., Kane, R. S., and Koratkar, N. 2007. Creep mitigation in composites using carbon nanotube additives. *Nanotechnology*, 18, 185703.
80. Yang, J., Zhang, Z., Friedrich, K., and Schlarb, A. K. 2007. Resistance to time-dependent deformation of nanoparticle/polymer composites. *Applied Physics Letters*, 91, 011901.
81. Zhou, T. H., Ruan, W. H., Yang, J. L., Rong, M. Z., Zhang, M. Q., and Zhang, Z. 2007. A novel route for improving creep resistance of polymers using nanoparticles. *Composites Science and Technology*, 67, 2297–2302.
82. Varela-Rizo, H., Weisenberger, M., Bortz, D. R., and Martin-Gullon, I. 2010. Fracture toughness and creep performance of PMMA composites containing micro and nanosized carbon filaments. *Composites Science and Technology*, 70, 1189–1195.

This page intentionally left blank

# 9

---

## *Analysis of Fracture*

---

### **9.1 Introduction**

Except for a brief discussion in Section 7.8.2, the previous chapters of this book have not considered the analysis of the effects of notches, cracks, delaminations, or other discontinuities in composites. For example, the conventional strength analyses outlined in Chapter 4 involved the use of gross “effective lamina strengths” in various semiempirical failure criteria irrespective of specific micromechanical failure modes that are related to such discontinuities. While such procedures, along with the use of empirical “safety factors,” may produce a satisfactory design for static loading, failures may still occur due to the growth of cracks or delaminations under dynamic loading. The purpose of this chapter is to give an introduction to the analysis of fracture of composites due to cracks, notches, and delaminations.

First, the prediction of the strength of composites with through-thickness cracks and notches is considered by using both fracture mechanics and stress fracture approaches. Next, the use of fracture mechanics in the analysis of interlaminar fracture will be discussed. Each of these topics is the subject of many publications. Thus, only brief introductions to the subjects are given here, along with key references where more detailed analyses may be found. Each of these topics is also the subject of considerable current research, and the reader is encouraged to consult technical journals for the results of the most recent research. Composites handbooks provide information on the basics of composite fracture [1]. The Special Technical Publication (STP) series by the American Society for Testing and Materials is a good source of recent research findings [2–7]. The application of fracture mechanics to composites is the subject of a book [8], as is delamination in composites [9].

---

### **9.2 Fracture Mechanics Analyses of Through-Thickness Cracks**

Much of the early work on fracture in composites involved investigations of the applicability of linear elastic fracture mechanics, which had been originally

developed for the analysis of through-thickness cracks in homogeneous, isotropic metals. The origin of fracture mechanics can be traced back to the seminal work of Griffith [10], who explained the discrepancy between the measured and predicted strength of glass by considering the stability of a small crack. The stability criterion was developed by using an energy balance on the crack.

Consider the through-thickness crack in the uniaxially loaded homogeneous, isotropic, linear elastic plate of infinite width shown in Figure 9.1. Griffith reasoned that the strain energy of the cracked plate would be less than the corresponding strain energy of the uncracked plate, and from a stress analysis, he estimated that the strain energy released by the creation of the crack under plane stress conditions would be

$$U_r = \frac{\pi\sigma^2 a^2 t}{E} \quad (9.1)$$

where

$U_r$  = strain energy released

$\sigma$  = applied stress

$a$  = half-crack length

$t$  = plate thickness

$E$  = modulus of elasticity of the plate

The corresponding expression in Griffith's original paper was later found to be in error, and Equation 9.1 is consistent with the corrected expression in more recent publications [11,12]. In addition, Griffith's energy terms were given on a per unit thickness basis. Equation 9.1 is also consistent with the strain energy released by relaxation of an elliptical zone having major and minor axes of lengths  $4a$  and  $2a$ , respectively, where the minor axis is coincident

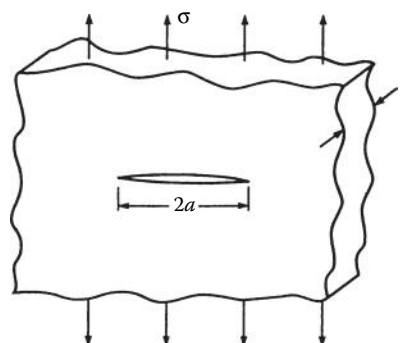


**FIGURE 9.1**

The Griffith crack: A through-thickness crack in a uniaxially stressed plate of infinite width.

with the crack and the major axis is perpendicular to the crack. The volume of such an ellipse is

$$V = \pi(2a)(a)(t) = 2\pi a^2 t \quad (9.2)$$

Since the plate was assumed to be uniformly stressed before the introduction of the crack, the strain energy released due to relaxation of the elliptical volume around the crack is

$$U_r = \frac{1}{2} \frac{\sigma^2}{E} V = \frac{\pi \sigma^2 a^2 t}{E} \quad (9.3)$$

Griffith also assumed that the creation of new crack surfaces required the absorption of an amount of energy given by

$$U_s = 4at\gamma_s \quad (9.4)$$

where

$U_s$  = energy absorbed by creation of new crack surfaces

$\gamma_s$  = surface energy per unit area

As the crack grows, if the rate at which energy is absorbed by creating new surfaces is greater than the rate at which strain energy is released, then

$$\frac{\partial U_s}{\partial a} > \frac{\partial U_r}{\partial a} \quad (9.5)$$

and crack growth is stable. If the strain energy is released at a greater rate than it can be absorbed, then

$$\frac{\partial U_r}{\partial a} > \frac{\partial U_s}{\partial a} \quad (9.6)$$

and crack growth is unstable. The threshold of stability, or the condition of neutral equilibrium, is therefore given by

$$\frac{\partial U_r}{\partial a} = \frac{\partial U_s}{\partial a} \quad (9.7)$$

or

$$\frac{\pi \sigma^2 a}{E} = 2\gamma_s \quad (9.8)$$

Thus, the critical stress,  $\sigma_c$ , for self-sustaining extension of the crack in plane stress is

$$\sigma_c = \sqrt{\frac{2E\gamma_s}{\pi a}} \quad (9.9)$$

Alternatively, the critical flaw size for plane stress at stress level  $\sigma$  is

$$a_c = \frac{2E\gamma_s}{\pi\sigma^2} \quad (9.10)$$

It is interesting to note that when we rearrange Equation 9.8 as

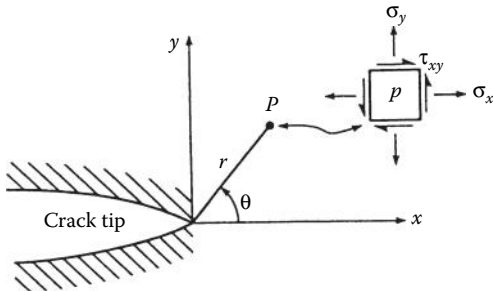
$$\sigma\sqrt{\pi a} = \sqrt{2E\gamma_s} \quad (9.11)$$

the terms on the left-hand side depend only on loading and geometry, whereas the terms on the right-hand side depend only on material properties. Thus, when the stress reaches the critical fracture stress,  $\sigma_c$ , the left-hand side becomes  $\sigma_c\sqrt{\pi a}$ . The term  $\sigma_c\sqrt{\pi a}$  is now referred to as the fracture toughness,  $K_c$ . This is a very important concept, which we will return to later.

The application of the Griffith-type analysis to composites presents some difficulties, but, fortunately, many of these problems have been solved over the years since Griffith's work. For example, for metals and many polymers the energy absorbed in crack extension is actually greater than the surface energy. Recognizing this, both Irwin [13] and Orowan [14] modified the Griffith analysis to include energy absorption due to plastic deformation at the crack tip. In this analysis the factor  $2\gamma_s$  on the right-hand side of Equation 9.8 and in all subsequent equations is replaced by the factor  $2(\gamma_s + \gamma_p)$ , where  $\gamma_p$  is the energy of plastic deformation. The solutions of several other problems encountered in the development of composite fracture mechanics have been made possible by the use of several different analytical techniques. Two of these techniques, now referred to as the "stress intensity factor" approach and the "strain energy release rate" approach, will be discussed in the following sections.

### 9.2.1 Stress Intensity Factor Approach

The Griffith analysis was originally developed for homogeneous, isotropic materials. Using effective modulus theory, we can replace the heterogeneous, anisotropic composite with an equivalent homogeneous, anisotropic material. It turns out that by considering the stress distribution around the crack tip, we can develop another interpretation of the Griffith analysis which can

**FIGURE 9.2**

Stresses at the tip of a crack under plane stress.

be applied equally well to homogeneous isotropic or anisotropic materials and to states of stress other than the simple uniaxial stress that Griffith used. Referring to the plane stress condition in the vicinity of the uniaxially loaded crack in Figure 9.2, Westergaard [15] used a complex stress function approach to show that the stresses for the isotropic case at a point  $P$  defined by polar coordinates  $(r, \theta)$  can be expressed as

$$\sigma_x = \frac{K_1}{\sqrt{2\pi r}} f_1(\theta) \quad (9.12)$$

$$\sigma_y = \frac{K_1}{\sqrt{2\pi r}} f_2(\theta) \quad (9.13)$$

$$\tau_{xy} = \frac{K_1}{\sqrt{2\pi r}} f_3(\theta) \quad (9.14)$$

where  $K_1$  is the stress intensity factor for the crack opening mode, as defined by

$$K_1 = \sigma \sqrt{\pi a} \quad (9.15)$$

and the  $f_i(\theta)$  are trigonometric functions of the angle. Irwin [16] recognized that the term  $\sigma \sqrt{\pi a}$  controls the magnitudes of the stresses at a point  $(r, \theta)$  near the crack tip. Returning to the discussion following Equation 9.11, we see that the critical value of the stress intensity factor,  $K_{lc}$ , corresponding to the critical stress,  $\sigma_c$ , is the fracture toughness. That is,

$$K_{lc} = \sigma_c \sqrt{\pi a} \quad (9.16)$$

The fracture toughness,  $K_{lc}$ , is a material property that can be determined experimentally, as shown later. Thus, if the fracture toughness of the material is known, the fracture mechanics analysis can be used in two ways, depending on whether the applied stress or the crack size is known. If the applied stress,  $\sigma$ , is known, equations such as Equation 9.15 can be used to find the critical crack size,  $a_c$ , which will lead to unstable and catastrophic crack growth. Knowing the critical crack size, we can specify inspection of the component in question to make sure that there are no cracks of that size. On the other hand, if the crack size,  $a$ , is known, then equations such as Equation 9.15 can be used to find the critical stress,  $\sigma_c$ , which will lead to unstable and catastrophic crack growth. Loading on the component in question would then be specified so as not to exceed this stress.

The reader is cautioned that the stress intensity factor is defined as  $k_1 = \sigma\sqrt{a}$  in some publications. This definition corresponds to the cancellation of  $\sqrt{\pi}$  in both the numerator and the denominator of Equations 9.12 through 9.14, so that the denominator corresponding to  $k_1$  would be  $\sqrt{2r}$  instead of  $\sqrt{2\pi r}$ , and thus  $K_1 = k_1\sqrt{\pi}$ .

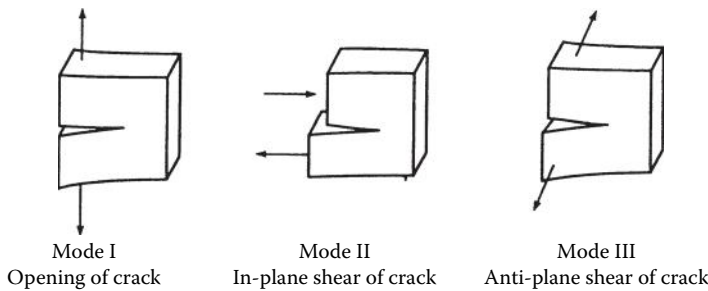
Expressions for stress distributions for other types of loading and crack geometries in isotropic materials lead to expressions that are similar to Equations 9.12 through 9.14, and the corresponding stress intensity factors can be found in the same way [17]. Other important results such as finite width correction factors (recall that the Griffith analysis is for a crack in an infinite width plate) have been tabulated in Ref. [17]. The three basic modes of crack deformation are shown in Figure 9.3. Thus, for the crack opening mode in the above example (mode I), we have the stress intensity factor  $K_I$ . For the in-plane shear mode (mode II) we have the stress intensity factor  $K_{II}$ , and for the antiplane shear mode (mode III) we have  $K_{III}$ . For example, for the cases of pure shear loading in modes II and III we have

$$K_{II} = \tau\sqrt{\pi a} \quad \text{and} \quad K_{III} = \tau\sqrt{\pi a} \quad (9.17)$$

respectively, where the shear stress,  $\tau$ , is different for modes II and III, as shown in Figure 9.3.

Although the stress analyses for the corresponding anisotropic material cases are more difficult and the expressions are more complicated, the stress intensity factors for certain loading conditions and crack geometries are the same as those for the isotropic case. For example, Lekhnitskii [18] has used a stress function approach to show that if the crack shown in Figures 9.1 and 9.2 lies in an anisotropic material for which the  $xy$ -plane is a plane of material property symmetry, then the stresses are given by

$$\sigma_x = \frac{K_I}{\sqrt{2\pi r}} F_1(\theta, s_1, s_2) \quad (9.18)$$

**FIGURE 9.3**

The three basic modes of crack deformation.

$$\sigma_y = \frac{K_I}{\sqrt{2\pi r}} F_2(\theta, s_1, s_2) \quad (9.19)$$

and

$$\tau_{xy} = \frac{K_I}{\sqrt{2\pi r}} F_3(\theta, s_1, s_2) \quad (9.20)$$

where the functions  $F_i(\theta, s_1, s_2)$  include not only trigonometric functions of the angle,  $\theta$ , but also  $s_1$  and  $s_2$ , which are complex roots of the characteristic equation corresponding to a differential equation in the stress function [18]. As pointed out by Wu [19], the magnitudes of the stresses at point  $(r, \theta)$  in an isotropic material (Equations 9.12 through 9.14) are completely determined by the stress intensity factors, but in the anisotropic case (Equations 9.18 through 9.20), these magnitudes also depend on  $s_1$  and  $s_2$ . Wu [19] has also shown, however, that if the crack lies along a principal material direction in the anisotropic material, then the stress intensity factors given by Equations 9.15 and 9.17 are still valid for their respective loading conditions shown in Figure 9.3.

Several experimental investigations have shown that the concept of a critical stress intensity factor can be used to describe the fracture behavior of through-thickness cracked unidirectional composites and laminates. Wu [19] reasoned that if the fracture toughness,  $K_{lc}$ , is a material constant, then by considering the logarithm of Equation 9.16, the slope of the  $\log \sigma_c$  versus  $\log a_c$  plot must be  $-0.5$ . Wu's experimental results for unidirectional E-glass/epoxy showed good agreement with this prediction. Konish et al. [20] showed that the critical stress intensity factors for  $0^\circ$ ,  $90^\circ$ ,  $45^\circ$  [ $\pm 45^\circ$ ]<sub>s</sub>, and  $[0^\circ \pm 45^\circ / 90^\circ]$ <sub>s</sub> graphite/epoxy laminates could be determined by using the same fracture toughness test method that had been developed for metals. Parhizgar et al. [21] showed both analytically and experimentally that the fracture toughness of unidirectional E-glass–epoxy composites is a constant

material property that does not depend on crack length but that does depend on fiber orientation.

The fracture toughness,  $K_{lc}$ , has been found to be an essentially constant material property for a variety of randomly oriented short fiber composites, as shown in papers by Alexander et al. [22] and Sun and Sierakowski [23]. Although the random fiber orientation in such materials allows one to use the numerous tabulated solutions for stress intensity factors of isotropic materials [17], it appears that the simple crack growth assumed in the Griffith-type analysis does not always occur in these materials. As an alternative to crack growth, the concept of a damage zone ahead of the crack tip in short-fiber composites has been proposed by Gaggar and Broutman [24].

### Example 9.1

A quasiisotropic graphite/epoxy laminate has a fracture toughness  $K_{lc} = 30 \text{ MPa m}^{1/2}$  and a tensile strength of 500 MPa. As shown in Figure 9.4, a 25-mm-wide structural element made from this material has an edge crack of length  $a = 3 \text{ mm}$ . If the element is subjected to a uniaxial stress,  $\sigma$ , determine the critical value of the stress that would cause unstable propagation of the crack. Compare this stress with the tensile strength of the material, which does not take cracks into account.

#### SOLUTION

From tabulated solutions [17], the stress intensity factor for the single-edge crack in Figure 9.4 is

$$K_I = \sigma \sqrt{\pi a f(a/b)}$$

where the function  $f(a/b)$  is given by the empirical formula [17]  $f(a/b) = 1.12 - 0.231(a/b) + 10.55(a/b)^2 - 21.72(a/b)^3 + 30.39(a/b)^4$  which is said to be accurate within 0.5% when  $a/b \leq 0.6$ . For this case,  $a/b = 3/25 = 0.12$  and  $f(a/b) = 1.213$ . The critical stress is then

$$\sigma_c = \frac{K_{lc}}{\sqrt{\pi a f(a/b)}} = \frac{30}{\sqrt{\pi}(0.003)(1.213)} = 255 \text{ MPa}$$

Comparing this stress with the tensile strength of 500 MPa, we see that in this case the cracked element can sustain only about 50% of the stress that an uncracked element could withstand.

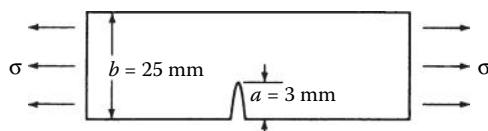


**FIGURE 9.4**  
Single-edge crack in a plate under uniaxial stress for Example 9.1.

### Example 9.2

A foam core sandwich beam in 4-point flexural loading is described in Example 7.17 and Figure 7.57. Core shear fracture is observed to occur in the regions of maximum shear force  $V$ . If the critical stress intensity factor for mode II shear fracture in the foam core is  $K_{IIC} = 0.0654 \text{ MPa} - \text{m}^{1/2}$  and a shear crack of size  $2a_{II} = 1.566 \text{ mm}$  is located at the point of maximum core shear stress, determine the critical value of the total applied load,  $P_c$ .

### SOLUTION

For the mode II crack shown in Figure 9.5, the critical stress intensity factor is

$$K_{IIC} = \tau_c \sqrt{\pi a_{II}}$$

so the critical shear stress is

$$\tau_c = \frac{K_{IIC}}{\sqrt{\pi a_{II}}} = \frac{0.0654}{\sqrt{\pi(0.000783)}} = 1.319 \text{ MPa}$$

It can be shown that the maximum transverse shear stress in the foam core occurs at the middle surface in the regions of maximum shear force  $V_{max} = P_{max}/2$  between the loading points and the support points (see the shear force diagram in Figure 7.57). From laminated beam theory, the transverse shear stress at the inner edge of the  $k$ th layer is given by Equation 7.19 as

$$(\tau_{xz})_k = \frac{V}{E_f I_{yy}} \sum_{j=k}^{N/2} \int_{z_{j-1}}^{z_j} (E_x)_j z \, dz = \frac{V}{2E_f I_{yy}} \sum_{j=k}^{N/2} (E_x)_j (z_j^2 - z_{j-1}^2)$$

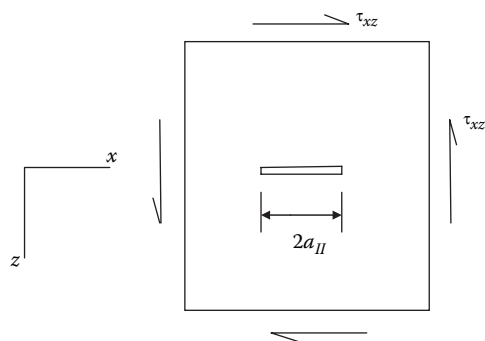


**FIGURE 9.5**  
Mode II shear crack for Example 9.2.

For the sandwich beam described in Example 7.17 and Figure 7.57, the above equation evaluated at the middle surface yields the following result for the maximum shear stress:

$$(\tau_{xz})_1 = \frac{V \left[ 0.092(6.35^2 - 0) + 139.4(7.061^2 - 6.35^2) \right]}{2(38.08)(25.4)(14.122)^3 / 12} = 0.002936 V \text{ MPa}$$

where  $V$  is in Newtons. Setting this result equal to the critical shear stress  $\tau_c = 1.319 \text{ MPa}$ , we find that the corresponding critical shear force is

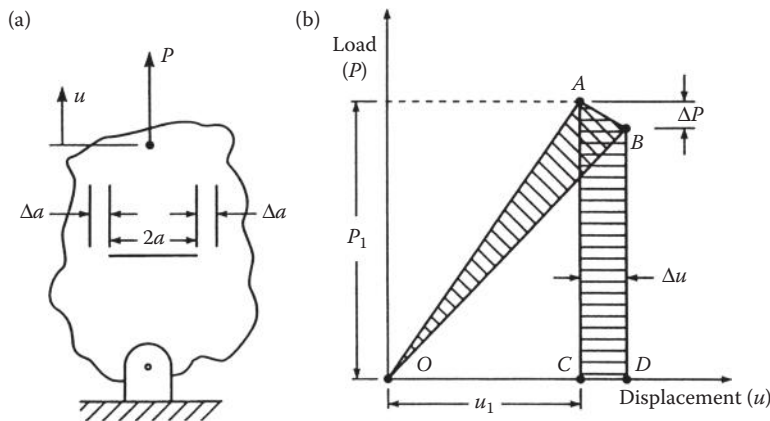
$$V = V_c = 449.25 \text{ N}$$

and the critical applied load is  $P_c = 2V_c = 898.5 \text{ N}$ .

### 9.2.2 Strain Energy Release Rate Approach

One of the major drawbacks of the stress intensity factor approach is that a stress analysis of the crack tip region is required. While such analyses have been done for a variety of loading conditions and crack geometries for isotropic materials [17], the corresponding analyses for anisotropic materials have only been done for relatively few cases because of mathematical difficulties. A very useful alternative to the stress intensity factor approach is referred to as the “strain energy release rate” approach. The strain energy release rate has an easily understood physical interpretation that is equally valid for either isotropic or anisotropic materials, and it turns out that this rate is also related to the stress intensity factor. The strain energy release rate approach has proved to be a powerful tool in both experimental and computational studies of crack growth.

The derivation of the strain energy release rate presented here follows that of Irwin [25], as explained by Corten [26]. We first consider a through-thickness cracked linear elastic plate under a uniaxial load, as shown in Figure 9.6a. An increase in the load,  $P$ , from the unloaded condition causes a linearly proportional change in the displacement,  $u$ , at the point of application of the load, as shown in the load–displacement plot in Figure 9.6b. We now assume that once the load reaches the value  $P_1$  and the corresponding displacement reaches  $u_1$ , the crack extends a small increment,  $\Delta a$ . The crack extension causes the load to drop by an amount  $\Delta P$  and the displacement to increase by an amount  $\Delta u$ . Just before the crack extension occurs, the potential energy,  $U$ , stored in the plate is given by the triangular area OAC in Figure 9.6b. The potential energy,  $\Delta U$ , released by the crack extension is given by the triangular area OAB. During the incremental displacement  $\Delta u$ , the increment of work done on the plate is  $\Delta W$  or the area ABDC. For this mode I crack deformation, the strain energy release rate,  $G_I$  (do not confuse with

**FIGURE 9.6**

Loaded plate and corresponding load–displacement curve used for strain energy release rate analysis. (a) Plate under uniaxial load and (b) load-displacement curve.

the shear modulus,  $G$ ), or the rate of change of the strain energy with respect to the crack extension area,  $A$ , is defined by [26]

$$G_I = \lim_{\Delta A \rightarrow 0} \frac{\Delta W - \Delta U}{\Delta A} = \frac{dW}{dA} - \frac{dU}{dA} \quad (9.21)$$

The system compliance,  $s$ , is given by

$$s = \frac{u}{P} \quad (9.22)$$

(Note that this is the system compliance,  $s$ , not the material compliance,  $S$ , defined earlier as being a ratio of strain to stress.) Thus, the potential energy of the plate in Figure 9.6a is

$$U = \frac{1}{2} Pu = \frac{1}{2} sP^2 \quad (9.23)$$

so that

$$\frac{dU}{dA} = sP \frac{\partial P}{\partial A} + \frac{1}{2} P^2 \frac{\partial s}{\partial A} \quad (9.24)$$

The incremental work done during the crack extension is approximately

$$\Delta W = P(\Delta u) \quad (9.25)$$

so that

$$\begin{aligned} \frac{dW}{dA} &= \lim_{\Delta A \rightarrow 0} \frac{\Delta W}{\Delta A} = \lim_{\Delta A \rightarrow 0} P \frac{\Delta u}{\Delta A} = P \frac{du}{dA} = P \frac{d}{dA}(sP) \\ &= Ps \frac{\partial P}{\partial A} + P^2 \frac{\partial s}{\partial A} \end{aligned} \quad (9.26)$$

Substitution of Equation 9.24 and Equation 9.26 into Equation 9.21 gives

$$G_I = \frac{P^2}{2} \frac{\partial s}{\partial A} \quad (9.27)$$

For a plate of constant thickness,  $t$ ,  $\partial A = t\partial a$  and

$$G_I = \frac{P^2}{2t} \frac{\partial s}{\partial a} \quad (9.28)$$

Thus, we can determine  $G_I$  by plotting the compliance as a function of crack length and finding the slope of the curve,  $ds/da$ , corresponding to the value of the load,  $P$ . The critical strain energy release rate,  $G_{Ic}$ , for this mode I crack deformation corresponds to the values  $P_c$  and  $(ds/da)_c$  at fracture. That is,

$$G_{Ic} = \frac{P_c^2}{2t} \left( \frac{\partial s}{\partial a} \right)_c \quad (9.29)$$

From the point of view of the experimentalist, the obvious advantage of Equation 9.29 is that knowledge of material properties or crack stress distributions is not needed since all the parameters can be determined from measurements on a test specimen. Note also that the method applies to either isotropic or anisotropic materials. As shown later in Section 9.4, Equation 9.21 has been used extensively for both measurement and calculation of the strain energy release rate for mode I delamination in laminates. Measurements of the strain energy release rate based on these equations will be discussed in Chapter 10.

Another major advantage of the strain energy release rate is that it is related to the stress intensity factor. As shown by Irwin [13], for mode I crack deformation in isotropic materials under plane stress,

$$K_I^2 = G_I E \quad (9.30)$$

so that the critical stress intensity factor or fracture toughness,  $K_{lc}$ , is related to the critical strain energy release rate,  $G_{lc}$ , by

$$K_{lc}^2 = G_{lc}E \quad (9.31)$$

This relationship has been used to determine the  $K_{lc}$  of composites from measurements of the  $G_{lc}$  [23] and to find  $G_{lc}$  from measurements of  $K_{lc}$  [20].

Cruse [27] has shown that for a through-thickness mode I crack in an orthotropic laminate having  $N$  angle-ply components and having strain compatibility among the plies ahead of the crack the critical strain energy release rate,  $G_{lc}$ , for the laminate is related to the corresponding lamina properties by a simple rule of mixtures of the form

$$G_{lc} = \frac{\sum_{i=1}^N G_{lic}t_i}{t} \quad (9.32)$$

where

$G_{lc}$  = critical strain energy release rate for the laminate

$G_{lic}$  = critical strain energy release rate for the  $i$ th angle-ply component

$t$  = total laminate thickness

$t_i$  = thickness of the  $i$ th angle-ply component

The predictions from this equation were found to show good agreement with experimental results for graphite/epoxy laminates [27].

The strain energy release rate has also proved to be useful in the characterization of the crack growth rate under cyclic loading. Interest in the possible relationship between fatigue crack growth rate and the strain energy release rate was prompted by the previous work of Paris and Erdogan [28], which showed that the mode I crack growth rate,  $da/dN$ , in many metals and polymers can be characterized by the equation

$$\frac{da}{dN} = B(\Delta K)^m \quad (9.33)$$

where

$N$  = number of cycles of repetitive loading

$\Delta K$  = stress intensity factor range =  $K_{I\max} - K_{I\min} = (\sigma_{\max} - \sigma_{\min})\sqrt{\pi a}$   
for mode I crack growth

$\sigma_{\max}$  = maximum stress

$\sigma_{\min}$  = minimum stress

$B, m$  = experimentally determined empirical factors for a given material, loading conditions, and environment.

Equation 9.33 has also found limited use in composites. For example, Kunz and Beaumont [29] observed that transverse crack growth in unidirectional

graphite–epoxy composites under cyclic compressive loading could be described by such an equation. Fatigue damage in composites cannot always be described in terms of self-similar crack growth, however. More often than not, fatigue damage is a very complex condition involving mixed modes of failure, and the analytical determination of the stress intensity factor for such a condition may be nearly impossible. Thus, the strain energy release rate range,  $\Delta G$ , may be a more convenient parameter to use than the stress intensity factor range,  $\Delta K$ . For example, Spearing et al. [30] have modeled fatigue damage growth in notched graphite/epoxy laminates by using an equation formed by combining Equations 9.30 and 9.33:

$$\frac{da}{dN} = C(\Delta G)^{m/2} \quad (9.34)$$

where  $C = BE^{m/2}$ .

### 9.2.3 Virtual Crack Closure Technique

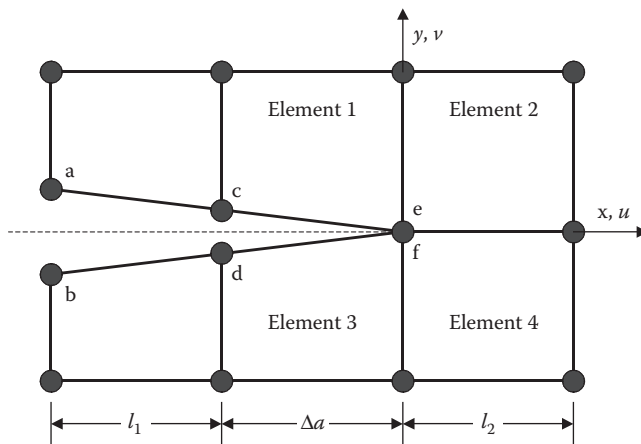
The so-called Virtual Crack Closure Technique (VCCT) has its origins in the seminal work of Irwin [25], was first implemented in finite element form by Rybicki and Kanninen [31], and has since evolved as a popular finite element computational tool for calculating the strain energy release rate and stress intensity factors. A recent review article by Krueger [32] summarizes the history, approach, and applications of the VCCT to composites, particularly to the case of delamination cracks.

Irwin [25] originally proposed that, when the crack tip shown schematically in Figure 9.2 has been extended by the amount  $\Delta a$ , the energy released during crack extension is equal to the energy required to close the crack to its original length. For the 2D state of stress in Figure 9.2, where the origin of the polar coordinates ( $r, \theta$ ) is located at the extended crack tip, Irwin suggested that the energy release rate  $G$  for a crack extension  $\Delta a$  is given by the crack closure integral [31]

$$G = \lim_{\Delta a \rightarrow 0} \frac{1}{2\Delta a} \int_0^{\Delta a} \sigma_y(\Delta a - r, 0)v(r, \pi)dr + \lim_{\Delta a \rightarrow 0} \frac{1}{2\Delta a} \int_0^{\Delta a} \tau_{xy}(\Delta a - r, 0)u(r, \pi)dr \quad (9.35)$$

where  $u$  and  $v$  are the relative sliding ( $x$ -direction) and opening ( $y$ -direction) displacements between points on the crack faces. The first and second integrals in Equation 9.35 are recognized to be  $G_I$  and  $G_{II}$ , the mode I and mode II energy release rates, respectively. Rybicki and Kanninen [31] later proposed that for the arrangement of four-noded 2D finite elements in Figure 9.7, Irwin's crack closure integrals could be approximated by

$$G_I = \lim_{\Delta a \rightarrow 0} \frac{1}{2\Delta a} F_{cy}(v_c - v_d) \quad (9.36)$$

**FIGURE 9.7**

Finite element nodes near the crack tip for the VCCT. (Reprinted from *Engineering Fracture Mechanics*, 9, Rybicki, E. F. and Kanninen, M. F., A finite element calculation of stress intensity factors by a modified crack closure integral, 931–938, Copyright (1997), with permission from Elsevier.)

and

$$G_{II} = \lim_{\Delta a \rightarrow 0} \frac{1}{2\Delta a} F_{cx}(u_c - u_d) \quad (9.37)$$

where  $\Delta a$  is the element length along the  $x$ -direction,  $F_{cx}$  and  $F_{cy}$  are the forces along  $x$  and  $y$  directions, respectively, that are required to hold nodes c and d together during crack closure,  $(u_c, v_c)$  are the  $x$  and  $y$  displacements, respectively, of point c, and  $(u_d, v_d)$  are the  $x$  and  $y$  displacements, respectively, of point d during crack closure. Since the publication of the paper by Rybicki and Kanninen [31], there have been numerous publications by others reporting on various improvements and applications of the VCCT to cracks in composites, particularly delamination cracks. Among the reported improvements are the use of eight-noded 2D finite elements, 20-noded 3D brick elements, plate or shell elements, and nonlinear finite elements, as well as the use of the VCCT to analyze fractures at bimaterial interfaces such as those in composites [32]. As noted in Section 9.4, many of the publications regarding the VCCT involve applications to composite delamination. One potential problem with the VCCT is the existence of the  $1/\sqrt{r}$  singularities in the stresses as  $r \rightarrow 0$  at the crack tip, as seen in Equations 9.12 through 9.14 and Equations 9.18 through 9.20. Special crack tip singularity elements have been shown to be effective in accurately approximating these singularities, but apparently these special elements are not readily available in many commonly used finite element codes [32].

### 9.3 Stress Fracture Criteria for Through-Thickness Notches

Although fracture mechanics concepts have been successfully used in some cases to analyze the effects of through-thickness cracks and notches in composite laminates, Whitney and Nuismer [33,34] questioned the need for such an approach and then proceeded to develop a simpler approach that is perhaps more useful to designers. As pointed out previously, the use of fracture mechanics in such applications has always been in question because the self-similar crack growth that occurs in metals does not always occur in composite laminates. Additional motivation for the work of Whitney and Nuismer was provided by the need to understand better experimental results that showed larger holes in laminates under tension cause greater strength reductions than do smaller holes. In a previous attempt to explain this effect, Waddoups et al. [35] had employed a fracture mechanics analysis of a hole in an isotropic plate with two symmetrically placed cracks extending from either side of the hole, as shown in Figure 9.8. The stress intensity factor for a mode I crack having this geometry was derived using the previous solution of Bowie [36] as

$$K_I = \sigma\sqrt{\pi a} f(a/R) \quad (9.38)$$

While the function  $f(a/R)$  has been tabulated for the isotropic case [17], it has not been determined for the anisotropic case. Thus, although the analysis of Waddoups et al. [35] predicted the experimentally observed trends regarding the effect of hole size, the effects of anisotropy were obviously not considered. In addition, no physical interpretation was given for the cracks at the edge of the hole (i.e., such cracks were used in the analysis but were not necessarily present in the experiments that showed the hole size effect).

Whitney and Nuismer [33,34] reasoned that the hole size effect could also be explained by observing the differences in the stress distributions near the hole for large and small holes. For example, the theory of elasticity solutions [37] for the normal stress distribution,  $\sigma_y$ , along the  $x$ -axis near a hole in an

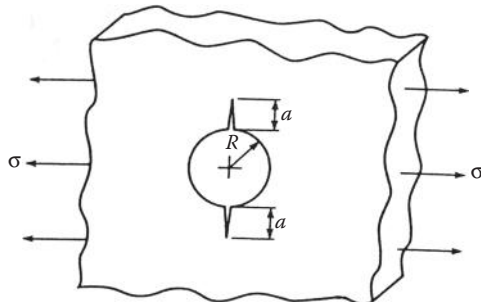


**FIGURE 9.8**  
Uniaxially stressed plate with an edge-cracked hole.

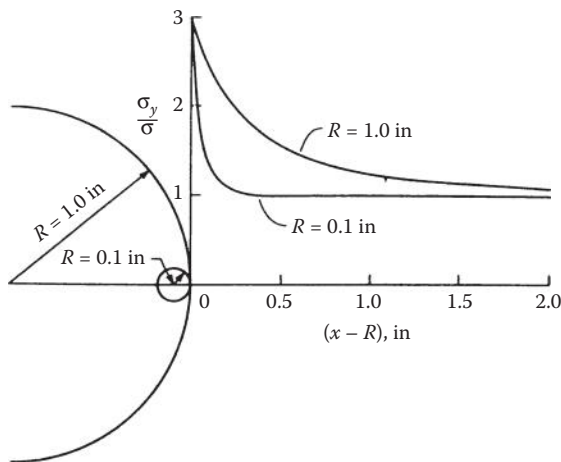
infinite isotropic plate under uniform tensile stress are shown in Figure 9.9 for small ( $R = 0.1$  in.) and large ( $R = 1.0$  in.) holes. The stress distribution for the smaller hole obviously has a sharper concentration near the hole than does the stress distribution for the larger hole. Whitney and Nuismer observed that since the plate with the smaller hole would be more capable of redistributing high stresses near the hole than would the plate with the larger hole, the plate with the smaller hole would be stronger. This observation led to the development of two failure criteria that were based on solutions for the normal stress,  $\sigma_y$ , along the  $x$ -axis near circular holes (Figure 9.9) and center cracks (Figure 9.10) in infinite orthotropic plates. The Whitney–Nuismer criteria [33,34] are now summarized.

The hole of radius  $R$  in Figure 9.9 is assumed to be in an infinite orthotropic plate that is under uniform stress,  $\sigma$ , at infinity. The normal stress,  $\sigma_y(x, 0)$ , along the  $x$ -axis near the hole is approximately

$$\sigma_y(x, 0) = \frac{\sigma}{2} \left\{ 2 + \left( \frac{R}{x} \right)^2 + 3 \left( \frac{R}{x} \right)^4 - (K_T^\infty - 3) \left[ 5 \left( \frac{R}{x} \right)^6 - 7 \left( \frac{R}{x} \right)^8 \right] \right\} \quad (9.39)$$

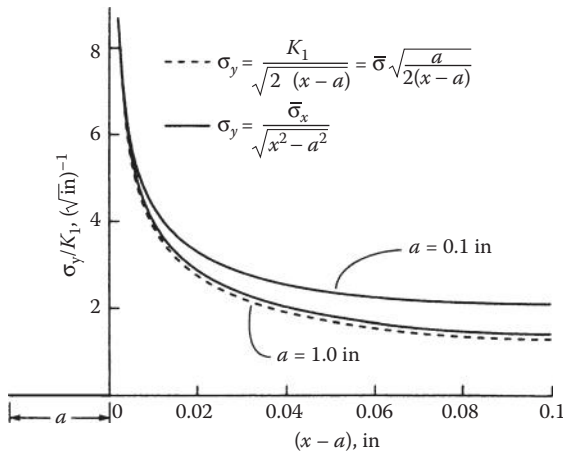
where  $x > R$  and the orthotropic stress concentration factor,  $K_T^\infty$ , for an infinite width plate is given by Lekhnitskii [38] as

$$K_T^\infty = 1 + \sqrt{\frac{2}{A_{22}} \left( \sqrt{A_{11}A_{22}} - A_{12} + \frac{A_{11}A_{22} - A_{12}^2}{2A_{66}} \right)} \quad (9.40)$$



**FIGURE 9.9**

Normal stress distribution for a circular hole in an infinite isotropic plate. (Reprinted from Nuismer, R. J. and Whitney, J. M. 1975. *Fracture Mechanics of Composites*, ASTM STP 593, pp. 117–142. American Society for Testing and Materials, Philadelphia, PA. Copyright ASTM. With permission.)

**FIGURE 9.10**

Normal stress distribution for a center crack in an infinite anisotropic plate. (Reprinted from Nuismer, R. J. and Whitney, J. M. 1975. *Fracture Mechanics of Composites*, ASTM STP 593, pp. 117–142. American Society for Testing and Materials, Philadelphia, PA. Copyright ASTM. With permission.)

where the  $A_{ij}$  are the laminate extensional stiffnesses from the CLT and the subscript 1 denotes the direction parallel to the applied stress,  $\sigma$ .

The first failure criterion proposed by Whitney and Nuismer, referred to as the “point stress criterion,” is based on the assumption that failure occurs when the stress  $\sigma_y$  at some fixed distance,  $d_0$ , away from the edge of the hole reaches the unnotched tensile strength of the material,  $\sigma_0$ . This criterion is given by

$$\sigma_y(R + d_0, 0) = \sigma_0 \quad (9.41)$$

By combining Equations 9.39 and 9.41, we find that the ratio of notched to unnotched strength is

$$\frac{\sigma_N^\infty}{\sigma_0} = \frac{2}{2 + \xi_1^2 + 3\xi_1^4 - (K_T^\infty - 3)(5\xi_1^6 - 7\xi_1^8)} \quad (9.42)$$

where

$$\xi_1 = \frac{R}{R + d_0}$$

and the notched tensile strength,  $\sigma_N^\infty$ , of the infinite width laminate is equal to the applied stress,  $\sigma$ , at failure. Whitney and Nuismer noted that for very large

holes  $\xi_1 \rightarrow 1$ , and the classical stress concentration result,  $\sigma_N^\infty / \sigma_0 = 1/K_T^\infty$ , is recovered. As  $\xi_1 \rightarrow 0$ , however,  $\sigma_N^\infty / \sigma_0 \rightarrow 1$ , as expected.

The second failure criterion proposed by Whitney and Nuismer, referred to as the "average stress criterion," is based on the assumption that failure occurs when the average value of  $\sigma_y$  over some fixed distance,  $a_0$ , from the edge of the hole reaches the unnotched tensile strength of the material,  $\sigma_0$ . This criterion is given by

$$\frac{1}{a_0} \int_R^{R+a_0} \sigma_y(x, 0) dx = \sigma_0 \quad (9.43)$$

By combining Equations 9.39 and 9.43, we find that the ratio of notched to unnotched strength is

$$\frac{\sigma_N^\infty}{\sigma_0} = \frac{2(1 - \xi_2)}{2 - \xi_2^2 - \xi_2^4 + (K_I^\infty - 3)(\xi_2^6 - \xi_2^8)} \quad (9.44)$$

where

$$\xi_2 = \frac{R}{R + a_0}$$

And  $\sigma_N^\infty$  is again the notched tensile strength of the infinite width laminate. As in the point stress criterion, the expected limits are recovered for the cases when  $\xi_2 \rightarrow 1$  and  $\xi_2 \rightarrow 0$ .

Whitney and Nuismer also applied the point stress criterion and the average stress criterion to the case of the center crack of length  $2a$  in an infinite anisotropic plate under uniform tensile stress,  $\sigma$ , as shown in Figure 9.10. They used Lekhnitskii's [38] exact elasticity solution for the normal stress,  $\sigma_y$ , along the  $x$ -axis near the edge of the crack, which is given by

$$\sigma_y(x, 0) = \frac{\sigma x}{\sqrt{x^2 - a^2}} = \frac{K_I x}{\sqrt{\pi a(x^2 - a^2)}} \quad (9.45)$$

where  $x > a$  and  $K_I = \sigma \sqrt{\pi a}$  is the mode I stress intensity factor. Substitution of this stress distribution in the point stress failure criterion given by Equation 9.41 leads to the expression

$$\frac{\sigma_N^\infty}{\sigma_0} = \sqrt{1 - \xi_3^2} \quad (9.46)$$

where

$$\xi_3 = \frac{a}{a + d_0}$$

Substitution of the stress distribution from Equation 9.45 in the average stress criterion given by Equation 9.43 yields

$$\frac{\sigma_N^\infty}{\sigma_0} = \sqrt{\frac{1 - \xi_4}{1 + \xi_4}} \quad (9.47)$$

where

$$\xi_4 = \frac{a}{a + a_0}$$

Whitney and Nuismer then reasoned that the effect of crack size on the measured fracture toughness of the notched laminate could be better understood by defining a parameter

$$K_Q = \sigma_N^\infty \sqrt{\pi a} \quad (9.48)$$

which is the fracture toughness corresponding to the notched tensile strength of the infinite width laminate. Substitution of Equation 9.46 into Equation 9.48 yields

$$K_Q = \sigma_0 \sqrt{\pi a (1 - \xi_3^2)} \quad (9.49)$$

for the point stress criterion. Similarly, substitution of Equation 9.47 into Equation 9.48 yields

$$K_Q = \sigma_0 \sqrt{\frac{\pi a (1 - \xi_4)}{1 + \xi_4}} \quad (9.50)$$

for the average stress criterion. For vanishingly small crack lengths,  $a$ , the numerical values of Equations 9.49 and 9.50 approach the limit  $K_Q = 0$ . For large crack lengths  $K_Q$  asymptotically approaches

$$K_Q = \sigma_0 \sqrt{2\pi d_0} \quad (9.51)$$

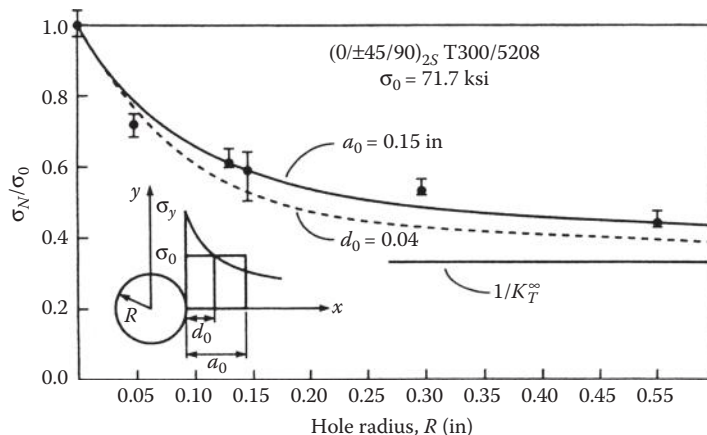
for the point stress criterion and

$$K_Q = \sigma_0 \sqrt{\pi a_0 / 2} \quad (9.52)$$

for the average stress criterion.

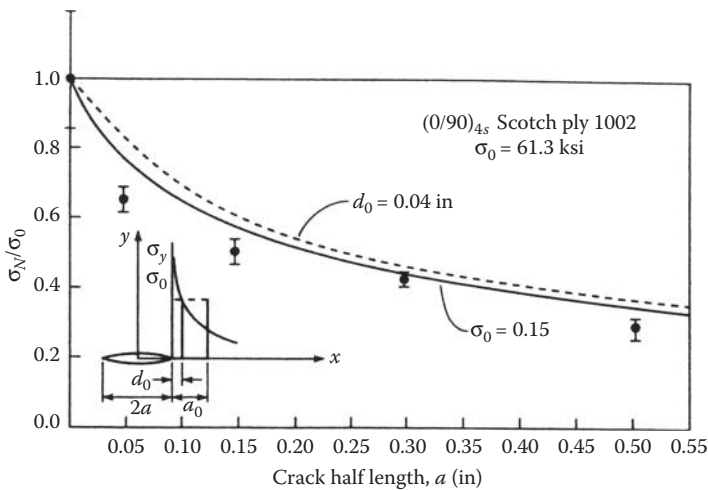
In order to use these stress fracture criteria, it is necessary to do enough experiments to establish values of  $d_0$  or  $a_0$  that give acceptable predicted values of  $\sigma_N^\infty$ . Whitney and Nuismer observed that the applicability of these criteria in design depends to a great extent on whether the distance  $d_0$  or  $a_0$  is constant for all hole or crack sizes in at least a particular laminate of a particular material system. If  $d_0$  or  $a_0$  was constant for all laminates of all material systems, the criteria would be even more useful.

Whitney and Nuismer showed that fixed values of  $d_0$  and  $a_0$  in the criteria gave reasonably good agreement with experimental results for graphite/epoxy and glass/epoxy laminates in two different laminate configurations [34]. For example, Figure 9.11 shows a comparison of the predictions from the point stress criterion for circular holes (Equation 9.42) and the average stress criterion for circular holes (Equation 9.44) with experimental data for  $[0/\pm 45/90]_{2s}$  graphite/epoxy laminates. Similarly, Figure 9.12 shows a comparison of the predictions from the point stress criterion for center cracks (Equation 9.46) and the average stress criterion for center cracks (Equation 9.47) with experimental data for  $[0/90]_{4s}$  glass/epoxy laminates. Note that the same values of  $d_0$  and  $a_0$  were used for both material systems and laminate configurations, and that both criteria correctly predict the effect of the hole



**FIGURE 9.11**

Comparison of predicted and measured failure stresses for circular holes in  $[0/\pm 45/90]_{2s}$  T300/5208 graphite/epoxy. (Reprinted from Nuismer, R. J. and Whitney, J. M. 1975. *Fracture Mechanics of Composites*, ASTM STP 593, pp. 117–142. American Society for Testing and Materials, Philadelphia, PA. Copyright ASTM. With permission.)

**FIGURE 9.12**

Comparison of predicted and measured failure stresses for center cracks in  $[0/90]_{4s}$  Scotchply 1002 E-glass/epoxy. (Reprinted from Nuismer, R. J. and Whitney, J. M. 1975. *Fracture Mechanics of Composites*, ASTM STP 593, pp. 117–142. American Society for Testing and Materials, Philadelphia, PA. Copyright ASTM. With permission.)

size or crack size on the notched strength. The results for graphite/epoxy are not quite so good as those for glass/epoxy, however. Even though it could not be concluded from this work that  $d_0$  and  $a_0$  are universal constants, the equations can be used with confidence for a particular material system under uniaxial loading. It should also be remembered that these criteria can be used for any through-thickness discontinuity for which the theoretical stress distribution can be found, not just for circular holes or straight cracks. Thus, given the relative simplicity of the equations, the Whitney–Nuismer criteria appear to be of considerable value to designers.

### Example 9.3

A large plate made from the quasiisotropic graphite/epoxy laminate in Example 9.1 has a center crack of length  $2a = 6$  mm and is subjected to a uniform uniaxial stress. Compare the predicted fracture strengths of the plate according to the fracture mechanics criterion, the point stress criterion, and the average stress criterion. Use the Whitney–Nuismer values of  $d_0$  and  $a_0$  from Figures 9.11 and 9.12.

### SOLUTION

For the fracture mechanics approach we rearrange Equation 9.16 as

$$\sigma_c = \frac{K_{Ic}}{\sqrt{\pi a}} = \frac{30}{\sqrt{\pi(0.003)}} = 309 \text{ MPa}$$

For the point stress criterion we use  $d_0 = 0.04$  in. = 1.016 mm and  $a = 3$  mm in Equation 9.46 as

$$\sigma_N^\infty = \sigma_0 \sqrt{1 - \xi_3^2} = (500) \sqrt{1 - [3.0/(3.0 + 1.016)]^2} = 332 \text{ MPa}$$

For the average stress criterion we use  $a_0 = 0.15$  in. = 3.81 mm and  $a = 3$  mm in Equation 9.47 as

$$\sigma_N^\infty = \sigma_0 \sqrt{\frac{1 - \xi_4}{1 + \xi_4}} = (500) \sqrt{\frac{1 - (3.0/(3.0 + 3.81))}{1 + (3.0/(3.0 + 3.81))}} = 312 \text{ MPa}$$

The results from all three analyses are reasonably close, and the fracture mechanics criterion is slightly more conservative than the point stress criterion and the average stress criterion in this case. Clearly, the predicted fracture strengths in all three cases are considerably lower than the unnotched tensile strength of 500 MPa, and we see that the effects of such cracks should not be ignored in design.

## 9.4 Interlaminar Fracture

Delamination or interlaminar fracture is a very important failure mode in composite laminates, and research activity regarding the onset and growth of delaminations has continued at a high level for the past several decades or so. The mechanics of interlaminar stresses and several mechanics of materials approaches to the prediction of the onset of delamination were discussed previously in Chapter 7. In this section, we discuss the use of fracture mechanics approaches, particularly those involving the use of the strain energy release rate, for the prediction of delamination growth and failure.

Delamination provides one of the few examples of self-similar crack growth in composite laminates. A delamination is in effect a crack separating adjacent laminae, and the plane of the crack lies in the plane of the interface between laminae. Like a crack in a metallic material, a delamination grows in a stable manner until it reaches a critical size, whereupon further growth occurs in an unstable manner. These characteristics make interlaminar fracture a prime candidate for the application of fracture mechanics analysis. On the other hand, as pointed out in Chapter 7, interlaminar stresses are part of a complex 3D state of stress that leads to delamination. While such a complex state of stress at the crack tip inhibits the effective use of the stress intensity factor approach, it makes the problem ideally suited for the strain energy release rate approach.

One of the first reports on the use of the strain energy release rate approach in the analysis of delamination was apparently that of Roderick et al. [39], who correlated strain energy release rates with the rates of cyclic debonding

between metal panels and composite reinforcement using an equation similar to Equation 9.34. Shortly thereafter, in a critical review of the applications of fracture mechanics in composites, Kanninen et al. [40] noted that the strain energy release rate had seen little application to composites. This observation led to the use of the strain energy release rate by Rybicki et al. [41] in an analytical and experimental study of free-edge delamination in boron/epoxy laminates. Rather than using Equation 9.21 to calculate the strain energy release rate, Rybicki et al. [41] employed a finite element implementation of the crack closure technique, described as VCCT in Section 9.2.3. This appears to be the first application of the VCCT to the analysis of delamination cracks, but since that time there have been numerous reports in the literature regarding the application of the VCCT to delamination cracks [32].

Wang [42] conducted experimental and analytical studies of delamination growth in unidirectional glass–epoxy composite specimens. As shown in Figure 9.13, delamination crack initiators were introduced in the specimens by cutting across several surface plies with a razor blade. The specimens were then subjected to cyclic tension–tension fatigue loading while the length of the delamination,  $l_d$ , was measured. Figure 9.14 shows typical data on delamination crack length versus the number of load cycles,  $N$ , at different stress levels. The delamination growth rate,  $dl_d/dN$ , at any number  $N$  is the tangent of the curve at that value of  $N$ . It is particularly important to note in Figure 9.14 that at a critical number of loading cycles,  $N_c$ , corresponding to a critical delamination size for a given stress level, the delamination growth becomes unstable and rapid crack propagation occurs. Such experiments provided further proof of the similarity between crack growth in metals and delamination growth in composite laminates and justified the use of the principles of fracture mechanics in the analysis of delamination.

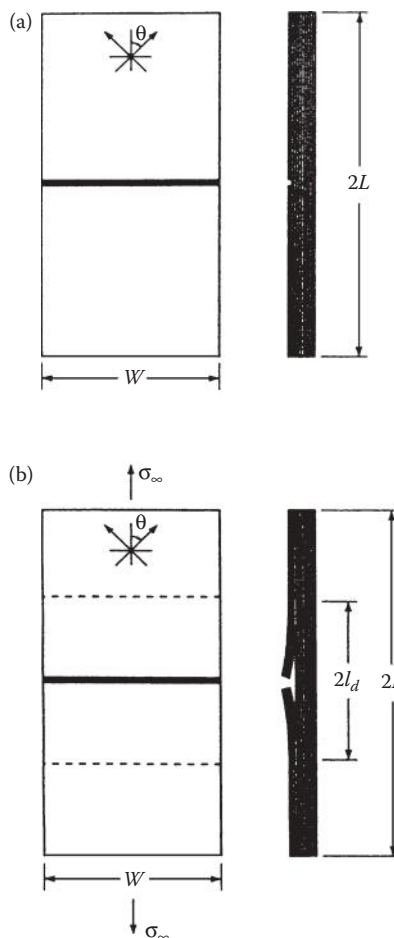
Wang [42] used a hybrid stress FEA to determine the stress intensity factors  $K_I$  and  $K_{II}$  for the mixed mode crack growth, which were then correlated with the delamination growth rate by equations similar to Equation 9.33. In this case, due to the mixed mode delamination, the relationships for the two crack deformation modes are

$$\frac{dl_d}{dN} \sim (\square K_I)^a \quad (9.53)$$

for mode I crack opening and

$$\frac{dl_d}{dN} \sim (\square K_{II})^b \quad (9.54)$$

for mode II crack shearing, where  $a$  and  $b$  are empirically determined exponents. Equations 9.53 and 9.54, when plotted on a log–log plot, should form a straight line. The validity of these equations is confirmed by plotting the experimental data on a 3D log–log plot, as shown in Figure 9.15. The data in

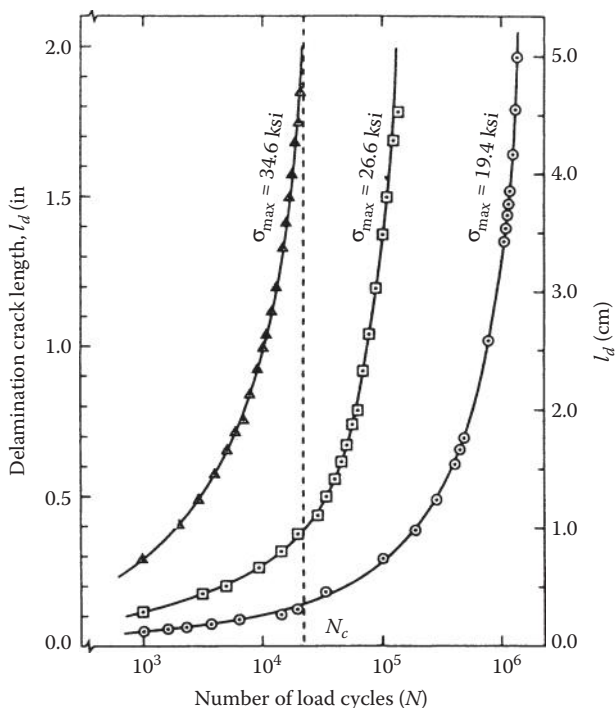
**FIGURE 9.13**

Specimen for delamination crack growth study ( $2L = 152.4$  mm,  $W = 25.4$  mm). (a) Before loading and (b) during loading. (Reprinted from Wang, S. S. 1979. In Tsai, S. W. ed., *Composite Materials: Testing and Design*, ASTM STP 674, pp. 642–663. American Society for Testing and Materials, Philadelphia, PA. Copyright ASTM. With permission.)

Figure 9.15 were found to follow a general relationship of the form

$$\frac{\log(dl_d/dN)}{\alpha_1} = \frac{\log(\Delta K_I) + C_1}{\alpha_2} = \frac{\log(\Delta K_{II}) + C_2}{\alpha_3} \quad (9.55)$$

where the  $\alpha_i$  ( $i = 1, 2, 3$ ) are the directional cosines of the line  $dl_d/dN = f(\Delta K_I, \Delta K_{II})$  with respect to the three axes, respectively, and  $C_1$  and  $C_2$  are constants associated with the opening and shearing modes, respectively.

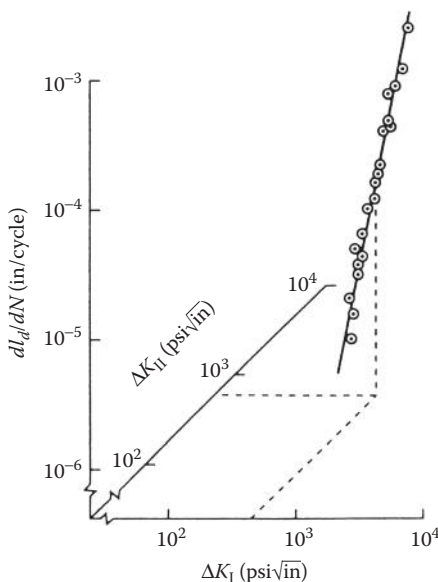
**FIGURE 9.14**

Delamination crack growth during fatigue in unidirectional glass/epoxy. (Reprinted from Wang, S. S. 1979. In Tsai, S. W. ed., *Composite Materials: Testing and Design*, ASTM STP 674, pp. 642–663. American Society for Testing and Materials, Philadelphia, PA. Copyright ASTM. With permission.)

Both mechanics of materials and fracture mechanics analyses were used by O'Brien [43] to study the onset and growth of edge delaminations (see Figure 7.37) in graphite/epoxy laminates. O'Brien's mechanics of materials approach was discussed previously in Chapter 7. A laminate-stacking sequence of  $[\pm 30/\pm 30/90/90]_s$  was selected so that edge delamination growth in tensile specimens would readily occur under cyclic loading, and delamination growth was monitored nondestructively. The strain energy release rate,  $G$ , associated with delamination growth was determined from two different analyses, only one of which will be discussed here. One method involved the use of the general equation for the strain energy release rate, Equation 9.21. The work done during crack extension,  $W$ , was ignored, so that

$$G = -\frac{dU}{dA} \quad (9.56)$$

The subscript I on  $G$  has been dropped here because the edge delamination growth is of the mixed mode type and the strain energy release rate may

**FIGURE 9.15**

Fatigue delamination crack growth rate,  $dl_d/dN$ , as a function of mixed mode stress intensity factor ranges  $\Delta K_I$ , and  $\Delta K_{II}$  for unidirectional glass/epoxy. (Reprinted from Wang, S. S. 1979. In Tsai, S. W. ed., *Composite Materials: Testing and Design*, ASTM STP 674, pp. 642–663. American Society for Testing and Materials, Philadelphia, PA. Copyright ASTM. With permission.)

have components due to  $G_I$ ,  $G_{II}$ , and  $G_{III}$ . Superposition of the strain energy release rates for different modes will be discussed later. Expressing the strain energy in terms of the strain energy density,  $E\epsilon^2/2$ , and the volume,  $V$ , Equation 9.56 becomes

$$G = -V \frac{\epsilon^2}{2} \frac{dE}{dA} \quad (9.57)$$

where

$\epsilon$  = nominal longitudinal strain

$E$  = longitudinal Young's modulus of a laminate partially delaminated along one or more interfaces.

In this case  $dA = 2L da$  and  $V = 2bt$ , where  $a$ ,  $b$ , and  $t$  were defined previously in Figure 7.37 and  $L$  is the length of the laminate. Substituting these definitions in Equation 9.57, along with the definition of  $E$  from Equation 7.122, O'Brien found that

$$G = \frac{\epsilon^2 t}{2} (E_x - E_{td}) \quad (9.58)$$

where  $E_x$  and  $E_{td}$  were defined previously along with Equation 7.122. Thus, the strain energy release rate is independent of delamination size and

depends only on  $E_x$  and  $E_{td}$  (which are determined by the laminate lay-up and the location of the delaminated interfaces), the strain,  $\epsilon$ , and the thickness,  $t$ . The critical strain,  $\epsilon_c$ , at the onset of delamination was measured for the  $[\pm 30/\pm 30/90/90]_s$  laminates and used in Equation 9.58 to determine the corresponding critical strain energy release rate,  $G_c$ . This value of  $G_c$  was then used to predict the critical value,  $\epsilon_c$ , at the onset of delamination in  $[+45_n/45_n/0_n/90_n]_s$  laminates. A comparison of measured and predicted values of  $\epsilon_c$  for different numbers of plies,  $n$ , is shown in Figure 9.16, and the agreement is seen to be very good.

As previously mentioned, the edge delamination test used by O'Brien [43] involved mixed mode crack deformations. He used a finite element implementation of a crack closure technique developed by Rybicki et al. [41] to find the components  $G_I$ ,  $G_{II}$ , and  $G_{III}$ . The total  $G$  was then found from the superposition relationship

$$G = G_I + G_{II} + G_{III} \quad (9.59)$$

In this case  $G_{III}$  turned out to be negligible. Equation 9.59 is valid when the plane of the crack and the plane of crack extension coincide with a principal axis of material property symmetry [26].

O'Brien also found excellent correlation between delamination growth rate,  $da/dN$ , and the maximum strain energy release rate,  $G_{max}$ , by using an equation of the form

$$\frac{da}{dN} = cG_{max}^\beta \quad (9.60)$$

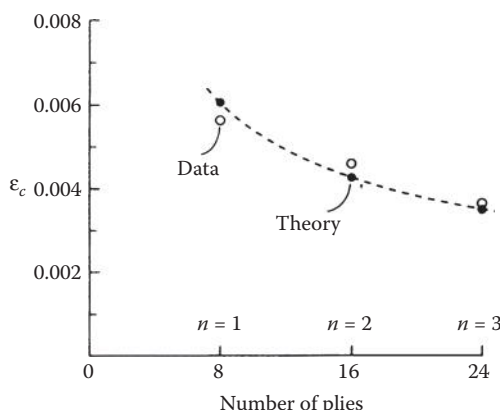


**FIGURE 9.16**

Edge delamination onset prediction compared with experimental data for  $[+45_n/45_n/0_n/90_n]_s$  graphite/epoxy, where  $n = 1, 2, 3$ . (Reprinted from O'Brien, T. K. 1982, in Reifsnider, K. L. ed., *Damage in Composite Materials*, ASTM STP 775, pp. 140–167. American Society for Testing and Materials, Philadelphia, PA. Copyright ASTM. With permission.)

where  $c$  and  $\beta$  are empirically determined constants. Figure 9.17 shows a comparison of predictions from this equation with experimental data, and the agreement is excellent.

As described above, the experiments of Wang [42] and O'Brien [43] involved mixed mode delamination, and the different components of the stress intensity factor or the strain energy release rate corresponding to modes I, II, and III had to be determined separately by using finite element techniques. In order to understand delamination better and, consequently, the best ways to improve interlaminar fracture toughness, there is an obvious need for delamination experiments which make it possible to isolate a single mode of crack growth. In the following paragraphs the most widely used experiments for single-mode measurement of interlaminar strain energy release rates will be briefly discussed, but details of the techniques will be left for Chapter 10 on mechanical testing of composites.

Mode I delamination has always been of interest because of the obvious weakness of the interlaminar region in through-thickness tension. Perhaps the most widely used mode I interlaminar fracture test method is the double cantilever beam (DCB) test, which was originally developed for studying fracture of adhesively bonded joints and then later adapted for interlaminar fracture of composite laminates [44–51]. A DCB specimen is shown in Figure 9.18a. In the DCB test the specimen is loaded transversely as shown in Figure 9.18a, so that mode I crack opening delamination occurs along the middle plane. The required test data are taken and the delamination  $G_{lc}$  is calculated by using one of several different forms of Equation 9.21 or Equation 9.27, as described later in Chapter 10. Typical values of delamination  $G_{lc}$  for several advanced composites, as determined by DCB tests, are tabulated in Table 9.1. The results of some of the attempts to improve the interlaminar fracture toughness are seen in Table 9.1, and these methods will be discussed in more detail later in this section.

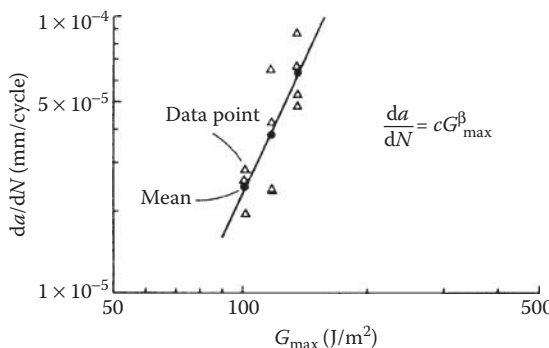


**FIGURE 9.17**

Power law curve fit for  $da/dN$  as a function of  $G_{\max}$  for  $[\pm 30/30/90/\bar{90}]_s$ , graphite/epoxy. (Reprinted from O'Brien, T. K. 1982, in Reifsnider, K. L. ed., *Damage in Composite Materials*, ASTM STP 775, pp. 140–167. American Society for Testing and Materials, Philadelphia, PA. Copyright ASTM. With permission.)

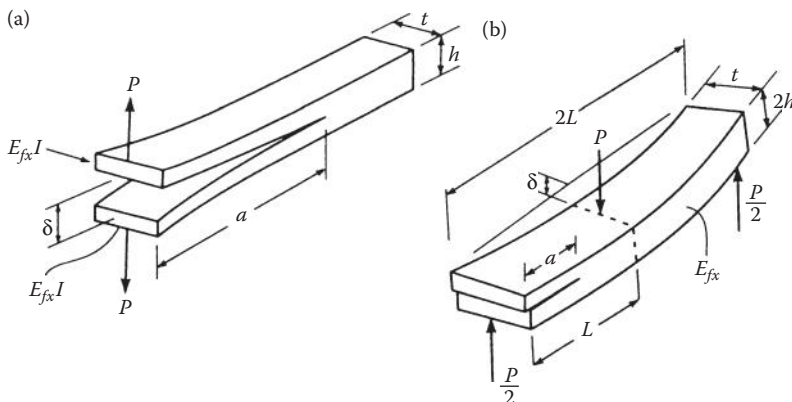


**FIGURE 9.18**  
DCB and ENF specimens. (a) Double cantilever beam (DCB) specimen and (b) end-notched flexure (ENF) specimen.

Although mode I delamination has received considerable attention in the literature, there is increased interest in mode II delamination because of its apparent relationship to impact damage tolerance of laminates [52]. As mentioned in Section 7.8.2, transverse impact can cause internal cracks and delaminations that may be difficult to detect. If the laminate is subsequently subjected to in-plane compressive loading, such cracks and delaminations can lead to local buckling and reductions of in-plane compressive strength (Figure 7.40). There is evidence that the so-called CAI strength is improved by increasing the mode II critical interlaminar strain energy release rate,  $G_{IIC}$  [52]. One of the most popular tests for measurement of the critical strain energy release rate for mode II delamination is the end-notched flexure (ENF) test. An ENF specimen is shown in Figure 9.18b. The strain energy release rate analysis of the ENF specimen, which has been improved and used by several investigators [52–57], will be discussed in more detail in the review of test methods in Chapter 10.

Once the capability to measure  $G_{Ic}$  and  $G_{IIC}$  separately had been developed, it became possible to evaluate various interactive criteria for mixed mode delamination growth. Although there is no universal agreement on which mixed mode delamination growth criterion is the most accurate, one of the simplest and most widely used of these criteria is given by the equation

$$\left(\frac{G_I}{G_{Ic}}\right)^m + \left(\frac{G_{II}}{G_{IIC}}\right)^n = 1 \quad (9.61)$$

where

$G_I$ ,  $G_{II}$  = strain energy release rates for delamination growth in modes I and II, respectively.

**TABLE 9.1**

Critical Interlaminar Strain Energy Release Rates,  $G_{lc}$ , for Several Advanced Composites, as Determined by DCB Tests

Fiber/Matrix Combination	Lay-Up	$G_{lc} \text{ J/m}^2 (\text{in-lb/in}^2)$	Source
T-300/5208 Graphite/epoxy	[0] <sub>24</sub>	87.6(0.50)	(1)
AS-1/3502 Graphite/epoxy	[0] <sub>24</sub>	140.1(0.80)	(2)
AS-4/3502 Graphite/epoxy	[0] <sub>24</sub>	161.1(0.92)	(2)
T-300/V387A Graphite/bismaleimide	[0] <sub>24</sub>	71.8(0.41)	(2)
AS-1/polysulfone Graphite/polysulfone	[0] <sub>12</sub>	585.0(3.34)	(2)
T-300/976 Graphite/epoxy bidirectional cloth	Woven, fabric, 10 plies	282.0(1.61)	(2)
AS-4/3501-6 Graphite/epoxy	[0] <sub>24</sub>	198–254(1.31–1.45) <sup>a</sup>	(3)
T-300/F-185 Graphite/epoxy	[0] <sub>24</sub>	1880–1500(10.7–8.6) <sup>b</sup>	(4)
AS-4/PEEK Graphite/polyetheretherketone	[0] <sub>40</sub>	2890–2410(16.5–13.8) <sup>c</sup>	(5)

Sources: (1) Wilkins, D. J., Eisenmann, J. R., Camin, R. A., Margolis, W. S., and Benson, R. A. 1982, in Reifsnider, K. L. ed., *Damage in Composite Materials*. ASTM STP 775, pp. 168–183. American Society for Testing and Materials, Philadelphia, PA; (2) Whitney, J. M., Browning, C. E., and Hoogsteen, W. 1982. *Journal of Reinforced Plastics and Composites*, 1, 297–313; (3) Aliyu, A. A. and Daniel, I. M. 1985, in Johnson, W. S., ed., *Delamination and Debonding of Materials*. ASTM STP 876, pp. 336–348. American Society for Testing and Materials, Philadelphia, PA; (4) Daniel, I. M., Shareef, I., and Aliyu, A. A. 1987, in Johnston, N. J. ed., *Toughened Composites*. ASTM STP 937, pp. 260–274. American Society for Testing and Materials, Philadelphia, PA; (5) Leach, D. C., Curtis, D. C., and Tamblin, D. R. 1987, in Johnston, N. J., ed., *Toughened Composites*. ASTM STP 937, pp. 358–380. American Society for Testing and Materials, Philadelphia, PA. Copyright ASTM. Reprinted with permission. Also from Whitney et al. Copyright Technomic Publishing Company. Reprinted with permission.

<sup>a</sup> Range of  $G_{lc}$  is given for crack velocities of 0.05–49.0 mm/s, respectively. Thus,  $G_{lc}$  increases with increasing strain rate for this material. The matrix is Hercules 3501-6, a standard prepreg-type epoxy resin [47].

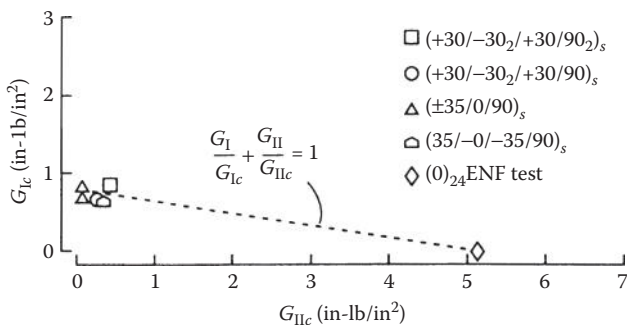
<sup>b</sup> Range of  $G_{lc}$  is given for crack velocities of 0.01–21.0 mm/s, respectively. Thus,  $G_{lc}$  decreases with increasing strain rate for this material. The matrix is Hexcel F-185, which is an elastomer-modified and toughened epoxy [48].

<sup>c</sup> Range of  $G_{lc}$  is given for stable and unstable crack growth, respectively [49].

$G_{lc}, G_{llc}$  = critical strain energy release rates for delamination growth in modes I and II, respectively.

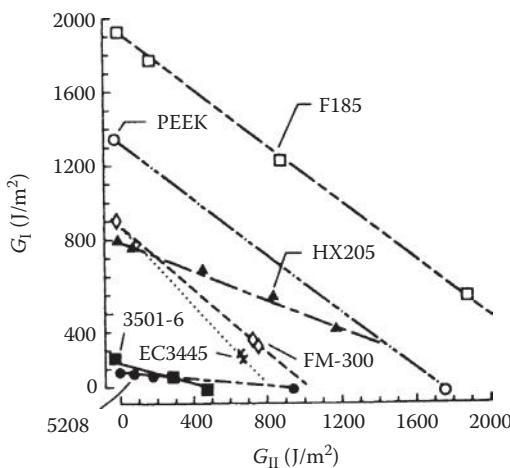
$m, n$  = empirically determined exponents.

Good agreement between the predictions from this equation and experimental data has been reported by O'Brien et al. [58] and Johnson and

**FIGURE 9.19**

Comparison of predictions from Equation 9.61 with mixed mode fracture data for T300/5208 graphite/epoxy laminates. (Reprinted from O'Brien, T. K., Johnston, N. J., Raju, I. S., Morris, D. H., and Simonds, R. A. 1987, in Johnston, N. J. ed., *Toughened Composites*, ASTM STP 937, pp. 199–221. American Society for Testing and Materials, Philadelphia, PA. Copyright ASTM. With permission.)

Mangalgiri [59] when  $m = n = 1$ . O'Brien et al. [58] investigated the use of Equation 9.61 for graphite/epoxy laminates having various lay-ups, and predictions are compared with experimental data from the edge delamination test [43] in Figure 9.19. Some previous data from Murri and O'Brien [60] are included in Figure 9.19. Johnson and Mangalgiri tested various matrix resins using the DCB, ENF, and several other methods, and comparisons of the

**FIGURE 9.20**

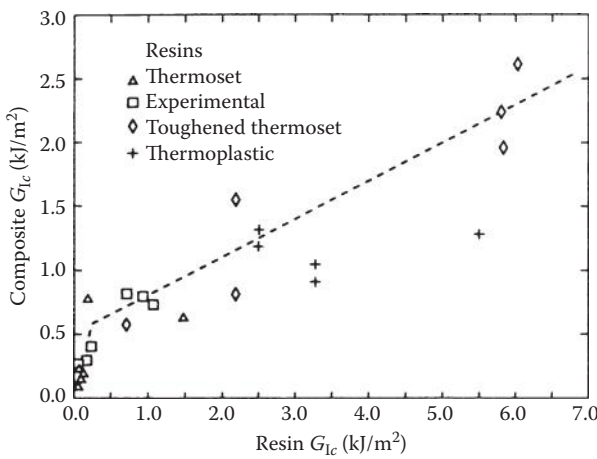
Comparison of predictions from Equation 9.61 with mixed mode fracture data for several matrix resins. (Reprinted from Johnson, W. S. and Mangalgiri, P. D. 1987, in Johnston, N. J. ed., *Toughened Composites*, ASTM STP 937, pp. 295–315. American Society for Testing and Materials, Philadelphia, PA. Copyright ASTM. With permission.)

predictions of Equation 9.61 with experimental data are shown in Figure 9.20. On the other hand, Ramkumar and Whitcomb [61] have concluded that Equation 9.61 is not a reliable delamination growth criterion for graphite/epoxy.

The measurement of mixed mode interlaminar fracture toughness (in particular, mixed mode I and mode II) has been the subject of numerous publications, and many methods have been proposed. One method, known as the mixed mode-bending test, was originally developed by Reeder and Crews [62] and later evolved as an ASTM standard [63]. This method will be discussed in more detail in Chapter 10.

In recent years much research has been done for the improvement of interlaminar fracture toughness of composites, and the results of some of this research can be seen in the  $G_{lc}$  data of Table 9.1. For example, since the interlaminar region consists primarily of matrix material, there has been considerable interest in the use of tough matrix materials. Significant improvements in the composite  $G_{lc}$  have been obtained by using tough matrix materials such as polysulfone [46], elastomer-modified epoxy [48], and polyetheretherketone [49]. It is not clear, however, that additional increases in resin matrix toughness will necessarily be translated into correspondingly higher composite toughness [50,51]. Figure 9.21 from Hunston et al. [51] shows that for resin  $G_{lc}$  values less than about 0.4 kJ/m<sup>2</sup> substantial gains in the corresponding graphite fiber composite,  $G_{lc}$  are obtained by increasing the resin  $G_{lc}$ . For resin  $G_{lc}$  values greater than about 0.4 kJ/m<sup>2</sup>, however, the gains in the composite  $G_{lc}$  from additional increases in resin  $G_{lc}$  are not nearly as great. SEM studies of delamination fracture surfaces have shown that increased toughness of the matrix causes an increase in the delamination fracture toughness by increasing the size of the plastic zone ahead of the crack tip [50,51]. Further increases in the size of this plastic zone are apparently prevented by the constraint of the fibers in the adjacent plies, however [50,51].

A variety of other methods for increasing interlaminar fracture toughness of laminates have been investigated. For example, thin films or "interleaves" made of a tough polymer resin can be embedded between the fiber-reinforced resin laminae [64–68]. Coating the fibers with a thin, tough polymer film [69–70], hybridization of different fiber types [71–72], and stitching of adjacent laminae [73] have also been investigated. A critical review of methods for improving fracture toughness of composites through interface control has also been published [74]. The so-called Z-pinning approach for improving delamination resistance involves the insertion of metal or composite pins through the thickness (i.e., in the z-direction) of the laminate in the same way that a nail would be driven into wooden boards to hold them together [75–77]. Three-dimensional braiding essentially eliminates delamination as a failure mode, since there are no distinct plies to separate [78,79]. However, the in-plane strength and stiffness of the braided composite will not be as great as the corresponding properties of a laminate constructed of unidirectional plies. These and other mechanical means of improving delamination resistance are illustrated schematically in Figure 9.22. Of particular relevance

**FIGURE 9.21**

Mode I interlaminar strain energy release rates for steady crack growth in graphite fiber composites as a function of the heat resin strain energy release rates for several matrix resins. (Reprinted from Hunston, D. L. et al. 1987, in Johnston, N. J. ed., *Toughened Composites*, ASTM STP 937, pp. 74–94. American Society for Testing and Materials, Philadelphia, PA. Copyright ASTM. With permission.)

here is a special issue of a well-known composites journal that has been devoted to papers on advances in statics and dynamics of delamination [80]. Unfortunately, improvements in interlaminar toughness often come at the expense of degradation in other properties such as hot/wet strength and stiffness or viscoelastic creep response. Although significant progress has been made in understanding delamination, much is still to be learned. The study of delamination continues to be a very active research topic, and the reader is encouraged to consult recent journal publications and conference proceedings for the latest findings. A highly relevant topic of recent interest is the use of nanoparticles, nanotubes, or nanofibers to enhance the fracture toughness of composites, which is discussed in Section 9.5.

### Example 9.4

Derive an equation for the mode I strain energy release rate of the DCB specimen shown in Figure 9.18a.

### SOLUTION

Analyze one half of the cracked DCB specimen as a single cantilever beam. Using the laminated beam theory, the tip deflection of the single laminated cantilever beam is

$$\frac{\delta}{2} = \frac{Pa^3}{3E_{\text{fix}}I}$$

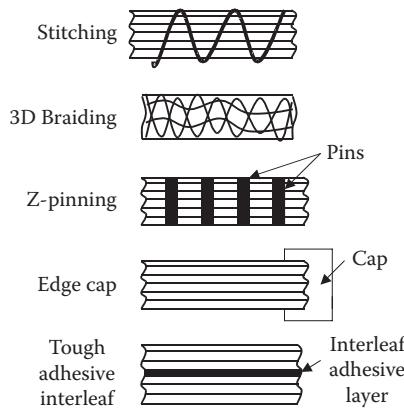
**FIGURE 9.22**

Illustration of some mechanical means of improving interlaminar fracture toughness.

where  $P$  is the applied load,  $a$  the beam length (same as the DCB crack length),  $E_{\text{fx}}$  is the flexural modulus of the cracked half of the DCB specimen along the  $x$ -direction (the beam axis),  $I = \frac{t(h/2)^3}{12} = \frac{th^3}{96}$  is the moment of inertia of the cracked half of the DCB about its centroidal axis,  $t$  is the DCB specimen width (the crack width) and  $h/2$  is the depth of the single cantilever. The tip compliance of the DCB specimen is then

$$s = \frac{\delta}{P} = \frac{64a^3}{E_{\text{fx}}th^3}$$

The mode I strain energy release rate,  $G_I$ , is then found by substituting this equation for the compliance in Equation 9.28 and differentiating with respect to the crack length,  $a$ . The result is

$$G_I = \frac{P^2}{2t} \frac{\partial s}{\partial a} = \frac{96P^2a^2}{E_{\text{fx}}t^2h^3}$$

or

$$G_I = \frac{3P\delta}{2ta}$$

## 9.5 Nanoenhancement of Fracture Toughness

Fracture toughness is a measure of resistance to crack growth, or energy dissipation at the crack tip during crack growth. In composites, several energy dissipation mechanisms such as debonding and pull-out are related to the amount of available fiber/matrix or particle/matrix interfacial area, and the

total interfacial surface area per unit volume increases substantially as the particle or fiber size is reduced. As shown in Example 1.1, the total surface area per unit volume of a group of small diameter fibers of diameter  $d_s$  is  $d_L/d_s$  times that of a single large diameter fiber of diameter  $d_L$ , and the same result holds for spherical particles. Thus, the fiber–matrix or particle–matrix interfacial area per unit volume available for debonding or pull-out is roughly a factor of 1000 times greater for nanosized reinforcements than for more conventional micron-sized reinforcements. Consider the analysis of Wichmann et al. [81] which compared the pull-out energy for a crack propagating through a single carbon microfiber with that of a crack propagating through a group of CNTs (Figure 9.23). This analysis was based on an earlier analysis of fiber pull-out energy which was published by Kelly [82], and later summarized by Sun et al. [83].

Following the developments in Refs. [81–83], the work done in pulling out a microfiber of radius  $r_{\text{mf}}$  over a distance  $x$  is

$$W_{\text{mf}} = \int_0^x 2\pi r_{\text{mf}} \tau_{\text{mf}} x \, dx = \pi r_{\text{mf}} \tau_{\text{mf}} x^2 \quad (9.62)$$

where  $\tau_{\text{mf}}$  is the microfiber/matrix interfacial shear strength. Taking into account the symmetry of the interfacial shear stress distribution about the half-length of the fiber (see Figure 6.6), the average pull-out work done per microfiber over the critical length  $L_{\text{cmf}}$  is then

$$\bar{W}_{\text{mf}} = \frac{\int_0^{L_{\text{cmf}}/2} W_{\text{mf}} \, dx}{L_{\text{cmf}}/2} = \frac{\pi r_{\text{mf}} \tau_{\text{mf}} L_{\text{cmf}}^2}{12} \quad (9.63)$$

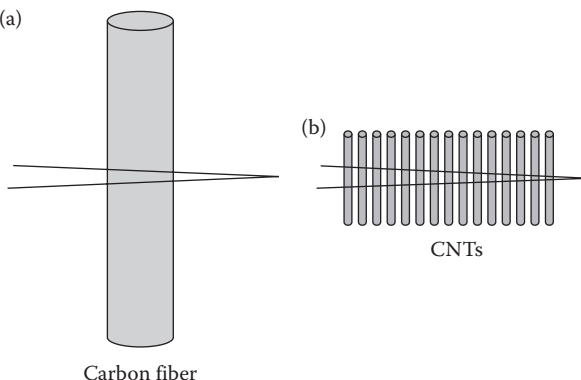


**FIGURE 9.23**

Schematic view of a crack propagating through (a) a single carbon microfiber, and (b) a group of CNTs having the same volume. (Reprinted from *Composites Science and Technology*, 68, Wichmann, M. H. G., Schulte, K., and Wagner, H. D., On nanocomposite toughness, 329–331, Copyright (2008), with permission from Elsevier.)

where, from Equation 6.9,

$$L_{\text{cmf}} = \frac{r_{\text{mf}} s_{\text{mf}}^{(+)}}{\tau_{\text{mf}}} \quad (9.64)$$

and  $s_{\text{mf}}^{(+)}$  is the tensile strength of the microfiber. The corresponding average work done in pulling out a single nanofiber or nanotube over the critical length  $L_{\text{cnf}}$  from the same matrix is therefore

$$\bar{W}_{\text{nf}} = \frac{\pi r_{\text{nf}} \tau_{\text{nf}} L_{\text{cnf}}^2}{12} \quad (9.65)$$

where

$$L_{\text{cnf}} = \frac{r_{\text{nf}} s_{\text{nf}}^{(+)}}{\tau_{\text{nf}}} \quad (9.66)$$

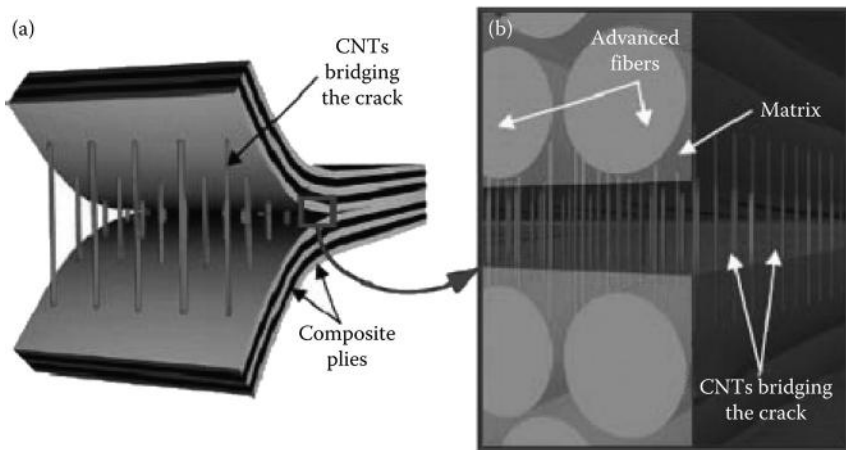
and  $r_{\text{nf}}$ ,  $\tau_{\text{nf}}$ , and  $s_{\text{nf}}^{(+)}$  are the radius, interfacial shear strength and tensile strength of the nanofiber or nanotube, respectively. Comparing the pull-out energy for single microfiber having volume  $V_{\text{mf}}$  and critical length  $L_{\text{cmf}}$  with that of a group of  $n$  nanofibers or nanotubes having the same volume but different critical length  $L_{\text{cnf}}$  requires that

$$n = \frac{V_{\text{mf}}}{V_{\text{nf}}} = \frac{r_{\text{mf}}^2 L_{\text{cmf}}}{r_{\text{nf}}^2 L_{\text{cnf}}} \quad (9.67)$$

where  $V_{\text{nf}}$  is the volume of a single nanofiber or nanotube. The ratio of the average work of pull-out of a group of  $n$  nanofibers or nanotubes to the corresponding average work of pull-out of a single microfiber is then

$$\frac{n \bar{W}_{\text{nf}}}{\bar{W}_{\text{mf}}} = \frac{r_{\text{mf}} \tau_{\text{nf}} L_{\text{cnf}}}{r_{\text{nf}} \tau_{\text{mf}} L_{\text{cmf}}} = \frac{s_{\text{nf}}^{(+)}}{s_{\text{mf}}^{(+)}} \quad (9.68)$$

where  $L_{\text{cmf}}$  and  $L_{\text{cnf}}$  are given by Equations 9.64 and 9.66, respectively. From the tensile strength properties in Table 1.1, it can be seen that the ratio  $s_{\text{nf}}^{(+)}/s_{\text{mf}}^{(+)}$  in Equation 9.68 can range from about 2 to greater than 10 when comparing CNTs with carbon microfibers. The corresponding range when comparing CNFs to carbon microfibers is about 0.5–1.5. So on the basis of the pull-out mechanism and its corresponding contribution to fracture toughness, there is a clear advantage of CNTs over conventional carbon microfibers. A similar analysis for fracture energy of fibers shows that CNTs are also superior to microfibers with regard to the fiber fracture contribution to fracture toughness, but a similar analysis for debonding of spherical particles indicates no advantage of nanoparticles over microparticles unless the particle–matrix interphase region is taken into account [83].

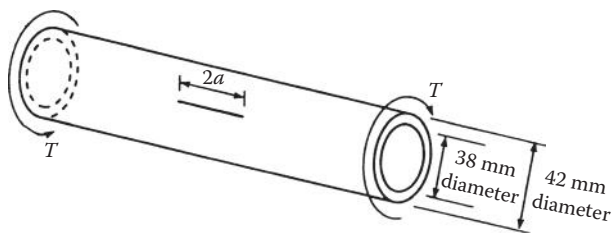
**FIGURE 9.24**

Use of aligned CNT forests to strengthen interlaminar region in composite laminates. (a) Vertically aligned carbon nanotubes (VACNTs) placed between two plies of a laminated composite and (b) close-up of the crack, showing VACNTs bridging the crack between the two plies. (Reprinted from *Composites Part A: Applied Science and Manufacturing*, 39, Garcia, E. J., Wardle, B. L., and Hart, A. J., Joining prepreg composite interfaces with aligned carbon nanotubes, 1065–1070, Copyright (2008), with permission from Elsevier.)

To take full advantage of the above-demonstrated potential pull-out energy of CNTs, they should be aligned parallel to each other and perpendicular to the crack plane, as shown in Figure 9.23b. Such a possibility has been realized by Garcia et al. [84], who demonstrated the use of aligned CNT forests to improve interlaminar strength and toughness of conventional CF/epoxy laminates. There are major concerns about conventional composite laminates because of the weak matrix resin-rich regions that exist between the composite laminae. As shown in Figure 9.24, vertically aligned CNT forests can bridge and strengthen this interlaminar region [84]. More specifically, the authors reported that the CNT-modified interfaces increased the mode I interlaminar fracture toughness of aerospace grade carbon/epoxy laminates by a factor of 1.5–2.5 and the corresponding mode II value by a factor of 3 [84]. Analytical modeling of fracture toughness of the CNT-modified laminates based on the crack closure technique for fiber bridging was reported later in [85]. Finally, as shown in a recent review article [83], there are numerous other reports in the literature regarding the use of other nanoparticles and related energy absorption mechanisms to improve the fracture toughness of polymers and composites.

### PROBLEMS

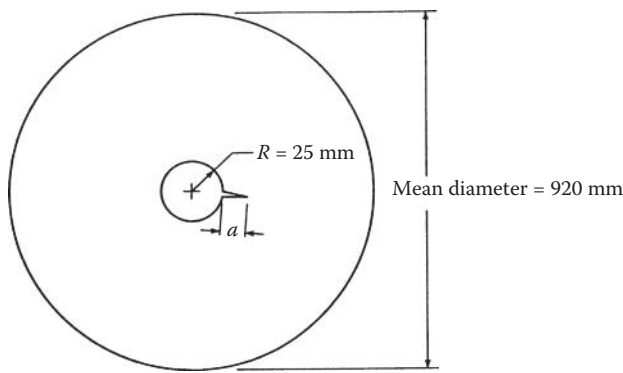
1. The thin-walled tubular shaft shown in Figure 9.25 is made of randomly oriented, short-fiber-reinforced metal matrix composite.

**FIGURE 9.25**

Thin-walled tubular composite shaft with longitudinal crack.

The shaft has a longitudinal through-thickness crack of length  $2a$  and is subjected to a torque  $T = 1 \text{ KN m}$ . If the mode II fracture toughness of the composite is  $K_{Ic} = 40 \text{ MPa m}^{1/2}$ , determine the critical crack size for self-sustaining crack growth.

2. a. Determine the allowable torque,  $T$ , if the crack length for the shaft in Figure 9.25 is  $2a = 10 \text{ mm}$ . Use the same dimensions and fracture toughness values that were given in Problem 1.
- b. If the uniaxial yield stress for the shaft material is  $\gamma = 1200 \text{ MPa}$ , and the crack is ignored, compare the answer from part (a) with the allowable torque based on the Maximum Shear Stress criterion for yielding.
3. The tube shown in Figure 9.25 is subjected to an internal pressure,  $p = 5 \text{ MPa}$ , instead of a torque. Neglecting the stress along the longitudinal axis of the tube, and assuming that the mode I fracture toughness is  $K_{Ic} = 10 \text{ MPa m}^{1/2}$ , determine the critical crack size.
4. As in Problem 3, assume that the tube in Figure 9.25 is subjected only to an internal pressure and neglect the longitudinal stress.
  - a. Determine the allowable internal pressure,  $p$ , if the crack length in Figure 9.25 is  $2a = 10 \text{ mm}$ . Use the same dimensions and fracture toughness values that were given in Problem 3.
  - b. Using the yield stress from Problem 2 and ignoring the crack, compare the answer from part (a) of this problem with the allowable internal pressure based on the Maximum Shear Stress criterion for yielding.
5. Use the Whitney–Nuismer average stress criterion to estimate the allowable internal pressure for Problem 4 if the unnotched tensile strength of the material is  $\sigma_0 = 1500 \text{ MPa}$  and the parameter  $a_0 = 3 \text{ mm}$ .
6. Repeat Problem 5 using the Whitney–Nuismer point stress criterion and the parameter  $d_0 = 1 \text{ mm}$ .
7. The 920 mm diameter, 1.6-mm-thick spherical pressure vessel in Figure 9.26 is a filament wound quasi-isotropic composite laminate with a single 50 mm diameter entrance hole. The vessel material has a mode I fracture toughness of  $K_{Ic} = 25 \text{ MPa m}^{1/2}$ . If the vessel is to contain gas at a pressure of  $0.69 \text{ MPa}$ , what is the critical length,  $a_c$ , of a single crack emanating from the edge of the hole? The Bowie equation (9.38) may be used for this problem, and the function  $f(a/R)$

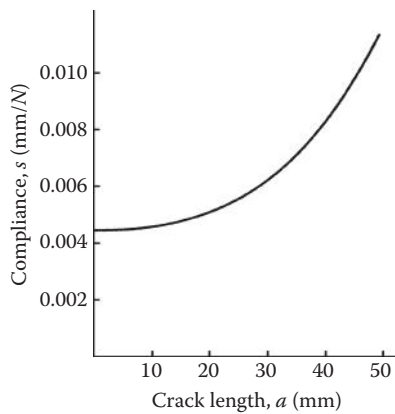
**FIGURE 9.26**

Spherical composite pressure vessel with single crack at the edge of entrance hole.

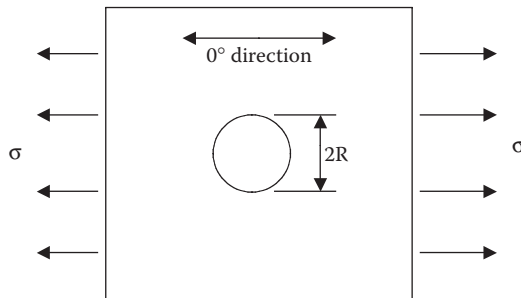
for a biaxial stress field and a single crack of length,  $a$ , at the edge of a hole of radius,  $R$ , is tabulated below for several values of  $a/R$ .

$a/R$	$f(a/R)$	$a/R$	$f(a/R)$
0.1	1.98	0.8	1.32
0.2	1.82	1.0	1.22
0.3	1.67	1.5	1.06
0.4	1.58	2.0	1.01
0.5	1.49	3.0	0.93
0.6	1.42	5.0	0.81

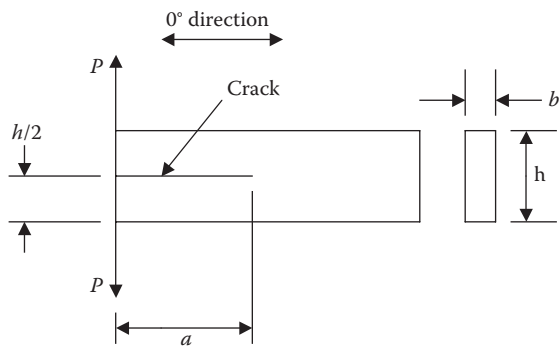
8. If the quasi-isotropic graphite/epoxy laminate in Example 7.6 has a centrally located 25 mm-diameter hole, determine the ratio of notched to unnotched uniaxial strength for the laminate using the Whitney–Nuismer average stress criterion. The parameter  $a_0 = 4 \text{ mm}$ .
9. A 3 mm-thick composite specimen is tested as shown in Figure 9.6a, and the compliance,  $s = u/P$ , as a function of the half-crack length,  $a$ , is shown in Figure 9.27. In a separate test the critical load for self-sustaining crack propagation,  $P_c$ , is measured for different crack lengths, and the critical load corresponding to a crack length  $2a = 50 \text{ mm}$  is found to be 100 N. Determine the critical mode I strain energy release rate,  $G_{lc}$ .
10. A laminated plate consisting of the  $[90/0/90]_s$  AS/3501 laminate described in Example 7.12 has a central hole as shown in Figure 9.28. The plate is loaded uniaxially along the  $0^\circ$  direction as shown. Using the Whitney–Nuismer average stress criterion for stress fracture with an unnotched laminate tensile strength of  $\sigma_0 = 500 \text{ MPa}$ , and an averaging distance  $a_0 = 10 \text{ mm}$ , plot the notched tensile strength  $\sigma_N^\infty$  as a function of hole radius

**FIGURE 9.27**

Variation of specimen compliance with crack length for Problem 9.

**FIGURE 9.28**

Uniaxially loaded laminated plate with central hole for Problem 10.

**FIGURE 9.29**

Cracked laminate subjected to bending for Problem 11.

- R. What are the maximum and minimum theoretical values of the notched tensile strength, and under what conditions do they occur?
11. A unidirectional [0] composite beam of longitudinal modulus  $E_1$ , thickness  $b$ , and depth  $h$  has a crack of length  $a$  and is loaded by the equal and opposite forces  $P$  as shown in Figure 9.29. Determine  $G_I$ , the mode I strain energy release rate for this crack. Your answer should be expressed in terms of the given parameters.
  12. The sandwich beam described in Example 9.2 is subjected to a total applied load  $P = 500$  N. Assuming that a shear crack is located at the middle surface of the beam in the region of maximum shear force, determine the critical crack size for mode II core shear fracture.
  13. For the sandwich beam described in Example 9.2, explain what would need to be done to find an equation for the crack growth rate  $da_{II}/dN$  under cyclic loading, where  $a_{II}$  is the shear crack half length and  $N$  is the number of loading cycles.

---

## References

1. Chan, W. F. 1997. Fracture and damage mechanics in laminated composites, in Mallick, P. K. ed., *Composites Engineering Handbook*, Chapter 7, pp. 309–370. Marcel Dekker, Inc., New York, NY.
2. Sendeckyj, G. P., ed. 1975. *Fracture Mechanics of Composites*, ASTM STP 593. American Society for Testing and Materials, Philadelphia, PA.
3. Reifsnider, K. L., ed. 1982. *Damage in Composite Materials*, ASTM STP 775. American Society for Testing and Materials, Philadelphia, PA.
4. Johnson, W. S., ed. 1985. *Delamination and Debonding of Materials*, ASTM STP 876. American Society for Testing and Materials, Philadelphia, PA.
5. Hahn, H. T., ed. 1986. *Composite Materials: Fatigue and Fracture*, ASTM STP 907. American Society for Testing and Materials, Philadelphia, PA.
6. Lagace, P. A., ed. 1989. *Composite Materials: Fatigue and Fracture*, ASTM STP 1012. American Society for Testing and Materials, Philadelphia, PA.
7. O'Brien, T. K., ed. 1991. *Composite Materials: Fatigue and Fracture*, ASTM STP 1110. American Society for Testing and Materials, Philadelphia, PA.
8. Friedrich, K., ed. 1989. Application of fracture mechanics to composite materials, in Pipes, R. B. ed., *Composite Material Series*, Vol. 6 (Series ed.). Elsevier Science Publisher, Amsterdam, The Netherlands.
9. Newaz, G. M., ed. 1991. *Delamination in Advanced Composites*. Technomic Publishing Co., Lancaster, PA.
10. Griffith, A. A. 1920. The phenomena of rupture and flow in solids. *Philosophical Transactions of the Royal Society*, 221A, 163–198.
11. Gilman, J. J. 1968. *Transactions of the American Society for Metals*, 61, 861–906. [Reprint of “Griffith, A. A. 1920. The phenomena of rupture and flow in solids. *Philosophical Transactions of the Royal Society*, 221A, 163–198.” with corrections and commentary.]

12. Sih, G. C. and Liebowitz, H. 1968. Mathematical theories of brittle fracture, in Liebowitz, H. ed., *Fracture—An Advanced Treatise*, Vol. II, *Mathematical Fundamentals*, pp. 67–190. Academic Press, New York, NY.
13. Irwin, G. R. 1949. *Fracturing of Metals*, pp. 147–166. American Society of Metals, Cleveland, OH.
14. Orowan, E. 1950. *Fatigue and Fracture of Metals*. MIT Press, Cambridge, MA.
15. Westergaard, H. M. 1939. Bearing pressures and cracks. *Transactions of the ASME, Series E, Journal of Applied Mechanics*, 61, A49–A53.
16. Irwin, G. R. 1957. Analysis of stresses and strains near the end of a crack traversing a plate. *Transactions of the ASME, Journal of Applied Mechanics*, 24, 361–364.
17. Tada, H., Paris, P. C., and Irwin, G. R. 1973. *The Stress Analysis of Cracks Handbook*. Del Research Corporation, Hellertown, PA.
18. Lekhnitskii, S. G. 1963. *Theory of Elasticity of an Anisotropic Elastic Body*. Holden-Day, Inc., San Francisco, CA.
19. Wu, E. M. 1968. Fracture mechanics of anisotropic plates, in Tsai, S. W., Halpin, J. C., and Pagano N. J. eds., *Composite Materials Workshop*, pp. 20–43. Technomic Publishing Co., Lancaster, PA.
20. Konish, H. J., Swedlow, J. L., and Cruse, T. A. 1972. Experimental investigation of fracture in an advanced composite. *Journal of Composite Materials*, 6, 114–124.
21. Parhizgar, S., Zachary, L. W., and Sun, C. T. 1982. Application of the principles of linear fracture mechanics to the composite materials. *International Journal of Fracture*, 20, 3–15.
22. Alexander, R. M., Schapery, R. A., Jerina, K. L., and Sanders, B. A. 1982. Fracture characterization of a random fiber composite material, in Sanders B. A. ed., *Short Fiber Reinforced Composite Materials*, ASTM STP 772, pp. 208–224. American Society for Testing and Materials, Philadelphia, PA.
23. Sun, C. T. and Sierakowski, R. L. 1980. Fracture characterization of composites with chopped fiberglass reinforcement. *SAMPE Quarterly*, 11(4), 15–21.4.
24. Gaggar, S. K. and Broutman, L. J. 1974. The development of a damage zone at the tip of a crack in a glass fiber reinforced polyester resin. *International Journal of Fracture*, 10, 606–608.
25. Irwin, G. R. 1958. Fracture, in Flugge, S. ed., *Handbuch der Physik*, Vol. 6, pp. 551–590. Springer, Berlin.
26. Corten, H. T. 1972. Fracture mechanics of composites, in Liebowitz, H. ed., *Fracture—An Advanced Treatise*, Vol. VII, *Fracture of Nonmetals and Composites*, pp. 675–769. Academic Press, New York, NY.
27. Cruse, T. A. 1973. Tensile strength of notched composites. *Journal of Composite Materials*, 7, 218–229.
28. Paris, P. C. and Erdogan, F. 1963. A critical analysis of crack propagation laws. *Transactions of ASME, Journal of Basic Engineering*, 85, 528–534.
29. Kunz, S. C. and Beaumont, P. W. R. 1975. Microcrack growth in graphite fiber-epoxy resin systems during compressive fatigue, in Hancock J. R. ed., *Fatigue of Composite Materials*, ASTM STP 569, pp. 71–91. American Society for Testing and Materials, Philadelphia, PA.
30. Spearing, M., Beaumont, P. W. R., and Ashby, M. F. 1991. Fatigue damage mechanics of notched graphite-epoxy laminates, in O'Brien, T. K. ed., *Composite Materials: Fatigue and Fracture*, Vol. 3, ASTM STP 1110, pp. 617–637. American Society for Testing and Materials, Philadelphia, PA.

31. Rybicki, E. F. and Kanninen, M. F. 1997. A finite element calculation of stress intensity factors by a modified crack closure integral. *Engineering Fracture Mechanics*, 9, 931–938.
32. Krueger, R. 2004. Virtual crack closure technique: History, approach and applications. *Applied Mechanics Reviews*, 57(2), 109–143.
33. Whitney, J. M. and Nuismer, R. J. 1974. Stress fracture criteria for laminated composites containing stress concentrations. *Journal of Composite Materials*, 8, 253–265.
34. Nuismer, R. J. and Whitney, J. M. 1975. Uniaxial failure of composite laminates containing stress concentrations, in *Fracture Mechanics of Composites*, ASTM STP 593, pp. 117–142. American Society for Testing and Materials, Philadelphia, PA.
35. Waddoups, M. E., Eisenmann, J. R., and Kaminski, B. E., 1971. Macroscopic fracture mechanics of advanced composite materials. *Journal of Composite Materials*, 5(4), 446–454.
36. Bowie, O. L., 1956. An analysis of an infinite plate containing radial cracks originating from the boundary of an internal circular hole. *Journal of Mathematics and Physics*, 35, 60–71.
37. Timoshenko, S. P. and Goodier, J. N. 1951. *Theory of Elasticity*, 2nd ed. McGraw-Hill, Inc., New York, NY.
38. Lekhnitskii, S. G. 1968. *Anisotropic Plates* (Translated from 2d Russian ed. by Tsai, S. W. and Cheron, T.). Gordon and Breach Science Publishers, New York, NY.
39. Roderick, G. L., Everett, R. A., and Crews, J. H. 1975. Debond propagation in composite-reinforced metals, in *Fatigue of Composite Materials*, ASTM STP 569, pp. 295–306. American Society for Testing and Materials, Philadelphia, PA.
40. Kanninen, M. F., Rybicki, E. F., and Brinson, H. F. 1977. A critical look at current applications of fracture mechanics to the failure of fiber reinforced composites. *Composites*, 8, 17–22.
41. Rybicki, E. F., Schmueser, D. W., and Fox, J. 1977. An energy release rate approach for stable crack growth in the free-edge delamination problem. *Journal of Composite Materials*, 11, 470–487.
42. Wang, S. S. 1979. Delamination crack growth in unidirectional fiber-reinforced composite under static and cyclic loading, in Tsai, S. W. ed., *Composite Materials: Testing and Design*, ASTM STP 674, pp. 642–663. American Society for Testing and Materials, Philadelphia, PA.
43. O'Brien, T. K. 1982. Characterization of delamination onset and growth in a composite laminate, in Reifsneider, K. L. ed., *Damage in Composite Materials*, ASTM STP 775, pp. 140–167. American Society for Testing and Materials, Philadelphia, PA.
44. Devitt, D. F., Schapery, R. A., and Bradley, W. L. 1980. A method for determining the mode I delamination fracture toughness of elastic and viscoelastic composite materials. *Journal of Composite Materials*, 14, 270–285.
45. Wilkins, D. J., Eisenmann, J. R., Camin, R. A., Margolis, W. S., and Benson, R. A. 1982. Characterizing delamination growth in graphite-epoxy, in Reifsneider, K. L. ed., *Damage in Composite Materials*, ASTM STP 775, pp. 168–183. American Society for Testing and Materials, Philadelphia, PA.
46. Whitney, J. M., Browning, C. E., and Hoogsteen, W. 1982. A double cantilever beam test for characterizing mode I delamination of composite materials. *Journal of Reinforced Plastics and Composites*, 1, 297–313.

47. Aliyu, A. A. and Daniel, I. M. 1985. Effects of strain rate on delamination fracture toughness of graphite/epoxy, in Johnson, W. S., ed., *Delamination and Debonding of Materials*, ASTM STP 876, pp. 336–348. American Society for Testing and Materials, Philadelphia, PA.
48. Daniel, I. M., Shareef, I., and Aliyu, A. A. 1987. Rate effects on delamination of a toughened graphite/epoxy, in Johnston, N. J. ed., *Toughened Composites*, ASTM STP 937, pp. 260–274. American Society for Testing and Materials, Philadelphia, PA.
49. Leach, D. C., Curtis, D. C., and Tamblin, D. R. 1987. Delamination behavior of carbon fiber/poly(etheretherketone) (PEEK) composites, in Johnson, N. J. ed., *Toughened Composites*, ASTM STP 937, pp. 358–380. American Society for Testing and Materials, Philadelphia, PA.
50. Bradley, W. L. 1989. Relationship of matrix toughness to interlaminar fracture toughness, in Friedrich, K. ed., *Application of Fracture Mechanics of Composite Materials*, Chapter 5, Vol. 6, *Composite Material Series*, Pipes, R. B. (Series ed.). Elsevier Science Publishers, Amsterdam, The Netherlands.
51. Hunston, D. L., Moulton, R. J., Johnston, N. J., and Bascom, W. 1987. Matrix resin effects in composite delamination: Mode I fracture aspects, in Johnston, N. J. ed., *Toughened Composites*, ASTM STP 937, pp. 74–94. American Society for Testing and Materials, Philadelphia, PA.
52. Carlsson, L. A. and Gillispie, J. W. 1989. Mode II interlaminar fracture of composites, in Friedrich, K. ed., *Application of Fracture Mechanics to Composite Materials*, Chapter 4, Vol. 6, *Composite Material Series*, Pipes, R. B. (Series ed.). Elsevier Science Publishers, Amsterdam, The Netherlands.
53. Russell, A. J. and Street, K. N. 1985. Moisture and temperature effects on the mixed mode delamination fracture of unidirectional graphite/epoxy, in Johnson, W. S. ed., *Delamination and Debonding of Materials*, ASTM STP, pp. 876, 349–370. American Society for Testing and Materials, Philadelphia, PA.
54. Carlsson, L. A., Gillispie, J. W. Jr., and Pipes, R. B. 1986. On the analysis and design of the end notched flexure (ENF) specimen for mode II testing. *Journal of Composite Materials*, 20, 594–604.
55. Carlsson, L. A. and Pipes, R. B. 1987. *Experimental Characterization of Advanced Composite Materials*. Prentice-Hall, Inc., Englewood Cliffs, NJ.
56. Kageyama, K., Kikuchi, M., and Yanagisawa, N. 1991. Stabilized end notched flexure test: Characterization of mode II interlaminar crack growth, in O'Brien, T. K. ed., *Composite Materials: Fatigue and Fracture*, Vol. 3, ASTM STP 1110, pp. 210–225. American Society for Testing and Materials, Philadelphia, PA.
57. Russell, A. J. 1991. Initiation and growth of Mode II delamination in toughened composites, in O'Brien, T. K. ed., *Composite Materials: Fatigue and Fracture*, Vol. 3, ASTM STP 1110, pp. 226–242. American Society for Testing and Materials, Philadelphia, PA.
58. O'Brien, T. K., Johnston, N. J., Raju, I. S., Morris, D. H., and Simonds, R. A. 1987. Comparisons of various configurations of the edge delamination test for interlaminar fracture toughness, in Johnston, N. J. ed., *Toughened Composites*, ASTM STP 937, pp. 199–221. American Society for Testing and Materials, Philadelphia, PA.
59. Johnson, W. S. and Mangalgiri, P. D. 1987. Influence of the resin on interlaminar mixed-mode fracture, in Johnston, N. J. ed., *Toughened Composites*, ASTM STP 937, pp. 295–315. American Society for Testing and Materials, Philadelphia, PA.

60. Murri, G. B. and O'Brien, T. K. 1985. Interlaminar  $G_{llc}$  evaluation of toughened resin matrix composites using the end notched flexure test, in *Proceedings of the 26th AIAA/ASCE/ASCE/AHS Structures, Structural Dynamics and Materials Conference*, pp. 197–202. American Institute for Aeronautics and Astronautics, New York.
61. Ramkumar, R. L. and Whitcomb, J. D. 1985. Characterization of mode I and mixed mode delamination growth in T300/5208 graphite/epoxy, in Johnson, W. S. ed., *Delamination and Debonding of Materials*, ASTM STP 876, pp. 315–335. American Society for Testing and Materials, Philadelphia, PA.
62. Reeder, J. R. and Crews, J. H. Jr. 1990. Mixed mode bending method for delamination testing. *AIAA Journal*, 28(7), 1270–1276.
63. D 6671/D 6771-M-04. 2005. Standard test method for mixed Mode I–Mode II interlaminar fracture toughness of unidirectional fiber reinforced polymer matrix composites. *Space Simulation; Aerospace and Aircraft; Composite Materials*, Vol. 15.03. ASTM International, West Conshohocken, PA
64. Chan, W. S., Rogers, C., and Aker, S. 1986. Improvement of edge delamination strength of composite laminates using adhesive layers, in Whitney, J. M. ed., *Composite Materials: Testing and Design (Seventh Conference)*, ASTM STP 893, pp. 266–285. American Society for Testing and Materials, Philadelphia, PA.
65. Evans, R. E. and Masters, J. E. 1987. A new generation of epoxy composites for primary structural applications: Materials and mechanics, in Johnston, N. J. ed., *Toughened Composites*, ASTM STP 937, pp. 413–436. American Society for Testing Materials, Philadelphia, PA.
66. Ishai, O., Rosenthal, H., Sela, N., and Drukker, E. 1988. Effect of selective adhesive interleaving on interlaminar fracture toughness of graphite/epoxy composite laminates. *Composites*, 19(1), 49–54.
67. Sela, N., Ishai, O., and Banks-Sills, L. 1989. The effect of adhesive thickness on interlaminar fracture toughness of interleaved CFRP specimens. *Composites*, 20(3), 257–264.
68. Lagace, P. A. and Bhat, N. V. 1992. Efficient use of film adhesive interlayers to suppress delamination, in Grimes, G. C. ed., *Composite Materials: Testing and Design*, Vol. 10, ASTM STP 1120, pp. 384–396. American Society for Testing and Materials, Philadelphia, PA.
69. Broutman, L. J. and Agarwal, B. D. 1974. A theoretical study of the effect of an interfacial layer on the properties of composites. *Polymer Engineering and Science*, 14(8), 581–588.
70. Schwartz, H. S. and Hartness, T. 1987. Effect of fiber coatings on interlaminar fracture toughness of composites, in Johnston, N. J. ed., *Toughened Composites*, ASTM STP 937, pp. 150–178. American Society for Testing and Materials, Philadelphia, PA.
71. Browning, C. E. and Schwartz, H. S. 1986. Delamination resistant composite concepts, in Whitney, J. M. ed., *Composite Materials: Testing and Design (Seventh Conference)*, ASTM STP 893, pp. 256–265. American Society for Testing and Materials, Philadelphia, PA.
72. Mignery, L. A., Tan, T. M., and Sun, C. T. 1985. The use of stitching to suppress delamination in laminated composites, in Johnson, W. S. ed., *Delamination and Debonding of Materials*, ASTM STP 876, pp. 371–385. American Society for Testing and Materials, Philadelphia, PA.

73. Garcia, R., Evans, R. E., and Palmer, R. J. 1987. Structural property improvements through hybridized composites, in Johnston, N. J. ed., *Toughened Composites*, ASTM STP 937, pp. 397–412. American Society for Testing and Materials, Philadelphia, PA.
74. Kim, J. K. and Mai, Y. W. 1991. High stretch, high fracture toughness fibre composites with interface control—A review. *Composites Science and Technology*, 41, 333–378.
75. Yan, W., Liu, H.-Y., and Mai, Y.-W. 2003. Numerical study on the Mode I delamination toughness of z-pinned laminates. *Composites Science and Technology*, 63(10), 1481–1493.
76. Byrd, L. W. and Birman, V. 2006. Effectiveness of z-pins in preventing delamination of co-cured composite joints on the example of a double cantilever test. *Composites Part B Engineering*, 37(4–5), 365–378.
77. Cartie, D. D. R., Troulis, M., and Partridge, I. K. 2006. Delamination of z-pinned carbon fibre reinforced laminates. *Composites Science and Technology*, 66(6), 855–861.
78. Mouritz, A. P., Baini, C., and Herszberg, I. 1999. Mode I interlaminar fracture toughness properties of advanced textile fiberglass composites. *Composites Part A Applied Science and Manufacturing*, 30A(7), 859–870.
79. Yau, S.-S., Chou, T.-W., and Ko, F. K. 1986. Flexural and axial compressive failures of three-dimensionally braided composite I-beams. *Composites*, 17(3), 227–232.
80. Allix, O. and Johnson, A., eds. 2006. Advances in statics and dynamics of delamination. *Composites Science and Technology* (special issue), 66(6), 695–862.
81. Wichmann, M. H. G., Schulte, K., and Wagner, H. D. 2008. On nanocomposite toughness. *Composites Science and Technology*, 68, 329–331.
82. Kelly, A. 1970. Interface effects and the work of fracture of fibrous composites. *Proceedings of the Royal Society of London A*, 319, 95–116.
83. Sun, L., Gibson, R. F., Gordaninejad, F., and Suhr, J. 2009. Energy absorption capability of nanocomposites: A review, *Composites Science and Technology*, 69(14), 2392–2409.
84. Garcia, E. J., Wardle, B. L., and Hart, A. J. 2008. Joining prepreg composite interfaces with aligned carbon nanotubes. *Composites Part A: Applied Science and Manufacturing*, 39, 1065–1070.
85. Blanco, J., Garcia, E. J., Guzman de Viloria, R., and Wardle, B. L. 2009. Limitations of Mode I interlaminar toughening of composites reinforced with aligned carbon nanotubes. *Journal of Composite Materials*, 43, 825–841.

This page intentionally left blank

# 10

---

## *Mechanical Testing of Composites and Their Constituents*

---

### **10.1 Introduction**

The purpose of this chapter is to review briefly the most widely used methods for mechanical testing of composite materials and their constituents. In previous chapters, the emphasis has been on the development of analytical models for mechanical behavior of composite materials. The usefulness and validation of such models depends heavily on the availability of measured intrinsic mechanical property data to use as input. In addition, some aspects of mechanical behavior of composites are so complex that the feasibility of proper analytical modeling is questionable, and experimental approaches become even more important. Much of our knowledge about the special nature of composite behavior has been derived from experimental observations. The measurement of mechanical properties is also an important element of the quality control and quality assurance processes associated with the manufacture of composite materials and structures.

Owing to the special characteristics of composites, such as anisotropy, coupling effects, and the variety of possible failure modes, it has been found that the mechanical test methods that are used for conventional metallic materials are usually not applicable to composites. Thus, the development and evaluation of new test methods for composites have been, and continues to be, a major challenge for the experimental mechanics community. The technology associated with composite test methods and test equipment has become just as sophisticated as that associated with the corresponding analytical methods. Many of these test methods have evolved into standards that have been adopted by ASTM International, formerly the American Society for Testing and Materials. The ASTM standards for testing of polymer matrix and metal matrix composites and their constituents are compiled mainly in ASTM Volume 15.03 [1], while the standards for testing ceramic matrix composites are compiled mainly in ASTM Volume 15.01 [2]. The emphasis in this chapter will be on mechanical testing of polymer matrix composites. Several useful books on experimental characterization of composites have been published [3,4], and all of the ASTM standards for testing polymer matrix composites are conveniently listed and summarized in the ASTM D4762-08 *Standard Guide for Testing Polymer Matrix Composite Materials* [5].

## 10.2 Measurement of Constituent Material Properties

From the earlier discussion of various micromechanical models, it should be obvious that experimentally determined constituent material properties are required as input to these models. Since the development of new composites depends so heavily on the development of new fiber and matrix materials, constituent material tests are often used for screening new materials before composites are made from them. This section deals with the test methods that are used to measure the mechanical properties of fiber and matrix materials.

### 10.2.1 Fiber Tests

The tensile strength and Young's modulus of individual reinforcing fibers under static longitudinal loading may be determined by the ASTM C1557.03R08 standard test method [6]. As shown in Figure 10.1, the fiber specimen is adhesively bonded to a thin paper, compliant metal, or plastic backing strip that has a central longitudinal slot or hole. Once the specimen is clamped in the grips of the tensile testing machine, the backing strip is burned or cut away, so that the filament transmits all the applied tensile load. The specimen is pulled to failure, the load and elongation are recorded, and the tensile strength and modulus are calculated from the usual formulas. For such small specimens, however, it is important to correct the measured compliance by subtracting out the system compliance. The system compliance can be determined by testing specimens of different gage lengths, plotting the compliance versus gage length, and extrapolating the curves to zero gage length. The compliance corresponding to zero gage length is assumed to be the system compliance [6]. This and other techniques for the measurement

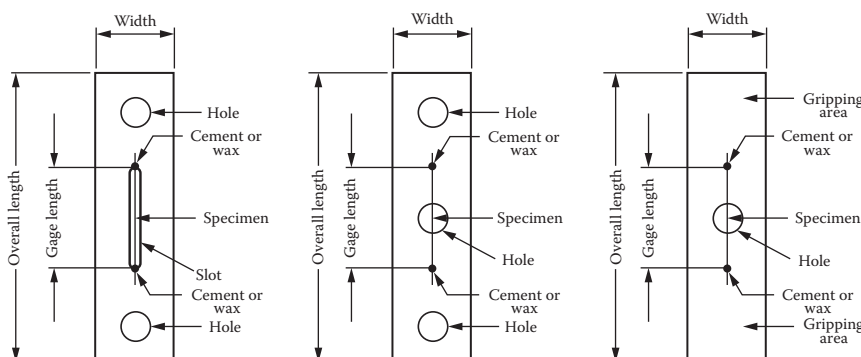


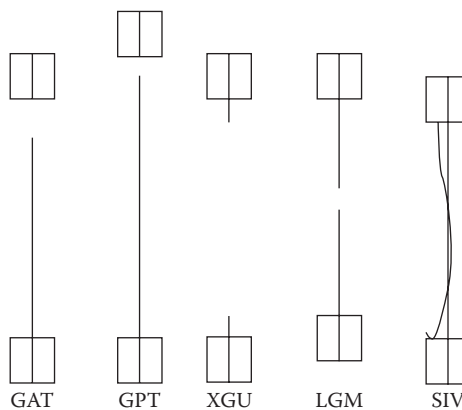
**FIGURE 10.1**

Different ways of mounting fiber specimens on backing strip. (Reprinted from C 1557.03R08. 2010. Vol. 15.01, *Refractories; Activated Carbon; Advanced Ceramics*. ASTM International, West Conshohocken, PA. Copyright ASTM International. With permission.)

of single graphite fiber, longitudinal tensile properties have been evaluated by McMahon [7].

Resin-impregnated and consolidated yarns, strands, rovings, and tows of carbon and graphite fibers may be tested by using ASTM D4018-99(2008) [8]. The impregnating resin is used to produce a rigid specimen that is easier to handle and test than a loose bundle of yarn and that should ensure uniform loading of the fibers in the bundle. The specimen test procedure is similar to that used in C1557.03R08, except that the tensile strength and modulus are calculated on the basis of the fiber stress, not the stress in the resin-impregnated strand. It is important to observe and record the failure mode, particularly any atypical failure modes (Figure 10.2).

The longitudinal modulus of single fibers has also been directly measured by Tsai and Daniel [9], who clamped the fiber specimen on each end and optically measured the transverse deflection of the fiber at midspan as small incremental weights were suspended transversely from the fiber at midspan. The same apparatus was used to measure the longitudinal coefficient of thermal expansion of fibers.

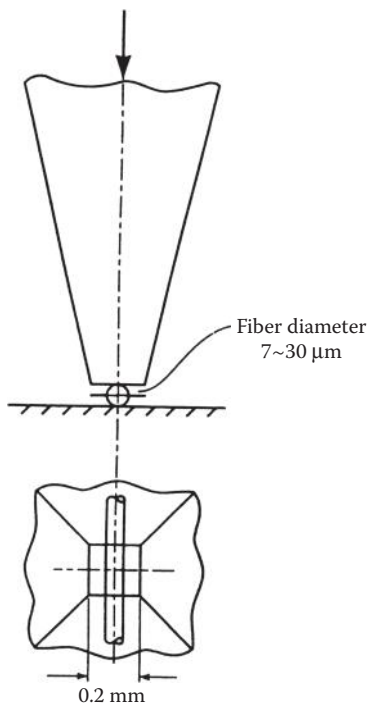


First character		Second character		Third character	
Failure type	Code	Failure area	Code	Failure location	Code
Grip/tab	G	Inside grip/tab	I	Bottom	B
Lateral	L	At grip/tab	A	Top	T
Long splitting (fiber pullout)	S	<1W from grip/tab	W	Middle	M
Explosive	X	Tab pullout	P	Various	V
Other	O	Various	V	Unknown	U
		Unknown	U		

**FIGURE 10.2**

Different failure modes for resin-impregnated strand test specimens. (Reprinted from D4018-99. 2008. Vol. 15.03, *Space Simulation; Aerospace and Aircraft; Composite Materials*. ASTM International, West Conshohocken, PA. Copyright ASTM International. With permission.)

Direct measurement of fiber properties under longitudinal compressive loading or longitudinal shear loading is very difficult. Such properties may be inferred from matrix and composite test data, however, and these tests will be discussed later in this chapter. As mentioned in Chapter 3, the transverse Young's modulus of fibers may also be inferred from matrix and composite test data, but direct measurement is possible. For example, Kawabata [10] has tested fibers in transverse diametral compression using the apparatus shown in Figure 10.3. The resulting load-deflection curve is compared with the corresponding load-deflection curve from a theoretical model of the fiber under transverse compression. One of the inputs to the model is the transverse Young's modulus of the fiber, which is used as a curve-fitting parameter to match the predictions with the measurements. Kawabata's measurements on graphite and aramid fibers showed even greater anisotropy than did the inferred properties. Tsai and Daniel [11] used a torsional pendulum to indirectly measure the longitudinal shear modulus of single fibers. The fiber specimen was clamped and vertically suspended from one end and a weight was attached at the bottom end. The weight was set into oscillation as a torsional pendulum, and the

**FIGURE 10.3**

Diametral compression of fiber for measurement of fiber transverse Young's modulus. (From Kawabata, S. 1989. In Vinson, J.R. ed., *Proceedings of the 4th Japan-U.S. Conference on Composite Materials*, pp. 253–262. CRC Press, Boca Raton, FL. With permission.)

measured frequency of oscillation was used in the frequency equation for the pendulum to solve for the longitudinal shear modulus of the fiber specimen.

Most of the methods described above are used to determine static mechanical properties of fibers. Dynamic test methods involving the use of vibration will be discussed later in this chapter.

### 10.2.2 Neat Resin Matrix Tests

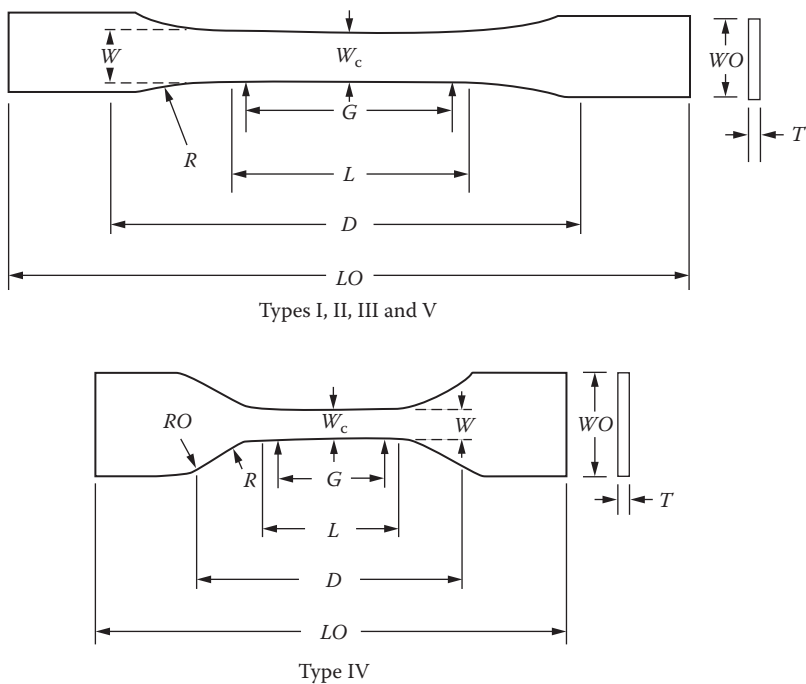
The tensile yield strength, tensile strength at break, modulus of elasticity, and elongation of neat resin matrix specimens may be determined by using the ASTM D638-10 method for tensile properties of plastics [12]. Several types of "dogbone-shaped" specimens are specified under this standard, depending on the thickness of the available material and whether the material is rigid or nonrigid. Specimens may be fabricated by machining or die cutting from sheets or plates of the material or by molding the resin to the desired shape. For example, the Specimen Types I-V for rigid or semirigid plastics are shown in Figure 10.4. Since plastics may be sensitive to temperature and relative humidity, the procedure used to condition specimens should be consistent from one test to another. The so-called "standard laboratory atmosphere" of 23°C (73.4°F) and 50% relative humidity is specified in the ASTM standard D618-08 [13]. Some plastics are also strain-rate sensitive, so the speed of testing should be consistent, as specified in D638-10. The details of the other test conditions and procedures are also given in the standard.

The ASTM D695-10 test method [14] can be used to determine compressive yield strength, compressive strength, and modulus of elasticity of neat resin matrix materials. Out-of-plane buckling failures are avoided by using a very short specimen (Figure 10.5) and a support jig on each side of the specimen (Figure 10.6). In order to generate true axial loading on the specimen without bending, a special compression fixture with a ball-and-socket arrangement is used (Figure 10.7).

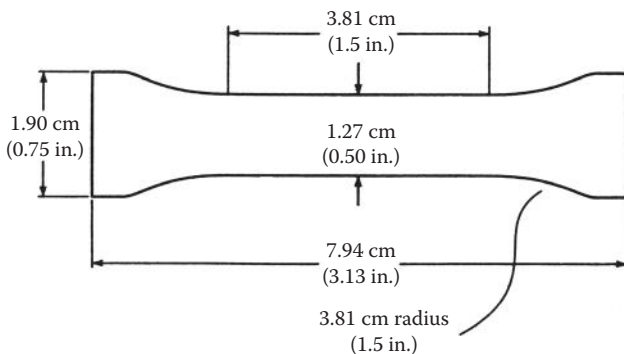
In either the tensile test or the compressive test of the neat resin matrix material, biaxial strain gages can be attached to the specimen so as to measure the longitudinal and transverse strains. The Young's modulus,  $E$ , and the Poisson's ratio,  $\nu$ , can then be determined from the standard definitions of those parameters. If desired, the shear modulus,  $G$ , can also be found from the isotropic relationship

$$G = \frac{E}{2(1 + \nu)} \quad (10.1)$$

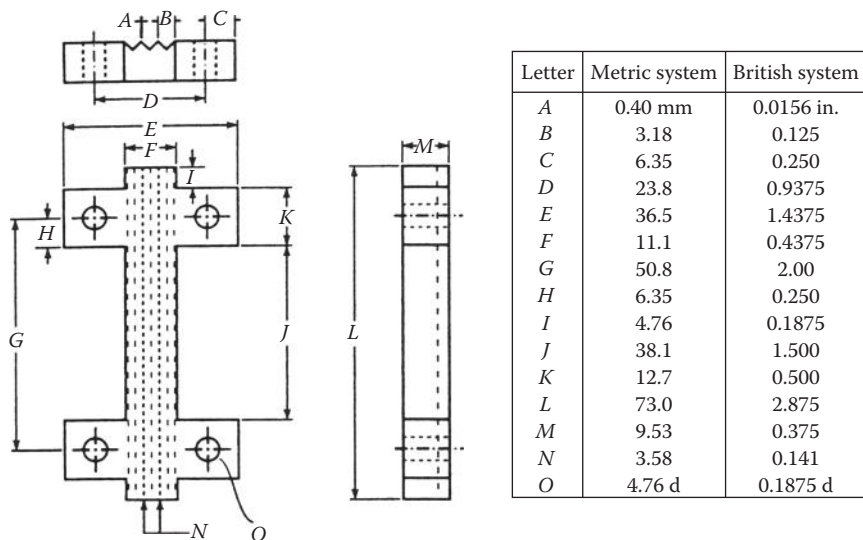
However, Novak and Bert [15] have reported that for some epoxies the values of  $G$  found from applying Equation 10.1 to either tensile or compressive tests differ substantially from directly measured values of  $G$ . Directly measured values of  $G$  were determined from a plot of angle of twist versus

**FIGURE 10.4**

ASTM D638-10 Type I, II, III, IV, and V neat resin tensile specimen geometries. (Reprinted from D638-10. 2010. Vol. 08.01, *Plastics*. ASTM International, West Conshohocken, PA. Copyright ASTM International. With permission.)

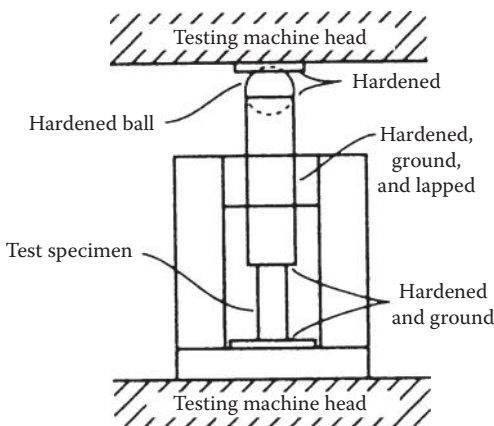
**FIGURE 10.5**

Neat resin compressive test specimen. (Reprinted from D695-10. 2010. Vol. 08.01, *Plastics*. ASTM International, West Conshohocken, PA. Copyright ASTM International. With permission.)

**FIGURE 10.6**

Support jig for D695-10 compressive test specimen. (Reprinted from D695-10. 2010. Vol. 08.01, Plastics. ASTM International, West Conshohocken, PA. Copyright ASTM International. With permission.)

torque for solid rod torsion tests. It was found that a more accurate calculation of  $G$  could be obtained by taking into account differences between tensile and compressive values of  $E$  and  $v$ . Their approach was based on the premise that since the elastic strain energy is invariant to a rotation of

**FIGURE 10.7**

Compression fixture with ball-and-socket joint to minimize bending. (Reprinted from D695-10. 2010. Vol. 08.01, Plastics. ASTM International, West Conshohocken, PA. Copyright ASTM International. With permission.)

coordinates, the strain energy for an isotropic material in pure shear along the  $x, y$  axes is equal to the strain energy associated with the corresponding biaxial tensile and compressive principal stresses oriented at  $45^\circ$  to the  $x, y$  axes. By equating these strain energy terms and using the Hooke's law for an isotropic material with different properties in tension and compression, Novak and Bert showed that the shear modulus,  $G$ , can be expressed as

$$\frac{1}{G} = \frac{(1 + v_t)}{E_t} + \frac{(1 + v_c)}{E_c} \quad (10.2)$$

where  $E_t$  is the Young's modulus from tensile test,  $E_c$  the Young's modulus from compressive test,  $v_t$  the Poisson's ratio from tensile test, and,  $v_c$  the Poisson's ratio from compressive test.

This equation, which involves both tensile and compressive properties, was found to give much better agreement with directly measured values of  $G$  than did Equation 10.1 when Equation 10.1 was used with either tensile compressive values of  $E$  and  $v$ . It is easily shown that when  $E_t = E_c = E$  and  $v_t = v_c = v$ , Equation 10.2 reduces to Equation 10.1.

The flexural yield strength, flexural strength, and modulus of elasticity of plastics may be determined by the ASTM D790-10 test method [16]. This test method involves three-point bending (Figure 10.8), and a separate standard D6272-10 describes a four-point bending test. Allowable ranges of radii for the loading noses and recommended specimen dimensions are provided in tables in D790-10 [16]. Test methods for measurement of mechanical properties of other constituents such as sandwich core materials and other constituent properties such as coefficient of thermal expansion, impact, creep, and fatigue response are also given in Ref. [1].

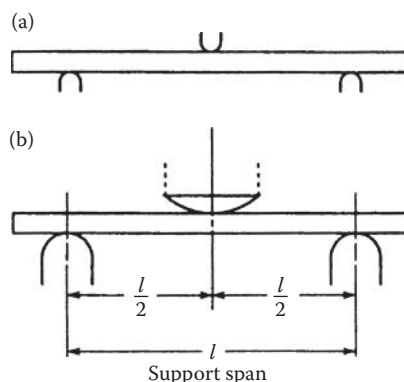


**FIGURE 10.8**

Three-point bending specimen for flexural properties of neat resin or composite. (a) Small radii loading and support fixtures and (b) large radii loading and support fixtures. (Reprinted from D790-10. 2010. Vol. 08.01, Plastics. ASTM International, West Conshohocken, PA. Copyright ASTM International. With permission.)

### 10.2.3 Constituent Volume Fraction Measurement

Knowledge of the volume fractions of fiber and matrix materials (and also void fractions, if possible) is essential for use in micromechanical analysis and for quality control during manufacturing of composites. For polymer matrix composites, ASTM standard D3171-09 [17] covers two basic approaches to the measurement of constituent volume fractions. Method I involves removal of the matrix resin from the composite sample using either chemical digestion (with acids or other chemicals) or ignition and burn-off in a furnace, in cases where it is safe to assume that the fibers are unaffected by the resin removal process. For example, by measuring the weight,  $W_c$ , and volume,  $V_c$ , of a composite sample before resin removal, then measuring the weight,  $W_f$ , and volume,  $V_f$ , of fibers remaining after resin removal, the fiber weight fraction can be calculated from  $w_f = W_f/W_c$ , and the fiber volume fraction can be calculated from  $v_f = V_f/V_c$ . From weight and volume measurements on a separate neat resin matrix sample, the matrix density  $\rho_m$  can be determined, then Equation 3.6 can be used to determine the matrix volume fraction,  $v_m$ . If the void fraction is desired, it can be calculated from Equation 3.9. Procedures A–F within Method I involve the use of different chemical mixtures to digest the resin matrix material, depending on the type of polymer matrix resin used in the composite. Procedure G within Method I involves ignition and burn-off of the matrix resin in a furnace if chemical digestion is not feasible. For example, the resin burn-off approach is typically used with glass fibers, but chemical digestion is the preferred approach for carbon fibers, which may suffer mass loss due to oxidation if the resin burn-off approach is used. Method II is based on the assumption that the fiber weight per unit area is known or controlled to within an acceptable degree, and involves measurement of laminate thickness.

A completely different and nondestructive approach to determining constituent volume fractions involves the use of computer-aided image analysis to determine the fiber area fraction in a photomicrograph of a polished composite specimen. A more detailed description of the procedure and equipment used in this approach is described by Adams et al. [3].

---

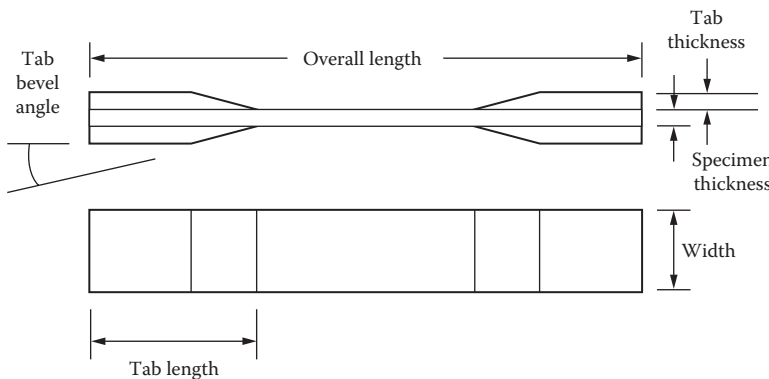
## 10.3 Measurement of Basic Composite Properties

This section is concerned with test methods for measurement of the basic composite mechanical properties that are needed in analysis and design. Methods for measurement of lamina properties such as tensile and compressive strength and stiffness, shear strength and stiffness, flexural strength and stiffness, fiber/matrix interfacial strength, and laminate properties such as interlaminar strength and fracture toughness are discussed. Both direct

and indirect methods are reviewed. Direct methods involve the application of uniaxial, shear, or flexural loading to a lamina or laminate specimen so as to determine the basic property that governs the response to such loading. Indirect methods may involve such techniques as “backing out” of lamina properties from tests of laminates. Difficulties encountered in some of these tests are discussed, along with limitations and possible sources of error.

### 10.3.1 Tensile Tests

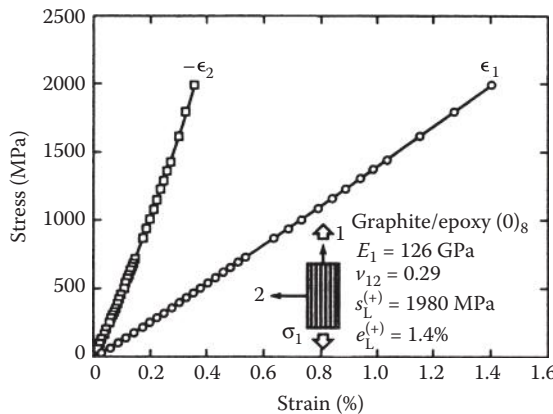
Lamina tensile strengths  $s_L^{(+)}$  and  $s_T^{(+)}$ , Young’s moduli,  $E_1$  and  $E_2$ , and Poisson’s ratios,  $\nu_{12}$  and  $\nu_{21}$ , may be measured by testing longitudinal ( $0^\circ$ ) and transverse ( $90^\circ$ ) unidirectional specimens according to the ASTM D3039/D3039M-08 standard test method [18]. The specimen geometry is shown in Figure 10.9. Laminated load transfer tabs are adhesively bonded to the ends of the specimen in order that the load may be transferred from the grips of the tensile testing machine to the specimen without damaging the specimen. Recommended dimensions for  $0^\circ$  and  $90^\circ$  specimens and several types of other laminates are provided in the standard, along with recommended test procedures and calculations. Typical longitudinal and transverse strain data from such a test on a  $[0]_8$  graphite/epoxy composite are given in Figure 10.10



Fiber orientation	Width mm (in.)	Overall length mm (in.)	Thickness mm (in.)	Tab length mm (in.)	Tab thickness mm (in.)	Tab bevel angle (°)
$0^\circ$ unidirectional	15 (0.5)	250 (10.0)	1.0 (0.040)	56 (2.25)	1.5 (0.062)	7 or 90
$90^\circ$ unidirectional	25 (1.0)	175 (7.0)	2.0 (0.080)	25 (1.0)	1.5 (0.062)	90
Balanced and symmetric	25 (1.0)	250 (10.0)	2.5 (0.100)	emery cloth	—	—
Random-discontinuous	25 (1.0)	250 (10.0)	2.5 (0.100)	emery cloth	—	—

**FIGURE 10.9**

Specimen geometry for ASTM D3039/D3039M-08 standard tensile test. (Reprinted from D3039/D3039M-08. 2008. Vol. 15.03, *Space Simulation; Aerospace and Aircraft; Composite Materials*. ASTM International, West Conshohocken, PA. Copyright ASTM International. With permission.)

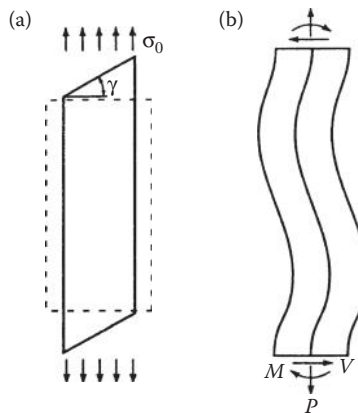
**FIGURE 10.10**

Longitudinal and transverse strain data at different stresses for  $[0]_8$  graphite/epoxy tensile specimen. (Reprinted from Carlsson, L.A. and Pipes, R.B. 1989. *Experimental Characterization of Advanced Composite Materials*. Prentice-Hall, Inc., Englewood Cliffs, NJ. With permission of Prentice-Hall, Englewood Cliffs, NJ.)

from [19] for various stresses along with the resulting values of  $E_1$ ,  $\nu_{12}$ ,  $s_L^{(+)}$ , and  $e_L^{(+)}$ . These results show the typical fiber-dominated linearity for the longitudinal strain response and a slight nonlinearity in the transverse strain response due to the influence of the matrix.

The D3039/D3039M-08 test method works well for specially orthotropic specimens because a uniform state of stress is produced across the specimen as it is loaded in tension. However, nonuniformities in the stress distribution may arise when the method is used for off-axis specimens that exhibit shear coupling. Such off-axis tests would typically be used to measure such properties as the off-axis Young's modulus,  $E_x$ , and the off-axis tensile strength,  $s_x^{(+)}$ . Pagano and Halpin [20] showed that a specimen that exhibits shear coupling will deform as shown in Figure 10.11a if the ends are unconstrained. But if the ends are constrained by clamping fixtures, the shear-coupling effects will produce shear forces and bending moments that distort the specimen, as shown in Figure 10.11b. Thus, in the latter case, the specimen is no longer under a uniform state of stress, and the usual definitions of the engineering constants are not valid. Pagano and Halpin found that the distortion shown in Figure 10.11b decreases with decreasing shear-coupling ratio,  $\eta_{x,xy}$  (recall Equation 2.41) and increasing length-to-width ratio of the specimen. They also suggested that in order to minimize such effects, angle-ply laminates could be used instead of off-axis specimens, or that a test fixture that allowed free rotation of the ends of the specimen could be used with off-axis specimens.

A similar conclusion regarding end constraint effects in off-axis specimens was proposed by Jones [21]. Jones suggested that for long, slender off-axis

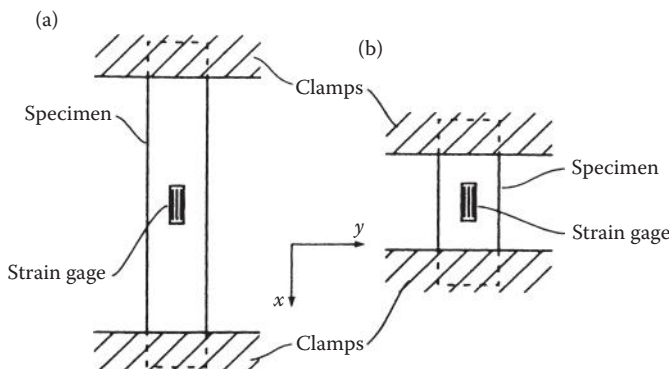
**FIGURE 10.11**

Effect of end conditions on deformation of an off-axis tensile specimen exhibiting shear coupling. (a) Ends unconstrained and (b) ends clamped. (From Pagano, N. J. and Halpin, J. C 1968. *Journal of Composite Materials*, 2, 18–31. With permission.)

specimens under a uniaxial stress, as shown in Figure 10.12a, the state of stress in the gage section of the specimen would be approximately

$$\sigma_y = \tau_{xy} = 0 \quad \text{and} \quad \sigma_x = E_x \epsilon_x \quad (10.3)$$

because the gage length is sufficiently far removed from the effects of the clamped ends. However, in a short, wide specimen (Figure 10.12b), the

**FIGURE 10.12**

Tensile specimens of different length showing relationship of gage length to specimen length. (a) Long, slender specimen and (b) short, wide specimen.

proximity of the clamped ends to the gage length will cause the strains in the gage length to be approximately

$$\varepsilon_y = \gamma_{xy} = 0 \quad (10.4)$$

When these strain conditions are substituted in Equation 2.35, the resulting stress condition in the gage length of the short, wide specimen is found to be

$$\sigma_x = \bar{Q}_{11}\varepsilon_x \quad (10.5)$$

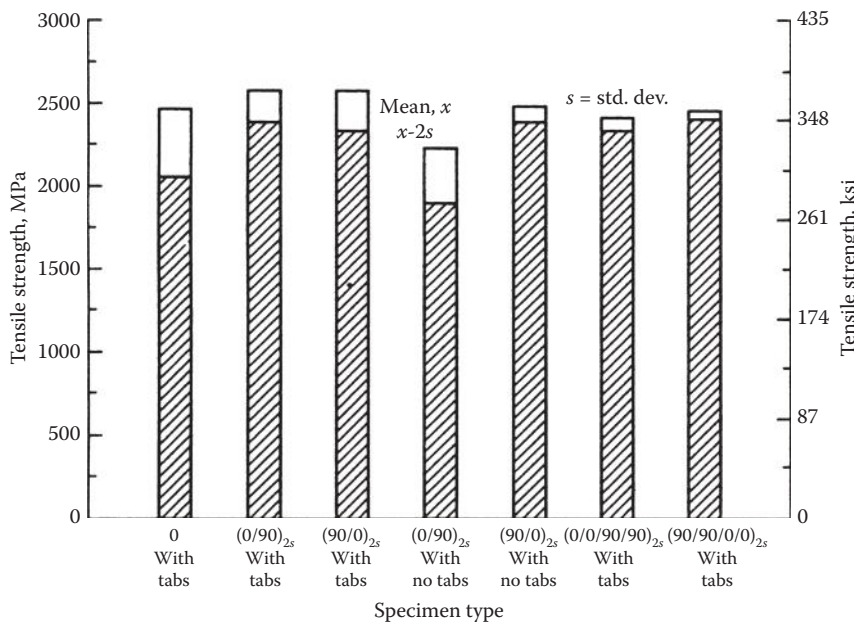
The conclusion here is that in the case of a long, slender specimen the off-axis Young's modulus,  $E_x$ , is measured. However, in the case of the short, wide specimen the transformed lamina stiffness,  $\bar{Q}_{11}$ , is measured instead of  $E_x$ . That is, if the specimen is too short, the measured ratio  $\sigma_x/\varepsilon_x$  may be closer to  $\bar{Q}_{11}$  than to  $E_x$ . As shown later in Example 10.1, the difference between the "apparent moduli"  $E_x$  and  $\bar{Q}_{11}$  depends on the fiber orientation  $\theta$  and can be quite large. Thus, the analyses of Pagano and Halpin [20] and Jones [21] lead to the same conclusion regarding the effect of specimen length in off-axis tensile tests, and one must be very careful in interpreting the results of such tests.

In the analysis of Jones [21], it is assumed that Equation 10.3 is valid when the specimen is "long enough," so that the end effects are not significant in the gage length. The decay of such localized effects with distance away from the source is justified by the use of Saint-Venant's principle. However, Horgan et al. [22–24] have shown that the characteristic decay length over which end effects are significant in orthotropic composites is generally several times greater than the corresponding decay length for isotropic materials. The decay length,  $\lambda$ , which is the distance from the end of the specimen over which the stress decays to  $1/e$  of the value of the stress at the end, was found to be

$$\lambda \approx \frac{b}{2\pi} \sqrt{\frac{E_1}{G_{12}}} \quad \text{as } \frac{G_{12}}{E_1} \rightarrow 0 \quad (10.6)$$

for an anisotropic, transversely isotropic, rectangular strip [24], where  $b$  is the width of the strip.

In the tests described above, lamina properties are measured directly by testing unidirectional specimens. A different approach involves the use of the classical lamination theory (CLT) to "back out" lamina properties from laminate test data [25,26]. For example, Rawlinson [25] has shown that CLT "back-out" factors for obtaining equivalent  $0^\circ$  tensile strengths from both angle-ply and cross-ply laminates showed good agreement with the

**FIGURE 10.13**

"Backed out" tensile strength data from seven different laminates of IM7G/8551-7 graphite/epoxy. (Reprinted from Rawlinson, R.A. 1991. *Proceedings of the 36th International SAMPE Symposium and Exhibition*, 36, Book 1, pp. 1058–1068. With permission of the Society for the Advancement of Material and Process Engineering.)

corresponding experimentally determined factors for several graphite/epoxy composites. As shown in Figure 10.13, Rawlinson's data for the equivalent  $0^\circ$  tensile strength of IM7G/8551-7 graphite/epoxy appear to be nearly the same regardless of whether unidirectional  $0^\circ$  specimens or various cross-ply laminate configurations are used. The one notable exception is the particular case of  $[0/90]_{2s}$  cross-ply specimens without load transfer tabs. It is seen in Figure 10.13 that the scatter in the data is generally less for the cross-ply specimens and that the data for the cross-ply specimens without load transfer tabs are generally just as good as the data for the corresponding specimens with tabs. Thus, there appears to be considerable potential for cost savings with the tests of untabbed cross-ply specimens.

### Example 10.1

As indicated above, if an off-axis tensile specimen is too short, the measured ratio  $\sigma_x/\varepsilon_x$  may be closer to  $\bar{Q}_{11}$  than to  $E_x$ , and the differences between the "apparent moduli"  $E_x$  and  $\bar{Q}_{11}$  can be quite large. Compare the values of  $E_x$  and  $\bar{Q}_{11}$  for a unidirectional T300/934 carbon/epoxy off-axis tensile specimen as functions of the fiber orientation  $\theta$ .

### SOLUTION

From Table 2.2, the lamina engineering constants for T300/934 carbon/epoxy are

$$E_1 = 131 \text{ GPa}, \quad E_2 = 10.3 \text{ GPa}, \quad G_{12} = 6.9 \text{ GPa}, \quad v_{12} = 0.22$$

From symmetry of the compliance matrix,  $v_{21} = v_{12}E_2/E_1 = 0.0173$ . Using this data, the lamina stiffnesses  $Q_{ij}$  are calculated from Equations 2.27, then  $\bar{Q}_{11}$  and  $E_x$  are calculated as functions of the angle  $\theta$  by using the first of Equations 2.36 and the first of Equations 2.40, respectively. As shown graphically in Figure 10.14, the “apparent moduli”  $\bar{Q}_{11}$  and  $E_x$  are only equal when  $\theta = 0^\circ$  or  $90^\circ$ , with  $\bar{Q}_{11}$  being significantly larger than  $E_x$  for other angles  $\theta$ . In the “worst case” for this material,  $Q_{11}$  is a factor of approximately 3 larger than  $E_x$  when  $\theta = 30^\circ$ .

#### 10.3.2 Compressive Tests

Compression testing has proved to be one of the most interesting and difficult challenges to those concerned with the testing of composites. There has been considerable discussion in the literature over the years about compression testing of composites, and numerous experimental approaches have been explored [3,27–31]. In general, test methods have been sought, which yield the greatest possible compressive strength, assuming that the greatest values must be closest to the true compressive strength. A great amount of effort has been expended in the design of test fixtures that load the specimen in pure compression and eliminate extraneous failure modes (e.g., global buckling of the specimen and local damage due to load introduction

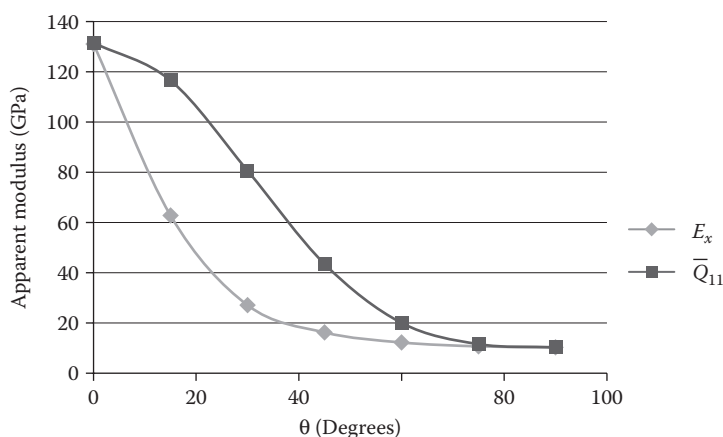
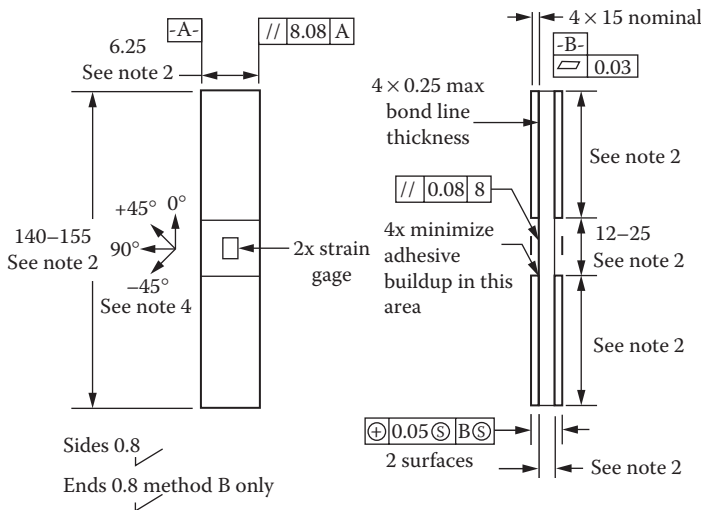


**FIGURE 10.14**

Variation of “apparent moduli”  $E_x$  and  $\bar{Q}_{11}$  with fiber orientation  $\theta$  for off-axis tensile test of a unidirectional T300/934 carbon/epoxy lamina. Lamina engineering constants are taken from Table 2.2.

in the grips), which lead to lower apparent compressive strengths. It is ironic that with all the effort that has been devoted to eliminating these other failure modes and achieving true compressive failure, the actual mode of failure of a compressively loaded composite structure in the field is more likely to be something other than pure compressive failure (i.e., it is just as difficult to achieve pure compressive failure in composite structures under service conditions as it is in laboratory test specimens). Three different ASTM standard test methods for compression testing of composites have been published [32–34], and each method will be briefly described in the following.

The ASTM D3410/D3410M-03 (Reapproved 2008) test method [32] involves the use of either a tabbed specimen (Figure 10.15) or an untabbed specimen in a special test fixture (Figure 10.16) that has been designed to introduce the compressive load in the specimen by virtue of side loading (i.e., shear transfer to the sides of the specimen from the grips of the test fixture), and to eliminate global buckling of the specimen. The wedge-shaped grips clamp the specimen ever tighter as the compressive load from the testing machine on the test fixture is increased, and all of the compressive load on the specimen

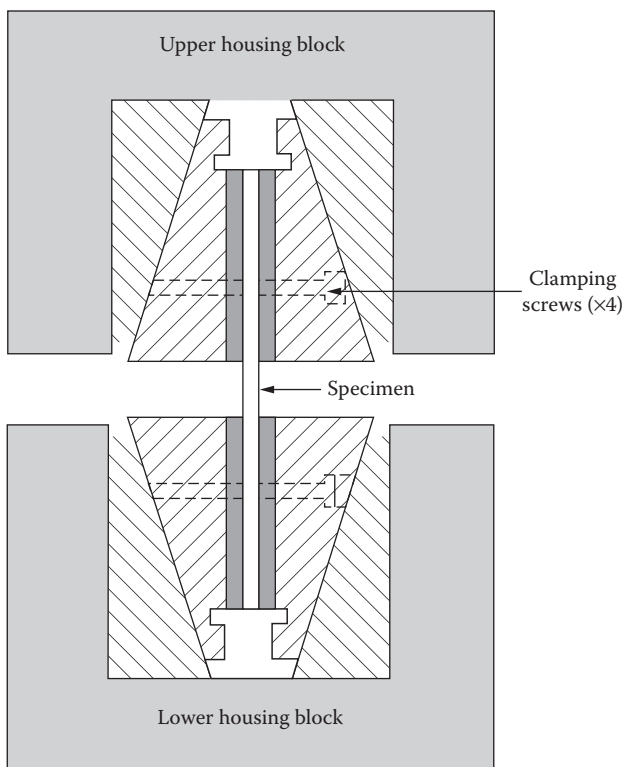


*Notes:*

1. Drawing interpretation per ANSI Y14.5M-1982 and ANSI/ASME 846.1-1985.
2. See section 8 and table 2 and Table 3 of the test standard for values of required or recommended width, thickness, gage length, tab length and overall length.
3. See test standard for values of material, ply orientation, use of tabs, tab material, tab angle, and tab adhesive.
4. Ply orientation tolerance relative to -A- = 0.5°.

**FIGURE 10.15**

Geometry for tabbed compression test specimen. (Reprinted from D3410/D3410M-03 (Reapproved 2008), Vol. 15.03, *Space Simulation; Aerospace and Aircraft; Composite Materials*. ASTM International, West Conshohocken, PA, 2009. Copyright ASTM International. With permission.)

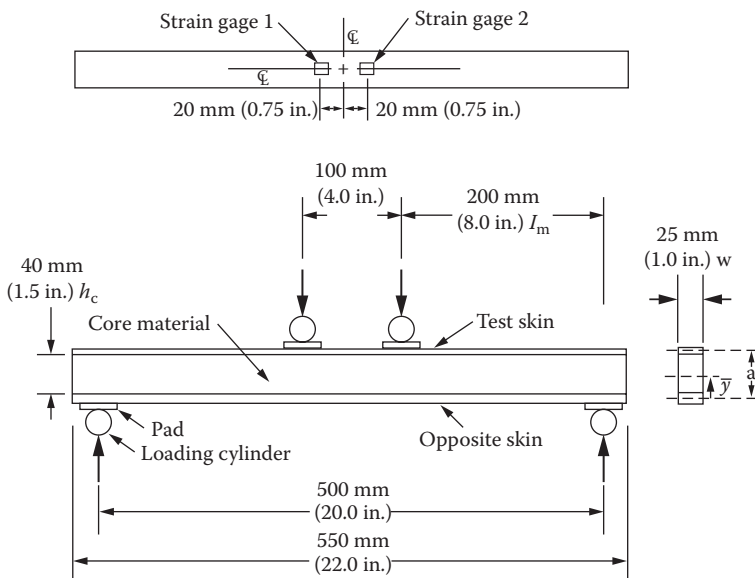
**FIGURE 10.16**

Cross-section view of ASTM D3410/D3410M-03 (Reapproved 2008) compression test fixture. (Reprinted from D3410/D3410M-03 (Reapproved 2008), Vol. 15.03, *Space Simulation; Aerospace and Aircraft; Composite Materials*. ASTM International, West Conshohocken, PA, 2009. Copyright ASTM International. With permission.)

comes from this shear transfer. With this fixture, there is no direct compression on the ends of the specimen as with the previously discussed neat resin compression test fixture of ASTM D695-10.

The sandwich beam specimen for ASTM D5467-97 (Reapproved 2004) [33] shown in Figure 10.17 is constructed so that the upper skin consists of the [0] unidirectional composite material of interest. The sandwich beam is bonded together with a structural adhesive, and the specimen is loaded in four-point bending, so that the upper skin is subjected to compressive stress. A honeycomb core material in the sandwich beam provides lateral support for the skin in order to avoid premature buckling of the skin, and thus the failure is due to compressive failure of the skin material.

In a comparison of several test methods that eventually led to the adoption of the current D3410 and D5467 standards, Adsit [35] showed that the methods gave equivalent results for compressive strength and modulus of graphite/epoxy, but that the D695 method for plastics (Figures 10.5 through 10.7) was

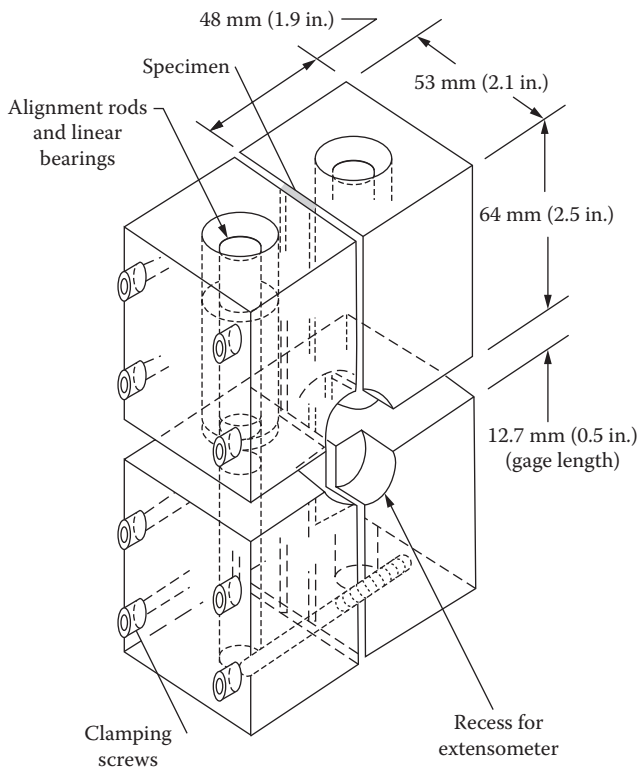
**FIGURE 10.17**

ASTM D5467/D5467M-97 (Reapproved 2004) sandwich beam specimen for face sheet compression. (Reprinted from D5467/D5467M-97 (Reapproved 2004), Vol. 15.03, *Space Simulation; Aerospace and Aircraft; Composite Materials*. ASTM International, West Conshohocken, PA, 2009. Copyright ASTM International. With permission.)

inadequate for high-modulus composites. Although all methods gave acceptable results for compression modulus, the D695 method produced premature delamination or shear failures due to end loading of the specimens.

The third version of the ASTM standard test methods for compression testing of composites is D6641/D6641M-09 [34], the combined loading compression (CLC) test. The CLC fixture (Figure 10.18) involves a combination of direct compression on the ends of an untabbed specimen and shear transfer through side loading to produce pure compression within the gage length of the specimen. Adams et al. [3] have suggested that the CLC method has several advantages over the other two methods. The CLC fixture is relatively simple and compact, no end tabs are required on the specimens, and the ratio of direct compressive load on the ends of the specimen to the shear load on the sides of the specimen can be adjusted for best results.

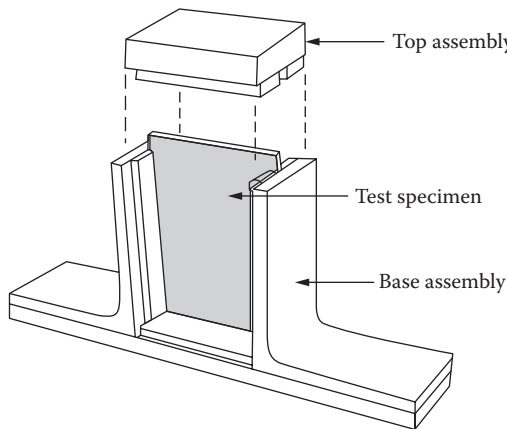
A number of alternative methods for measurement of compressive modulus and strength have been reported in the literature. The minisandwich specimen [36] is smaller than that used in ASTM D5467 and has a core consisting of the neat resin matrix material instead of a honeycomb material. Compressive properties of the [0] unidirectional lamina can also be “backed out” of [0/90] cross-ply laminate compression test data [37].

**FIGURE 10.18**

Test fixture for ASTM D6641/D6641M-09 CLC test method. (Reprinted from D6641/D6641M-09, 2009, Vol. 15.03, *Space Simulation; Aerospace and Aircraft; Composite Materials*. ASTM International, West Conshohocken, PA. Copyright ASTM International. With permission.)

The problem of local buckling and the corresponding reduction of in-plane compressive strength after delamination due to transverse impact have been discussed in Chapter 7 (Figure 7.40) and in Chapter 9. Concern about this failure mode has led to the development of the compression after impact (CAI) test [38,39].

Still more recent work on CAI has led to the development of ASTM Standard D7137/D7137M-07 on measurement of compressive residual strength properties of damaged polymer matrix composite plates [40], and the test fixture is shown in Figure 10.19. First, the test specimens are subjected to either quasistatic indentation damage according to ASTM D6264/D6264M-07 or drop-weight impact damage according to ASTM D7136/D7136M-07 and then the specimens are subjected to in-plane compression according to ASTM 7137/D7137M-07. The result of this sequence of tests is data on the compressive residual strength of composite plates with various amounts of statically induced or impact-induced damage.

**FIGURE 10.19**

Test fixture for compressive residual strength of polymer composite plates. (From D7137/D7137M-05e<sup>1</sup>. 2005. Standard test method for compressive residual strength properties of damaged polymer matrix composite plates, vol. 15.03, *Space Simulation; Aerospace and Aircraft; Composite Materials*. ASTM International, West Conshohocken, PA. Reprinted with permission.)

### Example 10.2

A [0] unidirectional AS/3501 carbon/epoxy specimen for the ASTM D3410 compression test (Figure 10.15) is subjected to longitudinal compression using the test fixture shown in Figure 10.16. The cross-sectional dimensions of the specimen are 10 mm wide  $\times$  1.5 mm thick, and the free length of the specimen between the clamping grips is 25 mm. Will this specimen fail as desired due to the compressive stress reaching the compressive strength of the material, or will it fail by buckling?

### SOLUTION

From Table 2.2, the relevant properties of AS/3501 are  $E_1 = 138 \text{ GPa}$ ,  $s_L^{(-)} = 1172 \text{ MPa}$ . The applied load necessary to cause longitudinal compressive failure is

$$P_{\text{comp}} = s_L^{(-)} A = (1172 \times 10^6 \text{ N/m}^2)(10 \text{ mm})(1.5 \text{ mm})/(m/10^3 \text{ mm})^2 = 17,580 \text{ N}$$

The critical buckling load is given by the Euler buckling formula for a clamped-clamped column of free length  $L$  and moment of inertia  $I$  as

$$P_{\text{cr}} = \frac{4\pi^2 E I}{L^2} = \frac{4\pi^2 (138 \times 10^9 \text{ N/m}^2)(10 \text{ mm})(1.5 \text{ mm})^3/(m/10^3 \text{ mm})^2}{12(25 \text{ mm})^2} = 24,512 \text{ N}$$

Since  $P_{\text{comp}} < P_{\text{cr}}$ , the specimen will fail first by compression, which is the desired result. If the specimen is too long, however, it will fail by buckling, and the test will not yield a valid measurement of the compressive strength. For example, it can be

easily shown that if the specimen free length  $L > 29.52$  mm and the other dimensions are held constant, the specimen will fail by buckling. Buckling is a structural instability which has nothing to do with the compressive strength, and is to be avoided in such compression tests.

### Example 10.3

It is proposed that the sandwich beam loaded in 4-point flexure as described in Example 7.17 and Figure 7.57 is to be used for face sheet compression testing similar to that described in ASTM D5467. If the longitudinal compressive strength of the unidirectional [0] face sheets is  $s_L^{(-)} = 1172 \text{ MPa}$ , what applied load  $P$  would cause face sheet compressive failure? Compare this result with the value of  $P$  that would cause core shear failure, as described in Example 7.18. Is this a good specimen design for determining the face sheet compressive strength?

### SOLUTION

Since the sandwich beam in Example 7.17 satisfies the assumptions associated with laminated beam theory, the longitudinal bending stresses in the  $j$ th ply are given by Equation 7.13 as

$$(\sigma_x)_j = \frac{Mz}{I_{yy}} \left[ \frac{(E_x)_j}{E_f} \right]$$

Applying this equation to the maximum compressive longitudinal stress in the upperface sheet,  $z = 7.061$  mm,  $M = Pd/2 = P(41.6 \text{ mm})/2 = 20.8P$  N mm, and  $I_{yy} = bh^3/12 = 25.4$  mm $(14.122 \text{ mm})^3/12 = 5961$  mm $^4$ . From Example 7.17, the face sheet longitudinal modulus is  $(E_x)_j = 139.4 \text{ GPa}$ , and the laminate flexural modulus is  $E_f = 38.08 \text{ GPa}$ . For upper face sheet compressive failure,  $(\sigma_x)_j = s_L^{(-)} = 1172 \times 10^6 \text{ N/m}^2$ . Substituting these values in Equation 7.13, we find that the applied load  $P = 12,994$  N. However, in Example 7.18 it was found that the load required to cause core shear failure in this sandwich beam is only  $P = 885.6$  N, therefore core shear failure would occur first and this is not a good specimen design for determining face sheet compressive strength. One way to modify the specimen design would be to increase the distance  $d$  between the loading points and the support points, thus increasing the bending moment  $M$ . This would increase the face sheet compressive stress without changing the core shear stress.

#### 10.3.3 Shear Tests

Shear testing of composites is complicated by the fact that, for an orthotropic material, there are three possible sets of shear properties associated with the three principal material axes (i.e., the in-plane shear modulus  $G_{12}$ , the out-of-plane shear moduli  $G_{13}$ , and  $G_{23}$  and the corresponding shear strengths associated with the 12, 13, and 23 axes). So it should be no surprise that numerous shear test methods have been proposed, that many of them are limited to only one or two of the three possible planes, and that some tests yield only

**TABLE 10.1**

Comparison of Shear Test Methods for Composites

Test Method (with ASTM Std. No., if Applicable)	Uniform Shear Stress State	All Three Stress States Practical	Shear Strength Obtained	Shear Stiffness Obtained
Short beam shear (D 2344)				
Iosipescu shear (D 5379)				
$\pm 45^\circ$ Tensile shear (D 3518)				
Two-rail shear (D 4255)				
Three-rail shear (D 4255)				
Double-notched shear (D 3846)				
Torsion of a thin tube (D 5448)				
Cross-beam sandwich				
Torsion of a solid rod				
Four-point shear				
Picture frame shear				
Plate twist				
10° Off-axis (tensile)				
V-notched rail shear (D 7078)				

Source: From Adams, D. F., 2005. *High Performance Composites*, 13(5), pp. 9–10. With permission.

shear modulus or shear strength, but not both. In a very practical, yet quantitative comparison of shear test methods, Adams [41] has reported that at least 14 shear test methods have been developed, 8 of which have been adopted as ASTM standards. Table 10.1 from Adams [41] provides a concise summary of these test methods and their capabilities, listed in decreasing order of frequency of use.

Of the available shear test methods, Adams concludes that only the Iosipescu shear test or V-notched beam test (ASTM D5379/ D5379M-05 [42]) and the V-notched rail shear test (ASTM D7078/D7078M-05 [43]) meet all four of the requirements listed in Table 10.1. That is, these two methods are the only ones that can presently produce a uniform shear stress state in any of the three possible planes and can be used to determine both the shear strengths and

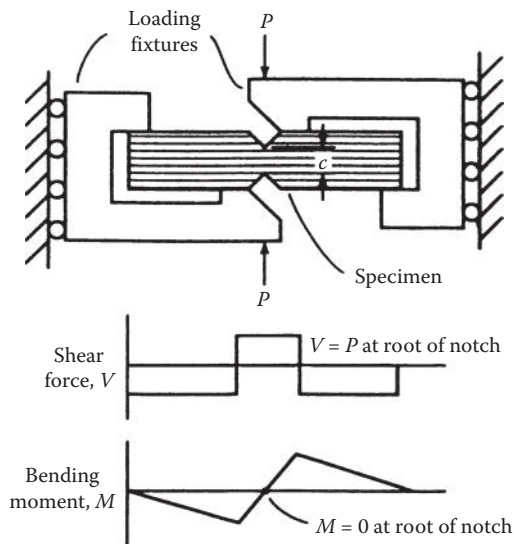


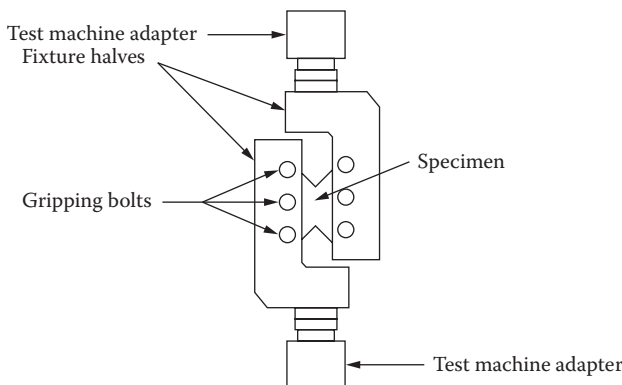
**FIGURE 10.20**  
Iosipescu test fixture with shear and moment diagrams.

the shear moduli associated with each of the three possible planes. Accordingly, the focus of the present coverage will be on these two methods.

The so-called Iosipescu shear test was first proposed for use with metals in 1967 [44] and was later adapted for use with composites by Adams et al. [45–48]. The Iosipescu test fixture and the corresponding shear and moment diagrams for the specimen are illustrated schematically in Figure 10.20, and more details regarding the fixture, specimen dimensions, and test procedures are given in ASTM D5379/ D5379M-05 [42]. The action of the test fixture is to produce pure shear loading with no bending at the midspan section of the specimen between the two notches. The average shear stress in that section is simply

$$\tau = \frac{P}{ct} \quad (10.7)$$

where  $P$  is the applied load,  $c$  is the distance between the roots of the notches, and  $t$  is the specimen thickness. No subscripts were used in Equation 10.7, because the test method can be used for either in-plane or out-of-plane shear testing, depending on the specimen configuration. Shear strains can be measured using strain gages to measure the normal strains at  $45^\circ$  to the specimen axis, then using the strain transformation equations to find the shear strain (e.g., see Example 2.3). The shear modulus is then the slope of the shear stress–shear strain curve in the elastic region, and the

**FIGURE 10.21**

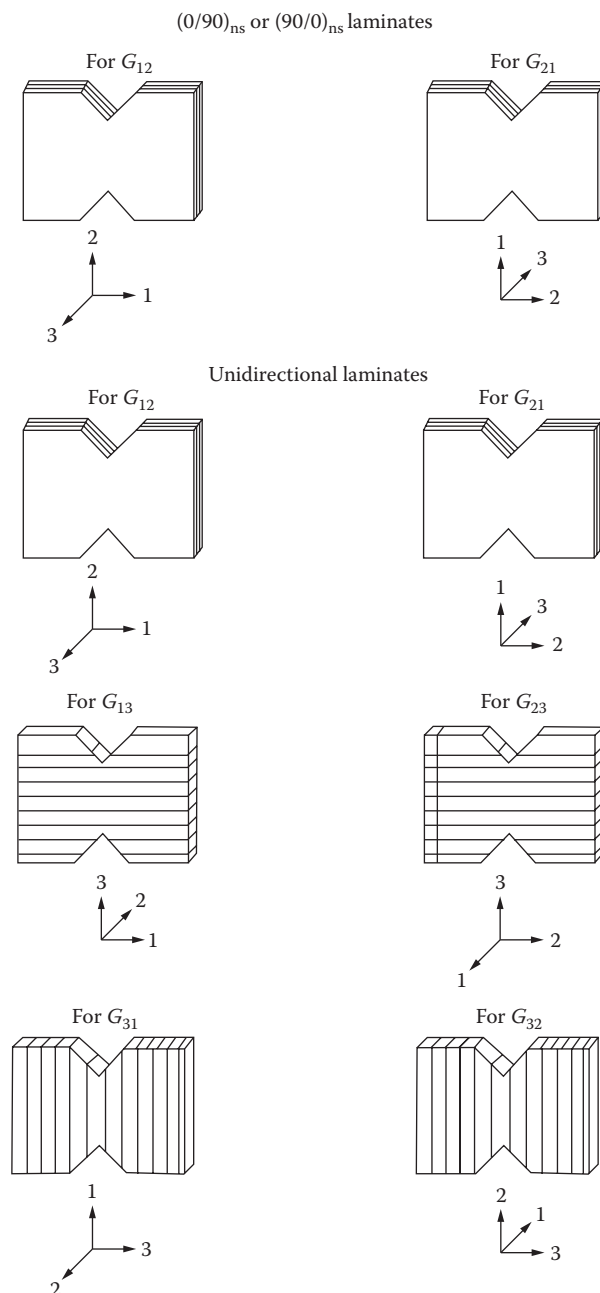
Test fixture for V-notched rail shear test. (Reprinted from D7078/D7078M-05, 2005, Vol. 15.03, *Space Simulation; Aerospace and Aircraft; Composite Materials*. ASTM International, West Conshohocken, PA. Copyright ASTM International. With permission.)

shear strength is the shear stress at failure. In addition to the advantages listed by Adams, the Iosipescu test specimens are small and easily fabricated. This method was also recommended by Lee and Munro [49], who ranked available in-plane shear test methods before the ASTM standard was adopted.

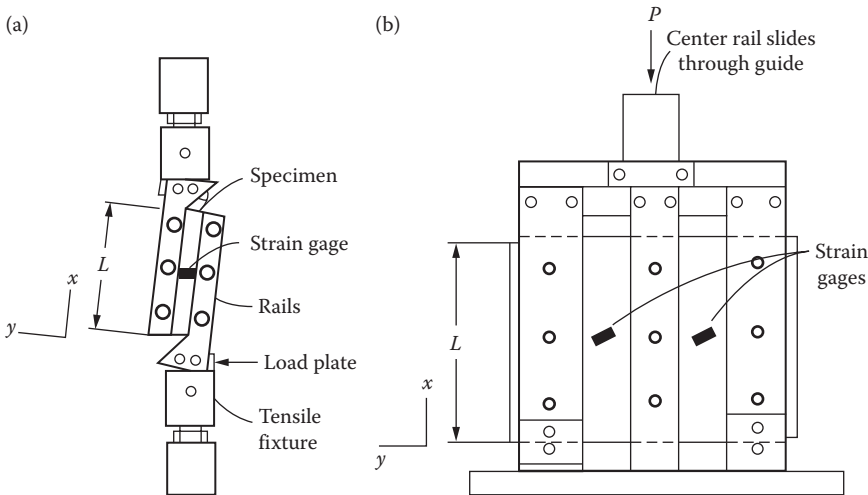
The test fixture for the V-notched rail shear test (ASTM D7078/D7078M-05 [43]) is shown in Figure 10.21, and the different possible arrangements for V-notched plate specimens are shown in Figure 10.22. Shear stress, shear strain, shear modulus, and shear strength calculations are similar to those used in the Iosipescu test method. As suggested by Adams [41], this method is the newest of the shear test methods, and, as such, it has not been used extensively yet.

Figure 10.23 shows the original rail shear test method, which can only be used to measure in-plane shear properties. The rail shear test standard, as described in ASTM D4255/D4255M-01(2007) [50], covers two separate procedures. Procedure A involves the use of the two-rail fixture shown in Figure 10.23a, whereas procedure B requires the use of the three-rail fixture shown in Figure 10.23b. In both procedures, a flat rectangular plate specimen is clamped in between the rail fixtures, and the fixture is subjected to uniaxial loading by a testing machine. The uniaxial loading on the fixture generates in-plane shear loading of the specimen and the resulting strains are monitored by the strain gages shown in Figure 10.23a and b. Simple equilibrium requires that the average shear stress along the specimen loading axes ( $x, y$ ) for procedure A with the two-rail fixture is

$$\tau_{xy} = \frac{P}{Lt} \quad (10.8)$$

**FIGURE 10.22**

Different test specimen arrangements for V-notched rail shear test. (Reprinted from D7078/D7078M-05, 2005. Vol. 15.03, *Space Simulation; Aerospace and Aircraft; Composite Materials*. ASTM International, West Conshohocken, PA. Copyright ASTM International. With permission.)

**FIGURE 10.23**

Rail shear test fixtures. (a) Two-rail fixture for procedure A and (b) three-rail fixture for procedure B. (Reprinted from D4255/D4255M-01, 2005. Vol. 15.03, *Space Simulation; Aerospace and Aircraft; Composite Materials*. ASTM International, West Conshohocken, PA. Copyright ASTM International. With permission.)

where  $L$  = specimen length along the  $x$  direction,  $P$  = applied load along the  $x$  direction, and  $t$  = specimen thickness, whereas the corresponding shear stress for procedure B with the three-rail fixture is

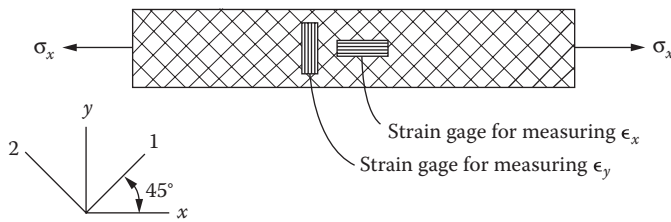
$$\tau_{xy} = \frac{P}{2Lt} \quad (10.9)$$

The shear strain along the  $x,y$  directions can be determined from the measured normal strain,  $\epsilon_{x'}$ , along the  $x'$  axis, which is oriented at  $45^\circ$  from the  $x$  axis. From the strain transformation relationship for a state of pure shear along the  $x, y$  axes, we have

$$\gamma_{xy} = 2\epsilon_{x'} \quad (10.10)$$

Thus, the shear stress–shear strain data can be generated from Equation 10.8 to Equation 10.10, and the corresponding modulus and strength can be found from the resulting stress–strain curve (see Example 10.4).

In-plane shear response can also be determined by testing a thin-walled composite tube in torsion and by measuring the resulting shear strain with a strain gage. If the strain gage is oriented at  $45^\circ$  to the tube axis, and if the applied torque creates a state of pure shear along the  $x, y$  axes, Equation 10.10 can again

**FIGURE 10.24**

A  $[ \pm 45 ]_s$  laminate tensile specimen for determination of in-plane shear properties.

be used to determine the shear strain. The shear stress can be estimated from the well-known mechanics of materials formula for a thin-walled tube:

$$\tau_{xy} = \frac{T}{2At} \quad (10.11)$$

where  $T$  is the applied torque,  $t$  the wall thickness,  $A$  the area enclosed by median line, which is equal to  $\pi R^2$  for the cylindrical tube, and  $R$  the mean radius of tube.

For the  $[ \pm 45 ]_s$  laminate tensile specimen ASTM D3518/D3518M-94 (2007) [51] (Figure 10.24), it can be shown from laminate analysis and a transformation of stresses that the lamina shear stress,  $\tau_{12}$ , along the principal material axes is related to the uniaxial tensile stress,  $\sigma_x$  acting on the laminate by

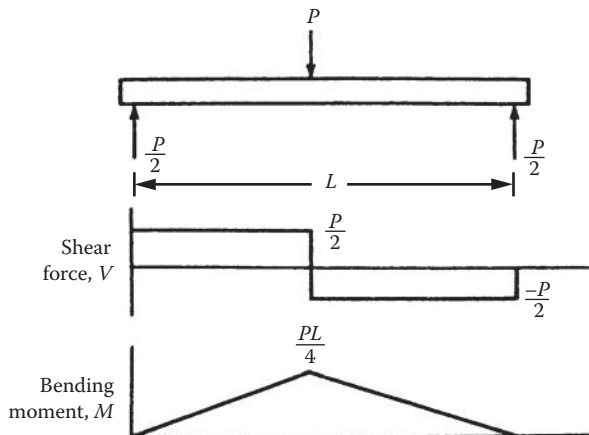
$$|\tau_{12}| = \left| \frac{\sigma_x}{2} \right| \quad (10.12)$$

The measured laminate strains,  $\varepsilon_x^o$  and  $\varepsilon_y^o$ , can be transformed to the lamina principal axes at  $\pm 45^\circ$ , so that the magnitude of the lamina shear strain is

$$|\gamma_{12}| = \left| \varepsilon_x^o - \varepsilon_y^o \right| \quad (10.13)$$

where  $\varepsilon_x^o$  is assumed to be a positive tensile strain and  $\varepsilon_y^o$  is assumed to be a negative Poisson strain. Thus, measurement of the applied stress,  $\sigma_x$ , and the laminate strains,  $\varepsilon_x^o$  and  $\varepsilon_y^o$ , during a tensile test of the  $[ \pm 45 ]_s$  laminate enables one to generate the shear stress–shear strain curve for the lamina material. The shear strength and the shear modulus can then be evaluated from this stress–strain curve.

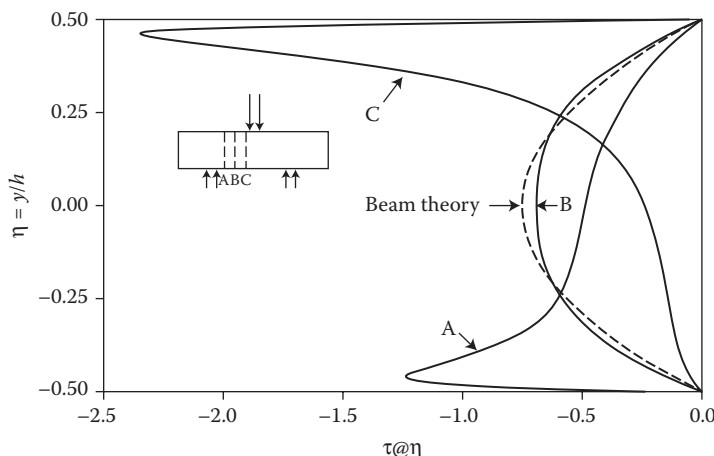
Although the off-axis tensile test is not yet a standard, it is a useful method. For example, a tensile test of an off-axis specimen can be used to determine the off-axis Young's modulus,  $E_x$ , as defined by Equation 2.39. If the values  $E_1$ ,  $E_2$ , and  $v_{12}$  are known from separate tests of longitudinal and transverse specimens, then the first of Equations 2.40 can be solved for the in-plane

**FIGURE 10.25**

Short-beam shear test specimen with shear and moment diagrams.

shear modulus,  $G_{12}$ . However, the off-axis tensile test cannot be expected to yield accurate results for the shear strength  $s_{LT}$  because of the biaxial stress state ( $\sigma_1, \sigma_2, \tau_{12}$ ) given in Equations 4.3. For example, if this stress state is substituted in the Tsai–Hill failure criterion (Equation 4.14), the failure is clearly due to all three stress components, but we can only have an accurate measurement of  $s_{LT}$  when the stress state along the 1,2 axes is pure shear, in which case Equation 4.14 reduces to  $\tau_{12} = s_{LT}$ . Such a pure shear condition is not possible with the off-axis tensile test.

In addition to the previously mentioned Iosipescu test, there is at least one other test that is used for interlaminar shear. The reader is cautioned in advance, however, that although this other test is widely used as a screening test, the interlaminar strength data from this test should not be used for design purposes. The ASTM D2344/D2344M-00(2006) short-beam shear test [52] involves the use of a short beam loaded in three-point bending, as shown in Figure 10.25. The resulting shear stress,  $\tau_{xy}$ , due to the shear force,  $V$ , and the normal stress,  $\sigma_x$ , due to the bending moment,  $M$ , can be estimated by using well-known mechanics of materials formulas. While the shear stress is independent of specimen length,  $L$ , the normal stress, because of its dependence on the bending moment, is a linear function of  $L$ . Thus, failure by interlaminar shear can theoretically be induced by making the beam short enough so that under load, the shear stress will reach its limiting value before the normal stress does. This is why the test is referred to as the “short-beam shear test.” However, Whitney [53] has used the theory of elasticity analyses of short-beam shear specimens to show that the actual state of stress in the vicinity of the applied load where failure initiates is much more complex than that predicted by the simple mechanics of materials formulas used in the D2344 standard. For example, Figure 10.26 from [53] shows clearly that the interlaminar shear stresses in short beam shear specimens predicted by

**FIGURE 10.26**

Comparison of predicted interlaminar shear stress distributions from theory of elasticity (solid curves) and beam theory (dotted curve) for a 50 ply short beam shear specimen with length-to-depth ratio of 4. Differences are particularly large near loading point (section C) and support points (section A). (Reprinted from *Composites Science and Technology*, 22, Whitney, J. M., Elasticity analysis of orthotropic beams under concentrated loads, 167–184, Copyright (1985), with permission from Elsevier.)

the theory of elasticity are substantially different from those predicted by mechanics of materials beam theory, particularly at sections near support points and the loading point (e.g., at Sections A and C). In Figure 10.26, the vertical axis is  $\eta = y / h$ , where  $y$  is the distance from the middle surface,  $h$  is the beam depth, and the horizontal axis is the shear stress  $\tau @ \eta$ . The classic parabolic shear stress distribution from beam theory is only valid at section B which is midway between the loading point and the support. Thus, the interlaminar strength derived from the beam theory used in the D2344 test is referred to only as “apparent” interlaminar shear strength and should not be used in design. According to D2344, such data can be used for quality control and specification purposes, however.

#### Example 10.4

A rail shear test of a unidirectional carbon/epoxy composite specimen is conducted using ASTM D4255 Procedure B with the three rail fixture shown in Figure 10.23b. The  $x$  and  $y$  axes in Figure 10.23b are aligned with the principal material axes of the specimen so that the  $x$  axis is the same as the 1 axis and the  $y$  axis is the same as the 2 axis. For an applied load  $P = 7.01$  kN, the measured strain  $\varepsilon_{x'} = 0.001$  from the strain gage along the  $x'$  axis which is oriented at  $45^\circ$  to the  $x$  axis. The specimen dimensions are length  $L = 254$  mm and thickness  $t = 1$  mm. What is the in-plane shear modulus  $G_{12}$  of the specimen? If the ultimate load  $P_U = 31.546$  kN at failure, what is the shear strength  $s_{LT}$  of the specimen?

## SOLUTION

Static equilibrium of the specimen requires that the shear force transmitted from the three rail fixture to the specimen is  $P/2$ , where  $P$  is the total applied load on the fixture. In this case, the  $x,y$  axes are coincident with the 1,2 axes, so the resulting shear stress in the specimen is

$$\tau_{xy} = \tau_{12} = \frac{P}{2Lt}$$

The strain transformation equation relating the measured strain  $\varepsilon_{x'}$  along the  $x'$  axis to the strains along the  $x,y$  axes is

$$\varepsilon_{x'} = \varepsilon_x \cos^2 \theta + \varepsilon_y \sin^2 \theta + 2 \cos \theta \sin \theta \frac{\gamma_{xy}}{2}$$

But in this case,  $\varepsilon_x = \varepsilon_y = 0$  and  $\theta = 45^\circ$ , so  $\varepsilon_{x'} = \gamma_{xy}/2 = \gamma_{12}/2$ . The shear modulus is then

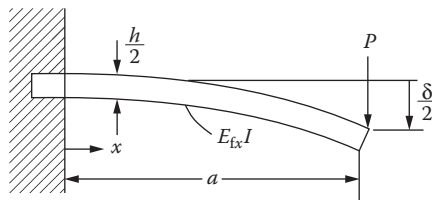
$$\begin{aligned} G_{12} &= \frac{\tau_{12}}{\gamma_{12}} = \frac{P}{2Lt(2\varepsilon_{x'})} = \frac{7010\text{N}}{4(254\text{mm})(1\text{mm})(0.001)} \left( \frac{10^3 \text{mm}}{m} \right)^2 \\ &= 6.9 \times 10^9 \text{N/m}^2 = 6.9 \text{GPa} \end{aligned}$$

At failure, the shear stress is equal to the shear strength as

$$\tau_{12} = s_{LT} = \frac{P_U}{2Lt} = \frac{31,546\text{N}}{2(254\text{mm})(1\text{mm})} \left( \frac{10^3 \text{mm}}{m} \right)^2 = 62.1 \times 10^6 \text{N/m}^2 = 62.1 \text{ MPa}$$

### 10.3.4 Flexure Tests

Recall from Chapter 7 that unlike homogeneous, isotropic materials, composite laminates have flexural properties that are not necessarily the same as the corresponding tensile properties. Since many laminates are used as flexural members, there is a need to determine the flexural properties experimentally. The ASTM D7264/D7264M-07 test method for flexural properties of polymer matrix composites [54] consists of Procedure A for three point flexure and Procedure B for four point flexure. This method differs from the previously described D790 and D6272 flexural tests for neat resin matrix materials. It is important to realize that in highly anisotropic composites such as unidirectional carbon/epoxy, through-thickness shear deformation can be significant unless the beam span-to-depth ratio is large enough. Thus, the recommended span-to-depth ratio for D7264 is 32:1 compared with 16:1 for D790 and D6272. D7264 is intended to cause long-beam, flexure-dominated behavior instead of

**FIGURE 10.27**

Cantilever beam representing half of the cracked DCB specimen.

short-beam, shear-dominated behavior in the D2344 method. It is also important to remember from Chapter 7 that the flexural modulus of highly anisotropic laminates depends on the ply-stacking sequence and is not necessarily the same as the in-plane Young's modulus of the laminate.

### 10.3.5 Interlaminar Fracture Tests

In Section 9.4, the importance of interlaminar fracture was discussed, and the use of the strain energy release rate to characterize the interlaminar fracture toughness was described. The most important modes of delamination seem to be modes I and II, and the corresponding fracture toughnesses are usually characterized by the strain energy release rates  $G_{lc}$  and  $G_{llc}$ , respectively. Although a number of test methods for measuring  $G_{lc}$  and  $G_{llc}$  have been reported in the literature, the most widely used methods appear to be the double cantilever beam (DCB) test for  $G_{lc}$  (Figure 9.18a) and the end-notched flexure (ENF) test for  $G_{llc}$  (Figure 9.18b).

The calculation of  $G_{lc}$  from experimental DCB data can be carried out by using the method of Whitney et al. [55], who analyzed each cracked half of the DCB specimen as though it were a cantilever beam (see Figure 9.18a and Figure 10.27). Using the mechanics of materials beam theory, the tip deflection of the cantilever beam in Figure 10.27 is

$$\frac{\delta}{2} = \frac{Pa^3}{3E_{fx}I} \quad (10.14)$$

where  $P$  is the applied load,  $a$  the beam length in Figure 10.27 is the DCB rack length in Figure 9.18a,  $E_{fx}$  the flexural modulus of cracked half of DCB along the  $x$  direction, and  $I$  the moment of inertia of cracked half of DCB about centroidal axis of cracked half.

From Equation 10.14, the compliance of the DCB specimen is found to be

$$s = \frac{\delta}{P} = \frac{64a^3}{E_{fx}th^3} \quad (10.15)$$

where  $t$  is the DCB specimen width (the crack width) and  $h$  is the DCB specimen depth.

The strain energy release rate,  $G_I$ , is then found by substituting Equation 10.15 in Equation 9.28 and differentiating with respect to the crack length,  $a$ . The result is

$$G_I = \frac{P^2}{2t} \frac{\partial s}{\partial a} = \frac{96P^2a^2}{E_{fx}t^2h^3} \quad (10.16)$$

or

$$G_I = \frac{3P\delta}{2ta} \quad (10.17)$$

where the deflection,  $\delta$ , is given by Equation 10.14. The critical strain energy release rate is then

$$G_{Ic} = \frac{96P_c^2a^2}{E_{fx}t^2h^3} \quad (10.18)$$

or

$$G_{Ic} = \frac{3P_c\delta_c}{2ta} \quad (10.19)$$

where  $P_c$  and  $\delta_c$  are the critical values of the load and deflection, respectively, measured at the onset of crack growth. Whitney et al. [55] suggested that  $G_{Ic}$  could also be determined by rearranging Equation 10.19 as

$$G_{Ic} = \frac{3H}{2t} \quad (10.20)$$

where  $H = P_c\delta_c/a$  is a constant, and averaging  $H$  over some number of data points during continuous loading and crack extension. The average value of  $H$  is given by

$$H = \frac{1}{N} \sum_{i=1}^N \frac{P_{ci}\delta_{ci}}{a_i} \quad (10.21)$$

where  $P_{ci}$ ,  $\delta_{ci}$  are the critical values of  $P$  and  $\delta$ , respectively, associated with the  $i$ th crack length  $a_i$ , and  $N$  the total number of data points. The relevant ASTM Standard for the DCB test is D5528-01 (2007)e3 [56].

The determination of  $G_{IIC}$  from ENF test data can be accomplished by using the method of Russell and Street [57,58], who employed the elementary beam theory to derive the expression

$$G_{II} = \frac{9P^2a^2s}{2t(2L^3 + 3a^3)} \quad (10.22)$$

where the parameters  $P$ ,  $a$ ,  $t$ , and  $L$  are all defined in Figure 9.18b and  $s = \delta/P$  is the midspan compliance. The critical strain energy release rate,  $G_{IIC}$ , then corresponds to the critical load,  $P_c$ , and the associated compliance,  $s_c$ , at the onset of crack growth. The compliance,  $s$ , can be determined experimentally or calculated from the following equation, which was also derived using the elementary beam theory [57]:

$$s = \frac{(2L^3 + 3a^3)}{8E_{fx}th^3} \quad (10.23)$$

where  $E_{fx}$  is now the flexural modulus of the beam of depth  $2h$ , as shown in Figure 9.18b. Carlsson et al. [59] have used the Timoshenko beam theory to modify Equations 10.22 and 10.23, so that the effects of shear deformation are included. Several other test methods for measurement of  $G_{Ic}$  and  $G_{IIC}$  are examined in detail by Adams et al. [3].

Since the loading conditions in most composite structures are generally such that more than one fracture mode would result, the experimental investigations of mixed mode fracture are of considerable interest. In composite laminates, Mixed Mode I and Mode II interlaminar fracture is probably the

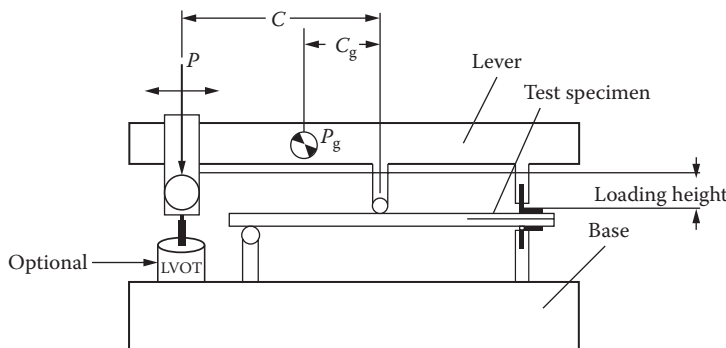


**FIGURE 10.28**

Test fixture for MMB test. (Reprinted from D6671/D6671M-06, 2009. Vol. 15.03, *Space Simulation; Aerospace and Aircraft; Composite Materials*. ASTM International, West Conshohocken, PA. Copyright ASTM International. With permission.)

most commonly occurring case of this type. The ASTM standard for mixed Mode I/Mode II interlaminar fracture is the mixed mode bending (MMB) test, D6671/D6671M-06 [60], which involves a laminated beam specimen with a delamination starter crack on one end. The MMB test was originally developed at NASA by Reeder and Crews [61,62]. As shown in Figure 10.28, the MMB test fixture is designed to produce pure Mode II delamination and measurement of the Mode II energy release rate,  $G_{II}$ , when the moment arm distance,  $c$ , is zero and the applied load  $P$  acts at specimen midspan. Then as the distance  $c$  is increased, and the applied load  $P$  moves away from midspan, the Mode I contribution and the mode mixity  $G_I/G_{II}$  increases accordingly. Thus, the MMB test is actually a combination of the DCB test for measuring  $G_I$  and the ENF test for measuring  $G_{II}$ , and by varying the distance  $c$ , various degrees of  $G_I/G_{II}$  mode mixity can be achieved. The MMB test has been modified for the measurement of mixed mode fracture in adhesively bonded joints by Liu et al. [63,64].

### 10.3.6 Fiber/Matrix Interface Tests

Good adhesion between the fiber and the matrix is a fundamental requirement if a composite is to be a useful structural material, and optimization of the fiber/matrix interface can only occur if reliable methods for measurement of fiber/matrix interfacial strength are available. One such method, a single-fiber fragmentation technique, has been developed and used by Drzal et al. [65–67]. The specimen, shown in Figure 10.29, consists of a single fiber embedded in a dogbone tensile specimen of matrix resin. This specimen is loaded in tension under a microscope until the fiber breaks up into segments corresponding to the critical length,  $L_c$ , which are measured by using the microscope. If the fiber tensile strength,  $s_{fl}^{(+)}$ , corresponding to the critical length, and the fiber diameter,  $d$ , are known, then the interfacial shear strength can be estimated from Equation 6.16, which is repeated here as Equation 10.24.

$$\tau_y = \frac{ds_{fl}^{(+)}}{2L_c} \quad (10.24)$$

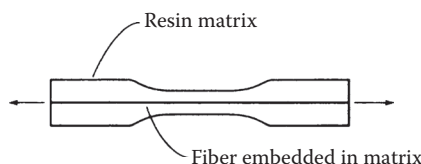


**FIGURE 10.29**

Single-fiber fragmentation specimen developed by Drzal et al. (From Drzal, L.T., Rich, M.J., and Lloyd, P.F. 1982. *Journal of Adhesion*, 16, 1–30.; Drzal, L.T., et al. 1983. *Journal of Adhesion* 16, 133–152. With permission.)

Since the observed lengths actually vary because of variations in fiber and matrix properties, a statistical distribution of fiber lengths must be used. If the measured values of  $L_c/d$  can be fitted by a two-parameter Weibull distribution, the mean value of interfacial shear strength can be expressed as [65]

$$\tau_y = \frac{s_{fl}^{(+)}}{2\beta} \Gamma\left(1 - \frac{1}{\alpha}\right) \quad (10.25)$$

where  $\Gamma$  is the gamma function and  $\alpha$  and  $\beta$  are the shape and scale parameters, respectively, for the two-parameter Weibull distribution.

In the so-called microbond test, single fiber is embedded in a resin droplet, and the free end of the fiber is loaded in tension until the fiber pulls out of the resin [68]. The interfacial strength is simply the pullout force divided by the interfacial area. One potential difficulty with this test is that it may be difficult to reproduce the composite resin matrix cure conditions in a small droplet of resin [68,69].

While a single-fiber specimen is required for the two techniques described above, *in situ* fiber/matrix interfacial shear strength in composite specimens may be measured by using the microindentation technique [69,70]. As shown in Figure 10.30, this approach involves the use of a diamond microindenter to load the end of a fiber in longitudinal compression until debonding between the fiber and the matrix occurs. The experimental data for debonding load are combined with a finite element analysis in order to calculate the interfacial strength.

A comparison of the three interfacial strength measurement techniques described above has been reported by McDonough et al. [68], and the results for carbon fibers having different surface treatments and the same epoxy matrix are shown in Table 10.2. It was concluded that while the single-fiber

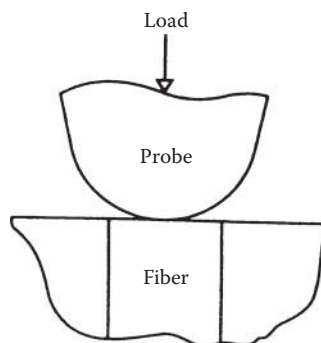


**FIGURE 10.30**

Microindenter test for fiber/matrix interfacial strength. (Reprinted from Mandell, J. F., et al. 1986. In Whitney, J. M. ed., *Composite Materials: Testing and Design (Seventh Conference)*, ASTM STP 893, pp. 87–108. American Society for Testing and Materials, Philadelphia, PA. Copyright ASTM. With permission.)

**TABLE 10.2**

Interfacial Shear Strength Values Obtained with Different Techniques

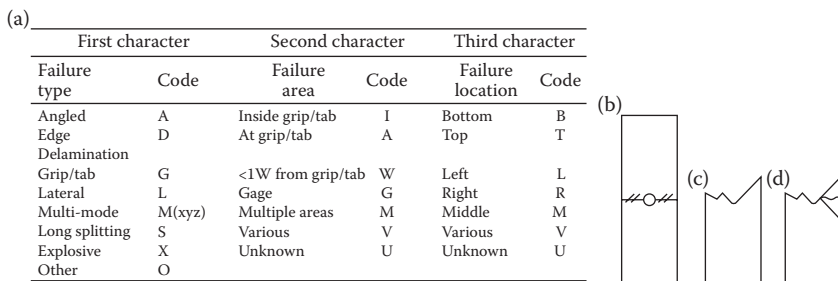
Fiber Type	Interfacial Shear Strength (MPa)		
	Fragmentation	Microbond	Microindentation
AS-4	68	50	71
AU-4	37	23	55
IM6-600	47	15	43
IM6-100	40	19	37
IM6-U	22	15	27

*Source:* Reprinted from McDonough, W. G., et al. 1991. In *Advanced Materials/Affordable Processes, Proceedings of 23rd International SAMPE Technical Conference*, Kiamesha Lake, NY, pp. 247–258. Society for Advancement of Material and Process Engineering, Covina, CA. With permission of the Society for the Advancement of Material and Process Engineering.

fragmentation technique and the microindentation techniques showed good agreement, the microbond technique produced interfacial strength values that were consistently lower than those of the other two methods. The above-mentioned uncertainty regarding the state of cure in the microbond droplet was given as the reason for these results.

### 10.3.7 Open Hole and Filled Hole Tests

Holes in composite structures are required when mechanical fasteners are used to connect different components, and the effects of such holes on composite strength must be characterized experimentally. ASTM standard test method D 5766/5766M-07 [71] may be used to determine the open hole tensile (OHT) strength or the notched tensile strength of polymer matrix composites. The test specimen is similar to that used in ASTM D3039/D3039M-08 [18] for tensile properties of polymer matrix composite materials, but with a centrally located hole. It is recommended that the test specimen geometry has a width-to-bolt-hole diameter ratio,  $w/d = 6$ , edge-distance to bolt-hole diameter ratio,  $e/d = 3$  and bolt-hole diameter-to-thickness ratio,  $d/t$ , in the range of 1.5–3.0, unless the experiment is investigating the effects of these ratios. The recommended centrally located hole/notch diameter is  $d = 6$  mm and the recommended specimen length,  $L$  is in the range of 200–300 mm. The ultimate OHT strength,  $F_x^{\text{OHTu}} = P^{\text{max}}/A$ , is calculated based on the gross cross-sectional area ( $A = wt$ ), neglecting the bolt-hole dimensions, and  $P^{\text{max}}$  is the maximum load before failure occurs in the composite. The OHT strength is recorded for only those specimens for which the fracture surface passes through the hole. Failures that do not occur at the hole are not acceptable. The three-character codes used to describe the failure modes are given in Figure 10.31a. The acceptable failure test codes for this test method are limited to LGM (laminate tensile

**FIGURE 10.31**

Acceptable test failure modes for ASTM D 5766/D 5766M-07 standard test method for open hole tensile strength (a) failure mode codes, (b) LGM, (c) AGM, and (d) MGM. (Reprinted from D5766/D5766M-07, 2009. Vol. 15.03. *Space Simulation; Aerospace and Aircraft; Composite Materials*. ASTM International. West Conshohocken, PA. Copyright ASTM International. With permission.)

failure laterally across the center of the hole, (Figure 10.31b), AGM (laminate generally fails in tension at the hole, but remnants of angle plies cross the hole lateral centerline, (Figure 10.31c) and MGM (laminate generally fails in tension at the hole and exhibits multiple failure modes in various sub laminates (Figure 10.31d).

Open hole compressive (OHC) strength of the composite can be determined using the standard test method ASTM D6484/D6484M-04e1 [72]. Two test procedures are recommended: Procedure A, in which the specimen/fixture assembly is directly clamped by the hydraulic wedge grips and Procedure B, in which the specimen/fixture are end-loaded by placing them between flat platens (on top and bottom). In both cases the load is transferred through shear to the specimens. The specimen geometry is similar to that used for OHT [71]. The test fixture used to support the specimens and prevent buckling can be used for both procedures A and B. Ultimate OHC strength,  $F_x^{\text{OHC}u} = P^{\max}/A$ , is calculated and again only gross cross-sectional area ignoring the bolt-hole is used for the calculation. As explained before, the failure modes that are acceptable are those in which the fracture surface passes through the bolt-hole (Figure 10.31 b-d).

ASTM D6742/D6742M-07 [73] may be used to determine the filled-hole tensile and compressive strengths of continuous fiber-reinforced polymer matrix composites. This test method and its specimen configuration are similar to those used for OHT [71] and OHC [72], but with a close-tolerance fastener or pin inserted in the bolt hole. Such a close-fitting fastener or pin may reduce the deformation in the composite around the hole, thus possibly affecting the failure stresses and failure modes as compared with the open hole case [74].

### 10.3.8 Bearing Tests

Bearing stress is generated by direct contact between the outer surface of the bolt or pin and the inner surface of the hole in the composite specimen

in which the bolt or pin is inserted. ASTM standard D 5961/D 5961M-08 [75] may be used to determine the bearing response of polymer matrix composite laminate specimens in double-shear tensile loading (Procedure A), single-shear tensile or compressive loading of a two-piece specimen (Procedure B), single-shear tensile loading of a one-piece specimen, (Procedure C), or double-shear compressive loading (Procedure D). This test also describes the procedure for a multi-fastener test to investigate the bearing/by-pass response for bolted joints, where the failure mode of the joint is either bearing failure or bypass bearing failure. In the case of a double shear test (Procedure A), the bearing load is applied by pulling the specimen in the fixture shown in Figure 10.32 through a lightly torqued fastener or pin.

In the case of a single-shear test (Procedure B), two identical specimens similar to the specimen used for double shear are fastened together through one or two holes located centrally near one end for a single-shear, single-fastener test or a single-shear, double fastener test, respectively. The single-shear test

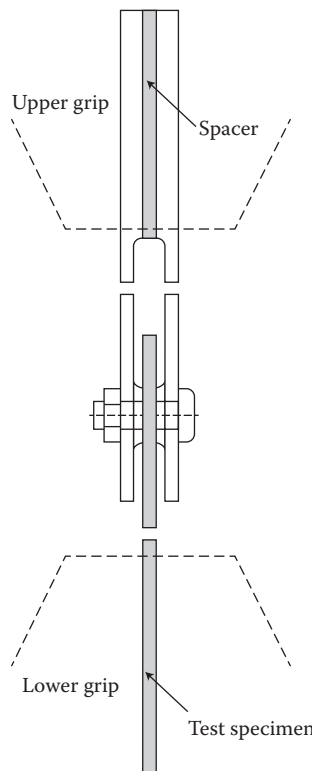


**FIGURE 10.32**

Fixture assembly for ASTM D5961/D5961M-08 (Procedure A) double shear test method for bearing response of polymer matrix composite laminates. (Reprinted from D5961/D5961M-08, 2009. Vol. 15.03, *Space Simulation; Aerospace and Aircraft; Composite Materials* ASTM International, West Conshohocken, PA. Copyright ASTM International. With permission.)

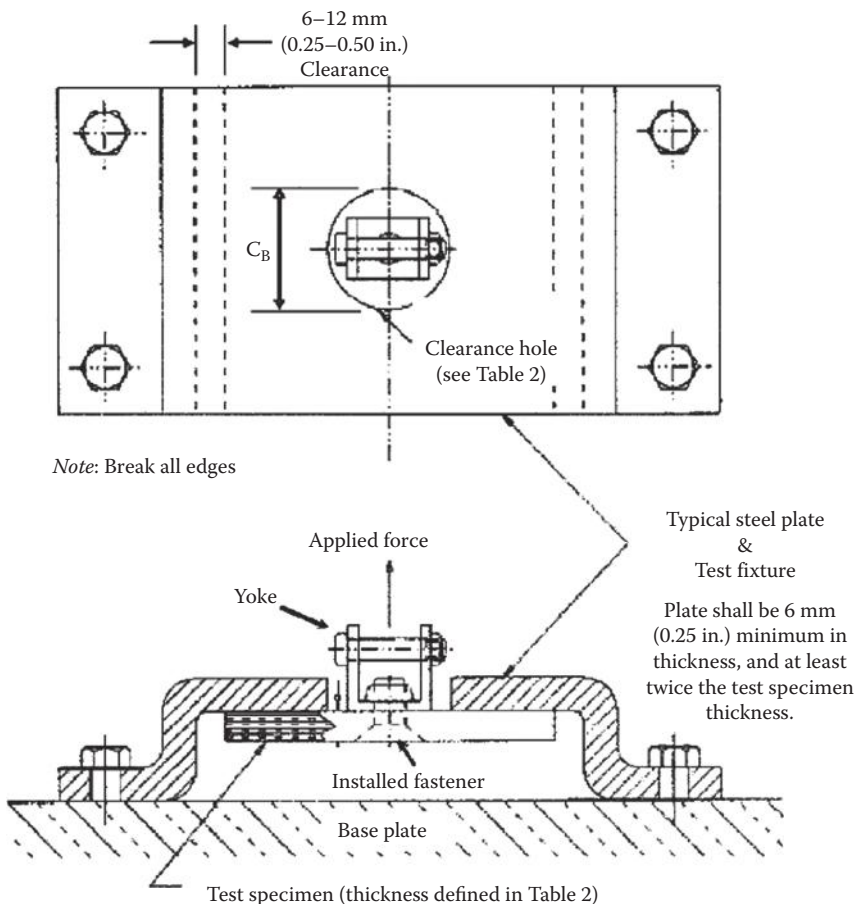
is carried out by pulling the lightly torqued specimens as explained before. The single-shear test can be carried out in either stabilized (with support fixture) or unstabilized (no support fixture) configuration. Although the stabilized configuration test fixture is designed to be used for both tension and compression, it is primarily intended to be used for compressive loading. The failure modes and the location of failures obtained during the bearing response tests are recorded, and the standard describes those failure modes which are acceptable or unacceptable.

Mechanically fastened joints in composite structures are often subjected to cyclic loading which may lead to bearing fatigue failure. ASTM D6873/D6873M-08 [76] may be used to determine the bearing fatigue behavior of composite materials subjected to cyclic bearing forces under specific loading and environmental conditions. This procedure is modified from the previously described static bearing test method [75] to include repetitive constant amplitude force (stress) cycles at a specified frequency. The repetitive loading may be tension-tension (T-T), compression-compression (C-C), or tension-compression (reversed) force-stress ratio,  $R$  (ratio of the minimum applied force-stress to the maximum applied force-stress). The loss of bearing strength due to fatigue damage can also be obtained by discontinuing the cyclic loading after a certain number of fatigue cycles,  $N$ , and performing a static bearing test using the static test method [75].

Bearing fatigue response of mechanically fastened composite joints is strongly affected by the selection of  $R$ -ratio. For example, for the case of a reversed load ratio ( $R = -1$ ), specimens may exhibit bearing damage on both sides of the bolt hole. Other factors that influence the fatigue response such as fastener selection, fastener preload/torque, fastener bolt-hole clearance, and environmental conditions are not specified in the test procedure. Specimen geometry, support fixtures and test configuration are similar to those used in test method D 5961/D 5961M [10]. For example, both procedure A (double shear with single fastener) and procedure B (single shear with single or double fastener) configurations can be used to determine the fatigue response.

### 10.3.9 Pull-Through Tests

Since composite structures often have poor transverse strength, it is important to establish pull-through characteristics as part of the design verification. Pull-through strength is the maximum load a mechanically fastened composite plate can sustain when the fastener is pulled through the plate perpendicular to the plane of the plate. ASTM D7332/D7332M-07e1 [77] may be used to determine the pull-through strength of a composite plate/fastener combination. This test can also be used to evaluate different components of the fastener, such as, bolt/nuts, pin/collars or washers. Two methods are recommended; the first method (Procedure A), is used for screening and fastener development and the second method (Procedure B), is used for

**FIGURE 10.33**

Test fixture and specimen for ASTM standard test method for measuring the fastener pull-through resistance of a fiber-reinforced polymer matrix composite, Procedure B. (Reprinted from D7332/D7332M-07e1. 2009. Standard test method for measuring the fastener pull-through resistance of a fiber-reinforced polymer matrix composite. Vol. 15.03, *Space Simulation; Aerospace and Aircraft; Composite Materials*, ASTM International, West Conshohocken, PA. With permission.)

developing design values. Both Procedures A and B require flat plate specimens having rectangular cross sections with a circular hole at the center for the fastener. Additionally, procedure A requires two plates and 4 more holes to be drilled on the periphery of the specimen to accommodate the test fixture. For Procedure A, the two plates are joined by a fastener and one plate is rotated by 45° with respect to the other plate. The plates are pried apart, which results in a tensile load on the fastener. In the case of Procedure B, the load is applied to a composite plate/fastener system through a yoke (Figure 10.33). It is recommended that the thickness,  $t$ , of the composite

plate should be 1.5 times greater than the normal fastener shank diameter,  $D$ . The pull-through strength is calculated corresponding to the first peak load observed in the load–displacement curve.

Finally, a number of other test methods are relevant to the characterization of the mechanical behavior of mechanically fastened joints in polymer composite structures, as shown in a recent review article [78].

---

## 10.4 Measurement of Viscoelastic and Dynamic Properties

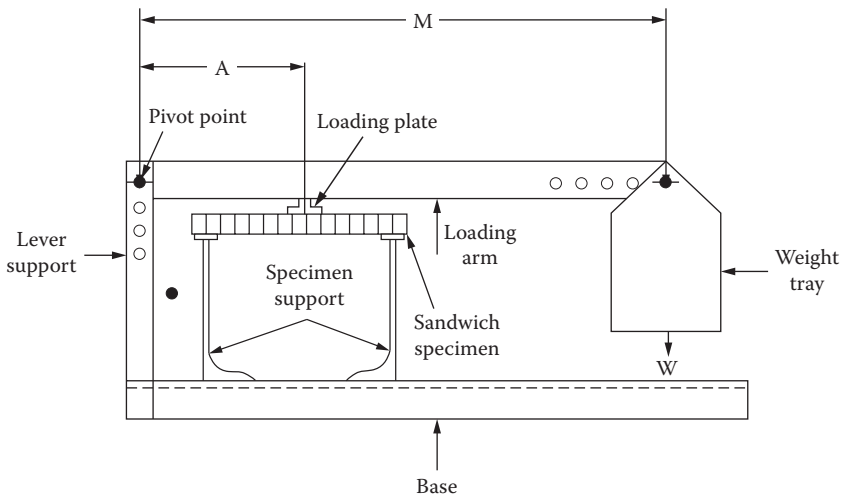
In Chapter 8, creep, relaxation, damping, and strain rate dependence were described as four important physical manifestations of viscoelastic behavior. All these characteristics can be determined experimentally, but in this section we will only describe test methods for the measurement of creep compliance and damping. Since the complex modulus notation conveniently describes both dynamic stiffness and damping of linear viscoelastic materials, vibration test methods for the measurement of the complex moduli of composites will be considered. The use of vibration tests of beams and plates to determine dynamic elastic moduli alone will also be reviewed. Wave propagation test methods will not be covered here.

### 10.4.1 Creep Tests

A creep test usually consists of the application of constant loading to a specimen, followed by measurement of the resulting time-dependent strains in the specimen, as shown schematically in Figure 8.1a. Although there are no standard creep test methods for composites at this time, a creep rupture test method has been standardized for tensile creep rupture of polymer composite reinforcing bars for concrete [79]. Creep rupture is a material failure that occurs after sustained loading over time. In a creep rupture test (or stress rupture test), the time to failure under constant load is measured rather than the time-dependent strain or deflection in the specimen. A relevant creep test method has been standardized for flexure creep testing of sandwich beams [80], and the apparatus is shown in Figure 10.34 from Ref. [80]. Through a mechanical lever arrangement, a constant load is applied at midspan of the simply supported sandwich beam, and midspan creep deflection is measured as a function of time.

In principle, any of the previously described composite test methods can be used to characterize creep if the following provisions are made:

1. The applied loading on the specimen should be constant.
2. The resulting strains or deflections in the specimen should be measured as a function of elapsed time under load.

**FIGURE 10.34**

Test apparatus for measurement of flexure creep of sandwich beams. (Reprinted from C480/C480M-08, 2009. Vol. 15.03, *Space Simulation; Aerospace and Aircraft; Composite Materials*. ASTM International, West Conshohocken, PA (2005). Copyright ASTM International. With permission.)

3. The specimen should be kept under controlled environmental conditions for the duration of the test.

Since viscoelastic behavior depends on temperature and humidity, the specimen would normally be enclosed in an environmental chamber. Stability of the measurement system electronics over long periods of time is also very important.

As shown by Halpin and Pagano [81], the principal creep compliances  $S_{11}(t)$ ,  $S_{22}(t)$ ,  $S_{12}(t) = S_{21}(t)$ , and  $S_{66}(t)$  for a linear viscoelastic, orthotropic lamina can be determined by conducting the three tensile creep tests in Figure 10.35. For example, in the creep test of the longitudinal specimen in Figure 10.35a the constant stress,  $\sigma_1$ , is applied; the time-dependent longitudinal strain,  $\epsilon_1(t)$ , and the transverse strain,  $\epsilon_2(t)$ , are measured, and the longitudinal creep compliance is determined from the equation

$$S_{11}(t) = \frac{\epsilon_1(t)}{\sigma_1} \quad (10.26)$$

whereas

$$S_{21}(t) = \frac{\epsilon_2(t)}{\sigma_1} \quad (10.27)$$

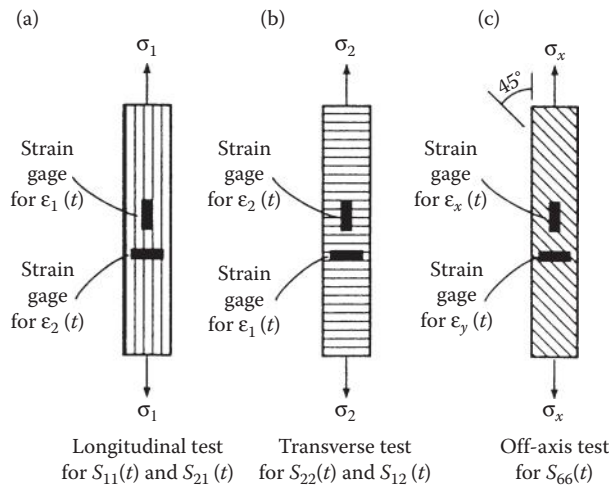


**FIGURE 10.35**

Tensile tests for measurement of creep compliances of an orthotropic, viscoelastic lamina.

For the transverse tensile creep test in Figure 10.35b, the constant transverse stress,  $\sigma_2$ , is applied, and the resulting strains are used to find the creep compliances

$$S_{22}(t) = \frac{\varepsilon_2(t)}{\sigma_2} \quad (10.28)$$

and

$$S_{12}(t) = \frac{\varepsilon_1(t)}{\sigma_2} \quad (10.29)$$

The data of Halpin and Pagano [81] and others from such tests have shown that  $S_{12}(t) = S_{21}(t)$ .

Finally, the off-axis tensile creep test in Figure 10.35c can be used to determine the shear creep compliance  $S_{66}(t)$ . For example, if the constant uniaxial stress is  $\sigma_x$  and the fiber orientation  $\theta = 45^\circ$ , a transformation of stresses gives the shear stress along the principal material axes as  $\tau_{12} = \sigma_x/2$ . The corresponding time-dependent shear strain,  $\gamma_{12}(t)$ , can be determined from the measured strains,  $\varepsilon_x(t)$  and  $\varepsilon_y(t)$ , by modifying Equation 10.13 as  $|\gamma_{12}(t)| = |\varepsilon_x(t)| - |\varepsilon_y(t)|$ . In practice, a more accurate determination of the shear strain  $\gamma_{12}(t)$  is possible by using a strain gage rosette that has three strain gages oriented at  $45^\circ$  to each other [82]. The shear compliance is given by

$$S_{66}(t) = \frac{\gamma_{12}(t)}{\tau_{12}} \quad (10.30)$$

Similar tensile creep tests of composites have been reported by Beckwith [83,84] and Sullivan (Ref. [30] of Chapter 8).

Uniaxial compressive creep testing presents the same difficulties that were discussed earlier in Section 10.3.2, and there appear to be few references dealing with such tests. For example, Irion and Adams [85] have used the Wyoming-modified Celanese fixture [27] for compressive creep testing of unidirectional composites.

Since viscoelastic behavior is dependent on the stress–time history, preconditioning of creep specimens is recommended. Lou and Schapery [86] have suggested that mechanical conditioning of specimens before creep testing leads to much more repeatable test results. Specimens are mechanically conditioned by subjecting them to specified numbers of cycles of creep and recovery (loading and unloading) at a certain stress level. The actual creep tests are then conducted at stresses less than or equal to the conditioning stress. In creep tests of polymer composites where the effects of physical aging are being studied, rejuvenation of the specimens at temperatures above  $T_g$  is necessary before the aging and/or creep tests begin (Ref. [30] of Chapter 8).

In the discussion of viscoelastic behavior in Chapter 8, linear viscoelastic behavior was assumed. Experiments have shown, however, that polymer composites may exhibit nonlinear viscoelastic behavior at relatively low stress levels [83,86]. For example, Beckwith [83,84] has shown that the creep compliances for filament-wound S-glass/epoxy composites at various lay-ups followed a power law of the form

$$S(t) = S_0 + S_1 t^n \quad (10.31)$$

where  $S(t)$  is the creep compliance,  $S_0$  the initial elastic compliance, and  $S_1$  and  $n$  the empirically determined parameters.

The exponent,  $n$ , was found to be approximately equal to 0.19 for all compliances in the linear range, but at high stress levels and after multiple cycles of loading and unloading microcracking in the materials caused the exponent  $n$  to increase substantially.

Recall from Chapter 8 that for a linear viscoelastic material, the time domain creep compliance is related to the frequency domain complex compliance by a Fourier transform pair, as are the relaxation modulus and the complex modulus. This relationship makes it possible to obtain time domain creep and relaxation characteristics from frequency domain test data and vice versa. Using frequency domain complex modulus data and the Fourier transform approach, Gibson et al. [87,88] have developed alternative techniques for determination of creep and relaxation behavior of linear viscoelastic composites in both tension and compression. A similar technique [89] involves using frequency domain vibration tests to determine the parameters in a spring–dashpot model (recall Section 8.2.2), and then substituting

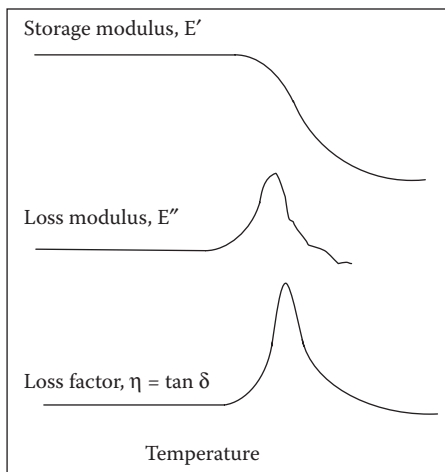
those same spring–dashpot parameters in the corresponding time domain creep compliance expression. Vibration test techniques for measurement of complex moduli will be discussed in the next section.

Finally, it is important to remember that, for polymer matrix composites, the viscoelastic behavior of the composite is dominated by the viscoelastic behavior of the polymer matrix material. So, for example, if it is not feasible or desirable to conduct creep tests of the composite material or structure, a viable alternative is to conduct creep tests of the neat resin polymer matrix material and then use micromechanical or macromechanical models to predict the corresponding creep behavior of the composite material or structure. Examples of such an approach involving the use of quasi-elastic analysis and the elastic–viscoelastic correspondence principle are given in Sections 8.2.3 and 8.2.5, respectively. However, since linear viscoelastic behavior is the underlying assumption of both quasielastic analysis and the elastic–viscoelastic correspondence principle, the use of this approach must be supported by experimental evidence of linear viscoelastic behavior of the polymer matrix material, as discussed in Section 8.2.

#### 10.4.2 Vibration Tests

The complex modulus notation, which is convenient for the characterization of dynamic behavior of linear viscoelastic composites, was developed in Chapter 8. The two measured components of the complex modulus (elastic storage modulus and damping loss factor) of a material are generally referred to as its dynamic mechanical properties. Measurement of these properties is often done using a dynamic mechanical analyzer (DMA), an instrument which imposes a vibratory deformation on a test specimen and measures its response.

The most relevant ASTM standards for DMA testing were developed for unreinforced plastics having elastic moduli in the range 0.5 MPa to 100 GPa [90]. Standard practice for determining dynamic mechanical properties of plastics using DMA instruments is described in ASTM D4065-06 [90], which includes the data reduction equations. According to D4065-06, DMA instruments typically operate in one of seven oscillatory modes. These modes and the associated standard test methods are: (1) freely decaying torsional oscillation (ASTM D5279-08 [91]), (2) forced constant amplitude, resonant, flexural oscillation (ASTM D5023-07 [92]), (3) forced constant amplitude, fixed frequency, compressive oscillation (ASTM D5024-07 [93]), (4) forced constant amplitude, fixed frequency, flexural oscillation (ASTM D5023-07 [92]), (5) forced, constant amplitude, fixed frequency, tensile oscillation (ASTM D5026-06 [94]), (6) forced constant amplitude, fixed frequency, torsional oscillation ASTM D 5279-08 [91], and (7) forced constant amplitude, fixed frequency, or variable frequency dual cantilever ASTM D5418-07 [95]. DMA instruments are typically automated to generate plots of storage modulus, loss modulus and loss factor (or  $\tan \delta$ ) vs. temperature (Figure 10.36) or frequency. As

**FIGURE 10.36**

Representation of automated DMA plot showing storage modulus, loss modulus and loss factor ( $\tan \delta$ ) vs. temperature.

discussed later, ASTM D7028-07e1 [96] describes the use of DMA measurements for the determination of the glass transition temperature,  $T_g$ , of polymer matrix composites.

In principle, some of the techniques described in these standards can also be used for high-modulus composites. In practice, however, there are many possible pitfalls, and DMA instruments are typically limited to materials having an elastic modulus less than 100 GPa. Commercially available DMA instruments were developed for testing small specimens of unreinforced low modulus polymers, and the stiffness of the specimen mounting hardware in the machines is generally insufficient for use with high-modulus composites. To reduce the composite specimen stiffness to the range required for valid data with these devices, it may be necessary to use specimen thicknesses on the order of the single ply thickness, so that testing of multiply laminates may not be possible. In addition, the equations used for data reduction in these machines typically do not take into account coupling effects, transverse shear effects, and other peculiarities of composite material behavior. Valid dynamic mechanical property measurements are difficult to obtain, particularly with composite materials. Only a brief overview of vibration test methods and difficulties will be given here, as a detailed review has been published elsewhere [97].

The complex modulus (recall Equation 8.75) for a particular vibration test specimen is obtained by measuring the storage modulus and the loss factor of the specimen as it vibrates in the desired mode. Specimens usually consist of rods, beams, or plates supported in such a way so as to minimize the extraneous damping due to the apparatus or the environment. Friction

damping at specimen support points and transducer attachments, aerodynamic drag on the vibrating specimen, and phase lag in the instrumentation may all lead to erroneous damping data. Cross-verification of damping measurements using several different techniques is always a good way to locate potential problems.

The storage modulus may be obtained by measuring a natural frequency of the specimen and by solving the appropriate frequency equation for the specimen. For example, Equation 8.111 can be used to solve for the longitudinal modulus,  $E$ , of a composite bar if the frequency,  $f_n$ , for the  $n$ th mode, the specimen length,  $L$ , and the density,  $\rho$ , are measured. Similarly, Equation 8.125 can be used to determine the flexural modulus,  $E_f$ , of a composite beam specimen [98]. Care must be taken to make sure that the effective modulus criteria have been met and that various effects such as coupling and transverse shear have been accounted for where necessary. As mentioned in Section 8.3.2, transverse shear effects are much more significant for high-modulus composites than they are for conventional materials, and Timoshenko beam theory may be required for valid results. Figure 10.37 shows correction factors, which, when multiplied by modulus values from the Bernoulli–Euler beam theory, yield corrected modulus values that are consistent with Timoshenko beam theory [99].

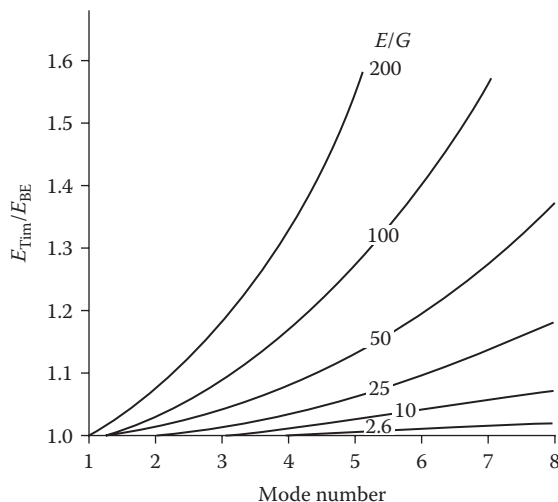
Damping is conveniently characterized by using the loss factor in the complex modulus notation. For lightly damped systems, the loss factor is related to the parameters that are used to characterize damping in a SDOF spring-mass system. The SDOF-damping parameters are typically estimated by curve fitting to the measured response of specimens in either free vibration or forced vibration if a single mode can be isolated for the analysis.

In the free vibration experiment, a specimen such as a rod or a beam is released from some initial displacement, or a steady-state excitation is removed, and the ensuing free vibration decay of the specimen is observed (Figure 10.38). The logarithmic decrement,  $\Delta$ , is calculated from such a decay curve by using the equation

$$\Delta = \frac{1}{n} \ln \frac{x_0}{x_n} \quad (10.32)$$

where  $x_0$  and  $x_n$  are amplitudes measured  $n$  cycles apart, as shown in Figure 10.38. Equation 10.32 is based on the assumption of viscous damping, but for light damping, the loss factor,  $\eta$ , is related to the logarithmic decrement by [100]

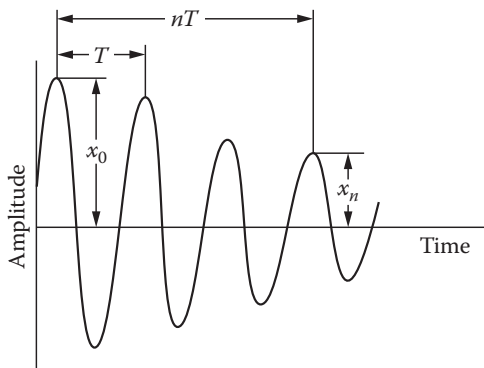
$$\eta = \frac{\Delta}{\pi} \quad (10.33)$$

**FIGURE 10.37**

Correction factors required to correct modulus values from resonant frequency measurements using the Bernoulli–Euler theory to values using the Timoshenko beam theory. Factors are plotted as a function of mode number for several values of  $E/G$  and length/thickness ratio of 100. (From Dudek, T. J. 1970. *Journal of Composite Materials*, 4, 232–241. With permission.)

Care must be taken to ensure that only one mode of vibration is present in the response decay curve, as the damping value should be measured for one particular mode.

One type of forced vibration test method involves fixed frequency oscillation of the specimen in a testing machine and simultaneous plotting of the resulting stress–strain hysteresis loop (Figure 10.39). Using the dimensions  $a$ ,

**FIGURE 10.38**

Free vibration decay curve for logarithmic decrement measurement.

$b$ , and  $c$  from such hysteresis loops at a frequency,  $f$ , the components of the complex modulus can then be estimated by the equations [97]

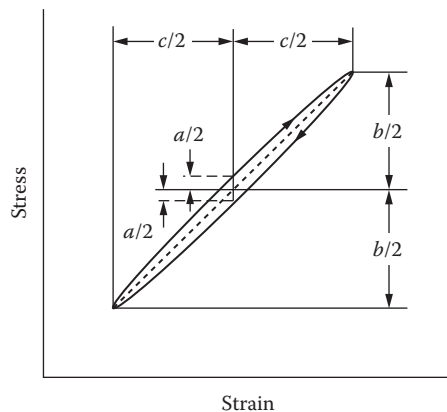
$$\eta(f) = \frac{a}{b} \quad (10.34)$$

and

$$E'(f) = \frac{b}{c} \quad (10.35)$$

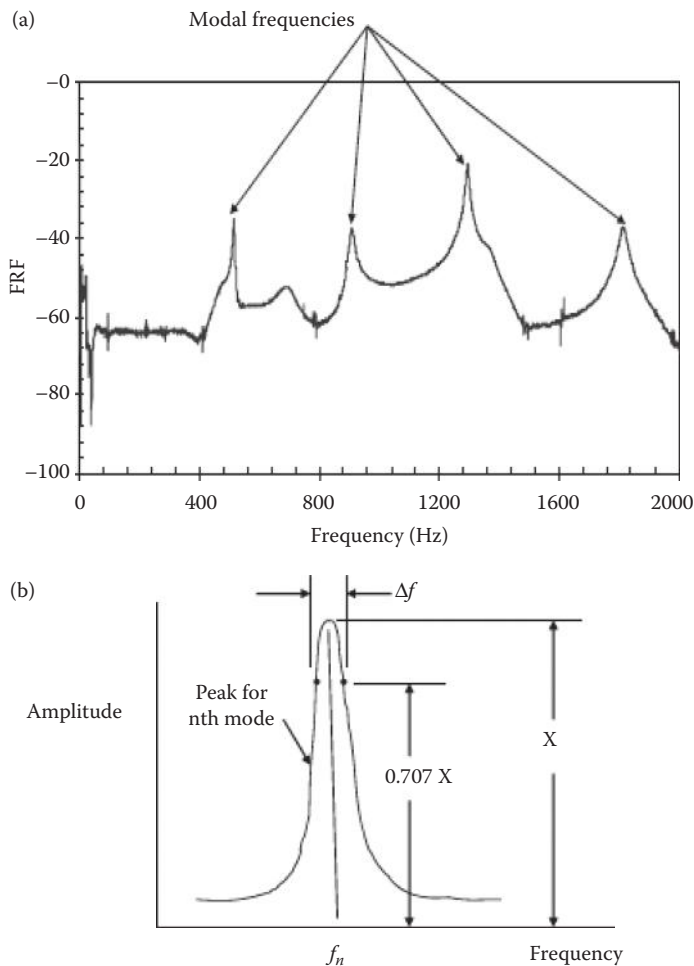
Another forced vibration technique is based on variation of the excitation frequency, simultaneous measurement of the response, and plotting of the magnitude and/or phase of the response in the frequency domain. The resulting frequency response function (FRF), or frequency response spectrum (Figure 10.40a), has a number of peaks that represent natural frequencies of the specimen, and SDOF curve-fitting techniques can be applied to these peaks to extract the data needed to compute the complex modulus. The storage modulus is determined by substituting the peak frequency for a particular mode into the appropriate specimen frequency equation as described previously. As shown in Figure 10.40b, the loss factor may be determined by using the half-power bandwidth equation at a particular peak as

$$\eta = \frac{\Delta f}{f_n} \quad (10.36)$$



**FIGURE 10.39**

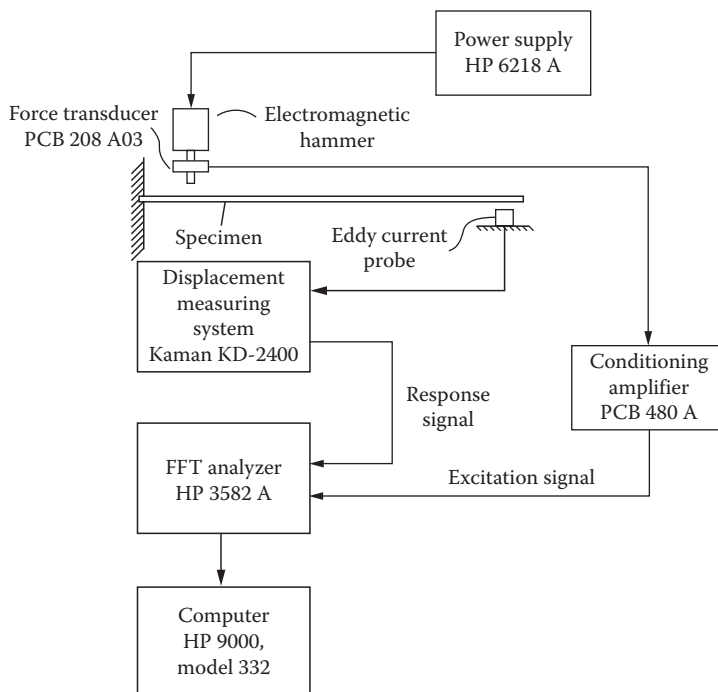
Hysteresis loop from fixed frequency forced oscillation test.

**FIGURE 10.40**

(a) Typical specimen frequency response function (FRF) vs. frequency with peaks corresponding to modal frequencies, and (b) single-degree-of-freedom (SDOF) curve-fit to peak at modal frequency  $f_n$  using half-power bandwidth method.

where  $\Delta f$  is the bandwidth at the half power points on the peak and  $f_n$  the peak frequency for the  $n$ th mode of vibration

Digital frequency spectrum analyzers or fast Fourier transform (FFT) analyzers are commonly used for this purpose. In recent years, virtual instrument software running on personal computers has become a popular alternative to dedicated spectrum analyzer instruments. Excitation may be variable frequency sinusoidal (or swept sine), random, or impulsive. The impulse–frequency response method is perhaps the fastest and simplest method in this category [98,101,102]. A cantilever beam test apparatus based

**FIGURE 10.41**

Cantilever beam test apparatus for impulse–frequency response method.

on the impulse–frequency response method is shown in Figure 10.41. In this apparatus the beam specimen is impulsively excited by a hammer that has a small force transducer in its tip, while the specimen response is monitored by a noncontacting displacement sensor. Excitation and response signals are fed into the FFT analyzer, which computes and displays the frequency response function in real time. Curve fitting to the frequency response curve and calculation of the complex modulus are accomplished by a desktop computer that is interfaced with the FFT analyzer. Frequency dependence of the complex moduli can be determined by testing beams of different lengths and/or by taking data for multiple modes of vibration. The experimental data in Figures 8.21 and 8.41 were obtained by using this method.

Impulse techniques have also been used in conjunction with laminated plate vibration models to determine the elastic constants of composite plates [103,104]. An impulse test apparatus based on this method has been developed for measurement of the complex extensional modulus of reinforcing fibers at elevated temperatures [105,106]. Damping has been found to be particularly sensitive to damage and degradation in composites, and the impulse-frequency response method has been successfully used in such studies [107,108].

In recent years, the use of modal vibration measurements to determine dynamic mechanical properties of composite materials and their constituents has been extended to numerous nontraditional applications such as determination of global elastic constants of composites, the distribution of reinforcing fibers within composites, time-domain creep response of composites, elevated-temperature behavior of composites and their constituents, interlaminar fracture toughness of composites, and the presence of defects, damage, and degradation in composites and adhesively bonded composite structures [109]. Similarly, investigations based on measurements of modal vibration response have been extended to the micromechanical and nanomechanical levels. For example, microscanning laser vibrometry has been used to investigate the modal vibration response of composite microelectromechanical systems such as microlayered ultrasonic sensors [110], and measured modal frequencies of cantilevered carbon nanotubes have been used in a combined experimental and numerical approach to indirectly determine the elastic modulus of the nanotubes [111].

In conclusion, dynamic test methods provide rapid and inexpensive alternatives to conventional static test methods in the measurement of composite stiffnesses. The dynamic test also yields information on the internal damping of the material, which is not only an important design property, but also a useful nondestructive test parameter that can be related to the integrity of the material. It is conceivable that such test methods could be integrated into the manufacturing process itself in order to provide on-line monitoring and control of composite material properties.

### Example 10.5

Describe a test method and the necessary equations for measurement of the frequency-dependent complex shear modulus  $G_{12}^*(f)$  of a unidirectional, specially orthotropic composite lamina at a frequency  $f$ , where  $f$  is in Hz.

#### SOLUTION

There are several possible test methods that could be used here. One possibility is to use forced vibration of a composite plate specimen mounted in a rail shear test fixture such as that shown in Figure 10.23b. Instead of a static load  $P$  as in Example 10.4, the applied load  $P(f)$  would vary sinusoidally with frequency  $f$ . The resulting frequency-dependent shear stress  $\tau_{12}(f) = P(f)/2Lt$  and shear strain  $\gamma_{12}(f) = 2\epsilon'_x(f)$  would be measured, where  $\epsilon'_x(f)$  is the strain measured by the strain gage which is oriented at  $45^\circ$  to the  $x$  axis as shown in Figure 10.23b. The oscillatory shear stress and shear strain are then plotted in  $x - y$  fashion to generate a hysteresis loop as in Figure 10.39. From the dimensions of the hysteresis loop, Equation 10.34 would then give the shear loss factor  $\eta_{12}(f) = a/b$  and Equation 10.35 would give the shear storage modulus  $G'_{12}(f) = b/c$ . Finally, the complex shear modulus  $G_{12}^*(f) = G'_{12}(f)[1 + i\eta_{12}(f)]$ . A potential problem with this test method would be extraneous friction damping between the specimen and the test fixture, which would cause errors in the loss factor measurement. Proper

fixture design and application of sufficient clamping force can help to minimize such extraneous losses. Calibration tests of specimens having known loss factors are also useful.

## 10.5 Measurement of Hygrothermal Properties

In Chapter 5, the analysis of hygrothermal behavior of polymers and polymer composites was shown to involve such important properties as the glass transition temperature, the coefficient of thermal expansion, the moisture diffusivity and the equilibrium moisture content. This section summarizes the relevant ASTM standards for measurement of these quantities.

### 10.5.1 Glass Transition Temperature Tests

ASTM D7028-07e1 [96] describes a method for determining the glass transition temperature,  $T_g$ , of polymer matrix composites by using dynamic mechanical analysis (DMA). In order to use this method, a DMA plot of the components of the complex modulus vs. temperature similar to that shown in Figure 10.36 must be generated by subjecting the specimen to vibration in a DMA instrument and measuring its response over the desired temperature range. The storage modulus,  $E'$ , decreases rapidly as the temperature rises through the glass transition region, and two straight lines A and B are fitted to the  $E'$  vs. temperature curve as shown in Figure 10.42, with line A tangent to the curve below the transition and line B tangent to the curve in the transition region. The so-called DMA  $T_g$  is defined to be the temperature at which the two tangent lines A and B intersect.

Another method for determining  $T_g$  was illustrated in Figure 8.23, but is not covered by an ASTM standard. In this method, the change in volume or

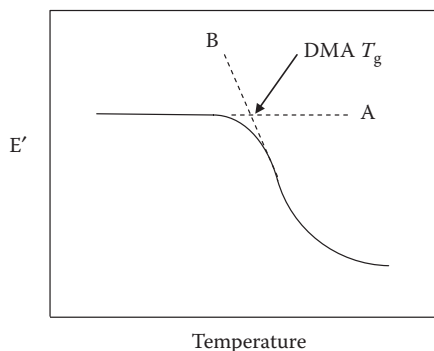


**FIGURE 10.42**

Determination of DMA  $T_g$  from storage modulus vs. temperature plot.

displacement of the specimen is measured with increasing temperature, and  $T_g$  is the temperature at which the slope of the volume vs. temperature begins to increase, indicating that the free volume between the polymer molecules is increasing faster than the volume occupied by the molecules.

### 10.5.2 Thermal Expansion Tests

All of the test methods for measurement of the coefficient of thermal expansion (CTE, or  $\alpha$ ) involve the measurement of thermal strain,  $\epsilon^T$ , or the change in length,  $\Delta L$ , of a specimen of original length  $L_0$  which is subjected to a temperature change  $\Delta T$  in an environmental chamber, and calculation according to the definition

$$\alpha = \frac{\epsilon^T}{\Delta T} = \frac{\Delta L}{L_0 \Delta T} \quad (10.37)$$

As indicated in Section 5.3, the CTE for composites may be dependent on reinforcement orientation, in which case the appropriate subscripts such as  $\alpha_1$  or  $\alpha_2$  are required and separate tests are needed for longitudinal and transverse CTEs (e.g., see Figure 5.15). Although there is no specific ASTM standard for measuring the coefficient of thermal expansion (CTE) of polymer composites, there are several relevant standards for determining the CTE of solid materials and plastics. D696-08 [112] for plastics and E228-06 [113] for solids both involve the use of a dilatometer, an instrument for precision measurement of the thermally induced change in length of the specimen. E289-04 [114] involves the use of an interferometer to measure the thermally induced displacements, and is particularly useful for low-CTE materials. Although not covered by the standards, direct measurement of thermally induced strains by using electrical resistance strain gages is a commonly used and inexpensive alternative. However, care must be taken to select strain gages that are temperature-compensated for the substrate material being tested and strain gage adhesives that are capable of withstanding elevated test temperatures without significant softening or creep.

#### Example 10.6

For the thermal expansion data plotted in Figure 5.15, determine the longitudinal CTE of the Kevlar 49/epoxy composite.

#### SOLUTION

From the slope of the thermal strain vs. temperature plots in Figure 5.15 over the temperature range from, say 25°C to 140°C ( $\Delta T = 115^\circ\text{C}$ ), and assuming that the curves converge to zero strain at 25°C, the longitudinal CTE for Kevlar 49/epoxy is

$$\alpha_1 = \frac{\epsilon_1^T}{\Delta T} = \frac{-0.0004 - 0}{140 - 25} = -3 \times 10^{-6} \text{ m/m}^\circ\text{C}$$

Several fibers such as Kevlar and carbon and their composites have negative longitudinal CTEs.

### 10.5.3 Moisture Absorption Tests

In Section 5.2, the through-the-thickness moisture diffusivity,  $D_z$ , and the saturation equilibrium moisture content,  $M_m$ , were shown to be the key properties that are needed to characterize moisture absorption in polymers and polymer composites. ASTM D5229 [115] deals with the measurement of these properties for polymer matrix composites. The test involves exposure of an initially dry test specimen to a moist environment on both sides and measurement of the moisture pickup (expressed as a percent of the specimen weight) as a function of time,  $t$ . Equation 5.6 and Figure 5.8 describe the moisture absorption as a function of time for an assumed Fickian diffusion process. D5229 [115] describes the conditions that must be met by the test data in order for the moisture absorption process to be treated as a Fickian process. Assuming that the test data meets these conditions, if the weight percent moisture  $M$  is plotted as a function of  $\sqrt{t}$  for an initially dry ( $M_i = 0$ ) specimen as shown in Figure 5.12, the initial part of the moisture absorption curve is essentially linear, and in this linear region Equation 5.6 can be approximated by [116]

$$G = \frac{M}{M_m} = \frac{4}{h} \sqrt{\frac{D_z t}{\pi}} \quad (10.38)$$

where all parameters have been defined in Section 5.2. The slope of the linear part of the  $M$  vs.  $\sqrt{t}$  curve can then be found by applying Equation 10.38 to two moisture contents  $M_2$  and  $M_1$  at  $\sqrt{t_2}$  and  $\sqrt{t_1}$ , respectively, where  $M_2 > M_1$ . The resulting slope is

$$\frac{M_2 - M_1}{\sqrt{t_2} - \sqrt{t_1}} = \frac{4M_m}{h} \sqrt{\frac{D_z}{\pi}} \quad (10.39)$$

and the resulting value of the through-the-thickness diffusivity is [115]

$$D_z = \pi \left( \frac{h}{4M_m} \right)^2 \left( \frac{M_2 - M_1}{\sqrt{t_2} - \sqrt{t_1}} \right)^2 \quad (10.40)$$

The saturation equilibrium moisture content,  $M_m$ , is the value of  $M$  to which the moisture absorption curve becomes asymptotic at long times. According to D5229,  $M_m$  has been reached when  $M$  changes less than 0.01% within the span of the reference time period, and a table of reference time periods is provided. For example, if  $D_z$  is unknown, the reference time period is 7 days.

## PROBLEMS

- Derive Equation 10.2.
- The results of longitudinal, transverse, and  $45^\circ$  off-axis tensile tests on samples from an orthotropic lamina are shown in Figure 10.43. Based on these results, find numerical values for the engineering constants  $E_1$ ,  $E_2$ ,  $v_{12}$ , and  $G_{12}$ .
- The in-plane shear modulus,  $G_{12}$ , of a carbon/epoxy lamina is to be measured by using the rail shear test shown in Figure 10.44. The test is conducted on a 10 in.  $\times$  10 in.  $\times$  0.1 in. (254 mm  $\times$  254 mm  $\times$  2.54 mm) panel specimen, which deforms under the applied load as shown. Determine the value of  $G_{12}$  from these data.
- The  $45^\circ$  off-axis test shown in Figure 10.45 is conducted on a 10 in.  $\times$  1 in.  $\times$  0.1 in. (254 mm  $\times$  25.4 mm  $\times$  2.54 mm) carbon/epoxy specimen, which deforms as shown under the applied load. It is also known from separate tensile tests that  $E_1 = 32 \times 10^6$  psi (220 GPa),  $E_2 = 1.0 \times 10^6$  psi (6.89 GPa), and  $v_{12} = 0.3$ . Determine the value of  $G_{12}$  from these test data.
- A  $45^\circ$  off-axis specimen cut from an AS/3501 carbon/epoxy lamina is subjected to a tensile test. The specimen is 3 mm thick and 25 mm wide, and a tensile load of  $F_x = 1$  kN on the specimen produces a corresponding strain  $\epsilon_x = 0.0003$ . It is claimed that the off-axis Young's modulus,  $E_x$ , can be determined from these results. Is this a valid claim? If so, why? If not, why not?
- Describe the measurements that must be taken and the equations that must be used to determine the shear creep compliance,  $S_{66}(t)$ , of a unidirectional viscoelastic lamina by using a rail shear test.
- Extensional vibration experiments are conducted on longitudinal, transverse, and  $45^\circ$  off-axis unidirectional composite specimens,

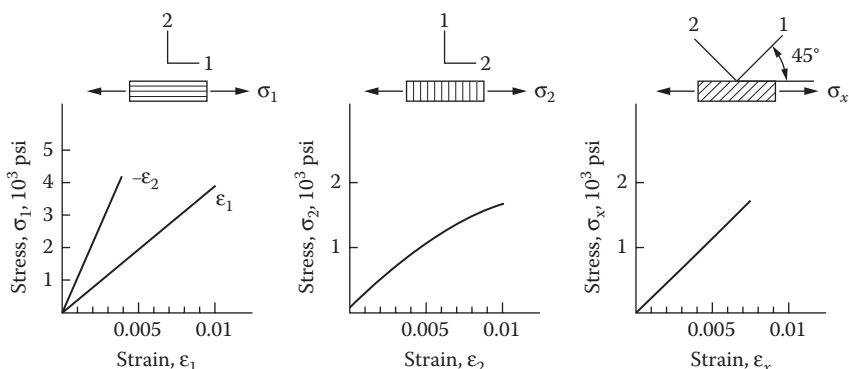


**FIGURE 10.43**

Stress-strain curves for longitudinal, transverse, and  $45^\circ$  off-axis tensile tests of an orthotropic lamina.

Specimen thickness = 0.1 in.

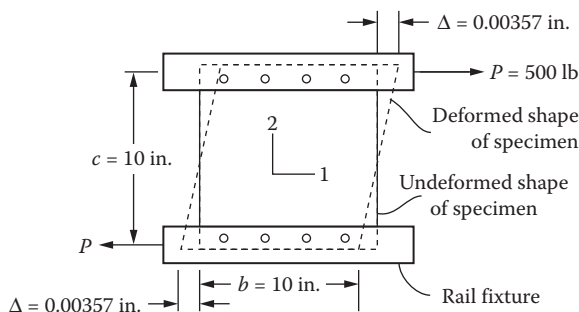


**FIGURE 10.44**

Shear deformation of a carbon/epoxy specimen during a rail shear test.

and the complex moduli results for a particular vibration frequency are, respectively:

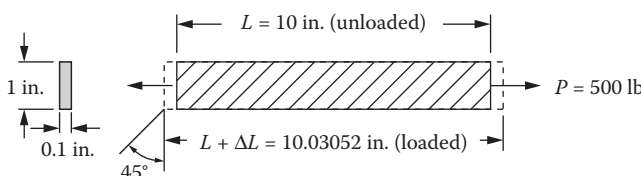
$$E_1^* = E'_1(1 + i\eta_1) = 35.6(1 + 0.004i)\text{GPa}, \quad \text{for } \theta = 0^\circ$$

$$E_2^* = E'_2(1 + i\eta_2) = 10.8(1 + 0.009i)\text{GPa}, \quad \text{for } \theta = 90^\circ$$

$$E_x^* = E'_x(1 + i\eta_x) = 11.6(1 + 0.011i)\text{GPa}, \quad \text{for } \theta = 45^\circ$$

Using the above data derive the equations for both parts of the complex shear modulus,  $G_{12}^* = G'_{12}(1 + i\eta_{12})$ , then find numerical values for both parts. Assume that all loss factors are very small ( $\ll 1$ ), and that the major Poisson's ratio  $\nu_{12} = 0.3$  is a real constant.

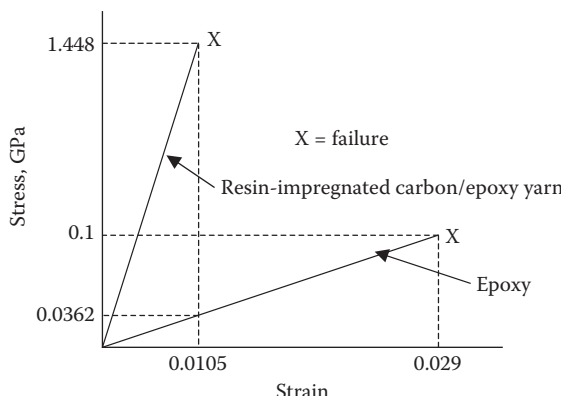
8. Using the results from Problem 7, derive the equations for both parts of the off-axis complex modulus,  $E_x^* = E'_x(1 + i\eta_x)$ , for an arbitrary angle  $\theta$ ; then find numerical values of both parts for an angle of  $\theta = 30^\circ$ .
9. Describe an experiment, and give the necessary equations for measurement of the complex flexural modulus,  $E_{fx}^*$ , of a symmetric laminated beam.
10. Describe an experiment, and give the necessary equations for the measurement of the complex extensional (or longitudinal) modulus,  $E_x^*$ , of a symmetric laminated bar.



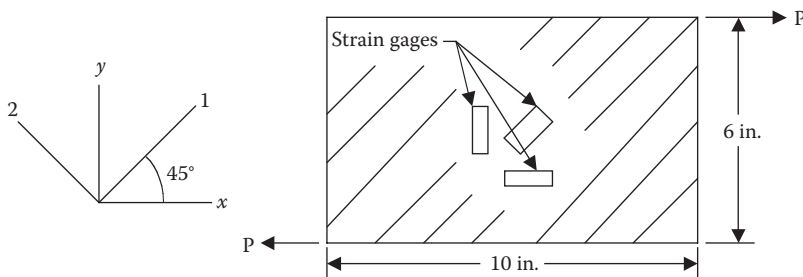
**FIGURE 10.45**

Extensional deformation of a carbon/epoxy specimen during a  $45^\circ$  off-axis tensile test.

11. Describe an experiment, and give the necessary equations for the measurement of the complex through-thickness shear modulus,  $G_{23}^*$ , of a unidirectional, specially orthotropic, transversely isotropic beam.
12. Describe an experiment, and give the necessary equations for measurement of the complex Young's modulus,  $E_m^*$ , of an isotropic matrix material.
13. Describe an experiment, and give the necessary equations for the measurement of the complex longitudinal modulus,  $E_{f1}^*$ , of a reinforcing fiber.
14. Describe an experiment, and give the necessary equations for measurement of the through-thickness creep compliance,  $S_{32}(t)$ , of a specially orthotropic, transversely isotropic lamina.
15. In order to determine the tensile Young's modulus and tensile strength of carbon fibers, a tensile test of a resin-impregnated carbon/epoxy yarn having a fiber volume fraction of 0.6 is conducted. A separate tensile test is conducted on the neat resin epoxy matrix material, and both stress-strain curves are shown in Figure 10.46. Using these two stress-strain curves and micromechanics models, determine the fiber tensile Young's modulus,  $E_{f1}$ , and the fiber tensile strength,  $s_{f1}^{(+)}$ .
16. A 45° off-axis rail shear test specimen of an orthotropic lamina is shown in Figure 10.47. Attached to the specimen are three strain gages that measure the normal strains  $\varepsilon_x$ ,  $\varepsilon_y$ , and  $\varepsilon_t$  along the  $x$ ,  $y$ , and 1 directions, respectively. The specimen thickness  $t = 0.1$  in. and the length and width are shown in Figure 10.47. The applied shear load along the  $x$  direction is  $P = 500$  lb, while the three measured strains are  $\varepsilon_x = 0.00056$ ,  $\varepsilon_y = 0.00075$ , and  $\varepsilon_t = 0.00078$ . Answer the following questions, giving both numerical values and units where appropriate. (a) Is it possible to determine the off-axis shear modulus  $G_{xy}$  from this data? If not, why not? If so, calculate  $G_{xy}$ . (b)

**FIGURE 10.46**

Stress-strain curves for epoxy and resin-impregnated carbon/epoxy yarn, for problem 15.

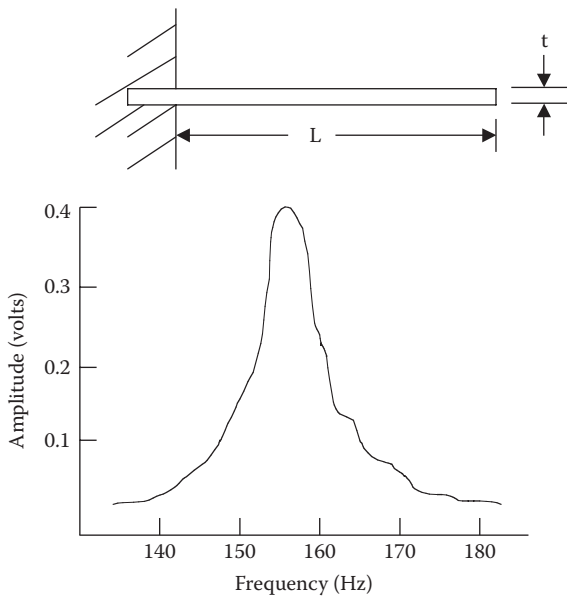
**FIGURE 10.47**

Strain-gaged rail shear test specimen for problem 16.

Is it possible to determine the Poisson's ratio  $\nu_{xy}$  from this data? If not, why not? If so, calculate  $\nu_{xy}$ . (c) Is it possible to determine the shear-coupling ratio  $\eta_{xy,x}$  from this data? If not, why not? If so, calculate  $\eta_{xy,x}$ . (d) Is it possible to determine the material shear strength  $s_{LT}$  from this data? If not, why not? If so, calculate  $s_{LT}$ .

*Hint:* Equation 10.10 is based on the assumption that the  $x,y$  axes are the same as the principal material axes 1,2 so that  $\varepsilon_x = \varepsilon_1 = \varepsilon_y = \varepsilon_2 = 0$ , but in this case the 1,2 axes are oriented at  $\theta = 45^\circ$  from the  $x,y$  axes and Equation 10.10 is not valid here.

17. The specimen geometry and the frequency response curve for the second mode flexural vibration of a laminated composite

**FIGURE 10.48**

Specimen geometry and measured frequency response curve for second flexural mode vibration of composite cantilever beam in problem 17.

cantilever beam specimen is shown in Figure 10.48. The specimen has length  $L = 8.913$  in, width  $w = 0.756$  in., thickness  $t = 0.04$  in., and specific weight of  $\gamma = 0.064$  lb/in.<sup>3</sup> (note:  $\gamma = \rho g$ , where  $\rho$  = density and  $g$  = gravitational acceleration = 386 in./s<sup>2</sup>). The specimen is clamped across the width as shown. Based on this data, give your best estimates for the following properties of the specimen, (a) the flexural modulus,  $E_f$ , and (b) the flexural loss factor,  $\eta_f$ .

18. Samples of unidirectional Kevlar 49/epoxy and S-glass/epoxy composites are subjected to elevated temperatures in an oven and the resulting thermal strains are measured by using strain gages oriented along the 1 and 2 directions, as shown in Figure 5.15. From the data in Figure 5.15, estimate the longitudinal thermal expansion coefficient  $\alpha_1$  and the transverse thermal expansion coefficient  $\alpha_2$  for both materials.
19. For the linear part of the moisture absorption curve for a temperature of 77°C in Figure 5.12, and assuming a specimen thickness of 2.54 mm, use the relevant analysis from ASTM D5229 to estimate the through-the-thickness diffusivity  $D_z$ .

---

## References

1. ASTM Standards 2009. Vol. 15.03, *Space Simulation; Aerospace and Aircraft; Composite Materials*. ASTM International, West Conshohocken, PA.
2. ASTM Standards 2009. Vol. 15.01, *Refractories; Activated Carbon; Advanced Ceramics*. ASTM International, West Conshohocken, PA.
3. Adams, D. F., Carlsson, L. A., and Pipes, R. B. 2003. *Experimental Characterization of Advanced Composite Materials*, 3rd edn. CRC Press, Boca Raton, FL.
4. Sharpe, W. N. Jr. Ed. 2008. *Springer Handbook of Experimental Solid Mechanics*. Springer, New York, NY.
5. D4762-08. 2009. Standard guide for testing polymer matrix composite materials, Vol. 15.03, *Space Simulation; Aerospace and Aircraft; Composite Materials*. ASTM International, West Conshohocken, PA.
6. C 1557.03R08. 2010. Standard test method for tensile strength and young's modulus of fibers, Vol. 15.01, *Refractories; Activated Carbon; Advanced Ceramics*. ASTM International, West Conshohocken, PA.
7. McMahon, P. E. 1973. Graphite fiber tensile property evaluation, *Analysis of Test Methods for High Modulus Fibers and Composites*, ASTM STP 521, pp. 367–389. ASTM International, West Conshohocken, PA.
8. D4018-99. 2008. Standard test methods for properties of continuous filament carbon and graphite fiber tows, Vol. 15.03, *Space Simulation; Aerospace and Aircraft; Composite Materials*. ASTM International, West Conshohocken, PA.
9. Tsai, C.-L. and Daniel, I. M. 1994. Method for thermo-mechanical characterization of single fibers. *Composites Science and Technology*, 50, 7–12.
10. Kawabata, S. 1989. Measurements of anisotropic mechanical property and thermal conductivity of single fiber for several high performance fibers, in Vinson,

- J. R. ed., *Proceedings of the 4th Japan-U.S. Conference on Composite Materials*, pp. 253–262. CRC Press, Boca Raton, FL.
11. Tsai, C. L. and Daniel, I. M. 1999. Determination of shear modulus of single fibers. *Experimental Mechanics*, 39(4), 284–286.
  12. D638-10. 2010. Standard test method for tensile properties of plastics, Vol. 08.01, *Plastics*. ASTM International, West Conshohocken, PA.
  13. D618-08. 2008. Standard practice for conditioning plastics for testing, Vol. 08.01, *Plastics*. ASTM International, West Conshohocken, PA.
  14. D695-10. 2010. Standard test method for compressive properties of rigid plastics, Vol. 08.01, *Plastics*. ASTM International, West Conshohocken, PA.
  15. Novak, R. C. and Bert, C. W. 1968. Theoretical and experimental bases for more precise elastic properties of epoxy. *Journal of Composite Materials*, 2, 506–508.
  16. D790-10. 2010. Standard test methods for flexural properties of unreinforced and reinforced plastics and electrical insulating materials, Vol. 08.01, *Plastics*. ASTM International, West Conshohocken, PA.
  17. D3171-09. 2005. Standard test methods for constituent content of composite materials, Vol. 15.03, *Space Simulation; Aerospace and Aircraft; Composite Materials*. ASTM International, West Conshohocken, PA.
  18. D3039/D3039M-08. 2008. Standard test method for tensile properties of polymer matrix composite materials, Vol. 15.03, *Space Simulation; Aerospace and Aircraft; Composite Materials*. ASTM International, West Conshohocken, PA.
  19. Carlsson, L. A. and Pipes, R. B. 1989. *Experimental Characterization of Advanced Composite Materials*. Prentice-Hall, Inc., Englewood Cliffs, NJ.
  20. Pagano, N. J. and Halpin, J. C. 1968. Influence of end constraint in the testing of anisotropic bodies. *Journal of Composite Materials*, 2, 18–31.
  21. Jones, R. M. 1975. *Mechanics of Composite Materials*. Hemisphere Publishing Co., New York, NY.
  22. Horgan, C. O. 1972. Some remarks on Saint-Venant's principle for transversely isotropic composites. *Journal of Elasticity*, 2(4), 335–339.
  23. Choi, I. and Horgan, C. O. 1977. Saint-Venant's principle and end effects in anisotropic elasticity. *Journal of Applied Mechanics*, 44, 424–430.
  24. Horgan, C. O. 1982. Saint-Venant end effects in composites. *Journal of Composite Materials*, 16, 411–422.
  25. Rawlinson, R. A. 1991. The use of crossply and angleply composite test specimens to generate improved material property data, How concept becomes reality, *Proceedings of the 36th International SAMPE Symposium and Exhibition*, 36, Book 1, pp. 1058–1068. Society for the Advancement of Material and Process Engineering, Covina, CA.
  26. Hart-Smith, L. J. 1992. Backing out equivalent unidirectional lamina strengths from tests on cross-plied laminates, in *Materials. Working for You in the 21st Century. Proceedings of the 37th International SAMPE Symposium and Exhibition*, 37, pp. 977–990. Society for the Advancement of Material and Process Engineering, Covina, CA.
  27. Berg, J. S. and Adams, D. F. 1989. An evaluation of composite material compression test methods. *Journal of Composites Technology and Research*, 11(2), 41–46.
  28. Schoeppner, G. A. and Sierakowski, R. L. 1990. A review of compression test methods for organic matrix composites. *Journal of Composites Technology and Research*, 12(1), 3–12.

29. Welsh, J. R. and Adams, D. F. 1997. Current status of compression test methods for composite materials. *SAMPE Journal*, 33(1), 35–43.
30. Odom, E. M. and Adams, D. F. 1990. Failure modes of unidirectional carbon/epoxy composite compression specimens. *Composites*, 21(4), 289–296.
31. Budiansky, B. and Fleck, N. A. 1993. Compressive failure of fibre composites. *Journal of the Mechanics and Physics of Solids*, 41(1), 183–211.
32. D3410/D3410M-03 (Reapproved 2008), Standard test method for compressive properties of polymer matrix composite materials with unsupported gage section by shear loading, Vol. 15.03, *Space Simulation; Aerospace and Aircraft; Composite Materials*. ASTM International, West Conshohocken, PA, 2009.
33. D5467/D5467M-97 (Reapproved 2004), Standard test method for compressive properties of unidirectional polymer matrix composite materials using a sandwich beam, Vol. 15.03, *Space Simulation; Aerospace and Aircraft; Composite Materials*. ASTM International, West Conshohocken, PA, 2009.
34. D6641/D6641M-09, Standard test method for determining compressive properties of laminated polymer matrix composite materials using a combined loading compression (CLC) test fixture, Vol. 15.03, *Space Simulation; Aerospace and Aircraft; Composite Materials*. ASTM International, West Conshohocken, PA, 2009.
35. Adsit, N. R. 1983. Compression testing of graphite/epoxy, in Chait, R. and Papirno, R. eds., *Compression Testing of Homogeneous Materials*, ASTM STP 808, pp. 175–186. American Society for Testing and Materials, Philadelphia, PA.
36. Crasto, A. S. and Kim, R. Y. 1991. Compression strength of advanced composites from a novel mini-sandwich beam. *SAMPE Quarterly*, 22(3), 29–39.
37. Wilson, D. W., Altstadt, V., and Prandy, J. 1992. On the use of laminate test methods to characterize lamina compression strength, in *Materials Working for You in the 21st Century, Proceedings of the 37th International SAMPE Symposium and Exhibition*, 37, pp. 606–619. Society for the Advancement of Material and Process Engineering, Covina, CA.
38. Boeing Specification Support Standard BSS 7260, *Advanced Composite Tests*. The Boeing Company, Seattle, WA, issued 1982, rev. 1988.
39. Nettles, A. T. and Hodge, A. J. 1991. Compression after impact testing of thin composite materials, in *Advanced materials/affordable processes, Proceedings of the 23rd International SAMPE Technical Conference*, 23, pp. 177–183. Society for the Advancement of Material and Process Engineering, Covina, CA.
40. D7137/D7137M-05e<sup>1</sup>, 2005. Standard test method for compressive residual strength properties of damaged polymer matrix composite plates, Vol. 15.03, *Space Simulation; Aerospace and Aircraft; Composite Materials*. ASTM International, West Conshohocken, PA.
41. Adams, D. F. 2005. A comparison of shear test methods. *High Performance Composites*, 13(5), 9–10.
42. D5379/D5379M-05, 2005. Standard test method for shear properties of composite materials by the V-notched beam test method, Vol. 15.03, *Space Simulation; Aerospace and Aircraft; Composite Materials*. ASTM International, West Conshohocken, PA.
43. D7078/D7078M-05, 2005. Standard test method for shear properties of composite materials by the V-notched rail shear test method, Vol. 15.03, *Space Simulation; Aerospace and Aircraft; Composite Materials*. ASTM International, West Conshohocken, PA.

44. Iosipescu, N. 1967. New accurate procedure for single shear testing of metals. *Journal of Materials*, 2(3), 537–566.
45. Walrath, D. E. and Adams, D. F. 1983. The Iosipescu shear test as applied to composite materials. *Experimental Mechanics*, 23(1), 105–110.
46. Adams, D. F. and Walrath, D. E. 1987. Current status of the Iosipescu shear test method. *Journal of Composite Materials*, 21, 484–505.
47. Adams, D. F. and Walrath, D. E. 1987. Further development of the Iosipescu shear test method. *Experimental Mechanics*, 27(2), 113–119.
48. Adams, D. F. 1990. The Iosipescu shear test method as used for testing polymers and composite materials. *Polymer Composites*, 11(5), 286–290.
49. Lee, S. and Munro, M. 1986. Evaluation of in-plane shear test methods for advanced composite materials by the decision analysis technique. *Composites*, 17(1), 13–22.
50. D4255/D4255M-01, 2005. Standard test method for in-plane shear properties of polymer matrix composite materials by the rail shear method, Vol. 15.03, *Space Simulation; Aerospace and Aircraft; Composite Materials*. ASTM International, West Conshohocken, PA.
51. D3518/D3518M-94, 2007. Standard test method for in-plane shear response of polymer matrix composite materials by tensile test of a  $\pm 45^\circ$  laminate, Vol. 15.03, *Space Simulation; Aerospace and Aircraft; Composite Materials*. ASTM International, West Conshohocken, PA.
52. D2344/D2344M-00, 2006. Standard test method for short-beam strength of polymer matrix composite materials and their laminates, Vol. 15.03, *Space Simulation; Aerospace and Aircraft; Composite Materials*. ASTM International, West Conshohocken, PA.
53. Whitney, J. M. 1985. Elasticity analysis of orthotropic beams under concentrated loads. *Composites Science and Technology*, 22, 167–184.
54. D7264/D7264M-07, 2009. Standard test method for flexural properties of polymer matrix composite materials. Vol. 15.03, *Space Simulation; Aerospace and Aircraft; Composite Materials*. ASTM International, West Conshohocken, PA.
55. Whitney, J. M., Browning, C. E., and Hoogsteden, W. 1982. A double cantilever beam test for characterizing mode I delamination of composite materials. *Journal of Reinforced Plastics and Composites*, 1, 297–313.
56. D5528-01(2007)e3, 2007. Standard test method for mode I interlaminar fracture toughness of unidirectional fiber-reinforced polymer matrix composites, Vol. 15.03, *Space Simulation; Aerospace and Aircraft; Composite Materials*. ASTM International, West Conshohocken, PA.
57. Russell, A. J. and Street, K. N. 1983. Moisture and temperature effects on the mixed mode delamination fracture of unidirectional graphite/epoxy, DREP Technical Memo 83-22, Defence Research Establishment Pacific, Victoria, B.C., Canada.
58. Russell, A. J. and Street, K. N. 1985. Moisture and temperature effects on the mixed mode delamination fracture of unidirectional graphite/epoxy, in Johnson, W. S. ed., *Delamination and Debonding of Materials*. ASTM STP 876, 349–370, American Society for Testing and Materials, Philadelphia, PA.
59. Carlsson, L. A., Gillispie, J. W., Jr., and Pipes, R. B. 1986. On the analysis and design of the end notched flexure (ENF) specimen for mode II testing. *Journal of Composite Materials*, 20, 594–604.
60. D6671/D6671M-06, 2009. Standard test method for mixed mode I—mode II interlaminar fracture toughness of unidirectional fiber-reinforced polymer

- matrix composites, Vol. 15.03, *Space Simulation; Aerospace and Aircraft; Composite Materials*. ASTM International, West Conshohocken, PA.
61. Reeder, J. R. and Crews, J. H., Jr. 1990. Mixed mode bending method for delamination testing. *AIAA Journal*, 28(7), 1270–1276.
  62. Reeder, J. R. and Crews, J. H., Jr. 1992. Redesign of the mixed mode bending delamination test to reduce nonlinear effects. *Journal of Composites Technology and Research*, 14(1), 12–19.
  63. Liu, Z., Gibson, R. F., and Newaz, G. M. 2002. The use of a mixed mode bending test for characterization of mixed mode fracture behavior of adhesively bonded metal joints. *The Journal of Adhesion*, 78, 223–244.
  64. Liu, Z., Gibson, R. F., and Newaz, G. M. 2002. Improved analytical models for mixed mode bending tests of adhesively bonded joints. *The Journal of Adhesion*, 78, 245–268.
  65. Drzal, L. T., Rich, M. J., and Lloyd, P. F. 1982. Adhesion of graphite fibers to epoxy matrices: I. The role of fiber surface treatment. *Journal of Adhesion*, 16, 1–30.
  66. Drzal, L. T., Rich, M. J., Koenig, M. F., and Lloyd, P. F. 1983. Adhesion of graphite fibers to epoxy matrices: II. The effect of fiber finish. *Journal of Adhesion*, 16, 133–152.
  67. Drzal, L. T., Rich, M. J., and Subramoney, S. 1987. Fiber-matrix bonding and its effect on composite properties, in *Advanced Composites III—Expanding the Technology, Proceedings of the 3rd Annual Conference on Advanced Composites*, pp. 305–308. ASM International, Materials Park, OH.
  68. McDonough, W. G., Herrera-Franco, P. J., Wu, W. L., Drzal, L. T., and Hunston, D. L. 1991. Fiber-matrix bond tests in composite materials, in *Advanced Materials/Affordable Processes, Proceedings of 23rd International SAMPE Technical Conference*, Kiamesha Lake, NY, pp. 247–258. Society for Advancement of Material and Process Engineering, Covina, CA.
  69. Mandell, J. F., Grande, D. H., Tsiang, T. H., and McGarry, F. J. 1986. Modified microbonding test for direct *in situ* fiber/matrix bond strength determination in fiber composites, in Whitney, J. M. ed., *Composite Materials: Testing and Design (Seventh Conference)*, ASTM STP 893, pp. 87–108. American Society for Testing and Materials, Philadelphia, PA.
  70. Caldwell, D. L. 1987. Determination of the interfacial strength of composites, in *Advanced Composites III—Expanding the Technology, Proceedings of the 3rd Annual Conference on Advanced Composites*, pp. 299–303. ASM International, Materials Park, OH.
  71. D5766/D5766M-07, 2009. Standard test method for open hole tensile strength of polymer matrix composite laminates, Vol. 15.03. *Space Simulation; Aerospace and Aircraft; Composite Materials*. ASTM International. West Conshohocken, PA.
  72. D6484/D6484M-04e1, 2009. Standard test method for open-hole compressive strength of polymer matrix composite laminates, Vol. 15.03, *Space Simulation; Aerospace and Aircraft; Composite Materials*. ASTM International, West Conshohocken, PA.
  73. D6742/D6742M-07, 2009. Standard practice for filled-hole tension and compression testing of polymer matrix composite laminates, Vol. 15.03, *Space Simulation; Aerospace and Aircraft; Composite Materials*, ASTM International, West Conshohocken, PA.

74. Sawicki, A. J. 2004. Development of compression design allowables for composite bolted joints using ASTM Standard D 6742. *Joining and Repair of Composite Structures*, ASTM STP 1455, Kedward, K. T. and Kim, H., eds., 199-216, ASTM International, West Conshohocken, PA.
75. D5961/D5961M-08, 2009. Standard test method for bearing response of polymer matrix composite laminates, Vol. 15.03, *Space Simulation; Aerospace and Aircraft; Composite Materials* ASTM International, West Conshohocken, PA.
76. D6873/D6873M-08, 2009. Standard practice for bearing fatigue response of polymer matrix composite laminates, Vol. 15.03, *Space Simulation; Aerospace and Aircraft; Composite Materials*, ASTM International, West Conshohocken, PA.
77. D 7332/D 7332M-07e1, 2009. Standard test method for measuring the fastener pull-through resistance of a fiber-reinforced polymer matrix composite, Vol. 15.03, *Space Simulation; Aerospace and Aircraft; Composite Materials*, ASTM International, West Conshohocken, PA.
78. Thoppul, S. D., Finegan, J., and Gibson, R. F. 2009. Mechanics of mechanically fastened joints in polymer matrix composite structures—A review. *Composites Science and Technology*, 69(3), 301–329.
79. D7337/D7337M-07, 2009. Standard test method for tensile creep rupture of fiber reinforced polymer matrix composite bars, Vol. 15.03, *Space Simulation; Aerospace and Aircraft; Composite Materials*, ASTM International, West Conshohocken, PA.
80. C480/C480M-08, 2009. Standard test method for flexure creep of sandwich constructions, Vol. 15.03, *Space Simulation; Aerospace and Aircraft; Composite Materials*. ASTM International, West Conshohocken, PA (2005).
81. Halpin, J. C. and Pagano, N. J. 1968. Observations on linear anisotropic viscoelasticity. *Journal of Composite Materials*, 2(1), 68–80.
82. Yeow, Y. T., Morris, D. H., and Brinson, H. F. 1979. Time-temperature behavior of a unidirectional graphite/epoxy composite, in Tsai S. W. ed., *Composite Materials: Testing and Design (Fifth Conference)*. ASTM STP 674, pp. 263–281. American Society for Testing and Materials, Philadelphia, PA.
83. Beckwith, S. W. 1984. Viscoelastic creep behavior of filament-wound case materials. *Journal of Spacecraft and Rockets*, 21(6), 546–552.
84. Beckwith, S. W. 1980. Creep evaluation of a glass/epoxy composite. *SAMPE Quarterly*, 11(2), 8–15.
85. Irion, M. N. and Adams, D. F. 1981. Compression creep testing of unidirectional composite materials. *Composites*, 2(2), 117–123.
86. Lou, Y. C. and Schapery, R. A. 1971. Viscoelastic characterization of a nonlinear fiber reinforced plastic. *Journal of Composite Materials*, 5, 208–234.
87. Gibson, R. F., Hwang, S. J., and Sheppard, C. H. 1990. Characterization of creep in polymer composites by the use of frequency-time transformations. *Journal of Composite Materials*, 24(4), 441–453.
88. Gibson, R. F., Hwang, S. J., Kathawate, G. R., and Sheppard, C. H. 1991. Measurement of compressive creep behavior of glass/PPS composites using the frequency-time transformation method, in *Advanced Materials/Affordable Processes, Proceedings of 23rd International SAMPE Technical Conference*, pp. 208–218. Society for the Advancement of Material and Process Engineering, Covina, CA.
89. Gibson, R. F. and Kathawate, G. R. 1991. Rapid screening of creep susceptibility of structural polymer composites, in Stokes, V. J. ed., *Plastics and Plastic Composites*:

- Material Properties, Part Performance and Process Simulation*, ASME MD, Vol. 29, pp. 161–171. American Society of Mechanical Engineers, New York, NY.
- 90. D4065-06, 2009. Standard practice for plastics: Dynamic mechanical properties: determination and report of procedures, Vol. 08.02, *Plastics (II)*. ASTM International, West Conshohocken, PA.
  - 91. D5279-08, 2009. Standard test method for plastics: dynamic mechanical properties: In Torsion, Vol. 08.03, *Plastics (III)*. ASTM International, West Conshohocken, PA.
  - 92. D5023-07, 2009. Standard test method for plastics: dynamic mechanical properties: In flexure (three point bending), Vol. 08.02, *Plastics (II)*. ASTM International, West Conshohocken, PA.
  - 93. D5024-07, 2009. Standard test method for plastics: dynamic mechanical properties: In compression, Vol. 08.02, *Plastics (II)*. ASTM International, West Conshohocken, PA.
  - 94. D5026-06, 2009. Standard test method for plastics: dynamic mechanical properties: In tension, Vol. 08.02, *Plastics (II)*. ASTM International, West Conshohocken, PA.
  - 95. D5418-07, 2009. Standard test method for plastics: dynamic mechanical properties: In flexure (dual cantilever beam), Vol. 08.03, *Plastics (III)*. ASTM International, West Conshohocken, PA.
  - 96. D7028-07e1, 2009. Standard test method for glass transition temperature (DMA  $T_g$ ) of polymer matrix composites by dynamic mechanical analysis (DMA), Vol. 15.03, *Space Simulation; Aerospace and Aircraft; Composite Materials* ASTM International, West Conshohocken, PA.
  - 97. Gibson, R. F. 1998. Vibration test methods for dynamic mechanical property characterization, in Jenkins, C. H. ed., *Manual on Experimental Methods for Mechanical Testing of Composites*, 2nd edn., Chapter 14. Society for Experimental Mechanics, The Fairmont Press, Inc., Lilburn, GA.
  - 98. Suarez, S. A. and Gibson, R. F. 1987. Improved impulse-frequency response techniques for measurement of dynamic mechanical properties of composite materials. *Journal of Testing and Evaluation*, 15(2), 114–121.
  - 99. Dudek, T. J. 1970. Young's and shear moduli of unidirectional composites by a resonant beam method. *Journal of Composite Materials*, 4, 232–241.
  - 100. Soovere, J. and Drake, M. L., 1985. Aerospace structures technology damping design guide: Volume I—Technology review, AFWAL-TR-84-3089, Vol. I. Air Force Wright Aeronautical Labs, Wright-Patterson AFB, OH.
  - 101. Suarez, S. A., Gibson, R. F., and Deobald, L. R., 1984. Random and impulse techniques for measurement of damping in composite materials. *Experimental Techniques*, M 8(10), 19–24.
  - 102. Crane, R. M. and Gillispie, J. W., Jr. 1992. A robust testing method for determination of the damping loss factor of composites. *Journal of Composites Technology and Research*, 14(2), 70–79.
  - 103. Deobald, L. R. and Gibson, R. F. 1988. Determination of Elastic Constants of orthotropic plates by a modal analysis/Rayleigh–Ritz technique. *Journal of Sound and Vibration*, 124(2), 269–284.
  - 104. Ayorinde, E. O. and Gibson, R. F. 1993. Elastic constants of orthotropic composite materials using plate resonance frequencies, classical lamination theory and an optimized three mode Rayleigh formulation. *Composites Engineering*, 3(5), 395–407.
  - 105. Gibson, R. F., Thirumalai, R., and Pant, R. 1991. Development of an apparatus to measure dynamic modulus and damping of reinforcing fibers at elevated

- temperature. *Proceedings 1991 Spring Conference on Experimental Mechanics*, pp. 860–869. Society for Experimental Mechanics, Bethel, CT.
- 106. Pant, R. H. and Gibson, R. F. 1996. Analysis and testing of dynamic micromechanical behavior of composite materials at elevated temperatures. *Journal of Engineering Materials and Technology*, 118, 554–560.
  - 107. Mantena, R., Place, T. A., and Gibson, R. F. 1985. Characterization of matrix cracking in composite laminates by the use of damping capacity measurements. *Role of Interfaces on Material Damping*, pp. 79–93. ASM International, Materials Park, OH.
  - 108. Mantena, R., Gibson, R. F., and Place, T. A. 1986. Damping capacity measurements of degradation in advanced materials. *SAMPE Quarterly*, 17(3), 20–31.
  - 109. Gibson, R. F. 2000. Modal vibration response measurements for characterization of composite materials and structures. *Composites Science and Technology*, 60, 2769–2780.
  - 110. Gibson, R. F., Srinivasan, N., Auner, G., Huang, C., Wang, Q., and Perooly, S. 2005. Vibration analysis of MEMS sensors for detection of ultrasound. *Proceedings of 2005 Society for Experimental Mechanics Conference*, Portland, Oregon, Paper # 279 on CD, Society for Experimental Mechanics, Bethel, CT.
  - 111. Gibson, R. F., Ayorinde, E. O., and Wen, Y.-F. 2007. Vibrations of carbon nanotubes and their composites: A review. *Composites Science and Technology*, 67(1), 1–28.
  - 112. D696-08, 2009. Standard test method for coefficient of linear thermal expansion of plastics between –30°C and 30°C with a vitreous silica dilatometer. Vol. 08.01 *Plastics (I)*. ASTM International, West Conshohocken, PA.
  - 113. E228-06, 2009. Standard test method for linear thermal expansion of solid materials with a push-rod dilatometer, Vol. 14.02, *General Test Methods*. ASTM International, West Conshohocken, PA.
  - 114. E289-04, 2010. Standard test method for linear thermal expansion of rigid solid materials with interferometry, Vol. 14.02, *General Test Methods*. ASTM International, West Conshohocken, PA.
  - 115. D5229/D5229M-92, 2010. Standard test method for moisture absorption properties and equilibrium conditioning of polymer matrix composites, Vol. 15.03, *Space Simulation; Aerospace and Aircraft; Composite Materials*. ASTM International, West Conshohocken, PA.
  - 116. Shen, C. H. and Springer, G. S. 1976. Moisture absorption and desorption of composite materials. *Journal of Composite Materials*, 10, 2–20.

This page intentionally left blank

---

## *Appendix A: Matrix Concepts and Operations*

---

Stress and strain transformation relationships such as Equations 2.30, 2.31, and 2.33, stress-strain relationships such as Equations 2.26, 2.35, and 2.37, and laminate force-deformation equations such as Equation 7.44 are all examples of linear algebraic equations of the general form

$$y_1 = a_{11}x_1 + a_{12}x_2 \cdots + a_{1n}x_n$$

$$y_2 = a_{21}x_1 + a_{22}x_2 \cdots + a_{2n}x_n$$

⋮

$$y_n = a_{n1}x_1 + a_{n2}x_2 \cdots + a_{nn}x_n$$

which can be conveniently expressed in matrix form as

$$\begin{Bmatrix} y_1 \\ y_2 \\ \vdots \\ y_n \end{Bmatrix} = \begin{bmatrix} a_{11} & a_{12} & \dots & a_{1n} \\ a_{21} & a_{22} & \dots & a_{2n} \\ \vdots & \vdots & \ddots & \vdots \\ a_{n1} & a_{n2} & \dots & a_{nn} \end{bmatrix} \begin{Bmatrix} x_1 \\ x_2 \\ \vdots \\ x_n \end{Bmatrix}$$

or in compact matrix form

$$\{y\} = [a]\{x\}$$

or in index notation form

$$y_i = \sum_{j=1}^n a_{ij}x_j = a_{ij}x_j,$$

where the indices  $i, j = 1, 2, \dots, n$  and summation on the repeated index  $j$  is implied, so that the right hand side of the equation involves element-by-element multiplication of the rows of the matrix  $[a]$  into the column of  $\{x\}$ . Matrix multiplication is discussed in more detail later in this appendix. In this example, the matrices  $\{y\} = [y]$  and  $\{x\} = [x]$  are *column matrices or column vectors* having  $n$  elements and the matrix  $[a]$  is a *square matrix* of order  $(n \times n)$  with  $n$  rows and  $n$  columns. The matrix element  $a_{ij}$  is located in the  $i$ th row

and the  $j$ th column of  $[a]$ . A *row matrix or row vector* has a single row of elements of the form

$$[c] = [c_1 \quad c_2 \quad \dots \quad c_n]$$

In general, a matrix  $[a]$  of order  $(m \times n)$  is a rectangular array of numbers having  $m$  rows and  $n$  columns such as

$$[a] = \begin{bmatrix} a_{11} & a_{12} & \dots & a_{1n} \\ a_{21} & a_{22} & \dots & a_{2n} \\ \dots & \dots & \dots & \dots \\ a_{m1} & a_{m2} & \dots & a_{mn} \end{bmatrix}$$

The *transpose* of the above  $(m \times n)$  matrix  $[a]$  is generated by interchanging its rows and columns, and is indicated by  $[a]^T$  as in

$$[a]^T = \begin{bmatrix} a_{11} & a_{21} & \dots & a_{m1} \\ a_{12} & a_{22} & \dots & a_{m2} \\ \dots & \dots & \dots & \dots \\ a_{1n} & a_{2n} & \dots & a_{mn} \end{bmatrix}$$

A *diagonal matrix* is a square matrix which only has elements along the main diagonal, and all off-diagonal elements are equal to zero, as in, for example,

$$[a] = \begin{bmatrix} a_{11} & 0 & 0 \\ 0 & a_{22} & 0 \\ 0 & 0 & a_{33} \end{bmatrix}$$

A *symmetric matrix* is a square matrix in which the elements are symmetrical about the main diagonal (i.e.,  $a_{ij} = a_{ji}$ ) as in, for example

$$[a] = \begin{bmatrix} 2 & 5 & 6 \\ 5 & 3 & 7 \\ 6 & 7 & 4 \end{bmatrix}$$

A symmetric matrix is also equal to its transpose. That is  $[a] = [a]^T$ . Two matrices  $[a]$  and  $[b]$  are said to be equal if they are both of order  $m \times n$  and their elements are identical, so that  $a_{ij} = b_{ij}$  and  $[a] = [b]$ .

If two matrices are of the same order, they can be added or subtracted by adding or subtracting their corresponding elements. For example, if

$$[a] = \begin{bmatrix} 1 & 2 \\ 3 & 4 \end{bmatrix} \quad \text{and} \quad [b] = \begin{bmatrix} 5 & 6 \\ 7 & 8 \end{bmatrix}$$

then

$$[a] + [b] = \begin{bmatrix} 6 & 8 \\ 10 & 12 \end{bmatrix} \quad \text{and} \quad [a] - [b] = \begin{bmatrix} -4 & -4 \\ -4 & -4 \end{bmatrix}$$

A matrix can be multiplied by a scalar by multiplying each element in the matrix by the scalar. For example, if

$$[a] = \begin{bmatrix} 1 & 2 \\ 3 & 4 \end{bmatrix} \quad \text{and} \quad c = 3, \quad \text{then} \quad c[a] = \begin{bmatrix} 3 & 6 \\ 9 & 12 \end{bmatrix}$$

The product  $[a][b]$  of two matrices  $[a]$  and  $[b]$  is only defined when the number of columns in  $[a]$  is equal to the number of rows in  $[b]$ . For example, if

$$[a] = \begin{bmatrix} a_{11} & a_{12} \\ a_{21} & a_{22} \end{bmatrix} \quad \text{and} \quad [b] = \begin{bmatrix} b_{11} & b_{12} & b_{13} \\ b_{21} & b_{22} & b_{23} \end{bmatrix}$$

the product  $[a][b]$  is possible because  $[a]$  has two columns and  $[b]$  has two rows. In such a matrix product, it is said that  $[b]$  is *premultiplied* by  $[a]$ , or that  $[a]$  is *postmultiplied* by  $[b]$ . If matrix  $[a]$  is of order  $(m \times n)$  and matrix  $[b]$  is of order  $(n \times p)$ , the product matrix  $[c] = [a][b]$  is of order  $(m \times p)$ . In the above example,  $m = 2$ ,  $n = 2$ , and  $p = 3$ , so the product matrix is of order  $(2 \times 3)$ . The element  $c_{ij}$  of the product matrix is found by multiplying each element in the  $i$ th row of  $[a]$  by the corresponding element in the  $j$ th column of  $[b]$  and adding the results. For the above example,

$$[c] = [a][b] = \begin{bmatrix} a_{11} & a_{12} \\ a_{21} & a_{22} \end{bmatrix} \begin{bmatrix} b_{11} & b_{12} & b_{13} \\ b_{21} & b_{22} & b_{23} \end{bmatrix} = \begin{bmatrix} c_{11} & c_{12} & c_{13} \\ c_{21} & c_{22} & c_{23} \end{bmatrix}$$

where the elements of  $[c]$  are

$$c_{11} = a_{11}b_{11} + a_{12}b_{21}$$

$$c_{12} = a_{11}b_{12} + a_{12}b_{22}$$

$$c_{13} = a_{11}b_{13} + a_{12}b_{23}$$

$$c_{21} = a_{21}b_{11} + a_{22}b_{21}$$

$$c_{22} = a_{21}b_{12} + a_{22}b_{22}$$

$$c_{23} = a_{21}b_{13} + a_{22}b_{23}$$

In general, the elements  $c_{ij}$  of the product matrix  $[c]$  are found from the elements  $a_{ij}$  of  $[a]$  and the elements  $b_{ij}$  of  $[b]$  by carrying out the following summations:

$$c_{ij} = \sum_{k=1}^n a_{ik}b_{kj}$$

where  $n$  is the number of columns in matrix  $[a]$ . It is important to know that *matrix multiplication is not commutative*, since  $[a][b] \neq [b][a]$  in general. Indeed, even when the product  $[a][b]$  is possible, the product  $[b][a]$  may not be possible if the number of rows in  $[a]$  is not equal to the number of columns in  $[b]$ .

Recall that, in the first matrix equation in this section,  $\{y\} = [a]\{x\}$ , the column matrix  $\{y\}$  is expressed as the product of matrix  $[a]$  and column matrix  $\{x\}$ . On the other hand, if we want to express  $\{x\}$  in terms of  $\{y\}$ , it is not possible to divide the equation by  $[a]$ . Indeed, there is no such operation in matrix algebra. Rather, in the case of a square matrix  $[a]$ , we use a matrix operation known as *matrix inversion* to find  $[a]^{-1}$ , the inverse of square matrix  $[a]$ , then we premultiply both sides of the equation by  $[a]^{-1}$ . The product of a square matrix  $[a]$  and its inverse  $[a]^{-1}$  yields the *identity matrix*  $[I]$ , which is a diagonal matrix consisting of elements  $I_{ij} = 1.0$  when  $i = j$ , with all off-diagonal elements  $I_{ij} = 0$  when  $i \neq j$ . Thus,

$$[a][a]^{-1} = [a]^{-1}[a] = [I]$$

so that

$$[a]^{-1}\{y\} = [a]^{-1}[a]\{x\} = [I]\{x\} = \{x\}$$

In order to find the *inverse* of a square matrix  $[a]$ , it is convenient to first define the *determinant* of  $[a]$ , the *minors* of  $[a]$ , the *cofactor matrix*, and the *adjoint matrix*.

The definition of a determinant and its associated notation are best explained by the use of examples. The determinant of a matrix is denoted by replacing the square brackets around the matrix with vertical lines, and the expansion of the determinant follows the rules demonstrated below. For example, a  $(2 \times 2)$  square matrix

$$[a] = \begin{bmatrix} a_{11} & a_{12} \\ a_{21} & a_{22} \end{bmatrix}$$

has the determinant and corresponding expansion

$$D = \begin{vmatrix} a_{11} & a_{12} \\ a_{21} & a_{22} \end{vmatrix} = a_{11}a_{22} - a_{12}a_{21}$$

A  $(3 \times 3)$  square matrix

$$[a] = \begin{bmatrix} a_{11} & a_{12} & a_{13} \\ a_{21} & a_{22} & a_{23} \\ a_{31} & a_{32} & a_{33} \end{bmatrix}$$

has the determinant and corresponding expansion along the first row

$$\begin{aligned} D &= \begin{vmatrix} a_{11} & a_{12} & a_{13} \\ a_{21} & a_{22} & a_{23} \\ a_{31} & a_{32} & a_{33} \end{vmatrix} = a_{11} \begin{vmatrix} a_{22} & a_{23} \\ a_{32} & a_{33} \end{vmatrix} - a_{12} \begin{vmatrix} a_{21} & a_{23} \\ a_{31} & a_{33} \end{vmatrix} + a_{13} \begin{vmatrix} a_{21} & a_{22} \\ a_{31} & a_{32} \end{vmatrix} \\ &= a_{11}M_{11} - a_{12}M_{12} + a_{13}M_{13} \end{aligned}$$

The element  $M_{ij}$  is referred to as the minor of element  $a_{ij}$ , and is defined to be the determinant formed by deleting the  $i$ th row and the  $j$ th column from the original determinant  $D$ . The minor  $M_{ij}$  multiplied by the number  $(-1)^{i+j}$  is called the cofactor of  $a_{ij}$ , and is denoted by

$$C_{ij} = (-1)^{i+j} M_{ij}$$

The pattern that emerges from the above examples is that a  $(n \times n)$  determinant may be expanded in terms of  $n$  determinants of order  $(n-1 \times n-1)$ , each of which is, in turn, expanded in terms of  $n-1$  determinants of order  $(n-2 \times n-2)$ , and so on. In summary, the  $(n \times n)$  determinant expanded along the first row may be defined as

$$D = \sum_{j=1}^n a_{ij} C_{ij}$$

where  $i = 1$  and the summation is on the index  $j$ . The determinant can also be expanded along any row or column with the appropriate changes in subscripts. It is important to note that if the elements of the original matrix are numbers, the determinant will also be a number. The cofactor matrix  $[C]$

consists of the cofactors  $C_{ij}$  arranged in matrix form. For example, for the  $(3 \times 3)$  matrix and associated determinants,

$$[C] = \begin{bmatrix} C_{11} & C_{12} & C_{13} \\ C_{21} & C_{22} & C_{23} \\ C_{31} & C_{32} & C_{33} \end{bmatrix}$$

The adjoint matrix  $[adj\ a]$  of a square matrix  $[a]$  is defined as the transpose of the cofactor matrix  $[C]$  as

$$[adj\ a] = [C]^T$$

For example, for the  $(3 \times 3)$  matrix defined above, the adjoint matrix is

$$[adj\ a] = [C]^T = \begin{bmatrix} C_{11} & C_{21} & C_{31} \\ C_{12} & C_{22} & C_{32} \\ C_{13} & C_{23} & C_{33} \end{bmatrix}$$

The inverse  $[a]^{-1}$  of a square matrix  $[a]$  having determinant  $D$  and adjoint matrix  $[adj\ a]$  is defined as

$$[a]^{-1} = \frac{[adj\ a]}{D}$$

It is important to note that the inverse of a matrix does not exist when its determinant  $D = 0$ . Such a matrix is referred to as a *singular* matrix.

To demonstrate these operations, it is instructive to find  $[S]^{-1}$ , the inverse of the lamina compliance matrix  $[S]$  for a specially orthotropic lamina, which is the same as the lamina stiffness matrix  $[Q]$ . Recalling from Equations 2.24 and 2.25 that the compliance matrix is symmetric,  $S_{ij} = S_{ji}$  and

$$[S] = \begin{bmatrix} S_{11} & S_{12} & 0 \\ S_{12} & S_{22} & 0 \\ 0 & 0 & S_{66} \end{bmatrix}$$

Expanding the determinant of  $[S]$  along the first row,

$$\begin{aligned} D &= \begin{vmatrix} S_{11} & S_{12} & 0 \\ S_{12} & S_{22} & 0 \\ 0 & 0 & S_{66} \end{vmatrix} = S_{11} \begin{vmatrix} S_{22} & 0 \\ 0 & S_{66} \end{vmatrix} - S_{12} \begin{vmatrix} S_{12} & 0 \\ 0 & S_{66} \end{vmatrix} + 0 \begin{vmatrix} S_{12} & S_{22} \\ 0 & 0 \end{vmatrix} \\ &= S_{66} (S_{11}S_{22} - S_{12}^2) \end{aligned}$$

The minors of the  $S_{ij}$  are

$$M_{11} = \begin{vmatrix} S_{22} & 0 \\ 0 & S_{66} \end{vmatrix} = S_{22}S_{66} \quad M_{12} = \begin{vmatrix} S_{12} & 0 \\ 0 & S_{66} \end{vmatrix} = S_{12}S_{66} \quad M_{13} = \begin{vmatrix} S_{12} & S_{22} \\ 0 & 0 \end{vmatrix} = 0$$

$$M_{21} = \begin{vmatrix} S_{12} & 0 \\ 0 & S_{66} \end{vmatrix} = S_{12}S_{66} \quad M_{22} = \begin{vmatrix} S_{11} & 0 \\ 0 & S_{66} \end{vmatrix} = S_{11}S_{66} \quad M_{23} = \begin{vmatrix} S_{11} & S_{12} \\ 0 & 0 \end{vmatrix} = 0$$

$$M_{31} = \begin{vmatrix} S_{12} & 0 \\ S_{22} & 0 \end{vmatrix} = 0 \quad M_{32} = \begin{vmatrix} S_{11} & 0 \\ S_{12} & 0 \end{vmatrix} = 0 \quad M_{33} = \begin{vmatrix} S_{11} & S_{12} \\ S_{12} & S_{22} \end{vmatrix} = S_{11}S_{22} - S_{12}^2$$

Applying the equation  $C_{ij} = (-1)^{i+j}M_{ij}$ , the cofactor matrix is found to be

$$[C] = \begin{bmatrix} S_{22}S_{66} & -S_{12}S_{66} & 0 \\ -S_{12}S_{66} & S_{11}S_{66} & 0 \\ 0 & 0 & S_{11}S_{22} - S_{12}^2 \end{bmatrix}$$

Noting that the cofactor matrix is symmetric for this case, the adjoint matrix is

$$[\text{adj } S] = [C]^T = [C] = \begin{bmatrix} S_{22}S_{66} & -S_{12}S_{66} & 0 \\ -S_{12}S_{66} & S_{11}S_{66} & 0 \\ 0 & 0 & S_{11}S_{22} - S_{12}^2 \end{bmatrix}$$

The inverse of matrix  $[S]$  is then

$$[S]^{-1} = \frac{[\text{adj } S]}{D} = \begin{bmatrix} \frac{S_{22}}{S_{11}S_{22} - S_{12}^2} & -\frac{S_{12}}{S_{11}S_{22} - S_{12}^2} & 0 \\ -\frac{S_{12}}{S_{11}S_{22} - S_{12}^2} & \frac{S_{11}}{S_{11}S_{22} - S_{12}^2} & 0 \\ 0 & 0 & \frac{1}{S_{66}} \end{bmatrix} = \begin{bmatrix} Q_{11} & Q_{12} & 0 \\ Q_{12} & Q_{22} & 0 \\ 0 & 0 & Q_{66} \end{bmatrix}$$

which was previously given in Equation 2.27.

As another example of matrix inversion, recall from Chapter 2 that the 2D transformation of stresses and strains from the  $xy$ -coordinate

system to the 12-coordinate system is governed by the transformation matrix

$$[T] = \begin{bmatrix} c^2 & s^2 & 2cs \\ s^2 & c^2 & -2cs \\ -cs & cs & c^2 - s^2 \end{bmatrix}$$

and the corresponding transformation from 12 to  $xy$  coordinates is governed by the inverse matrix  $[T]^{-1}$ , where  $c = \cos \theta$  and  $s = \sin \theta$ . The determinant of  $[T]$  is

$$\begin{aligned} D &= \begin{vmatrix} c^2 & s^2 & 2cs \\ s^2 & c^2 & -2cs \\ -cs & cs & c^2 - s^2 \end{vmatrix} = c^2 \begin{vmatrix} c^2 & -2cs \\ cs & c^2 - s^2 \end{vmatrix} - s^2 \begin{vmatrix} -2cs & 2cs \\ -cs & c^2 - s^2 \end{vmatrix} + 2cs \begin{vmatrix} s^2 & c^2 \\ -cs & cs \end{vmatrix} \\ &= c^6 + 3c^4s^2 + 3c^2s^4 + s^6 = (c^2 + s^2)^3 = 1 \end{aligned}$$

After finding the minors, the cofactor matrix, and the adjoint matrix, the resulting inverse matrix is

$$[T]^{-1} = \frac{[\text{adj } T]}{D} = \begin{bmatrix} c^2 & s^2 & -2cs \\ s^2 & c^2 & 2cs \\ cs & -cs & c^2 - s^2 \end{bmatrix}$$

which was previously given in Equation 2.30.

For a numerical example, consider the inverse of the nonsymmetric matrix

$$[a] = \begin{bmatrix} 5 & 4 & 1 \\ 1 & 2 & 2 \\ 1 & 0 & 3 \end{bmatrix}$$

The determinant expanded along the first row is

$$D = \begin{vmatrix} 5 & 4 & 1 \\ 1 & 2 & 2 \\ 1 & 0 & 3 \end{vmatrix} = (5) \begin{vmatrix} 2 & 1 \\ 0 & 3 \end{vmatrix} - (4) \begin{vmatrix} 1 & 2 \\ 1 & 3 \end{vmatrix} + (1) \begin{vmatrix} 1 & 2 \\ 1 & 0 \end{vmatrix} = 30 - 4 - 2 = 24$$

The minors of the  $a_{ij}$  are

$$M_{11} = \begin{vmatrix} 2 & 2 \\ 0 & 3 \end{vmatrix} = 6, \quad M_{12} = \begin{vmatrix} 1 & 2 \\ 1 & 3 \end{vmatrix} = 1, \quad M_{13} = \begin{vmatrix} 1 & 2 \\ 1 & 0 \end{vmatrix} = -2$$

$$M_{21} = \begin{vmatrix} 4 & 1 \\ 0 & 3 \end{vmatrix} = 12, \quad M_{22} = \begin{vmatrix} 5 & 1 \\ 1 & 3 \end{vmatrix} = 14, \quad M_{23} = \begin{vmatrix} 5 & 4 \\ 1 & 0 \end{vmatrix} = -4$$

$$M_{31} = \begin{vmatrix} 4 & 1 \\ 2 & 2 \end{vmatrix} = 6, \quad M_{32} = \begin{vmatrix} 5 & 1 \\ 1 & 2 \end{vmatrix} = 9, \quad M_{33} = \begin{vmatrix} 5 & 4 \\ 1 & 2 \end{vmatrix} = 6$$

Applying the equation  $C_{ij} = (-1)^{i+j} M_{ij}$ , the cofactor matrix is found to be

$$[C] = \begin{bmatrix} 6 & -1 & -2 \\ -12 & 14 & 4 \\ 6 & -9 & 6 \end{bmatrix}$$

The adjoint matrix is

$$[\text{adj } a] = [C]^T = \begin{bmatrix} 6 & -12 & 6 \\ -1 & 14 & -9 \\ -2 & 4 & 6 \end{bmatrix}$$

and the inverse of  $[a]$  is

$$[a]^{-1} = \frac{[\text{adj } a]}{D} = \frac{1}{24} \begin{bmatrix} 6 & -12 & 6 \\ -1 & 14 & -9 \\ -2 & 4 & 6 \end{bmatrix} = \begin{bmatrix} 0.25 & -0.5 & 0.25 \\ -0.042 & 0.583 & -0.375 \\ -0.083 & 0.166 & 0.25 \end{bmatrix}$$

For large matrices, this inversion method may be cumbersome due to the large number of determinants that is required, and other methods such as Gauss–Jordan elimination may be more computationally efficient. The reader is referred to books on numerical methods for more details on such methods.

This page intentionally left blank

---

## Appendix B: Stress Equilibrium Equations

---

For a body under static loading, the stresses at every point in the body must satisfy the static equilibrium conditions,  $\Sigma \bar{F} = 0$  and  $\Sigma \bar{M} = 0$ , where  $\bar{F}$  and  $\bar{M}$  are the resultant external forces and moments, respectively, acting at the point. Consider the infinitesimal two-dimensional element of unit thickness shown in Figure B1, where normal stresses are denoted by  $\sigma$  and shear stresses are denoted by  $\tau$ .

The fact that the stresses in a body generally vary from point-to-point is accounted for by including differential changes in stresses from one face to another. For example, while the normal stress,  $\sigma_x$ , acts on the left face of the element, the variation of stresses from point-to-point is accounted for by assigning the normal stress,  $\sigma_x + (\partial\sigma_x/\partial x)dx$ , to the right face of the element (i.e., the stress,  $\sigma_x$ , changes at the rate  $\partial\sigma_x/\partial x$  over the increment  $dx$  along the  $x$  direction). Similarly, the other stress components,  $\sigma_y$  and  $\tau_{xy}$ , must vary from the left face to the right face, and from the bottom face to the top face of the element. Now, the scalar component of the moment equilibrium condition,  $\Sigma \bar{M}_O = 0$ , at the center point O can be written as

$$\begin{aligned}\sum M_O &= \tau_{xy}dy(1)\frac{dx}{2} + \left[ \left( \tau_{xy} + \frac{\partial\tau_{xy}}{\partial x}dx \right) dy(1) \right] \frac{dx}{2} - \tau_{yx}dx(1)\frac{dy}{2} \\ &\quad - \left[ \left( \tau_{yx} + \frac{\partial\tau_{yx}}{\partial y}dy \right) dx(1) \right] \frac{dy}{2} = 0\end{aligned}$$

After dividing each term by  $dx dy$ , the remaining terms are

$$\tau_{xy} + \frac{\partial\tau_{xy}}{\partial x}\frac{dx}{2} - \tau_{yx} - \frac{\partial\tau_{yx}}{\partial y}\frac{dy}{2} = 0$$

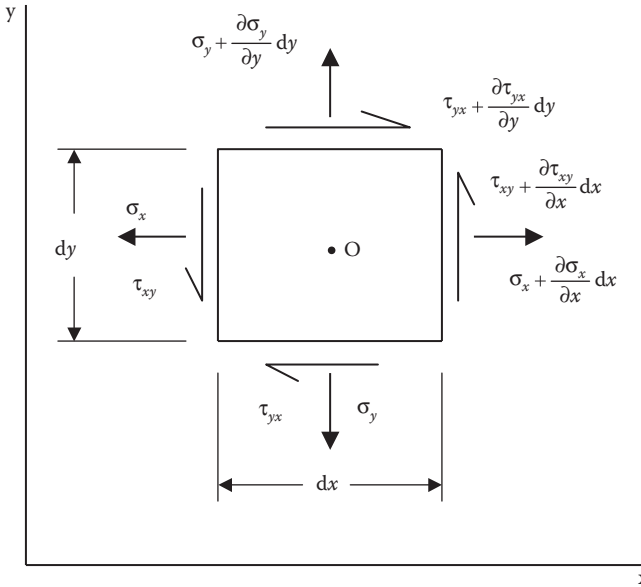
At a point in the body, where  $dx$  and  $dy$  both approach zero, the result is the proof of symmetry of the shear stresses

$$\tau_{xy} = \tau_{yx}$$

and in the general 3D case,

$$\tau_{ij} = \tau_{ji}$$

where  $i, j = 1, 2, 3$ .

**FIGURE B1**

Infinitesimal element representing stresses at a point in a body.

Thus, moment equilibrium requires that the shear stresses be symmetric. Recall that symmetry of the stresses is a key assumption leading to the development of the contracted notation in Chapter 2.

Now with regard to the force equilibrium requirement, the scalar component of the force equilibrium condition  $\sum \bar{F} = 0$  along the  $x$  direction is

$$\begin{aligned}\sum F_x &= -\sigma_x dy(1) + \left( \sigma_x + \frac{\partial \sigma_x}{\partial x} dx \right) dy(1) \\ &\quad - \tau_{yx} dx(1) + \left( \tau_{yx} + \frac{\partial \tau_{yx}}{\partial y} dy \right) dx(1) = 0\end{aligned}$$

Simplifying the above equation, writing a similar equilibrium equation  $\sum F_y = 0$ , and making use of the symmetry condition  $\tau_{xy} = \tau_{yx}$ , we get the 2D stress equilibrium equations

$$\frac{\partial \sigma_x}{\partial x} + \frac{\partial \tau_{yx}}{\partial y} = 0$$

$$\frac{\partial \tau_{xy}}{\partial x} + \frac{\partial \sigma_y}{\partial y} = 0$$

A similar derivation for a 3D infinitesimal element including the force equilibrium requirement,  $\Sigma F_z = 0$ , leads to the full set of stress equilibrium equations

$$\frac{\partial \sigma_x}{\partial x} + \frac{\partial \tau_{yx}}{\partial y} + \frac{\partial \tau_{zx}}{\partial z} = 0$$

$$\frac{\partial \tau_{xy}}{\partial x} + \frac{\partial \sigma_y}{\partial y} + \frac{\partial \tau_{zy}}{\partial z} = 0$$

$$\frac{\partial \tau_{xz}}{\partial x} + \frac{\partial \tau_{yz}}{\partial y} + \frac{\partial \sigma_z}{\partial z} = 0$$

This page intentionally left blank

---

## Appendix C: Strain–Displacement Equations

---

The relationships between strains and displacements at a point in a stressed body can be derived by considering the geometry of deformation of an infinitesimal element. Figure C1 shows the geometry of deformation for a 2D plane strain condition, where the original undeformed element is denoted by  $ABCD$  and the deformed element is denoted by  $A'B'C'D'$ .

So during deformation, point  $A$  deforms to point  $A'$ , point  $B$  deforms to point  $B'$ , and so forth. The displacement along the  $x$  direction is  $u$ , and the corresponding displacement along the  $y$  direction is  $v$ . Using the definition of normal strain (i.e., the change in length per unit length), for small deformations and strains, the normal strain along the  $x$  direction can be written as

$$\varepsilon_x = \frac{A'B' - AB}{AB} = \frac{\left[ dx + \frac{\partial u}{\partial x} dx \right] - dx}{dx} = \frac{\partial u}{\partial x}$$

Similarly, the normal strain along the  $y$  direction is given by

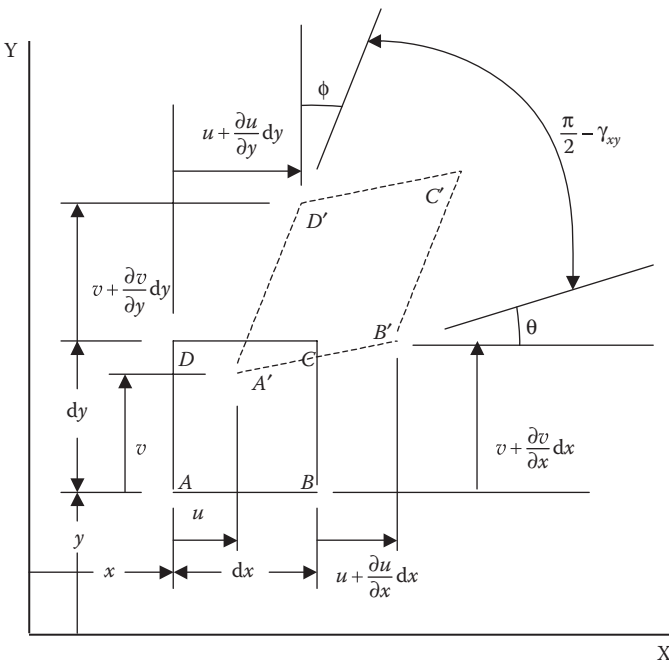
$$\varepsilon_y = \frac{A'D' - AD}{AD} = \frac{\left[ dy + \frac{\partial v}{\partial y} dy \right] - dy}{dy} = \frac{\partial v}{\partial y}$$

Referring to Figure 2.2 and the definition of engineering shear strain,  $\gamma_{xy}$ , it is seen that  $\gamma_{xy}$  is equal to the difference between original right angle  $DAB$  in the undeformed element and the angle  $D'A'B'$  in the deformed element. If we assume small deformations and a correspondingly small angle between line  $A'B'$  and line  $AB$ , and define this small angle as  $\theta$ , then we can write

$$\theta \equiv \tan \theta = \frac{\partial v / \partial x}{dx}$$

Similarly, if we define the small angle between line  $A'D'$  and line  $AD$  as  $\phi$ , we can write

$$\phi \equiv \tan \phi = \frac{\partial u / \partial y}{dy}$$

**FIGURE C1**

Geometry of deformation at a point in a stressed body.  $ABCD$  is undeformed element and  $A'B'C'D'$  is deformed element.

As a result, the shear strain is given by

$$\gamma_{xy} = \frac{\pi}{2} - \left[ \frac{\pi}{2} - \theta - \phi \right] = \theta + \phi = \frac{(\partial v / \partial x) dx}{dx} + \frac{(\partial u / \partial y) dy}{dy} = \frac{\partial v}{\partial x} + \frac{\partial u}{\partial y}$$

In summary, the 2D strain–displacement equations are

$$\epsilon_x = \frac{\partial u}{\partial x}$$

$$\epsilon_y = \frac{\partial v}{\partial y}$$

$$\gamma_{xy} = \frac{\partial v}{\partial x} + \frac{\partial u}{\partial y}$$

Similarly, the full 3D strain–displacement equations are

$$\begin{aligned}\varepsilon_x &= \frac{\partial u}{\partial x} & \gamma_{xy} &= \frac{\partial v}{\partial x} + \frac{\partial u}{\partial y} \\ \varepsilon_y &= \frac{\partial v}{\partial y} & \gamma_{yz} &= \frac{\partial w}{\partial y} + \frac{\partial v}{\partial z} \\ \varepsilon_z &= \frac{\partial w}{\partial z} & \gamma_{zx} &= \frac{\partial u}{\partial z} + \frac{\partial w}{\partial x}\end{aligned}$$

This page intentionally left blank

This page intentionally left blank

# PRINCIPLES OF COMPOSITE MATERIAL MECHANICS

*"Professor Ron Gibson provides a comprehensive textbook to cover the basic concept of anisotropy and inhomogeneity of composites as well as state-of-art issues such as dynamic behavior, fracture and testing. The many worked-out examples and homework problems are most useful for readers to understand the basic concepts to be used in practical applications of composites. Such knowledge is essential for advanced composite materials to be further applied to lightweight structures successfully."*

—Nobuo Takeda, University of Tokyo, Japan

**Principles of Composite Material Mechanics, Third Edition** presents a unique blend of classical and contemporary mechanics of composites technologies. While continuing to cover classical methods, this edition also includes frequent references to current state-of-the-art composites technology and research findings.

## New to the Third Edition

- Many new worked-out example problems, homework problems, figures, and references
- An appendix on matrix concepts and operations
- Coverage of particle composites, nanocomposites, nanoenhancement of conventional fiber composites, and hybrid multiscale composites
- Expanded coverage of finite element modeling and test methods

Easily accessible to students, this popular bestseller incorporates the most worked-out example problems and exercises of any available textbook on mechanics of composite materials. It offers a rich, comprehensive, and up-to-date foundation for students to begin their work in composite materials science and engineering.



CRC Press

Taylor & Francis Group  
an informa business

[www.crcpress.com](http://www.crcpress.com)

6000 Broken Sound Parkway, NW  
Suite 300, Boca Raton, FL 33487  
711 Third Avenue  
New York, NY 10017  
2 Park Square, Milton Park  
Abingdon, Oxon OX14 4RN, UK

K12275

ISBN: 978-1-4398-5005-3

9 781439 850053

90000